Genome engineering on a large scale *pp. 849 & 922*

Monkeyflower research begins to bloom *p. 854*

Protecting elections from social media manipulation *p. 858*

Science

$15
30 AUGUST 2019
sciencemag.org

AAAS

CALLING OUR BLUFF

AI masters multiplayer poker

pp. 864 & 885

CONTENTS

858
Measuring manipulation: Social media and elections

30 AUGUST 2019 • VOLUME 365 • ISSUE 6456

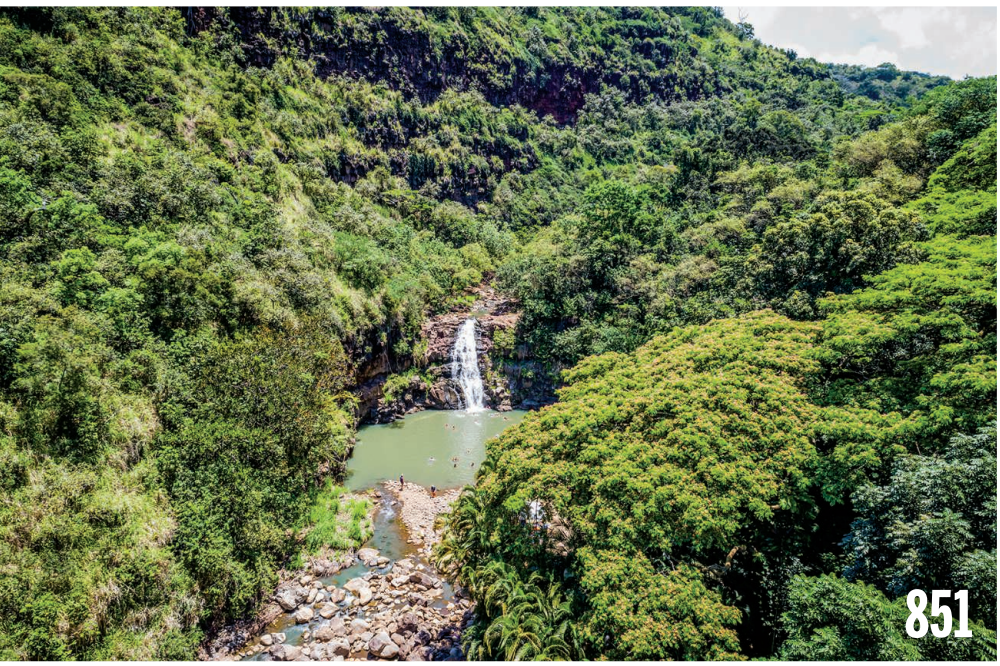

851

NEWS

IN BRIEF

844 News at a glance

IN DEPTH

847 ERADICATION GOAL SPLITS MALARIA COMMUNITY
A *Lancet* panel wants to end the disease by 2050. A WHO panel says that's not realistic *By M. Enserink*

848 ANCIENT SITE IN IDAHO IMPLIES FIRST AMERICANS CAME BY SEA
16,000-year-old occupation predates possible land route *By L. Wade*
▸ RESEARCH ARTICLE P. 891

849 MODIFIED CRISPR CUTS AND SPLICES WHOLE GENOMES
New tools bring editing to synthetic biology *By R. F. Service*
▸ REPORT P. 922

850 STUNNING SKULL SHAKES HUMAN FAMILY TREE
Researchers reveal the 4-million-year-old face of the most ancient australopithecine *By M. Price*

851 NO MICROBIOME IS AN ISLAND, SURVEY REVEALS
Sampling in Hawaiian valley shows wider environment shapes each organism's microbial community
By E. Pennisi
▸ PODCAST

852 WORLD'S OLDEST IMPACT CRATER DATED IN AUSTRALIAN OUTBACK
The 2.2-billion-year-old Yarrabubba impact came at the end of a planetwide deep freeze
By E. Hand

853 AMAZON FIRES CLEARLY LINKED TO DEFORESTATION, SCIENTISTS SAY
Brazilian government deflects blame for rise in fire activity
By H. Escobar

FEATURES

854 THE ALLURE OF MONKEYFLOWERS
A tough, diverse, colorful weed used in evolutionary studies is becoming a key model for plant biology
By E. Pennisi

INSIGHTS

POLICY FORUM

858 PROTECTING ELECTIONS FROM SOCIAL MEDIA MANIPULATION
Rigorous causal analysis could help harden democracy against future attacks *By S. Aral and D. Eckles*

PERSPECTIVES

862 THE IMMUNOLOGICAL CODE OF PREGNANCY
Maternal immune cells interact with the placenta and influence pregnancy complications
By F. Colucci

864 AI SURPASSES HUMANS AT SIX-PLAYER POKER
Self-learning Pluribus beats five humans in Texas hold'em showdown
By A. Blair and A. Saffidine
▸ RESEARCH ARTICLE P. 885

865 HOW HUMANS CHANGED THE FACE OF EARTH
Archaeological evidence shows that anthropogenic changes began earlier and spread faster than previously estimated *By N. Roberts*
▸ RESEARCH ARTICLE P. 897

866 THE MITSUNOBU REACTION, REIMAGINED
Catalytic nucleophilic substitution of alcohols makes organic synthesis greener *By L. Longwitz and T. Werner*
▸ REPORT P. 910

868 BACTERIA SEND MESSAGES TO COLONIZE PLANT ROOTS
Bacteria-derived RNA fragments target host plant genes to promote root colonization
By P. Baldrich and B. C. Meyers
▸ REPORT P. 919

869 HOW DO GENES AFFECT SAME-SEX BEHAVIOR?
Genetic loci linked with same-sex sexual behavior cannot predict orientation of individuals
By M. C. Mills
▸ RESEARCH ARTICLE P. 882

CREDITS: (FROM TOP) BROBEL DESIGN; WAIMEA VALLEY BOTANICAL GARDENS; YAOWU YUAN

Published by AAAS

BOOKS *ET AL.*

871 LESSONS IN BLACK EXCELLENCE
Data and success stories reveal how to ensure that African American students thrive in the STEM classroom
By D. Riley

872 CHANGING CONCEPTION
A thought-provoking volume traces the medical, social, and political histories of in vitro fertilization
By I. G. Cohen

LETTERS

873 MAKING OLIVE OIL SUSTAINABLE
By F. Moreira et al.

873 WILL DNA BARCODING MEET TAXONOMIC NEEDS?
By H. T. Pinheiro et al.

874 TROPHY HUNTING BANS IMPERIL BIODIVERSITY
By A. Dickman et al.

RESEARCH

IN BRIEF

878 From *Science* and other journals

REVIEW

881 NEURODEVELOPMENT
Cell migration and axon guidance at the border between central and peripheral nervous system
T. A. C. S. Suter and A. Jaworski
REVIEW SUMMARY; FOR FULL TEXT:
dx.doi.org/10.1126/science.aaw8231

RESEARCH ARTICLES

882 HUMAN GENETICS
Large-scale GWAS reveals insights into the genetic architecture of same-sex sexual behavior *A. Ganna* et al.
RESEARCH ARTICLE SUMMARY; FOR FULL TEXT:
dx.doi.org/10.1126/science.aat7693
▸ PERSPECTIVE P. 869

883 IMMUNOLOGY
Identification of a T follicular helper cell subset that drives anaphylactic IgE *U. Gowthaman* et al.
RESEARCH ARTICLE SUMMARY; FOR FULL TEXT:
dx.doi.org/10.1126/science.aaw6433

884 MALARIA
Validation of the protein kinase *Pf*CLK3 as a multistage cross-species malarial drug target *M. M. Alam* et al.
RESEARCH ARTICLE SUMMARY; FOR FULL TEXT:
dx.doi.org/10.1126/science.aau1682

885 COMPUTER SCIENCE
Superhuman AI for multiplayer poker
N. Brown and T. Sandholm
▸ PERSPECTIVE P. 864

891 ARCHAEOLOGY
Late Upper Paleolithic occupation at Cooper's Ferry, Idaho, USA, ~16,000 years ago *L. G. Davis* et al.
▸ NEWS STORY P. 848

897 ARCHAEOLOGY
Archaeological assessment reveals Earth's early transformation through land use *ArchaeoGLOBE Project*
▸ PERSPECTIVE P. 865; PODCAST

REPORTS

903 MANTLE CHEMISTRY
Deep magma ocean formation set the oxidation state of Earth's mantle
K. Armstrong et al.

906 SUPERCONDUCTIVITY
Dynamical charge density fluctuations pervading the phase diagram of a Cu-based high-T_c superconductor
R. Arpaia et al.

910 ORGANIC CHEMISTRY
Redox-neutral organocatalytic Mitsunobu reactions *R. H. Beddoe* et al.
▸ PERSPECTIVE P. 866

914 MAGNETISM
Skyrmion lattice with a giant topological Hall effect in a frustrated triangular-lattice magnet
T. Kurumaji et al.

919 PLANT SCIENCE
Rhizobial tRNA-derived small RNAs are signal molecules regulating plant nodulation *B. Ren* et al.
▸ PERSPECTIVE P. 868

922 SYNTHETIC BIOLOGY
Programmed chromosome fission and fusion enable precise large-scale genome rearrangement and assembly
K. Wang et al.
▸ NEWS STORY P. 849

926 ASTROCHRONOLOGY
Solar System chaos and the Paleocene–Eocene boundary age constrained by geology and astronomy
R. E. Zeebe and L. J. Lourens

929 SIGNAL TRANSDUCTION
Membrane-associated periodic skeleton is a signaling platform for RTK transactivation in neurons
R. Zhou et al.

DEPARTMENTS

843 EDITORIAL
Evidence lights the way
By Adam Gamoran

946 WORKING LIFE
Between two worlds
By Luis Alexis Rodríguez-Cruz

ON THE COVER

Many real-world settings involve interacting parties with private information. As the prototypical such setting, poker has been a grand challenge in game theory and artificial intelligence (AI) for seven decades. A new poker AI, Pluribus, has reached the key remaining milestone: superhuman performance when there are multiple opponents at the table. Prior superhuman game-playing milestones—even in perfect-information games—have been limited to two-player games. See pages 864 and 885. *Illustration: Jason Solo/The Jacky Winter Group*

Science Staff 842
AAAS News & Notes 875
New Products 935
Science Careers 936

SCIENCE (ISSN 0036-8075) is published weekly on Friday, except last week in December, by the American Association for the Advancement of Science, 1200 New York Avenue, NW, Washington, DC 20005. Periodicals mail postage (publication No. 484460) paid at Washington, DC, and additional mailing offices. Copyright © 2019 by the American Association for the Advancement of Science. The title SCIENCE is a registered trademark of the AAAS. Domestic individual membership, including subscription (12 months): $165 ($74 allocated to subscription). Domestic institutional subscription (51 issues): $1971; Foreign postage extra: Mexico, Caribbean (surface mail) $55; other countries (air assist delivery): $98. First class, airmail, student, and emeritus rates on request. Canadian rates with GST available upon request, GST #125488122. Publications Mail Agreement Number 1069624. **Printed in the U.S.A.**
Change of address: Allow 4 weeks, giving old and new addresses and 8-digit account number. **Postmaster:** Send change of address to AAAS, P.O. Box 96178, Washington, DC 20090–6178. **Single-copy sales:** $15 each plus shipping and handling; bulk rate on request. **Authorization to reproduce** material for internal or personal use under circumstances not falling within the fair use provisions of the Copyright Act can be obtained through the Copyright Clearance Center (CCC), www.copyright.com. The identification code for *Science* is 0036-8075. *Science* is indexed in the *Reader's Guide to Periodical Literature* and in several specialized indexes.

PHOTO: FUNKYFOOD LONDON/PAUL WILLIAMS/ALAMY STOCK PHOTO

Published by AAAS

Science AAAS

Editor-in-Chief Jeremy Berg, jberg@aaas.org

Executive Editor Monica M. Bradford

Editors, Research Valda Vinson, Jake S. Yeston **Editor, Insights** Lisa D. Chong

DEPUTY EDITORS Julia Fahrenkamp-Uppenbrink (UK), Stella M. Hurtley (UK), Phillip D. Szuromi, Sacha Vignieri **SR. EDITORIAL FELLOW** Andrew M. Sugden (UK) **SR. EDITORS** Gemma Alderton (UK), Caroline Ash (UK), Brent Grocholski, Pamela J. Hines, Paula A. Kiberstis, Marc S. Lavine (Canada), Steve Mao, Ian S. Osborne (UK), Beverly A. Purnell, L. Bryan Ray, H. Jesse Smith, Jelena Stajic, Peter Stern (UK), Valerie B. Thompson, Brad Wible, Laura M. Zahn **ASSOCIATE EDITORS** Michael A. Funk, Priscilla N. Kelly, Tage S. Rai, Seth Thomas Scanlon (UK), Keith T. Smith (UK), Yury V. Suleymanov **LETTERS EDITOR** Jennifer Sills **LEAD CONTENT PRODUCTION EDITORS** Harry Jach, Lauren Kmec **CONTENT PRODUCTION EDITORS** Amelia Beyna, Jeffrey E. Cook, Chris Filiatreau, Nida Masiulis, Suzanne M. White **SR. EDITORIAL COORDINATORS** Carolyn Kyle, Beverly Shields **EDITORIAL COORDINATORS** Aneera Dobbins, Joi S. Granger, Jeffrey Hearn, Lisa Johnson, Maryrose Madrid, Ope Martins, Shannon McMahon, Jerry Richardson, Alana Warnke, Alice Whaley (UK), Anita Wynn **PUBLICATIONS ASSISTANTS** Jeremy Dow, Alexander Kief, Ronmel Navas, Hilary Stewart (UK), Brian White **EXECUTIVE ASSISTANT** Jessica Slater **ASI DIRECTOR, OPERATIONS** Janet Clements (UK) **ASI SR. OFFICE ADMINISTRATOR** Jessica Waldock (UK)

News Editor Tim Appenzeller

NEWS MANAGING EDITOR John Travis **INTERNATIONAL EDITOR** Martin Enserink **DEPUTY NEWS EDITORS** Elizabeth Culotta, Lila Guterman, David Grimm, Eric Hand (Europe), David Malakoff **SR. CORRESPONDENTS** Daniel Clery (UK), Jon Cohen, Jeffrey Mervis, Elizabeth Pennisi **ASSOCIATE EDITORS** Jeffrey Brainard, Catherine Matacic **NEWS REPORTERS** Adrian Cho, Jennifer Couzin-Frankel, Jocelyn Kaiser, Kelly Servick, Robert F. Service, Erik Stokstad (Cambridge, UK), Paul Voosen, Meredith Wadman **INTERN** Alex Fox **CONTRIBUTING CORRESPONDENTS** Warren Cornwall, Ann Gibbons, Mara Hvistendahl, Sam Kean, Eli Kintisch, Kai Kupferschmidt (Berlin), Andrew Lawler, Mitch Leslie, Eliot Marshall, Virginia Morell, Dennis Normile (Shanghai), Elisabeth Pain (Careers), Charles Piller, Michael Price, Tania Rabesandratana (Barcelona), Emily Underwood, Gretchen Vogel (Berlin), Lizzie Wade (Mexico City) **CAREERS** Donisha Adams, Rachel Bernstein (Editor), Katie Langin **COPY EDITORS** Julia Cole (Senior Copy Editor), Cyra Master (Copy Chief) **ADMINISTRATIVE SUPPORT** Meagan Weiland

Creative Director Beth Rakouskas

DESIGN MANAGING EDITOR Marcy Atarod **GRAPHICS MANAGING EDITOR** Alberto Cuadra **PHOTOGRAPHY MANAGING EDITOR** William Douthitt **WEB CONTENT STRATEGY MANAGER** Kara Estelle-Powers **SENIOR DESIGNER** Chrystal Smith **DESIGNER** Christina Aycock **PHOTO EDITOR** Emily Petersen **GRAPHICS EDITOR** Nirja Desai **SENIOR SCIENTIFIC ILLUSTRATORS** Valerie Altounian, Chris Bickel **SCIENTIFIC ILLUSTRATOR** Alice Kitterman **SENIOR GRAPHICS SPECIALISTS** Holly Bishop, Nathalie Cary

Interim Chief Executive Officer and Executive Publisher Alan Leshner

Publisher, Science Family of Journals Bill Moran

DIRECTOR, BUSINESS SYSTEMS AND FINANCIAL ANALYSIS Randy Yi **DIRECTOR, BUSINESS OPERATIONS & ANALYSIS** Eric Knott **DIRECTOR OF ANALYTICS** Enrique Gonzales **MANAGER, BUSINESS OPERATIONS** Jessica Tierney **SENIOR BUSINESS ANALYST** Cory Lipman, Meron Kebede **FINANCIAL ANALYST** Alexander Lee **ADVERTISING SYSTEM ADMINISTRATOR** Tina Burks **SENIOR SALES COORDINATOR** Shirley Young **DIGITAL/PRINT STRATEGY MANAGER** Jason Hillman **QUALITY TECHNICAL MANAGER** Marcus Spiegler **ASSISTANT MANAGER DIGITAL/PRINT** Rebecca Doshi **SENIOR CONTENT SPECIALISTS** Steve Forrester, Jacob Hedrick, Antoinette Hodal, Lori Murphy **DIGITAL PRODUCTION MANAGER** Lisa Stanford **CONTENT SPECIALIST** Kimberley Oster **DIGITAL AD-OPS SPECIALIST** Patrick Gerrits **ADVERTISING PRODUCTION OPERATIONS MANAGER** Deborah Tompkins **DESIGNER, CUSTOM PUBLISHING** Jeremy Huntsinger **SR. TRAFFIC ASSOCIATE** Christine Hall **SPECIAL PROJECTS ASSOCIATE** Sarah Dhere

ASSOCIATE DIRECTOR, BUSINESS DEVELOPMENT Justin Sawyers **GLOBAL MARKETING MANAGER** Allison Pritchard **DIGITAL MARKETING MANAGER** Aimee Aponte **MARKETING MANAGER** Shawana Arnold **MARKETING ASSOCIATES** Tori Velasquez, Mike Romano, Ashley Hylton **SENIOR DESIGNER** Kim Huynh **TRADE SHOW AND MEETINGS ASSOCIATE** Andrew Clamp

DIRECTOR AND SENIOR EDITOR, CUSTOM PUBLISHING Sean Sanders **ASSISTANT EDITOR, CUSTOM PUBLISHING** Jackie Oberst

DIRECTOR, BUSINESS STRATEGY AND PORTFOLIO MANAGEMENT Sarah Whalen **ASSOCIATE DIRECTOR, PRODUCT MANAGMENT** Kris Bishop **ASSOCIATE DIRECTOR, PRODUCT DEVELOPMENT AND SPJ** Hannah Heckner **SR. PRODUCT ASSOCIATE** Robert Koepke **DIGITAL PRODUCT STRATEGIST** Michael Hardesty **SPJ ASSOCIATE** Samantha Bruno Fuller

DIRECTOR, INSTITUTIONAL LICENSING Iquo Edim **ASSOCIATE DIRECTOR, RESEARCH & DEVELOPMENT** Elisabeth Leonard **SENIOR INSTITUTIONAL LICENSING MANAGER** Ryan Rexroth **INSTITUTIONAL LICENSING MANAGERS** Marco Castellan, Christos Skoutas **MANAGER, SYSTEMS AND OPERATIONS** Brian Holiahn **MANAGER, AGENT RELATIONS & CUSTOMER SUCCESS** Judy Lillibridge **SENIOR OPERATIONS ANALYST** Lana Guz **FULFILLMENT COORDINATOR** Melody Stringer

DIRECTOR, GLOBAL SALES Tracy Holmes **ASSOCIATE DIRECTOR, ADVERTISING SALES, US** Laurie Faraday **US EAST COAST AND MID WEST SALES** Glen Cox **US WEST COAST SALES** Lynne Stickrod **US SALES MANAGER, SCIENCE CAREERS** Claudia Paulsen-Young **US SALES REP, SCIENCE CAREERS** Tracy Anderson **ASSOCIATE DIRECTOR, ROW** Roger Goncalves **SALES REP, ROW** Sarah Lelarge **SALES ADMIN ASSISTANT, ROW** Bryony Cousins **DIRECTOR OF GLOBAL COLLABORATION AND ACADEMIC PUBLISHING RELATIONS, ASIA** Xiaoying Chu **ASSOCIATE DIRECTOR, INTERNATIONAL COLLABORATION** Grace Yao **SALES MANAGER** Danny Zhao **PROJECT MANAGER** Kilo Lan **ASCA CORPORATION, JAPAN** Kaoru Sasaki (Tokyo), Miyuki Tani (Osaka) **COLLABORATION/CUSTOM PUBLICATIONS/JAPAN** Adarsh Sandhu

DIRECTOR, COPYRIGHT, LICENSING AND SPECIAL PROJECTS Emilie David **RIGHTS AND LICENSING COORDINATOR** Jessica Adams **RIGHTS AND PERMISSIONS ASSOCIATE** Elizabeth Sandler **CONTRACTS AND LICENSING ASSOCIATE** Lili Catlett

---

MAIN HEADQUARTERS
Science/AAAS
1200 New York Ave. NW
Washington, DC 20005

SCIENCE INTERNATIONAL
Clarendon House
Clarendon Road
Cambridge, CB2 8FH, UK

SCIENCE CHINA
Room 1004, Culture Square
No. 59 Zhongguancun St.
Haidian District, Beijing, 100872

SCIENCE JAPAN
ASCA Corporation
Sibaura TY Bldg. 4F, 1-14-5
Shibaura Minato-ku
Tokyo, 108-0073 Japan

EDITORIAL
science_editors@aaas.org

NEWS
science_news@aaas.org

INFORMATION FOR AUTHORS
sciencemag.org/authors/science-information-authors

REPRINTS AND PERMISSIONS
sciencemag.org/help/reprints-and-permissions

MEDIA CONTACTS
scipak@aaas.org

MULTIMEDIA CONTACTS
SciencePodcast@aaas.org
ScienceVideo@aaas.org

INSTITUTIONAL SALES AND SITE LICENSES
sciencemag.org/librarian

PRODUCT ADVERTISING & CUSTOM PUBLISHING
advertising.sciencemag.org/products-services
science_advertising@aaas.org

CLASSIFIED ADVERTISING
advertising.sciencemag.org/science-careers
advertise@sciencecareers.org

JOB POSTING CUSTOMER SERVICE
employers.sciencecareers.org
support@sciencecareers.org

MEMBERSHIP AND INDIVIDUAL SUBSCRIPTIONS
sciencemag.org/subscriptions

MEMBER BENEFITS
aaas.org/membercentral

AAAS BOARD OF DIRECTORS
CHAIR Margaret A. Hamburg
PRESIDENT Steven Chu
PRESIDENT-ELECT Claire M. Fraser
TREASURER Carolyn N. Ainslie
INTERIM CHIEF EXECUTIVE OFFICER Alan Leshner
BOARD Cynthia M. Beall, May R. Berenbaum, Rosina M. Bierbaum, Ann Bostrom, Stephen P. A. Fodor, S. James Gates, Jr., Laura H. Greene, Kaye Husbands Fealing, Maria Klawe, Robert B. Millard, William D. Provine

Science serves as a forum for discussion of important issues related to the advancement of science by publishing material on which a consensus has been reached as well as including the presentation of minority or conflicting points of view. Accordingly, all articles published in *Science*—including editorials, news and comment, and book reviews—are signed and reflect the individual views of the authors and not official points of view adopted by AAAS or the institutions with which the authors are affiliated.

BOARD OF REVIEWING EDITORS (Statistics board members indicated with **(S)**)

Adriano Aguzzi, *U. Hospital Zürich*
Takuzo Aida, *U. of Tokyo*
Leslie Aiello, *Wenner-Gren Foundation*
Judith Allen, *U. of Manchester*
Sebastian Amigorena, *Institut Curie*
James Analytis, *U. of California, Berkeley*
Paola Arlotta, *Harvard U.*
Johan Auwerx, *EPFL*
David Awschalom, *U. of Chicago*
Clare Baker, *U. of Cambridge*
Nenad Ban, *ETH Zürich*
Franz Bauer, *Pontificia Universidad Católica de Chile*
Ray H. Baughman, *U. of Texas at Dallas*
Peter Bearman, *Columbia U.*
Carlo Beenakker, *Leiden U.*
Yasmine Belkaid, *NIAID, NIH*
Philip Benfey, *Duke U.*
Gabriele Bergers, *VIB*
Bradley Bernstein, *Mass. General Hospital*
Alessandra Biffi, *Harvard Med. School*
Peer Bork, *EMBL*
Chris Bowler, *École Normale Supérieure*
Ian Boyd, *U. of St. Andrews*
Emily Brodsky, *U. of California, Santa Cruz*
Ron Brookmeyer, *U. of California, Los Angeles* **(S)**
Christian Büchel, *UKE Hamburg*
Dennis Burton, *Scripps Research*
Carter Tribley Butts, *U. of California, Irvine*
György Buzsáki, *New York U. School of Med.*
Blanche Capel, *Duke U.*
Annmarie Carlton, *U. of California, Irvine*
Lars-Erik Cederman, *ETH Zürich*
Nick Chater, *U. of Warwick*
Zhijian Chen, *UT Southwestern Med. Ctr.*
Ib Chorkendorff, *Denmark TU*
James J. Collins, *MIT*
Robert Cook-Deegan, *Arizona State U.*
Alan Cowman, *Walter & Eliza Hall Inst.*
Carolyn Coyne, *U. of Pittsburgh*
Roberta Croce, *VU Amsterdam*
Jeff L. Dangl, *U. of North Carolina*
Tom Daniel, *U. of Washington*
Chiara Daraio, *Caltech*
Nicolas Dauphas, *U. of Chicago*
Frans de Waal, *Emory U.*
Claude Desplan, *New York U.*
Sandra Díaz, *Universidad Nacional de Córdoba*
Hong Ding, *Inst. of Physics, CAS*
Jennifer Dionne, *Stanford U.*
Dennis Discher, *U. of Penn.*
Jennifer A. Doudna, *U. of California, Berkeley*
Bruce Dunn, *U. of California, Los Angeles*
William Dunphy, *Caltech*
Christopher Dye, *U. of Oxford*
Todd Ehlers, *U. of Tübingen*
Jennifer Elisseeff, *Johns Hopkins U.*
Tim Elston, *U. of North Carolina*
Andrea Encalada, *U. San Francisco de Quito*
Nader Engheta, *U. of Penn.*
Karen Ersche, *U. of Cambridge*
Barry Everitt, *U. of Cambridge*
Vanessa Ezenwa, *U. of Georgia*
Michael Feuer, *The George Washington U.*
Toren Finkel, *U. of Pittsburgh Med. Ctr.*
Gwenn Flowers, *Simon Fraser U.*
Peter Fratzl, *Max Planck Inst. Potsdam*
Elaine Fuchs, *Rockefeller U.*
Eileen Furlong, *EMBL*
Jay Gallagher, *U. of Wisconsin*
Susan Gelman, *U. of Michigan*
Daniel Geschwind, *U. of California, Los Angeles*
Karl-Heinz Glassmeier, *TU Braunschweig*
Ramon Gonzalez, *U. of South Florida*
Elizabeth Grove, *U. of Chicago*
Nicolas Gruber, *ETH Zürich*
Kip Guy, *U. of Kentucky College of Pharmacy*
Taekjip Ha, *Johns Hopkins U.*
Christian Haass, *Ludwig Maximilians U.*
Sharon Hammes-Schiffer, *Yale U.*
Wolf-Dietrich Hardt, *ETH Zürich*
Louise Harra, *U. College London*
Jian He, *Clemson U.*
Carl-Philipp Heisenberg, *IST Austria*
Ykä Helariutta, *U. of Cambridge*
Janet G. Hering, *Eawag*
Hans Hilgenkamp, *U. of Twente*
Kai-Uwe Hinrichs, *U. of Bremen*
David Hodell, *U. of Cambridge*
Lora Hooper, *UT Southwestern Med. Ctr.*
Fred Hughson, *Princeton U.*
Randall Hulet, *Rice U.*
Auke Ijspeert, *EPFL*
Akiko Iwasaki, *Yale U.*
Stephen Jackson, *USGS and U. of Arizona*
Kai Johnsson, *EPFL*
Peter Jonas, *IST Austria*
Matt Kaeberlein, *U. of Washington*
William Kaelin Jr., *Dana-Farber Cancer Inst.*
Daniel Kammen, *U. of California, Berkeley*
V. Narry Kim, *Seoul Nat. U.*
Robert Kingston, *Harvard Med. School*
Nancy Knowlton, *Smithsonian Institution*
Etienne Koechlin, *École Normale Supérieure*
Alexander Kolodkin, *Johns Hopkins U.*
Thomas Langer, *U. of Cologne*
Mitchell A. Lazar, *U. of Penn.*
Ottoline Leyser, *U. of Cambridge*
Wendell Lim, *U. of California, San Francisco*
Marcia C. Linn, *U. of California, Berkeley*
Jianguo Liu, *Michigan State U.*
Luis Liz-Marzán, *CIC biomaGUNE*
Jonathan Losos, *Washington U. in St. Louis*
Ke Lu, *Chinese Acad. of Sciences*
Christian Lüscher, *U. of Geneva*
Fabienne Mackay, *U. of Melbourne*
Anne Magurran, *U. of St. Andrews*
Oscar Marín, *King's College London*
Charles Marshall, *U. of California, Berkeley*
Christopher Marx, *U. of Idaho*
Geraldine Masson, *CNRS*
C. Robertson McClung, *Dartmouth College*
Rodrigo Medellín, *U. of Mexico*
Graham Medley, *London School of Hygiene & Tropical Med.*
Jane Memmott, *U. of Bristol*
Edward Miguel, *U. of California, Berkeley*
Tom Misteli, *NCI, NIH*
Yasushi Miyashita, *U. of Tokyo*
Alison Motsinger-Reif, *NC State U.* **(S)**
Daniel Nettle, *Newcastle U.*
Daniel Neumark, *U. of California, Berkeley*
Beatriz Noheda, *U. of Groningen*
Helga Nowotny, *Austrian Council*
Rachel O'Reilly, *U. of Warwick*
Harry Orr, *U. of Minnesota*
Pilar Ossorio, *U. of Wisconsin*
Andrew Oswald, *U. of Warwick*
Isabella Pagano, *Istituto Nazionale di Astrofisica*
Margaret Palmer, *U. of Maryland*
Elizabeth Levy Paluck, *Princeton U.*
Jane Parker, *Max Planck Inst. Cologne*
Giovanni Parmigiani, *Dana-Farber Cancer Inst.* **(S)**
Samuel Pfaff, *Salk Inst. for Biological Studies*
Julie Pfeiffer, *UT Southwestern Med. Ctr.*
Matthieu Piel, *Institut Curie*
Kathrin Plath, *U. of California, Los Angeles*
Martin Plenio, *Ulm U.*
Elvira Poloczanska, *Alfred-Wegener-Inst.*
Julia Pongratz, *Ludwig Maximilians U.*
Philippe Poulin, *CNRS*
Jonathan Pritchard, *Stanford U.*
David Randall, *Colorado State U.*
Félix A. Rey, *Institut Pasteur*
Trevor Robbins, *U. of Cambridge*
Amy Rosenzweig, *Northwestern U.*
Mike Ryan, *U. of Texas at Austin*
Mitinori Saitou, *Kyoto U.*
Shimon Sakaguchi, *Osaka U.*
Miquel Salmeron, *Lawrence Berkeley Nat. Lab*
Nitin Samarth, *Penn. State U.*
Jürgen Sandkühler, *Med. U. of Vienna*
Alexander Schier, *Harvard U.*
Wolfram Schlenker, *Columbia U.*
Susannah Scott, *U. of California, Santa Barbara*
Rebecca Sear, *London School of Hygiene & Tropical Med.*
Vladimir Shalaev, *Purdue U.*
Jie Shan, *Cornell U.*
Beth Shapiro, *U. of California, Santa Cruz*
Jay Shendure, *U. of Washington*
Brian Shoichet, *U. of California, San Francisco*
Robert Siliciano, *Johns Hopkins U. School of Med.*
Lucia Sivilotti, *U. College London*
Alison Smith, *John Innes Centre*
Richard Smith, *U. of North Carolina* **(S)**
Mark Smyth, *QIMR Berghofer*
Pam Soltis, *U. of Florida*
John Speakman, *U. of Aberdeen*
Tara Spires-Jones, *U. of Edinburgh*
Allan C. Spradling, *Carnegie Institution for Science*
V. S. Subrahmanian, *U. of Maryland*
Ira Tabas, *Columbia U.*
Sarah Teichmann, *U. of Cambridge*
Rocio Titiunik, *Princeton U.*
Shubha Tole, *Tata Inst. of Fundamental Research*
Wim van der Putten, *Netherlands Inst. of Ecology*
Reinhilde Veugelers, *KU Leuven*
Bert Vogelstein, *Johns Hopkins U.*
Kathleen Vohs, *U. of Minnesota*
David Wallach, *Weizmann Inst. of Science*
Jane-Ling Wang, *U. of California, Davis* **(S)**
David Waxman, *Fudan U.*
Jonathan Weissman, *U. of California, San Francisco*
Chris Wikle, *U. of Missouri* **(S)**
Terrie Williams, *U. of California, Santa Cruz*
Ian A. Wilson, *Scripps Research* **(S)**
Yu Xie, *Princeton U.*
Jan Zaanen, *Leiden U.*
Kenneth Zaret, *U. of Penn. School of Med.*
Jonathan Zehr, *U. of California, Santa Cruz*
Maria Zuber, *MIT*

Published by AAAS

EDITORIAL

Evidence lights the way

Adam Gamoran
is president of the William T. Grant Foundation, New York, NY, USA.
agamoran@wtgrantfdn.org

These are dark times for science and public policy in the United States. In June, it was revealed that the White House suppressed the congressional testimony of a State Department scientist on the implications of climate change for national security—just the latest example of evidence undercut by ideology. Yet, despite this gloomy backdrop, there are glimmers of scientific evidence used to improve policy and practice. In July, a bipartisan group formed the Congressional What Works Caucus to encourage federal investments in evidence-based programs and policies. Since January, the Foundations for Evidence-Based Policymaking Act has pushed federal agencies to develop learning agendas and appoint chief data officers to make better use of government data. What will it take to keep the light of evidence burning and ensure that the best science informs important decisions of our time?

"What will it take to...ensure that the best science informs important decisions of our time?"

The current administration has taken steps to undermine the integrity of federal statistics agencies, eliminate or marginalize science units in federal agencies, slim down or drop expert advisory boards, remove scientific information from federal websites, and ban agency employees from using the term "scientific evidence" in budget requests. In June, President Trump directed federal agencies to disband at least one-third of their expert advisory committees by 30 September.

Nevertheless, there are signs that data, evidence, and rigorous evaluation persist. In June, the nonprofit Bipartisan Policy Center published Evidence Works, a compendium of 20 cases of evidence use at the federal, state, and local levels in the United States, with many reflecting action since 2017. One case is the Family First Prevention Services Act of 2018. Guided by years of research, this federal law has created funding opportunities to encourage states to provide services to meet families' mental health, substance use, and parenting needs to help keep children at home instead of sending them to foster care. Ultimately, Family First will provide better lives for thousands of children and families.

State and local leaders are also seeking to use evidence, often in collaboration with researchers. By investing in research-informed programs, for example, the New Hampshire Charitable Foundation has made progress on early childhood education, family and youth supports, substance abuse prevention, and education and career pathways. Likewise, the National Network of Education Research-Practice Partnerships is fortifying the capacity of state education agencies and school districts to collaborate with researchers to identify ways to improve academic and socio-emotional outcomes for students. Findings from such collaborations are often consequential in policy and practice because the questions examined derive from the needs of the local districts and state agencies involved. In one well-known example, high school graduation rates in Chicago increased by more than a third after the district implemented an early warning system (to identify students at risk of dropping out) informed by findings from a research–practice partnership between district officials and university researchers.

So how can research, science, and evidence remain integral to public policy? Public and private funders must redouble their commitments to support scientific inquiry, as in 2018 when Congress increased the budgets of several science agencies after the administration had proposed cuts. Philanthropy must also fund evidence-based solutions and the science behind them. The Community Foundation Opportunity Network, for instance, which unites local philanthropies committed to equity, is mobilizing leaders to adopt evidence-based approaches to narrow opportunity gaps for young people in their communities. More researchers should collaborate with policy-makers to develop research agendas, to increase the chances that research findings will be used. One example of the promise of such partnerships comes from the United Kingdom, where government-funded Applied Research Collaborations have helped narrow the divide between research production and the use of research evidence in health care policy and practice.

It's clear that contributions from government, philanthropy, and research organizations are keeping evidence aglow, even in dark times. Let's make sure that such efforts continue to light the path ahead.

–Adam Gamoran

PHOTO: MONICA FELIX

10.1126/science.aaz2301

Published by AAAS

Edited by **Jeffrey Brainard**

A giraffe calf at Maasai Mara National Reserve in Kenya represents a new generation.

CONSERVATION

Giraffe trade to be tracked

Nations this week agreed to monitor trade in giraffes and their body parts to help conserve the species, now deemed vulnerable to extinction. From 1985 to 2015, the wild giraffe population shrank by about 40% to approximately 68,000 adults. The declines were especially sharp in eastern and Central Africa where giraffes' savanna and forest habitat has been turned into farms and the animals are poached for meat; most trophy hunting of giraffes happens in southern Africa, where populations have been increasing. Environmental groups welcomed the new monitoring requirement, enacted by the Convention on International Trade in Endangered Species of Wild Fauna and Flora at its meeting in Geneva, Switzerland, as data are sparse. The only figures on trade in giraffe parts show that about 40,000—including hides, carved bones, and hunting trophies such as mounted heads—were brought into the United States from 2006 to 2015.

Huge study offers DNA counseling

BIOMEDICINE | The U.S. National Institutes of Health's All of Us study, which will explore genetic links to illnesses, on 21 August selected a company to offer counseling to the planned 1 million participants. Study volunteers can request their DNA test results for ancestry and genetic risks of certain diseases and drug reactions—an unusual step for a research study. The counseling company, Color, of Burlingame, California, will counsel participants by phone to help them understand how the findings could affect their health care; counselors will provide in-depth sessions for the estimated 3% of study subjects with genes that significantly raise the risk of cancer and other diseases.

Germany seals open-access deal

PUBLISHING | A consortium of more than 700 German research institutions and libraries last week announced an agreement with publisher Springer Nature that gives member institutions online access to most of its scholarly journals while making all papers authored by their researchers in those journals immediately free to read. The 3-year agreement with the consortium, called Project DEAL, is the largest national deal of this kind to date. But it doesn't include *Nature* or its sister journals, which now have no open-access option for authors. The "publish and read" agreement gives member institutions full access to content in 2500 other Springer Nature journals, including archives back to 1997. Charges are based not on subscriptions, but on a fee per research article, paid by the consortium institutions, for the estimated 13,000 papers published annually in those journals by scholars based in Germany. Project DEAL reached a similar agreement with publisher Wiley in February but remains at an impasse in its attempt to reach one with Elsevier, the world's largest scientific publisher.

'Polypill' yields positive results

CLINICAL RESEARCH | A large study of taking a daily "polypill" shows it slashes the rate of heart attacks by half. However, experts are divided on the ethics of distributing the pills prophylactically to healthy people over age 50 without a prescription, as some advocates suggest. Taking a polypill—a capsule containing aspirin, two blood-pressure drugs, and a cholesterol-lowering statin—drastically

PHOTO: EASTCOTT MOMATIUK/GETTY IMAGES

Published by AAAS

reduced cardiovascular illnesses in nearly 7000 Iranians, says a study in the 24 August issue of *The Lancet*. These diseases are the world's top killer. Polypills could benefit the many patients worldwide who have trouble sticking to a regimen of multiple heart pills. But some experts argue that physicians should first screen patients for risk factors for these diseases because the medications in polypills can cause side effects.

United States targets Huawei R&D

NATIONAL SECURITY | The U.S. Department of Commerce last week barred several research centers run by Chinese communications powerhouse Huawei Technologies from receiving U.S. products and software. The ban, prompted by national security concerns, will not take effect for 90 days. At least five China-based research centers as well as facilities in Milan, Italy, and Martlesham, U.K., will be affected, but how the ban might hinder Huawei's research activities is unclear. Huawei has 14 research centers worldwide and is investing 120 billion Chinese yuan ($16.8 billion) this year in R&D in telecommunications, networking technologies, electronics, artificial intelligence, and other fields, putting it among the world's top corporate R&D spenders.

More Ebola vaccine ordered

INFECTIOUS DISEASE | The U.S. Department of Health and Human Services announced last week it would give pharmaceutical company Merck $23 million to manufacture more doses of its experimental Ebola vaccine to help control the continuing outbreak in the Democratic Republic of the Congo. Public health officials worry the supply might run low if the outbreak worsens or spreads to other areas.

Chile eyes harassment rules

#METOO | Chile's Senate approved a bill on 20 August that requires state-supported colleges and universities to create comprehensive protocols to respond to sexual harassment or risk losing accreditation and funding. A 2017 study found that at least 39% of Chilean students and 41% of academics reported encountering unsolicited attention of a sexual nature. Chile's laws protect employees of universities and other research institutes against sexual harassment, but students, postdoctoral scholars, and some others are left to fall through the cracks, says biochemist Adriana Bastías, president of the Chilean Network of Women Researchers. The bill will now move to Chile's Chamber of Deputies. Its supporters hope it will become law as early as next year.

MIT apologizes for Epstein gifts

PHILANTHROPY | A history of ties to Jeffrey Epstein, the jailed sex offender and hedge fund manager who killed himself earlier this month, caused upheaval at the Massachusetts Institute of Technology (MIT) in Cambridge and its interdisciplinary Media Lab last week. MIT President Rafael Reif said the school would donate $800,000— the amount Epstein is believed to have given the lab and MIT engineering professor Seth Lloyd—to help victims of sex abuse. Reif also offered a "profound and humble apology" for enhancing Epstein's reputation. Lloyd, who visited Epstein in prison after his 2008 conviction, asked Epstein's victims to forgive him for "protecting a powerful abuser." Media Lab Director Joi Ito also apologized, and Ethan Zuckerman, head of the lab's center for civic

MARINE BIOLOGY

Caribbean coral bred in lab

Scientists for the first time have induced Caribbean coral to spawn in a laboratory, which could help conserve near-extinct species and pave the way for large-scale coral production in labs to replenish damaged reefs. The procreation, which started on 17 August at the Florida Aquarium's research center in Apollo Beach, capped a 2-year effort to trick pillar coral (*Dendrogyra cylindrus*) into releasing a blizzard of eggs and sperm. Pillar coral has dwindled to just 115 colonies in the Florida Keys, partly because of stony coral tissue loss disease, which is ravaging Caribbean reefs. Over months, researchers used lighting and heating systems to mimic changes in the sun, moon, and water temperature that in the wild act as coral spawning triggers. The success with the Atlantic Ocean species comes 3 years after researchers learned to trigger spawning by some captive Pacific Ocean corals.

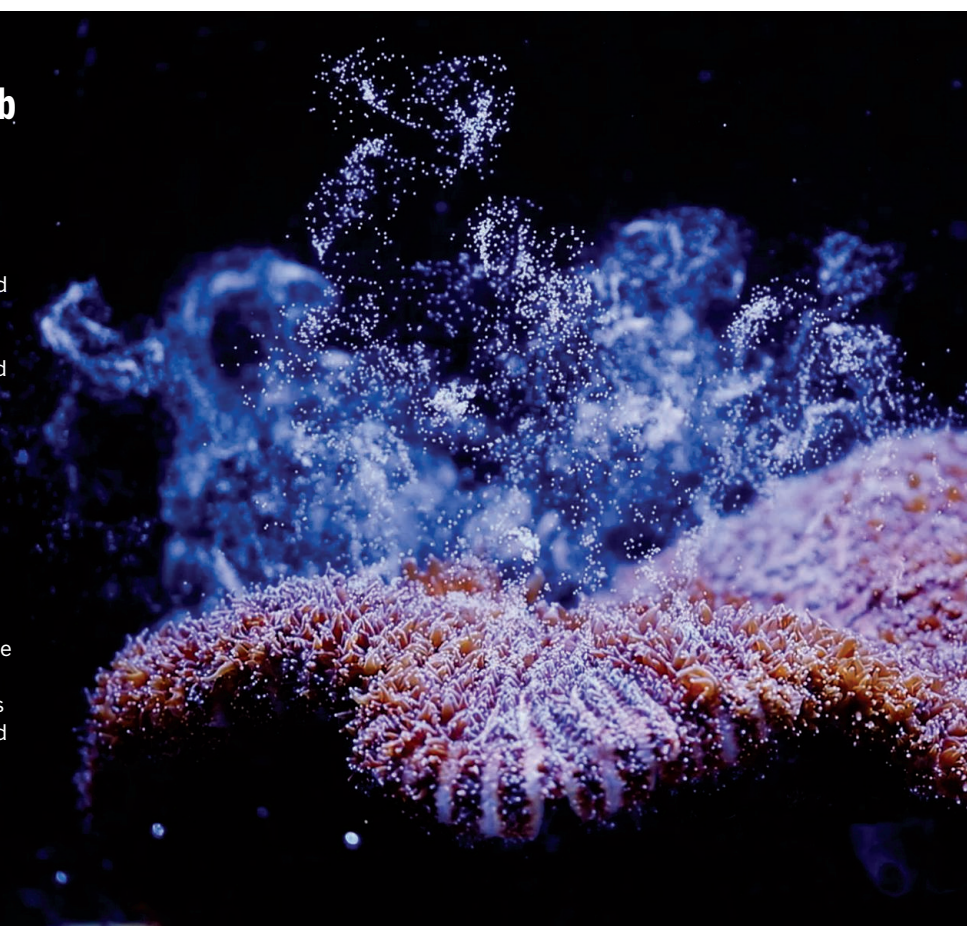

Eggs rise in the water column from a pillar coral in a lab at the Florida Aquarium.

PHOTO: © THE FLORIDA AQUARIUM

Published by AAAS

media, announced plans to leave because "it's hard to do that work with a straight face in a place that violated its own values so clearly in working with Epstein."

NSF fellowships show skew

GRADUATE STUDIES | Recipients at a handful of elite universities again reaped a large portion of the U.S. National Science Foundation's prestigious fellowships for early career graduate students for this year, a *Science* analysis indicates. Just 10 institutions garnered 31% of the 2052 fellowships, and 14% went to the top three—the University of California, Berkeley; the Massachusetts Institute of Technology in Cambridge; and Stanford University in Palo Alto, California. The reason for the pattern, which has persisted for many years, is unclear; top institutions contacted by *Science* declined to say how many of their students applied. But the universities' financial resources appear to be one factor in helping applicants prepare. The fellowships are open to U.S. citizens who have completed no more than 12 months of a graduate program in science, technology, engineering, or math. Fellows are paid at the high end of what a standard research assistantship or teaching assistantship stipend would net. They also receive access to international research collaborations and career development internships.

Solar power could replace hydro

ENERGY | Solar panels could produce just as much electricity as the 2603 hydroelectric dams in the contiguous United States, but use much less land, says a study published online this week in *Nature Sustainability*. If the dams were removed and solar arrays installed on just 13% of the area that had been submerged under reservoirs, the solar cells could match the dams' annual generation of 275,000 gigawatt hours. Many of the dams are aging and will require maintenance or removal before long; replacing them with solar would bring environmental benefits such as allowing fish to swim upstream, say study authors John Waldman, a biologist at Queens College, part of the City University of New York, and colleagues. Among the obstacles: Until engineers develop better batteries and systems for storing intermittent solar power, hydropower is a more dependable electricity supply. And dams provide other benefits including flood control, water supply, and recreation.

Alarm over Indonesia capital plan

ENVIRONMENT | Indonesian President Joko Widodo worried conservationists this week by announcing a $33 billion plan to move the country's capital to the island of Borneo from Jakarta, which endures air pollution and crowding and is one of the world's fastest-sinking cities, making it prone to floods. The shift, if approved by Parliament, is to be completed by 2024; it could accelerate development on Borneo that is harming its endangered orangutans and native tropical forests, environmental groups say. It's unclear how much the government would spend to help Jakarta, home to more than 10 million people and the country's economic capital, to solve its environmental problems.

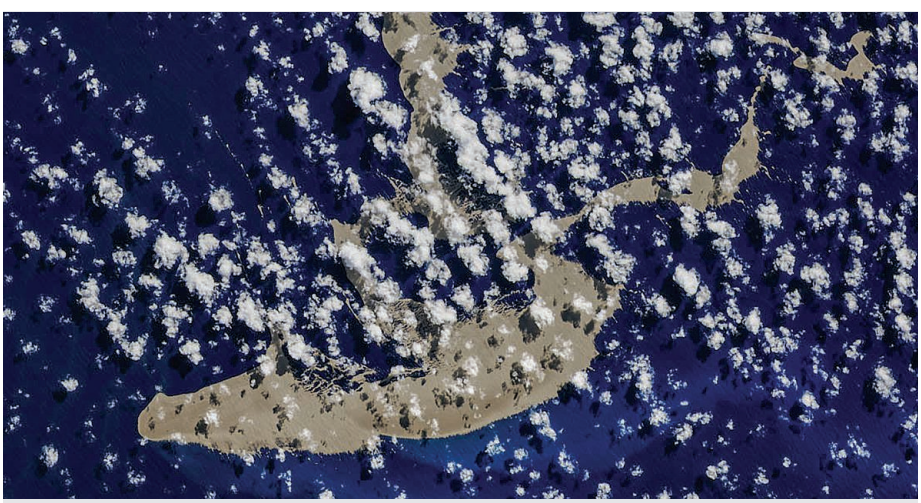

PHOTO: NASA EARTH OBSERVATORY/JOSHUA STEVENS/U.S. GEOLOGICAL SURVEY

OCEAN SCIENCE

Subsea eruption creates pumice 'raft' in Pacific

Sailors and scientists alike were surprised this month to discover a "raft" of pumice larger than Manhattan floating in the Pacific Ocean, about 50 kilometers northwest of Vava'u in Tonga. The suspected source: the eruption of an unnamed undersea volcano, just 40 meters down. The pumice—formed from lava that cooled and hardened—floats because it is porous. NASA's Earth Observatory said the agency's Landsat 8 satellite recorded the raft on 13 August (above). Two days later, the husband-and-wife crew of the catamaran *ROAM* reported on Facebook that they had sailed into it, surrounded as far as they could see by "rocks from marble to basketball size such that water was not visible." An undersea eruption in the same location was reported in 2001, according to the Smithsonian Institution's Global Volcanism Program. Pumice rafts can drift for weeks or years before breaking up, and they play an important role in long-distance dispersal of marine organisms, scientists say.

AWARDS

Science wins journalism prizes

Members of our news team were honored for articles published in 2018:

Ann Gibbons won the David Perlman Award for Excellence in Science Journalism-News from the American Geophysical Union for her 16 November 2018 story about the worst year to be alive: 536.

Paul Voosen received the Award for Distinguished Science Journalism in the Atmospheric and Related Sciences from the American Meteorological Society for his 27 July 2018 feature about the creation of a new climate model.

Jon Cohen and **Jennifer Couzin-Frankel** were given a Health Care Print Journalism Award by the National Institute for Health Care Management for a 13 June 2018 article about why Florida is struggling to control HIV.

Sanjay Kumar won a Red Ink Award special mention from the Mumbai Press Club for a 4 April 2018 article about threats to fossil sites in India.

SCIENCEMAG.ORG/NEWS
Read more news from *Science* online.

Published by AAAS

A woman watches over a child with malaria in a hospital in Jacqueville, Ivory Coast, in April.

PHOTO: SIA KAMBOU/AFP/GETTY IMAGES

GLOBAL HEALTH

Eradication goal splits malaria community

A *Lancet* panel wants to end the disease by 2050. A WHO panel says that's not realistic

By **Martin Enserink**

In 2007, philanthropists Bill and Melinda Gates stunned many scientists when, at a meeting in Seattle, Washington, they called for the worldwide eradication of malaria. Many felt malaria was so entrenched—there were almost 250 million cases annually—and so difficult to fight that any talk of eradication was premature. But it's hard to ignore two of the world's most generous funders, and both the World Health Organization (WHO) and researchers embraced the idea. Soon, a flurry of working groups, scientific papers, and public health strategies were laying the groundwork.

But the consensus is dissolving. Last week, WHO dropped a minor bombshell of its own when it released the summary of a report that says malaria eradication isn't feasible in the foreseeable future. And it argues that setting any deadline will undermine disease control efforts, as it did when WHO set a similar goal 64 years ago. "We must not set the world up for another failed malaria eradication effort that could derail attempts to achieve our vision for decades," says the report from WHO's Strategic Advisory Group on Malaria Eradication (SAGme).

"It's a watershed moment," says Willem Takken, a retired medical entomologist from Wageningen University & Research in the Netherlands. "Basically WHO now admits we won't get rid of malaria anytime soon."

A second high-caliber group, however, disagrees. On 9 September, the *Lancet* Commission on Malaria Eradication, a group of 26 academics from around the globe, will publish a study recommending that the world set a 2050 target for eradication, sources tell *Science*. The commission will also offer a timeline and concrete steps for reaching the goal. A deadline will help raise money and keep the field energized, says Arjen Dondorp, head of the Mahidol Oxford Tropical Medicine Research Unit in Bangkok and a member of the *Lancet* group: "It's mainly about keeping up the spirit."

The *Lancet* commission plans a high-profile announcement at WHO headquarters in Geneva, Switzerland. That prompted a preemptive strike by SAGme. It published its summary and held a press conference on 22 August, even though the full report is months away, "partly because of the noise that may be generated around" the *Lancet* report, says Pedro Alonso, director of WHO's Global Malaria Programme. "It is making sure that the community doesn't go down a single line of thinking."

The debate is about more than just the usefulness of bold goals in global health. The focus on eradication has skewed scientists' and funders' priorities, says Brian Greenwood, a malariologist at the London School of Hygiene & Tropical Medicine. For instance, much energy has been spent in countries on the fringes of the malaria map—such as Sri Lanka, Bhutan, and El Salvador—where eliminating the parasite was relatively easy. Such "early wins" boosted morale but diverted attention from African countries where thousands of children were dying of malaria, Greenwood says. He recalls seeing 16 children with cerebral malaria in a hospital in Sierra Leone and thinking that talk of eradication was premature.

WHO first adopted the goal of malaria eradication in 1955, after the insecticide DDT made killing mosquitoes easy and cheap. The effort saw major successes, until insecticide resistance emerged. The campaign made little headway in Africa, however, and in 1969 the World Health Assembly moved to effectively end it by shifting responsibility for malaria control to national governments, while still retaining eradication as a long-term goal. That caused interest in the disease to plummet and the parasite to resurge.

When the Bill & Melinda Gates Foundation

Published by AAAS

revived the E word in 2007, it didn't mention a deadline. Bill Gates later said it would take "multiple decades" and acknowledged it was "dangerous" to set unattainable goals (*Science*, 7 December 2007, p. 1544). Still, Margaret Chan, then WHO's director, pledged the agency's support, and the eradication goal began to shape policy and research.

But Alonso thought the feasibility of eradication needed a closer look, and in 2016 he convened SAGme and asked Marcel Tanner, a former director of the Swiss Tropical and Public Health Institute in Basel, to lead the panel. Its report, which partly relied on modeling by a team at the University of Oxford in the United Kingdom, says eradication is still a long-term goal worth pursuing, and that time is on humanity's side: Megatrends such as socio-economic development, urbanization, and climate change—which can influence transmission by changing temperature, humidity, and rainfall—will all help drive down malaria incidence. But it concludes that even in the rosiest of scenarios there will still be 11 million cases in 2050.

The *Lancet* panel used models from the same Oxford group and will concur with many of SAGme's findings, Dondorp says. But he and others argue that the Gates Foundation's embrace of eradication reinvigorated malaria research, attracted money, and boosted control efforts. That helped trigger a decadelong decline in cases, from an estimated 247 million in 2006 to 214 million in 2015. (The decline has flattened since then, however, and a WHO plan to reduce incidence by 40% between 2015 and 2020 is badly off track.)

Whether the *Lancet* commission's 2050 target could deliver a similar boost is unclear; 2050 is so distant that "it's not really a target at all," says William Moss, a malaria researcher at the Johns Hopkins Bloomberg School of Public Health in Baltimore, Maryland. He notes that other Gates-backed eradication campaigns, such as those for polio and Guinea worm, have repeatedly missed deadlines. "What you end up with," he says, "is donor fatigue, public fatigue, and loss of political will and commitment."

How Bill and Melinda Gates feel about the rift is unclear. Philip Welkhoff, director for malaria at the Gates Foundation in Seattle, says he can't speak for the couple, but he is a member of SAGme and supports its conclusions. "My personal take is that the most effective goals are the ones that are in a 10- to 12-year time frame," he says. "That's where the energy should go." At the same time, he says, "Our leadership and myself are completely committed to carrying through all the way to eradication. We are in it for the long haul." ■

Ancient people apparently followed rivers more than 500 kilometers inland to Cooper's Ferry in western Idaho.

ARCHAEOLOGY

Ancient site in Idaho implies first Americans came by sea

16,000-year-old occupation predates possible land route

By **Lizzie Wade**

About 16,000 years ago, on the banks of a river in western Idaho, people kindled fires, shaped stone blades and spearpoints, and butchered large mammals. All were routine activities in prehistory, but their legacy today is anything but. The charcoal and bone left at that ancient site, now called Cooper's Ferry, are some 16,000 years old—the oldest radiocarbon-dated record of human presence in North America, according to work reported on p. 891.

The findings do more than add a few centuries to the timeline of people in the Americas. They also shore up a new picture of how humans first arrived, by showing that people lived at Cooper's Ferry more than 1 millennium before melting glaciers opened an ice-free corridor through Canada about 14,800 years ago. That implies the first people in the Americas must have come by sea, moving rapidly down the Pacific coast and up rivers. The dates from Cooper's Ferry "fit really nicely with the [coastal] model that we're increasingly getting a consensus on from genetics and archaeology," says Jennifer Raff, a geneticist at the University of Kansas in Lawrence who studies the peopling of the Americas.

The Clovis people, big game hunters who made characteristic stone tools dated to about 13,000 years ago, were once thought to have been the first to reach the Americas, presumably through the ice-free corridor. But a handful of earlier sites have persuaded many researchers that the coastal route is more likely. Archaeologists have questioned the signs of occupation at some putative pre-Clovis sites, but the stone tools and dating at Cooper's Ferry pass the test with flying colors, says David Meltzer, an archaeologist at Southern Methodist University in Dallas, Texas. "It's pre-Clovis. I'm convinced."

A 6-centimeter blade is among the oldest at an Idaho site.

Over 10 years of excavations, the Cooper's Ferry team uncovered dozens of stone spear points, blades, and multipurpose tools called bifaces, as well as hundreds of pieces of debris from their manufacture. Although the site is near the Salmon River, most of the ancient bones belonged to mammals, including extinct horses. The team also found a hearth and pits dug by the site's ancient residents, containing stone artifacts and animal bones.

Radiocarbon dates on the charcoal and bone are as old as 15,500 years. In North America, few tree ring records can precisely calibrate such early radiocarbon dates, but a state-of-the-art probabilistic model placed the start of the occupation at between 16,560 and 15,280 years. "I may not think it goes back to 16,000 years ago, but I surely can be-

PHOTOS: (TOP TO BOTTOM) LOREN DAVIS; L. DAVIS *ET AL.*, *SCIENCE*, VOL. 365, 891 (2019)

Published by AAAS

lieve it goes back 15,000 years," says Michael Waters, an archaeologist at Texas A&M University in College Station.

The only rival to Cooper's Ferry as the oldest site in North America is the Gault site in Texas. Researchers dated that site to about 16,000 years ago by optical luminescence, a method with larger error bars than radiocarbon dating.

It's easy to see how seafaring people might have reached Cooper's Ferry, says Loren Davis, an archaeologist at Oregon State University in Corvallis who led the excavations. Although the site is more than 500 kilometers from the coast, the Salmon, Snake, and Columbia rivers link it to the sea. "As people come down the coast, the first left-hand turn to get south of the ice comes up the Columbia River Basin," Davis says. "It's the first off-ramp."

The area is now federal land but was long occupied by the Nez Perce Tribe, or the Niimíipuu. They know Cooper's Ferry as Nipéhe, an ancient village founded by a young couple after a flood destroyed their previous home, says Nakia Williamson, the tribe's director of cultural resources. "Our stories already tell us how long we've been here. ... This [study] only reaffirms that," Williamson says. He hopes the excavations—in which Nez Perce archaeologists and interns participated—will help others recognize the deep ties the Nez Perce have to their ancestral lands. "This is not just something that happened 16,000 years ago. It's something that is still important to us today," he says.

Cooper's Ferry may also offer a glimpse of the tools carried by the first arrivals to the Americas. Many of the spearpoints found there belong to the western stemmed point tradition, smaller—about the size of a pinkie—and lighter than the hefty Clovis points. Such tools have been found at early sites from British Columbia to Peru, and as far inland as Texas. Similar points are known from Japan from about 16,000 to 13,000 years ago, Davis says. He and others argue that western stemmed points are emerging as the best markers of the first people to arrive in the Americas, and that they carried the tradition with them from Asia.

But Meltzer isn't convinced the western stemmed tradition conclusively predates Clovis or represents a coastal connection around the Pacific Rim. There are plenty of sites in Siberia in Russia without the technology, he says, and the complete points at Cooper's Ferry are almost the same age as Clovis. (The site's oldest tools are blades, bifaces, and fragments of points, fashioned with the same methods used to make western stemmed points.) Just as archaeology puts one debate about stone tools in the Americas to rest, it could be gearing up for the next one. ■

SYNTHETIC BIOLOGY

Modified CRISPR cuts and splices whole genomes

New tools bring editing to synthetic biology

By **Robert F. Service**

Imagine a word processor that allowed you to change letters or words but balked when you tried to cut or rearrange whole paragraphs. Biologists have faced such constraints for decades. They could add or disable genes in a cell or even—with the genome-editing technology CRISPR—make precise changes within genes. Those capabilities have led to recombinant DNA technology, genetically modified organisms, and gene therapies. But a long-sought goal remained out of reach: manipulating much larger chunks of chromosomes in *Escherichia coli*, the workhorse bacterium. Now, researchers report they've adapted CRISPR and combined it with other tools to cut and splice large genome fragments with ease.

"This new paper is incredibly exciting and a huge step forward for synthetic biology," says Anne Meyer, a synthetic biologist at the University of Rochester in New York who was not involved in the paper on p. 922. The technique will enable synthetic biologists to take on "grand challenges," she says, such as "writing of information to DNA and storing it in a bacterial genome or creating new hybrid bacterial species that can carry out novel [metabolic reactions] for biochemistry or materials production."

> ***"This new paper is incredibly exciting and a huge step forward for synthetic biology."***
>
> **Anne Meyer**, University of Rochester

The tried and true tools of genetic engineering simply can't handle long stretches of DNA. Restriction enzymes, the standard tool for cutting DNA, can snip chunks of genetic material and join the ends to form small circular segments that can be moved out of one cell and into another. (Stretches of linear DNA don't survive long before other enzymes, called endonucleases, destroy them.) But the circles can accommodate at most a couple of hundred thousand bases, and synthetic biologists often want to move large segments of chromosomes containing multiple genes, which can be millions of bases long or more. "You can't get very large pieces of DNA in and out of cells," says Jason Chin, a synthetic biologist at the Medical Research Council (MRC) Laboratory of Molecular Biology in Cambridge, U.K.

What's more, those cutting and pasting tools can't be targeted precisely, and they leave unwanted DNA at the splicing sites—the equivalent of genetic scars. The errors build up as more changes are made. Another problem is that traditional editing tools can't faithfully glue large segments together. These issues can be a deal-breaker when biologists want to make hundreds or thousands of changes to an organism's genome, says Chang Liu, a synthetic biologist at the University of California, Irvine.

Now, Chin and his MRC colleagues report they have solved these problems. First, the team adapted CRISPR to precisely excise long stretches of DNA without leaving scars. They then altered another well-known tool, an enzyme called lambda red recombinase, so it could glue the ends of the original chromosome—minus the removed portion—back together, as well as fuse the ends of the removed portion. Both circular strands of DNA are protected from endonucleases. The technique can create different circular chromosome pairs in other cells, and researchers can then swap chromosomes at will, eventually inserting whatever chunk they choose into the original genome. "Now, I can make a series of changes in one segment and then another and combine them together. That's a big deal," Liu says.

The new tools will bolster industrial biotechnology by making it easier to vary the levels of proteins that microbes make, Liu and others say. They also promise an easy way to rewrite bacterial genomes wholesale, Meyer adds. One such project aims to alter genomes so they can code not just for proteins' normal 20 amino acids, but also for large numbers of nonnatural amino acids throughout the genome. That could lead to synthetic life forms capable of producing molecules far beyond the reach of natural organisms. ■

Corrected 30 August 2019. See full text.

Published by AAAS

PALEOANTHROPOLOGY

Stunning skull shakes human family tree

Researchers reveal the 4-million-year-old face of the most ancient australopithecine

By **Michael Price**

For months, herder Ali Bereino had been trying to get a job working for a team of fossil hunters in northeastern Ethiopia. The Afar man hung around, watching and learning. One day in February 2016, Bereino dug a burrow to keep his baby goats safe from hyenas. He noticed teeth protruding from the hard-packed sand and pulled out a jawbone, which he brought to the team's leader, Ethiopian paleoanthropologist Yohannes Haile-Selassie of the Cleveland Museum of Natural History in Ohio. Shoveling aside nearly half a meter of old goat droppings and sieving through sediment, the team unearthed the nearly complete skull of an enigmatic human ancestor, the oldest member of the genus that eventually led to our own.

After 3 years of analysis, researchers have dated the fossil to 3.8 million years old and identified it as *Australopithecus anamensis*, a hominin long thought to be the direct predecessor of the famed "Lucy" species, *A. afarensis*. The new fossil could reshuffle that ancient relationship, the authors argue this week in two papers in *Nature*.

Researchers hail the skull as one of the most significant hominin discoveries in decades. "It's a spectacular find," says Carol Ward, an evolutionary anatomist at the University of Missouri School of Medicine in Columbia. "A number of teams—mine included—have been looking for an australopith skull like this. … This is the specimen we've been waiting for."

Still, not everyone is convinced it clarifies the relations of the australopithecines, a genus of upright apes that lived between 4.2 million and 2 million years ago throughout eastern and southern Africa.

A. anamensis was first identified in 1995, mostly on the basis of 4-million-year-old teeth and jaws from Kenya. Given the dates, plus several telltale anatomical similarities, most researchers concluded that *A. anamensis* gradually transitioned into and was replaced by *A. afarensis*, which lived from about 3.7 million to 3 million years ago.

The new Ethiopian specimen, named MRD after Miro Dora, the site where it was found, was probably a male with a brain size of about 370 cubic centimeters, about that of a chimpanzee. He had jutting cheekbones, elongated canine teeth and oval-shaped earholes—all features that strongly suggest membership in *A. anamensis* rather than the bigger-brained, flatter-faced *A. afarensis*, Haile-Selassie says. The team dated the skull using the radioactive decay of isotopes of argon in the surrounding sediments.

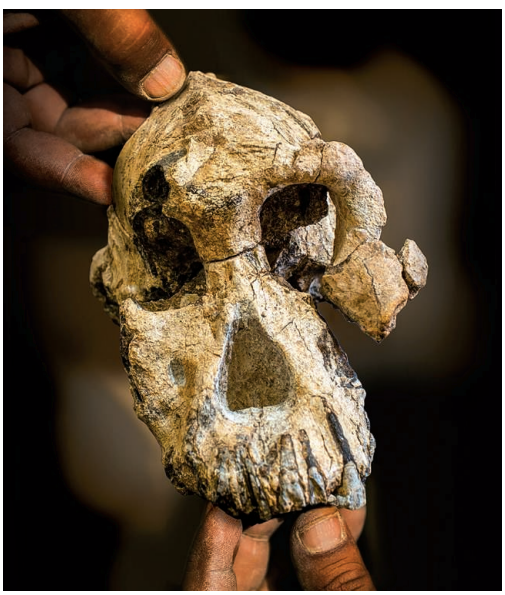

A skull (top) shows that *Australopithecus anamensis* (artist's reconstruction, bottom) had a small brain and a protruding face.

PHOTOS: (TOP TO BOTTOM) JENNIFER TAYLOR/CLEVELAND MUSEUM OF NATURAL HISTORY/DALE MORI AND LIZ RUSSELL; JOHN GURCHE AND MATT CROW/CLEVELAND MUSEUM OF NATURAL HISTORY

Fred Spoor, a paleoanthropologist at the Natural History Museum in London, says features such as MRD's projecting cheekbones and primitive earholes resemble those of later hominins, including South Africa's *A. africanus* and Kenya's *Kenyanthropus platyops*. The similarities, he says, may make some researchers wonder whether *A. anamensis*—and not *A. afarensis*, as thought—was the ancestor of those later hominins.

MRD's anatomy also helps pin down the identity of a puzzling 3.9-million-year-old forehead bone found in Ethiopia in 1981; Haile-Selassie says the comparison suggests the skull fragment belonged to *A. afarensis*. If he's correct, Lucy's species would predate the new *anamensis* skull. Haile-Selassie concludes that the two species overlapped for about 100,000 years. The team still thinks *A. afarensis* descends from *A. anamensis*, but suggests Lucy's species branched off *anamensis*, rather than simply replacing it.

Ward and William Kimbel, a paleoanthropologist at Arizona State University in Tempe, agree that the new skull belongs to *A. anamensis*, but both say it will take more fossils to convince them that two distinct species of australopithecines roamed the Afar region at the same time. "That issue rests on the comparison of the new specimen with the single frontal" bone, which is the only *A. afarensis* specimen suspected of such antiquity, Kimbel says. "It's difficult to make a strong argument because we have only the two specimens."

In a statement, Tim White, a paleoanthropologist at the University of California, Berkeley, who served as Haile-Selassie's doctoral adviser years ago, praised the discovery but says the studies' evolutionary implications are "a bridge too far." He thinks individual variation alone can account for the differences between the two specimens, and that the idea that *afarensis* replaced *anamensis* still makes sense.

Regardless of how things shake out for hominin taxonomy, the finding proved a boon for Bereino. "Obviously, it guaranteed him a hire," Haile-Selassie says. ■

Published by AAAS

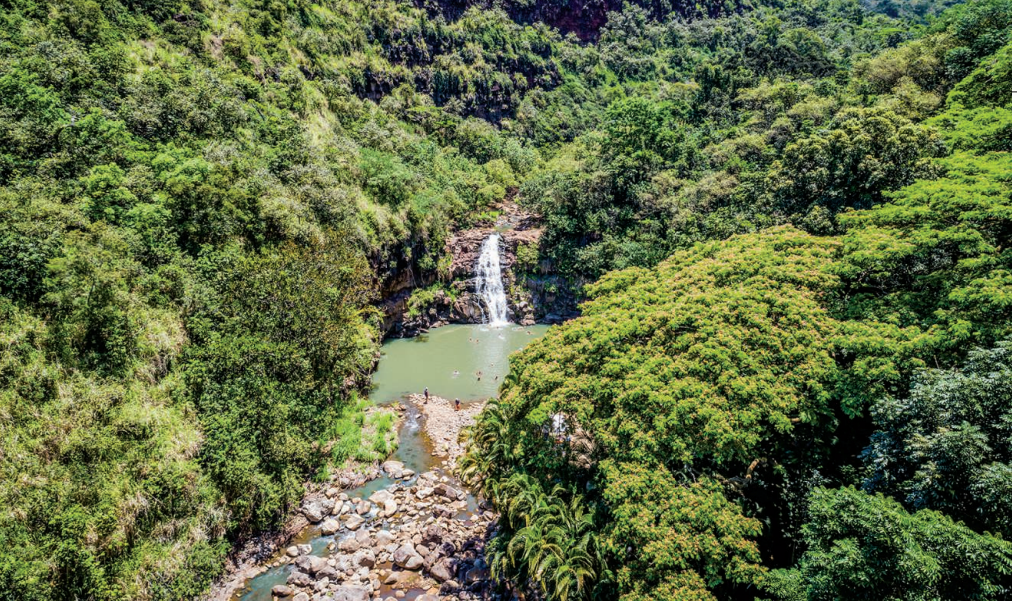

The Waimea Valley in Hawaii includes a wide variety of habitats for microbes and their plant and animal hosts.

MICROBIAL ECOLOGY

No microbiome is an island, survey reveals

Sampling in Hawaiian valley shows wider environment shapes each organism's microbial community

By **Elizabeth Pennisi**, *in Louisville, Kentucky*

Even the internal world of microbes on which almost every plant and animal depends is part of a larger ecosystem, findings from a Hawaiian valley suggest. Researchers have tended to study such microbial communities—found in animal guts and in nitrogen-fixing nodules on legume roots, for example—in isolation. But by sampling and analyzing bacteria throughout Oahu's Waimea Valley, a team has found that each organism's microbiome is a subset of what exists in the broader environment and in organisms lower on the food web. "The real surprise was the extent to which microbes are spread across hosts and habitats," said microbial ecologist Anthony Amend, one of about two dozen researchers at the University of Hawaii (UH) in Honolulu who conducted the survey. "We have been wearing blinders."

Instead of individual microbiomes, picture a single "ecosystem microbiome," says Amend, who presented the findings here at the annual meeting of the Ecological Society of America this month. The work "has the possibility of giving us a whole picture of how microbes move within and across environments," adds Kabir Gabriel Peay, an ecologist at Stanford University in Palo Alto, California, who heard the meeting presentation. "This approach is really critical if we really want to know how microbiomes assemble."

UH's Margaret McFall Ngai, whose studies of bioluminescent microbes in squid over the past several decades revealed how intimate the connections between microbes and their hosts can be, thought the Hawaiian islands might do for microbes what they have for other flora and fauna: provide a laboratory for testing key ecological principles. And she realized that newly hired UH microbiome researchers had the range of expertise needed to do the work. Her colleagues were quickly sold on the idea, and they identified the Waimea Valley as a promising setting. A watershed just 12 kilometers long, Waimea encompasses a wide range of habitats, from dry beach to tropical rainforest.

During the survey, researchers captured birds, sampled their microbiomes, and released them.

Students and faculty fanned out across the valley to collect microbes, sampling plants, animals, soil, rocks, streams, and even the ocean, as divers took stock of the microbes in the coral reefs at the valley's base. They analyzed all the DNA in their samples and compared those sequences to DNA databases of known organisms. "I can't think of anyone else who has taken that [broad brush] effort," says Stephanie Kivlin, a microbial and ecosystems ecologist at the University of Tennessee in Knoxville. "We never thought to look how [the microbes in] nearby animals might affect the plants," she adds. "What they found is that there's this really nice pattern."

The data revealed nested microbiomes, akin to Russian dolls. The soil and free-living samples contained the widest range of microbes. Primary producers—plants and algae—hosted the next greatest range, although just a subset of the diversity seen in the valley environment. The plant and algae eaters had a subset of that subset, and carnivores had the least diverse microbiomes of all. Amend and his colleagues concluded that the microbes in the landscape set the stage for those found within hosts. And somehow each organism's place in the food web helps determine what microbes it acquires.

Many researchers have assumed that an organism's microbiome is somehow seeded from the environment, but few had delved into the specifics. This study is "a demonstration of how connected our world is, all the way down to the microbiological level," says Colin Averill, a microbial ecologist at ETH Zurich in Switzerland who studies how soil microbes influence the trees above them. The Waimea survey "implies that I need to take an even broader approach," he says.

The work also revealed that some microbes are surprisingly widespread. Many so-called marine fungi were common in the stream and even on land, Amend reported. That's surprising to Peay. "It suggests that they may have much more complex life cycles or natural histories than we have previously imagined."

Amend and his colleagues now hope to watch the ecosystemwide microbial traffic in action. They are taking lab-grown strawberry seedlings and caged, lab-reared, germ-free fruit flies to different places in the valley, hoping to see how they acquire microbiomes from the environment and how their new microbial guests affect their health and reproductive fitness. "That could have a practical pay-off," Peay says. "Understanding how plants and animals acquire their microbiomes has the potential to improve efforts to restore ecosystems, improve agricultural sustainability, and manage diseases." ■

PHOTOS: (TOP TO BOTTOM) WAIMEA VALLEY BOTANICAL GARDENS; UH FOUNDATION

Published by AAAS

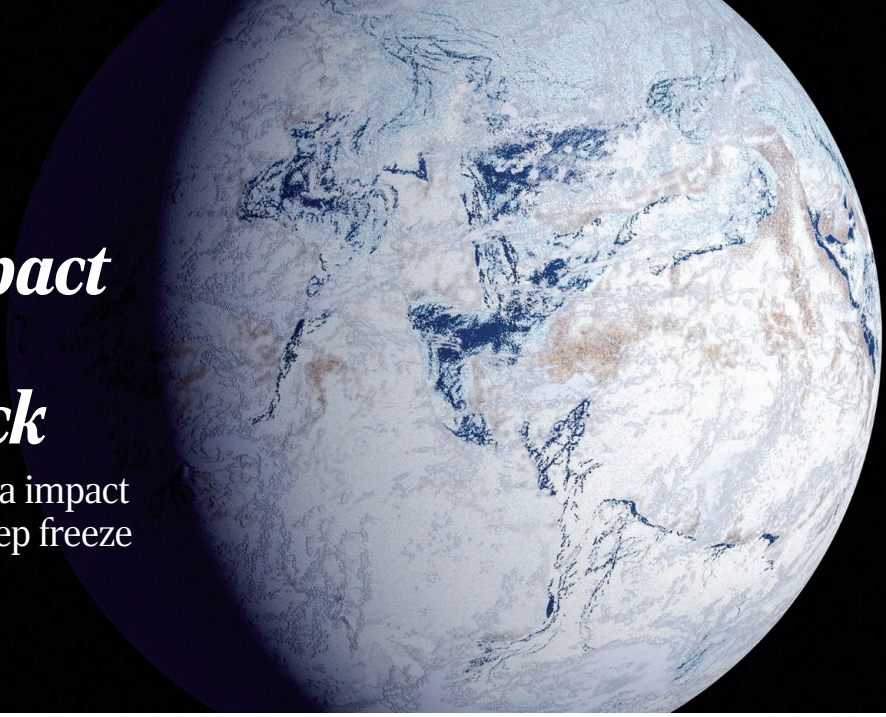

EARTH SCIENCE

World's oldest impact crater dated in Australian outback

The 2.2-billion-year-old Yarrabubba impact came at the end of a planetwide deep freeze

By **Eric Hand**, *in Barcelona, Spain*

Barlangi Rock, an ancient hill in the outback of Western Australia, is dimpled by the quarries of Aboriginal people who chiseled its fine-grained rocks into sharp tools. Now, geologists have added a much deeper layer of history to those rocks by showing they were forged 2.229 billion years ago, when an asteroid crashed into our planet. The finding makes Yarrabubba crater, the 70-kilometer-wide scar left by the collision, Earth's oldest.

The geologists who reported the date last week, here at the Goldschmidt geochemistry conference, also point out a conspicuous coincidence: The impact came at the tail end of a planetwide deep freeze known as Snowball Earth. They say the impact may have helped thaw Earth by vaporizing thick ice sheets and lofting steam into the stratosphere, creating a powerful greenhouse effect.

"It's intriguing to think what a moderate to large impact event could do in this time period," says Timmons Erickson, a geochronologist at NASA's Johnson Space Center in Houston, Texas, who led the study. "The temporal coincidence is striking," agrees Eva Stüeken, a geobiologist at the University of St. Andrews in the United Kingdom. But she and other researchers are skeptical that Yarrabubba—which is just one-third the size of the crater left by the dinosaur-killing impact 66 million years ago—could have had such a profound effect on the climate. Still, Stüeken says, paleoclimate studies should consider the possible role of such violent collisions. "It forces us to think more about these impacts and these potential feedbacks."

Earth likes to cover its tracks. Erosion from wind and water, as well as the churn of plate tectonics, mean impact craters are scarcer the further one goes back in time—even though the cratered surfaces of the moon and Mars show impacts were actually more common in the tumultuous early solar system. Prior to the dating of Yarrabubba crater, the oldest known impact was the Vredefort Dome, a 2.02-billion-year-old feature in South Africa that, at 300 kilometers wide, is the world's largest.

Western Australia is a good place to look for old craters because it contains the Yilgarn Craton, one of Earth's oldest surviving pieces of crust. In 2001, a magnetic survey near Yarrabubba revealed circular features in the bedrock, although no crater rim can be seen at the surface. And when Francis Macdonald, a geologist at the University of California (UC), Santa Barbara, took a close look at rocks from the region, he found the signatures of an impact's shock: microscopic planar patterns in mineral crystals and shatter cones, horsetail fracture patterns up to 1 meter long. Some of the melted and recrystallized rocks from beneath the crater—including Barlangi Rock—had also survived. "We're looking at the roots of it," Macdonald says. In a 2003 discovery paper, he and his colleagues named the crater after the local sheep shearing station. They knew the impact was ancient, but could not give it a firm date.

In 2014, Erickson saw an opportunity while on his way to field work elsewhere in Western Australia. He camped near Barlangi Rock and crisscrossed the hill with a sledgehammer, filling a backpack with a dozen chunks of rock. In a laboratory tub, he zapped the rocks with 100,000 volts of electricity, breaking them up into their component minerals without damaging delicate textures.

Next, Erickson had to sift for crystals suitable for dating. Like a gold prospector, he used pans to float off less dense quartz and feldspar, and he extracted other unwanted minerals with a magnet. Finally, with tweezers and a microscope, he picked out several hundred grains of zircon and monazite, each smaller than the width of a human hair. "You need a good podcast or music when you're doing that," he says.

He wanted crystals with rims that had melted and recrystallized, an assurance that the impact had reset a clock in which small amounts of radioactive uranium, trapped within the crystal, decay into lead. He mounted some of the best crystals in epoxy, polished them down to a fresh face, and vaporized spots on the rims with an ion beam. A mass spectrometer measured the abundance of uranium and lead in the vapor;

Shock and thaw?

Yarrabubba crater is in the Yilgarn Craton, an ancient piece of crust. Dust and steam from the impact may have helped end a global ice age, researchers suggest.

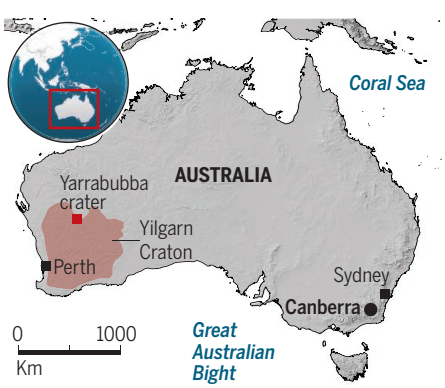

Oxygen from ancient life may have led to Snowball Earth (artist's concept). Did an impact help it thaw?

CREDITS: (PHOTO) CHRIS BUTLER/SCIENCE SOURCE; (MAP) A. CUADRA/*SCIENCE*

Published by AAAS

from the proportions and the known half-life of the uranium, he and his colleagues could calculate an age. They ended up with a date of 2.229 billion years old, plus or minus 5 million years.

That puts the impact at a turbulent time in Earth's history. Life had existed for more than 1 billion years, but photosynthetic life—cyanobacteria living in shallow waters—was a recent evolutionary invention, one that triggered a sharp rise in atmospheric oxygen about 2.4 billion years ago. Previously, high levels of methane in the atmosphere had generated a greenhouse effect that warmed the planet. But many scientists think the methane was destroyed by chemical reactions with Earth's first ozone, produced when ultraviolet light from the sun struck the oxygen molecules. They suspect loss of methane sent Earth crashing into a set of severe and long-lived ice ages, even at low latitudes. Three or maybe four of these icy episodes took place between 2.45 billion and 2.22 billion years ago, which means Australia might have been covered in ice at the time of the Yarrabubba impact.

Scientists have assumed that volcanic eruptions ended the ice ages, by belching carbon dioxide and warming the planet. But Erickson and his colleagues speculate that Yarrabubba could have helped. They modeled the effect of a 7-kilometer-wide asteroid striking an ice sheet between 2 and 5 kilometers thick. They found the impact could have spread dust thousands of kilometers, darkening ice and enhancing its ability to absorb heat. It also would have sent half a trillion tons of steam into the stratosphere—orders of magnitude more water vapor than in today's stratosphere—where it would have trapped heat.

Andrey Bekker, a geologist at UC Riverside, doubts that the water vapor would have persisted for the centuries needed to thaw Earth. "I'm not convinced that by itself it could do this job," he says. Christian Koeberl, an impact expert and the director general of the Natural History Museum in Vienna, shares those doubts, but says paleoclimate researchers need to model the effects explicitly.

If the Yarrabubba impact did thaw the planet, allowing life to reclaim icy continents and oceans, it wouldn't be the first example of life benefiting from a cosmic blow, Koeberl says. Although the public tends to associate impacts with extinctions, he notes that impacts 4 billion years ago could have jump-started life. Asteroids delivered phosphorus, a key nutrient, and the impacts also created the protected, energy-rich hydrothermal systems where some biologists believe life began. "Impacts can be bringers of life, impacts can be destroyers of life," he says. ■

ENVIRONMENTAL POLICY

Amazon fires clearly linked to deforestation, scientists say

Brazilian government deflects blame for rise in fire activity

By **Herton Escobar**

Brazil's government claims its policies aren't responsible for the fires that are ravaging the Amazon rainforest and triggered worldwide indignation last week. President Jair Bolsonaro suggested nongovernmental organizations were setting the forest ablaze to discredit his government; his minister of the environment, Ricardo Salles, tweeted that "dry weather, wind, and heat" were to blame.

Scientists dismiss those claims. "There is no doubt that this rise in fire activity is associated with a sharp rise in deforestation," says Paulo Artaxo, an atmospheric physicist at the University of São Paulo in São Paulo.

Thousands of fires occur in the Amazon annually, but the numbers have risen since Bolsonaro became president on 1 January and began to encourage development. In satellite images, Brazil's National Institute for Space Research (INPE) counted more than 41,000 "fire spots" between 1 January and 24 August, compared with 22,000 in the same period last year. The Global Fire Emissions Database, a collaboration between NASA 's Goddard Space Flight Center in Greenbelt, Maryland and two universities, sees a similar trend. The numbers are the highest since 2010, when the Amazon experienced a severe drought triggered by El Niño and a warming of the North Atlantic Ocean. This time, climatic anomalies can't explain the uptick, scientists say.

Deforestation can, at least partly. To clear land for farming, settlers fell trees, remove valuable timber, and then set fire to the remainder. Recent INPE data showed deforestation to be on the rise, although Bolsonaro called the numbers "a lie" and had INPE Director Ricardo Galvão fired (*Science*, 2 August, p. 419). The 10 municipalities with the highest rate of fire activity are also the ones where the forest disappeared most rapidly this year, according to the Amazon Environmental Research Institute in Belém, Brazil. And many of the recently detected spots are active for more than a day, burning with intense heat and producing tall, thick, smoke pillars—all indicators that trees are on fire, not overgrown pastures, crop residues, or roadside vegetation.

Bolsonaro has so far rejected international pressure to protect the rainforest. He hurled insults at Norway and Germany after they suspended contributions to the Amazon Fund, which supports conservation and sustainable development, and refused $20 million offered by the G-7 nations to help fight the fires. But facing mounting criticism at home, Bolsonaro ordered the military to help combat the fires and made a 5-minute TV address to profess his "deep love and respect for the Amazon" and promise that his administration would "act strongly" against the blazes. ■

Herton Escobar is a science journalist in São Paulo, Brazil.

PHOTO: © VICTOR MORIYAMA/GREENPEACE

A forest fire in Altamira, in Brazil's Pará state. President Jair Bolsonaro has rejected help from G-7 members.

Published by AAAS

THE ALLURE OF MONKEYFLOWERS

A tough, diverse, colorful weed used in evolutionary studies is becoming a key model for plant biology

By **Elizabeth Pennisi**

Yaowu Yuan's passion for monkeyflowers began in 2004 with a slideshow. Then a budding plant taxonomist at the University of Washington in Seattle and an avid hiker, he was amazed at the variety of wildflowers he saw on his outings in the Cascade mountains. Like Charles Darwin, he was vexed by what Darwin called an abominable mystery: How did nature generate such a diversity of flower colors and forms? During a campus seminar, Yuan encountered a plant that he thought might yield answers. University of Washington plant molecular biologist H. D. "Toby" Bradshaw and his graduate student showed slides documenting as much floral diversity within a single monkeyflower species as Yuan had seen in the meadows and streambanks of the Cascades—all generated by mutating the genome of this one *Mimulus* species.

The revelation changed the course of Yuan's research because he realized such mutants could lead to a better understanding of flower development in all plants. Since starting a faculty job at the University of Connecticut (UConn) in Storrs 6 years ago, he has been tracking down genes that control color, shape, size, and other traits in *Mimulus* flowers—and that may have similar effects in other plants. And he is far from the only scientist to have fallen under the spell of a plant best known as a weed that thrives where few plants, even other weeds, can grow—around abandoned copper mines and hot springs and in other inhospitable, mineral-laden soil.

Like plant scientists' traditional lab workhorse, the mustard weed *Arabidopsis thaliana*, monkeyflowers grow fast, produce a lot of seeds, and have a simple genome—appealing traits for lab studies. But their explosion of flower colors and forms, diverse lifestyles, and extraordinary hardiness—dramatic contrasts to the unassuming *Arabidopsis*—have seduced researchers studying plant evolution and adaptations. "You can use *Mimulus* to study traits that don't even exist in *Arabidopsis*," Yuan says.

More than 40 labs now focus on select members of *Mimulus*, a number that has doubled in the past decade, says Andrea Sweigart, an evolutionary geneticist at the University of Georgia in Athens. The National Science Foundation (NSF) has funded both

PHOTO: DENA GROSSENBACHER

Published by AAAS

The great diversity of flowers within *Mimulus* is one reason the plants have become a popular subject of study.

PHOTO: BENJAMIN BLACKMAN

individual evolution and ecology projects with *Mimulus* and, more recently, supported a $1 million effort to develop efficient techniques for altering traits in those plants.

"A large, organized, and growing research community is using this system," says evolutionary geneticist Theodore Morgan, a program officer at NSF in Alexandria, Virginia. A monkeyflower meeting in Providence in June drew about 70 biologists, more than triple the number who attended the first one 13 years ago. The number of publications on *Mimulus* still isn't huge—about 425—but that tally has grown rapidly in the past decade.

Some researchers are exploring monkeyflowers' own unusual adaptations. But other scientists are turning the flowers into a window on widespread biological processes. Yuan, for example, recently teamed up with another lab to use *Mimulus* mutants with odd petal color patterns to provide the most detailed example yet of mathematician Alan Turing's scenario for how zebra stripes, leopard spots, and some floral patterns arise in nature. Another team examining how monkeyflowers mutate as they grow revealed a mechanism that may enable many plants to evolve faster than animals.

The field may even have its first serious controversy: Some researchers are rejecting a recent revision of the monkeyflower family tree that split the more than 100 *Mimulus* species into multiple genera, creating confusion in the scientific literature by renaming the most studied monkeyflower species. The researchers' passion is a measure of the enthusiasm the new model plant arouses. One opponent of the new tree, John Willis, an evolutionary geneticist at Duke University in Durham, North Carolina, says flatly, "We're not going to take it anymore."

LAB SCIENTISTS AREN'T THE FIRST to be fascinated by *Mimulus*, which is found worldwide, often in the harshest spots, such as the bare islands of "serpentine" soil that dot the forests of California's Sierra Nevada mountains. Plant ecologists have conducted field studies of wild *Mimulus* for 80 years. Last year, for example, researchers documented populations of *Mimulus guttatus* that contain a mix of individuals with different flowering times, flower sizes, and number of seeds produced. The late-flowering plants do better in wet years, and early-flowering ones do better in years when drought hits early in the season. Because the amount of rain varies from year to year, the two variants coexist in a population, although the proportions change over time. The work, reported last year in *Science* (3 August 2018, p. 475), provided long-sought proof of an evolutionary phenomenon called fluctuating selection, in which changing conditions cause a species to evolve in multiple directions. Theorists have proposed that fluctuating selection helps explain the extensive variation seen in many other species besides monkeyflowers.

Red "tongue" *Mimulus* mutants revealed how coloration arises.

At the June *Mimulus* meeting, Willis revealed a major clue to another monkeyflower mystery: the plants' affinity for serpentine soils. Because they derive from Earth mantle rock, those soils are rich in iron and magnesium but low in potassium and calcium, which plants depend on to maintain their cell walls. The soils also tend to have little nitrogen, vital for plants, but plenty of toxic heavy metals, such as nickel and chromium.

Willis and his Duke postdoc Jessica Selby recently crossed serpentine-tolerant monkeyflowers with versions of the plant that were not growing on serpentine soil. The duo tested several generations to identify DNA important to the trait. To narrow the hunt for relevant genes, Selby collected *M. guttatus* specimens from serpentine soils in seven places across California and Oregon and compared their DNA with that of populations of *M. guttatus* living nearby, on richer soil.

Both approaches pointed to a gene for an enzyme that makes arabinose, a sugar found primarily in the plant cell wall, Willis reported. That gene varies among *M. guttatus* plants, but every plant that can grow on serpentine soils has the same mutation. It may alter how arabinose interacts with other components of the cell wall, somehow compensating for the low calcium and high magnesium and keeping cell walls intact—an idea Willis's team is testing with researchers from the University of California (UC), Berkeley, and Stanford University.

By harnessing population genetics and other gene-finding techniques, Willis "was way ahead of the curve in seeing how genomics could make the tremendous natural variation in plants knowable at the level of the gene," says Lila Fishman, an evolutionary biologist at the University of Montana in Missoula. The work could have practical benefits as well, adds Benjamin Blackman, an evolutionary biologist at UC Berkeley: "Learning how plants have already adapted to cope with marginal soil environments can inform breeding efforts aimed at developing crops that can cope with poor soil."

Besides probing monkeyflowers' own special biology, researchers are using them to glean more general lessons about plants and animals. Take Yuan and Blackman's work on color patterning. Blackman's lab originally studied sunflowers. But *M. guttatus* appealed to him for studies of the genetic basis of patterning because its simple genome had been sequenced—making it easier to test the role of particular genes and proteins by genetically modifying the plant. Independently, he and Yuan homed in on the same protein, which they thought might be a key to flower color patterns.

Yuan and UConn postdoc Baoqing Ding had recently tracked down the gene that causes red pigment to appear on the yellow

Published by AAAS

lower petal of some *Mimulus* flowers. The red usually appears as a band of speckles, which serve as a "nectar guide" for incoming pollinators. Many types of coloration in plants and animals are the result of a network of proteins that activate pigment genes at specific places and times in the body. But Yuan and Blackman wondered whether the monkeyflower spots might be generated instead through a patterning mechanism proposed in the 1950s by Turing, who is best known for breaking the Germans' Enigma code in World War II but was also a theoretical biologist.

Turing predicted that some patterns emerge from the natural diffusion and interactions of proteins whose concentrations regulate each other's production. For spots, when the gene encoding a cell's "activator" of pigment production turns on, the activator protein stimulates its own production and that of a "repressor" protein, which diffuses beyond the pigmented spot. That second molecule shuts down any activator in the surrounding cells—causing a white halo. But the repressor gets more dilute the farther it travels, eventually losing its effect. Then the activator can turn on, and a new spot of color can form. Color patterns emerge depending on the differences in the two proteins' diffusion rates (see diagram, below).

Biologists have long assumed that Turing's mechanism is responsible for zebra stripes and leopard spots and perhaps even for monkeyflower nectar guides. Indeed, Yuan had identified a monkeyflower protein that might serve as the activator. But no one had identified a full activator-repressor system involved in periodic pigmentation patterns.

Blackman, however, had noticed a clue in some wild *M. guttatus*: They either lacked spots or else had just one large red patch, which he called a tongue, suggesting part of the system was missing. Independently, Yuan uncovered a similar red tongue variety among mutants he made in another *Mimulus* species. When they learned of each other's work, the two joined forces. And at the June *Mimulus* meeting, they reported using the red tongue varieties to track down a protein dubbed R3-MYB, the repressor counterpart to the already known activator protein.

To confirm that R3-MYB really acted as a repressor, Yuan and Blackman both wielded molecular tools to block its production. Yuan relied on RNA interference, whereas Blackman's team enlisted CRISPR—the first use of the genome-editing technology in *Mimulus*. Both techniques led to full red tongues on the plants' petals, Blackman reported—vivid testimony that the mechanism Turing hypothesized can account for some of nature's tapestry. "This work shows how *Mimulus* can provide broad insight into processes that shape biodiversity," Sweigart says.

ANOTHER LINE OF WORK with monkeyflowers sheds light on biodiversity by revealing a mechanism, unique to plants, for rapidly adapting to new conditions. Their advantage, graduate student Jaime Schwoch of Portland State University in Oregon found, is rooted in the way they produce reproductive cells. In animals, the cells that mature into eggs and sperm are sequestered early in development, and they don't divide until the organism sexually matures. That protects them from division-related mutations that occur in the organism's nongerm, or somatic, tissues. But flowers, which contain both kinds of germ cells—pollen and ova—form from active somatic tissue at the tips of growing stems. Any mutations occurring in the dividing cells of a stem will be locked into the germ cells and can pass on to the next generation.

Given that somatic tissue mutations should accumulate in a plant's germ cells over successive generations, Schwoch wondered why plants don't wind up with many more such mutations than animals—and a greater burden of harmful ones. In fact, as the somatic parts of both plants and animals grow, their cells accumulate about one mutation per million bases per cell division, so plant germ cells should have far

Turing's idea takes root

Spots, stripes, and monkeyflower petal speckles arise through "reaction-diffusion" (top right), which involves an activator protein that turns on pigment pathways and the production of a second protein, which inhibits the activator.

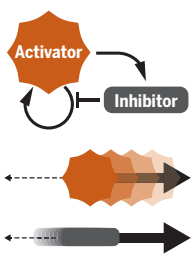

Both the activator and the inhibitor diffuse away from the cells that produce them, with the inhibitor moving faster (above).

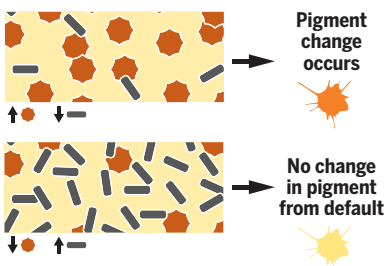

The balance of concentrations between the two proteins determines whether pigment is produced.

Spot on

Unimpeded by the inhibitor, an activator colors a cell and spreads to and colors nearby cells. The inhibitor quickly diffuses away from the colored cells, causing a nonpigmented halo to form. As this process repeats throughout the tissue, multiple spots form, resulting in a periodic pattern.

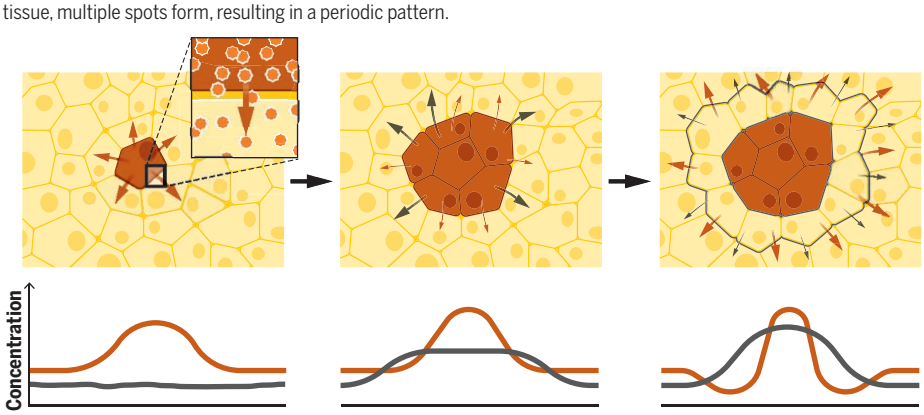

Initial condition: high concentration of activator because of self-activation. Activator diffuses.

Pigment spot develops, but inhibitor concentration grows because of activator activity.

Activator levels decline at the border of the spot because of competition from faster-diffusing inhibitors. Spot is isolated.

Patterns galore

Monkeyflower hybrids mix different species' activators and inhibitors, altering petal speckle patterns.

CREDITS: (GRAPHIC) V. ALTOUNIAN/*SCIENCE*; (IMAGES) QIAOSHAN LIN AND BAOQING DING

Published by AAAS

Many monkeyflowers thrive in inhospitable, mineral-laden soils, like this spot in Lake County in California, and plant biologists are starting to understand how they do it.

more mutations than animal germ cells. But they don't. And deleterious mutations are surprisingly scarce in plants, Schwoch found when she compared two sets of monkeyflowers. She produced one by self-fertilizing *Mimulus* flowers with each flower's own pollen, the other by fertilizing flowers with pollen from flowers on another stem of the same plant. The latter is the equivalent of a cross between different parents, because each stem acquires a unique set of mutations as it grows.

Self-fertilization, like inbreeding in animals, should pair up harmful recessive mutations, so Schwoch expected the crosses that used pollen from one stem on flowers from another to do better. But some of the more prolific, healthier plants came from progeny derived from a single stem, she reported at the Evolution 2019 meeting, also in Providence in June. That finding suggested the plants were somehow eliminating harmful mutations in their somatic cells and accumulating beneficial ones for their reproductive cells.

To verify that sorting process, Schwoch grew *Mimulus* plants for 6 months in saltier-than-normal conditions and then sequenced DNA from their tips, taking note of new mutations and how often the mutations appeared in the sequenced material. Such mutations should occur in low frequencies, so when she found one that occurred in many cells of the plant tip, she inferred that the original cell with that mutation had grown much faster than cells without it and replaced them.

The rate of mutations doubled under the salt stress, she reported. Moreover, cells carrying mutations that improve salt tolerance proved more likely to persist in stems, whereas less well-adapted cells died out. The survivors made it into the germ line, so the within-lifetime innovations were passed on to subsequent flowers and pollen. The process means "plants can adapt very quickly" to tough situations, Schwoch said.

Duke evolutionary biologist Jennifer Coughlan is impressed. "This work has broad significance for all plants, but in particular for long-lived perennial plants, [which] accumulate many mutations across their lifetimes," she says. Sweigart predicts that Schwoch will quickly unearth the specific mutations that produced the salt tolerance: *Mimulus* "has great genetic and genomic resources, so it should be possible to identify the precise molecular changes that have occurred" in her salt-tolerant plants, Sweigart says. And the lessons from monkeyflowers may point to ways to make other plants, including crops, more tolerant of salty soils, researchers suggest.

Growing monkeyflowers in salty conditions has helped reveal how plants weed out deleterious mutations.

JUST WHEN INVESTIGATORS are flocking to monkeyflowers, the monkeyflowers may be scattering—at least taxonomically. A 2012 evaluation of the *Mimulus* family tree placed some of the better-studied monkeyflower species in other genera. For example, the popular *M. guttatus* is now named *Erythranthe guttata*. The *Mimulus* genus itself kept only seven species of the original 165-plus. Adopting new designations for many *Mimulus* species will lead to chaos in the scientific literature, some researchers in the field say.

Among monkeyflower researchers, the reclassification provoked a minor rebellion. Most did not use the new names in their presentations at the *Mimulus* conference or the subsequent Evolution meeting. A paper in press in the journal *Taxon* argues for a different, less disruptive reclassification, and Willis says that makes sense. "You either rename 150 species, or you rename 20 somewhat obscure species and call them all *Mimulus*," he notes.

A *Mimulus* by any other name might smell as sweet, but most biologists don't want to monkey around with their new favorite plant. ■

PHOTOS: (TOP TO BOTTOM) JESSICA PACKARD SELBY; JAIME SCHWOCH

Published by AAAS

INSIGHTS

POLICY FORUM

SCIENCE AND DEMOCRACY

Protecting elections from social media manipulation

Rigorous causal analysis could help harden democracy against future attacks

By **Sinan Aral**[1,2,3] *and* **Dean Eckles**[1,2]

To what extent are democratic elections vulnerable to social media manipulation? The fractured state of research and evidence on this most important question facing democracy is reflected in the range of disagreement among experts. Facebook chief executive officer Mark Zuckerberg has repeatedly called on the U.S. government to regulate election manipulation through social media. But we cannot manage what we do not measure. Without an organized research agenda that informs policy, democracies will remain vulnerable to foreign and domestic attacks. Thankfully, social media's effects are, in our view, eminently measurable. Here, we advocate a research agenda for measuring social media manipulation of elections, highlight underutilized approaches to rigorous causal inference, and discuss political, legal, and ethical implications of undertaking such analysis. Consideration of this research agenda illuminates the need to overcome important trade-offs for public and corporate policy—for example, between election integrity and privacy. We have promising research tools, but they have not been applied to election manipulation, mainly because of a lack of access to data and lack of cooperation from the platforms (driven in part by public policy and political constraints).

Two recent studies commissioned by the U.S. Senate Intelligence Committee detail Russian misinformation campaigns targeting hundreds of millions of U.S. citizens during the 2016 presidential election. The reports highlight, but do not answer,

[1]*Sloan School of Management, Massachusetts Institute of Technology (MIT), Cambridge, MA, USA.* [2]*Institute for Data, Systems, and Society, MIT, Cambridge, MA, USA.* [3]*Manifest Investment Partners, Tiburon, CA, USA. Email: sinan@mit.edu*

ILLUSTRATION: BROBEL DESIGN

Published by AAAS

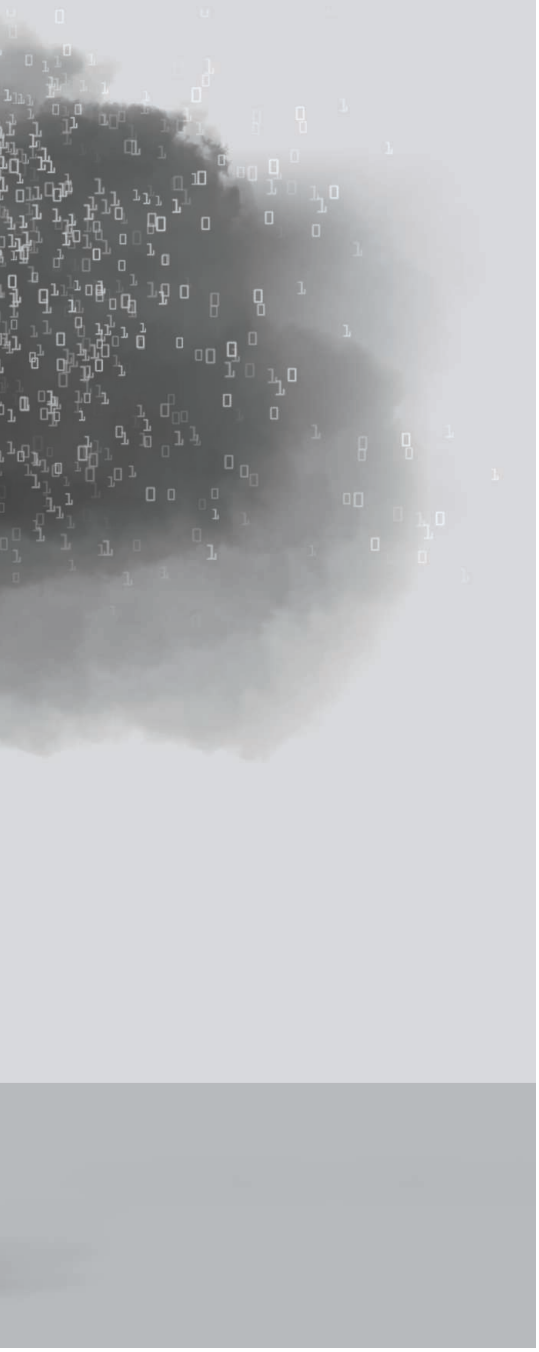

whether social media manipulation may have influenced the outcome. Some experts argue that Russia-sponsored content on social media likely did not decide the election because Russian-linked spending and exposure to fake news (*1*, *2*) were small-scale. Others contend that a combination of Russian trolls and hacking likely tipped the election for Donald Trump (*3*). Similar disagreements exist about the UK referendum on leaving the European Union and recent elections in Brazil, Sweden, and India.

Such disagreement is understandable, given the distinctive challenges of studying social media manipulation of elections. For example, unlike the majority of linear television advertising, social media can be personally targeted; assessing its reach requires analysis of paid and unpaid media, ranking algorithms and advertising auctions; and causal analysis is necessary to understand how social media changes opinions and voting.

Luckily, much of the necessary methodology has already been developed. A growing body of literature illuminates how social media influences behavior. Analysis of misinformation on Twitter and Facebook (*4*, *5*), and randomized and natural experiments involving hundreds of millions of people on various platforms, have shown how social media changes how we shop, read, and exercise [e.g., (*6*, *7*)]. Similar methods can and should be applied to voting (*8*).

Research on election manipulation will be enabled and constrained by parallel policy initiatives that aim, for example, to protect privacy. Although privacy legislation may prohibit retention of consumer data, such data may also be critical to understanding how to harden our democracies against manipulation. To preserve democracy in the digital age, we must manage these tradeoffs and overcome multidisciplinary methodological challenges simultaneously.

MEASURING MANIPULATION

We propose a four-step research agenda for estimating the causal effects of social media manipulation on voter turnout and vote choice (see the figure). We also describe analysis of the indirect, systemic effects of social media manipulation on campaign messaging and the news cycle (see supplementary materials for further details).

Step 1: We must catalog exposures to manipulation, which we define as impressions (i.e., serving of an ad or message to a viewer) of paid and organic manipulative content (*9*) (e.g., false content intended to deceive voters, or even true content propagated by foreign actors, who are banned from participating in domestic political processes, with the intent of manipulating voters). To do so, we must evaluate the reach of manipulation campaigns and analyze the targeting strategies that distribute these impressions. For example, we need to know which text, image, and video messages were advertised, organically posted, and "boosted" through paid advertising, and on which platforms, as well as when and how each of these messages was shared and reshared by voters (*2*) and inauthentic accounts. Here, understanding social multiplier effects, or how individuals influence each other, will be essential, and the literature on peer effects in social networks describes how our peers change our behavior (*6*–*8*). The content of the messages should also be analyzed to assess the effectiveness of particular textual, image, and video content in changing opinions and behavior.

Much prior work on exposure to and diffusion of (mis)information has relied on proxies for exposure, such as who follows whom on social media (*2*, *4*), though some has also investigated logs of impressions, recognizing the role of algorithmic ranking and auctions in determining exposure [e.g., (*5*, *10*)]. Given prior work on the rapid decay of advertising effects, it is important to consider when these exposures occurred, as recent work suggests that exposure to misinformation may increase just prior to an election and wane immediately afterward (*2*).

Step 2: We must combine exposure data with data on voting behavior. Data about voter turnout in the United States are readily available in public records (e.g., registered voters' names, addresses, party affiliations, and when they voted). Prior work has matched social media accounts and public voting records using relatively coarse data (e.g., residences inferred from self-reported profile data and group-level, anonymous matching procedures) (*2*, *8*), in part because of privacy concerns, resulting in low match rates that limit statistical power and representativeness. This could be substantially improved, for example, by using the rich location data possessed by social media platforms, similar to that already sold and reused for marketing purposes (e.g., matching voter registrations with inferred home addresses based on mobile and other location data), rather than simply matching voters by name and age at the state level.

In contrast to turnout data, vote choices in the United States are secret and thus only measurable in aggregate (e.g., precinct-level vote totals and shares) or sparsely and indirectly through surveys (e.g., exit polls). Thus, exposure data would need to be aggregated, at the precinct, district, or state levels, before combining it with vote choice data, making it likely that estimates of voter turnout effects will be more precise than estimates of vote choice effects.

Experiments demonstrate that persuasive interventions can substantially affect voter turnout. But, when assessing turnout, it is important to remember that voting is habitual. Effective manipulation therefore likely requires targeting occasional voters in battleground regions. In social media, however, this type of targeting is possible and took place during the 2016 U.S. presidential election. Analysis of the precision of targeting efforts is essential to understanding voter turnout effects.

Influencing vote choice is more difficult because likely voters have strong prior beliefs. However, even the pessimistic litera-

Published by AAAS

ture on vote choice allows for substantial effects, especially when targeted messages change voters' beliefs. In a meta-analysis of 16 field experiments, Kalla and Broockman (*11*) report a wide 95% confidence interval (CI) of [−0.27%, 0.83%] for the effect of impersonal contact (e.g., mail, ads) on vote choice within 2 months of general elections, and larger, more significant effects in primaries and on issue-specific ballot measures. In Rogers and Nickerson (*12*), informing recipients in favor of abortion rights that a candidate was not consistently supportive of such rights had a 3.90% [95% CI: 1.16%, 6.64%] effect on reported vote choice. Such prior beliefs are predictable and addressable in manipulation campaigns through social media targeting and thus measurable in studies of the effectiveness of such manipulation.

Step 3: We must assess the effects of manipulative messages on opinions and behavior. This requires a rigorous approach to causal inference, as naïve, observational approaches would neglect the confounding factors that cause both exposure and voting behavior (e.g., voters targeted with such content are more likely to be sympathetic to it). Evaluations using randomized experiments have shown that observational estimates of social media influence without careful causal inference are frequently off by more than 100%. Effects of nonpaid exposures, estimated without causal inference, have been off by as much as 300 to 700%. Yet, causal claims about why social media messages spread are routinely made without any discussion of causal inference. Widely publicized claims about the effectiveness of targeting voters by inferred personality traits, as allegedly conducted by Cambridge Analytica, were not based on randomized experiments or any other rigorous causal inference and therefore plausibly suffer from similar biases.

To credibly estimate the effects of misinformation on changes in opinions and behaviors, we must change our approach and embrace causal inference. We must analyze similar people exposed to varying levels of misinformation, perhaps due to random chance or explicit randomization by firms and campaigns. Fortunately, there are many, until-now largely ignored, sources of such random variation. For example, Facebook and Twitter constantly test new variations on their feed ranking algorithms, which cause people to be exposed to varying levels of different types of content. Some preliminary analysis suggests that an A/B test run by Facebook during the 2012 U.S. presidential election caused over 1 million Americans to be exposed to more "hard news" from established sources, affecting political knowledge, policy preferences, and voter turnout (*10*). Most of these routine experiments are not intended specifically to modulate exposure to political content, but recent work has illustrated how the random variation produced by hundreds or thousands of routine tests, of the kind these platforms conduct every day, can be used to estimate the effects of exposure to such content (*13*). Such experiments could facilitate measurement of both direct effects (e.g., effects of manipulative content on recipients) and indirect "spillover" effects (e.g., word of mouth from recipients to peers), though other methods for estimating the latter also exist (*6*–*8*).

One important challenge is that statistical precision is often inadequate to answer many questions about effects on voter behavior. For example, randomized experiments conducted by Facebook in the 2010 and 2012 U.S. elections only barely detected effects on turnout—even though the estimated effects imply that a minimal intervention caused hundreds of thousands of additional votes to be cast [e.g., (*8*)]. The lack of statistical precision in those studies arose in part because only about a tenth of users were uniquely matched to voter records, which, as we note, could be improved upon. Furthermore, unlike television advertising, much less of the as-good-as-random variation in exposure to social media may be within, not between, geographic areas, making effects on aggregate vote shares more difficult to detect. Such imprecision can be misleading, suggesting that online advertising does not work simply because the effects were too small to detect in a given study (*14*), even though the results were consistent with markedly low costs per incremental vote, making engagement in such campaigns economically rational.

Step 4: We must compute the aggregate consequences of changes in voting behavior for election outcomes. To do so, we would combine summaries of individual-level counterfactuals (i.e., predicted voter behavior with and without exposure) with data on the abundance of exposed voters by geographic, demographic, and other characteristics in specific elections. This would enable estimates and confidence intervals for vote totals in specific states or regions if a social media manipulation campaign had not been conducted. Although some of these confidence intervals will include vote totals that do or do not alter the winner in a particular contest, the ranges of counterfactual outcomes would still be informative about how such manipulation can alter elections. Although it remains to be seen exactly how precise the resulting estimates of the effects of exposure to misinformation would be, even sufficiently precise and carefully communicated null results could exclude scenarios currently posited by many commentators.

Research should also address the systemic effects of social media manipulation, like countermessaging and feedback on the news cycle itself. Countermessaging could be studied in, for example, the replies to and debunking of fake news on Facebook and Twitter (*4*, *5*) and whether the emergence of fake stories alters the narrative trajectories of messaging by campaigns or other interested groups. Feedback into the news cycle could be studied by examining the causal impact of manipulation on the topical content of news coverage. For example, Ananya Sen and Pinar Yildirim have used as-good-as-random variation in the weather to show that more viewership to particular news stories causes publishers to write more stories on those topics. A similar approach could determine whether attention to misinformation alters the topical trajectory of the news cycle.

We believe near-real-time and ex post analysis are both possible and helpful. The bulk of what we are proposing is ex post analysis of what happened, which can then be used to design platforms and policy to

A blueprint for empirical investigations of social media manipulation

ASSESS MESSAGE CONTENT AND REACH	→	ASSESS TARGETING AND EXPOSURE	→	ASSESS CAUSAL BEHAVIOR CHANGE	→	ASSESS EFFECTS ON VOTING BEHAVIOR
How many messages spread?		Who was exposed to which messages?		How did messages change opinions and behavior?		How did opinion and behavior change alter voting outcomes?
Analysis of paid and organic information diffusion		Analysis of targeting and messaging exposure		Causal statistical analysis of opinion and behavior change		Counterfactual analysis of deviations from expected voting
Measure impressions through paid media and sharing		Evaluate targeting campaigns and impression distributions		Evaluate causal effects across individuals and segments		Measure deviations from expected voting behavior

Published by AAAS

prevent future manipulation. The pace at which voting data (whether in primaries or general elections) become available is a key limitation. But real-time detection of manipulation efforts and reaction to them could also be designed, similar to tactics in digital advertising that estimate targeting models offline and then implement real-time bidding based on those estimates. Experimental analysis of the effect of social media on behavior change can be spun up and conducted by the platforms in a matter of days and analyzed in a week.

LEGAL, ETHICAL, AND POLITICAL IMPLICATIONS

We have described what a rigorous analysis of social media manipulation would entail, but have also assumed that the data required to conduct it are available for analysis. But does the social media data that we describe above, especially data about the content that individuals were exposed to, exist retrospectively or going forward? Social media companies routinely log what users are exposed to for research and retraining algorithms. But current regulatory regimes disincentivize the lossless retention of this data. For example, the European Union's General Data Protection Regulation (GDPR) encourages firms to comply with user requests to delete data about them, including content that they have posted. An audit by the office of the Irish Data Protection Commissioner caused Facebook to implement similar policies in 2012. Thus, without targeted retention, it may be difficult for firms to accurately quantify exposures for users who deleted their accounts or were exposed to content deleted by others. We should recognize that well-intentioned privacy regulations, though important, may also impede assessments like the one that we propose. Similarly, proposed legislation in the United States (the DETOUR Act) could make many routine randomized experiments by these firms illegal (Senate Bill 1084), making future retrospective analyses more difficult and, of course, making ongoing efforts by those firms to limit such manipulation less data-driven.

Even if such data are available, it is not obvious that we should accept world governments demanding access to or analyses of those data to quantify the effects of speech in elections. Although we suggest that linking datasets could be achieved using rich location data routinely used for marketing, such use may be reasonably regarded as data misuse. Thus, we do not unconditionally advocate the use of any and all existing data for the proposed analyses. Instead, privacy-preserving methods for record linkage and content analysis, such as differential privacy (*15*), could help manage trade-offs between the need for privacy and the need to protect democracy.

Hardening democracies to manipulation will take extraordinary political and commercial will. Politicians in the United States, for example, may have countervailing incentives to support or oppose a postmortem on Russian interference, and companies like Facebook, Twitter, and Google face pressure to secure personal data. Perhaps this is why Social Science One, the forward-looking industry–academic partnership working to provide access to funding and Facebook data to study the effects of social media on democracy, faced long delays in securing access to any data, and why its most recent release does not include any data relevant to a postmortem on Russian interference in the 2016 or 2018 elections in the United States. Moreover, this cannot just be about any single company or platform. Comprehensive analysis must include Facebook, Twitter, YouTube, and others. Perhaps only mounting pressure from legislators and the public will empower experts with the access they need to do the work that is required.

> ***"...begin a public discussion of the trade-offs between privacy, free speech, and democracy..."***

Research collaborations with social media platforms, like that being undertaken by Social Science One, can facilitate access to important data for understanding democracy's vulnerability to social media manipulation. We hope the realization that the analysis we propose is bigger than any one election and essential to protecting democracies worldwide will help overcome partisanship and myopic commercial interests in making the necessary data available, in privacy-preserving ways.

However, it is important to note that prior work has linked social media messaging to validated voting, both with the assistance of the social media platforms (*8*) and without it (*2*). Although collaboration with the platforms is preferable, it is not the only way to assess manipulation. In the absence of commercial or governmental support for postmortems on past elections, active analysis of ongoing information operations, conducted according to the framework that we propose, is a viable and valuable alternative. A detailed understanding of country-specific regulations and election procedures is necessary for robust analysis of the effects of social media manipulation on democracies worldwide.

Our suggested approach emphasizes precise causal inference, but this should be complemented with surveys, ethnographies, and analysis of observational data to understand the mechanisms through which manipulation can affect opinions and behavior.

Achieving a scientific understanding of the effects of social media manipulation on elections is an important civic duty. Without it, democracies remain vulnerable. The sooner we begin a public discussion of the trade-offs between privacy, free speech, and democracy that arise from the pursuit of this science, the sooner we can realize a path forward. ■

REFERENCES AND NOTES

1. H. Allcott, M. Gentzkow, *J. Econ. Perspect.* **31**, 211 (2017).
2. N. Grinberg, K. Joseph, L. Friedland, B. Swire-Thompson, D. Lazer, *Science* **363**, 374 (2019).
3. K. H. Jamieson, *Cyberwar: How Russian Hackers and Trolls Helped Elect a President* (Oxford Univ. Press, 2018).
4. S. Vosoughi, D. Roy, S. Aral, *Science* **359**, 1146 (2018).
5. A. Friggeri, L. A. Adamic, D. Eckles, J. Cheng, in *Proceedings of the International Conference on Web and Social Media* (Association for the Advancement of Artificial Intelligence, 2014).
6. S. Aral, D. Walker, *Science* **337**, 337 (2012).
7. S. Aral, C. Nicolaides, *Nat. Commun.* **8**, 14753 (2017).
8. R. M. Bond *et al.*, *Nature* **489**, 295 (2012).
9. A. Guess, B. Nyhan, J. Reifler, Selective exposure to misinformation: Evidence from the consumption of fake news during the 2016 US presidential campaign (European Research Council, 2018).
10. S. Messing, *Friends that Matter: How Social Transmission of Elite Discourse Shapes Political Knowledge, Attitudes, and Behavior*, Ph.D. thesis, Stanford University (2013).
11. J. L. Kalla, D. E. Broockman, *Am. Polit. Sci. Rev.* **112**, 148 (2018).
12. T. Rogers, D. Nickerson, Can inaccurate beliefs about incumbents be changed? And can reframing change votes? HKS Working Paper no. RWP13-018 (2013).
13. A. Peysakhovich, D. Eckles, Learning causal effects from many randomized experiments using regularized instrumental variables, in *Proceedings of the 2018 World Wide Web Conference* (International World Wide Web Conferences Steering Committee, 2018), pp. 699–707.
14. D. E. Broockman, D. P. Green, *Polit. Behav.* **36**, 263 (2014).
15. C. Dwork, Differential privacy: A survey of results, in *Proceedings of the International Conference on Theory and Applications of Models of Computation* (Springer, 2008).

ACKNOWLEDGMENTS

We thank A. J. Berinsky and B. Nyhan for comments. S.A. has financial interest in Alibaba, Google, Amazon, and Twitter. S.A. was a Scholar in Residence at the *New York Times* in 2013 and visiting researcher at Microsoft in 2016. S.A. has received research funding from *The Boston Globe* and speaking fees from Microsoft. S.A. is an inventor on a related patent pending. D.E. has financial interest in Facebook, Amazon, Google, and Twitter. D.E. was a consultant at Microsoft in 2018. D.E. was an employee and consultant at Facebook from 2010 to 2017. D.E. has recently received funding from Amazon. D.E.'s attendance at conferences has recently been funded by DARPA, Microsoft, and Technology Crossover Ventures. D.E. is an inventor on a related patent, which is assigned to Facebook. S.A. and D.E. contributed equally to this work.

SUPPLEMENTARY MATERIALS

science.sciencemag.org/content/365/6456/858/suppl/DC1

10.1126/science.aaw8243

Published by AAAS

PERSPECTIVES

IMMUNOLOGY

The immunological code of pregnancy

Maternal immune cells interact with the placenta and influence pregnancy complications

By **Francesco Colucci**

Various factors contribute to the hypertensive placental disease preeclampsia, fetal growth restriction (FGR), spontaneous abortion, preterm labor, and stillbirth. Some of these problems are due to placental dysfunction (*1*). The placenta attaches to and invades deep into the decidua, the specialized uterine mucosa that is rich in maternal immune cells. Because the placenta is formed from the fetus and contains genetic material from another individual (the father), it should be targeted by the maternal immune system but it usually is not. By understanding the interactions between the placenta and the maternal immune system, interventions to improve pregnancy outcomes could be developed.

An example of how immunological incompatibility can cause pathology is rhesus (Rh) disease. Immunity is passed from mother to fetus through neonatal Fc receptors on placental cells (trophoblasts) that bind immunoglobulin G (IgG) antibodies. These maternal antibodies protect neonates while their own antibodies are developing. But in blood group–mismatched pregnancies, maternal antibodies against the RhD antigen made by Rh-negative mothers are also transported through the placenta and destroy Rh-positive fetal red blood cells, causing severe anemia. Understanding the basic mechanisms of this fetal disease has led to a successful preventive treatment with immunotherapy.

Interactions within the decidua are important to understand most pregnancy complications (see the figure). The placenta is formed from embryonic trophoblast cells, and their invasion into the decidua ensures that the developing embryo acquires nutrients and oxygen from maternal blood. The interactions between maternal decidual immune cells and fetal trophoblast cells transforms uterine arteries into flaccid, large conduits, called spiral arteries, where circulation is slowed down. Appendices (villi) of the placenta bathe in the blood within spiral arteries, absorbing nutrients and exchanging gases needed for fetal growth. Shallow trophoblast invasion is associated with preeclampsia, FGR, and miscarriage (*1*), whereas excessive invasion causes placenta accreta, which can lead to fatal hemorrhage during birth. The cross-talk between trophoblast and immune cells in the decidua is key to the depth of trophoblast invasion (*2*).

Obstetrics research is challenging because of the constantly changing nature of tissues and the difficulty in accessing them, especially during the first trimester. An additional challenge is to decode the function of tissue-resident immune cells, which may adapt to specific microenvironments. Moreover, each mammalian species has evolved its own placentation process. The placenta in mice and humans is hemochorial, meaning that extravillous trophoblast (EVT) cells invade the decidua, although the degree of invasion is greater in humans. Another similarity is that cells of the innate immune system are most abundant in the decidua compared to other tissues. These include decidual natural killer (dNK) cells and macrophages, as well as dendritic cells (DCs) and T cells, including immunosuppressive regulatory T cells (T_{regs}) (*2*). In mice, T_{regs} are induced at conception in the female reproductive tract by cytokines in semen, they expand in subsequent pregnancies, and their depletion causes abortion. In humans, T_{regs} are fewer and less functional in preeclampsia (*3*). The role of decidual T_{regs} may not be to suppress immune responses, because maternal immune cells that might cause placental dysfunction by targeting paternal antigens and must therefore be controlled by T_{regs} have never been identified. Directly or indirectly through modulating the functions of dNK cells, macrophages, and DCs in the decidua, T_{regs} may participate in tissue remodeling, as demonstrated in adipose tissue, muscle, and intestine (*4*). They may also regulate the transformation of the endometrial lining of the uterus into decidua (decidualization), implantation, and vascular adaptations during placentation.

Exaggerated inflammation during pregnancy in response to infections such as influenza can be fatal to mother and fetus. Placental ischemia triggers systemic inflammatory responses of maternal endothelial cells (which line blood vessels), leading to hypertension in preeclampsia. However, inflammation and the innate immune system might have become integral to the necessary destruction and regeneration of the uterine mucosa during the menstrual cycle and in pregnancy. Immunological mechanisms that had originally evolved to destroy and repair might have been co-opted to participate in successful placental invasion. Traditional ideas about immunity and pregnancy suggest that immunological tolerance of non-self tissues must prevail and, for the pregnancy to succeed, maternal immune cells must be prevented from responding to paternal antigens in the fetus. The emerging idea is that the invasive type of placentation in humans and mice has coevolved with the immune system to both maximize the benefits and minimize the hazards of cross-talk between trophoblast and immune cells, rather than avoiding maternal immune responses in the decidua.

The need for functional immune cells at the maternal-fetal interface is exemplified by dNK cells. Although blood NK cells kill virally infected and cancerous cells, dNK cells are involved in tissue homeostasis rather than in killing. In mice, dNK cells are necessary for uterine vascular adaptations during pregnancy (*5*). In humans and mice, dNK cells seem to participate in controlling trophoblast invasion and transforming uterine blood vessels into spiral arteries. Genetic evidence in humans and mice suggests that excessive inhibition of dNK cell function impedes both decidual arterial remodeling and fetal growth (*6*). Maternal dNK cells and fetal trophoblast cells establish intimate connections through receptor-ligand interactions, and these may be the key to cracking the immunological code of pregnancy. The main determinants of immune tolerance—the extremely variable human leukocyte antigen (HLA) molecules that present antigens to T cells—are not expressed by the outer layer of the placenta (syncytiotrophoblast), thereby avoiding any possible recognition of paternal antigens by maternal immune cells. However, human fetal EVT cells express invariable HLA-E and HLA-G, and variable HLA-C, which can be derived from either parent and

Department of Obstetrics and Gynaecology, University of Cambridge School of Clinical Medicine and Centre for Trophoblast Research. National Institute for Health Research Cambridge Biomedical Research Centre, Cambridge CB2 0SW, UK. Email: fc287@medschl.cam.ac.uk

Published by AAAS

can differ from pregnancy to pregnancy, even in the same couple. All HLA-C allotypes can bind variable dNK receptors, called killer cell immunoglobulin-like receptors (KIRs), which can be activating or inhibitory. Combinations of maternal *KIR* and fetal *HLA-C* genetic variants that activate dNK cells may attract EVT cells and enhance placental perfusion, thus improving placental invasion and promoting fetal growth. Conversely, combinations that inhibit dNK cells may impede trophoblast invasion and contribute to preeclampsia and FGR (*6*). Similar mechanisms also seem to occur in mice (*7*).

Other receptor-ligand pairs between dNK cells and trophoblasts may also be important to human placentation, such as the inhibitory receptors NK group 2A (NKG2A) and leukocyte immunoglobulin-like receptor B1 (LILRB1) (also expressed on macrophages), which bind to HLA-E and HLA-G, respectively. It has become apparent that, like adaptive immune responses, innate immunity also has some form of memory. During first pregnancies, LILRB1 and the activating receptor NKG2C (which also binds HLA-E) may trigger epigenetic DNA modifications in some dNK cells, potentially making them more active in subsequent pregnancies, which are less prone to preeclampsia provided the male partner does not change (*8*). Therefore, some form of immunological memory may facilitate placental invasion into the decidua.

The cellular networks operating in the decidua and placenta are starting to be revealed by technological advances. RNA sequencing in mouse dNK cells and related innate lymphoid cells (ILCs) has revealed further specialization of these cells in the decidua, where subpopulations of ILCs may play distinct roles in trophoblast invasion and vascular remodeling, immune defenses, and immunological memory (*9*). Single-cell RNA sequencing of the human maternal-fetal interface has begun to identify cellular and molecular networks (*10*). Decidual stromal cells produce interleukin-15 (IL-15), the key dNK cell growth factor. Fetal EVT cells produce transforming growth factor β (TGFβ), which promotes differentiation of maternal T_{regs}. Three subpopulations of dNK cells interact with both maternal and fetal cells using different receptor-ligand combinations (*10*). Analysis of both cell suspensions and tissue sections by mass cytometry should provide new functional and spatial information. Organoids (three-dimensional cell cultures that form structures morphologically similar to tissues in vivo) (*11*) of human trophoblasts cocultured with maternal immune cells with defined genetic backgrounds could also help to study these complex interactions.

Maternal and fetal cells in the decidua and placenta do not operate in isolation, and metabolism has a considerable impact on immune cell function. How do nutrition and oxygen concentration influence these interactions? Metabolomics analyses of the human placenta have started to decipher the differences between metabolites in maternal and fetal tissues (*12*) and might eventually integrate our growing appreciation of how metabolism shapes immune functions. Do microorganisms influence the immunology of placentation, thereby contributing to pregnancy complications? Labor may be precipitated by intrauterine infections, leading to preterm birth. The human genome harbors DNA from retroviruses that have helped trophoblasts to fuse together to form the syncytiotrophoblast, which separates the fetus from maternal blood. Maternal microbes or their products may influence fetal-placental development, and some evidence suggests that microbiota in the placenta and amniotic fluid may colonize the fetal gut in utero (*13*). However, other findings do not support the existence of a placental microbiota (*14*), and further research is needed.

Once cellular and molecular networks that regulate placentation are identified, the challenge will be to understand how these are altered in pregnancy complications. Are we ready to manipulate the human immune system during pregnancy to prevent complications? Despite the precedent of immunotherapy to prevent Rh disease, it remains too risky to interfere with the maternal immune system. Currently, anti-inflammatory and immunosuppressive drugs such as aspirin, hydroxychloroquine, and steroids are used to improve the outcome of preeclampsia, antiphospholipid syndrome (in which antibodies cause thrombosis and, in turn, potentially miscarriage), and chronic inflammation of the placental villi, or even to improve fertility. The benefit of these treatments is generally minimal and probably not specific. For example, aspirin may help treat preeclampsia because it reduces systemic endothelial inflammatory responses, but its use does not correct the primary defect at the maternal-fetal interface. There is optimism about immune checkpoint inhibitors (ICIs) to treat patients with cancer. These antibodies block inhibitory receptors and can reawaken antitumor immune responses to cancer cells, thereby improving survival. Subsets of dNK cells and T cells in the decidua express inhibitory receptors that can be targeted by ICIs, and trophoblasts express ligands for some of these receptors (*10*). Treating pregnant mice with ICIs causes fetal loss. However, three patients with melanoma treated with ICIs survived and had successful pregnancy outcomes [one case reported in (*15*)], illustrating the possibility of immunotherapy to target the maternal-fetal interface. Researchers are just starting to crack the immunological code of pregnancy and may one day intervene to improve outcomes. ■

Some maternal-fetal interactions in the decidua

Trophoblast cells transform uterine arteries into spiral arteries. Extravillous trophoblast cells bud off the placental villi to invade the decidua, where they interact with maternal immune cells through ligand-receptor pairs.

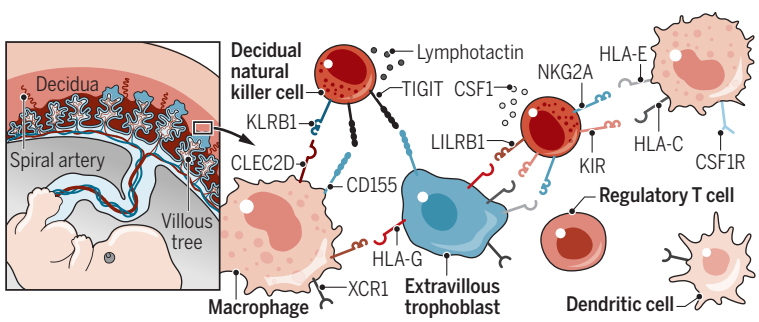

CLEC2D, C-type lectin domain family 2 member D; CSF1, colony-stimulating factor 1; CSF1R, CSF1 receptor; HLA, human leukocyte antigen; KIR, killer cell immunoglobulin-like receptor; KLRB1, killer cell lectin-like receptor B1; LILRB1, leukocyte immunoglobulin-like receptor B1; NKG2A, natural killer cell receptor G2A; TIGIT, T cell immunoreceptor with Ig and ITIM domains; XCR1, lymphotactin receptor; CD155, cluster of differentiation 155.

GRAPHIC: KELLIE HOLOSKI/*SCIENCE*

REFERENCES AND NOTES

1. I. Brosens, R. Pijnenborg, L. Vercruysse, R. Romero, *Am. J. Obstet. Gynecol.* **204**, 193 (2011).
2. A. Erlebacher, *Annu. Rev. Immunol.* **31**, 387 (2013).
3. S. A. Robertson *et al.*, *Front. Immunol.* **10**, 478 (2019).
4. M. Panduro, C. Benoist, D. Mathis, *Annu. Rev. Immunol.* **34**, 609 (2016).
5. A. A. Ashkar, J. P. Di Santo, B. A. Croy, *J. Exp. Med.* **192**, 259 (2000).
6. A. Moffett, F. Colucci, *J. Clin. Invest.* **124**, 1872 (2014).
7. J. Kieckbusch, L. M. Gaynor, A. Moffett, F. Colucci, *Nat. Commun.* **5**, 3359 (2014).
8. M. Gamliel *et al.*, *Immunity* **48**, 951 (2018).
9. I. Filipovic *et al.*, *Nat. Commun.* **9**, 4492 (2018).
10. R. Vento-Tormo *et al.*, *Nature* **563**, 347 (2018).
11. M. Y. Turco *et al.*, *Nature* **564**, 263 (2018).
12. J. M. Walejko, A. Chelliah, M. Keller-Wood, A. Gregg, A. Edison, *Metabolites* **8**, 10 (2018).
13. M. C. Collado, S. Rautava, J. Aakko, E. Isolauri, S. Salminen, *Sci. Rep.* **6**, 23129 (2016).
14. M. C. de Goffau *et al.*, *Nature* **572**, 329 (2019).
15. M. Burotto *et al.*, *Semin. Oncol.* **45**, 164 (2018).

ACKNOWLEDGMENTS

Supported by Wellcome Trust grant 200841/Z/16/Z.

10.1126/science.aaw1300

Published by AAAS

COMPUTER SCIENCE

AI surpasses humans at six-player poker

Self-learning Pluribus beats five humans in Texas hold'em showdown

By **Alan Blair** *and* **Abdallah Saffidine**

Superhuman performance by artificial intelligence (AI) has been demonstrated in two-player, deterministic, zero-sum, perfect-information games (*1*) such as chess, checkers (*2*), Hex, and Go (*3*). Research using AI has broadened to include games with challenging attributes such as randomness, multiple players, or imperfect information. Randomness is a feature of dice games, and card games include the additional complexity that each player sees some cards that are hidden from others. These aspects more closely resemble real-world situations, and this research may thus lead to algorithms with wider applicability. On page 885 of this issue, Brown and Sandholm (*4*) show that a new computer player called Pluribus exceeds human performance for six-player Texas hold'em poker.

Texas hold'em is a variant of poker where each player has two hidden cards and five communal cards from which to make the best poker hand. Scientists have previously demonstrated superhuman performance for two-player versions of the game: limit hold'em, where bets are capped (*5*), and no-limit hold'em, where they are not capped (*6*). Exceeding human performance in the six-player version had remained a challenge.

Games with three or more players represent a challenge for game theory. For two player, zero-sum games, a strategy exists where no player can improve their chances by switching to a different strategy. This so-called Nash equilibrium is considered a solution to the game. For multiplayer games, the expected reward may vary from one Nash equilibrium to another. Fast algorithms guaranteed to converge to a Nash equilibrium, such as counterfactual regret minimization (CFR), may fail to do so in multiplayer games. Nevertheless, CFR still shows promising empirical performance in some multiplayer domains.

Pluribus first learns a generic or "blueprint" strategy by self-play. Then, during actual play, it computes a real-time strategy to refine the blueprint strategy, depending on the current state of the game. The program learns the blueprint strategy through a CFR variant called Monte Carlo CFR (MCCFR) (*7*), with a number of enhancements. Pluribus repeatedly simulates hands of poker in which all players use the same strategy; after each hand, it recursively examines each decision and estimates the expected outcome from that decision, compared to other possible actions that could have been chosen in the same situation.

To improve the efficiency of MCCFR in Pluribus, the authors introduced linear weighted discounting in the early stages of training, and strategic pruning of negative-regret actions in the later stages. The most intricate part of the system is the real-time strategy component. To deal with imperfect information, Pluribus performs a nested search, maintaining a probability distribution of root nodes for the search tree and of the cards held by each player, conditioned on the assumption that all players are using the same (known) strategy. To evaluate leaf nodes robustly, Pluribus considers four different variants of the blueprint strategy.

For large and complex games, abstraction of states and actions can be used to restrain the growth of the search tree (*8*). This is necessary for the full six-player no-limit Texas hold'em game, which is too complex to search directly. Instead, Pluribus simulates a simpler version of the game by bucketing similar decision points together and eliminating some actions (see the figure). For example, the blueprint strategy considers

Abstraction in game tree search

In its abstraction mechanism, Pluribus shrinks the number of decision points on whether to call, raise, or fold by bucketing similar situations together. This reduces the game tree search complexity in poker from an intractable to a solvable problem, using Monte Carlo counterfactual regret minimization (MCCFR).

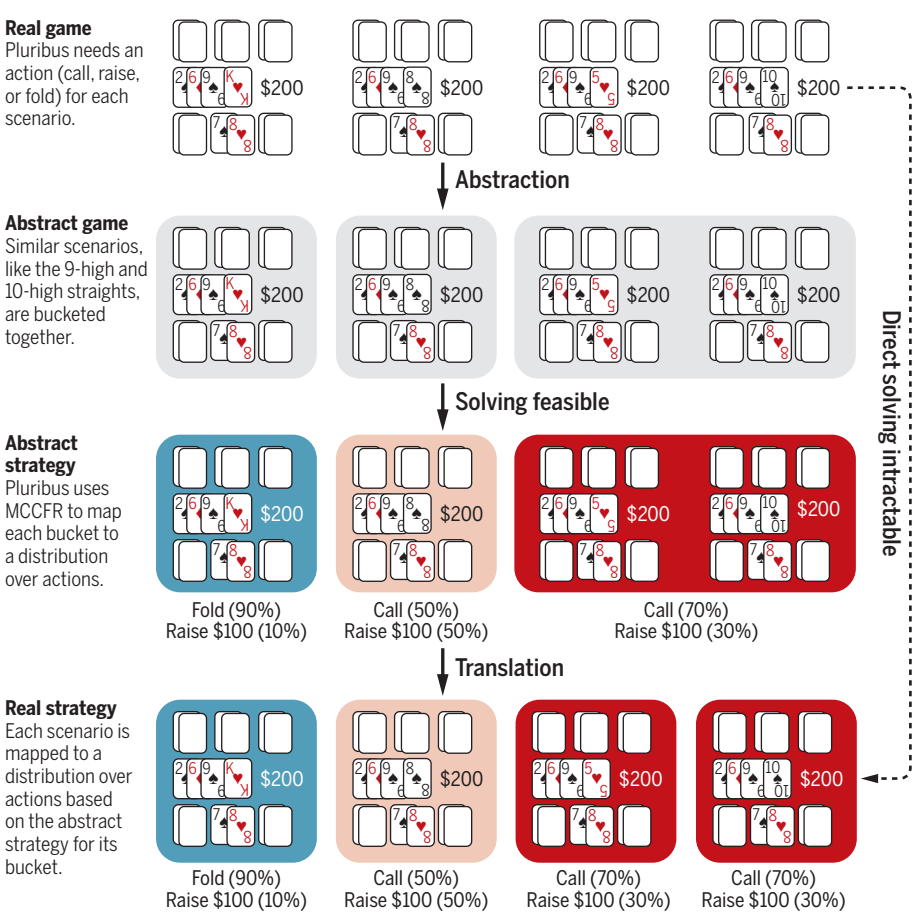

GRAPHIC: A. KITTERMAN/*SCIENCE*

School of Computer Science and Engineering, University of New South Wales, Sydney 2052, Australia. Email: blair@cse.unsw.edu.au; abdallahs@cse.unsw.edu.au

Published by AAAS

only a limited number of standard bet sizes, depending on the situation. During actual play, if the opponent bet is close enough to a standard bet size, action translation can be used to apply the blueprint strategy directly. Otherwise, Pluribus uses a real-time search, based on the actual bet size. These and other enhancements make Pluribus very computationally efficient.

The authors tested Pluribus in a series of matches. It played both against five professional human players and with one human against five Pluribus copies. Pluribus achieved superhuman performance in both cases. It plays in a style that is generally consistent with human preferences; nevertheless, just as the AI programs Chinook, TD-Gammon, and AlphaGo Zero led to a reexamining of accepted opening moves and replies, Pluribus may also challenge certain traditional beliefs about poker strategy.

Many challenges remain in the area of game learning. One target is the card game bridge, which has a larger number of game positions. Real-time strategy (RTS) games such as StarCraft (*9*) require continuous actions, and hidden information often grows as the game progresses. Coordination with teammates is a factor in some RTS games like Dota (*10*), and RoboCup Soccer, which also involves physical embodiment. Nimble adaptation to exploit the weaknesses of its opponents is another challenging area for an AI player that has only been explored to a limited degree for complex games. Algorithms like CFR have recently been applied to security games (*11*), potentially allowing methods such as those developed by Brown and Sandholm to tackle real-world problems, including infrastructure and environmental resource protection (*12*). ■

REFERENCES AND NOTES

1. H. J. van den Herik, J. W. H. M. Uiterwijk, J. van Rijswijck, *Artif. Intell.* **134**, 277 (2002).
2. J. Schaeffer *et al.*, *Science* **317**, 1518 (2007).
3. D. Silver *et al.*, *Nature* **550**, 354 (2017).
4. N. Brown, T. Sandholm, *Science* **365**, 885 (2019).
5. M. Bowling, N. Burch, M. Johanson, O. Tammelin, *Science* **347**, 145 (2015).
6. N. Brown, T. Sandholm, *Science* **359**, 418 (2018).
7. M. Zinkevich, M. I Johanson, M. Bowling, C. Piccione, *Advances in Neural Information Processing Systems* (MIT Press, 2008), pp. 1729–1736.
8. M. Johanson, N. Burch, R. Valenzano, M. Bowling, *in Proceedings of the 2013 International Conference on Autonomous Agents and Multiagent Systems* (IFAAMAS, 2013), pp. 271–278.
9. M. Čertický, D. Churchill, in *Thirteenth Artificial Intelligence and Interactive Digital Entertainment Conference* (2017).
10. J. M. F. Fernandez, T. Mahlmann, in *IEEE Transactions on Games* 10:1109/TG.2018.283456 (2018).
11. V. Lisy, T. Davis, M. Bowling, in *Thirtieth AAAI Conference on Artificial Intelligence* (AAAI, 2016), pp. 544–550.
12. F. Fang, P. Stone, M. Tambe, in *Twenty-Fourth International Joint Conference on Artificial Intelligence* (2015), pp. 2589–2595.

ACKNOWLEDGMENTS

The authors contributed equally to this work.

10.1126/science.aay7774

PHOTO: FUNKYFOOD LONDON/PAUL WILLIAMS/ALAMY STOCK PHOTO

ENVIRONMENTAL SCIENCE

How humans changed the face of Earth

Archaeological evidence shows that anthropogenic changes began earlier and spread faster than previously estimated

By **Neil Roberts**[1,2]

Scientists across disciplines have been debating potential dates for the beginning of the Anthropocene—the period during which human activity has become a dominant influence on climate change and the global environment (*1*, *2*). Recorded history has provided information with which to chart Earth's environmental changes during recent centuries. But how can it be determined if and when human activities transformed Earth during the time before written records? This question is prompted in part by the hypothesis that prehistoric deforestation and rice farming might explain the preindustrial upturn in atmospheric methane and carbon dioxide concentrations after ~7000 years ago (*3*). On page 897 of this issue, Stephens *et al.* (*4*) describe efforts by the ArchaeoGLOBE Project to crowdsource information from the global archaeological community, synthesize the data, and generate semiquantitative estimates of how various types of land use have altered Earth during the past ten millennia.

For much of the past millennium, scientists have used documentary records to reconstruct historical changes in Earth's land cover. For example, information in William the Conqueror's Domesday Survey (*5*) showed that only 15% of the surveyed land was still forested in 1086 CE; evidently, much of England's primeval wildwood had already been cleared by medieval times. Further back in time, documentary sources dry up, forcing scientists to turn to other "proxy" data sources, such as archaeology and paleoecology. Archaeological data have long been recognized as a vital source of evidence, but until recently, scaling up the data to reconstruct global trends and patterns has been done only qualitatively and incompletely.

The work by Stephens *et al.* concludes that Earth had already been substantially transformed by human activities as early as 3000 years ago. This time point for anthropogenic changes in land cover fits with several other lines of evidence (for example, reconstructions of forest loss in temperate Europe) (*6*, *7*) and broadly supports the hypothesis of Ruddiman *et al.* (*3*). On the other hand, the conclusions of Stephens *et al.* stand in contrast to the limited amount of prehistoric change reconstructed by the widely used History Database of the Global Environment (HYDE) model, which simulates past global land cover (*8*). In light of the ArchaeoGLOBE synthesis, low-end estimates for early human impact, such as in the HYDE model, become less tenable.

By the time humans abandoned this archaeological site (Mycenae, Greece) ~3000 years ago, they had already substantially transformed Earth's land surface.

The ArchaeoGLOBE synthesis is by no means the last word in the story, and by its very nature, archaeological evidence carries a number of inherent biases. In particular, archaeological data come from places inhabited by people, especially farmers (the Ecumene), rather than from parts of Earth's surface where few or no humans lived—what might today be called "wilderness areas." The ArchaeoGLOBE results, therefore, say more about the villages, fields, and paths where the proverbial Goldilocks safely lived, but much less about the surrounding wildwood inhabited by wolves and bears, and almost nothing about remote high mountains or polar deserts. Thus, it is perhaps unsurprising that Stephens *et al.* conclude that human transformation of Earth's land surface occurred at an early date.

[1]*School of Geography, Earth and Environmental Sciences, University of Plymouth, Plymouth, UK.* [2]*School of Archaeology, University of Oxford, Oxford, UK.*
Email: c.n.roberts@plymouth.ac.uk

Published by AAAS

Other empirical datasets exist that are free of this bias (for example, pollen, insect, and other paleoecological evidence); an obvious next step is to conduct a systematic comparison of these paleodata, archaeological datasets, and modeled simulations. Comparisons of regions with long histories of farming and pastoralism (such as Europe and China) over the past six millennia should show similar overall trajectories for land-cover change regardless of which data source is used, but this is clearly not the case for most regions (see the figure). In temperate Europe and northeastern China, the HYDE model shows an exponential increase in agricultural and grazing land after ~1000 years ago. By contrast, the ArchaeoGLOBE results for these regions show substantial human land conversion prior to 3000 years ago, whereas the curve for the proportion of open land according to pollen-based estimates lies somewhere in between the other two. A similar contrast is evident at a global scale, for which pollen data are not yet available. Only in Europe's boreal forest zone do temporal trends look similar regardless of the method used (see the figure). The Past Global Changes LandCover6k program is currently performing systematic intercomparison among the three data sources (*9*). These efforts must be harmonized with those of the ArchaeoGLOBE community to achieve truly multiproxy reconstructions of past land-cover changes.

The impressive results of collaborative "big data" analyses by the ArchaeoGLOBE team indicate that human transformation of Earth's land surface began well before the testing of the first atomic bomb, invention of the steam engine, or other proposed markers for the onset of the Anthropocene (*1*, *2*). A recent report from the Intergovernmental Panel on Climate Change (IPCC) (*10*) makes clear that better land management has a key role to play in keeping global warming to below 2°C. For this to occur, it is essential to take a long-term view on carbon release and the changing use of land. The ArchaeoGLOBE results should aid scientists in this endeavor. ■

REFERENCES AND NOTES

1. B. D. Smith, M. A. Zeder, *Anthropocene* **4**, 8 (2013).
2. S. L. Lewis, M. A. Maslin, *Nature* **519**, 171 (2015).
3. W. F. Ruddiman *et al.*, *Rev. Geophys.* **54**, 93 (2016).
4. ArchaeoGLOBE Project, *Science* **365**, 897 (2019).
5. O. Rackham, *Ancient Woodland: Its History, Vegetation and Uses in England* (Castlepoint Press, ed. 2, 2003).
6. J. O. Kaplan *et al.*, *Land* **6**, 91 (2017).
7. N. Roberts *et al.*, *Sci. Rep.* **8**, 716 (2018).
8. K. Klein Goldewijk, A. Beusen, J. Doelman, E. Stehfest, *Earth Syst. Sci. Data* **9**, 927 (2017).
9. S. P. Harrison *et al.*, *Geosci. Model Dev. Discuss.* 10.5194/gmd-2019-125 (2019).
10. IPCC, *Climate Change and Land, Summary for Policymakers* (2019); www.ipcc.ch/report/srccl.
11. F. Li *et al.*, *Past Glob. Changes Mag.* **26**, 32 (2018).
12. L. Marquer *et al.*, Pollen-based REVEALS estimates of plant cover in Europe for 36 grid-cells and the last 11700 years, PANGAEA (2019) ; https://doi.org/10.1594/PANGAEA.900966.

ACKNOWLEDGMENTS

The author thanks M.-J. Gaillard, F. Li, L. Marquer, and L. Stephens for providing data used in the figure.

10.1126/science.aay4627

Human-driven changes in Earth's land cover

Reconstructions of the extent of agricultural and pasture land based on archaeological, modeled, and pollen data show agreement in some regions but differ widely in others. Changes after 1850 CE are not shown.

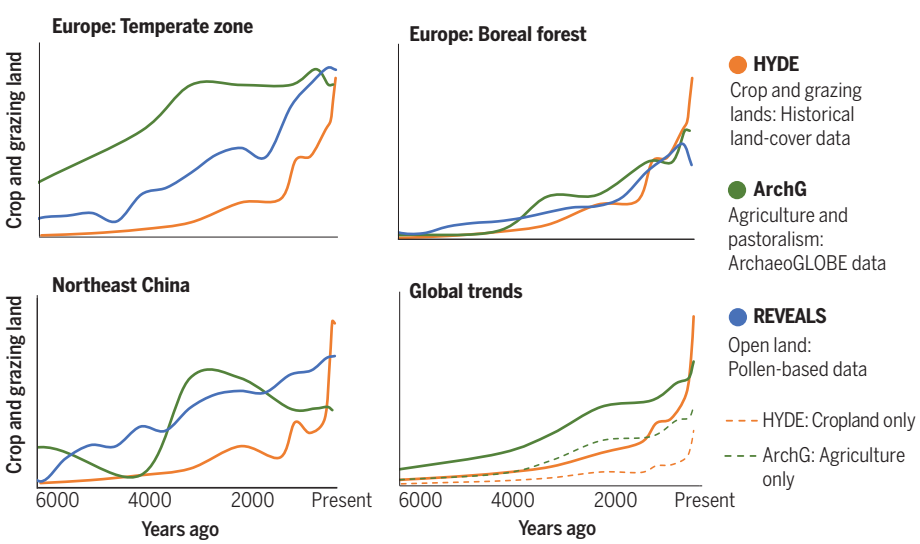

Units of measurement differ among the methods; for simplification, the graphs show indicative trends on the *y* axis. History Database of the Global Environment (HYDE) simulations in million hectares (for all of Europe and all of China), from (*8*); pollen-based Regional Estimates of Vegetation Abundance from Large Sites (REVEALS) estimates are percentage of total land area, from (*11*, *12*); ArchaeoGLOBE (ArchG) data are minimum percentage areas, from (*4*). Global HYDE data for cropland (dashed orange) and ArchG data for all agriculture (dashed green) are shown separately and combined with grazing land.

CATALYSIS

The Mitsunobu reaction, reimagined

Catalytic nucleophilic substitution of alcohols makes organic synthesis greener

By **Lars Longwitz** *and* **Thomas Werner**

Nucleophilic substitution reactions are widely used to create carbon–heteroatom and carbon–carbon bonds as part of the synthesis of natural products and other organic molecules. These reactions typically involve a pronucleophile (NuH) and an electrophile that bears a suitable leaving group. Alcohols are often used as electrophiles because they are inexpensive and readily available. During the direct nucleophilic substitution between an alcohol and a pronucleophile, the alcohol's hydroxyl group would be replaced with the nucleophile, forming water as the sole byproduct. In the case of chiral secondary alcohols, the bimolecular substitution would lead to the substituted product with inverted stereochemistry. However, alcohols usually do not react with pronucleophiles without being activated prior to the substitution. On page 910 of this issue, Beddoe *et al.* (*1*) report an easily accessible catalyst that facilitates the direct nucleophilic substitution.

The authors' work is based on the Mitsunobu reaction, in which stoichiometric amounts of a phosphane and azodicarboxylate reagent activate the otherwise inert alcohol, promoting coupling with a wide variety of nucleophilic reaction partners (*2*, *3*). This chemistry was first reported in 1967 by Oyo Mitsunobu (*4*) and has since become a powerful synthetic tool. However, the need for stoichiometric quantitites of hazardous reagents leads to a substantial amount of waste, which does not comply with the main principles of green chemistry and sustainable synthesis, such as the principle of atom economy (*5*). A method using catalytic amounts of both the azo reagent and phosphane—called a fully catalytic Mitsunobu reaction system—could be a greener alternative but is difficult to achieve (*6*).

Leibniz Institute for Catalysis, Albert-Einstein-Str. 29a, 18059 Rostock, Germany. Email: thomas.werner@catalysis.de

GRAPHIC: N. CARY/*SCIENCE*

Published by AAAS

Beddoe *et al.* now achieve this goal, by means of a redox-neutral organocatalytic Mitsunobu reaction. Most notably, their protocol is based on a single, easily accessible catalyst; no further stoichiometric reductants or oxidants are required. Furthermore, the only by-product is water, greatly increasing the overall atom economy of the reaction. The structure of the catalyst seems simple: a tertiary phosphane oxide bearing a phenolic group (see the figure). On second glance, however, it becomes clear that the design is brilliant, because it enables the dehydrative coupling of primary and secondary alcohols with various pronucleophiles. Initially, the catalyst reacts with the pronucleophile to form a cyclic oxyphosphonium salt while releasing water. The alcohol then reacts with the phosphonium salt, forming a new P–O bond and simultaneously liberating the phenolic side chain of the catalyst. This represents the activated substrate, which eventually reacts with the nucleophile, forming the substitution product under liberation of the catalyst.

The authors show that this reaction works for a broad range of primary (R= H) and secondary (R, R′ ≠ H) alcohols. They converted chiral alcohols under stereochemical inversion to the respective substituted products with excellent selectivity. As they demonstrate, the methodology allows the use of various pronucleophiles, leading to the formation of C–O, C–N, and C–S bonds.

Beddoe *et al.*'s approach differs conceptually from earlier attempts to realize catalytic Mitsunobu reactions. Previous strategies stayed close to the original procedure, introducing additional reagents and catalysts to regenerate the phosphane or azodicarboxylate and thereby realize protocols that were catalytic in these components.

In 2006, But and Toy reported a variant of the Mitsunobu reaction that was catalytic in the azo reagent, using an iodine-based oxidant to regenerate the azo reagent (*7*). In 2013, Taniguchi *et al.* (*8*) described further developments in this direction, showing that molecular oxygen from air could serve as the terminal oxidant in the presence of an iron catalyst. However, besides the increased complexity of the overall systems, both procedures still required overstoichiometric amounts of the phosphane.

Two years later, Buonomo and Aldrich realized a protocol that was catalytic in phosphane by using stoichiometric amounts of a silane to regenerate the phosphane. The authors combined this with the above-mentioned catalytic system of Taniguchi to realize a fully catalytic Mitsunobu reaction (*9*). However, these findings were reevaluated and critically discussed in the community (*10*, *11*). Taniguchi and co-workers performed a detailed study on the fully catalytic system and showed that the reaction proceeds under retention of configuration and that the azo reagent does not participate (*10*). They concluded that the fully catalytic Mitsunobu reaction was not realized.

These previous findings underline the tremendous challenges associated with the development of a fully catalytic system based on the original Mitsunobu protocol. It has proved difficult to realize a catalytic system by implementing a selective reducing agent to regenerate the phosphane in the presence of an oxidizing agent to regain the azodicarboxylate.

Instead of trying to find a perhaps unachievable balance in reactivity and selectivity, Beddoe *et al.*'s catalyst circumvents the above-mentioned challenges. Their system provides an exciting approach to the long-standing challenge of the direct bimolecular substitution of nonactivated chiral alcohols, delivers a new platform in organocatalysis, and offers new possibilities for sustainable organic synthesis. ■

Catalytic substitution of alcohols

Beddoe *et al.* report a redox-neutral organocatalytic analog of the stoichiometric Mitsunobu reaction for substituting otherwise inert alcohols.

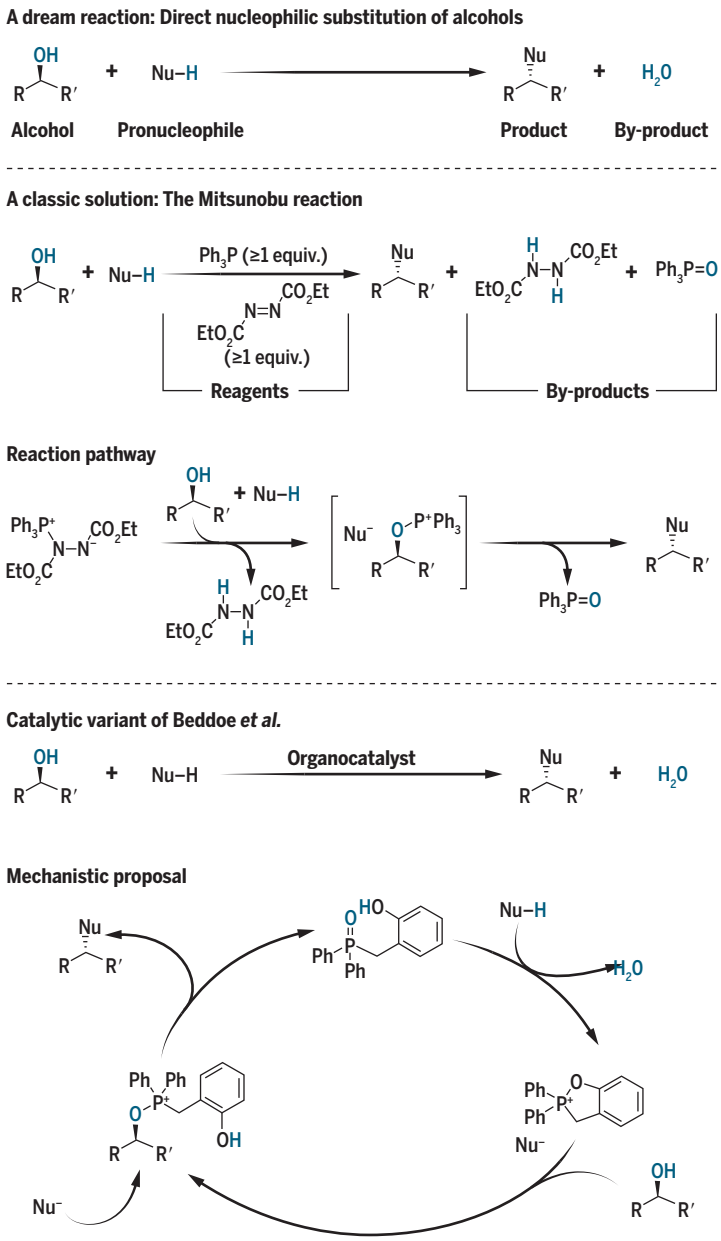

Nu, nucleophile; R and/or R′, H, alkyl, aryl, etc.; Et, ethyl; Ph, phenyl.

GRAPHIC: C. BICKEL/*SCIENCE*

REFERENCES AND NOTES

1. R. H. Beddoe *et al.*, *Science* **365**, 910 (2019).
2. K. C. K. Swamy, N. N. B. Kumar, E. Balaraman, K. V. P. P. Kumar, *Chem. Rev.* **109**, 2551 (2009).
3. O. Mitsunobu, *Synthesis* **1981**, 1 (1981).
4. M. Oyo, Y. Masaaki, M. Teruaki, *Bull. Chem. Soc. Jpn.* **40**, 935 (1967).
5. B. M. Trost, *Science* **254**, 1471 (1991).
6. S. Fletcher, *Org. Chem. Front.* **2**, 739 (2015).
7. T. Y. S. But, P. H. Toy, *J. Am. Chem. Soc.* **128**, 9636 (2006).
8. D. Hirose, T. Taniguchi, H. Ishibashi, *Angew. Chem. Int. Ed.* **52**, 4613 (2013).
9. J. A. Buonomo, C. C. Aldrich, *Angew. Chem. Int. Ed.* **54**, 13041 (2015).
10. D. Hirose, M. Gazvoda, J. Košmrlj, T. Taniguchi, *Org. Lett.* **18**, 4036 (2016).
11. R. H. Beddoe, H. F. Sneddon, R. M. Denton, *Org. Biomol. Chem.* **16**, 7774 (2018).

ACKNOWLEDGMENTS

We are grateful for support from the Leibniz ScienceCampus Phosphorus Research Rostock (www.sciencecampus-rostock.de).

10.1126/science.aay6635

Published by AAAS

PLANT BIOLOGY

Bacteria send messages to colonize plant roots

Bacteria-derived RNA fragments target host plant genes to promote root colonization

By **Patricia Baldrich**[1] and **Blake C. Meyers**[1,2]

Studied for more than 130 years (*1*), the intimate and unusual relationship established between legumes and nitrogen-fixing bacteria (*Rhizobia*) allows plants to use atmospheric nitrogen in exchange for their photosynthetic-derived carbohydrates. The production of root nodules in which the symbiotic interaction takes place requires complex developmental regulation by the plant. Nodules are relatively distinct organs among plant species, essentially representing a controlled microbial invasion of the root. Somewhat like the human gut, the plant provides an environment in which specific microbes can thrive—but unlike the gut, nodule microbial composition is limited to a small number of species. The genetic control of nodulation development is complex, with recent work showing a dependency on small RNAs (sRNAs) trafficked from shoot to root (*2*). On page 919 of this issue, Ren *et al.* (*3*) identify bacteria-derived transfer RNA (tRNA)–derived fragments (tRFs) as modulators of the process of nodulation.

In plants, sRNAs are classified into at least three pathways: microRNAs, heterochromatic short-interfering RNAs (hc-siRNAs), and phased secondary siRNAs (phasiRNAs). All three of these pathways require the enzyme Dicer, which processes longer RNAs into smaller RNAs. However, since the earliest days of large-scale RNA sequencing studies, a large class of structural RNA fragments have been identified but largely ignored. These sequences, mostly originating from ribosomal RNAs and tRNAs, were considered degradation products, unavoidably captured during RNA sequencing and of little functional importance.

tRNAs are one of the most conserved and abundant RNA species in cells; they function to decode messenger RNA (mRNA) into proteins in ribosomes. tRNAs have a distinctive cloverleaf structure, containing three hairpin loops, with a specific amino acid attached to the end that is used to translate codons in the mRNA to an amino acid transferred to the end of a growing protein. During the tRNA biogenesis process, or under specific conditions, cleavage yields tRFs. These ~17- to 22-nucleotide (nt) fragments have few known functions, one of which is a role in genome protection against transposable elements (TEs) (*4*, *5*). TEs are widespread repetitive genome sequences derived from viruses that have the ability to mobilize. Their mobilization in the "host" genome is typically suppressed because the potential disruption of host genome sequences (mutations or genome rearrangements) might be detrimental for fitness. The association of tRFs with the ARGONAUTE (AGO) proteins that mediate sRNA-target interactions has also been described (*6*), as well as their Dicer dependency (*5*), suggesting that tRFs function in posttranscriptional control.

From sRNA sequencing data, Ren *et al.* identified tRFs from the rhizobium *Bradyrhizobium japonicum*, which are enriched in planta and predicted to target 52 genes in the soybean (*Glycine max*) genome. Three of these genes—*GmRHD3*, *GmHAM4*, and *GmLRX5*, which are orthologs of *Arabidopsis thaliana* genes *ROOT HAIR DEFECTIVE 3* (*RHD3*), *HAIRY MERISTEM 4* (*HAM4*), and *LEUCINE-RICH REPEAT EXTENSIN-LIKE 5* (*LRX5*), respectively—are directly involved in development, including that of root hairs. This is particularly important because nodulation starts when the tip of a hair root curls around a rhyzobial cell, creating a small tube, the infection thread, that will provide a path for the bacteria to reach the root epidermal cells. Ren *et al.* found that the 21-nt tRFs produced by the bacteria are loaded into the soybean AGO1 protein, subsequently interacting with target genes in a sequence homology–dependent manner (see the figure). A series of experiments demonstrated that these genes are critical for the early stages of the establishment of the root nodulation process, and in planta suppression of the tRFs supports a role for them in promoting the infection process.

To determine whether this regulatory process is conserved across evolutionarily related nodulating legumes, Ren *et al.* examined the compatible symbiotic interaction established between the common bean and its symbiotic partner, *Rhizobium etli*. The authors found that a different set of tRFs target a different set of genes in this host plant. These results suggest that the use of bacterial tRFs to target host genes might be conserved, whereas the tRFs and their target genes may vary across species. These findings, combined with previous studies on plant sRNAs involved in the nodulation process (*2*), highlight the complexity of the regulatory network that occurs during the establishment of nodulation.

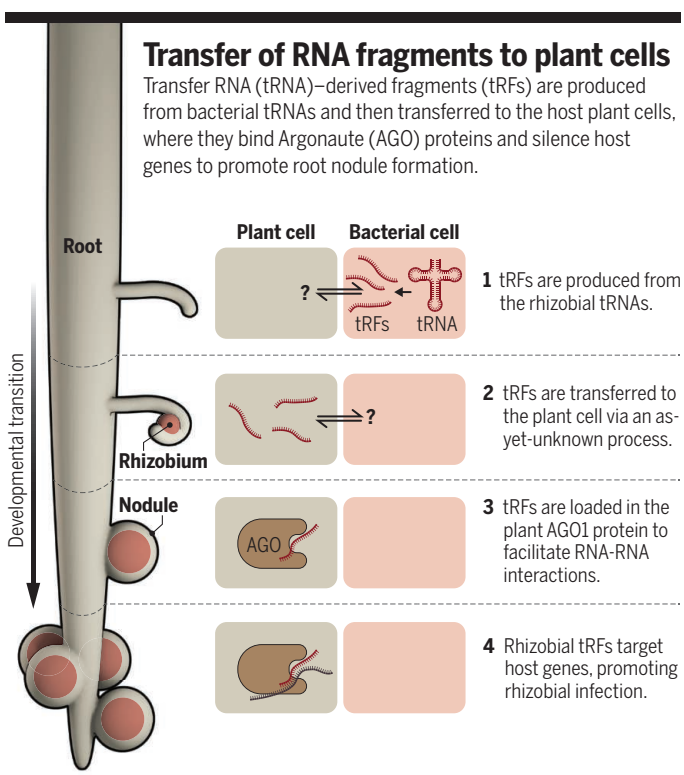

GRAPHIC: V. ALTOUNIAN/*SCIENCE*

[1]*Donald Danforth Plant Science Center, Saint Louis, MO 63132, USA.* [2]*Division of Plant Sciences, University of Missouri–Columbia, Columbia, MO 65211, USA. Email: pbaldrich@danforthcenter.org; bmeyers@danforthcenter.org*

Published by AAAS

There are still many questions to be addressed. Plants have a remarkable ability to distinguish between friends and foes, allowing *Rhizobia* to enter the root while keeping other pathogenic bacteria outside. Could this tRF regulation be critical to distinguish symbiotic and pathogenic bacteria? In other words, do plant pathogenic bacteria also use tRFs to hijack the host cellular machinery and trigger disease? It is also unknown how bacteria produce tRFs or whether they are produced under normal growing conditions or the specific tRFs necessary to trigger nodulation are only produced when needed. Recent studies have demonstrated that sRNAs are transferred from pathogen to host by using extracellular vesicles (*7*, *8*). Future work might address whether tRFs are also transported in vesicles from the bacterial cell to the host and whether the vesicles guide the tRFs to the appropriate AGO protein.

"...these genes are critical for the early stages of the establishment of the root nodulation process..."

Since the discovery in the late 19th century of biological symbiotic nitrogen fixation, efforts have focused on the transfer of the trait into cereals and other nonleguminous crops (*9*). This would reduce the use of nitrogen-based fertilizers, cutting down the economic and environmental cost of agriculture, without diminishing yield. However, this naturally occurring process is complex and finely regulated, and success in its transfer depends on a comprehensive understanding of the mechanics behind the legume-rhizobium symbiosis. The discovery of tRFs as key symbiotic regulators arguably brings us one step closer to the use of this beneficial natural phenomenon in a broader range of plant species. ■

REFERENCES AND NOTES

1. J. B. Lawes, J. H. Gilbert, *Philos. Trans. R. Soc. Biol. Sci.* **180**, 1 (1889).
2. D. Tsikou *et al.*, *Science* **362**, 233 (2018).
3. B. Ren, X. Wang, J. Duan, J. Ma, *Science* **365**, 919 (2019).
4. G. Martinez, *Mob. Genet. Elements* **7**, 1 (2017).
5. G. Martinez, S. G. Choudury, R. K. Slotkin, *Nucleic Acids Res.* **45**, 5142 (2017).
6. G. Loss-Morais, P. M. Waterhouse, R. Margis, *Biol. Direct* **8**, 1 (2013).
7. Q. Cai *et al.*, *Science* **360**, 1126 (2018).
8. P. Baldrich *et al.*, *Plant Cell* **31**, 315 (2019).
9. A. Quispel, *Acta Bot. Neerl.* **3**, 495 (1954).

ACKNOWLEDGMENTS

We acknowledge the support of the National Science Foundation (IOS award 1842698).

10.1126/science.aay7101

GENOMICS

How do genes affect same-sex behavior?

Genetic loci linked with same-sex sexual behavior cannot predict orientation of individuals

By **Melinda C. Mills**

Studies have indicated that same-sex orientation and behavior has a genetic basis and runs in families, yet specific genetic variants have not been isolated (*1*). Evidence that sexual orientation has a biological component could shape acceptance and legal protection: 4 to 10% of individuals report ever engaging in same-sex behavior in the United States, so this could affect a sizeable proportion of the population (*2*). On page 882 of this issue, Ganna *et al.* (*3*) report the largest study to date, comprising almost half a million individuals in the United Kingdom and United States, identifying genetic variants associated with same-sex sexual behavior. They provide evidence that genetic variation accounts for a small fraction of same-sex sexual behavior and uncover a relationship to the regulation of the sex hormones testosterone and estrogen as well as sex-specific differences. They also reveal complexity of human sexuality.

The genetic basis of same-sex orientation and sexual behavior has evaded discovery, largely because of the challenges of using small and nonrepresentative cohorts. Initial evidence focused mostly on gay men, providing indirect and often speculative evidence of a relationship with fraternal birth order, prenatal exposure to sex hormones, neurodevelopmental traits, or maternal immunization to sex-specific proteins (*4*). Work in the 1990s isolated a relationship with the Xq28 region on the X chromosome (*5*, *6*). Subsequent studies found similarity in the sexual orientation of identical twins, with genetics explaining 18% (for women) and 37% (for men), with the remainder accounted for by directly shared environments (such as family or school) and nonshared environments (such as legalization or norms regarding same-sex behavior) (*7*). Many of these studies could not be replicated, and although twin and family studies found a genetic basis, they could not isolate variants associated with same-sex orientation at specific genetic loci.

Department of Sociology, University of Oxford, 42 Park End Street, Oxford, OX1 1JD, UK. Email: melinda.mills@nuffield.ox.ac.uk

The study of Ganna *et al.* involved a genome-wide association study (GWAS), in which the genome is analyzed for statistically significant associations between single-nucleotide polymorphisms (SNPs) and a particular trait. SNPs are single-nucleotide base differences in DNA that allow the measurement of variation in a population. The approach of using a large cohort, sex-specific analyses, and complex measures of sexuality (for example, proportion of same-sex partners to total sexual partners, attraction, and identity) allowed the detection of genetic—and even sex-specific—variants that had evaded prior research.

Ganna *et al.* analyzed the association of ever having sex with a same-sex partner with SNPs in genomes from the UK Biobank (408,995 individuals) and from 23andMe (68,527 individuals from the United States), with more males having engaged in same sex behavior than females across equally sex-divided cohorts. They discovered five loci that correlate with ever having same-sex behavior: two loci across both sexes, two in males, and one in females. Comparatively, the average number of loci found in all GWASs from 2005 to 2018 is 13.6, but as cohort sizes increased to over a million, many GWASs since 2016 now find hundreds or even thousands of loci (*8*). One of the most intriguing findings of Ganna *et al.* are differences in genetic contribution between males and females to same-sex sexual behavior and the weak across-sex genetic correlation of 0.63. A genetic correlation of 1 denotes perfect association with genetic variation between the sexes, a score of 0 denotes no correlation. For comparison, related traits such as reproductive behavior have a high genetic correlation between males and females of 0.86 for an individual's age when they have their first baby and 0.97 for the number of children ever born to an individual (*9*). They speculate that the reason for the differences in genetic contribution between the sexes may be biological (related to testosterone and estrogen) and nongenetic factors, such as gendered social norms about sexual behavior. It is also noteworthy that Ganna *et al.* do not find evidence that sexual orientation is associated with variants on the X chromosome (*5*, *6*).

Published by AAAS

When using a different technique called SNP-heritability—comparing the genetic similarity of all unrelated individuals in the sample with their phenotypic similarity of same-sex sexual behavior—Ganna *et al.* found that genetics could eventually account for an upper limit of 8 to 25% of same-sex sexual behavior of the population. However, when all of the SNPs they identified from the GWAS are considered together in a combined score, they explain less than 1%. Thus, although they did find particular genetic loci associated with same-sex behavior, when they combine the effects of these loci together into one comprehensive score, the effects are so small (under 1%) that this genetic score cannot in any way be used to predict same-sex sexual behavior of an individual. This difference between the population SNP-based estimates of 8 to 25% versus individual polygenic estimates (multiple SNPs combined) of the influence of genetic variation on same-sex sexual behavior of 1% is attributed to a lack of measuring rare variants; polygenicity, in which many variants have small effects; or nonadditive genetic effects, such as dominance or epistasis.

In 1948, the biologist Alfred Kinsey proposed the "heterosexual-homosexual rating scale," specific to men, which ranges from exclusively heterosexual to exclusively homosexual, measured with the same scale for all sexualities (*10*). Ganna *et al.* nuanced this approach and undertook an additional GWAS of the proportion of same-sex partners to total partners (using the UK Biobank data), and from 23andMe, the question "With whom have you had sex?" with answers ranging from "other sex mostly" across six categories to "same sex only." The genetic correlation identified in the GWAS of whether a person had ever engaged in sex with someone of the same sex and the more complex measure of proportion of same-sex partners was 0.73 for men but only 0.52 for women. This means that genetic variation has a higher influence on same-sex sexual behavior in men than in women and also demonstrates the complexity of women's sexuality. This may also reflect sex-specific social norms regarding the number of sexual partners women have, particularly given the age range of participants in this study. In addition to showing sex differences, what is striking is that these different measures of sexuality—proportion of same-sex partners and engagement in same-sex sexual behavior—are associated with different genetic loci and with other traits. The finding that the genetic effects differentiating heterosexual from same-sex sexual behavior are distinctive, particularly in relation to the number of sexual partners and other sexual measures (identification and attraction), challenges the use of Kinsey's scale across all groups. This reflects voices from the LGBTQ+ (lesbian, gay, bisexual, transgender, queer+) community arguing that a range of sexualities exist. Sexuality is dynamic, with the ability to express and realize sexual preferences, and is thus also shaped and regulated by cultural, political, social, legal, and religious structures.

Ganna *et al.* did not find evidence of any specific cells and tissues related to the loci they identified. Male-specific loci that were associated with ever experiencing same-sex behavior were linked to olfactory receptor genes, sensitivity to certain scents, and regulation of testosterone and estrogen by a variant located upstream of the transcription factor 12 (*TCF12*) gene, which is essential for gonad development in mice, and a variant located downstream of the sex-determining region Y (*SRY*) gene, which is responsible for male sex determination in humans.

A caveat common to most genetic discoveries (*8*) is that the study of Ganna *et al.* includes only European-ancestry populations from Western high-income countries (United Kingdom, United States, and Sweden for replication). The data also come from older individuals living under stricter social norms and legislative regulations (23andMe, mean age 51.3 years; UK Biobank, aged 40 to 69 years), overrepresented by higher socioeconomic status groups (*11*). Although a more complex continuum beyond two categories of ever having sex with someone of the same sex was possible by using the 23andMe cohort, these data had an unusually high number of individuals who ever had same-sex partners (19%), potentially biasing the data.

There is an inclination to reduce sexuality to genetic determinism or to resent this reduction. Attributing same-sex orientation to genetics could enhance civil rights or reduce stigma. Conversely, there are fears it provides a tool for intervention or "cure." Same-sex orientation has been classified as pathological and illegal and remains criminalized in more than 70 countries, some with the death penalty. Because Ganna *et al.* found that the genetic loci they isolated predict less than 1% of same-sex behavior of individuals, using these results for prediction, intervention, or a supposed "cure" is wholly and unreservedly impossible. Rather, by calculating the ceiling of what is potentially attributed to genetics with a SNP-heritability of 8 to 25% and isolating specific loci, this study serves as a guide to the potential magnitude of genetic effects we may eventually measure and a sign that complex behaviors continue to have small, likely polygenic, influences. Future work should investigate how genetic predispositions are altered by environmental factors, with this study highlighting the need for a multidisciplinary sociogenomic approach. ■

REFERENCES AND NOTES

1. R. C. Pillard, J. M. Bailey, *Hum. Biol.* **70**, 347 (1998).
2. D. Herbenick *et al.*, *J. Sex. Med.* **7**, 255 (2010).
3. A. Ganna *et al.*, *Science* **365**, eaat7693 (2019).
4. Q. Rahman, *Neurosci. Biobehav. Rev.* **29**, 1057 (2005).
5. S. Hu *et al.*, *Nat. Genet.* **11**, 248 (1995).
6. D. H. Hamer, S. Hu, V. L. Magnuson, N. Hu, A. M. Pattatucci, *Science* **261**, 321 (1993).
7. N. Långström, Q. Rahman, E. Carlström, P. Lichtenstein, *Arch. Sex. Behav.* **39**, 75 (2010).
8. M. C. Mills, C. Rahal, *Commun. Biol.* **2**, 9 (2019).
9. N. Barban *et al.*; BIOS Consortium; LifeLines Cohort Study, *Nat. Genet.* **48**, 1462 (2016).
10. A. C. Kinsey *et al.*, *Sexual Behavior in the Human Male* (W. B. Sanders, 1948).
11. A. Fry *et al.*, *Am. J. Epi.* **186**, 1026 (2017).

ACKNOWLEDGMENTS

I thank X. Woltjer and F. C. Tropf for comments. I am supported by European Research Council grants 615603 and 835079 and The Leverhulme Trust, Leverhulme Centre for Demographic Science.

10.1126/science.aay2726

PHOTO: ISTOCK.COM/ANEESE

Published by AAAS

BOOKS *et al.*

Naomi Mburu, a former Meyerhoff Scholar, is currently pursuing a graduate degree at Oxford University.

PHOTO: MARLAYNA DEMOND FOR UMBC

EDUCATION

Lessons in black excellence

Data and success stories reveal how to ensure that African American students thrive in the STEM classroom

By **Donna Riley**

Building a diverse STEM (science, technology, engineering, and mathematics) workforce is an enduring priority in the United States, but predominantly white institutions (PWIs) have been slow to correct the systematic exclusion of Native Americans, Hispanics, and African Americans from educational opportunities. In *Making Black Scientists*, Marybeth Gasman and Thai-Huy Nguyen examine African American access to STEM careers through stories and data that describe the successful experiences of faculty, staff, and students at historically black colleges and universities (HBCUs).

Whereas PWIs have failed to make substantial progress in ensuring positive educational experiences for African Americans, HBCUs have been steadily "making black scientists" (and technologists, engineers, and mathematicians). HBCUs represent only 3% of postsecondary institutions but produce nearly a fifth of all bachelor's degrees awarded to African Americans in engineering and nearly a third in mathematics and physical sciences, despite differences in size, resources, and student preparedness.

The reviewer is the Kamyar Haghighi Head of the School of Engineering Education, Purdue University, West Lafayette, IN 47907, USA. E-mail: riley@purdue.edu

The book's power lies in artfully sharing the stories of HBCU students, faculty, and administrators, inviting us into student lives, faculty minds, and institutional cultures. It is organized thematically, describing key overlapping and reinforcing characteristics that create environments supporting African American excellence in STEM. These passages are bookended by an introduction and first chapter that concisely capture the landscape of racial inequality in STEM education—a section worth reading slowly, especially for faculty who are not familiar with the history and context of HBCUs—and a final chapter that distills action items for PWIs to improve the experiences of African American STEM students.

Gasman and Nguyen argue that African American success in STEM begins with an institutional commitment to the education of black students. This notion, built into the mission of HBCUs, is in many ways precluded at PWIs through the history of segregation in U.S. education. The book details how HBCUs do not anxiously perseverate over math preparation, test scores, and other dubious meritocratic measures. Instead, faculty and administrators offer educational experiences tailored to students' needs. This entails a variety of approaches, including making STEM socially relevant, recognizing students' life circumstances, highlighting student strengths, beginning wherever K–12 preparation left off, celebrating black achievement in STEM, and believing in students even when they might not believe in themselves.

Making Black Scientists
A Call to Action
Marybeth Gasman and Thai-Huy Nguyen
Harvard University Press, 2019. 253 pp.

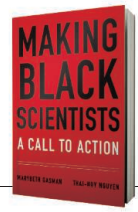

The authors foreground the sense of community at HBCUs, describing how peer collaboration facilitates student accountability and self-confidence. Emphasizing community success and intellectual generosity rather than individual achievement and competition contrasts strongly with traditional STEM education at PWIs.

HBCU faculty collaborate in putting students first and innovating supportive learning environments. Achieving excellence and needing help in learning are both normalized and expected from each student rather than viewed as aberrations. Faculty serve as caregivers to students, creating a sense of kinship and family that is rare in many other institutions of higher education.

Gasman and Nguyen argue that PWIs have much to learn from HBCUs' decades of accomplishment in black students' STEM education, a challenge to which I hope they will rise. But critical questions remain: How does one eradicate meritocratic thinking and elitist policies that maintain de facto segregation at PWIs? How does one radically upend reward structures and institutional budgets to truly put (traditionally marginalized) students first?

I do not doubt the transformative power of faculty showing up for African American students or of institutional reform to improve African American graduation rates in STEM at PWIs. But moving beyond incremental change requires striking at root causes such as racism and classism and confronting unjust relations of knowledge and power in a system that reliably reproduces inequality. This book provides a roadmap of actions within individual faculty members' control and sustenance for students, faculty, and administrators engaging in the struggle for racial justice in STEM education.

It may be helpful to read the book remembering that HBCUs are both the product of a racist system and a challenge to that system. With this in mind, I could not help but wonder what more HBCUs and their students might accomplish if they were equitably resourced, and what the appropriate moral correction might be for PWIs that have benefited from decades of privilege. ■

10.1126/science.aay3052

Published by AAAS

REPRODUCTIVE TECHNOLOGY

Changing conception

A thought-provoking volume traces the medical, social, and political histories of in vitro fertilization

The Pursuit of Parenthood
Margaret S. Marsh and Wanda Ronner
Johns Hopkins University Press, 2019. 274 pp.

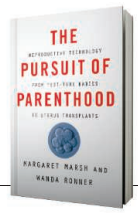

By **I. Glenn Cohen**

Major academic figures admonish "immoral experiments on the unborn." An advertisement in *The New York Times* cautions about the "unknowable risks to human lives." A government official calls for an ethics board to investigate "attempts to control the genetic makeup of offspring." No, these are not the latest outcries over germline gene editing. The concerns raised above came from debates in the 1970s about a technology many of us now take for granted: in vitro fertilization (IVF). In their illuminating and highly readable new book, *The Pursuit of Parenthood*, historian Margaret Marsh and physician Wanda Ronner tell the medical, social, and political story of IVF from its prehistory in the mid-1900s to the present day, sweeping in adjacent technologies toward the book's end.

In the first half of the book, Marsh and Ronner masterfully interweave narrative, historical, and demographic materials in beautiful prose to tell a compelling story that will enlighten even those who specialize in this area. That story begins with John Rock, born in 1890, who would go on to become the director of the Fertility and Endocrine Clinic at the Free Hospital for Women in Brookline, Massachusetts. Together with his research assistant Miriam Menkin, in August 1944 Rock published a report in *Science* describing a procedure in which four fully fertilized eggs from three women were cultured in a glass dish.

While Rock, Menkin, and others made huge progress toward realizing IVF, efforts in the United States ultimately waned, setting the stage for the United Kingdom to bring the technology to fruition. Here, Marsh and Ronner shift to describing the academic odd couple of Patrick Steptoe and Robert Edwards, who enabled the birth of the world's first IVF baby in Oldham, England, on 25 July 1978. Far from a dry recitation of the medical history, the book goes deep into each man's background, describing their somewhat unlikely pairing—the two were separated by age, class, and training—and peppering the story with engaging anecdotes along the way. (My favorite was an incident in which Edwards was denounced by Princeton theologian Paul Ramsey at a 1971 forum on medical ethics. Edwards described his response: "I was a Yorkshireman and I would be blunt as Yorkshiremen are reputed to be.")

The book then pivots to early efforts to bring IVF to the United States. Here, the authors describe Howard and Georgeanna Jones's pioneering IVF work in Norfolk, Virginia, and Richard Marrs's establishment of an IVF practice in California. They also present a deep dive into the accompanying political maneuverings around federal funding of human embryo and IVF research. The book then insightfully traces the expansion of IVF practices and explores some of the shadier elements of today's reproductive medicine—including fertility fraud and the infamous case of Ricardo Asch, who stole eggs and embryos from patients—before more briefly surveying IVF-adjacent technologies, including surrogacy and egg and embryo freezing.

Although more careful than most commentators, Marsh and Ronner do buy into the common trope that paints the United States as the "wild west" of reproductive technology usage. They describe, for example, how a shift to a "consumer protection" model facilitated what little federal legislation exists with regard to IVF—the Fertility Clinic Success Rate and Certification Act of 1992—and correctly call out its relatively weak enforcement mechanism. Where they misstep slightly, however, is in focusing almost exclusively on federal-level legislation, and especially in their comparison to the UK Human Fertilisation and Embryology Authority (HFEA).

Although the United Kingdom, like many other countries, has adopted a unitary country-wide approach, the authors give too short a shrift to a distinctly American regulatory configuration that has largely left much of IVF governance to individual states. The result is a continuum of legal approaches to reproductive technologies. Regarding surrogacy, for example, in the United States one sees everything from criminalization of the practice to judicial approval and enforcement of contracts. Meanwhile, in states such as California, huge reproductive technology industries thrive, whereas in Louisiana, fertilized embryos have been declared "juridical persons."

Another minor disappointment of the book was how rushed its last two chapters felt. Although the subtitle references uterus transplants, the book only manages three pages on this topic. I also wished the authors had taken the time to more deeply reflect on what implications the history of IVF might have for technologies such as gene editing. But these are minor quibbles.

Ultimately, Marsh and Ronner have stitched together an amazing amount of historical, legal, medical, and quantitative material. This book is a must-read for anyone interested in the history of reproductive technology. ■

10.1126/science.aay4220

The reviewer is at the Petrie-Flom Center for Health Law Policy, Biotechnology, and Bioethics, Harvard Law School, Cambridge, MA 02138, USA. Email: igcohen@law.harvard.edu

What if you suddenly remembered details from a life you never led?

PHOTO: ISTOCK.COM/ELLENAZ

PODCAST

Recursion
A Novel
Blake Crouch
Crown, 2019. 336 pp.

In his latest science fiction thriller, Blake Crouch imagines a world thrown into chaos by a mysterious condition that causes those afflicted to experience false memories. This week on the *Science* podcast, Crouch reveals the real-life research that inspired the story (*Science*, 26 July 2013, p. 387).

10.1126/science.aay7800

Published by AAAS

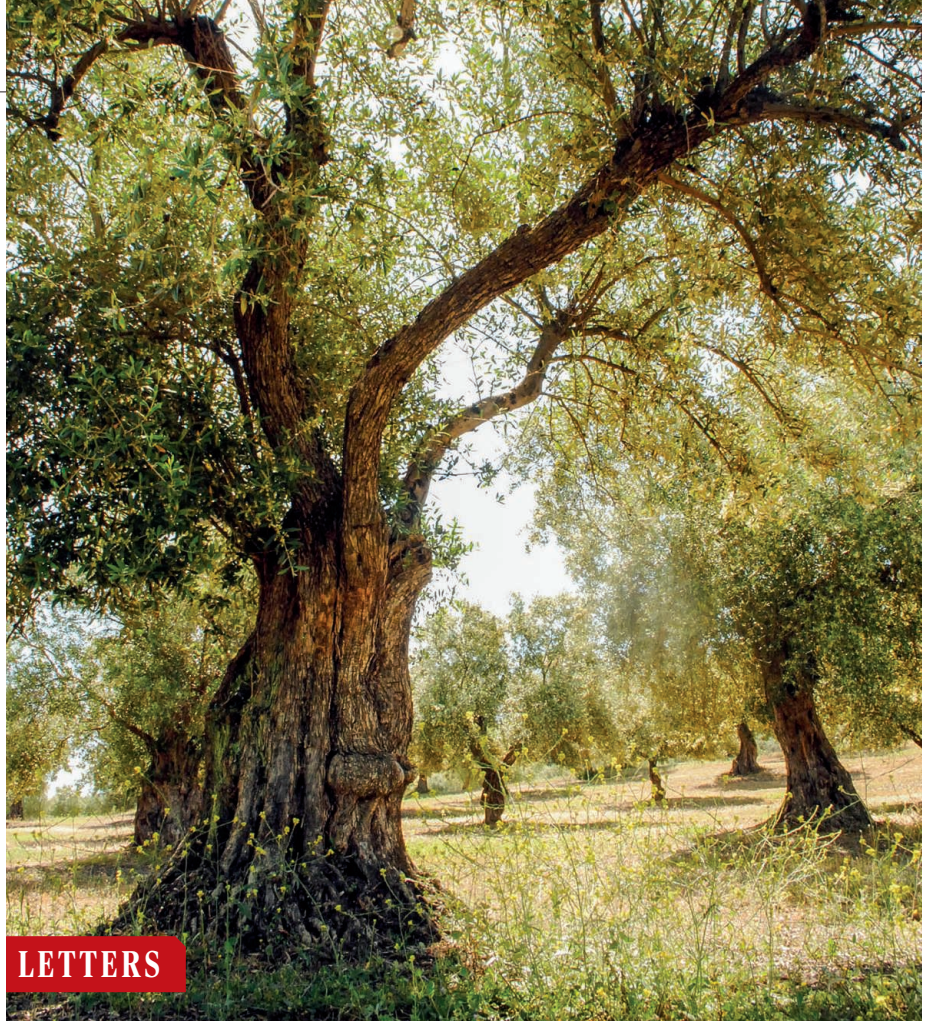

The environmental value of traditional olive groves, such as this one in Portugal, has been overlooked.

PHOTO: NEREIDA MELGUIZO-RUIZ

REFERENCES AND NOTES

1. D. Zohary, P. Spiegel-Roy, *Science* **187**, 319 (1975).
2. A. Loumou, C. Giourga, *Agric. Hum. Values* **20**, 87 (2003).
3. B. Neves, I. M. Pires, *Region* **5**, 101 (2018).
4. C. Vasilopoulos, "200,000 olive farms in Spain could vanish in next decade, report finds," Olive Oil Times (2019).
5. G. Beaufoy, "The environmental impact of olive oil production in the European Union: Practical options for improving the environmental impact" (2001); http://ec.europa.eu/environment/agriculture/pdf/oliveoil.pdf.
6. J. M. Herrera *et al.*, *Anim. Conserv.* **18**, 557 (2015).
7. P. J. Rey *et al.*, *Ecosyst. Environ.* **277**, 61 (2019).
8. L. P. Silva, V. Mata, *Nature* **569**, 192 (2019).
9. European Commission, "Proposal for a Regulation of the European Parliament and of the Council establishing rules on support for strategic plans to be drawn up by Member States under the Common agricultural policy (CAP Strategic Plans) and financed by the European Agricultural Guarantee Fund (EAGF) and by the European Agricultural Fund for Rural Development (EAFRD)" (2018).
10. G. Pe'er *et al.*, *Science* **365**, 449 (2019).

10.1126/science.aay7899

LETTERS

Edited by **Jennifer Sills**

Making olive oil sustainable

Traditional olive groves, typical of Mediterranean landscapes, date back at least to the ancient Greek civilizations (*1*) and hold cultural, scenic, and biodiversity value (*2*). However, as demand for olives and olive oil has increased (*3*), traditional groves, the least viable in economic terms, have been abandoned and production has shifted to large-scale intensive plantations to maximize yields (*3*–*5*). These vast groves use irrigation, high tree densities, agrochemicals, and mechanization (*6*). The resulting landscape simplification and habitat loss and degradation contribute to substantial biodiversity decline (*6*, *7*). There are also claims that harvesting olives at night leads to mass bird mortality (*8*) and that the olive industry affects water, soil, and human health (*5*).

A thorough understanding of the environmental impacts of modern olive farming is urgent to inform agricultural policies and consumers. In the European post-2020 agricultural policy proposal (*9*), currently under discussion, most farmers are required to comply with basic environmental standards. However, the olive sector is exempted from environmental requirements (*10*). This should be changed in order to promote the maintenance of traditional olive groves, limit the area occupied by continuous olive tree monocultures, and introduce environmentally friendly management practices. Because organic production labels focus mostly on fertilizers and pesticides, they do not provide enough information to consumers. To facilitate informed choices, new labels should be created. Olive oil packaging should provide consumers with details about the grove from which the product was sourced. Biodiversity-rich groves that host rare species of plants and animals could benefit from this marketing. Enhancing and highlighting the sustainability of olive farming are important not only for the environment but also for the economic revenues of olive oil producers.

Francisco Moreira[1,2]*, José M. Herrera[3], Pedro Beja[1,2]

[1]CIBIO/InBIO, Universidade do Porto, 4485-601 Vairão, Portugal. [2]CIBIO/InBIO, Instituto Superior de Agronomia, Universidade de Lisboa, 1349-017 Lisbon, Portugal. [3]MED, Universidade de Évora, 7000–651 Évora, Portugal.
*Corresponding author.
Email: fmoreira@isa.ulisboa.pt

Will DNA barcoding meet taxonomic needs?

In her In Depth News story "DNA barcodes jump-start search for new species" (7 June, p. 920), E. Pennisi celebrates a global effort to identify 2 million new species and suggests that a "golden era" for biodiversity science is about to begin. The effort is mainly driven by an injection of $180 million toward sequencing short DNA segments that distinguish species—DNA barcodes—across a wide diversity of multicellular species, both in the field and the laboratory. The commendable goal is to document new species before they disappear, and the effort will undoubtedly find at least as many new species as they estimate. However, the massive gap in our taxonomic knowledge is not a problem of finding new species but rather a delay in formally describing them (*1*).

Natural history museum collections already house a substantial amount of the biodiversity awaiting formal description, including specimens of species likely to be "discovered" through the proposed DNA barcoding effort. Although DNA can be an invaluable tool for identifying new species, formal descriptions provide the names and accounts of anatomy, biology, and provenance that make species visible and useful to the scientific community and to the resource managers who aim to protect and conserve biodiversity. Additionally, taxonomy requires context and expertise, including comparisons to previously documented species for which DNA sequences have yet to be obtained.

The current average shelf life of new species between discovery and description is

Published by AAAS

estimated at 21 years (*2*). This slow pace and ever-increasing backlog are the result of the decreasing number of taxonomists and the lack of financial investment in the field of taxonomy and museum collections (*3*). Many megadiverse groups, including less charismatic plants, fungi, and invertebrates, have very few or no specialists with the necessary knowledge to describe them, whereas most scientists study charismatic groups and dedicate their time to ecological and evolutionary science (*4*). Without support for proper long-term housing and morphological descriptions, which is what is required to officially name a species under the rules of the International Codes of Nomenclature (*5*), species identified by DNA barcode will likely just add to the already massive backlog.

The lack of investment in natural history collections and research worldwide is clear and especially apparent in developing countries (*6*) that hold most of the biodiversity on our planet. Many new species that might be at risk of extinction in nature have the same risk of disappearing from museum shelves due to the lack of maintenance (*6*). DNA barcodes alone are not enough to document the biological diversity. Overcoming the taxonomic backlog can lead to incredible advances in conservation and biodiversity science, but this will only happen if governments, societies, and institutions recognize and invest in taxonomists, museum collections, and their staff.

H. T. Pinheiro[1], C. S. Moreau[2], M. Daly[3], L. A. Rocha[1]*
[1]California Academy of Sciences, San Francisco, CA 94118, USA. [2]Cornell University, Ithaca, NY 14853, USA. [3]Ohio State University, Columbus, OH 43212, USA.
*Corresponding author.
Email: lrocha@calacademy.org

REFERENCES AND NOTES

1. Q. D. Wheeler, P. H. Raven, E. O. Wilson, *Science* **303**, 285 (2004).
2. B. Fontaine, A. Perrard, P. Bouchet, *Curr. Biol.* **22**, R943 (2012).
3. M. C. Ebach, A. G. Valdecasas, Q. D. Wheeler, *Cladistics* **27**, 550 (2011).
4. L. W. Drew, *BioScience* **61**, 942 (2011).
5. International Commission on Zoological Nomenclature, *International code of Zoological Nomenclature. Fourth Edition* (The International Trust for Zoological Nomenclature, London, UK, 1999).
6. K. A. Zamudio *et al.*, *Science* **361**, 1322 (2018).

10.1126/science.aay7174

Trophy hunting bans imperil biodiversity

Trophy hunting is under pressure: There are high-profile campaigns to ban it, and several governments have legislated against it (*1*). In the United States, the CECIL Act (*2*) would prohibit lion and elephant trophy imports from Tanzania, Zambia, and Zimbabwe and restrict imports of species listed as threatened or endangered on the Endangered Species Act. Australia, the Netherlands, and France have also restricted trophy imports (*1*), and the United Kingdom is under pressure to follow. Calls for hunting bans usually cite conservation concerns. However, there is compelling evidence that banning trophy hunting would negatively affect conservation.

In African trophy hunting countries, more land has been conserved under trophy hunting than under national parks (*3*), and ending trophy hunting risks land conversion and biodiversity loss (*4*). Poorly managed trophy hunting can cause local population declines (*5*), but unless better land-use alternatives exist, hunting reforms—which have proved effective (*6*)—should be prioritized over bans (*7*). Positive population impacts of well-regulated hunting have been demonstrated for many species, including rhinos, markhor, argali, bighorn sheep, and many African ungulates (*7*).

Banning trophy hunting can have unintended consequences for species such as lions.

Trophy hunting can also provide income for marginalized and impoverished rural communities (*7*). Viable alternatives are often lacking; opponents of hunting promote the substitution of photo-tourism, but many hunting areas are too remote or unappealing to attract sufficient visitors (*8*). Species such as lions fare worst in areas without photo-tourism or trophy hunting (*9*), where unregulated killing can be far more prevalent than in hunting zones, with serious repercussions for conservation and animal welfare (*10*). Focusing on trophy hunting also distracts attention from the major threats to wildlife.

The International Union for Conservation of Nature (IUCN), a global conservation authority, clearly concludes that "with effective governance and management trophy hunting can and does have positive impacts" on conservation and local livelihoods (*7*). Although there is considerable room for improvement, including in governance, management, and transparency of funding flows and community benefits (*11*), the IUCN calls for multiple steps to be taken before decisions are made that restrict or end trophy hunting programs (*7*). Crucially, as African countries call for a "New Deal" for rural communities (*12*) that allows them to achieve the self-determination to sustainably manage wildlife and reduce poverty, it is incumbent on the international community not to undermine that. Some people find trophy hunting repugnant (including many of us), but conservation policy that is not based on science threatens habitat and biodiversity and risks disempowering and impoverishing rural communities.

Amy Dickman[1,2], Rosie Cooney[2,3], Paul J. Johnson[1]*, Maxi Pia Louis[4], Dilys Roe[2,5], and 128 signatories
[1]Wildlife Conservation Research Unit, Department of Zoology, University of Oxford, The Recanati-Kaplan Centre, Tubney, Oxfordshire, OX13 5QL, UK. [2]IUCN SSC Sustainable Use and Livelihoods Specialist Group, 1196, Gland, Switzerland. [3]Fenner School of Environment and Society, Australian National University, 0200 ACT, Australia. [4]Namibian Association of CBNRM Support Organisations, Windhoek, Namibia. [5]Natural Resources Group, International Institute for Environment and Development, London WC1X 8NH, UK.
*Corresponding author.
Email: paul.johnson@zoo.ox.ac.uk

REFERENCES AND NOTES

1. E. Ares, "Trophy hunting," House of Commons Library Briefing Paper Number 7908 (2019); https://researchbriefings.parliament.uk/ResearchBriefing/Summary/CBP-7908.
2. U.S. Congress, H.R.2245—CECIL Act (2019); www.congress.gov/bill/116th-congress/house-bill/2245/text.
3. P. A. Lindsey, P. A. Roulet, S. S. Romanach, *Biol. Conserv.* **134**, 455 (2007).
4. E. Di Minin *et al.*, *Conserv. Biol.* **27**, 808 (2013).
5. C. Packer *et al.*, *Conserv. Biol.* **25**, 142 (2011).
6. C. M. Begg, J. R. B. Miller, K. S. Begg, *J. Appl. Ecol.* **55**, 139 (2018).
7. IUCN, "Informing decisions on trophy hunting" (IUCN, Gland, Switzerland, 2016).
8. C. W. Winterbach, C. Whitesell, M. J. Somers, *PLOS One* **10**, e0135595 (2015).
9. P. A. Lindsey *et al.*, *Biol. Conserv.* **209**, 137 (2017).
10. A. J. Dickman, in *Conflicts in Conservation: Navigating Towards Solutions*, S. M. Redpath, R. J. Gutierrez, K. A. Wood, J. C. Young, Eds. (Cambridge University Press, Cambridge, 2015), pp. 30–32.
11. IUCN SSC, "Guiding principles on trophy hunting as a tool for conservation incentives v 1.0" (IUCN SSC, Gland, Switzerland, 2012).
12. Southern Africa Trust, "Declaration—Voices of the communities: A new deal for rural communities and wildlife and natural resources" (2019); www.southernafricatrust.org/2019/06/25/declaration-voices-of-the-communities-a-new-deal-for-rural-communities-and-wildlife-and-natural-resources/.

SUPPLEMENTARY MATERIAL

science.sciencemag.org/content/365/6456/874/suppl/DC1
List of Signatories

10.1126/science.aaz0735

PHOTO: KEN SILLS

Published by AAAS

Kip Thorne accepts the Nobel Prize in Physics in 2017 for his "decisive contributions to the LIGO detector and the observation of gravitational waves."

Science diplomacy leverages alliances to build global bridges

History of U.S. and Soviet scientific research collaborations and exchanges offers lessons for today

By **Anne Q. Hoy**

Nobel laureate and theoretical physicist Kip Thorne counts his decades-long collaboration with Russian experimental physicist Vladimir Braginsky as pivotal to scientific research that led to the first detection of two colliding black holes in the distant universe.

The 2015 detection of gravitational waves by the Laser Interferometer Gravitational-Wave Observatory (LIGO) was not only the birth of a whole new way of studying the universe, a realization predicted by Albert Einstein's general theory of relativity, and a discovery that earned Thorne and two other physicists the 2017 Nobel Prize in Physics. It also validated the enduring benefits of science diplomacy across the globe.

"Braginsky was my principal mentor on research at the interface between theory and experiment. His mentoring made possible many of my contributions to LIGO, and our tight collaboration led to his own major LIGO contributions," said Thorne. "He became the 'conscience' of LIGO in the 1990s and 2000s, identifying a series of sources of noise that we had not been aware of, and triggering the LIGO Scientific Collaboration to scope out those noise sources and devise ways to deal with them."

Thorne and Braginsky, who died in 2016, traveled to each other's laboratories, coauthored scientific papers, shared findings, traded questions, and formed a lasting friendship that began with Thorne's first visit to Braginsky's lab in 1968 and extended into the 2000s.

As scientists forged such cooperative relationships despite tensions between their governments, the American Association for the Advancement of Science (AAAS) was pioneering efforts to spread the global reach of science and technology by engaging in scientific leadership initiatives through international exchanges and scientific partnerships.

In 2008, AAAS formally established the Center for Science Diplomacy to advance the value of what then AAAS CEO Alan I. Leshner described as a program "guided by the overarching goal of using science and scientific cooperation to promote international understanding and prosperity. AAAS believes this use of scientific collaboration and communication is essential both to the advancement of science and its use for the benefit of our global society." Leshner is now serving as AAAS's interim CEO.

At the center's opening, Vaughan Turekian, then AAAS's chief international officer, said the center would "contribute to the long and methodical building of relationships" and pursue advances to address global challenges such as climate change, sustainability, and health care innovation.

A year later, AAAS joined five representatives of other leading scientific organizations in a meeting with North Korea's State Academy of Science. During the rare visit, U.S. scientists met with their counterparts, toured government research institutions, and reached an agreement to pursue cooperative issues that paved the way for a reciprocal visit of North Korean scientists to U.S. laboratories.

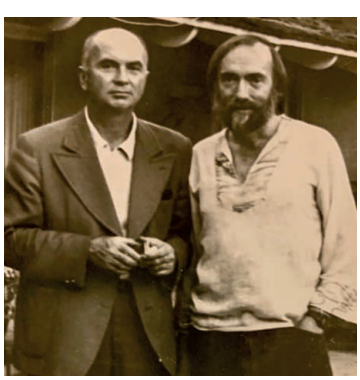

Vladimir Braginsky, left, meets with Kip Thorne at his Pasadena, California, home.

AAAS has continued to develop such scientific agreements, including a 2013 agreement with China's Association for Science Technology, a 2014 pact between AAAS and the Cuban Academy of Sciences, a 2017 agreement with Mexico's Presidential Science Advisory Council, and a 2018 agreement with the Science Commission of Chile's Senate.

It also has tapped into long-standing collaborations to offer training sessions and expand global scientific alliances. Last year, for instance, AAAS held a regional training workshop with The World Academy of Sciences and the Academy of Science of South Africa to introduce regional scientists to scientific collaborations that inform science and advance diplomacy.

(PHOTOS TOP TO BOTTOM) © NOBEL MEDIA AB; VALENTIN RUDENKO, COURTESY KIP THORNE

Published by AAAS

The AAAS Center for Science Diplomacy also provides training for scientists and graduate students in the U.S., and, since 2014, it has cohosted international sessions with The World Academy of Sciences at its headquarters in Italy.

Throughout the ebb and flow of relations between the United States and the Soviet Union, then Russia, scientists, like Thorne, continue to build professional relationships and keep in touch with their foreign counterparts.

"The Cold War Iron Curtain was not a significant barrier to my collaborations with Braginsky and other Russian scientists," said Thorne. "I hope the soaring paranoia in Washington about China does not create major barriers to the very fruitful collaborations that my colleagues today have with Chinese scientists."

The parallel with China was not raised during a 16 July AAAS symposium hosted by the AAAS Center for Science Diplomacy that centered on the history of U.S.-Soviet scientific activities. In examining scientific interactions between the two powers, Gerson S. Sher, author of *From Pugwash to Putin: A Critical History of US-Soviet Scientific Cooperation* and former coordinator of the National Science Foundation's U.S.-Soviet and East European program, used the U.S.-Soviet relationship as a case study of what drives, benefits, and sometimes interrupts international scientific collaborations.

Today, six decades of formal bilateral exchanges between U.S. and Soviet scientific academies have "all but descended to zero," after Russia's annexation of the Crimean Peninsula and its intervention in the Ukraine crisis in 2014, said Sher during the symposium held at AAAS's Washington, D.C., headquarters.

Sher walked through earlier collaborations during post–World War II, post–Joseph Stalin and post-Soviet periods to demonstrate that despite any strained relations between governments, scientific cooperation endures in strengthening civil relationships, improving understanding of each society, and advancing science.

Among early U.S. collaborations was President Dwight D. Eisenhower's "people to people" exchange initiative. Backed by private sponsors, it amplified the scientific communities' prevalence to nurture relationships with fellow researchers. This led to the emergence of multiple public and private scientific efforts designed to support international scientific alliances in the wake of the Soviet Union's demise in 1991.

The U.S. National Science Foundation, for instance, established the nonprofit U.S. Civilian Research and Development Foundation (CRDF) in 1995 to provide scientists grants, technical resources, and training support for global scientific and technical collaborations. Sher served as its founding president.

CRDF's emergence came amid heightened U.S. concerns about unsecured weapons of mass destruction and set off calls for nonproliferation programs, said Sher. Particularly unsettling was the sidelining of Russian nuclear weapons experts under the weight of a stagnant Soviet economy and amid the chaotic fallout of the Soviet Union's collapse.

In remarks at the AAAS symposium, Cathleen A. Campbell, who also served as a CRDF president beginning in 2006, underscored the importance of such nongovernmental organizations in fostering scientific collaborations through science and technology agreements between the United States and the former Soviet Union and its republics.

"That was a unique period in history that I don't think we will ever see again anywhere," said Campbell, a former visiting scholar at the AAAS Center for Science Diplomacy and now a board member of the U.S.-Israel Bilateral Science Foundation. "It's just an incredible interconnection of opportunities and challenges and issues we were facing that prompted this whole array of programs."

Turekian, now executive director of policy and global affairs at the National Academies of Sciences, Engineering, and Medicine, said the Cold War had a profound impact in shaping science diplomacy, then and today.

"The creation of the AAAS Center for Science Diplomacy was a response to the need to refocus how science and science cooperation could be better utilized as a bridge outside of a polar world and to deal with complex issues at regional and global scales," said Turekian. "But it also looked to the U.S.-USSR science diplomacy experiences to understand how to make science diplomacy work."

Interactive early education builds STEM literacy in children

AAAS programs introduce STEM careers through hands-on activities and interaction with scientists

By **Andrea Korte**

Wildlife biologists have turned to creative solutions like 3D printing technologies to fashion prosthetic beaks, limbs, and shells to aid injured animals. A group of Maryland elementary school students were given their own opportunity to tackle a similar project, designing and printing shells for turtles, hermit crabs, or snails under the guidance of a retired scientist.

Throughout the process, systems biologist Gertraud Robinson encouraged the students to think like a scientist. "You have a problem; you think about the solution; you test it out; and you improve," she coached.

Robinson has leaned in to science education after retiring from the National Institutes of Health, trading her laboratory for elementary school classrooms and forgoing a full retirement. She participates in the American Association for the Advancement of Science's STEM Volunteer Program, which pairs scientists and engineers with elementary, middle, and high school teachers at nine school districts in the Washington, D.C., area, including those in three Virginia counties and three cities, and two in Maryland. In support of primary and secondary education, the volunteers work to spark interest in science, technology, engineering, and mathematics (STEM) with an eye toward drawing students into relevant careers.

Nearly 200 volunteers visit classrooms throughout the school year, helping teachers set up experiments, answering student questions, and drawing connections between classroom projects and the real-life research and activities scientists pursue.

The program is one of several AAAS initiatives that foster science literacy in children and cultivate interest in STEM careers. Along with Science in the Summer, a seasonal enrichment program, and Family Science Days, a public event held at the AAAS Annual Meeting, the STEM Volunteer Program complements an array of AAAS education and public engagement activities that take a hands-on approach.

"In the face of AAAS's goal to foster education in science and technology for all, we have worked to improve K–12 STEM education at a system level and have coupled this work with direct engagement with students," said Shirley Malcom, AAAS senior adviser

Published by AAAS

Participants extracted DNA from strawberries among the many hands-on activities offered at the 2019 Family Science Days in Washington, D.C.

PHOTO: ADAM COHEN/AAAS

and head of the SEA Change program, a AAAS initiative to spur institutional change at colleges and universities to support diversity and inclusion. "Through these programs, the value of STEM education has been reinforced for students and parents alike, and we are encouraged by engagement activities through the positive changes we realize."

The STEM Volunteer Program dates to 2004, when Alan I. Leshner, then AAAS CEO and now AAAS's interim CEO, penned a relevant editorial for *Science*. "Reaching out to the public is not a strong tradition for the science community, perhaps because we may think that nonscientists cannot understand our work. We're wrong about that," Leshner wrote.

The editorial inspired Donald Rea, a retired NASA Jet Propulsion Laboratory scientist, who joined other AAAS members in volunteering as science educators at public schools in Maryland's Montgomery County, the state's largest school district. Together, they launched what was then called the AAAS Senior Scientists and Engineers program.

In 2016, the program became the STEM Volunteer Program to reflect a broader volunteer base that expanded beyond senior citizens. Today, about 20% of participants in the program take time away from their STEM jobs to volunteer in classrooms, according to Betty Calinger, senior project director at AAAS.

AAAS activities for children do not end with the school year. Science in the Summer is a free, hands-on program geared toward 2nd through 6th grade students. Launched in the Philadelphia area in the 1980s by pharmaceutical company GSK, Science in the Summer expanded nationwide with the help of AAAS in 2015. AAAS now oversees Science in the Summer at dozens of sites in Washington, D.C.; Maryland; and Virginia, bringing local teachers to libraries, museums, and Boys & Girls Clubs to lead students in hands-on science experiments.

The goal of this program is to keep children from losing skills and knowledge during summer breaks, Calinger said, and instill perspectives that extend beyond the next school year. Children get excited about science and build science literacy for the long term, she said.

Each summer's curriculum is centered on a theme to demonstrate the relevance of science in their everyday lives and interests. A sports-focused curriculum, for instance, taught children how their favorite athletes benefit from quick reflexes. They also were given an opportunity to be scientists in testing their own hand-eye coordination. First, though, they had to establish a hypothesis and collect data before they could draw conclusions.

Last summer, educator Monica Padgett led Science in the Summer participants in experiments related to space travel. To learn about rocket propulsion, Padgett guided students as they used film canisters to create their own miniature rocket ships. When the fuel—a mixture of water and Alka-Seltzer—was added, the rockets zoomed toward the ceiling, just one part of a curriculum that is "hands-on and exciting for the kids," said Padgett.

Experiencing fun science firsthand is a hallmark of AAAS's Family Science Days, the AAAS Annual Meeting's well-attended public event. Since 2004, the event has offered children and their parents opportunities to hold a real human brain, pilot a robot and build their own pinball game at activity stations run by museums, universities, laboratories, and other science organizations.

Older children are particularly interested in exhibits about virtual reality, 3D printing, and computer programming, while younger children crowd around areas that feature anything they can touch, said Stacey Baker, public engagement associate with AAAS's Center for Public Engagement with Science and Technology.

Stage shows featured at Family Science Days also are interactive. Scientists give a short presentation and answer questions from the audience before heading to the "Meet a Scientist" area, where children can ask scientists questions in a one-on-one setting. Children engage in conversations with a diverse slate of scientists across genders, races, and ethnicities and from a variety of STEM careers. Children realize that "they, too, can be scientists," said Baker.

From the start of her transition from NIH to the classroom, Robinson recognized an inspiration along with the importance of bringing science to elementary schools. As a STEM Volunteer, she wanted to represent science diversity. The participation of female scientists in the program sends many students a powerful message by their presence as a volunteer. "That was one of my motivations—to show them that there are women working in this job," she said.

The goal was validated when students, as part of a class project, were asked to draw a scientist. The majority of the drawings depicted women. Robinson said, "I was pleased."

Published by AAAS

RESEARCH

Skyrmion lattice in a centrosymmetric magnet

Kurumaji et al., *p. 914*

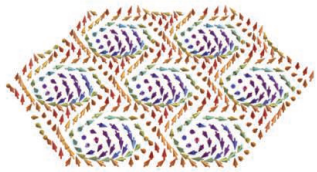

IN *SCIENCE* JOURNALS

Edited by **Michael Funk**

Fields and managed forests, such as these in Eifel, Germany, are common agricultural land uses.

ARCHAEOLOGY

A synthetic history of human land use

Humans began to leave lasting impacts on Earth's surface starting 10,000 to 8000 years ago. Through a synthetic collaboration with archaeologists around the globe, Stephens *et al*. compiled a comprehensive picture of the trajectory of human land use worldwide during the Holocene (see the Perspective by Roberts). Hunter-gatherers, farmers, and pastoralists transformed the face of Earth earlier and to a greater extent than has been widely appreciated, a transformation that was essentially global by 3000 years before the present. —AMS

Science, this issue p. 897; see also p. 865

COMPUTER SCIENCE

AI now masters six-player poker

Computer programs have shown superiority over humans in two-player games such as chess, Go, and heads-up, no-limit Texas hold'em poker. However, poker games usually include six players—a much trickier challenge for artificial intelligence than the two-player variant. Brown and Sandholm developed a program, dubbed Pluribus, that learned how to play six-player no-limit Texas hold'em by playing against five copies of itself (see the Perspective by Blair and Saffidine). When pitted against five elite professional poker players, or with five copies of Pluribus playing against one professional, the computer performed significantly better than humans over the course of 10,000 hands of poker. —JS

Science, this issue p. 885; see also p. 864

ORGANIC CHEMISTRY

Displacing OH groups catalytically

The Mitsunobu reaction is widely used to invert the configuration of alcohols. However, its major drawback is the need to activate the alcohol with a full equivalent of phosphine, thereby generating a phosphine oxide co-product. Beddoe *et al*. report a phosphine oxide compound that achieves the same result catalytically (see the Perspective by Longwitz and Werner). The key is a phenol substituent that can reversibly bond through its oxygen to phosphorus, forming a ring that the alcohol opens. The phosphorus thus remains in the +5 oxidation state throughout the reaction, and water is the only by-product. —JSY

Science, this issue p. 910; see also p. 866

MANTLE CHEMISTRY

Deep divide in fate of iron

A large component of Earth's atmosphere comes from the interior, where the gas species are dictated by the redox state of the mantle. After formation of Earth's iron core, the mantle became several orders of magnitude more oxidized. Armstrong *et al*. conducted a set of experiments looking at the redox state of silicate melt representative of Earth's early magma oceans. They found that at some depth, iron oxide disproportionates into iron(III) oxide and metallic iron. The reduced iron sinks to the core, leaving an oxidized rocky mantle that emits carbon dioxide and water instead of more reduced species. —BG

Science, this issue p. 903

ASTROCHRONOLOGY

Filling a dating hole

The periodic nature of Earth's orbit around the Sun produces cycles of insolation reflected in climate records. Conversely, these climate records can be used to infer changes in the dynamics of the Solar System, which is inherently chaotic and not always similarly periodic. A particular obstacle is the lack of well-defined planetary orbital constraints between 50 and 60 million years ago. Zeebe and Lourens found an astronomical

CREDITS: (TOP TO BOTTOM) KURUMAJI *ET AL*.; LOOK/ALAMY STOCK PHOTO

Published by AAAS

solution for that interval showing that the Solar System experienced a specific resonance transition pattern. These data provide a measure of the duration of the Paleocene-Eocene Thermal Maximum. —HJS

Science, this issue p. 926

PLANT SCIENCE

Microbial tRNA pieces regulate nodulation

To fix nitrogen, leguminous plants enter into a symbiotic relationship with nodulating bacteria. Ren *et al*. now reveal the bacteria as active regulators in this process (see the Perspective by Baldrich and Meyers). Small fragments cleaved from rhizobial tRNA molecules tap into the hosts' RNA interference machinery to silence key host genes. Thus, both host and microbe shape the symbiotic environment. —PJH

Science, this issue p. 919; see also p. 868

IMMUNOLOGY

Empowering NK cells against cancer

Tumors release factors, such as the cytokine transforming growth factor–β (TGF-β), that block antitumor immunity mediated by natural killer (NK) immune cells by promoting their differentiation into a less suppressive cell type. Rautela *et al.* found that activin-A, another member of the TGF-β family, had similar effects on both mouse and human NK cells but through a pathway independent of TGF-β. Inhibition of activin-A reduced skin cancer growth in a mouse melanoma model, suggesting that targeting this pathway could enhance NK cell function and antitumor immunity. —JFF

Sci. Signal. **12**, eaat7527 (2019).

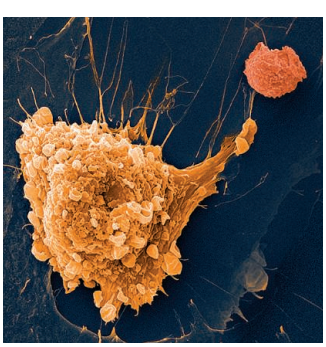

Natural killer cell (top) and melanoma cell in a scanning electron micrograph

PHOTOS: (LEFT TO RIGHT) FERNANDO S. F. GUIMARAES/WEHI; CAROLINA C. CAMARGO/UFPR AND SIMON TAPLIN/WEHI; DPA PICTURE ALLIANCE/ALAMY STOCK PHOTO

SYNTHETIC BIOLOGY

Programmable genome engineering

The model bacterium *Escherichia coli* has a single circular chromosome. Wang *et al*. created a method to fragment the *E. coli* genome into independent chromosomes that can be modified, rearranged, and recombined. The efficient fission of the unmodified *E. coli* genome into two defined, stable pairs of synthetic chromosomes provides common intermediates for large-scale genome manipulations such as inversion and translocation. Fusion of synthetic chromosomes from distinct cells generated a single genome in a target cell. Precise, rapid, large-scale genome engineering operations are useful tools for creating diverse synthetic genomes. —SYM

Science, this issue p. 922

MICROBIOTA

Superantigens spur IgA secretion

Mucosal immunoglobulin A (IgA) is abundant and interacts with the gut microbiome. To examine microbial induction of IgA in humans, Bunker *et al.* screened microbiota from infants against mouse and human IgA. A subset of samples bound IgA in a way that indicated the presence of superantigens, which bind T cell receptors or B cell receptors outside of the typical antigen-binding region, leading to nonspecific activation. Putative superantigens in commensal members of Lachnospiraceae activated human VH3-positive B cells and induced IgA production in mice. The authors suggest that commensal superantigens may be dominant forces behind IgA production in humans. —LP

Sci. Transl. Med. **11**, eaau9356 (2019).

IN OTHER JOURNALS

Edited by **Caroline Ash** *and* **Jesse Smith**

The ubiquitous protist parasite *Toxoplasma gondii* infects many species but only develops sexually in cats.

PARASITES

Breaking the species barrier

The protozoan parasite *Toxoplasma gondii* is found in most mammals and is spread by ingestion of contaminated food and water. It is a health risk to humans because it can form brain cysts and cause life-changing complications during pregnancy. Despite this parasite's ability to infect many mammals, it can only complete its life cycle in felids, including domestic cats. Martorelli di Genova *et al.* sought to understand the basis for the specificity of the sexual stages for the gut epithelium of cats. Using cat gut organoids, they found that the parasite's sexual stages are stimulated to develop by the plant fat linoleic acid. Cats uniquely lack the enzyme needed for linoleic acid digestion, delta-6-desaturase. To test whether intact linoleic acid acts as a parasite signal, mice were given a chemical treatment to inhibit their desaturase, then fed linoleic acid and infected. *T. gondii* promptly initiated sexual development and the mice shed infectious oocysts in their feces 6 days later. —CA

PLOS Biol. **17**, e3000364 (2019).

PHYSICS

Twisted multilayer graphene

Since the recent discovery of superconductivity in twisted bilayer graphene, physicists have been exploring other twisted heterostructures, including those in which two bilayers of graphene are twisted with respect to each other. These experiments have shown signatures of exotic states, inspiring theorists to try to understand their properties. Liu *et al.* undertook a theoretical study of the general case of two graphene multilayers, each of which could contain an arbitrary number of graphene monolayers, twisted with respect to each other. They found that such heterostructures retained the approximately flat bands characteristic of twisted bilayer graphene at the same "magic" twist angle. Additionally, twisted

Published by AAAS

The fairy ring–forming fungus *Marasmius oreades*

FUNGAL GENETICS

Fairy rings magically prevent mutation

Mutation can often occur as part of the process of cellular division and may have deleterious consequences for multicellular organisms. Through genomic sequencing of *Marasmius oreades*, a species of fairy ring mushroom, Hiltunen *et al.* found that in this relatively long-lived species, the accumulation of mutations is an order of magnitude less than previously discovered for any organism. This could not be attributed to purifying selection and indicates that this species has evolved high-fidelity replication and/or repair mechanisms to prevent mutation accumulation. Given that fungi, unlike mammals, do not sequester their reproductive germ cells, this is of interest in understanding how an organism can police its own cell division to maintain a low rate of mutation accumulation. —LMZ

Curr. Biol. **29**, 2758 (2019).

multilayer graphene showed interesting topological properties that depended on the number and stacking of monolayers in each multilayer. —JS

Phys. Rev. X **9**, 031021 (2019)

BIOSYNTHESIS

Building psychoactives with purpose

Plants are skilled, if unwitting, organic chemists that produce a panoply of natural products that influence human biochemistry and cognition. Farrow *et al.* identified a suite of enzymes in the iboga plant, *Tabernanthe iboga*, that produce (−)-ibogaine from a complex precursor alkaloid. The carbon scaffold is rearranged in a series of steps that follow or mirror the synthesis of (+)-catharanthine, an intermediate in the formation of the anticancer drug vinblastine. Knowledge of their biosynthetic pathways may stimulate research into the psychoactive properties of iboga alkaloids, including potential antiaddictive activities. —MAF

J. Am. Chem. Soc. **141**, 12979 (2019).

CELL BIOLOGY

Born in the ribosomal tunnel

The correct folding and processing of nascent polypeptides requires ribosome-associated chaperones. One such chaperone, the ribosome-bound nascent polypeptide–associated complex (NAC), cross-links to newly assembled polypeptides. Gamerdinger *et al.* discovered that NAC is positioned above the ribosomal exit site, from where it antagonizes incorrect endoplasmic reticulum protein targeting. Remarkably, the extended N-terminal tail of the β subunit inserts deeply inside the ribosomal tunnel to facilitate their folding and sorting. As the peptide elongates, it displaces NAC from the ribosomal tunnel. NAC then rearranges on the surface of the ribosome, ready to coordinate further cotranslational activities. —SMH

Mol. Cell 10.1016/j.molcel.2019.06.030 (2019).

PHYSICS

Controlling exciton lifetimes

Excitons are electron-hole pairs optically induced in condensed matter systems which reemit a photon when they recombine. Monolayer transition metal dichalcogenides, e.g., $MoSe_2$, are of particular interest owing to the strong binding energy of the excitons and an ultrafast response time. By sandwiching the monolayers of $MoSe_2$ between layers of hexagonal boron nitride (hBN), Fang *et al.* show that the lifetime of the excitons can be controlled across an order of magnitude from 1 to 10 picoseconds with the lifetime determined simply by the thickness of the hBN sandwiching layers. Such control of the exciton lifetime and transport properties should be applicable to other two-dimensional materials and could be exploited for use in a variety of ultrafast optoelectronic applications. —ISO

Phys. Rev. Lett. **123**, 067401 (2019).

REGENERATIVE MEDICINE

Improving heart muscle

Heart failure is caused by injury to the myocardium, the heart muscle, which results in irreversible loss because this tissue cannot regenerate itself. Bargehr *et al.* investigated whether regenerative medicine approaches involving human embryonic stem cell (hESC)–derived epicardial cells, which produce stromal cells, smooth muscle cells, and growth factors, can remuscularize injured heart. They showed that hESC-derived epicardial cells improved the structure and function of heart tissue in vitro and improved hESC-derived cardiomyocyte grafts in rats with heart tissue loss. The improvements to heart function in vivo persisted for 3 months, suggesting an approach for improving heart regenerative medicine. —GKA

Nat. Biotech. **37**, 895 (2019).

PHOTO: WALLY EBERHART/GETTY IMAGES

Published by AAAS

ALSO IN *SCIENCE* JOURNALS

Edited by **Michael Funk**

NEURODEVELOPMENT

Neurons negotiating boundaries

Barriers around the brain and spinal cord separate central from peripheral nervous systems, yet the two systems are interlinked. Suter and Jaworski review what is known about how cells, axons, and signals negotiate the boundary zone. Understanding what goes wrong in boundary transgressions reveals the inner workings of multiple, partially redundant mechanisms built during development that separate the two compartments in adulthood. —PJH

Science, this issue p. 881

HUMAN GENETICS

The genetics of sexual orientation

Twin studies and other analyses of inheritance of sexual orientation in humans has indicated that same-sex sexual behavior has a genetic component. Previous searches for the specific genes involved have been underpowered and thus unable to detect genetic signals. Ganna *et al*. perform a genome-wide association study on 493,001 participants from the United States, the United Kingdom, and Sweden to study genes associated with sexual orientation (see the Perspective by Mills). They find multiple loci implicated in same-sex sexual behavior indicating that, like other behavioral traits, nonheterosexual behavior is polygenic. —LMZ

Science, this issue p. 882; see also p. 869

IMMUNOLOGY

Thirteen is the charm in anaphylaxis

Immunoglobulin E (IgE) is a type of antibody associated with allergies and response to parasites such as worms. When high-affinity, allergen-specific IgE binds its target, it can cross-link receptors on mast cells that induce anaphylaxis. It remains unclear, however, how B cells are instructed to generate high-affinity IgE. Gowthaman *et al*. discovered a subset of T follicular helper cells ($T_{FH}13$) that direct B cells to do just that. $T_{FH}13$ cells are induced by allergens but not during parasite infection. Transgenic mice lacking these cells show impaired production of high-affinity, anaphylactic IgE. $T_{FH}13$ cells, which are elevated in patients with food and aeroallergies, may be targeted in future antianaphylaxis therapies. —STS

Science, this issue p. 883

MALARIA

Targeting parasite's protein kinase

Malaria elimination goals are constantly eroded by the challenge of emerging drug and insecticide resistance. Alam *et al*. have taken established drug targets—CLK protein kinases involved in regulation of RNA splicing—and investigated how inhibition of the parasite's enzymes blocks completion of its complex life cycle. They identified an inhibitor of the parasite's CLK protein kinase that was 100-fold less active against the most closely related human protein kinase and effective at clearing rodent malaria parasites. Not only does this compound halt the development of sexual stages but it also limits transmission to the mosquito vector of the parasite, a key requirement for malaria drugs. —CA

Science, this issue p. 884

SUPERCONDUCTIVITY

Pervasive fluctuations

Among the many intertwined phases in the cuprate superconductor phase diagram is the charge density wave (CDW) order, which has been detected in all major cuprate families. It is thought that CDW competes with superconductivity, but whether it has bearing on the mechanism of superconductivity remains unclear. Arpaia *et al*. undertook a comprehensive study of charge density fluctuations in a cuprate family, varying doping and temperature. They found that short-range dynamic charge fluctuations were present in a large portion of the phase diagram, at temperatures considerably higher than those at which the CDW order disappears. —JS

Science, this issue p. 906

SIGNAL TRANSDUCTION

A dynamic signaling scaffold

In neurons, many cellular processes are regulated by receptor tyrosine kinases (RTKs), cell surface receptors whose activation can depend on other signaling pathways. Zhou *et al*. used super-resolution imaging to visualize colocalization of signaling proteins on the membrane-associated periodic skeleton (MPS) that is formed by actin, spectrin, and related molecules in the axons and dendrites of neurons. The colocalization of signaling proteins in different pathways leads to transactivation of RTK, which initiates intracellular signaling. In a negative feedback loop, the downstream signaling in turn leads to degradation of the MPS. Thus, the MPS is a dynamically regulated platform that coordinates signal transduction in neurons. —VV

Science, this issue p. 929

IMMUNOLOGY

Distinct immunology of the placenta

The placenta is formed when specialized cells from an embryo invade the maternal uterus. The effectiveness of this process can determine whether complications in pregnancy, such as preeclampsia, arise. In a Perspective, Colucci discusses the emerging role of immune cells in the formation of the placenta. Homeostatic immune cell activities facilitate placental implantation without inducing an immune response to foreign antigens expressed on fetal-derived tissues. Understanding this process more fully could help to prevent or treat placenta-associated complications of pregnancy. —GKA

Science, this issue p. 862

SKIN INFLAMMATION

Resurrecting sentinels in the skin

Langerhans cells are resident innate immune cells in the skin that play essential roles in promoting local immune responses and maintaining skin homeostasis. Langerhans cells arise from fetal progenitors that seed the skin early in development. In a mouse hematopoietic stem cell transplant model, Ferrer *et al*. found that monocytes from the blood infiltrate the skin and eventually replenish the Langerhans cell network. These observations are in agreement with previous studies looking at other sites, but the process by which monocytes give rise to Langerhans cells is inefficient, limiting the extent to which they can be renewed in the skin. —AB

Sci. Immunol. **4**, eaax8704 (2019).

ARCHAEOLOGY

The early occupation of America

The Cooper's Ferry archaeological site in western North America has provided evidence for the pattern and time course of the early peopling of the Americas. Davis *et al*. describe new evidence of human activity from this site, including stemmed projectile points. Radiocarbon dating and Bayesian analysis indicate an age between 16,560

Published by AAAS

and 15,280 years before present. Humans therefore arrived in the Americas before an inland ice-free corridor had opened, so a Pacific coastal route was the probable entry route. The stemmed projectile points closely resemble those found in Upper Paleolithic Japan, also supporting the hypothesis of a coastal route. —AMS

Science, this issue p. 891

MAGNETISM

Skyrmions in a frustrated magnet

Skyrmions—tiny, topologically protected whirlpools of spin—have been investigated as potential information carriers in spintronic devices. Usually, skyrmions appear in noncentrosymmetric materials or at interfaces between materials. In contrast to this rule of thumb, Kurumaji *et al*. observed a skyrmion lattice phase in the centrosymmetric material Gd_2PdSi_3. The magnetic frustration present in this material helped stabilize the skyrmion phase, which was detected through transport measurements in magnetic field. —JS

Science, this issue p. 914

Published by AAAS

REVIEW SUMMARY

NEURODEVELOPMENT

Cell migration and axon guidance at the border between central and peripheral nervous system

Tracey A. C. S. Suter and Alexander Jaworski*

BACKGROUND: In vertebrates, the central and peripheral nervous system (CNS and PNS, respectively) are segregated at the cellular level. The CNS encompasses the brain and spinal cord, and the PNS is composed of numerous ganglia and nerves in the body periphery. Each subsystem is characterized by specialized neurons and unique glial cell types critical for neural circuit function. During development, virtually all CNS neurons and glia arise from progenitors located within this subdivision of the nervous system, and the vast majority of PNS-resident cells originate from the neural crest and ectodermal placodes in the periphery. However, it has become evident that at least a subset of peripheral glia is generated in the CNS and migrates into the PNS. Further, whereas most CNS and PNS neurons project axons exclusively within the same subdivision that houses their cell body, hindbrain and spinal cord motor neurons innervate various peripheral targets, and peripheral sensory neurons send axons into the CNS. Therefore, during development, when neurons and glia migrate to their destinations and axons navigate to their targets, the CNS-PNS interface must be permeable to select cells and axons at specific locations but prevent intermixing of most other CNS and PNS components. The cellular and molecular mechanisms that establish this pattern of segregation and selective connectivity are now beginning to be understood.

ADVANCES: Multiple cell types and signaling pathways exert tight control over the movement of cells and axons between the developing vertebrate CNS and PNS. A multilayered barrier surrounds most of the brain and spinal cord to prevent aberrant spillover of CNS and PNS components, but specialized access points called transition zones allow regulated cell migration and axon growth across the CNS-PNS boundary. Studies in various vertebrate species have begun to unravel some of the rules that govern cellular traffic at the CNS-PNS interface. It has become apparent that inhibitory signals from specialized cells located at the CNS-PNS border help to confine migrating cells and nascent axons to one nervous system subdivision; the cues that attract cells and axons to their correct targets are also important for preventing aberrant crossing of the CNS-PNS border. When these signaling pathways are disrupted, transition zones are particularly vulnerable to transgressions by cells and axons that would normally remain within their nervous system compartment. The permissive nature of transition zones is further underscored by the fact that cells in the mature nervous system can occasionally traverse these windows in response to injury. The developmental mechanisms that direct the correct cells and axons toward and across transition zones are still poorly understood, but attractive signals from cells at or beyond the CNS-PNS interface appear to play important roles. Furthermore, axons that need to cross the border are guided there by cues that repel them from inappropriate targets within their nervous system subdivision of origin, and they actively filter out guidance information that would otherwise steer them away from transition zones. Beyond this selective responsiveness to directional signals, these axons also use specialized subcellular structures to penetrate CNS-PNS barrier constituents.

ON OUR WEBSITE

Read the full article at http://dx.doi.org/10.1126/science.aaw8231

OUTLOOK: The tight regulation of cell migration and axon navigation at the developing CNS-PNS interface is critical for establishing proper neuronal connectivity and allocating functionally specialized cells to the two major nervous system subdivisions. Further investigation of the relevant mechanisms holds the promise to elucidate the full repertoire of cellular interactions, guidance molecules, and signal transduction pathways that control this key dividing line in the nervous system. Because the fundamental division of the nervous system into central and peripheral compartments appears conserved across species, including some invertebrates, continuing to study the CNS-PNS boundary in multiple model organisms will contribute to understanding the evolution of nervous system organizing principles. Moreover, insights into signaling mechanisms at the CNS-PNS interface could aid in the development of therapeutic approaches that rekindle developmental plasticity at transition zones in the mature nervous system and promote regeneration after injury or onset of neurodegenerative disease. ■

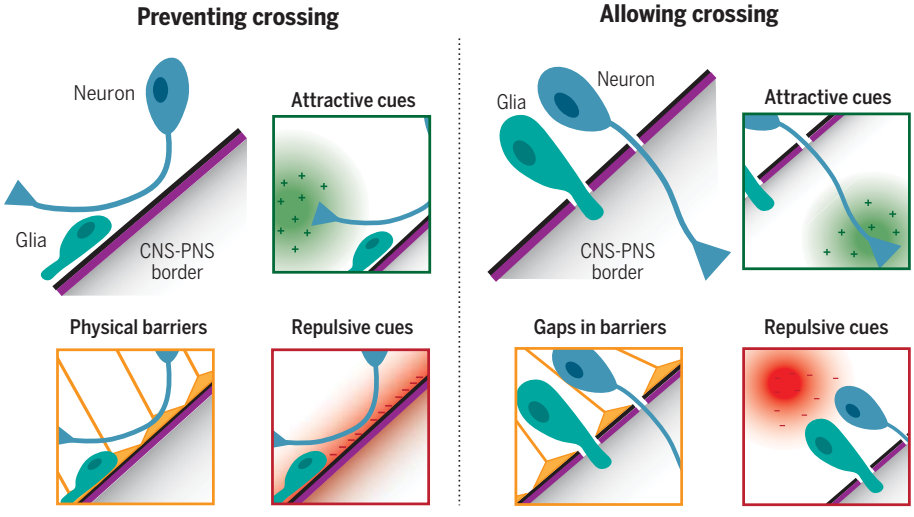

Control of the CNS-PNS boundary. During nervous system development, most glia, neurons, and axons are prevented from crossing the CNS-PNS border, whereas select subsets are allowed to move between the two compartments. Physical barriers and combinations of attractive and repulsive cues control cell behaviors at the CNS-PNS dividing line.

The list of author affiliations is available in the full article online.
*Corresponding author. Email: alexander_jaworski@brown.edu
Cite this article as T. A. C. S. Suter and A. Jaworski, *Science* **365**, eaaw8231 (2019). DOI: 10.1126/science.aaw8231

REVIEW

NEURODEVELOPMENT

Cell migration and axon guidance at the border between central and peripheral nervous system

Tracey A. C. S. Suter[1,2] and Alexander Jaworski[1,2]*

The central and peripheral nervous system (CNS and PNS, respectively) are composed of distinct neuronal and glial cell types with specialized functional properties. However, a small number of select cells traverse the CNS-PNS boundary and connect these two major subdivisions of the nervous system. This pattern of segregation and selective connectivity is established during embryonic development, when neurons and glia migrate to their destinations and axons project to their targets. Here, we provide an overview of the cellular and molecular mechanisms that control cell migration and axon guidance at the vertebrate CNS-PNS border. We highlight recent advances on how cell bodies and axons are instructed to either cross or respect this boundary, and present open questions concerning the development and plasticity of the CNS-PNS interface.

In the vertebrate nervous system, the central nervous system (CNS) and peripheral nervous system (PNS) are characterized by functionally specialized neurons and unique glial cell types. The CNS is composed of the brain and spinal cord, and the PNS encompasses the sympathetic, parasympathetic, and enteric subdivisions and ganglia containing various sensory neurons with their associated nerves and glia. Virtually all CNS-resident neurons and glia arise locally, and the vast majority of cells in the PNS originate from the neural crest and ectodermal placodes in the periphery. However, at least a subset of glia is generated in the CNS and migrates into the PNS. Further, most CNS and PNS neurons send axons to targets within the same subdivision that houses their cell body, but motor and sensory axons project out of and into the CNS, respectively, to allow CNS-PNS communication. Therefore, although intermixing of most CNS and PNS components is prevented by cellular interactions at the boundary between the two nervous system compartments, this barrier must be permeable to select cells and axons at specific locations during development. The mechanisms that restrict and facilitate cell migration and axon growth across the CNS-PNS interface have long remained elusive, but recent research has begun to uncover some of the underlying developmental principles. In this review, we first describe the anatomy of the CNS-PNS border before summarizing our current understanding of how the behavior of neurons and glia at this dividing line is controlled. We also highlight promising research directions regarding the formation and function of this boundary.

[1]Department of Neuroscience, Division of Biology and Medicine, Brown University, Providence, RI 02912, USA. [2]Robert J. and Nancy D. Carney Institute for Brain Science, Providence, RI 02912, USA.
*Corresponding author. Email: alexander_jaworski@brown.edu (A.J.)

Cellular constituents of the CNS-PNS boundary

The surface of the CNS is a mostly uniform, impenetrable barrier preventing the movement of neurons, glia, and axons between the CNS and surrounding tissues, including the PNS. This boundary is formed by various cellular and extracellular components, including radial glia and astrocytic endfeet (forming a structure called the glia limitans), the meninges, and a specialized extracellular matrix (ECM) (Fig. 1). However, during development, specific access points called transition zones are selectively permeable for subsets of cells and axons, allowing for connectivity between the CNS and PNS. Transition zones are regions of the nerve rootlets protruding from the neural tube surface where CNS and PNS tissues meet and partially interdigitate (Fig. 1, B to D). They are characterized by local disruption of some of the CNS-PNS barrier components and the presence of dedicated cell types—boundary cap (BC) cells in mice (Fig. 1, A to C) and motor exit point (MEP) glia in fish (Fig. 2A)—which help to regulate CNS-PNS access.

Radial glia and astrocytes

During development, neuroectodermally derived neural progenitors, termed radial glia, form elongated processes that extend from the ventricular to the pial surface of the brain and spinal cord (Fig. 1, A to C). Radial glia are not only the essential, primary contributors to CNS neurogenesis and gliogenesis, but also serve as a scaffold for migration of their cellular offspring away from the ventricular zone (*1*). Additionally, radial glia aid both in the architectural organization of the CNS and in establishing the CNS-PNS boundary. At the pial surface, radial glia processes contact the basement membrane, which surrounds the CNS (see below), and their endfeet form a tight physical barrier essential for preserving the separation of the CNS and PNS compartments (*1*). As proliferative activity ceases, radial glia gradually disappear or, in rare instances, directly transform into astrocytes with a similar morphology. Concurrently, astrocyte precursors, which arise from radial glia in the ventricular zone, begin to migrate from their birthplace, and astrocytic processes fill the gaps vacated by radial glia endfeet at the pial surface (*2*, *3*). Ultimately, astrocytes completely replace radial glia to form the glia limitans at the CNS-PNS border (Fig. 1, C and D), but the timing of this substitution remains poorly understood. At mature transition zones, where axons have crossed the CNS-PNS boundary, the peripheral portion of the transition zone apparatus contains a funnel-shaped sleeve of glial processes, which surround and separate each axon (*4*–*6*).

Meninges and basement membrane

The basement membrane is a thin, protective layer of ECM molecules that surrounds most tissues in the body, including the neural tube (Fig. 1). It is largely composed of laminins, collagens, nidogens, and proteoglycans, and it further contains a variety of signaling molecules that interact with the core ECM constituents and instruct numerous cellular behaviors (*7*). The CNS basement membrane is produced predominantly by radial glia and the mesenchyme surrounding the neural tube, and it plays an integral role in neural development. It provides an adhesive surface for radial glia endfeet and helps to control neural crest cell migration and axon growth at the CNS-PNS boundary. After neural crest delamination, the basement membrane forms a complete seal around the neural tube surface (*8*, *9*) (Fig. 1).

The meninges are membranes of connective tissue enveloping and protecting the entire CNS (Fig. 1). Three layers compose the mature meninges: the pia, arachnoid, and dura mater (*10*). During development, the meninges surrounding the forebrain arise from cranial neural crest cells, but the origin of the meninges surrounding the caudal CNS had long been controversial. Over time, consensus emerged that spinal cord meninges are not neural crest derived and instead form by condensation of mesodermal mesenchyme around the neural tube (*11*–*13*). The initial, primitive meningeal layer, termed leptomeninges, is located in direct apposition to the outer basement membrane of the neural tube (*8*, *10*). During development, the meninges fulfill multiple functions: they control the migration and positioning of various neuronal populations, regulate radial glia proliferation and survival, and organize and maintain the basement membrane (*10*, *14*, *15*). They also produce signaling molecules that appear to control axon behavior at the CNS-PNS interface (*16*).

Boundary cap cells and motor exit point glia

Transition zones allow movement of select cells and axons between the CNS and PNS (*6*, *17*). They

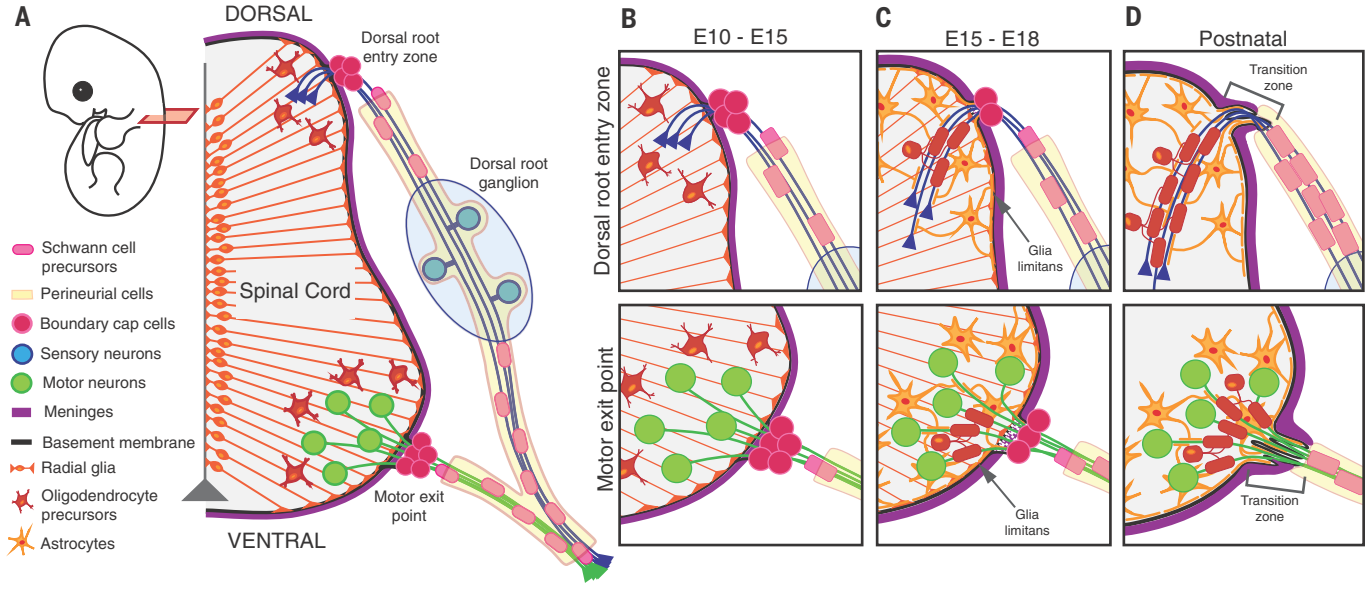

Fig. 1. Anatomy of the CNS-PNS border during development. (**A**) Schematic of mouse embryo indicating the plane of the spinal cord sections shown on the right. Depicted are the various constituents of the CNS-PNS border. (**B** to **D**) Developmental changes in cellular composition and arrangement of spinal cord transition zones.

are best characterized in the spinal cord, where most motor axons leave the CNS through MEPs and dorsal root ganglion sensory axons enter the CNS at the dorsal root entry zone (DREZ) (Fig. 1). The importance of these transition zones is highlighted in human patients with Friedreich ataxia, in which DREZs are disorganized and exhibit intrusions of CNS and PNS components into the inappropriate compartment (*18*). In rodents and chicks, BC cells, a transient population of multipotent neural crest cells, play an integral role in the establishment and maintenance of transition zones during development (*19*). BC cells migrate in close association with the neural tube surface before arresting at axon entry and exit points (*20*, *21*) (Fig. 1, A to C). BC cells at DREZs and MEPs have distinct gene expression profiles, and ventral, but not dorsal, BC cells appear to extend protrusions into the neural tube, suggesting that they each fulfill specialized functions (*19*, *22*). Moreover, the timing of BC cell arrival relative to axon exit and/or entry differs between MEPs and DREZs. BC cells arrive at the presumptive DREZ before sensory axons, consistent with the idea that they could guide sensory axons into the spinal cord; in contrast, motor axons emerge from the spinal cord before BC cell clustering at MEPs, suggesting that nascent motor axons might recruit BC cells to MEPs (*8*, *21*). After axon growth through MEPs and DREZs has concluded, BC cells differentiate into multiple peripheral cell types (*19*). Although BC cells associate with all exit and entry points of hindbrain and spinal nerves (*19*, *20*), it remains elusive whether an analogous cell population is present at the transition zone for olfactory sensory axons.

Zebrafish do not possess a neural crest–derived equivalent of BC cells. Instead, MEP glia, a specialized subset of myelinating glia whose gene expression signature combines CNS and PNS characteristics, originates in the CNS and localizes to the proximal portion of motor axon tracts just outside of the neural tube (*23*). To date, no similar cell type has been identified at sensory axon entry points. MEP glia in fish localize to the same region that ventral BC cells do in birds and mammals and similarly function to maintain the integrity of the CNS-PNS boundary, but they appear to do so through distinct mechanisms (*23*, *24*). This suggests that these cell types represent convergent evolutionary solutions to a common problem in CNS-PNS border development across fish and amniotes.

Positioning CNS and PNS glia

With the exception of microglia, all glia of the CNS and PNS arise from neural ectoderm during development. We focus here on the behavior of these neuroectoderm-derived glia at the CNS-PNS interface and refer the interested reader to other excellent reviews on the development of microglia, which originate in the embryonic yolk sac and, shortly after onset of neuronal differentiation, migrate into the developing CNS by breaking through the neural tube basal lamina using matrix metalloproteases (*25*, *26*). CNS-resident astrocytes and oligodendrocytes are born in the neural tube, whereas PNS Schwann cells, satellite glia, BC cells, olfactory ensheathing glia, and most perineurial glia arise from neural crest progenitors in the periphery. By contrast, MEP glia and a small subset of perineurial glia are CNS derived and enter the PNS through transition zones. However, in the intact, mature nervous system, astrocytes and oligodendrocytes are not observed in the PNS and peripheral glia do not enter the CNS. This segregation is likely of functional importance, e.g., peripheral Schwann cells produce basement membrane, which would interfere with cellular interactions in the CNS (*27*, *28*). Nevertheless, transition zones remain plastic enough to adapt to environmental perturbations or developmental defects that deplete the glial pool in one compartment, allowing Schwann cells, oligodendrocytes, and astrocytes to cross the CNS-PNS boundary and partially compensate for the absence of their missing counterpart. Thus, the CNS and PNS environments are seemingly able to support the survival and differentiation of glial cells originating in the other compartment (*24*, *29*, *30*). The mechanisms that permit and restrict movement of glia between the CNS and PNS are now beginning to be understood.

Regulated glial crossing between the CNS and PNS

The long-standing idea that some peripheral glia might originate in the neural tube has been confirmed by recent work in zebrafish and mice, raising the question of how these cells penetrate the CNS-PNS boundary. In zebrafish, MEP glia leave the neural tube through MEPs and myelinate motor axons in spinal cord–proximal regions of ventral roots (*23*). Although MEP glia have not been observed in birds or mammals, at least one glial cell type appears to emigrate from the CNS into the PNS as part of normal development across vertebrates: a subset of perineurial cells (Fig. 1) (*31*, *32*). Perineurial glia envelop peripheral nerves to protect them from toxins and infection, regulate extracellular ion concentrations, and provide metabolic support (*33*). Although most perineurial cells originate from the neural crest, the CNS-proximal aspect of the ventral root perineurium in both zebrafish and mice is derived from Nkx2.2^{+}

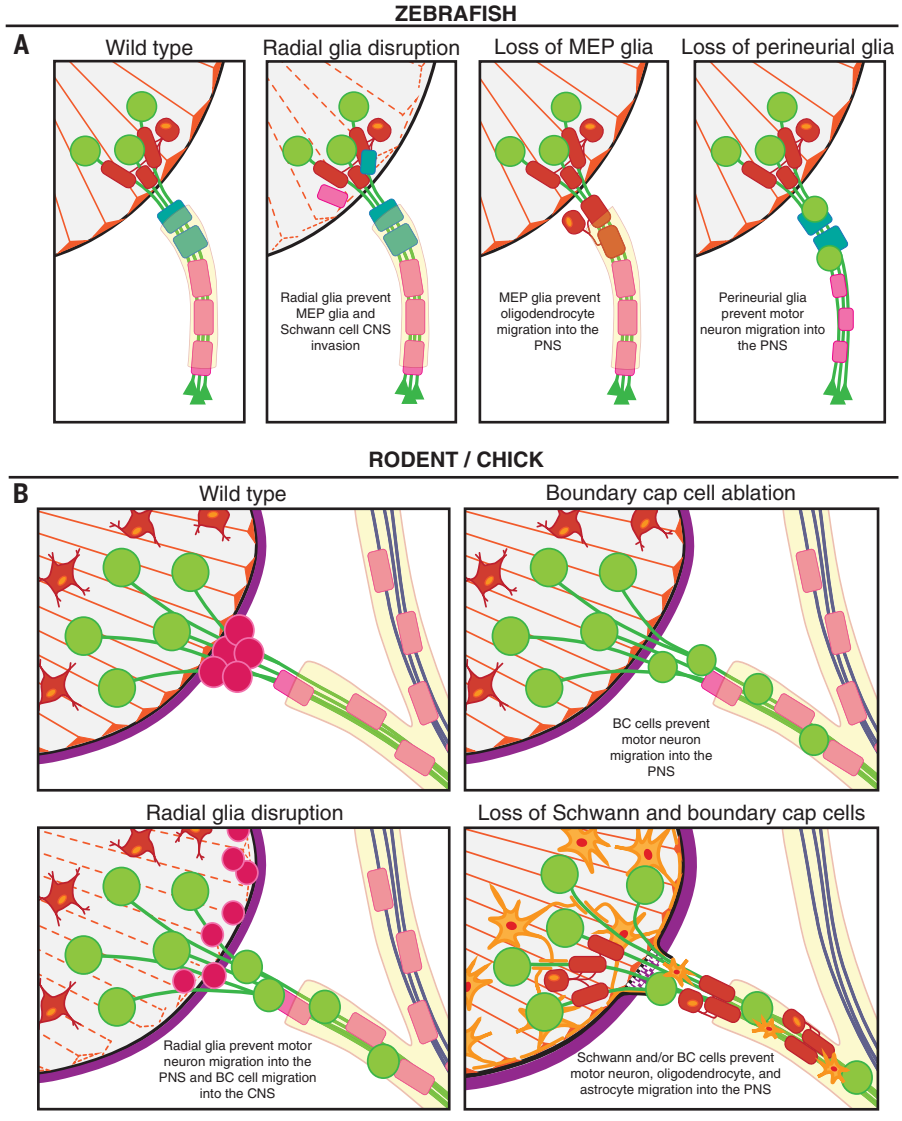

Fig. 2. Migration of neurons and glia across the CNS-PNS border. (**A**) Schematic of wild-type zebrafish motor exit point, followed by depictions of the effects resulting from disruption or loss of various cell types. (**B**) Schematic of wild-type rodent/chick motor exit point, followed by three examples of events occurring after the disruption and/or loss of a particular cell type. Text within each panel summarizes the effect on CNS-PNS segregation.

progenitors in the ventral spinal cord. These CNS-derived perineurial glia leave the spinal cord through MEPs and join their peripherally generated counterparts to form a continuous sleeve around motor nerves (*31*, *32*).

Transition zones also allow peripheral glia to transiently enter the CNS during development. Live-imaging studies in zebrafish have demonstrated that a small number of $Sox10^+$ neural crest–derived peripheral glia enter the spinal cord through MEPs after motor axon exit but before MEP glia emigration. After a few hours, all of these PNS-derived cells relocate back into the periphery and remain restricted to the PNS afterward (*34*). This transient migration of peripheral glia into the CNS has not been observed in higher vertebrates, raising questions about its evolutionary conservation and functional significance.

Together, these recent studies have uncovered a selective permeability of transition zones for glial migration during development, but the specific mechanisms that permit and instruct the movement of MEP glia, $Nkx2.2^+$ perineurial cells, and $Sox10^+$ peripheral glia across the CNS-PNS border have not yet been elucidated. However, these migrations appear to be restricted to the time before radial glia endfeet form a continuous seal at MEPs, suggesting that gaps between these endfeet are a prerequisite for glial crossing between the CNS and PNS.

Preventing aberrant intermixing of CNS and PNS glia

The vast majority of CNS and PNS glia remain confined to their respective compartment of origin. This raises the question of how aberrant intermixing of CNS and PNS glia is prevented, and experimental manipulations that erode this segregation have begun to provide insights into some of the relevant mechanisms. In zebrafish, ablation of MEP glia causes oligodendrocytes to emigrate from the spinal cord through MEPs and myelinate motor axons (Fig. 2A). Even during normal development, oligodendrocyte processes constantly probe the peripheral space outside of the spinal cord, but these cellular extensions retract upon contacting MEP glia (*23*). Contact-mediated inhibition from MEP glia therefore appears essential for preventing oligodendrocyte exit from the fish spinal cord, even though the precise molecular mechanism remains elusive. In mice, BC cells appear to fulfill a similar role, as oligodendrocytes exit through MEPs and DREZs after genetic ablation of the BC (*29*), but it is unknown whether this function involves direct physical contact between oligodendrocytes and BC cells (Fig. 2B). Interfering with Schwann cell differentiation or survival in fish and mice by genetic deletion of *Sox10* or *ErbB3* also leads to oligodendrocyte (and in mice astrocyte) emigration from the CNS through transition zones (*23*, *35*, *36*) (Fig. 2B). However, because these manipulations also affect MEP glia and BC cells, it is not entirely clear whether Schwann cells help to confine glia to the CNS, but the presence of CNS glia in peripheral nerves from a human patient lacking Schwann cell myelin is consistent with this idea (*29*). Lastly, pharmacological inhibition of A2a adenosine receptors or blockade of neurotransmitter release in zebrafish results in ectopic oligodendrocyte migration through MEPs without affecting MEP glia development (*37*). Although the precise mechanism underlying this effect has not been elucidated, this finding suggests that, in addition to interactions with peripherally located glia, neuronal activity helps to prevent oligodendrocyte migration across the CNS-PNS border.

PNS-resident glia also need to be prevented from entering the CNS. Radial glia appear to fulfill an essential function in this process. As mentioned, in zebrafish, $Sox10^+$ peripheral glia freely cross between the CNS and PNS at the MEP until radial glia endfeet form a continuous barrier (*34*). When radial glia are selectively ablated, peripherally located glia, including MEP glia, continue to migrate into the spinal cord throughout later stages of development (*34*) (Fig. 2A). Similarly, in mice, genetic inactivation of the chemokine CXCL12 or its receptor, CXCR4, leads to the formation of gaps between radial glia endfeet in the developing spinal cord, resulting in immigration of BC cells into the neural tube through DREZs and MEPs (*38*) (Fig. 2B). Together, these studies support the idea that radial glia endfeet prevent peripheral glia from invading the CNS. Lesion studies in the adult rodent spinal cord suggest that astrocytic endfeet fulfill the same function after the disappearance of radial glia. After spinal cord injury, Schwann cells often invade the CNS and remyelinate axons at the lesion site while retaining their original compartment identity

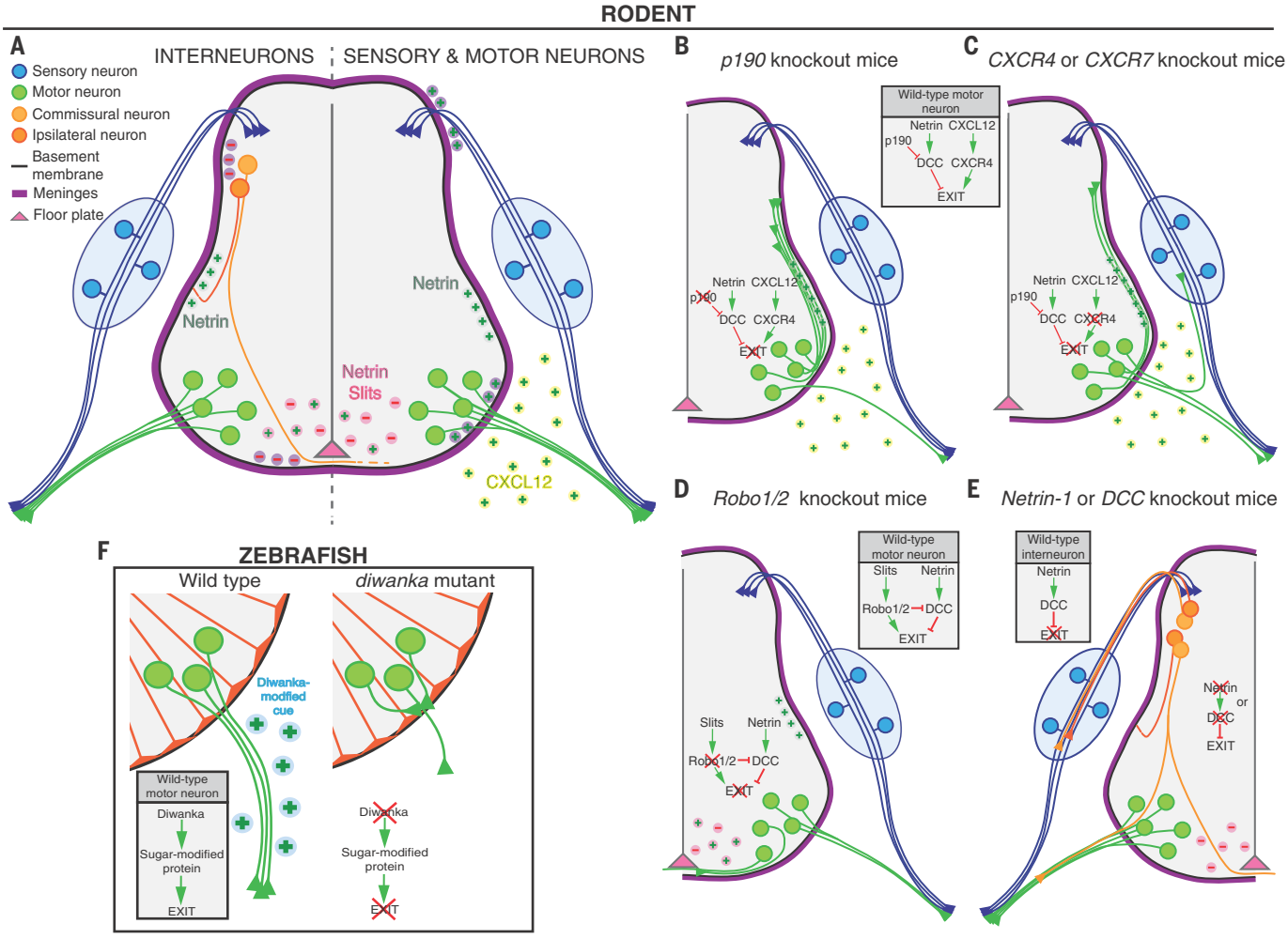

Fig. 3. Aberrant axonal crossing of the CNS-PNS border. (**A**) Schematic of rodent spinal cord and relevant axonal populations. Colored circles signify attractive and repulsive guidance cues, with colors indicating tissue of origin, e.g., purple circles represent meninges-derived cues. (**B**) Failure of motor axon exit due to gain of attraction to basement membrane–associated Netrin-1. (**C**) Failure of motor axon exit due to loss of CXCL12 attraction toward the periphery. (**D**) Failure of motor axon exit due to loss of responsiveness to spinal cord–intrinsic repulsive guidance cues. (**E**) Misprojection into the PNS by axons that are normally confined to the CNS caused by loss of attraction to their appropriate targets. (**F**) Peripheral attraction is necessary for motor axon exit in zebrafish. Gray boxes depict the wild-type signaling pathway, and notes within panels show how these pathways are perturbed.

and myelination characteristics (*39*–*41*). Early work attributed this migration of peripheral glia into the injured spinal cord to the disruption of the astrocytic endfeet barrier (*41*–*44*). However, Schwann cells also enter the spinal cord and remyelinate CNS axons in multiple rat lines in which CNS myelin is eliminated but the glia limitans appears intact (*30*). This indicates that CNS myelin provides inhibitory signals that prevent Schwann cell invasion of the CNS. Myelin-associated glycoprotein is one such potential signal, as it inhibits the migration of Schwann cells and induces their death through the p75 neurotrophin receptor (*45*). Overall, the precise interplay of mechanisms that restrict and, in the case of injury, trigger Schwann cell crossing of the CNS-PNS border remain poorly understood. However, these spinal cord injury studies unmask a notable plasticity in the allocation of glia to the CNS and PNS compartments, endowing the nervous system with the capacity to repair itself.

Controlling neuronal cell body and axon behavior at the CNS-PNS interface

Neurons that arise in the CNS do not enter the PNS, even though their cell bodies often migrate over long distances within the brain and spinal cord. Similarly, peripherally born neurons remain confined to the PNS, with one notable exception: Gonadotropin-releasing hormone (GnRH) neurons migrate from the olfactory placode into the brain (*46*). Although the vast majority of axonal projections are confined to either the CNS or PNS, a substantial number of axons grow across the CNS-PNS interface to connect the two subdivisions. Motor neurons are located in the hindbrain and spinal cord, and their axons leave the CNS through MEPs to innervate peripheral muscles and ganglia. Neural crest–derived somatosensory neurons localize to dorsal root ganglia and multiple cranial ganglia and project axons into the CNS through DREZs (Figs. 1 and 3) or various cranial nerves. Gustatory and audiovestibular information is similarly carried into the CNS by sensory neurons, which arise from the cranial neural crest and otic placode, reside in specialized ganglia, and project through cranial nerves. Lastly, olfactory sensory neurons are born in the nasal placode, reside in the olfactory epithelium, and send axons through the cribriform plate into the olfactory bulb. The mechanisms that selectively allow some neurons and axons to cross the CNS-PNS border while preventing most others from traversing this boundary are only now beginning to be understood.

Migration of select neurons across the CNS-PNS border

GnRH neurons are currently the only known neuronal population that migrates across the CNS-PNS boundary, raising the question of what allows them to accomplish this unique feat. However, they reach the CNS as part of a larger "migratory mass," which contains additional, as yet unidentified cells that express neuronal markers (*46*, *47*). Failure of GnRH neurons to populate the hypothalamus causes hypogonadotropic hypogonadism, underscoring the functional importance of their journey into the CNS (*47*). GnRH neurons originate peripherally in the nasal placode and translocate along bundles of olfactory, vomeronasal, and terminal nerve axons to leave the olfactory pit. These neurons then use this axonal scaffold to cross the developing cribriform plate and enter the brain, either through or just ventral to the olfactory bulb, at which point they continue migrating toward their final destination in the hypothalamus (*46*, *47*). Association with axons that project from the nose into the CNS is instructive for GnRH neuron migration, as genetic manipulations that cause misrouting of these axons before penetrating into the brain non-cell autonomously prevent GnRH neurons from entering the CNS (*46*–*49*). The comorbidity of anosmia and hypogonadotropic hypogonadism in patients with Kallmann syndrome has been commonly interpreted as a link between olfactory sensory axon guidance and GnRH neuron migration (*46*, *47*). However, recent evidence strongly suggests that most GnRH neurons follow terminal nerve fibers, whereas only a small subpopulation migrates along olfactory and/or vomeronasal axons (*50*). In addition to following these axons, which are steered toward the brain by various guidance molecules, GnRH neurons appear to also require their own chemoattractive cues to migrate into the CNS. Hepatocyte growth factor and CXCL12, which are expressed by mesenchymal cells along the GnRH neuron migratory route and increase in concentration toward the olfactory bulb, have been implicated as two such cues; however, their precise mechanism of action remains elusive, and it is not entirely clear whether these factors do indeed control GnRH neuron migration directly without affecting axon guidance (*51*–*53*). Therefore, GnRH neurons appear to require attractive guidance cues and a correctly targeted axonal substrate for their migration across the CNS-PNS boundary. The complete repertoire of guidance cues, receptors, and cellular mechanisms that regulate GnRH neuron entry into the CNS awaits identification.

Prohibiting CNS exit of neuronal cell bodies

How are the vast majority of neuronal cell bodies contained within either the CNS or PNS? Motor neurons are the only pan-vertebrate, CNS-resident neurons with axons that project into the PNS. This renders their cell bodies particularly vulnerable to accidental CNS exit, and multiple mechanisms prevent motor neurons from leaving the neural tube by helping to uncouple cell body translocation from axon extension. Both fish and mammals depend on CNS-derived perineurial glia to contain motor neurons within the spinal cord, and the radial glia endfeet barrier and additional signaling from BC cells help to solidify this confinement in mammals (Fig. 2B). In *Reelin* knockout mice, radial glia endfeet in the spinal cord fail to form a continuous barrier along the basement membrane, and motor neurons emigrate from the spinal cord through MEPs (*54*). Thus, radial glia endfeet appear to prevent motor neuron exit from the CNS, but it is unclear whether this is mediated by inhibitory signals or the formation of a physical seal at MEPs. Ablation of BC cells also causes motor neuron CNS exit through MEPs in both chicks and mice (*55*) (Fig. 2B). At least two BC-derived signals appear to mediate this function of confining motor neurons to the CNS: the transmembrane Semaphorin Sema6A (*56*, *57*) and the Netrin family member Netrin-5 (*58*). Knockdown of *Sema6A* in chick BC cells or genetic deletion in mice causes motor neuron emigration from the spinal cord; however, the identity of the receptor(s) mediating the effect of Sema6A on motor neurons remains controversial, as conflicting RNA interference evidence in chick embryos implicates either PlexinA1 or PlexinA2, whereas knockout studies in mice implicate the class III Semaphorin receptor Neuropilin-2 (*56*, *57*). Mice lacking Netrin-5, which is expressed by BC cells, or the Netrin receptor DCC, expressed in motor neurons, also exhibit motor neuron emigration through MEPs. This supports the idea that BC-derived Netrin-5 restricts motor neuron exit from the CNS through DCC (*58*). Sema6A and Netrin-5 might well function as BC-derived repellants that prevent the migration of motor neurons into the PNS, but this mechanism of action has yet to be confirmed. CNS-derived perineurial glia in the proximal ventral roots further help to confine motor neurons to the CNS. When the development of these cells is perturbed by inactivation of *Nkx2.2*, motor neuron somata leave the CNS through MEPs in both fish and mice (Fig. 2A) (*31*, *32*), but the mechanisms through which perineurial glia control motor neuron positioning are still unclear. Multiple studies in mice have shown that inactivating motor neuron–specific transcription factors, including HB9, Islet1, and Islet2, causes motor neuron cell body migration into peripheral nerves without affecting BC cell clustering at MEPs or radial glia endfeet morphology (*59*–*62*). These findings suggest that these transcriptional regulators control the expression of genes required for motor neurons to sense guidance cues that keep their cell bodies within the CNS. The identity of the relevant misregulated effector molecules remains elusive, but components of the repulsive Semaphorin-Neuropilin and Slit-Robo signaling pathways have been implicated as downstream mediators of Islet1/2 in preventing motor neuron emigration into the PNS (*62*). Together, these studies show that motor neurons rely on multiple, nonredundant signaling mechanisms to remain within the CNS.

In fish and amphibians, but not in amniotes, an additional population of CNS neurons projects axons across the CNS-PNS border: Rohon–Beard sensory neurons. These neurons reside in the dorsal spinal cord and send axons into the periphery, but the mechanisms that contain their cell bodies within the CNS are unknown.

Behaving as a mirror image of motor and Rohon–Beard neurons, peripheral sensory neurons project axons into the CNS. The only documented instance of neurons aberrantly entering the CNS occurs in mice lacking Six1 and Six4—loss of these transcription factors impairs differentiation of dorsal root ganglion neurons and causes their migration into the spinal cord through the DREZ (*63*). It is not known whether this reflects impaired responsiveness of sensory neurons to inhibitory signals or pleiotropic effects on the structure of the CNS-PNS border.

When motor or sensory neuron somata aberrantly cross between the CNS and PNS, they always do so through transition zones, suggesting that these exit and entry points are more permissive for neuronal migration than the rest of the CNS-PNS boundary. Consistent with this idea, transition zones in the hindbrain are also vulnerable to ectopic migration of nonmotor neurons out of the CNS. Rhombic lip–derived pontine neurons migrate long distances underneath the hindbrain pial surface, where they must maneuver around multiple cranial nerve exit points before reaching their final location (*64*). Netrin-1 is present in the basement membrane at the pial surface and functions as a guidance substrate for pontine neurons, which express DCC. When *Netrin-1* or *DCC* are deleted, pontine neurons aberrantly leave the hindbrain through cranial nerves and enter the PNS (*65*, *66*). Because these defects arise despite normal BC cell localization and radial glia morphology, this suggests that Netrin-1 chemotactic or haptotactic activity keeps pontine neurons on the correct path to promote their retention in the CNS (*65*, *66*) and supports the idea that CNS neurons are vulnerable to exiting into the PNS when their normal migratory trajectories are disrupted.

Transgressions of the CNS-PNS boundary by neurons at sites other than transition zones are rare and appear to require a more dramatic breakdown of the barrier. Defects in radial glia or basement membrane formation in the cerebral cortex result in overmigration of neurons into the marginal zone and subarachnoid space of the meninges (*67*–*73*), indicating that these components of the CNS-PNS border keep neuronal cell bodies confined to the cortex. Disruptions of the radial glia scaffold in the spinal cord have not been reported to cause similar nonspecific breaching of the CNS-PNS border outside of transition zones, but the reasons underlying this difference between cortex and spinal cord are unclear.

Allowing the right axons to connect the CNS and PNS

To project across the CNS-PNS interface, axons must penetrate between radial glia endfeet and

through the basement membrane and meninges (Figs. 1 and 3A). At the time when motor and sensory axons navigate through MEPs and DREZs, respectively, radial glia endfeet form an incomplete barrier with numerous gaps (*8*), and olfactory sensory axons enter the olfactory bulb through small fenestrations in the basement membrane (*74*). This suggests that gaps in the CNS-PNS barrier might be required to permit axon growth through transition zones. However, recent work has also highlighted the importance of transient morphological and functional changes in sensory and motor axon growth cones for crossing the CNS-PNS border. When pioneer axons reach prospective CNS exit and entry points, they pause, reorganize their growth cones into a structure called an invadopodium, and secrete matrix metalloproteases to digest the ECM and puncture through the basement membrane (*75*, *76*). Therefore, axons can themselves create gaps necessary for crossing the CNS-PNS barrier. When the radial glia endfeet barrier at the DREZ is removed, sensory axon growth cones enter the CNS without transforming into invadopodia (*75*), suggesting that invadopodium formation is triggered by contact with radial glia or radial glia–derived ECM and is only required for neural tube entry when the CNS-PNS border is intact.

Local disruption of the CNS-PNS boundary is likely a prerequisite for axon crossing at transition zones, but instructive cues are needed to guide axons toward and across the CNS-PNS interface. Consistent with this notion, multiple studies indicate that motor axons exit the CNS in response to signals provided by peripheral tissues. In zebrafish, a myotome-expressed glycosyltransferase, LH3, is required for motor axon exit from the spinal cord, embryonic motility, and survival. LH3 (encoded by the *diwanka* gene) likely functions by adding sugar modifications to myotomal type XVIII collagen, which are needed for this ECM molecule to direct pioneer motor axons into the spinal cord periphery (Fig. 3F) (*77*, *78*). In mice, the CXCL12-CXCR4 signaling pathway has been implicated in motor axon exit from the spinal cord. CXCR4 is expressed by motor neurons, whereas CXCL12 is expressed by the meninges and mesenchyme surrounding the spinal cord (Fig. 3A), and many motor axons fail to leave the spinal cord in *Cxcl12* and *Cxcr4* mutant mice, instead projecting either medially to the ventricular zone or dorsally to the DREZ (*79*) (Fig. 3C). This suggests that CXCL12 functions as an attractive peripheral cue that promotes motor axon exit. Guidance molecules that direct sensory axons to DREZs and into the spinal cord remain elusive, but BC cells have been implicated as a likely source of such cues (*21*). Only slightly more is known about signaling mechanisms that promote olfactory sensory axon entry into the brain (*74*, *80*). The only clear-cut example of a molecule that guides these axons across the CNS-PNS border is the secreted Semaphorin Sema3A, which is expressed in the olfactory bulb. In *Sema3A*-knockout mice, most olfactory and vomeronasal axons fail to cross the CNS-PNS boundary and instead accumulate at the cribriform plate or misroute dorsally into meningeal tissue, but how exactly Sema3A steers olfactory axons in this system is unclear (*81*). Additional cues that direct motor and sensory axons to their transition zones, as well as the tissues producing these cues, remain to be identified. Recent in vitro studies provide evidence that the developing mouse spinal cord meninges secrete diffusible, as yet unidentified chemoattractants for somatosensory and motor axons, which could help to guide these axons to the CNS-PNS interface (*16*) (Fig. 3A).

Although attractive signals appear instrumental in guiding motor and sensory axons across transition zones, multiple studies have highlighted that these axons also need to avoid navigating to inappropriate targets en route to CNS exit and entry points. In *Robo1/2* double-knockout mice, a subset of motor axons fails to reach the MEP and instead projects across the spinal cord midline (Fig. 3D) (*82*–*84*). Robos can mediate axon repulsion from their Slit ligands while suppressing DCC-mediated attraction to Netrin-1 (*85*, *86*), and the motor axon guidance defect in *Robo1/2* mutant mice is therefore likely a result of reduced repulsion from midline-derived Slits and/or increased Netrin-1 attraction. Similarly, the Rho-GTPase antagonist p190RhoGAP was recently shown to suppress Netrin-DCC attractive signaling in motor axons, thereby allowing motor axons to ignore attraction to basement membrane–associated Netrin-1 and project into the periphery through the MEP (*87*) (Fig. 3B). This pathway seems to function in parallel to the CXCL12-CXCR4 pathway to collaboratively steer motor axons out of the spinal cord (*79*, *87*). In summary, motor axon exit from the CNS requires suppression of attractive signals within the spinal cord in addition to attraction to the MEP and peripheral tissues. Consistent with a direct role for repulsive signaling in directing axons of CNS-resident neurons to their exit points, Rohon–Beard sensory axons in embryonic zebrafish require Sema3D, which is expressed in the spinal cord roof plate, to leave the CNS (*88*). Similar pathways that steer peripheral sensory axons to their CNS entry points have so far remained elusive.

Lastly, the location of spinal cord MEPs appears sensitive to signals that change motor neuron cell body or axon positioning. In both mice and zebrafish, loss of CNS-derived perineurial glia after *Nkx2.2* deletion causes not only motor neuron emigration but also aberrant motor axon exit from the CNS at sites lateral to the MEP (*31*–*33*). Owing to the additional expression of Nkx2.2 in ventral spinal cord neurons, it is unclear whether these changes result exclusively from effects on perineurial glia. Mutations in *Netrin-1* or *DCC* affect motor neuron cell body positioning and cause the MEP to shift dorsolaterally, whereas mutations in *Slit* genes or *Robo1/2* result in a ventral shift. When both signaling pathways are inactivated simultaneously, the MEP remains in its normal position, suggesting that push/pull signals from spinal cord midline–derived Netrin-1 and Slits dictate MEP location (*84*, *89*). Therefore, the positioning of transition zones is, at least partially, shaped by the axons that cross the border.

Preventing the wrong axons from leaving the CNS

How most axons are forced to remain within either the CNS or PNS has not been extensively investigated, but several studies support the existence of mechanisms that actively prevent CNS axons from projecting into the PNS. In vitro experiments demonstrate that the meninges secrete repulsive axon guidance molecules for dorsal spinal cord neurons and suggest that these still unidentified cues could aid in preventing axons from aberrantly exiting the CNS (*16*) (Fig. 3A). Moreover, in *Netrin-1* knockout mice, axons of commissural and ipsilaterally projecting neurons in the spinal cord, as well as pontine neuron axons in the hindbrain, aberrantly exit the CNS through transition zones (*65*, *66*, *90*–*92*) (Fig. 3E). Similar defects are observed in mice lacking the Netrin receptors DCC or Unc5c; however, in *Unc5c* knockout mice, CNS axons invade the DREZ but do not fully exit the CNS (*90*). Analysis of these mutant lines suggests two possible mechanisms through which Netrin-1 could prevent CNS axons from projecting into the PNS: (i) drawing axons away from transition zones by attractive signaling and (ii) creating an inhibitory environment at the DREZ (*90*). The full complement of mechanisms that prevent axons from crossing the CNS-PNS border remains to be uncovered.

Outlook

Multiple cell types and signaling pathways exert tight control over the movement of cells and axons between the developing vertebrate CNS and PNS. A multilayered barrier surrounds the brain and spinal cord to prevent aberrant intermixing of CNS and PNS components, and specialized transition zones allow regulated cell migration and axon growth across the CNS-PNS boundary. Studies in various vertebrate species have begun to unravel some of the rules that govern cellular traffic at the CNS-PNS interface; it appears that these findings frequently arose fortuitously through chance discovery of instances in which cells and axons aberrantly crossed between the two subdivisions of the nervous system or failed to do so in cases when they should have. Tellingly, for the overwhelming majority of aberrant CNS-PNS boundary transgressions, defects are restricted to transition zones. This underscores the permissive nature of these access points, the importance of multiple mechanisms to regulate cell migration and axon growth at these sites, and their plasticity in response to physical injury or developmental defects. It also highlights the fact that, aside from transition zones, the CNS-PNS border appears to be very robust, likely using numerous, at least partially redundant mechanisms to restrict aberrant movement across this boundary. More directed research efforts to understand the CNS-PNS interface promise to elucidate the full

repertoire of cellular interactions and molecular signaling pathways that control this key dividing line in the nervous system. These future studies will likely also provide additional insights into the roles of transition zones in response to nervous system injury and regeneration. Finally, some of the cell types and molecules controlling axon guidance at the *Drosophila* CNS-PNS boundary have been uncovered (*93*–*97*), and continued study of this interface in multiple model organisms, including invertebrates, will contribute to our understanding of the evolution of CNS-PNS segregation and connectivity.

REFERENCES AND NOTES

1. D. S. Barry, J. M. Pakan, K. W. McDermott, Radial glial cells: Key organisers in CNS development. *Int. J. Biochem. Cell Biol.* **46**, 76–79 (2014). doi: 10.1016/j.biocel.2013.11.013; pmid: 24269781
2. X. Liu *et al*., The superficial glia limitans of mouse and monkey brain and spinal cord. *Anat. Rec.* **296**, 995–1007 (2013). doi: 10.1002/ar.22717; pmid: 23674345
3. D. Ohayon *et al*., Onset of Spinal Cord Astrocyte Precursor Emigration from the Ventricular Zone Involves the Zeb1 Transcription Factor. *Cell Rep.* **17**, 1473–1481 (2016). doi: 10.1016/j.celrep.2016.10.016; pmid: 27806288
4. J. P. Fraher, Axon-glial relationships in early CNS-PNS transitional zone development: An ultrastructural study. *J. Neurocytol.* **26**, 41–52 (1997). doi: 10.1023/A:1018511425126; pmid: 9154528
5. D. O'Brien, P. Dockery, K. McDermott, J. P. Fraher, The ventral motoneurone axon bundle in the CNS—A cordone system? *J. Neurocytol.* **27**, 247–258 (1998). doi: 10.1023/A:1006932931160; pmid: 10640183
6. J. P. Fraher, The CNS-PNS transitional zone of the rat. Morphometric studies at cranial and spinal levels. *Prog. Neurobiol.* **38**, 261–316 (1992). doi: 10.1016/0301-0082(92)90022-7; pmid: 1546164
7. P. D. Yurchenco, Basement membranes: Cell scaffoldings and signaling platforms. *Cold Spring Harb. Perspect. Biol.* **3**, a004911 (2011). doi: 10.1101/cshperspect.a004911; pmid: 21421915
8. J. P. Fraher, P. Dockery, O. O'Donoghue, B. Riedewald, D. O'Leary, Initial motor axon outgrowth from the developing central nervous system. *J. Anat.* **211**, 600–611 (2007). doi: 10.1111/j.1469-7580.2007.00807.x; pmid: 17850285
9. M. Martins-Green, C. A. Erickson, Development of neural tube basal lamina during neurulation and neural crest cell emigration in the trunk of the mouse embryo. *J. Embryol. Exp. Morphol.* **98**, 219–236 (1986). pmid: 3655650
10. J. A. Siegenthaler, S. J. Pleasure, We have got you 'covered': How the meninges control brain development. *Curr. Opin. Genet. Dev.* **21**, 249–255 (2011). doi: 10.1016/j.gde.2010.12.005; pmid: 21251809
11. G. F. Couly, N. M. Le Douarin, Mapping of the early neural primordium in quail-chick chimeras. II. The prosencephalic neural plate and neural folds: Implications for the genesis of cephalic human congenital abnormalities. *Dev. Biol.* **120**, 198–214 (1987). doi: 10.1016/0012-1606(87)90118-7; pmid: 3817289
12. G. F. Couly, P. M. Coltey, N. M. Le Douarin, The developmental fate of the cephalic mesoderm in quail-chick chimeras. *Development* **114**, 1–15 (1992). pmid: 1576952
13. X. Jiang, S. Iseki, R. E. Maxson, H. M. Sucov, G. M. Morriss-Kay, Tissue origins and interactions in the mammalian skull vault. *Dev. Biol.* **241**, 106–116 (2002). doi: 10.1006/dbio.2001.0487; pmid: 11784098
14. Y. Choe, J. A. Siegenthaler, S. J. Pleasure, A cascade of morphogenic signaling initiated by the meninges controls corpus callosum formation. *Neuron* **73**, 698–712 (2012). doi: 10.1016/j.neuron.2011.11.036; pmid: 22365545
15. K. Zarbalis, Y. Choe, J. A. Siegenthaler, L. A. Orosco, S. J. Pleasure, Meningeal defects alter the tangential migration of cortical interneurons in Foxc1hith/hith mice. *Neural Dev.* **7**, 2 (2012). doi: 10.1186/1749-8104-7-2; pmid: 22248045
16. T. A. C. S. Suter, Z. J. DeLoughery, A. Jaworski, Meninges-derived cues control axon guidance. *Dev. Biol.* **430**, 1–10 (2017). doi: 10.1016/j.ydbio.2017.08.005; pmid: 28784295
17. J. P. Fraher, D. C. Bristol, High density of nodes of Ranvier in the CNS-PNS transitional zone. *J. Anat.* **170**, 131–137 (1990). pmid: 2254159
18. A. H. Koeppen, A. B. Becker, J. Qian, B. B. Gelman, J. E. Mazurkiewicz, Friedreich Ataxia: Developmental Failure of the Dorsal Root Entry Zone. *J. Neuropathol. Exp. Neurol.* **76**, 969–977 (2017). doi: 10.1093/jnen/nlx087; pmid: 29044418
19. K. J. Radomska, P. Topilko, Boundary cap cells in development and disease. *Curr. Opin. Neurobiol.* **47**, 209–215 (2017). doi: 10.1016/j.conb.2017.11.003; pmid: 29174469
20. C. Niederländer, A. Lumsden, Late emigrating neural crest cells migrate specifically to the exit points of cranial branchiomotor nerves. *Development* **122**, 2367–2374 (1996). pmid: 8756282
21. J. P. Golding, J. Cohen, Border controls at the mammalian spinal cord: Late-surviving neural crest boundary cap cells at dorsal root entry sites may regulate sensory afferent ingrowth and entry zone morphogenesis. *Mol. Cell. Neurosci.* **9**, 381–396 (1997). doi: 10.1006/mcne.1997.0647; pmid: 9361276
22. F. Coulpier *et al*., Novel features of boundary cap cells revealed by the analysis of newly identified molecular markers. *Glia* **57**, 1450–1457 (2009). doi: 10.1002/glia.20862; pmid: 19243017
23. C. J. Smith, A. D. Morris, T. G. Welsh, S. Kucenas, Contact-mediated inhibition between oligodendrocyte progenitor cells and motor exit point glia establishes the spinal cord transition zone. *PLOS Biol.* **12**, e1001961 (2014). doi: 10.1371/journal.pbio.1001961; pmid: 25268888
24. S. Kucenas, W. D. Wang, E. W. Knapik, B. Appel, A selective glial barrier at motor axon exit points prevents oligodendrocyte migration from the spinal cord. *J. Neurosci.* **29**, 15187–15194 (2009). doi: 10.1523/JNEUROSCI.4193-09.2009; pmid: 19955371
25. D. Nayak, T. L. Roth, D. B. McGavern, Microglia development and function. *Annu. Rev. Immunol.* **32**, 367–402 (2014). doi: 10.1146/annurev-immunol-032713-120240; pmid: 24471431
26. F. Ginhoux, M. Prinz, Origin of microglia: Current concepts and past controversies. *Cold Spring Harb. Perspect. Biol.* **7**, a020537 (2015). doi: 10.1101/cshperspect.a020537; pmid: 26134003
27. F. A. Court, L. Wrabetz, M. L. Feltri, Basal lamina: Schwann cells wrap to the rhythm of space-time. *Curr. Opin. Neurobiol.* **16**, 501–507 (2006). doi: 10.1016/j.conb.2006.08.005; pmid: 16956757
28. W. Halfter, J. Yip, An organizing function of basement membranes in the developing nervous system. *Mech. Dev.* **133**, 1–10 (2014). doi: 10.1016/j.mod.2014.07.003; pmid: 25058486
29. F. Coulpier *et al*., CNS/PNS boundary transgression by central glia in the absence of Schwann cells or Krox20/Egr2 function. *J. Neurosci.* **30**, 5958–5967 (2010). doi: 10.1523/JNEUROSCI.0017-10.2010; pmid: 20427655
30. I. D. Duncan, R. L. Hoffman, Schwann cell invasion of the central nervous system of the myelin mutants. *J. Anat.* **190**, 35–49 (1997). doi: 10.1046/j.1469-7580.1997.19010035.x; pmid: 9034880
31. J. K. Clark *et al*., Mammalian *Nkx2.2*$^{+}$ perineurial glia are essential for motor nerve development. *Dev. Dyn.* **243**, 1116–1129 (2014). doi: 10.1002/dvdy.24158; pmid: 24979729
32. S. Kucenas *et al*., CNS-derived glia ensheath peripheral nerves and mediate motor root development. *Nat. Neurosci.* **11**, 143–151 (2008). doi: 10.1038/nn2025; pmid: 18176560
33. S. Kucenas, Perineurial glia. *Cold Spring Harb. Perspect. Biol.* **7**, a020511 (2015). doi: 10.1101/cshperspect.a020511; pmid: 25818566
34. C. J. Smith, K. Johnson, T. G. Welsh, M. J. Barresi, S. Kucenas, Radial glia inhibit peripheral glial infiltration into the spinal cord at motor exit point transition zones. *Glia* **64**, 1138–1153 (2016). doi: 10.1002/glia.22987; pmid: 27029762
35. F. Fröb *et al*., Establishment of myelinating Schwann cells and barrier integrity between central and peripheral nervous systems depend on Sox10. *Glia* **60**, 806–819 (2012). doi: 10.1002/glia.22310; pmid: 22337526
36. D. A. Lyons *et al*., erbb3 and erbb2 are essential for schwann cell migration and myelination in zebrafish. *Curr. Biol.* **15**, 513–524 (2005). doi: 10.1016/j.cub.2005.02.030; pmid: 15797019
37. L. Fontenas *et al*., The Neuromodulator Adenosine Regulates Oligodendrocyte Migration at Motor Exit Point Transition Zones. *Cell Rep.* **27**, 115–128.e5 (2019). doi: 10.1016/j.celrep.2019.03.013; pmid: 30943395
38. Y. Zhu, T. Matsumoto, T. Nagasawa, F. Mackay, F. Murakami, Chemokine Signaling Controls Integrity of Radial Glial Scaffold in Developing Spinal Cord and Consequential Proper Position of Boundary Cap Cells. *J. Neurosci.* **35**, 9211–9224 (2015). doi: 10.1523/JNEUROSCI.0156-15.2015; pmid: 26085643
39. T. J. Sims, S. A. Gilmore, Schwann cells can misdirect regrowing neuronal processes. *Brain Res.* **763**, 141–144 (1997). doi: 10.1016/S0006-8993(97)00501-5; pmid: 9272840
40. S. A. Gilmore, T. J. Sims, J. K. Heard, Autoradiographic and ultrastructural studies of areas of spinal cord occupied by Schwann cells and Schwann cell myelin. *Brain Res.* **239**, 365–375 (1982). doi: 10.1016/0006-8993(82)90515-7; pmid: 7093696
41. T. J. Sims, S. A. Gilmore, Interactions between intraspinal Schwann cells and the cellular constituents normally occurring in the spinal cord: An ultrastructural study in the irradiated rat. *Brain Res.* **276**, 17–30 (1983). doi: 10.1016/0006-8993(83)90544-9; pmid: 6626996
42. W. F. Blakemore, R. C. Patterson, Observations on the interactions of Schwann cells and astrocytes following X-irradiation of neonatal rat spinal cord. *J. Neurocytol.* **4**, 573–585 (1975). doi: 10.1007/BF01351538; pmid: 1177001
43. W. F. Blakemore, Invasion of Schwann cells into the spinal cord of the rat following local injections of lysolecithin. *Neuropathol. Appl. Neurobiol.* **2**, 21–39 (1976). doi: 10.1111/j.1365-2990.1976.tb00559.x
44. L. Jasmin, G. Janni, T. M. Moallem, D. A. Lappi, P. T. Ohara, Schwann cells are removed from the spinal cord after effecting recovery from paraplegia. *J. Neurosci.* **20**, 9215–9223 (2000). doi: 10.1523/JNEUROSCI.20-24-09215.2000; pmid: 11124999
45. N. Chaudhry *et al*., Myelin-Associated Glycoprotein Inhibits Schwann Cell Migration and Induces Their Death. *J. Neurosci.* **37**, 5885–5899 (2017). doi: 10.1523/JNEUROSCI.1822-16.2017; pmid: 28522736
46. S. Wray, From nose to brain: Development of gonadotrophin-releasing hormone-1 neurones. *J. Neuroendocrinol.* **22**, 743–753 (2010). doi: 10.1111/j.1365-2826.2010.02034.x; pmid: 20646175
47. P. E. Forni, S. Wray, GnRH, anosmia and hypogonadotropic hypogonadism—Where are we? *Front. Neuroendocrinol.* **36**, 165–177 (2015). doi: 10.1016/j.yfrne.2014.09.004; pmid: 25306902
48. V. Pingault *et al*., Loss-of-function mutations in SOX10 cause Kallmann syndrome with deafness. *Am. J. Hum. Genet.* **92**, 707–724 (2013). doi: 10.1016/j.ajhg.2013.03.024; pmid: 23643381
49. A. Cariboni *et al*., Defective gonadotropin-releasing hormone neuron migration in mice lacking SEMA3A signalling through NRP1 and NRP2: Implications for the aetiology of hypogonadotropic hypogonadism. *Hum. Mol. Genet.* **20**, 336–344 (2011). doi: 10.1093/hmg/ddq468; pmid: 21059704
50. E. Z. M. Taroc, A. Prasad, J. M. Lin, P. E. Forni, The terminal nerve plays a prominent role in GnRH-1 neuronal migration independent from proper olfactory and vomeronasal connections to the olfactory bulbs. *Biol. Open* **6**, 1552–1568 (2017). doi: 10.1242/bio.029074; pmid: 28970231
51. Y. Toba, J. D. Tiong, Q. Ma, S. Wray, CXCR4/SDF-1 system modulates development of GnRH-1 neurons and the olfactory system. *Dev. Neurobiol.* **68**, 487–503 (2008). doi: 10.1002/dneu.20594; pmid: 18188864
52. G. A. Schwarting, T. R. Henion, J. D. Nugent, B. Caplan, S. Tobet, Stromal cell-derived factor-1 (chemokine C-X-C motif ligand 12) and chemokine C-X-C motif receptor 4 are required for migration of gonadotropin-releasing hormone neurons to the forebrain. *J. Neurosci.* **26**, 6834–6840 (2006). doi: 10.1523/JNEUROSCI.1728-06.2006; pmid: 16793890
53. P. Giacobini *et al*., Hepatocyte growth factor acts as a motogen and guidance signal for gonadotropin hormone-releasing hormone-1 neuronal migration. *J. Neurosci.* **27**, 431–445 (2007). doi: 10.1523/JNEUROSCI.4979-06.2007; pmid: 17215404
54. H. Lee, M. R. Song, The structural role of radial glial endfeet in confining spinal motor neuron somata is controlled by the Reelin and Notch pathways. *Exp. Neurol.* **249**, 83–94 (2013). doi: 10.1016/j.expneurol.2013.08.010; pmid: 23988635
55. M. Vermeren *et al*., Integrity of developing spinal motor columns is regulated by neural crest derivatives at motor exit points. *Neuron* **37**, 403–415 (2003). doi: 10.1016/S0896-6273(02)01188-1; pmid: 12575949
56. R. Bron *et al*., Boundary cap cells constrain spinal motor neuron somal migration at motor exit points by a semaphorin-plexin mechanism. *Neural Dev.* **2**, 21 (2007). doi: 10.1186/1749-8104-2-21; pmid: 17971221
57. O. Mauti, E. Domanitskaya, I. Andermatt, R. Sadhu, E. T. Stoeckli, Semaphorin6A acts as a gate keeper between

the central and the peripheral nervous system. *Neural Dev.* **2**, 28 (2007). doi: 10.1186/1749-8104-2-28; pmid: 18088409
58. A. M. Garrett *et al*., Analysis of Expression Pattern and Genetic Deletion of Netrin5 in the Developing Mouse. *Front. Mol. Neurosci.* **9**, 3 (2016). doi: 10.3389/fnmol.2016.00003; pmid: 26858598
59. S. Arber *et al*., Requirement for the homeobox gene Hb9 in the consolidation of motor neuron identity. *Neuron* **23**, 659–674 (1999). doi: 10.1016/S0896-6273(01)80026-X; pmid: 10482234
60. J. P. Thaler *et al*., A postmitotic role for Isl-class LIM homeodomain proteins in the assignment of visceral spinal motor neuron identity. *Neuron* **41**, 337–350 (2004). doi: 10.1016/S0896-6273(04)00011-X; pmid: 14766174
61. S. Lee, B. Lee, J. W. Lee, S. K. Lee, Retinoid signaling and neurogenin2 function are coupled for the specification of spinal motor neurons through a chromatin modifier CBP. *Neuron* **62**, 641–654 (2009). doi: 10.1016/j.neuron.2009.04.025; pmid: 19524524
62. H. Lee *et al*., Slit and Semaphorin signaling governed by Islet transcription factors positions motor neuron somata within the neural tube. *Exp. Neurol.* **269**, 17–27 (2015). doi: 10.1016/j.expneurol.2015.03.024; pmid: 25843547
63. H. Yajima *et al*., Six1 is a key regulator of the developmental and evolutionary architecture of sensory neurons in craniates. *BMC Biol.* **12**, 40 (2014). doi: 10.1186/1741-7007-12-40; pmid: 24885223
64. D. H. Nichols, L. L. Bruce, Migratory routes and fates of cells transcribing the Wnt-1 gene in the murine hindbrain. *Dev. Dyn.* **235**, 285–300 (2006). doi: 10.1002/dvdy.20611; pmid: 16273520
65. A. R. Yung *et al*., Netrin-1 Confines Rhombic Lip-Derived Neurons to the CNS. *Cell Rep.* **22**, 1666–1680 (2018). doi: 10.1016/j.celrep.2018.01.068; pmid: 29444422
66. J. A. Moreno-Bravo *et al*., Commissural neurons transgress the CNS/PNS boundary in absence of ventricular zone-derived netrin 1. *Development* **145**, dev159400 (2018). doi: 10.1242/dev.159400; pmid: 29343638
67. D. Graus-Porta *et al*., β1-class integrins regulate the development of laminae and folia in the cerebral and cerebellar cortex. *Neuron* **31**, 367–379 (2001). doi: 10.1016/S0896-6273(01)00374-9; pmid: 11516395
68. S. A. Moore *et al*., Deletion of brain dystroglycan recapitulates aspects of congenital muscular dystrophy. *Nature* **418**, 422–425 (2002). doi: 10.1038/nature00838; pmid: 12140559
69. H. E. Beggs *et al*., FAK deficiency in cells contributing to the basal lamina results in cortical abnormalities resembling congenital muscular dystrophies. *Neuron* **40**, 501–514 (2003). doi: 10.1016/S0896-6273(03)00666-4; pmid: 14642275
70. A. Niewmierzycka, J. Mills, R. St-Arnaud, S. Dedhar, L. F. Reichardt, Integrin-linked kinase deletion from mouse cortex results in cortical lamination defects resembling cobblestone lissencephaly. *J. Neurosci.* **25**, 7022–7031 (2005). doi: 10.1523/JNEUROSCI.1695-05.2005; pmid: 16049178
71. T. D. Myshrall *et al*., Dystroglycan on radial glia end feet is required for pial basement membrane integrity and columnar organization of the developing cerebral cortex. *J. Neuropathol. Exp. Neurol.* **71**, 1047–1063 (2012). doi: 10.1097/NEN.0b013e318274a128; pmid: 23147502
72. W. Halfter, S. Dong, Y. P. Yip, M. Willem, U. Mayer, A critical function of the pial basement membrane in cortical histogenesis. *J. Neurosci.* **22**, 6029–6040 (2002). doi: 10.1523/JNEUROSCI.22-14-06029.2002; pmid: 12122064
73. H. Hu, Y. Yang, A. Eade, Y. Xiong, Y. Qi, Breaches of the pial basement membrane and disappearance of the glia limitans during development underlie the cortical lamination defect in the mouse model of muscle-eye-brain disease. *J. Comp. Neurol.* **501**, 168–183 (2007). doi: 10.1002/cne.21238; pmid: 17206611
74. H. Treloar, A. Miller, A. Ray, C. Greer, "Development of the olfactory system," in *The Neurobiology of Olfaction*, A. Menini, Ed. (CRC/Taylor & Francis, 2010).
75. E. L. Nichols, C. J. Smith, Pioneer axons employ Cajal's battering ram to enter the spinal cord. *Nat. Commun.* **10**, 562 (2019). doi: 10.1038/s41467-019-08421-9; pmid: 30718484
76. M. Santiago-Medina, K. A. Gregus, R. H. Nichol, S. M. O'Toole, T. M. Gomez, Regulation of ECM degradation and axon guidance by growth cone invadosomes. *Development* **142**, 486–496 (2015). doi: 10.1242/dev.108266; pmid: 25564649
77. V. A. Schneider, M. Granato, The myotomal diwanka (lh3) glycosyltransferase and type XVIII collagen are critical for motor growth cone migration. *Neuron* **142**, 683–695 (2006). doi: 10.1016/j.neuron.2006.04.024; pmid: 16731508
78. J. Zeller, M. Granato, The zebrafish diwanka gene controls an early step of motor growth cone migration. *Development* **126**, 3461–3472 (1999). pmid: 10393124
79. I. Lieberam, D. Agalliu, T. Nagasawa, J. Ericson, T. M. Jessell, A Cxcl12-CXCR4 chemokine signaling pathway defines the initial trajectory of mammalian motor axons. *Neuron* **47**, 667–679 (2005). doi: 10.1016/j.neuron.2005.08.011; pmid: 16129397
80. H. Nishizumi, H. Sakano, Developmental regulation of neural map formation in the mouse olfactory system. *Dev. Neurobiol.* **75**, 594–607 (2015). doi: 10.1002/dneu.22268; pmid: 25649346
81. G. A. Schwarting *et al*., Semaphorin 3A is required for guidance of olfactory axons in mice. *J. Neurosci.* **20**, 7691–7697 (2000). doi: 10.1523/JNEUROSCI.20-20-07691.2000; pmid: 11027230
82. G. Bai *et al*., Presenilin-dependent receptor processing is required for axon guidance. *Cell* **144**, 106–118 (2011). doi: 10.1016/j.cell.2010.11.053; pmid: 21215373
83. H. N. Gruner, M. Kim, G. S. Mastick, Robo1 and 2 Repellent Receptors Cooperate to Guide Facial Neuron Cell Migration and Axon Projections in the Embryonic Mouse Hindbrain. *Neuroscience* **402**, 116–129 (2019). doi: 10.1016/j.neuroscience.2019.01.017; pmid: 30685539
84. M. Kim *et al*., Motor neuron cell bodies are actively positioned by Slit/Robo repulsion and Netrin/DCC attraction. *Dev. Biol.* **399**, 68–79 (2015). doi: 10.1016/j.ydbio.2014.12.014; pmid: 25530182
85. H. Blockus, A. Chédotal, Slit-Robo signaling. *Development* **143**, 3037–3044 (2016). doi: 10.1242/dev.132829; pmid: 27578174
86. E. Stein, Y. Zou, M. Poo, M. Tessier-Lavigne, Binding of DCC by netrin-1 to mediate axon guidance independent of adenosine A2B receptor activation. *Science* **291**, 1976–1982 (2001). doi: 10.1126/science.1059391; pmid: 11239160
87. D. Bonanomi *et al*., p190RhoGAP Filters Competing Signals to Resolve Axon Guidance Conflicts. *Neuron* **102**, 602–620.e9 (2019). doi: 10.1016/j.neuron.2019.02.034; pmid: 30902550
88. Y. Liu, M. C. Halloran, Central and peripheral axon branches from one neuron are guided differentially by Semaphorin3D and transient axonal glycoprotein-1. *J. Neurosci.* **25**, 10556–10563 (2005). doi: 10.1523/JNEUROSCI.2710-05.2005; pmid: 16280593
89. M. Kim, T. M. Fontelonga, C. H. Lee, S. J. Barnum, G. S. Mastick, Motor axons are guided to exit points in the spinal cord by Slit and Netrin signals. *Dev. Biol.* **432**, 178–191 (2017). doi: 10.1016/j.ydbio.2017.09.038; pmid: 28986144
90. C. Laumonnerie, R. V. Da Silva, A. Kania, S. I. Wilson, Netrin 1 and Dcc signalling are required for confinement of central axons within the central nervous system. *Development* **141**, 594–603 (2014). doi: 10.1242/dev.099606; pmid: 24449837
91. Z. Wu *et al*., Long-Range Guidance of Spinal Commissural Axons by Netrin1 and Sonic Hedgehog from Midline Floor Plate Cells. *Neuron* **101**, 635–647.e4 (2019). doi: 10.1016/j.neuron.2018.12.025; pmid: 30661738
92. J. A. Moreno-Bravo, S. Roig Puiggros, P. Mehlen, A. Chédotal, Synergistic Activity of Floor-Plate- and Ventricular-Zone-Derived Netrin-1 in Spinal Cord Commissural Axon Guidance. *Neuron* **101**, 625–634.e3 (2019). doi: 10.1016/j.neuron.2018.12.024; pmid: 30661739
93. T. Bossing, A. H. Brand, Dephrin, a transmembrane ephrin with a unique structure, prevents interneuronal axons from exiting the *Drosophila* embryonic CNS. *Development* **129**, 4205–4218 (2002). pmid: 12183373
94. K. J. Sepp, J. Schulte, V. J. Auld, Peripheral glia direct axon guidance across the CNS/PNS transition zone. *Dev. Biol.* **238**, 47–63 (2001). doi: 10.1006/dbio.2001.0411; pmid: 11783993
95. J. P. Labrador *et al*., The homeobox transcription factor even-skipped regulates netrin-receptor expression to control dorsal motor-axon projections in Drosophila. *Curr. Biol.* **15**, 1413–1419 (2005). doi: 10.1016/j.cub.2005.06.058; pmid: 16085495
96. H. T. Broihier, A. Kuzin, Y. Zhu, W. Odenwald, J. B. Skeath, Drosophila homeodomain protein Nkx6 coordinates motoneuron subtype identity and axonogenesis. *Development* **131**, 5233–5242 (2004). doi: 10.1242/dev.01394; pmid: 15456721
97. M. J. Layden *et al*., Zfh1, a somatic motor neuron transcription factor, regulates axon exit from the CNS. *Dev. Biol.* **291**, 253–263 (2006). doi: 10.1016/j.ydbio.2005.12.009; pmid: 16458285

ACKNOWLEDGMENTS

We thank members of the Jaworski laboratory and P. Forni for thoughtful comments on the manuscript. **Funding:** This work was supported by NIH grants F31 NS098643 (T.A.C.S.S.), T32 GM077995 (T.A.C.S.S.), RI-INBRE P20 GM103430 (A.J.), and R01 NS095908 (A.J.); a grant from the Rhode Island Foundation and a New Frontiers Award from the Rhode Island Neuroscience Consortium to A.J.; and funding from Brown University. **Author contributions:** Conceptualization: T.A.C.S.S. and A.J.; Supervision: A.J.; Visualization: T.A.C.S.S.; Writing – original draft: T.A.C.S.S. and A.J.; Writing – review and editing: T.A.C.S.S. and A.J. **Competing interests:** The authors declare no competing interests. **Data and materials availability**: All experimental data are available in the text.

10.1126/science.aaw8231

RESEARCH ARTICLE SUMMARY

HUMAN GENETICS

Large-scale GWAS reveals insights into the genetic architecture of same-sex sexual behavior

Andrea Ganna, Karin J. H. Verweij, Michel G. Nivard, Robert Maier, Robbee Wedow, Alexander S. Busch, Abdel Abdellaoui, Shengru Guo, J. Fah Sathirapongsasuti, 23andMe Research Team, Paul Lichtenstein, Sebastian Lundström, Niklas Långström, Adam Auton, Kathleen Mullan Harris, Gary W. Beecham, Eden R. Martin, Alan R. Sanders, John R. B. Perry, Benjamin M. Neale, Brendan P. Zietsch*

INTRODUCTION: Across human societies and in both sexes, some 2 to 10% of individuals report engaging in sex with same-sex partners, either exclusively or in addition to sex with opposite-sex partners. Twin and family studies have shown that same-sex sexual behavior is partly genetically influenced, but previous searches for the specific genes involved have been underpowered to detect effect sizes realistic for complex traits.

RATIONALE: For the first time, new large-scale datasets afford sufficient statistical power to identify genetic variants associated with same-sex sexual behavior (ever versus never had a same-sex partner), estimate the proportion of variation in the trait accounted for by all variants in aggregate, estimate the genetic correlation of same-sex sexual behavior with other traits, and probe the biology and complexity of the trait. To these ends, we performed genome-wide association discovery analyses on 477,522 individuals from the United Kingdom and United States, replication analyses in 15,142 individuals from the United States and Sweden, and follow-up analyses using different aspects of sexual preference.

RESULTS: In the discovery samples (UK Biobank and 23andMe), five autosomal loci were significantly associated with same-sex sexual behavior. Follow-up of these loci suggested links to biological pathways that involve sex hormone regulation and olfaction. Three of the loci were significant in a meta-analysis of smaller, independent replication samples. Although only a few loci passed the stringent statistical corrections for genome-wide multiple testing and were replicated in other samples, our analyses show that many loci underlie same-sex sexual behavior in both sexes. In aggregate, all tested genetic variants accounted for 8 to 25% of variation in male and female same-sex sexual behavior, and the genetic influences were positively but imperfectly correlated between the sexes [genetic correlation coefficient (r_g) = 0.63; 95% confidence intervals, 0.48 to 0.78]. These aggregate genetic influences partly overlapped with those on a variety of other traits, including externalizing behaviors such as smoking, cannabis use, risk-taking, and the personality trait "openness to experience." Additional analyses suggested that sexual behavior, attraction, identity, and fantasies are influenced by a similar set of genetic variants (r_g > 0.83); however, the genetic effects that differentiate heterosexual from same-sex sexual behavior are not the same as those that differ among nonheterosexuals with lower versus higher proportions of same-sex partners, which suggests that there is no single continuum from opposite-sex to same-sex preference.

ON OUR WEBSITE

Read the full article at http://dx.doi.org/10.1126/science.aat7693

CONCLUSION: Same-sex sexual behavior is influenced by not one or a few genes but many. Overlap with genetic influences on other traits provides insights into the underlying biology of same-sex sexual behavior, and analysis of different aspects of sexual preference underscore its complexity and call into question the validity of bipolar continuum measures such as the Kinsey scale. Nevertheless, many uncertainties remain to be explored, including how sociocultural influences on sexual preference might interact with genetic influences. To help communicate our study to the broader public, we organized workshops in which representatives of the public, activists, and researchers discussed the rationale, results, and implications of our study. ■

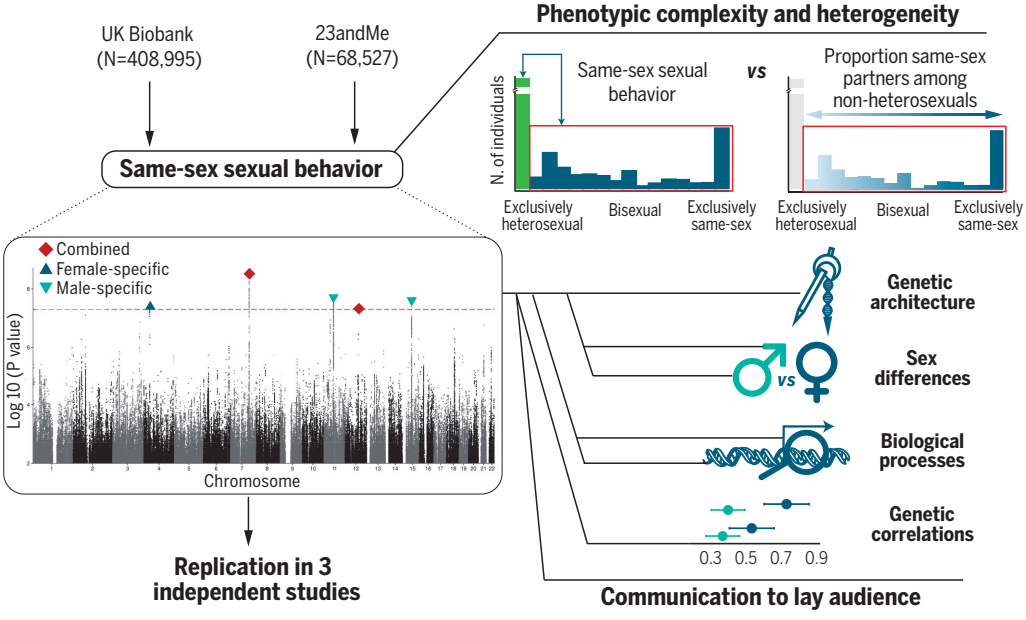

A genome-wide association study (GWAS) of same-sex sexual behavior reveals five loci and high polygenicity. Follow-up analyses show potential biological pathways; show genetic correlations with various traits; and indicate that sexual preference is a complex, heterogeneous phenotype.

The list of author affiliations is available in the full article online.
*Corresponding author.
Email: zietsch@psy.uq.edu.au
Cite this article as A. Ganna *et al.*, *Science* **365**, eaat7693 (2019). DOI: 10.1126/science.aat7693

RESEARCH ARTICLE

HUMAN GENETICS

Large-scale GWAS reveals insights into the genetic architecture of same-sex sexual behavior

Andrea Ganna[1,2,3,4]*, Karin J. H. Verweij[5]*, Michel G. Nivard[6], Robert Maier[1,2,3], Robbee Wedow[1,3,7,8,9,10,11], Alexander S. Busch[12,13,14], Abdel Abdellaoui[5], Shengru Guo[15], J. Fah Sathirapongsasuti[16], 23andMe Research Team[16], Paul Lichtenstein[4], Sebastian Lundström[17], Niklas Långström[4], Adam Auton[16], Kathleen Mullan Harris[18,19], Gary W. Beecham[15], Eden R. Martin[15], Alan R. Sanders[20,21], John R. B. Perry[12]†, Benjamin M. Neale[1,2,3]†, Brendan P. Zietsch[22]†‡

Twin and family studies have shown that same-sex sexual behavior is partly genetically influenced, but previous searches for specific genes involved have been underpowered. We performed a genome-wide association study (GWAS) on 477,522 individuals, revealing five loci significantly associated with same-sex sexual behavior. In aggregate, all tested genetic variants accounted for 8 to 25% of variation in same-sex sexual behavior, only partially overlapped between males and females, and do not allow meaningful prediction of an individual's sexual behavior. Comparing these GWAS results with those for the proportion of same-sex to total number of sexual partners among nonheterosexuals suggests that there is no single continuum from opposite-sex to same-sex sexual behavior. Overall, our findings provide insights into the genetics underlying same-sex sexual behavior and underscore the complexity of sexuality.

Across human societies and in both sexes, some 2 to 10% of individuals report engaging in sex with same-sex partners, either exclusively or in addition to sex with opposite-sex partners (*1*–*4*). The biological factors that contribute to sexual preference are largely unknown (*5*), but genetic influences are suggested by the observation that same-sex sexual behavior appears to run in families (*6*) and is concordant more often in genetically identical (monozygotic) twin pairs than in fraternal twin pairs or siblings (*7*).

With respect to genetic influences, several questions arise. First, what genes are involved and what biological processes do they affect? Previous reports of genetic variants associated with sexual orientation (*8*–*10*) were based on relatively small samples and did not meet current standards of genome-wide significance ($P < 5 \times 10^{-8}$). Identification of robustly associated variants could enable exploration of the biological pathways and processes involved in development of same-sex sexual behavior. One hypothesis suggests that sex hormones are involved (*11*–*13*), but little direct genetic or biological evidence is available. Second, to what extent are genetic influences the same or different for females and males; behavior, attraction, and identity; and heterosexuality and different same-sex sexual behaviors (such as bisexuality)?

In order to identify genetic variants associated with same-sex sexual behavior and explore its genetic architecture and underlying biology, we performed a genome-wide association study (GWAS) of same-sex sexual behavior. Analyses were conducted in the UK Biobank from the United Kingdom and a cohort of research participants from 23andMe, predominantly located in the United States, and replications were performed in three other smaller studies. This study is part of a preregistered research plan (Open Science Framework; https://osf.io/357tn), and we explain our deviations from that plan in (*14*).

Phenotypic characterization

The UK Biobank study comprises a sample of ~500,000 genotyped UK residents aged 40 to 70 years (tables S1 and S2) (*14*). Our primary phenotype of interest is a binary, self-reported measure of whether respondents had ever had sex with someone of the same sex (here termed "nonheterosexuals") or had not (here termed "heterosexuals") (Box 1).

In the UK Biobank sample, 4.1% of males and 2.8% of females reported ever having had sex with someone of the same sex (tables S1 and S2), with higher rates among younger participants (Fig. 1A). This binary phenotype follows from previous work proposing that sexual preference is taxonic rather than dimensional in structure, with individuals reporting exclusively opposite-sex preference differing from individuals reporting any same-sex preference (*15*). However, the binary variable also collapses rich and multifaceted diversity among nonheterosexual individuals (*15*), so we explored finer-scaled measurements and some of the complexities of the phenotype, although intricacies of the social and cultural influences on sexuality made it impossible to fully explore this complexity. The 23andMe sample comprised 23andMe customers who consented to participate in research and chose to complete a survey about sexual orientation (from many possible survey topics). Individuals who engage in same-sex sexual behavior may be more likely to self-select the sexual orientation survey, which would explain the unusually high proportion of individuals who had had same-sex sexual partners in this sample (18.9%) (table S3) (*14*).

We also performed replication analyses in three smaller datasets (*14*): (i) Molecular Genetic Study of Sexual Orientation (MGSOSO) (n = 2308 U.S. adult males), in which respondents were asked about their sexual identity; (ii) Add Health (n = 4755 U.S. young adults), in which respondents were asked whether they ever had same-sex intercourse and whether they were romantically attracted to the same sex; and (iii) Child and Adolescent Twin Study in Sweden (CATSS) (n = 8093 Swedish adolescents), in which

[1]Analytic and Translational Genetics Unit, Center for Genomic Medicine, Massachusetts General Hospital, Boston, MA 02114, USA. [2]Program in Medical and Population Genetics, Broad Institute of MIT and Harvard, Cambridge, MA 02142, USA. [3]Stanley Center for Psychiatric Research, Broad Institute of MIT and Harvard, Cambridge, MA 02142, USA. [4]Department of Medical Epidemiology and Biostatistics, Karolinska Institutet, Stockholm, Sweden. [5]Department of Psychiatry, Amsterdam University Medical Centers (UMC), location AMC, University of Amsterdam, Meibergdreef 5, 1105 AZ Amsterdam, Netherlands. [6]Department of Biological Psychology, Vrije Universiteit Amsterdam, 1081 BT, Amsterdam, Netherlands. [7]Department of Sociology, Harvard University, Cambridge, MA 02138, USA. [8]Department of Epidemiology, Harvard T. H. Chan School of Public Health, Boston, MA 02115, USA. [9]Department of Sociology, University of Colorado, Boulder, CO 80309-0483, USA. [10]Health and Society Program and Population Program, Institute of Behavioral Science, University of Colorado, Boulder, CO 80309-0483, USA. [11]Institute for Behavioral Genetics, University of Colorado, Boulder, CO 80309-0483, USA. [12]Medical Research Council (MRC) Epidemiology Unit, University of Cambridge School of Clinical Medicine, Institute of Metabolic Science, Cambridge Biomedical Campus, Cambridge, UK. [13]Department of Growth and Reproduction, Rigshospitalet, University of Copenhagen, Copenhagen, Denmark. [14]International Center for Research and Research Training in Endocrine Disruption of Male Reproduction and Child Health (EDMaRC), Rigshospitalet, Copenhagen, Denmark. [15]Department of Human Genetics, University of Miami, Miami, FL 33136, USA. [16]23andMe, Mountain View, CA 94041, USA. [17]Centre for Ethics, Law and Mental Health, Gillberg Neuropsychiatry Centre, University of Gothenburg, Sweden. [18]Carolina Population Center, University of North Carolina at Chapel Hill, Chapel Hill, NC 27516, USA. [19]Department of Sociology, University of North Carolina at Chapel Hill, Chapel Hill, NC 27599, USA. [20]Department of Psychiatry and Behavioral Sciences, NorthShore University HealthSystem Research Institute, Evanston, IL 60201, USA. [21]Department of Psychiatry and Behavioral Neuroscience, University of Chicago, Chicago, IL 60637, USA. [22]Centre for Psychology and Evolution, School of Psychology, University of Queensland, St. Lucia, Brisbane QLD 4072, Australia.
*These authors contributed equally to this work. †These authors contributed equally to this work.
‡Corresponding author. Email: zietsch@psy.uq.edu.au

Box 1. Phenotype and sample definition and limitations.

In this study, we use the term "same-sex sexual behavior," which is defined as having ever had sex with someone of the same sex. Detailed descriptions of the variables used in the different cohorts can be found in the supplementary materials (*14*).

To aid in readability throughout the manuscript, in some places we refer to individuals who have ever had sex with someone of the same sex as "nonheterosexuals," whereas we refer to individuals who have never had sex with someone of the same sex as "heterosexuals."

We acknowledge that the grouping phrase "nonheterosexuals" has the potential to present messages of othering (that is, undesirable marginalization of another person or group on the basis of their sexual expression)—by defining an "outgroup" in reference to an "ingroup" and implying that "nonheterosexual behavior" may have a negative connotation, whereas "heterosexual behavior" may have a positive one. We wish to make clear that our choice of language is not meant to forward messages of othering on the basis of sexual behavior.

Throughout this manuscript, we use the terms "female" and "male" rather than "woman" and "man." This is because our analyses and results relate to biologically defined sex, not to gender.

As is common in genetic analyses, we dropped individuals from our study whose biological sex and self-identified sex/gender did not match. This is an important limitation of our analyses because the analyses do not include transgender persons, intersex persons, and other important persons and groups within the queer community. We hope that this limitation will be addressed in future work.

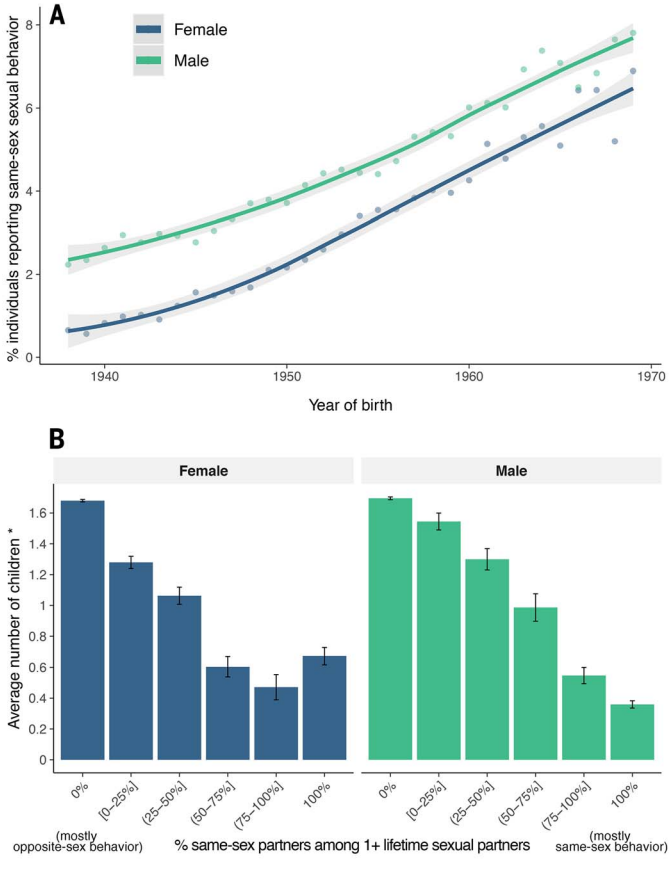

Fig. 1. Descriptive statistics regarding same-sex sexual behavior in the UK Biobank. (**A**) The percentage of participants in the UK Biobank who reported having had at least one same-sex sexual partner (*y* axis) increased with participants' year of birth (*x* axis). (**B**) Among participants reporting at least one same-sex partner, those with a greater proportion of same-sex partners (*x* axis) have a larger reproductive disadvantage (lower birth-year adjusted number of children) (*y* axis). Vertical bars represent 95% CIs.

participants reported the degree of attraction to the same versus opposite sex.

We observed in the UK Biobank that individuals who reported same-sex sexual behavior had on average fewer offspring than those of individuals who engaged exclusively in heterosexual behavior, even for individuals reporting only a minority of same-sex partners (Fig. 1B). This reduction in number of children is comparable with or greater than for other traits that have been linked to lower fertility rates (fig. S1) (*14*). This reproductive deficit raises questions about the evolutionary maintenance of the trait, but we do not address these here.

Genetic architecture of same-sex sexual behavior

We first assessed whether same-sex sexual behavior clustered in families in a manner consistent with genetic influences on the phenotype. Among pairs of individuals in the UK Biobank related at full cousin or closer [as identified by genomic similarity (*14*); *n* pairs = 106,979], more closely related individuals were more likely to be concordant in terms of same-sex sexual behavior. By modeling the correspondence of relatedness among individuals and the similarity of their sexual behavior, we estimated broad-sense heritability—the percentage of variation in a trait attributable to genetic variation—at 32.4% [95% confidence intervals (CIs), 10.6 to 54.3] (table S4). This estimate is consistent with previous estimates from smaller twin studies (*7*).

To identify genetic variants [largely single-nucleotide polymorphisms (SNPs)] associated with same-sex sexual behavior, we performed a GWAS in the UK Biobank study (*n* = 408,995 individuals) (*14*). To increase power and generalizability of our results, we also performed a GWAS in the cohort from 23andMe using an equivalent variable (individuals who reported having had sex with "Other sex only" versus the other options on a seven-point scale regarding participants' sexual partners) (*n* = 68,527 individuals, of which 12,933 reported same-sex sexual behavior) (table S3) (*14*). We estimated the genetic correlation (*16*) between different heritable traits to determine the degree of consistency of genetic influences on same-sex sexual behavior in the two studies, which was high [genetic correlation coefficient (r_g) = 0.87; 95% CIs, 0.67 to 1.06] (table S5) (*14*). Genetic correlations between same-sex sexual behavior and 28 different traits were largely similar in the UK Biobank and 23andMe (fig. S2) (*14*), although a few differences were observed; for example, in females, the genetic correlations between same-sex sexual behavior and anorexia were in opposite directions in the UK Biobank (r_g = –0.36; 95% CIs, –0.60 and –0.09) and 23andMe data (r_g = 0.36; 95% CIs, 0.08 to 0.65; Wald test *P* value for differences = 0.0001). Overall, these results indicate that the genetic influences on same-sex sexual behavior in the two samples is similar, although there is some suggestion of phenotypic heterogeneity. We meta-analyzed the two sample sets using MTAG (*17*), which models

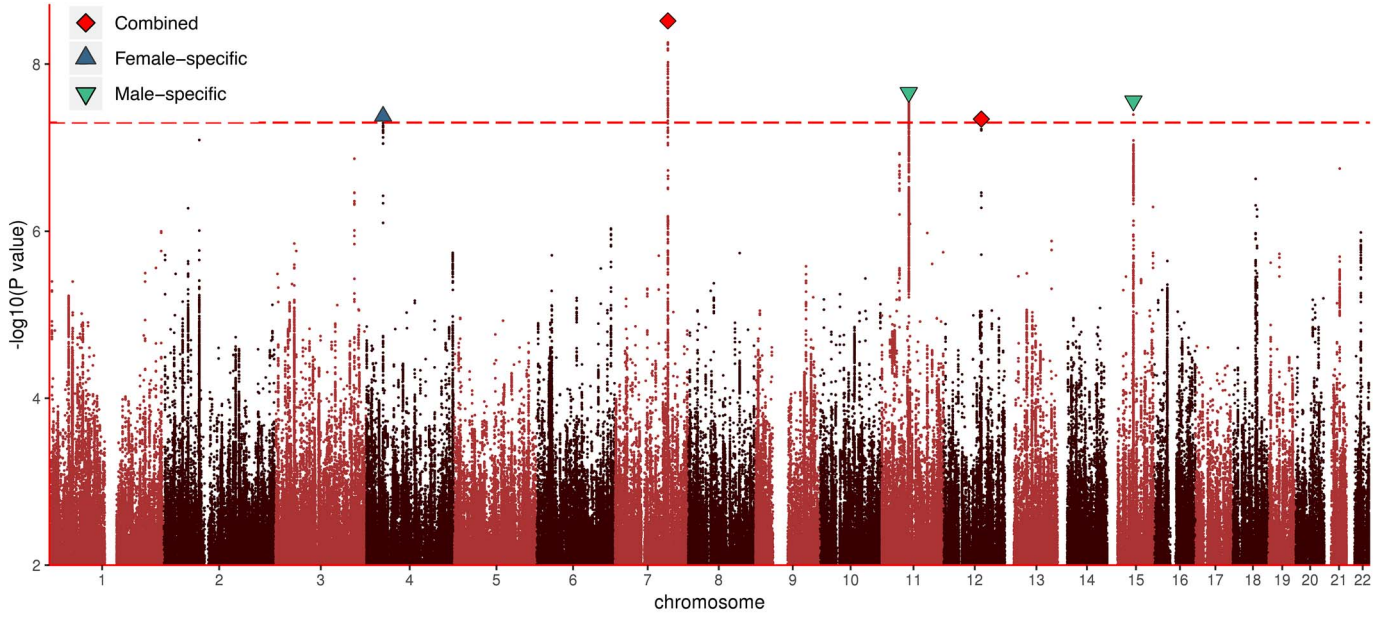

Fig. 2. Manhattan plot for a GWAS of same-sex sexual behavior. Diamonds (red) represent genome-wide significant signals from analysis of males and females combined, and triangles represent genome-wide significant signals that are female (pointing up, blue) or male (pointing down, green) specific.

their genetic correlation to determine the meta-analytic weights, yielding a total sample size of 477,522 individuals (26,827 individuals reporting same-sex sexual behavior).

After standard quality control checks (table S6) (*14*), we identified two genome-wide significant signals for same-sex sexual behavior (rs11114975-12q21.31 and rs10261857-7q31.2) (Fig. 2 and tables S7 and S8). We discuss these SNPs further in the section "In-silico follow-up of GWAS results." To assess differences in effects between females and males, we also performed sex-specific analyses. These results suggested only a partially shared genetic architecture across the sexes; the across-sex genetic correlation was 0.63 (95% CIs, 0.48 to 0.78) (table S9). This is noteworthy given that most other studied traits show much higher across-sex genetic correlations, often close to 1 (*18*–*21*). Through the sex-specific analyses, we identified two additional signals in males (rs28371400-15q21.3 and rs34730029-11q12.1), which showed no significant association in females, and one in females (rs13135637-4p14), which showed no significant association in males. Overall, three of the SNPs replicated at a nominal *P* value in the meta-analyzed replication datasets (Wald test $P = 0.027$ for rs34730029, $P = 0.003$ for rs28371400, and $P = 0.006$ for rs11114975) (table S10), despite the much smaller sample size (MGSOSO, Add Health, and CATSS; total sample size = 15,156 individuals, effective sample size = 4887 individuals).

The SNPs that reached genome-wide significance had very small effects (odds ratios ~1.1) (table S7). For example, in the UK Biobank, males with a GT genotype at the rs34730029 locus had 0.4% higher prevalence of same-sex sexual behavior than those with a TT genotype (4.0 versus 3.6%). Nevertheless, the contribution of all

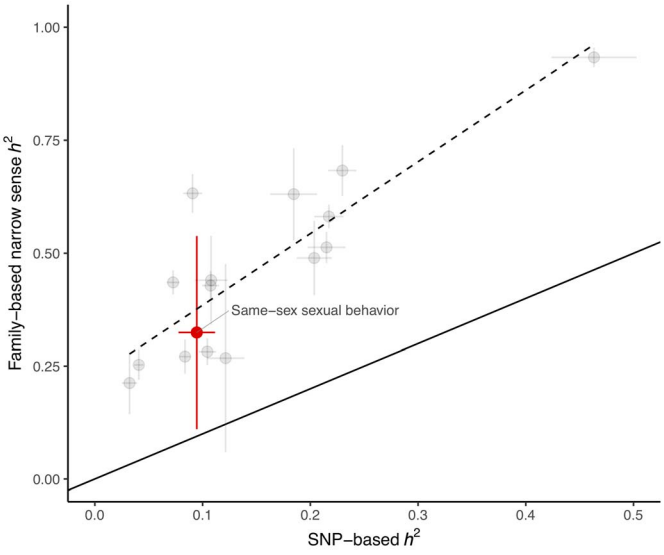

Fig. 3. SNP-based versus family-based heritability estimates for same-sex sexual behavior compared with a variety of other traits. Heritability, h^2; same-sex sexual behavior, red dot; other traits, gray dots. The estimates for all traits are provided in table S23. Horizontal bars represent 95% CIs for the SNP-based estimate, and vertical bars represent 95% CIs for the family-based estimate. Dashed and solid lines represent the observed (obtained by linear regression) and expected relationship between family-based and SNP-based heritability, respectively.

measured common SNPs in aggregate (SNP-based heritability) was estimated to be 8 to 25% (95% CIs, 5 to 30%) of variation in female and male same-sex sexual behavior, in which the range reflects differing estimates by using different analysis methods or prevalence assumptions (table S11) (*14*). The discrepancy between the variance captured by the significant SNPs and all common SNPs suggests that same-sex sexual behavior, like most complex human traits, is influenced by the small, additive effects of very many genetic variants, most of which cannot be detected at the current sample size (*22*). Consistent with this interpretation, we show that the contribution of each chromosome to heritability is broadly proportional to its size (fig. S3) (*14*). In contrast to linkage studies that found substantial association of sexual

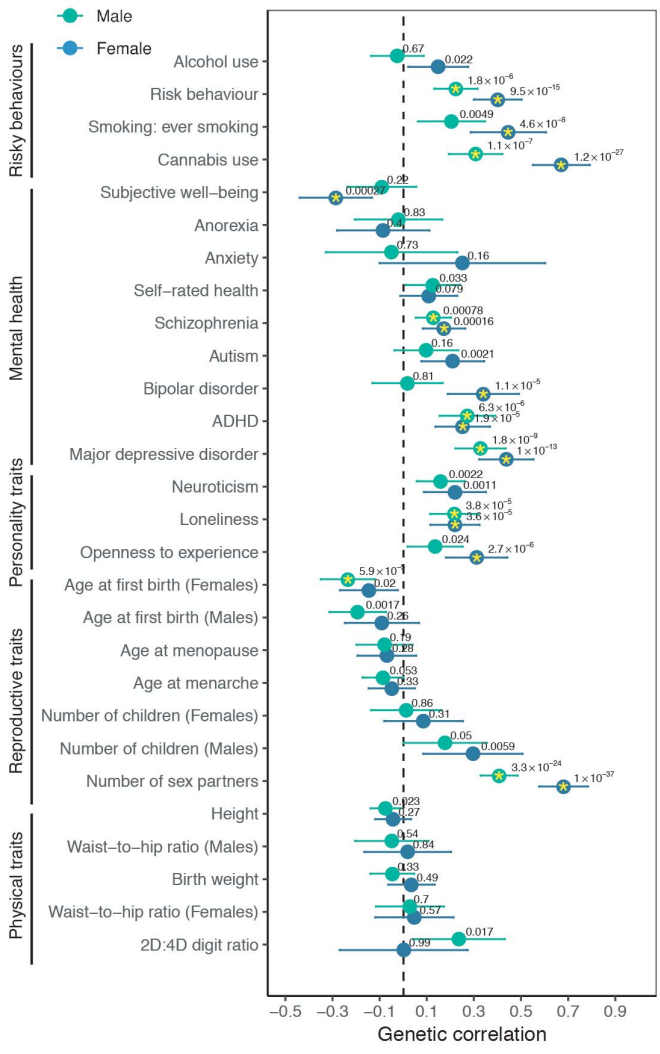

Fig. 4. Genetic correlations of same-sex sexual behavior with various preselected traits and disorders, separately for males and females. Males, green; females, blue. Yellow asterisks denote the genetic correlations that were experiment-wise significant ($P < 8.9 \times 10^{-4}$; references, definitions, and full results can be found in table S19). Wald test P values for the genetic correlations are reported above each dot. Horizontal bars represent 95% CIs.

orientation with variants on the X-chromosome (*8*, *23*), we found no excess of signal (and no individual genome-wide significant loci) on the X-chromosome (fig. S4).

To test whether these aggregate estimates of genetic effects correlate with sexuality in other samples, we constructed polygenic scores for same-sex sexual behavior (*14*, *24*). These polygenic scores were significantly associated with sexual identity in MGSOSO (Wald test, $P = 0.001$) and same-sex attraction in the Add Health ($P = 0.017$) and CATSS ($P = 3.5 \times 10^{-6}$) studies (tables S12, S13, and S14). In CATSS, polygenic scores were also significantly associated with sexual attraction in participants at age 15 years ($P = 6.4 \times 10^{-5}$), suggesting that at least some of the genetic influences on same-sex sexual behavior manifest early in sexual development. The purpose of these analyses is to further characterize the genetic influences on same-sex sexual behavior and not to predict same-sex sexual behavior on the individual level. In all cases, the variance explained by the polygenic scores was extremely low (<1%); these scores could not be used to accurately predict sexual behavior in an individual.

Overall, these findings suggest that genetic influences on same-sex sexual behavior are highly polygenic and are not specific to the discovery samples or measures. All the SNPs measured, when combined, do not capture the entirety of family-based heritability (8 to 25% from GWAS versus 32% from family-based methods). In this, same-sex sexual behavior is similar to many other complex traits; the ratio between family-based heritability and SNP-heritability estimated in the same sample is consistent with empirical findings for the other 16 traits we tested (family heritability approximately three times larger than SNP-heritability) (Fig. 3) (*14*). There are many possible reasons for this discrepancy, including, but not limited to, variants not captured by genotyping arrays, nonadditive genetic effects, and phenotypic heterogeneity.

In silico follow-up of GWAS results

To explore the biological processes that may influence same-sex sexual behavior, we performed cell- and tissue-type enrichment analyses using the GWAS discovery dataset (*14*, *25*). We did not find clear evidence of enrichment for any particular cell or tissue (fig S5). However, we did find that genes near variants associated with same-sex sexual behavior are more likely than chance to be highly constrained [having unusually low prevalence of loss-of-function variants, suggesting stronger evolutionary constraint (*14*, *26*)], even after controlling for expression in the brain (table S15).

At the level of individual loci, we investigated biological pathways by integrating information from expression quantitative trait loci (eQTL) analyses (*27*), phenome-wide association study (PheWAS) (table S16) (*28*), and gene-based analysis by using MAGMA (*14*, *29*). A full report can be found in table S17. Here, we highlight findings relating to the two SNPs associated with male same-sex sexual behavior: rs34730029 and rs28371400. First, the locus encompassing rs34730029-11q12.1 contains a number of olfactory receptor genes (several of which were significantly associated with same-sex sexual behavior in a gene-based test) (fig. S6 and table S18). This SNP is correlated [linkage disequilibrium, coefficient of determination (R^2) = 0.70] with a missense variant (rs6591536) in *OR5A1* that has been reported to have a substantial effect on the sensitivity to certain scents (*30*). Second, rs28371400-15q21.3 had several indications of being involved in sex hormone regulation: The allele positively associated with same-sex sexual behavior is associated with higher rate of male pattern balding [in which sex-hormone sensitivity is implicated (*31*)] and is located ~20 kb upstream of the *TCF12* gene. *TCF12* is the primary heterodimerization partner for *TCF21*, a transcription factor essential for normal development of the gonads in mice (*32*), and is involved in the downstream actions of the *SRY* gene (which is responsible for the initiation of male sex determination) in humans (*33*).

Genetic correlations with other traits

Next, we explored the genetic correlations between same-sex sexual behavior and 28 other relevant traits chosen before the analyses, using summary statistics from other GWASs (Fig. 4 and table S19) (*14*). In particular, we included mental health traits because they are substantially heritable (*34*), and previous population surveys have shown elevated risk of adverse mental health outcomes (such as depression, anxiety, or substance use) in sexual minority populations, including individuals engaging in same-sex sexual behavior (*35*, *36*).

We found several personality traits (loneliness and openness to experience), risky behaviors (smoking and cannabis use) and mental health

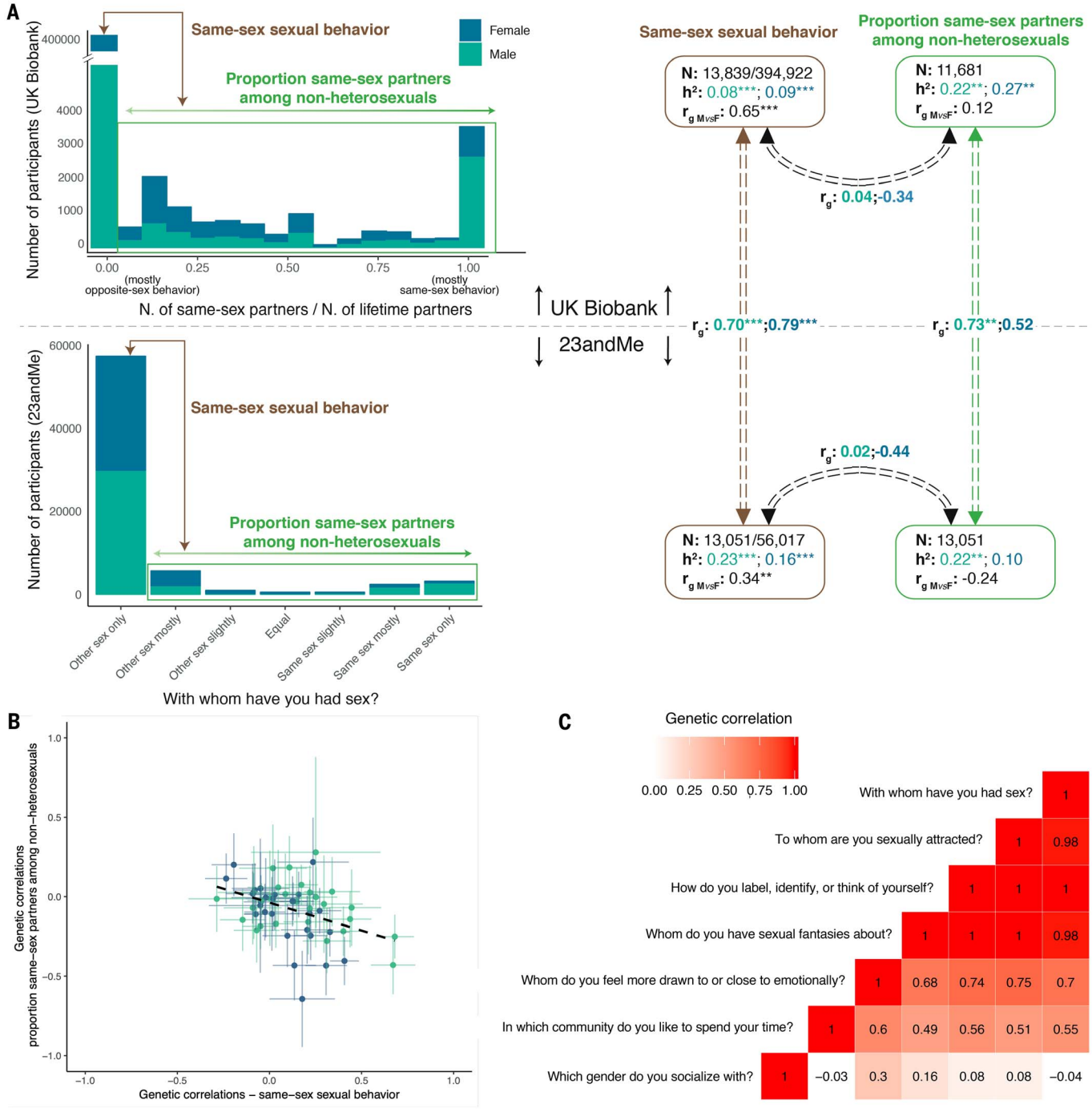

Fig. 5. Complexity and heterogeneity of genetic influences. (**A**) Genetic correlations between the main phenotype (same-sex sexual behavior; heterosexuals versus nonheterosexuals) and proportion of same-sex to total sexual partners among nonheterosexuals, in the UK Biobank and 23andMe samples. (**B**) Scatterplot showing genetic correlations of the main phenotype (*x* axis) and the proportion of same-sex to total partners among nonheterosexuals (*y* axis) with various other traits (table S21). (**C**) Genetic correlations among different sexual preference items in the 23andMe sample.

disorders, but not physical traits, to be significantly genetically correlated with same-sex sexual behavior. We found in both sexes that same-sex sexual behavior was positively genetically correlated with several psychiatric or mental health traits [for example, depression, r_g = 0.44 in females (95% CIs, 0.32 and 0.55), r_g = 0.33 in males (95% CIs, 0.22 and 0.43); schizophrenia, r_g = 0.17 in females (95% CIs 0.08 and 0.35), r_g = 0.13 in males (95% CIs, 0.05 and 0.26); all Wald test $P < 0.001$]. We emphasize that the causal processes underlying these genetic correlations are unclear and could be generated by environmental factors relating to prejudice against individuals engaging in same-sex sexual behavior, among other possibilities, which we discuss in (*14*). Some associations were sex specific. In particular, the genetic correlations with bipolar disorder, cannabis use, and number of sexual partners were significantly higher in females than in males (Wald test $P = 0.001$, 1.47×10^{-6}, and 3.13×10^{-5} respectively) (table S19).

Last, given the potential roles of sex hormones in sexual behaviors, we directly explored whether

Box 2. Communication and interpretation.

The topic explored in this study is complex and intersects with sexuality, identity, and attraction and potentially has civil and political implications for sexual minority groups. Therefore, we have

Engaged with science communication teams,

Engaged with LGBTQIA+ advocacy groups nationally and within our local institutions, and

Tried to make clear the many limitations and nuances of our study and our phenotypes.

We wish to make it clear that our results overwhelmingly point toward the richness and diversity of human sexuality. Our results do not point toward a role for discrimination on the basis of sexual identity or attraction, nor do our results make any conclusive statements about the degree to which "nature" and "nurture" influence sexual preference.

there is a genetic correlation with serum sex-hormone–binding globulin (SHBG) levels (*37*), which are thought to be inversely related to bioactive testosterone and estrogen in females and males, respectively (*38*). There was a significant correlation in females (r_g = 0.25, Wald test P = 0.03) but not in males (r_g = 0.10, Wald test P = 0.32).

Complexity and heterogeneity

To maximize our sample size and increase the power to detect SNP associations, we defined our primary phenotype as ever or never having had a same sex partner. Such a measure fails to capture the multifaceted richness and complexity of human sexual orientation. To explore the consequences of this simplification, we pursued genetic analyses across different aspects of sexual preference and behavior.

First, within participants reporting same-sex sexual behavior, we performed a GWAS on the proportion of same-sex partners to total partners, with a higher value indicating a higher proportion of same-sex partners (*14*). In the UK Biobank, this is measured directly from participants' reported number of same-sex and all partners, whereas in 23andMe, we used participants' raw responses to the item "With whom have you had sex?", which in individuals reporting same-sex sexual behavior could be "other sex mostly," "other sex slightly," "equal," "same sex slightly," "same sex mostly," or "same sex only." The UK Biobank and 23andMe variables were heritable (table S20A) and genetically correlated with each other (r_g = 0.52 and 95% CIs, −0.16 to 1.20 for females; r_g = 0.73 and 95% CIs, 0.18 to 1.27 for males) (Fig. 5A and table S20C), so we used MTAG to meta-analyze across the two studies for subsequent analyses.

We found little evidence for genetic correlation of the proportion of same-sex to total partners among individuals reporting same-sex sexual behavior (nonheterosexuals) with the binary same-sex sexual behavior variable [r_g = −0.31 (95% CIs, −0.62 to 0.00) for females and r_g = 0.03 (95% CIs, −0.18 to 0.23) for males] (table S20B). Further, this phenotype showed a markedly different pattern of genetic correlations with other traits, as compared with corresponding genetic correlations with the binary same-sex sexual behavior variable (Fig. 5B and table S21). These findings suggest that the same-sex sexual behavior variable and the proportion of same-sex partners among nonheterosexuals capture aspects of sexuality that are distinct on the genetic level, which in turn suggests that there is no single continuum from opposite-sex to same-sex sexual behavior. Interpretations of any one set of results in our study must consider this complexity.

With this in mind, we examined the possibility of different genetic variants distinguishing heterosexual behavior from differing proportions of same-sex partners within nonheterosexuals. To do so, we performed additional GWASs in the UK Biobank data on the following traits: those whose partners were (i) less than a third same-sex, (ii) between a third and two-thirds same-sex, (iii) more than a third same-sex, and (iv) exclusively same-sex. Genetic correlations of the first three categories with the fourth were 0.13, 0.80, and 0.95 (table S22), indicating partly different genetic variants distinguishing heterosexual behavior from differing proportions of same-sex partners within nonheterosexuals.

Last, using additional measures from 23andMe, we showed strong genetic correlations (all $r_g \geq 0.83$) (Fig. 5C and fig. S7) of same-sex sexual behavior with items assessing same-sex attraction, identity, and fantasies (a full list of items is provided in table S5), suggesting that these different aspects of sexual orientation are influenced by largely the same genetic variants. The full set of results of phenotypic and genetic correlations for females, males, and the whole sample is available in fig. S7 and table S5.

Discussion

We identified genome-wide significant loci associated with same-sex sexual behavior and found evidence of a broader contribution of common genetic variation. We established that the underlying genetic architecture is highly complex; there is certainly no single genetic determinant (sometimes referred to as the "gay gene" in the media). Rather, many loci with individually small effects, spread across the whole genome and partly overlapping in females and males, additively contribute to individual differences in predisposition to same-sex sexual behavior. All measured common variants together explain only part of the genetic heritability at the population level and do not allow meaningful prediction of an individual's sexual preference.

The knowledge that the variants involved are numerous and spread across the genome enabled us to leverage whole-genome analytic techniques to explore human sexual behavior in ways previously impossible. We determined that the genetic effects that differentiate heterosexual from same-sex sexual behavior are not the same as those that differ among nonheterosexuals with lower versus higher proportions of same-sex partners. This finding suggests that on the genetic level, there is no single dimension from opposite-sex to same-sex preference. The existence of such a dimension, in which the more someone is attracted to the same-sex the less they are attracted to the opposite-sex, is the premise of the Kinsey scale (*39*), a research tool ubiquitously used to measure sexual orientation. Another measure, the Klein Grid (*40*), retains the same premise but separately measures sexual attraction, behavior, fantasies, and identification (as well as nonsexual preferences); however, we found that these sexual measures are influenced by similar genetic factors. Overall, our findings suggest that the most popular measures are based on a misconception of the underlying structure of sexual orientation and may need to be rethought. In particular, using separate measures of attraction to the opposite sex and attraction to the same sex, such as in the Sell Assessment of Sexual Orientation (*41*), would remove the assumption that these variables are perfectly inversely related and would enable more nuanced exploration of the full diversity of sexual orientation, including bisexuality and asexuality.

Although we emphasize the polygenicity of the genetic effects on same-sex sexual behavior, we identified five SNPs whose association with same-sex sexual behavior reached genome-wide significance. Three of these replicated in other independent samples whose measures related to identity and attraction rather than behavior. These SNPs may serve to generate new lines of enquiry. In particular, the finding that one of the replicated SNPs (rs28371400-15q21.3) is linked to male pattern balding and is nearby a gene (*TCF12*) relevant to sexual differentiation strengthens the idea that sex-hormone regulation may be involved in the development of same-sex sexual behavior. Also, that another replicated SNP (rs34730029-11q12.1) is strongly linked to several genes involved in olfaction raises intriguing questions. Although the underlying mechanism at this locus is unclear, a link between olfaction and reproductive function has previously been established. Individuals with Kallmann syndrome exhibit both delayed or absent pubertal development and an impaired sense of smell because of the close developmental origin of fetal gonadotropin-releasing hormone and olfactory neurons (*42*).

Our study focused on the genetic basis of same-sex sexual behavior, but several of our results point to the importance of sociocultural context as well. We observed changes in prevalence of

reported same-sex sexual behavior across time, raising questions about how genetic and sociocultural influences on sexual behavior might interact. We also observed partly different genetic influences on same-sex sexual behavior in females and males; this could reflect sex differences in hormonal influences on sexual behavior (for example, importance of testosterone versus estrogen) but could also relate to different sociocultural contexts of female and male same-sex behavior and different demographics of gay, lesbian, and bisexual groups (*43*). With these points in mind, we acknowledge the limitation that we only studied participants of European ancestry and from a few Western countries; research involving larger and more diverse samples will afford greater insight into how these findings fare across different sociocultural contexts.

Our findings provide insights into the biological underpinnings of same-sex sexual behavior but also underscore the importance of resisting simplistic conclusions (Box 2)—because the behavioral phenotypes are complex, because our genetic insights are rudimentary, and because there is a long history of misusing genetic results for social purposes.

Materials and methods summary

Study samples

We used data from genotyped individuals from five cohorts (total n = 492,678) who provided self-report information using different questionnaire-based measurement scales. Informed consent was provided from all individuals participating in the studies, which were approved by their local research ethic committee.

Genetic association analyses

After standard quality control, we performed GWASs for "same-sex sexual behavior" (defined as ever versus never having had sex with a same-sex partner) in the UK Biobank and 23andMe samples, which we meta-analysed using MTAG (*17*). We also conducted GWASs separately by sex. Genome-wide significant SNPs were replicated in three independent samples. Also, using LD-pred (*24*), we derived polygenic score for same-sex sexual behavior according to the meta-analyzed GWAS results and tested the association between this polygenic score and same-sex sexual behavior in three independent samples. To explore diversity among individuals reporting same-sex sexual behavior, we also conducted GWASs in the UK-Biobank and 23andMe samples (meta-analyzed using MTAG) on the "proportion of same-sex to total number of sexual partners among nonheterosexuals."

Heritability estimation

We estimated family-based heritability of same-sex sexual behavior on the basis of known familial relationships in the UK Biobank study. The relatedness between pairs of participants was estimated by using KING (*44*). Additive genetic effects as well as shared and unshared environmental variance components were estimated on the basis of the covariance between different pairs of relatives. Second, heritability explained by all measured common SNPs (SNP-based heritability) was estimated by using linkage disequilibrium (LD) score regression (*45*) and transformed to the liability scale (*46*). Using a similar approach, we also estimated the SNP-based heritability per chromosome and evaluated heritability enrichment across various tissues on the basis of Genotype-Tissue Expression (GTEx) gene-expression results (*47*).

In silico follow-up

The GWAS results for same-sex sexual behavior were followed up with gene-based tests of association in MAGMA (*29*) and an enrichment analysis of evolutionarily constrained genes by using partitioned LD score regression (*45*) and MAGMA. We also performed a PheWAS (*28*) to examine whether the SNPs we identified for same-sex sexual behavior have also been associated with other phenotypes and eQTL mapping (*27*) to link SNPs with gene expression.

Genetic correlations and phenotypic heterogeneity

Using cross-trait LD score regression (*16*), we estimated the genetic correlations of same-sex sexual behavior and proportion of same-sex to total number of sexual partners among non-heterosexuals with a range of traits, including mental health, personality, and sexually dimorphic traits. To examine heterogeneity of genetic influences, we looked at the genetic correlations between sexes, between cohorts, and between different measures of sexual preference.

Science communication strategy

To communicate the results of the study to the broader audience, we engaged with different LGBTQIA+ (lesbian, gay, bisexual, transgender, queer, intersex, asexual, and other+) and science communication organizations and created multimedia materials for a lay audience.

Detailed materials and methods can be found in the supplementary materials (*14*).

REFERENCES AND NOTES

1. ACSF investigators, AIDS and sexual behaviour in France. ACSF investigators. *Nature* **360**, 407–409 (1992). doi: 10.1038/360407a0; pmid: 1448162
2. M. Melbye, R. J. Biggar, Interactions between persons at risk for AIDS and the general population in Denmark. *Am. J. Epidemiol.* **135**, 593–602 (1992). doi: 10.1093/oxfordjournals.aje.a116338; pmid: 1580235
3. S. W. Semenyna, D. P. VanderLaan, L. J. Petterson, P. L. Vasey, Familial patterning and prevalence of male androphilia in Samoa. *J. Sex Res.* **54**, 1077–1084 (2017). doi: 10.1080/00224499.2016.1218416; pmid: 27593894
4. J. M. Bailey *et al.*, Sexual orientation, controversy, and science. *Psychol. Sci. Public Interest* **17**, 45–101 (2016). doi: 10.1177/1529100616637616; pmid: 27113562
5. D. Scasta, P. Bialer, American Psychiatric Association, Position statement on issues related to homosexuality (American Psychiatric Association, 2013); www.psychiatry.org/psychiatrists/search-directories-databases/policy-finder (accessed on 26 February 2019).
6. R. C. Pillard, J. M. Bailey, Human sexual orientation has a heritable component. *Hum. Biol.* **70**, 347–365 (1998). pmid: 9549243
7. N. Långström, Q. Rahman, E. Carlström, P. Lichtenstein, Genetic and environmental effects on same-sex sexual behavior: A population study of twins in Sweden. *Arch. Sex. Behav.* **39**, 75–80 (2010). doi: 10.1007/s10508-008-9386-1; pmid: 18536986
8. D. H. Hamer, S. Hu, V. L. Magnuson, N. Hu, A. M. Pattatucci, A linkage between DNA markers on the X chromosome and male sexual orientation. *Science* **261**, 321–327 (1993). doi: 10.1126/science.8332896; pmid: 8332896
9. G. Rice, C. Anderson, N. Risch, G. Ebers, Male homosexuality: Absence of linkage to microsatellite markers at Xq28. *Science* **284**, 665–667 (1999). doi: 10.1126/science.284.5414.665; pmid: 10213693
10. A. R. Sanders *et al.*, Genome-wide association study of male sexual orientation. *Sci. Rep.* **7**, 16950 (2017). doi: 10.1038/s41598-017-15736-4; pmid: 29217827
11. R. A. Lippa, Sex differences and sexual orientation differences in personality: Findings from the BBC Internet survey. *Arch. Sex. Behav.* **37**, 173–187 (2008). doi: 10.1007/s10508-007-9267-z; pmid: 18074219
12. Y. Wang, M. Kosinski, Deep neural networks are more accurate than humans at detecting sexual orientation from facial images. *J. Pers. Soc. Psychol.* **114**, 246–257 (2018). doi: 10.1037/pspa0000098; pmid: 29389215
13. J. M. Bailey, M. P. Dunne, N. G. Martin, Genetic and environmental influences on sexual orientation and its correlates in an Australian twin sample. *J. Pers. Soc. Psychol.* **78**, 524–536 (2000). doi: 10.1037/0022-3514.78.3.524; pmid: 10743878
14. Materials and methods are available as supplementary materials.
15. A. L. Norris, D. K. Marcus, B. A. Green, Homosexuality as a discrete class. *Psychol. Sci.* **26**, 1843–1853 (2015). doi: 10.1177/0956797615598617; pmid: 26499203
16. B. Bulik-Sullivan *et al.*, An atlas of genetic correlations across human diseases and traits. *Nat. Genet.* **47**, 1236–1241 (2015). doi: 10.1038/ng.3406; pmid: 26414676
17. P. Turley *et al.*, Multi-trait analysis of genome-wide association summary statistics using MTAG. *Nat. Genet.* **50**, 229–237 (2018). doi: 10.1038/s41588-017-0009-4; pmid: 29292387
18. K. Rawlik, O. Canela-Xandri, A. Tenesa, Evidence for sex-specific genetic architectures across a spectrum of human complex traits. *Genome Biol.* **17**, 166 (2016). doi: 10.1186/s13059-016-1025-x; pmid: 27473438
19. A. Okbay *et al.*, Genome-wide association study identifies 74 loci associated with educational attainment. *Nature* **533**, 539–542 (2016). doi: 10.1038/nature17671; pmid: 27225129
20. J. Martin *et al.*, A Genetic investigation of sex bias in the prevalence of attention-deficit/hyperactivity disorder. *Biol. Psychiatry* **83**, 1044–1053 (2018). doi: 10.1016/j.biopsych.2017.11.026; pmid: 29325848
21. R. Karlsson Linnér *et al.*, Genome-wide association analyses of risk tolerance and risky behaviors in over 1 million individuals identify hundreds of loci and shared genetic influences. *Nat. Genet.* **51**, 245–257 (2019). doi: 10.1038/s41588-018-0309-3; pmid: 30643258
22. M. E. Goddard, K. E. Kemper, I. M. MacLeod, A. J. Chamberlain, B. J. Hayes, Genetics of complex traits: Prediction of phenotype, identification of causal polymorphisms and genetic architecture. *Proc. Biol. Sci.* **283**, 20160569 (2016). doi: 10.1098/rspb.2016.0569; pmid: 27440663
23. A. R. Sanders *et al.*, Genome-wide scan demonstrates significant linkage for male sexual orientation. *Psychol. Med.* **45**, 1379–1388 (2015). doi: 10.1017/S0033291714002451; pmid: 25399360
24. B. J. Vilhjálmsson *et al.*, modeling linkage disequilibrium increases accuracy of polygenic risk scores. *Am. J. Hum. Genet.* **97**, 576–592 (2015). doi: 10.1016/j.ajhg.2015.09.001; pmid: 26430803
25. H. K. Finucane *et al.*, Partitioning heritability by functional annotation using genome-wide association summary statistics. *Nat. Genet.* **47**, 1228–1235 (2015). doi: 10.1038/ng.3404; pmid: 26414678
26. M. Lek *et al.*, Analysis of protein-coding genetic variation in 60,706 humans. *Nature* **536**, 285–291 (2016). doi: 10.1038/nature19057; pmid: 27535533
27. A. Gusev *et al.*, Integrative approaches for large-scale transcriptome-wide association studies. *Nat. Genet.* **48**, 245–252 (2016). doi: 10.1038/ng.3506; pmid: 26854917
28. J. C. Denny *et al.*, PheWAS: Demonstrating the feasibility of a phenome-wide scan to discover gene-disease associations. *Bioinformatics* **26**, 1205–1210 (2010). doi: 10.1093/bioinformatics/btq126; pmid: 20335276
29. C. A. de Leeuw, J. M. Mooij, T. Heskes, D. Posthuma, MAGMA: Generalized gene-set analysis of GWAS data. *PLOS Comput.*

Biol. **11**, e1004219 (2015). doi: 10.1371/journal.pcbi.1004219; pmid: 25885710
30. S. R. Jaeger *et al*., A Mendelian trait for olfactory sensitivity affects odor experience and food selection. *Curr. Biol.* **23**, 1601–1605 (2013). doi: 10.1016/j.cub.2013.07.030; pmid: 23910657
31. H. Kische *et al*., Sex hormones and hair loss in men from the general population of northeastern Germany. *JAMA Dermatol.* **153**, 935–937 (2017). doi: 10.1001/jamadermatol.2017.0297; pmid: 28403384
32. S. Cui *et al*., Disrupted gonadogenesis and male-to-female sex reversal in Pod1 knockout mice. *Development* **131**, 4095–4105 (2004). doi: 10.1242/dev.01266; pmid: 15289436
33. R. K. Bhandari, I. Sadler-Riggleman, T. M. Clement, M. K. Skinner, Basic helix-loop-helix transcription factor TCF21 is a downstream target of the male sex determining gene SRY. *PLOS ONE* **6**, e19935 (2011). doi: 10.1371/journal.pone.0019935; pmid: 21637323
34. P. F. Sullivan, M. J. Daly, M. O'Donovan, Genetic architectures of psychiatric disorders: The emerging picture and its implications. *Nat. Rev. Genet.* **13**, 537–551 (2012). doi: 10.1038/nrg3240; pmid: 22777127
35. T. G. M. Sandfort, R. de Graaf, R. V. Bijl, P. Schnabel, Same-sex sexual behavior and psychiatric disorders: Findings from the Netherlands Mental Health Survey and Incidence Study (NEMESIS). *Arch. Gen. Psychiatry* **58**, 85–91 (2001). doi: 10.1001/archpsyc.58.1.85; pmid: 11146762
36. J. Semlyen, M. King, J. Varney, G. Hagger-Johnson, Sexual orientation and symptoms of common mental disorder or low wellbeing: Combined meta-analysis of 12 UK population health surveys. *BMC Psychiatry* **16**, 67 (2016). doi: 10.1186/s12888-016-0767-z; pmid: 27009565
37. A. D. Coviello *et al*., A genome-wide association meta-analysis of circulating sex hormone-binding globulin reveals multiple Loci implicated in sex steroid hormone regulation. *PLOS Genet.* **8**, e1002805 (2012). doi: 10.1371/journal.pgen.1002805; pmid: 22829776
38. C. W. Burke, D. C. Anderson, Sex-hormone-binding globulin is an oestrogen amplifier. *Nature* **240**, 38–40 (1972). doi: 10.1038/240038a0; pmid: 4120573
39. A. C. Kinsey, W. B. Pomeroy, C. E. Martin, *Sexual Behavior in the Human Male* (W.B. Saunders, 1948).
40. F. Klein, *The Bisexual Option* (Routledge, ed. 2, 1993).
41. R. L. Sell, Defining and measuring sexual orientation: A review. *Arch. Sex. Behav.* **26**, 643–658 (1997). doi: 10.1023/A:1024528427013; pmid: 9415799
42. H. Valdes-Socin *et al*., Reproduction, smell, and neurodevelopmental disorders: Genetic defects in different hypogonadotropic hypogonadal syndromes. *Front. Endocrinol.* **5**, 109 (2014). doi: 10.3389/fendo.2014.00109; pmid: 25071724
43. G. M. Herek, A. T. Norton, T. J. Allen, C. L. Sims, Demographic, Psychological, and Social Characteristics of Self-Identified Lesbian, Gay, and Bisexual Adults in a US Probability Sample. *Sex. Res. Social Policy* **7**, 176–200 (2010). doi: 10.1007/s13178-010-0017-y; pmid: 20835383
44. A. Manichaikul *et al*., Robust relationship inference in genome-wide association studies. *Bioinformatics* **26**, 2867–2873 (2010). doi: 10.1093/bioinformatics/btq559; pmid: 20926424
45. B. K. Bulik-Sullivan *et al*., LD Score regression distinguishes confounding from polygenicity in genome-wide association studies. *Nat. Genet.* **47**, 291–295 (2015). doi: 10.1038/ng.3211; pmid: 25642630
46. S. H. Lee, N. R. Wray, M. E. Goddard, P. M. Visscher, Estimating missing heritability for disease from genome-wide association studies. *Am. J. Hum. Genet.* **88**, 294–305 (2011). doi: 10.1016/j.ajhg.2011.02.002; pmid: 21376301
47. J. Lonsdale *et al*., The Genotype-Tissue Expression (GTEx) project. *Nat. Genet.* **45**, 580–585 (2013). doi: 10.1038/ng.2653; pmid: 23715323
48. A. Ganna, andgan/sexual_orientation_GWAS v1.0. Zenodo (2019); doi:10.5281/zenodo.3232892

ACKNOWLEDGMENTS

We thank N. J. Cox, M. C. Keller, and E. S. Lander for carefully reading and commenting on the manuscript. We thank P. Turley and R. Walters for constructive discussion about MTAG. This research was conducted by using the UK Biobank Resource under application 25995. We thank all cohort participants for making this study possible. **Funding:** A.R.S. received funding from the Eunice Kennedy Shriver National Institute of Child Health and Human Development specifically to investigate the genetics of sexual orientation: R01HD041563 (A.R.S., principal investigator) and R21HD080410 (A.R.S. and E.R.M., multiple principal investigators). E.R.M., G.W.B., and S.G. are also supported by R21HD080410. No other member of the group received funding specifically for this study, but members of our team received salary funding from organizations as well as our own universities. B.P.Z. received funding from The Australian Research Council (FT160100298). A.G. was supported by the Knut and Alice Wallenberg Foundation (2015.0327) and the Swedish Research Council (2016-00250). A.G., R.M., and B.M.N. were supported by National Institutes of Health (NIH) grant 1R01MH107649-03 (to B.M.N.). R.W. was supported by the National Science Foundation's Graduate Research Fellowship Program (DGE 1144083). Any opinion, findings, conclusions, or recommendations expressed in this material are those of the authors and do not necessarily reflect the views of the National Science Foundation. M.G.N. is supported by ZonMw grants 849200011 and 531003014 from the Netherlands Organisation for Health Research and Development. This research used data from Add Health, a program project directed by K.M.H. (principal investigator) and designed by J. R. Udry, P. S. Bearman, and K.M.H. at the University of North Carolina at Chapel Hill, and funded by grant P01-HD031921 from the Eunice Kennedy Shriver National Institute of Child Health and Human Development, with cooperative funding from 23 other federal agencies and foundations. Information on how to obtain the Add Health data files is available on the Add Health website (www.cpc.unc.edu/addhealth). This research used Add Health GWAS data funded by Eunice Kennedy Shriver National Institute of Child Health and Human Development (NICHD) grants R01 HD073342 to K.M.H. (principal investigator) and R01 HD060726 to K.M.H., J. D. Boardman, and M. B. McQueen (multiple principal investigators). The genetic part of the CATSS study was supported by grant 2014-0834 from the Swedish Council for Working Life and Social Research. We thank the research participants of 23andMe and the other contributing cohorts for making this study possible. Collaborators for the 23andMe Research Team are M. Agee, B. Alipanahi, A. Auton, R. K. Bell, K. Bryc, S. L. Elson, P. Fontanillas, N. A. Furlotte, B. Hicks, K. E. Huber, E. M. Jewett, Y. Jiang, A. Kleinman, K.-H. Lin, N. K. Litterman, J. C. McCreight, M. H. McIntyre, K. F. McManus, J. L. Mountain, E. S. Noblin, C. A. M. Northover, S. J. Pitts, G. D. Poznik, A. J. Shastri, J. F. Shelton, S. Shringarpure, C. Tian, J. Y. Tung, V. Vacic, X. Wang, and C. H. Wilson. **Author contributions:** A.G., K.J.H.V., M.G.N., J.R.B.P., B.M.N., and B.P.Z. were responsible for the study concept and the design of the study. A.G. was the main analyst, performed the majority of analyses, and created most of the figures and tables. J.F.S., 23andMe Research Team, and A.Au. contributed to data acquisition and analysis of the 23andMe dataset. R.W. and K.M.H. contributed to data acquisition and analysis of the Add Health data. S.G., G.W.B., E.R.M., and A.R.S. contributed to data acquisition and analysis of the MGSOSO data. A.G., P.L., S.L., and N.L. contributed to data acquisition and analysis of the CATSS data. K.J.H.V., M.G.N., R.M., R.W., A.S.B., A.Ab., S.G., J.F.S., G.W.B., E.R.M. contributed to secondary analyses of the data. B.P.Z. wrote most of the manuscript; A.G., K.J.H.V., M.G.N., R.W., J.R.B.P., and B.M.N. contributed substantially to the writing of the manuscript. K.J.H.V. was in charge of writing the supplementary material. A.G., M.G.N., R.M., R.W., A.S.B., E.R.M., A.R.S., and B.P.Z. provided important input for the supplementary materials. A.G., K.J.H.V., R.W., A.R.S., B.M.N., and B.P.Z. contributed to engaging in community-based outreach with alliance and advocacy groups. All authors provided critical revision of the manuscript for important intellectual content. **Competing interests:** J.F.S., A.Au., and members of the 23andMe Research Team are employees of 23andMe and hold stock or stock options in 23andMe. B.M.N. is a member of the scientific advisory board at Deep Genomics and a paid consultant for Camp4 Therapeutics Corporation, Takeda Pharmaceutical, and Biogen. **Data and materials availability:** The code is available through GitHub (https://github.com/andgan/sexual_orientation_GWAS), archived at Zenodo (*48*), and the GWAS summary statistics of the UK Biobank sample (and the top 10,000 independent SNPs from the meta-analysis including 23andMe data) are available at GWAS Catalog (www.ebi.ac.uk/gwas/downloads/summary-statistics). Access to the full summary statistics of the 23andMe sample (for all SNPs) can be obtained by qualified researchers through a data transfer agreement with 23andMe that protects the privacy of the 23andMe participants. Researchers interested in the full meta-analysis summary statistics containing 23andMe data must also apply to 23andMe. Please visit (https://research.23andme.com/dataset-access) for more information and to apply to access the data. Access to individual level data from the UK Biobank can be obtained by bona fide scientists through application with UK Biobank (www.ukbiobank.ac.uk/researchers). Summary statistics from the Neale Lab database used for the pheWAS are available at GWAS Catalog (www.ebi.ac.uk/gwas/downloads/summary-statistics).

SUPPLEMENTARY MATERIALS

science.sciencemag.org/content/365/6456/eaat7693/suppl/DC1
Materials and Methods
Figs. S1 to S7
Tables S1 to S23
References (*49*–*108*)

10 September 2018; accepted 22 July 2019
10.1126/science.aat7693

RESEARCH ARTICLE SUMMARY

IMMUNOLOGY

Identification of a T follicular helper cell subset that drives anaphylactic IgE

Uthaman Gowthaman, Jennifer S. Chen*, Biyan Zhang*, William F. Flynn, Yisi Lu, Wenzhi Song, Julie Joseph, Jake A. Gertie, Lan Xu, Magalie A. Collet, Jessica D. S. Grassmann, Tregony Simoneau, David Chiang, M. Cecilia Berin, Joseph E. Craft, Jason S. Weinstein, Adam Williams*†, Stephanie C. Eisenbarth*†

INTRODUCTION: Cross-linking of high-affinity, allergen-specific immunoglobulin E (IgE) on mast cells results in anaphylaxis, a potentially life-threatening allergic reaction. The cellular mechanisms that induce B cells to produce high-affinity IgE to allergens remain poorly understood and likely differ from those that generate low-affinity IgE. T follicular helper (T_{FH}) cells are the primary T cell subset responsible for directing the affinity, longevity, and isotype of antibodies produced by B cells; they have recently been found to be responsible for IgE responses as well. Yet the nature of the T_{FH} cells that induce high-affinity IgE in allergic disease remains unclear.

RATIONALE: T_{FH} cells guide B cell isotype switching via cytokine production. Although interleukin-4 (IL-4) has long been recognized to guide IgE switching, IL-4 is also a canonical T_{FH} cell cytokine, expressed even when IgE is not made. This suggests that although IL-4 is necessary for high-affinity IgE, it is not sufficient, and additional T_{FH} cell–derived signals are required. We hypothesized that a distinct but rare T_{FH} cell population regulates the production of high-affinity IgE. To test this hypothesis, we used a model of dedicator of cytokinesis 8 (DOCK8) deficiency, which causes a monogenic form of allergy associated with aberrant production of IgE. Comparison of the T_{FH} populations present in this model with wild-type mice immunized to food and aeroallergens enabled us to identify the nature of the T cell that induces anaphylactic IgE antibody production by B cells.

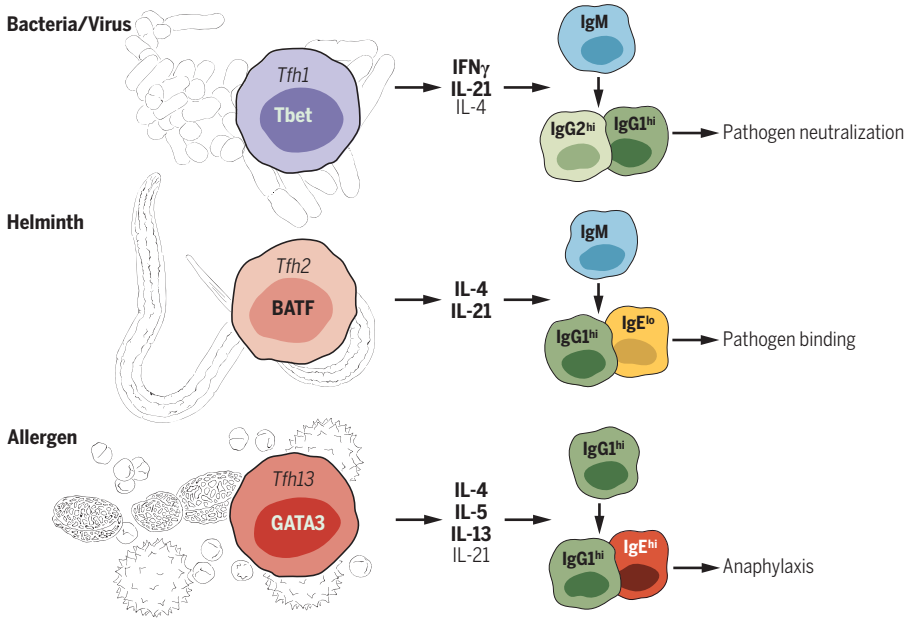

Model of T_{FH} cell–driven antibody production. Distinct T_{FH} cell subsets dictate the outcome of antibody responses. $T_{FH}1$ cells elicited to type 1 immunizations (bacterial or viral infections) do not induce IgE but promote pathogen neutralizing IgGs via production of IL-21 and interferon-γ (IFN-γ), with limited IL-4 production. During the type 2 immune responses to helminth infection, IL-4– and IL-21–producing $T_{FH}2$ cells are induced, resulting in production of IgG and low-affinity IgE antibodies but not anaphylaxis. The IgE^+ B cells in this case are derived from direct switching from low-affinity IgM^+ B cells. In contrast, $T_{FH}13$ cells are induced during allergic conditions and are necessary for the generation of high-affinity IgE, which results in anaphylactic responses. The high-affinity IgE^+ B cells in this case are derived from sequentially switched and activated $IgG1^+$ B cells.

RESULTS: Regardless of immunization conditions, mice with T cell–specific *Dock8* deficiency made allergen-reactive and anaphylactic IgE. This was associated with the presence of an unusual IL-4– and IL-13–producing T_{FH} cell population in lymph nodes, which we call $T_{FH}13$ cells. $T_{FH}13$ cells demonstrated a distinctive transcription factor profile, including expression of BCL6 and GATA3. $T_{FH}13$ cells were also induced in wild-type mice but only during immune responses when high-affinity IgE was made, including during food or aeroallergen sensitization. These cells were absent during immune responses lacking high-affinity IgE, including those induced by bacterial products or helminth infection. Patients who were allergic to peanut or aeroallergens also had elevated circulating $T_{FH}13$ cells. Single-cell RNA sequencing analysis confirmed that $T_{FH}13$ cells were distinct from related T helper 2 (T_H2) or IL-4–expressing $T_{FH}2$ cells. $T_{FH}13$ cells could also be distinguished from IL-13–expressing effector T_H2 cells by their subanatomical location in the germinal center. Conditional ablation of $T_{FH}13$ cells or isolated loss of IL-13 in T_{FH} cells resulted in impaired high-affinity, anaphylactic IgE responses to allergens. IgE and IgG1 germinal center B cells, but not naïve B cells, expressed the receptor for IL-13, suggesting that IL-13 may promote sequential switching of affinity-matured $IgG1^+$ to high-affinity IgE^+ B cells.

ON OUR WEBSITE

Read the full article at http://dx.doi.org/10.1126/science.aaw6433

CONCLUSION: Our work describes a subset of T cells necessary for inducing anaphylactic IgE production to allergens. $T_{FH}13$ cells and the molecular pathways operative in this distinctive population represent targets that could be leveraged diagnostically and therapeutically for allergies. Furthermore, the identification of $T_{FH}13$ cells and the immune context in which they are induced solves the long-standing question of how, under rare circumstances, anaphylaxis-inducing IgE is produced by high-affinity B cells. ■

The list of author affiliations is available in the full article online.
*These authors contributed equally to this work.
†Corresponding author. Email: stephanie.eisenbarth@yale.edu (S.C.E.); adam.williams@jax.org (A.W.)
Cite this article as U. Gowthaman *et al.*, *Science* **365**, eaaw6433 (2019). DOI: 10.1126/science.aaw6433

RESEARCH ARTICLE

IMMUNOLOGY

Identification of a T follicular helper cell subset that drives anaphylactic IgE

Uthaman Gowthaman[1,2], Jennifer S. Chen[1,2]*, Biyan Zhang[1,2]*, William F. Flynn[3], Yisi Lu[2], Wenzhi Song[2], Julie Joseph[1], Jake A. Gertie[1,2], Lan Xu[1,2], Magalie A. Collet[3], Jessica D. S. Grassmann[3], Tregony Simoneau[4], David Chiang[5], M. Cecilia Berin[5], Joseph E. Craft[2], Jason S. Weinstein[6], Adam Williams[3,7]*†, Stephanie C. Eisenbarth[1,2]*†

Cross-linking of high-affinity immunoglobulin E (IgE) results in the life-threatening allergic reaction anaphylaxis. Yet the cellular mechanisms that induce B cells to produce IgE in response to allergens remain poorly understood. T follicular helper (T_{FH}) cells direct the affinity and isotype of antibodies produced by B cells. Although T_{FH} cell–derived interleukin-4 (IL-4) is necessary for IgE production, it is not sufficient. We report a rare population of IL-13–producing T_{FH} cells present in mice and humans with IgE to allergens, but not when allergen-specific IgE was absent or only low-affinity. These "$T_{FH}13$" cells have an unusual cytokine profile (IL-13^{hi}IL-4^{hi}IL-5^{hi}IL-21^{lo}) and coexpress the transcription factors BCL6 and GATA3. $T_{FH}13$ cells are required for production of high- but not low-affinity IgE and subsequent allergen-induced anaphylaxis. Blocking $T_{FH}13$ cells may represent an alternative therapeutic target to ameliorate anaphylaxis.

Anaphylaxis is a severe form of allergic reaction precipitated by degranulation of immunoglobulin E (IgE)–laden mast cells after allergen recognition (*1*). Studies from food-allergic patients and murine models indicate that high-affinity, but not low-affinity, IgE induces mast-cell degranulation and anaphylaxis (*2*–*4*) and that the nature of the B cell that switches to low- versus high-affinity IgE differs (*5*, *6*). Unlike other antibody isotypes, how B cells are instructed to make affinity-matured IgE remains unclear.

Early work on IgE regulation demonstrated that the deletion of T helper 2 (T_H2) lineage-defining transcription factors (TFs) such as STAT6 or GATA3 or the prototypical T_H2 cytokine interleukin-4 (IL-4) reduced total IgE. Thus, T_H2 cells were proposed to control the IgE response (*7*–*9*). However, more recent work has demonstrated that IL-4^+ T follicular helper (T_{FH}) cells, not T_H2 cells, are required for IgE production (*10*–*15*). T_{FH} cells are the primary helper T cell subset responsible for directing the affinity, longevity, and isotype of antibody produced by B cells. Recent work has supported this functional T_H2-T_{FH} lineage distinction by identifying a distinctive *Il4* enhancer locus bound by BATF in T_{FH} cells that is distinct from the T_H2 DNA regulatory element for IL-4, IL-5, and IL-13 bound by GATA3 (*16*–*19*). Therefore, it has been argued that GATA3, IL-5, and IL-13 are restricted to T_H2 cells and type 2 innate lymphoid cells (ILC2s) (*14*, *20*).

IL-4 is a B cell survival factor expressed by T_{FH} cells during a variety of immune responses, including those in which IgE is not made (*21*–*23*). This suggests that IL-4 from T_{FH} cells is necessary but not sufficient for the induction of IgE. We hypothesized that IL-4^+ T_{FH} cells induce direct switching of B cells to low-affinity IgE during certain type 2 immune responses, but a distinct T_{FH} population producing additional signals regulates high-affinity IgE during allergen responses.

Using a murine model of a rare monogenic form of IgE-mediated allergy, dedicator of cytokinesis 8 (*Dock8*) deficiency, we discovered a subset of T_{FH} cells associated with high-affinity IgE production. These "$T_{FH}13$" cells produced IL-13 along with IL-4 but down-regulated IL-21. Accordingly, they expressed GATA3 in addition to the T_{FH} TF BCL6. We found the same $T_{FH}13$ cells in wild-type (WT) mice immunized with multiple allergens, but not other stimuli that failed to induce high-affinity IgE, including bacterial products or helminth infection. Circulating $T_{FH}13$ cells were also found in patients with IgE to aeroallergens or peanut. Conditional deletion of $T_{FH}13$ cells or IL-13 in T_{FH} cells abrogated the generation of high-affinity anaphylactic IgE to allergens. Thus, our study identifies the context in which a rare subset of T_{FH} cells are elicited and uncovers their critical role in the induction of anaphylactic IgE to allergens.

Dock8 deficiency reveals the presence of a distinct T_{FH} cell population associated with a hyper-IgE state

Patients with mutations in *DOCK8* are immunodeficient, but, paradoxically, they present with hyper-IgE syndrome (HIES) and associated food allergies and asthma. The precise reasons for HIES in this condition are not yet understood (*24*, *25*). DOCK8 was originally described as a guanine nucleotide exchange factor that regulates the actin cytoskeleton, but recent evidence reveals diverse roles of DOCK8 in nearly every cell of the immune system (*25*). We generated both total and immune cell–specific knockouts of *Dock8* in mice to study the cellular mechanisms of IgE induction.

IgE antibodies are a characteristic component of type 2 immunity, which is induced in response to allergens and helminths. In contrast, type 1 responses, induced by viral and certain bacterial infections, do not classically elicit the production of IgE. To determine whether *Dock8* deficiency promotes an aberrant hyper-IgE response to type 1 immunization, we immunized mice with lipopolysaccharide (LPS) along with the model antigen 4-hydroxy-3-nitrophenylacetyl (NP) conjugated to ovalbumin (NP-OVA), henceforth called LPS+OVA. The hapten NP allows measurement of antigen specificity and affinity. Using conditional *Dock8*-knockout mice, we discovered that isolated loss of *Dock8* in T cells (T-$Dock8^{-/-}$), but not in B cells or dendritic cells (DCs), recapitulated the hyper-IgE phenotype seen in patients (Fig. 1A). The hyper-IgE phenotype was not present in complete *Dock8*-knockout mice, which was not surprising given their DC-dependent defect in T_{FH} cell induction (*26*). The use of T-$Dock8^{-/-}$ mice bypassed the effect of *Dock8* deficiency on DC migration (fig. S1A) and B cell development (fig. S1B). T cell–specific deletion of *Dock8* was confirmed by immunoblot (fig. S1C) and via known T cell–intrinsic phenotypes of *Dock8*, including reduced T cell frequencies (fig. S1D) (*27*). However, $Dock8^{-/-}$ OVA-specific $CD4^+$ T cells (OT-II cells) demonstrated comparable in vivo proliferation and T_{FH} cell differentiation to $Dock8^{WT}$ OT-II cells to LPS+OVA immunization (fig. S1, E and F).

In addition to atypical total IgE production, type 1 immunization in T-$Dock8^{-/-}$ mice resulted in reduced NP-OVA–specific IgG antibodies and elevated NP-OVA–specific IgE antibodies (fig. S2, A to C). Additionally, there was reduced high-affinity NP-specific IgG1 and elevated high-affinity NP-specific IgE (Fig. 1, B and C). Previously immunized T-$Dock8^{-/-}$ mice challenged with NP-conjugated bovine serum albumin (BSA) showed robust acute mast-cell degranulation and systemic tissue edema (fig. S2, D and E) (*28*). The anaphylactic capacity of IgE from T-$Dock8^{-/-}$ mice was confirmed using a passive cutaneous anaphylaxis (PCA) assay (Fig. 1D) (*6*, *28*). T-$Dock8^{-/-}$ mice also spontaneously developed

[1]Department of Laboratory Medicine, Yale University School of Medicine, New Haven, CT 06520, USA. [2]Department of Immunobiology, Yale University School of Medicine, New Haven, CT 06520, USA. [3]The Jackson Laboratory for Genomic Medicine, Farmington, CT 06030, USA. [4]The Asthma Center, CT Children's Medical Center, Hartford, CT 06106, USA. [5]Jaffe Food Allergy Institute and Precision Immunology Institute, Icahn School of Medicine at Mount Sinai, New York, NY 10029, USA. [6]Center for Immunity and Inflammation, Rutgers New Jersey Medical School, Newark, NJ 07101, USA. [7]The Department of Genetics and Genome Sciences, University of Connecticut Health Center, Farmington, CT 06032, USA.
*These authors contributed equally to this work.
†Corresponding author. Email: stephanie.eisenbarth@yale.edu (S.C.E.); adam.williams@jax.org (A.W.)

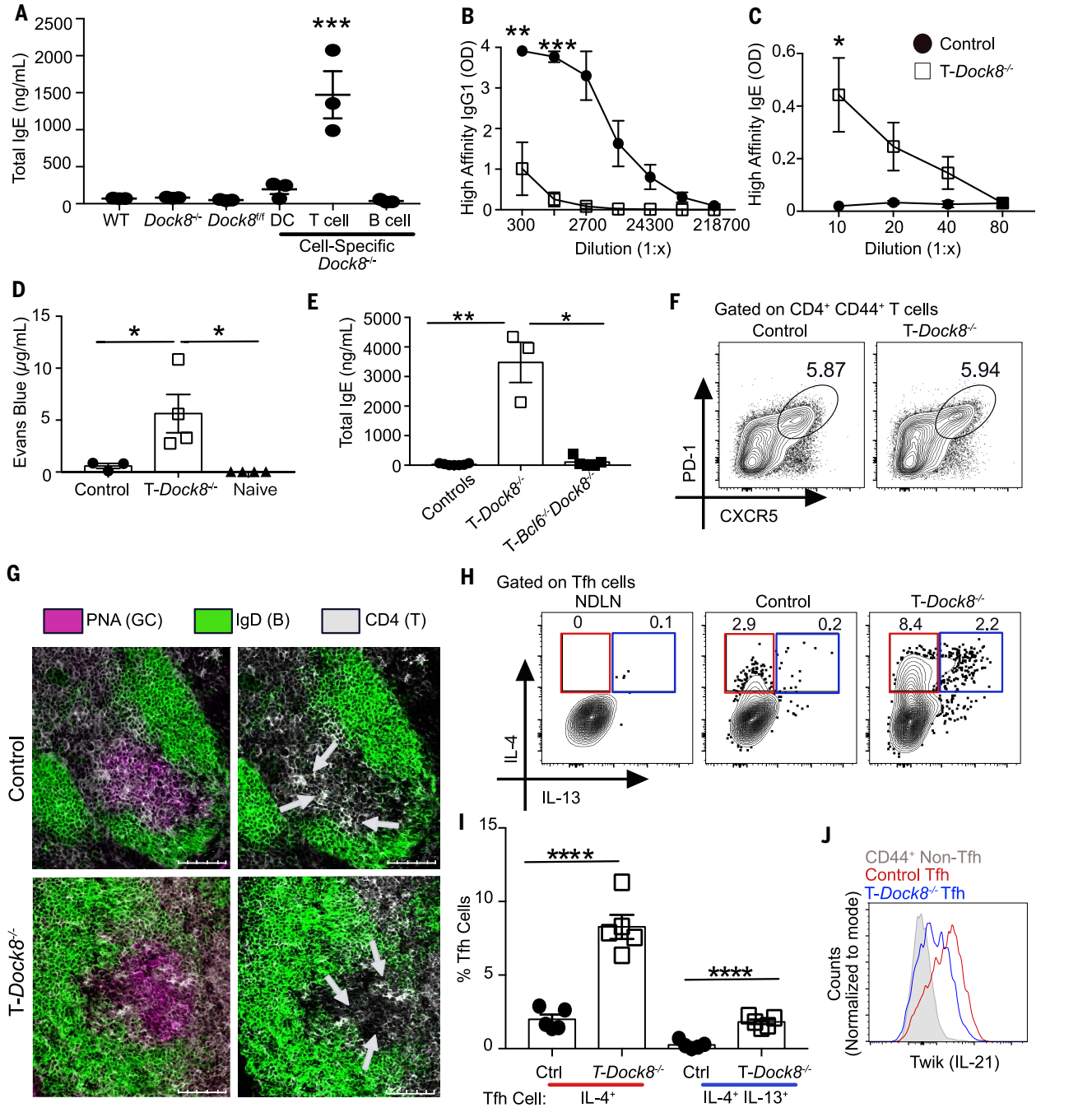

Fig. 1. DOCK8 deficiency reveals the presence of a specific T_{FH} cell population associated with a hyper-IgE state. (**A**) WT, *Dock8*$^{-/-}$, *Dock8*$^{fl/fl}$, *Cd11c*^{Cre}*Dock8*$^{fl/fl}$ (DC-*Dock8*$^{-/-}$), *Cd4*^{Cre}*Dock8*$^{fl/fl}$ (T-*Dock8*$^{-/-}$), and *Cd19*^{Cre}*Dock8*$^{fl/fl}$ (B-*Dock8*$^{-/-}$) mice were immunized intranasally (i.n.) with LPS and NP16-OVA (LPS+OVA). Day 12 total serum IgE was measured by ELISA. (**B** and **C**) T-*Dock8*$^{-/-}$ or control mice (*Dock8*$^{fl/fl}$) were immunized and boosted with LPS+OVA. Day 8 post-boost sera were analyzed by ELISA for (B) NP4-specific IgG1 and (C) NP4-specific IgE. OD, optical density. (**D**) PCA assay performed by transferring day 8 post-boost sera into naïve recipients and challenging with NP7-BSA and 1% Evans blue. Dye extravasation quantification is shown. (**E**) Day 12 serum IgE from T-*Dock8*$^{-/-}$, T-*Bcl6*$^{-/-}$*Dock8*$^{-/-}$, or control mice (*Dock8*$^{fl/fl}$ and *Bcl6* $^{fl/fl}$ *Dock8*$^{fl/fl}$) immunized i.n. with LPS+OVA. (**F**) Day 8 T_{FH} cell frequencies are depicted as representative flow cytometry contour plots. (**G**) Immunofluorescent images of day 9 MedLN GCs from immunized T-*Dock8*$^{-/-}$ or control *Dock8*$^{fl/fl}$ mice stained for IgD (green) and CD4 (white) with or without (left and right, respectively) peanut agglutinin (PNA, purple) are shown. Scale bars: 100 μm. Arrows indicate clusters of CD4^{+} T cells in the GC. (**H** and **I**) Intracellular expression of IL-4 and IL-13 by day 8 T_{FH} cells (gated as in fig. S4A) depicted as (H) flow cytometry plots and (I) bar graphs. NDLN, nondraining lymph node. (**J**) IL-21 reporter expression in T_{FH} cells from IL-21 TWIK T-*Dock8*$^{-/-}$ or control *Dock8*$^{fl/fl}$ reporter mice on day 8 after immunization depicted as histogram overlay. In (A), (D), (E), and (I), each symbol indicates an individual mouse. Numbers in flow plots indicate percentages. Error bars indicate SEM. Statistical tests: analysis of variance (ANOVA) (A and D); Student's *t* test (B, C, and I); Kruskal-Wallis *H* test (E). *$P < 0.05$, **$P < 0.01$, ***$P < 0.001$, ****$P < 0.0001$. Data representative of at least two independent experiments with three to seven mice per group.

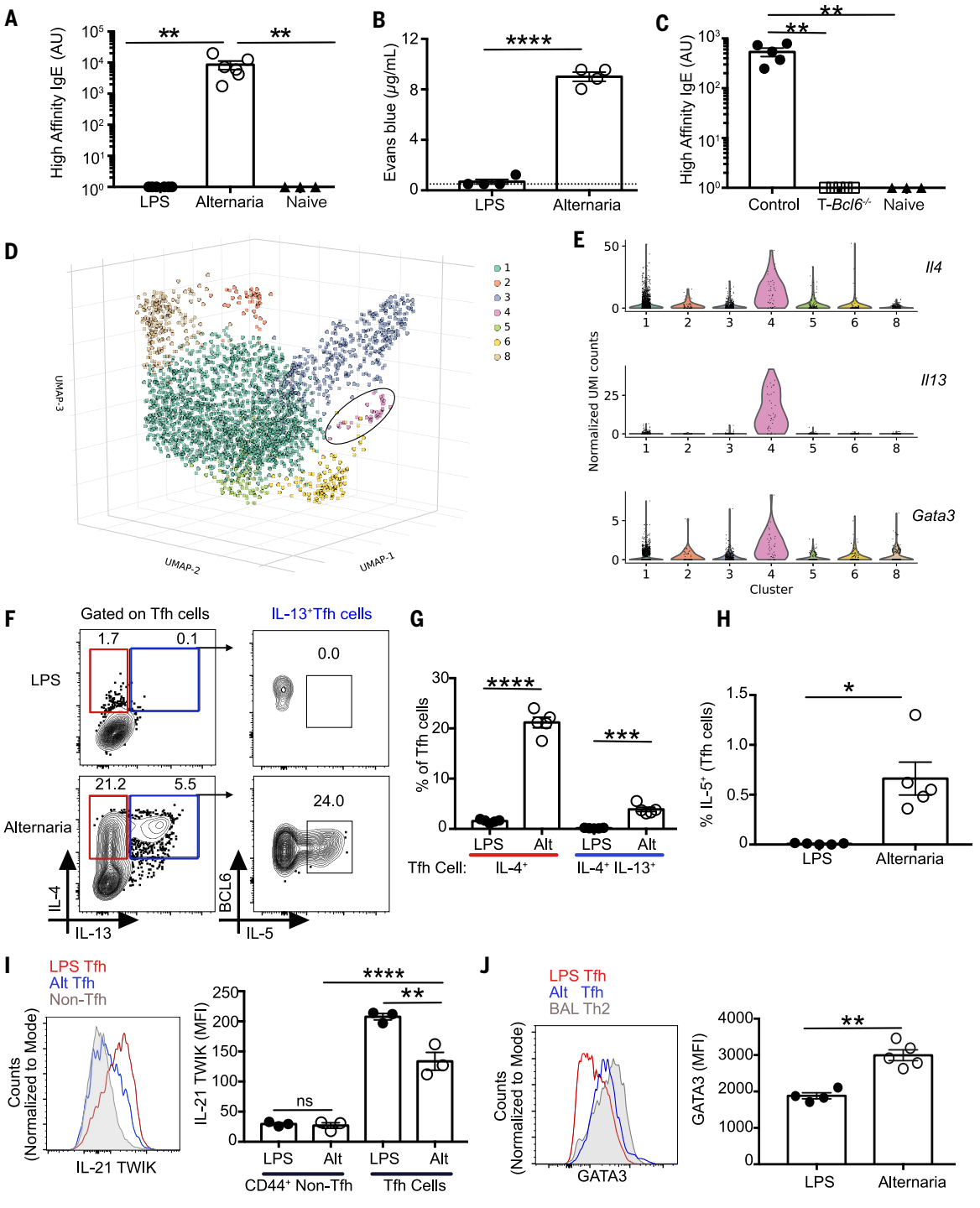

Fig. 2. $T_{FH}13$ cells are induced in WT mice during allergic sensitization. WT mice were immunized and boosted i.n. with LPS or *Alternaria* extract and NP16-OVA. (**A**) Day 8 sera from boosted mice were analyzed for high-affinity IgE by ELISA with NP7-BSA–coated plates. (**B**) Evans blue dye extravasation quantification after PCA with day 8 post-boost sera and NP7-BSA challenge. Dotted line represents background readings of sera from naïve mice. (**C**) $Cd4^{Cre}Bcl6^{fl/fl}$ ($T\text{-}Bcl6^{-/-}$) or control $Bcl6^{fl/fl}$ mice were immunized and boosted with *Alternaria* extract and NP16-OVA. Eight days later, high-affinity IgE was quantitated using NP4-BSA by ELISA. (**D**) 3D uniform manifold approximation and projection (UMAP) embedding of the single-cell expression profiles of n = 3002 single T_{FH} cells sorted from WT C57BL/6 mice immunized i.n. with *Alternaria* extract and NP-OVA. Leiden community detection on the cell-cell k = 10 nearest neighbor graph segregates cells into seven clusters, five of which were identifiable on the basis of the expression of previously known markers: 1, $T_{FH}2$; 2, type 1 IFN T cell population; 3, proliferating T cells; 4, $T_{FH}13$ cells; and 6, T_{FR} cells. The circle identifies cluster 4, a cluster of $Il13^{+}$ T_{FH} cells (n = 39). (**E**) Violin plots showing the expression of distinctive marker genes of $Il13^{+}$ T_{FH} cluster (*Il4*, *Il13*, *Gata3*). (**F** to **H**) Intracellular expression of IL-4, IL-13, and IL-5 in day 8 MedLN T_{FH} cells induced after primary immunization with LPS or *Alternaria* and NP-OVA depicted as flow cytometry plots (F) and bar graphs for IL-4 and IL-13 (G) and IL-5 (H). (**I**) IL-21 expression in T_{FH} cells from IL-21-TWIK reporter mice at day 8 after immunization, depicted as histogram overlay (left) and bar graphs (right). (**J**) GATA3 expression in T_H2 cells from bronchioalveolar lavage fluid of mice immunized with *Alternaria* and NP-OVA, and T_{FH} cells from MedLN of mice immunized with LPS or *Alternaria* and NP-OVA. Data are depicted as histogram overlay (left) and bar graphs (right). Each symbol indicates an individual mouse. Numbers in flow plots indicate percentages. Error bars indicate SEM. Statistical tests: Kruskal-Wallis H test (A and C); Student's t test (B, G, and J); ANOVA (I); Mann-Whitney U test (H). *P < 0.05, **P < 0.01, ***P < 0.001, ****P < 0.0001; ns, not significant. Data representative of two or three independent experiments with three to five mice per group (A to C and F to J). Data representative of three biological replicates (D and E).

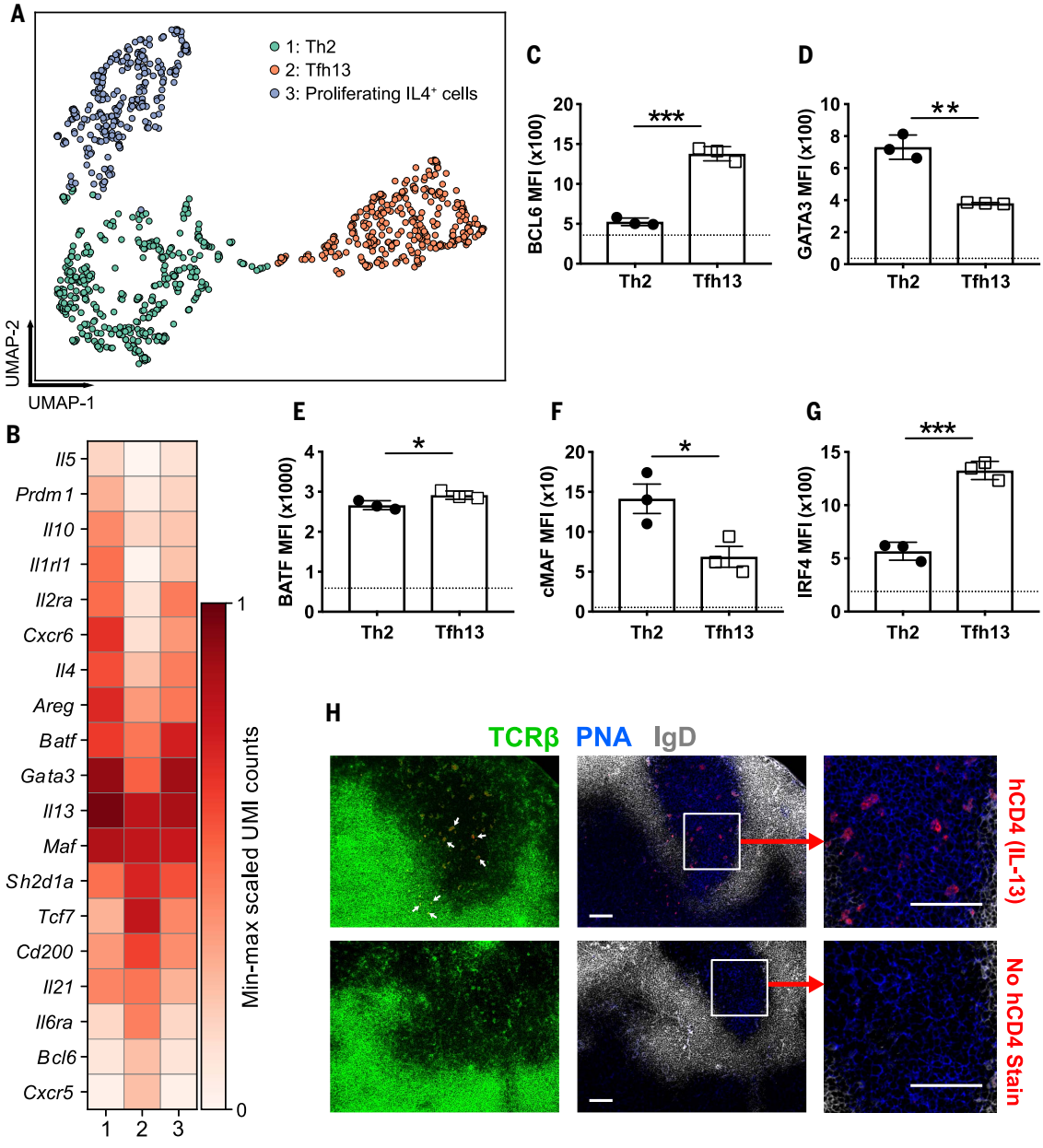

Fig. 3. $T_{FH}13$ cells are a distinct T cell subset. 4Get/*Il4*-reporter mice were immunized i.n. with *Alternaria* extract and NP19-OVA. GFP(*Il4*)$^+$CD44$^+$CD4$^+$ T cells were sorted for scRNA-seq. Cells expressing one or more *Il13* transcripts were isolated and subjected to dimensionality reduction and clustering. (**A**) A 2D UMAP embedding of $n = 1040$ *Il13*$^+$ cells. Low-resolution (0.2) Leiden community detection on the $k = 10$ cell-cell nearest neighbor graph reveals three subpopulations comprising 405, 340, and 295 cells, respectively. Populations 1, 2, and 3 were putatively identified as T_H2 cells, $T_{FH}13$ cells, and proliferating IL-4$^+$ cells, respectively. (**B**) A matrix plot showing the expression of key marker genes that are similarly and differentially expressed between *Il13*$^+$ T_H2 and $T_{FH}13$ cells. Color scale represents log-transformed normalized unique molecular identifier (UMI) counts scaled between 0 and 1, separately for each gene. (**C** to **H**) Smart13 (*Il13*) reporter mice were immunized with *Alternaria* extract and NP-OVA. Day 3 after boost, analysis of transcription factors (C) BCL6, (D) GATA3, (E) BATF, (F) cMAF, and (G) IRF4 was performed by intracellular staining of $T_{FH}13$ cells and IL-13$^+$ T_H2 cells (gated as in fig. S12A). Dotted lines indicate mean fluorescence intensity (MFI) of naïve CD4$^+$ T cells. (H) Microscopic images of MedLN GCs from immunized reporter mice stained for human CD4 (IL-13) (red), TCRβ (green), IgD (white), and PNA (blue) are shown. Arrows in the leftmost panel indicate TCRβ and hCD4 costaining. Scale bars: 100 μm. Statistical tests: Student's *t* test (C to G). *$P < 0.05$, **$P < 0.01$, ***$P < 0.001$. Data representative of three biological replicates (A and B). Data representative of two independent experiments (C to H) with three mice.

high levels of serum IgE as they aged (fig. S2, F and G). Thus, T-*Dock8*$^{-/-}$ mice appear to recapitulate the hyper-IgE and dysgammaglobulinemic presentation of *DOCK8*-deficient patients.

DOCK8 deficiency has been reported to inhibit FOXP3$^+$ regulatory T cell (T_{reg}) function (*29*, *30*). However, the inducible deletion of *Dock8* in T_{regs} did not develop high-affinity IgE in response to LPS+OVA immunization (fig. S2H). Further, *Dock8*-deficient T_{regs} were competent in suppressing T cell activation in vitro (fig. S2I). To determine whether T_{FH} cells in T-*Dock8*$^{-/-}$ mice were responsible for the hyper-IgE response to type 1 immunization, we crossed T-*Dock8*$^{-/-}$ mice to *Bcl6*$^{fl/fl}$ mice to generate T-*Bcl6*$^{-/-}$*Dock8*$^{-/-}$ (*Cd4*^{Cre}*Bcl6*$^{fl/fl}$*Dock8*$^{fl/fl}$) mice. In contrast to T-*Dock8*$^{-/-}$ mice, T-*Bcl6*$^{-/-}$*Dock8*$^{-/-}$ mice did not develop a hyper-IgE response, suggesting

that the hyper-IgE phenotype in T-*Dock8*$^{-/-}$ mice is dependent on T_{FH} cells but not on other cell types (e.g., $CD4^+$ DCs or $CD8^+$ T cells) that may have lost *Dock8* expression as a result of *Cd4*^{Cre}-mediated deletion (Fig. 1E). Finally, T-*Dock8*$^{-/-}$ mice immunized with the model type 2 allergen *Alternaria alternata* along with NP-OVA (henceforth called Alt+OVA) showed high-affinity and total IgE titers similar to control mice (fig. S2, J and K). Thus, DOCK8 in T_{FH} cells blocks inappropriate induction of IgE during type 1 immune responses. Our analysis of T_{FH} cells showed no difference in frequency or expression of programmed cell death 1 (PD-1) or CXCR5 between control and T-*Dock8*$^{-/-}$ mice post LPS+OVA immunization (Fig. 1F and fig. S3, A and B). Germinal center (GC) structure, T_{FH} cell localization, and GC B cell frequencies were also comparable between control and T-*Dock8*$^{-/-}$ mice (Fig. 1G and fig. S3, C to E). However, in contrast to control mice, there was a significantly greater population of IL-4–producing T_{FH} cells as well as an unexpected population of IL-4 and IL-13 coproducing T_{FH} cells in T-*Dock8*$^{-/-}$ mice (Fig. 1, H and I, and fig. S4A). A fraction of these $IL\text{-}4^+IL\text{-}13^+$ T_{FH} cells, which we call $T_{FH}13$ cells, also produced the canonical type 2 cytokine IL-5 (fig. S4B). $T_{FH}13$ cells induced in T-*Dock8*$^{-/-}$ mice expressed the lineage-defining T_{FH} TF BCL6 at levels similar to $IL\text{-}4^+$ T_{FH} cells induced in control mice (fig. S4C).

The cytokine IL-21 has been associated with the negative regulation of IgE and promoting IgG1 in mice (*31*–*33*) as well as in humans in the presence of IL-13 (*34*). Hence, we assessed IL-21 levels in T_{FH} cells in T-*Dock8*$^{-/-}$ mice by crossing them with IL-21 TWIK reporter mice (*21*). IL-21 production by T_{FH} cells was reduced in T-*Dock8*$^{-/-}$ mice relative to control mice (Fig. 1J and fig. S4, D and E). T_{FH} cells from T-*Dock8*$^{-/-}$ mice expressed more of the canonical T_H2 TF GATA3 compared with control T_{FH} cells and non-T_{FH} effector cells (fig. S4F). Aged T-*Dock8*$^{-/-}$ mice that developed the spontaneous hyper-IgE phenotype also had elevated frequencies of $T_{FH}13$ cells (fig. S4G). Thus, a rare population of T_{FH} cells that expressed GATA3 and unexpectedly produced IL-5 and IL-13 in addition to IL-4, while secreting less IL-21, was associated with the hyper-IgE state in T cell–specific *Dock8* deficiency.

$T_{FH}13$ cells are induced in WT mice during allergic sensitization

We next asked whether $T_{FH}13$ cells are also induced in genetically unmanipulated WT mice during allergic sensitization, which also generates high-affinity anaphylactic IgE. WT mice immunized with Alt+OVA, but not those immunized with LPS+OVA, produced high-affinity IgE that was anaphylactic (Fig. 2, A and B). Alt+OVA immunization induced less high-affinity IgG1 compared with LPS+OVA (fig. S5A). IgE induction in *Alternaria* immunization was dependent on T_{FH} cells, as *Cd4*^{Cre}*Bcl6*$^{fl/fl}$ (T-*Bcl6*$^{-/-}$) mice did not generate high-affinity or total IgE (Fig. 2C and fig. S5, B and C). However, eosinophilia in these mice was similar to controls, indicating that the type 2 cellular response was intact but could not compensate for T_{FH} cell loss in IgE induction, consistent with published studies (fig. S5D) (*10*, *13*).

To determine whether $T_{FH}13$ cells could be identified as a transcriptionally distinct population in WT mice, we performed single-cell RNA sequencing (scRNA-seq) on sorted T_{FH} cells after Alt+OVA immunization (n = 3 mice). After data processing (fig. S6 and tables S1 to S3), $CXCR5^+PD1^+$ T cells formed seven clusters with distinct transcriptional signatures (Fig. 2D and fig. S7A). We could readily identify a $T_{FH}2$ cell population (cluster 1), a T_{FH} cell population with a type I interferon signature (cluster 2), a T follicular regulatory (T_{FR}) population (cluster 6), and a $T_{FH}13$ cell population (cluster 4). Although all clusters similarly expressed T_{FH} cell markers such as *Batf*, *Cd40lg*, *Icos*, and *Pdcd1*, $T_{FH}13$ cells uniquely expressed high levels of *Il4*, *Il13*, and *Gata3* (Fig. 2E). Pairwise analysis between the $T_{FH}2$ and $T_{FH}13$ clusters identified additional genes that discriminate between these two populations, demonstrating that $T_{FH}13$ cells are a transcriptionally distinct population (fig. S7B).

We also identified $T_{FH}13$ cells by flow cytometry in *Alternaria*-immunized WT mice. Although the overall magnitude of T_{FH} cell and GC B cell induction was comparable between LPS- and *Alternaria*-immunized mice (fig. S8, A to C), a significant $T_{FH}13$ population was induced by Alt+OVA but not LPS+OVA immunization (Fig. 2, F and G, and fig. S8, D to F). Related cell types induced during type 2 immune responses—T_H2 effector cells and IL-4 single-positive T_{FH} cells ($T_{FH}2$ cells)—were also more abundant with Alt+OVA immunization. However, these populations were distinguished from $T_{FH}13$ cells via flow cytometric staining of BCL6, PD-1, and CXCR5 (fig. S8, G to I). *Il13* transcripts were detected in unstimulated T_{FH} cells sorted from mice immunized with *Alternaria* but not LPS, whereas *Il4* transcripts were present in T_{FH} cells from both conditions (fig. S9, A and B). Like $T_{FH}13$ cells in T-*Dock8*$^{-/-}$ mice, $T_{FH}13$ cells in Alt+OVA-immunized WT mice also produced IL-5 (Fig. 2, F and H). As IL-5 promotes eosinophilia (*10*, *14*, *35*) and the majority of $IL\text{-}5^+$ T cells in the lymph node (LN) were T_{FH} cells, we accordingly observed eosinophil infiltration of the LNs in Alt+OVA-immunized mice (fig. S9, C to E).

Alternaria-induced T_{FH} cells produced substantial levels of IL-21 compared with non-T_{FH} effector $CD4^+$ T cells, but reduced levels of IL-21 compared with LPS+OVA-induced T_{FH} cells (Fig. 2I). T_{FH} cells from Alt+OVA immunization also demonstrated significant GATA3 expression, albeit less than differentiated T_H2 cells from the lungs (Fig. 2J). However, T_{FH} TFs such as BCL6, BATF, IRF4, and TCF1 (*36*) were expressed at equivalent levels in both immunizations (fig. S10). Thus, $T_{FH}13$ cells are also induced in WT mice but only during type 2 high-affinity IgE responses.

$T_{FH}13$ cells are a distinct T cell subset

Given the similar phenotype of $T_{FH}13$ cells and conventional T_H2 effector cells (i.e., IL-4, IL-5, IL-13, and GATA3 expression), we evaluated whether the two populations were transcriptionally distinct. We performed scRNA-seq on *Il4*-reporter–positive activated $CD4^+$ T cells from Alt+OVA-immunized 4Get/*Il4*-reporter mice (n = 3) (*37*). The data were processed as before (fig. S6 and tables S1 to S3), followed by selection of *Il13*-expressing cells. The *Il13*-expressing T cells formed three transcriptionally distinct clusters (Fig. 3A). Among these clusters, we could identify a population of T_H2 effectors (cluster 1), $T_{FH}13$ cells (cluster 2), and $Il4^+$ T cells expressing high levels of proliferation markers such as *Top2a* and *Mki67* (cluster 3). Pairwise analysis between T_H2 effector and $T_{FH}13$ cells confirmed differential expression of T effector versus T_{FH} cell markers, including *Prdm1* (BLIMP1), *Bcl6*, *Il21*, and *Areg* (Fig. 3B and fig. S11A). We verified select targets at the protein level (Fig. 3, C to G). We also analyzed the scRNA-seq data from *Bcl6*-expressing cells and identified two distinct clusters, one with a transcriptional profile consistent with $T_{FH}13$ cells (cluster 2) and the other consistent with $T_{FH}2$ cells (cluster 1) (fig. S11, B and C).

To determine the location of $T_{FH}13$ cells in the LN, we used the Smart13 reporter, which reports *Il13* via the expression of human CD4 (hCD4) (*14*). hCD4 expression was concordant with IL-13 intracellular cytokine staining (fig. S12, A and B). With immunofluorescence, *Il13* reporter$^+$ T cells could be visualized in both the GC and T cell zone, corresponding to $T_{FH}13$ cells and $IL\text{-}13^+$ T effectors, respectively (Fig. 3H). Altogether, by transcriptional profile, protein expression, and subanatomic location, we show that $T_{FH}13$ cells are a distinct subset from T_H2 effector and $T_{FH}2$ cells.

$T_{FH}13$ cells are induced to multiple allergens in mice and humans

Two other common allergens, house dust mite extract (HDM) and peanut (PN), were then assessed for their ability to induce $T_{FH}13$ cells. HDM-induced allergic airway responses lead to T_{FH} and GC B cell induction in the mediastinal LN (MedLN) (*38*). Similar to Alt+OVA immunization, HDM+OVA immunization elicited $T_{FH}13$ cells and antigen-specific IgE (Fig. 4, A and B, and fig. S13, A and B). Peanut administered with the mucosal adjuvant cholera toxin (CT) is a commonly used model of IgE-mediated food allergy (*39*). There was a significant induction of mesenteric LN $T_{FH}13$ cells and PN-specific IgE in response to PN+CT but not PN alone (Fig. 4, C and D, and fig. S13, C and D).

We next explored whether $T_{FH}13$ cells were present in humans with IgE-mediated allergy by examining "circulating" T_{FH} (cT_{FH}) cells from a cohort of PN-allergic individuals (*40*) with PN-specific IgE (Fig. 4E). We selected PN-allergic or healthy individuals whose peripheral blood T cells responded in vitro to PN extract by upregulating CD40L (fig. S14). $IL\text{-}4^+IL13^+$ $T_{FH}13$ cells could be

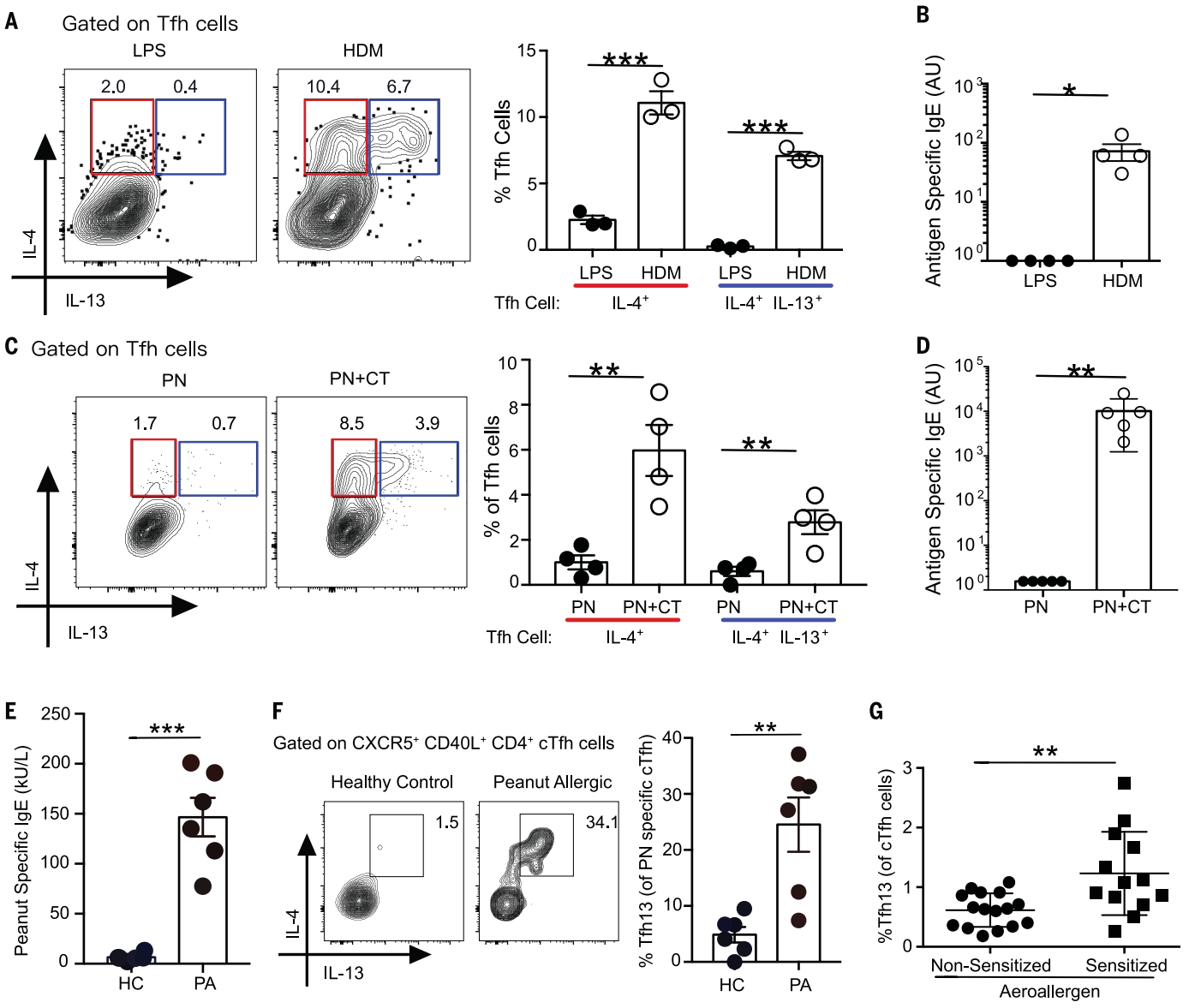

Fig. 4. $T_{FH}13$ cells are induced to multiple allergens in mice and humans. WT C57BL/6 mice were immunized i.n. with HDM and NP16-OVA and boosted with HDM and NP16-OVA twice, or with LPS and NP16-OVA as described in Fig. 1. (**A**) Intracellular expression of IL-4 and IL-13 from day 8 MedLN T_{FH} cells induced after primary immunization is depicted as representative flow cytometry plots (left) and summary bar graphs (right). (**B**) Day 8 sera from boosted mice were analyzed for NP16-OVA–specific IgE by ELISA. (**C** and **D**) WT mice were intragastrically immunized with ground peanut (PN) alone with or without CT in 0.2 M $NaHCO_3$ and boosted with the same immunization up to four times at weekly intervals. (C) Intracellular expression of IL-4 and IL-13 in day 8 mesenteric lymph node (MesLN) T_{FH} cells induced after primary immunization is depicted as representative flow cytometry plots (left) and summary bar graphs (right). (D) Day 8 sera from boosted mice were analyzed for crude PN extract–specific IgE by ELISA. (**E**) PN-specific serum IgE ELISA performed with sera from PN-allergic patients (PA) or healthy controls (HC). (**F**) Cytokine profiles of PN-specific circulating T_{FH} (cT_{FH}) cells (gated as in fig. S14) obtained from PA or HC. (**G**) IL-4^+ IL-13^+ cT_{FH} cells from aeroallergen sensitized or control nonsensitized individuals. Each symbol indicates an individual mouse or subject. Numbers in flow plots indicate percentages. Error bars indicate SEM. Statistical tests: Student's *t* test (A, C, and E to G); Mann-Whitney *U* test (B and D). $*P < 0.05$, $**P < 0.01$, $***P < 0.001$. Data representative of at least two independent experiments (A to D) with three to five mice per group. (E to F) Data from healthy controls ($n = 6$) or PN-allergic patients ($n = 6$). (G) Data from aeroallergen sensitized allergic patients ($n = 13$) or nonsensitized individuals ($n = 16$).

identified within the cT_{FH} cell compartment of PN-allergic patients but not those of healthy controls (Fig. 4F). We also examined cT_{FH} cells from patients with IgE to aeroallergens (table S4). Compared with nonsensitized individuals, aeroallergen-sensitized individuals had a significantly higher frequency of $T_{FH}13$ cells (Fig. 4G). Thus, $T_{FH}13$ cells are induced in both mice and humans with antigen-specific IgE responses to multiple allergens.

$T_{FH}13$ cells and high-affinity IgE are not induced to helminth infections

Although T_{FH} cells are required for IgE production in both allergen and helminth models, it is unclear whether the T_{FH} cell phenotype in these type 2 immune responses is the same. Previous studies of T_{FH} cells during helminth-induced type 2 responses have reported IL-4 but not IL-5 or IL-13 production (*14*, *21*). Helminth infections elicit a strong type 2 response characterized by the induction of ILC2s, T_H2 cells, eosinophilia, and IgE. Although substantial IgE is produced, little is affinity-matured (*6*, *41*). This suggests

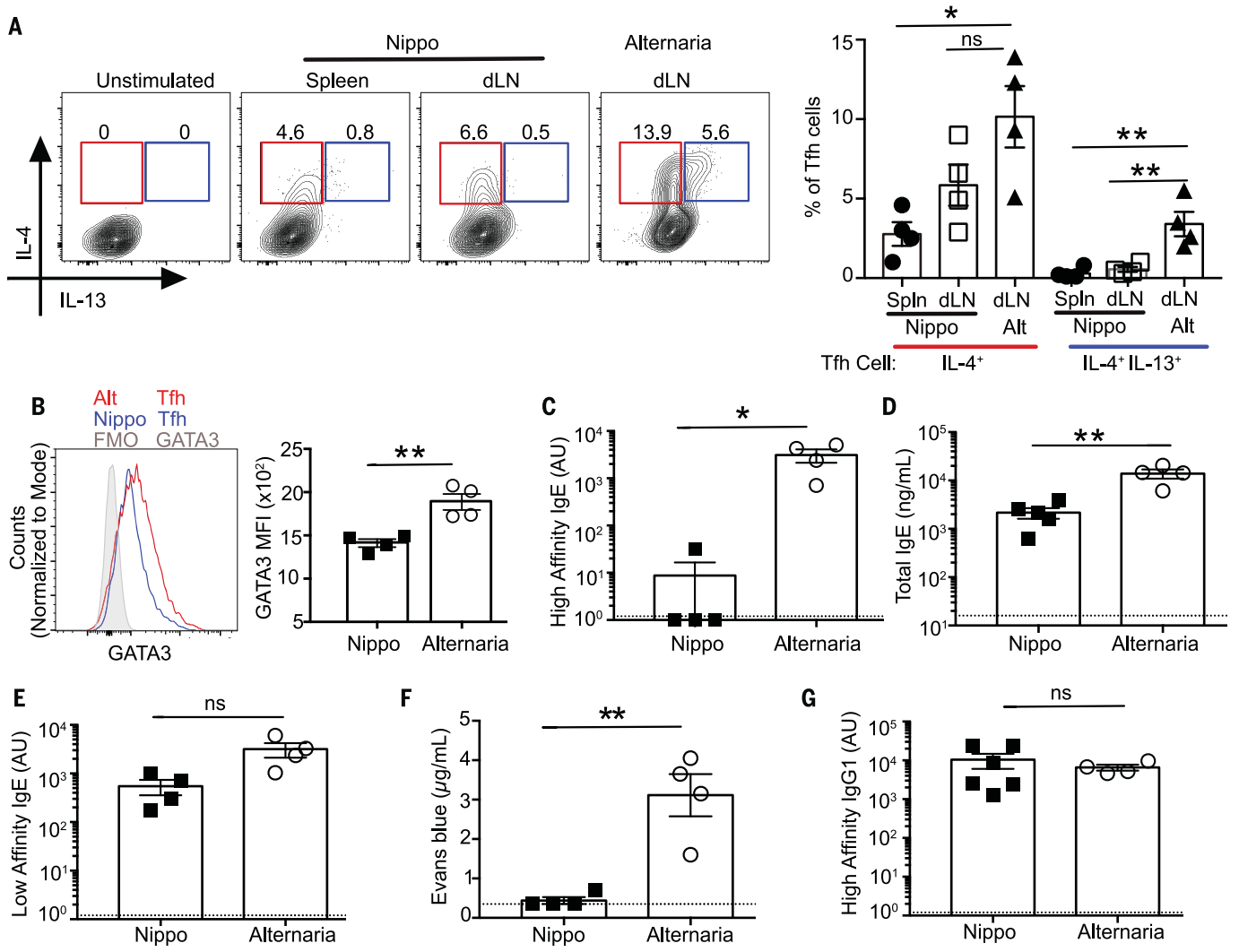

Fig. 5. $T_{FH}13$ cells and high-affinity IgE are not induced to helminth infections. WT C57BL/6 mice were either immunized and boosted with *Alternaria* extract and NP16-OVA (Alt+OVA) or infected with *N. brasiliensis* and co-immunized with NP16-OVA and boosted (Nippo+OVA). (**A**) IL-4 and IL-13 expression in day 8 T_{FH} cells from *N. brasiliensis or Alternaria* immunization is shown as flow cytometry plots (left) or as summary bar graphs (right). (**B**) GATA3 expression in day 8 splenic T_{FH} cells induced by *N. brasiliensis* or MedLN T_{FH} cells from *Alternaria* immunization. (**C** to **E**) Day 8 post-boost sera from mice immunized with Nippo+OVA or Alt+OVA were analyzed by ELISA for (C) high-affinity IgE using NP7-BSA, (D) total IgE, and (E) low-affinity IgE using NP40-BSA. (**F**) Evans blue dye quantification from PCA assay (with i.v. NP7-BSA challenge) using day 8 post-boost sera from Nippo+OVA or Alt+OVA immunized mice. (**G**) ELISA for high-affinity IgG1 using NP7-BSA performed on day 8 post-boost sera from mice immunized with Nippo+OVA or Alt+OVA. Each symbol indicates an individual mouse. Numbers in flow plots indicate percentages. Error bars indicate SEM. Dotted lines in bar graphs represent background readings of sera from naïve mice. Statistical tests: ANOVA (A); Student's *t* test (B and D to F); Mann-Whitney *U* test (C and G). $*P < 0.05$, $**P < 0.01$. Data representative of two independent experiments with four to six mice per group.

that IL-4 production by T_{FH} cells may be necessary for any IgE induction but insufficient for the production of high-affinity IgE. We analyzed T_{FH} cells in mice infected with the helminth *Nippostrongylus brasiliensis* and coimmunized with NP-OVA (Nippo+OVA). Nippo+OVA induced a strong IL-4–producing T_{FH} population in the draining LN and spleen. However, in contrast to Alt+OVA, $T_{FH}13$ cells were absent (Fig. 5A). We hypothesized that the absence of $T_{FH}13$ cells in *N. brasiliensis* infection was the result of low GATA3 expression in T_{FH} cells. Indeed, T_{FH} cells in *N. brasiliensis* infection did not up-regulate GATA3 (Fig. 5B).

Nippo+OVA immunization therefore provided a model in which $T_{FH}13$ cells were absent but IL-4$^+$IL-13$^-$ $T_{FH}2$ cells remained present. In the setting where only $T_{FH}2$ cells were present, there was strong induction of total IgE but little was of high affinity (Fig. 5, C and D). However, low-affinity IgE levels were comparable between Nippo+OVA and Alt+OVA immunization (Fig. 5E). This suggests that $T_{FH}2$ cells may promote low-affinity IgE but not high-affinity IgE. Serum from Nippo+OVA mice did not contain anaphylactic IgE (Fig. 5F). Similar IgG1 responses in both Nippo+OVA and Alt+OVA models were observed (Fig. 5G). Thus, $T_{FH}13$ cells are uniquely induced during type 2 allergen but not helminth responses and may be responsible for the production of anaphylactic IgE.

Loss of $T_{FH}13$ cells abrogates production of high-affinity IgE

To test whether $T_{FH}13$ cells are necessary to induce high-affinity IgE, we bred *Il13*^{Cre} (*14*) to *Bcl6*$^{fl//fl}$ (13Cre*Bcl6*$^{fl/fl}$) mice to specifically delete $T_{FH}13$ cells. In 13Cre*Bcl6*$^{fl/fl}$ mice, *Il13*-expressing cells lost *Bcl6* expression and could not differentiate into $T_{FH}13$ cells. 13Cre*Bcl6*$^{fl/fl}$ mice had severely reduced $T_{FH}13$ cells but retained similar frequencies of IL-4$^+$ $T_{FH}2$ or IL-13$^+$

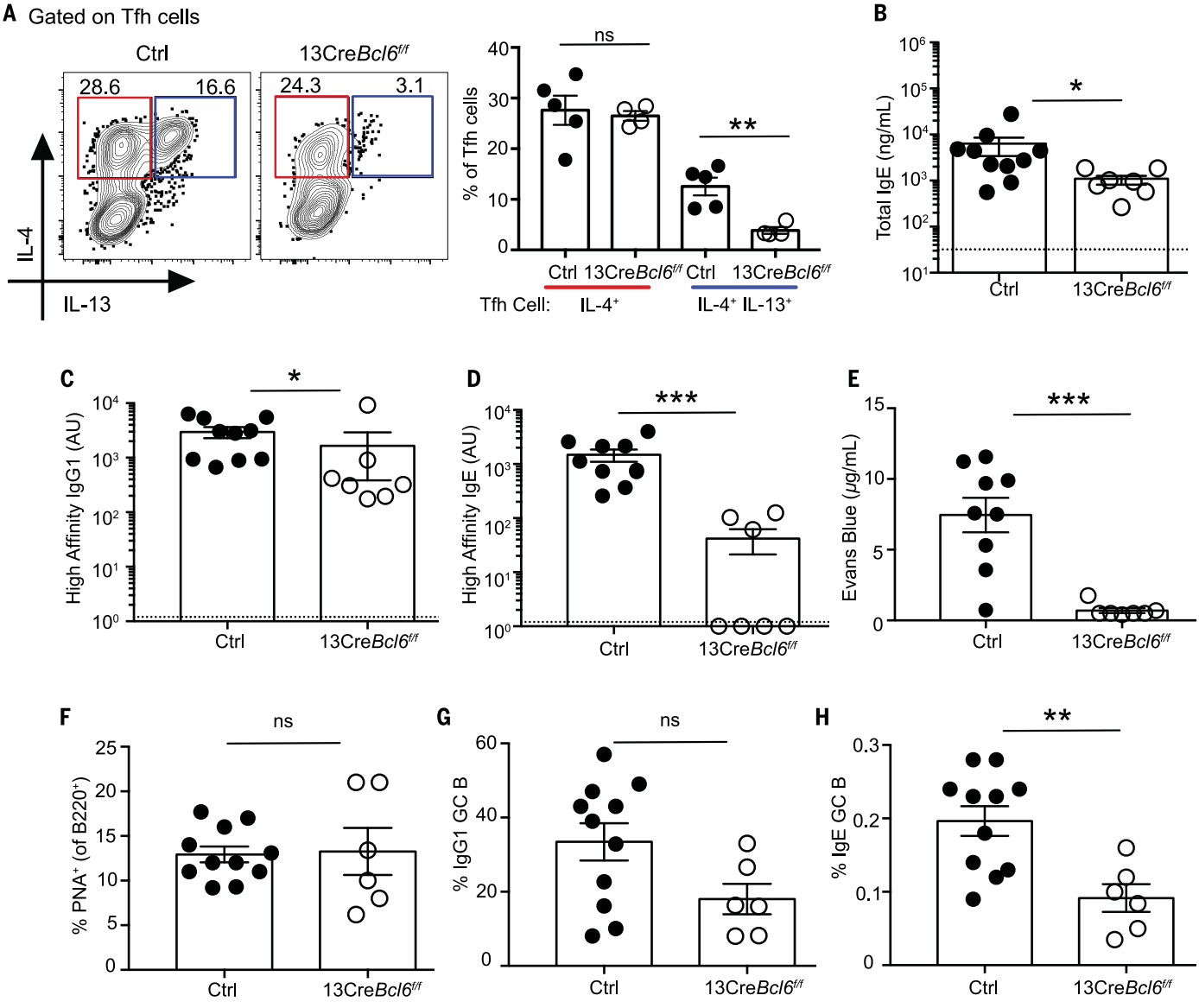

Fig. 6. Loss of $T_{FH}13$ cells abrogates the production of high-affinity IgE. 13Cre*Bcl6*$^{fl/fl}$ or control *Bcl6*$^{fl/fl}$ mice were immunized and boosted with *Alternaria* extract and NP19-OVA. (**A**) Intracellular expression of IL-4 and IL-13 from day 8 MedLN T_{FH} cells induced after primary immunization is depicted as representative flow cytometry plots (left) and summary bar graphs (right). (**B** to **E**) Day 8 post-boost sera were analyzed for (B) total IgE, (C) NP7-specific high-affinity IgG1, (D) NP7-specific high-affinity IgE, and (E) anaphylactic ability by PCA after i.v. challenge with NP7-BSA. (**F** to **H**) Day 7 post-boost MedLN cells were analyzed for (F) B220$^+$PNA$^+$ GC B cells, (G) percentage of GC B cells expressing IgG1, and (H) percentage of GC B cells expressing IgE. Each symbol indicates an individual mouse. Numbers in flow plots indicate percentages. Error bars indicate SEM. Statistical tests: Student's *t* test (A and F to H); Mann-Whitney *U* test (B to E). *$P < 0.05$, **$P < 0.01$. Dotted lines in bar graphs represent background readings of sera from naïve mice. Data are either representative of two independent experiments (A) or from two pooled experiments (B to H) with three to six mice per group.

T_H2 cells to Alt+OVA (Fig. 6A and fig. S15A). 13Cre*Bcl6*$^{fl/fl}$ mice demonstrated minimal reduction of total IgE and high-affinity IgG1 (Fig. 6, B and C); however, high-affinity IgE was reduced by one to three logs, and serum from 13Cre*Bcl6*$^{fl/fl}$ mice failed to elicit anaphylaxis (Fig. 6, D and E). Although total GC and IgG1 GC B cell frequencies were comparable, IgE GC B cell frequencies (gated as in fig. S15B) were significantly reduced in mice lacking $T_{FH}13$ cells (Fig. 6, F to H). Thus, although IL-4$^+$ $T_{FH}2$ cells may be sufficient to promote total IgE and affinity-matured IgG1 responses, the induction of high-affinity IgE critically depends on $T_{FH}13$ cells.

T_{FH} cell–derived IL-13 is required for anaphylactic IgE production

The loss of IgE$^+$ GC B cells in 13Cre*Bcl6*$^{fl/fl}$ mice suggested that GC B cells might be able to respond to IL-13. Indeed, after allergic sensitization, GC B cells significantly up-regulated IL-13Rα1 (fig. S16). IgG1 GC B cells had significantly higher expression of IL-13Rα1 compared with IgM GC B cells, and IgE GC B cells expressed the highest levels (Fig. 7A). Further, IL-13 worked synergistically with IL-4 in ex vivo anti-CD40–stimulated B cells from *Alternaria*-immunized mice to increase IgE$^+$ plasma cells (Fig. 7B), suggesting that $T_{FH}13$-derived IL-4 and IL-13 may together promote IgE in vivo.

Although the loss of IL-13 or its receptor impairs total IgE production (*42*–*44*), its role in promoting high-affinity IgE is unclear. To address whether IL-13 produced by $T_{FH}13$ cells was necessary for anaphylactic IgE induction, we generated mixed bone marrow chimeras using

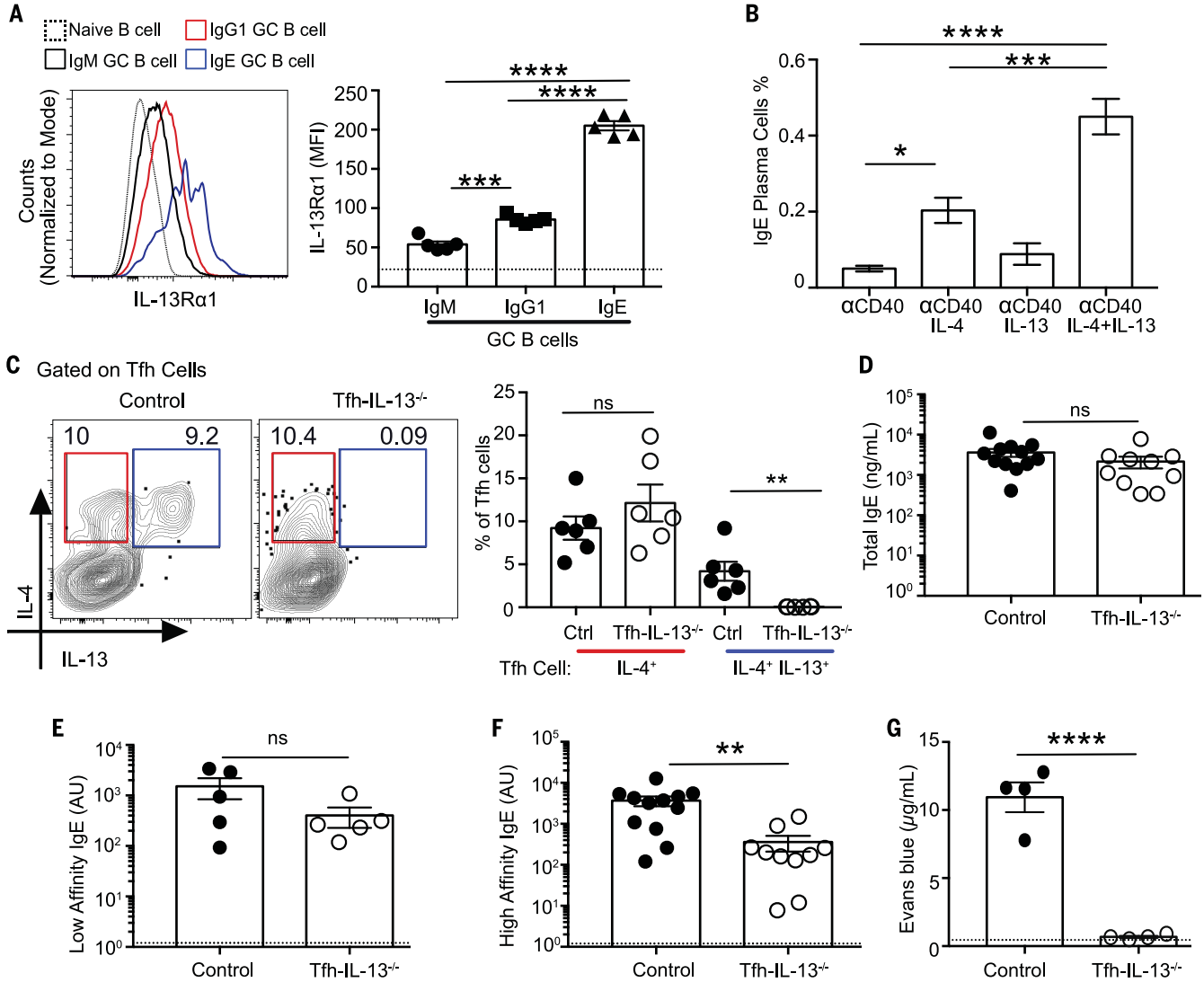

Fig. 7. T_{FH} cell–derived IL-13 is required for anaphylactic IgE production. (**A**) Expression of IL-13Rα1 on MedLN GC B cells at day 9 after immunization with *Alternaria* and NP-OVA is shown as histogram overlay (left) and summary bar graphs (right). Gating strategy as in fig. S15B. (**B**) Day 8 MedLN lymphocytes from *Alternaria* and NP-OVA immunized WT mice were cultured with α-CD40 and IL-4 and/or IL-13 for 3 days, and IgE plasma cells were quantified by staining the cells for intracellular IgE and CD138. (**C** to **G**) Mixed bone marrow chimeric mice were generated from *Il13*$^{-/-}$ and *Cd4*^{Cre} *Bcl6*$^{fl/fl}$ donor bone marrow (T_{FH}-*Il13*$^{-/-}$ chimeric mice) or WT and *Cd4*^{Cre} *Bcl6*$^{fl/fl}$ donor bone marrow (control chimeric mice). Chimeric mice were immunized and boosted with *Alternaria* and NP20-OVA. (C) IL-4 and IL-13 expression by day 8 T_{FH} cells after boost from T_{FH}-*Il13*$^{-/-}$ or control chimeras is shown as flow cytometry plots (left) or summary bar graphs (right). (D to F) Day 8 post-boost sera from T_{FH}-*Il13*$^{-/-}$ or control chimeras were analyzed by ELISA for (D) total IgE, (E) low-affinity IgE using NP-40 BSA, and (F) high-affinity IgE using NP7-BSA. (G) Evans blue dye quantification after PCA assay with day 9 post-boost sera from T_{FH}-*Il13*$^{-/-}$ or control chimeras after i.v. challenge with NP7-BSA. Each symbol indicates an individual mouse. Error bars indicate SEM. Dotted lines in bar graphs represent (A) IL-13Rα1 expression on naïve B cells or (E to G) background readings of sera from naïve mice. Statistical tests: ANOVA (A and B); Student's *t* test (C and G); Mann-Whitney *U* test (D to F). **P* < 0.05, ***P* < 0.01, ****P* < 0.001, *****P* < 0.0001. Data are either from two pooled experiments (D and F) or are representative of at least two independent experiments with three to seven mice per group.

Cd4^{Cre}*Bcl6*$^{fl/fl}$ and *Il13*$^{-/-}$ mice as donors. T_{FH} cells in these chimeras did not produce IL-13 but still made IL-4 to Alt+OVA immunization (Fig. 7C). Like 13Cre*Bcl6*$^{fl/fl}$ mice, T_{FH}-*Il13*$^{-/-}$ chimeric mice produced comparable titers of total and low-affinity IgE to that of controls (Fig. 7, D and E) but had impaired high-affinity IgE (Fig. 7F). The residual high-affinity IgE induced in T_{FH}-*Il13*$^{-/-}$ mice was unable to elicit a PCA response (Fig. 7G). Thus, two complementary experimental approaches revealed that T_{FH}13 cells and the IL-13 they produce are both required for the induction of anaphylactic IgE to allergens.

Discussion

The signals that instruct B cells to make high-affinity IgE remain unresolved. Our work demonstrated that a rare T_{FH}13 cell population coexpressing IL-4, IL-5, IL-13, BCL6, and GATA3 was responsible for the production of high-affinity anaphylactic IgE. Eliminating T_{FH}13 cells or T_{FH} cell–derived IL-13 during allergen immunization resulted in the abrogation of high-affinity anaphylactic IgE while leaving low-affinity IgE intact. Using scRNA-seq, we confirmed that T_{FH}13 cells are transcriptionally distinct from T_{FH}2 and T_H2 cells. Previous work demonstrates that T_H2 and T_{FH} cells can interconvert during type 2 responses (*45*, *46*). A transitional stage during T_{FH} development may exist between

T effector and T_{FH} cells during multiple types of immune responses, but there is little reason to believe that a shared developmental stage indicates functional homology (*23*, *47*). We observe functionally discrete T_H2 and $T_{FH}13$ populations after allergen immunization.

Our data from T-*Dock8*$^{-/-}$ mice provides insight into possible signaling pathways regulating $T_{FH}13$ cells. In humans, DOCK8 has been shown to promote nuclear translocation of STAT3 upon IL-6 or IL-21 stimulation (*48*, *49*). *Stat3*-deficient mice demonstrate increased GATA3 expression in T_{FH} cells (*50*). These studies, along with our data, suggest a T cell–intrinsic pathway by which DOCK8 may promote STAT3-dependent suppression of GATA3, thereby blocking inappropriate T_{FH}-induced IgE during type 1 immune responses.

On the basis of previous studies of IgE-producing B cells and the present work, we propose a two-tiered model of IgE induction that allows for different forms of IgE to be produced depending on the nature of the T_{FH} cell generated during the type 2 response. Switching to IgE can proceed either directly from IgM or sequentially via IgG1 (*6*). Directly switched IgE is often of low affinity with poor anaphylactic capabilities and can even protect against anaphylaxis by competing for FcεR occupancy (*5*, *6*, *41*, *51*–*54*). This is the dominant pathway to IgE during a helminth infection (*51*, *53*). In contrast, allergens are associated with high-affinity anaphylaxis-inducing IgE. During allergic sensitization in both mice and humans, IgE-producing plasma cells show evidence of sequential switching from affinity-matured IgG^+ GC B cells (*5*, *6*, *55*, *56*). We propose that $T_{FH}2$ cells instruct the switching of IgM to IgE plasma cells via BATF-driven IL-4, resulting in low-affinity IgE antibodies. These $T_{FH}2$ cells, which do not express GATA3, cannot make IL-13. In contrast, allergens induce $GATA3^+$ $T_{FH}13$ cells, which instruct sequential switching of $IgG1^+$ B cells, driving high-affinity IgE production and anaphylaxis. This is consistent with our data showing that IgG1 GC B cells express IL-13Rα1 and that loss of $T_{FH}13$ cells impairs both high-affinity IgE and GC IgE B cell induction. However, loss of IL-13 does not impair IgE responses in instances where low-affinity IgE is made, such as in helminth infections (*43*), which is consistent with our findings and the two-tiered IgE model. As loss of IL-4 abrogates all IgE (*53*), IL-13 likely works synergistically with IL-4 to promote high-affinity IgE by stably engaging the type II IL-4 receptor complex leading to sustained STAT6 activation (*57*, *58*).

Our study defines the role of $T_{FH}13$ cells in eliciting anaphylactic IgE to allergens, identifying specific molecular targets that could be leveraged diagnostically and therapeutically for allergies. Identification of $T_{FH}13$ cells answers the long-standing question of how, under rare circumstances, anaphylaxis-inducing IgE is produced by high-affinity B cells. It reconciles conflicting literature, including discrepancies between murine and human studies, on whether IL-13 and GATA3 are T_{FH}-relevant effector molecules. Human T_{FH} cells expressing GATA3, IL-13, and IL-4 have been identified (*15*, *59*, *60*) and *Il13* remains one of the most replicated genetic associations with elevated IgE, food allergy, atopy, and asthma in humans (*61*–*63*). Although this role is typically ascribed to effector $T_{FH}2$ cells, $T_{FH}13$ cells likely drive the humoral arm of the allergic response. It will be interesting to see whether monotherapies targeting IL-13 in patients affect more than tissue-restricted pathology, specifically allergen-reactive IgE levels. Similarly, recent clinical trials of a GATA3 deoxyribozyme to inhibit GATA3 activity in T_H2 cells in asthmatics showed efficacy in reducing eosinophilia (*64*). The effect of these antisense molecules on T_{FH} cells and IgE has not been considered given that GATA3 has not typically been associated with T_{FH} cells (*16*–*19*). Thus, the identification of GATA3-expressing $T_{FH}13$ cells changes the T_H2 paradigm for IgE responses.

Materials and methods

Human subjects

Peanut allergy study: Peanut-allergic subjects were selected from a cohort previously described (*40*). The clinical study (CoFAR6) provided samples for this study, which is registered with ClinicalTrials.gov with ID NCT01904604. Informed consent was obtained from all subjects or parents/guardians, and all procedures were approved by the institutional review boards at each of the five clinical sites. Peanut allergy was confirmed by double-blind placebo controlled oral challenge with peanut. Controls were sensitized but did not react to peanut challenge. All individuals were avoiding peanut at time of blood draw. Aeroallergen study: Patients 7 to 14 years old, with and without allergies and asthma, were recruited from the pediatric pulmonary and pediatric primary care clinics at Connecticut Children's Medical Center (CCMC). The allergic phenotype was confirmed with a positive ImmunoCAP clinical laboratory test or positive skin prick testing to at least one environmental allergen (*Dermatophagoides farinae*, *Dermatophagoides pteronyssinus*, *Alternaria alternata*, *Cladosporium herbarum*, dog, cat, mugwort, mouse, rat, or cockroach). Participants with self-reported food allergies were excluded from analysis ($n = 1$). Clinical details are provided in table S4. CCMC IRB# 15-007.

Mice

C57BL/6 and congenic C57BL/6-Ly5.1 [B6.SJL-$Ptprc^aPepc^b$/BoyCrl] WT mice were purchased from Charles River Laboratories (Wilmington, MA). *Cd4*^{cre} [Tg(*Cd4*-cre)1Cwi/BfluJ], *Cd11c*^{cre} (*Itgax*-Cre) [B6.Cg-Tg(Itgax-Cre)1-1Reiz/J], *Cd19*^{cre} [B6.129P2(C)-Cd19$^{tm1(cre)Cgn}$/J], *Il13*^{cre} [C.129S4(B6)-Il13$^{tm1(YFP/cre)Lky}$/J], *Foxp3*$^{EGFP\text{-}cre\text{-}ERT2}$ [Foxp3$^{tm9(EGFP/cre/ERT2)Ayr}$/J], *Bcl6*^{flox} [B6.129S(FVB)-*Bcl6*$^{tm1.1Dent}$/J] Smart13[B6.129S4(C)- *Il13*$^{tm2.1Lky}$/J], and OT-II [B6.Cg-Tg(TcraTcrb)425Cbn/J] mice were all purchased from Jackson Laboratories (Bar Harbor, ME). Bone marrow from *Il13*$^{-/-}$ mice (*42*) in a C57BL6/J background were kindly provided by Dr. E. Gelfand (National Jewish Health, CO). IL-4 4Get reporter mice [C.129-*Il4*$^{tm1.1Lky}$/J] were back crossed to C57BL/6 background. OT-II mice were crossed onto the CD45.1 or *Dock8*$^{-/-}$ mice. *Dock8*$^{-/-}$ and *Dock8*$^{fl/fl}$ mice were generated as described previously (*26*). To generate T-*Dock8*$^{-/-}$, DC-*Dock8*$^{-/-}$ mice or B-*Dock8*$^{-/-}$ mice, *Dock8*$^{fl/fl}$ were crossed with *Cd4*^{Cre}, *Cd11c*^{cre}, or *Cd19*^{Cre} mice, respectively. IL-13^{cre} mice were in Balb/c background and were backcrossed to *Bcl6*^{flox} (C57BL6/J background) for three generations and intercrossed to generate *Il-13*$^{cre/cre}$ *Bcl6*$^{flox/flox}$ mice in a mixed background and were used for experiments; Cre negative littermates were used as controls. All protocols used in this study were approved by the Institutional Animal Care and Use Committee at the Yale University School of Medicine.

Immunizations

Type 1 LPS model: Mice were immunized intranasally (i.n.) with 2 μg of LPS (Sigma) and 25 μg of 4-hydroxy-3-nitrophenylacetyl conjugated ovalbumin (NP16-OVA) (LGC Biosearch Technologies) for primary immunizations. Mice were boosted twice (i.n.) with 10 μg NP16-OVA in weekly intervals 10 to 12 days after primary immunization. Type 2 models: Mice were immunized with 10 μg *Alternaria* (Greer; Lot# 322776) or house dust mite extract (Greer; Lot# 248041) with 25 μg NP16-OVA (i.n.) for primary immunizations. Mice were boosted twice (i.n.) with 2 μg of the extract and 10 μg NP16-OVA in weekly intervals 10 to 12 days after primary immunization. We observed lot-to-lot variability in house dust mite extract's ability to elicit $T_{FH}13$ cells and antigen-specific IgE. Peanut model: Mice were immunized weekly by oral gavage with 5 mg of ground raw blanched peanut (Western Mixers Produce & Nuts) with or without 10 μg of cholera toxin (List Biologicals) in 200 μl of 0.2 M sodium bicarbonate buffer per mouse. *N. brasiliensis* and NP-OVA model: Mice were injected with 100 μg NP16-OVA mixed with *N. brasiliensis* (500 third-stage larvae/mouse) subcutaneously. Mice subsequently were boosted intraperitoneally twice with 50 μg of NP16-OVA in weekly intervals 10 to 12 days after primary immunization. For some experiments, NP19-OVA or NP20-OVA were used depending on the lot.

Flow cytometry and cell sorting

Single-cell suspensions from lymph nodes and spleen were prepared and stained as described previously (*21*, *26*). For intracellular cytokine staining (ICS), cells were restimulated with phorbol 12-myristate 13-acetate (PMA) (50 ng/ml) and ionomycin (1 μg/ml) in 96-well U bottom plates in complete IMDM media for 4 hours, and Golgiplug (BD Biosciences) was added for the last 3 hours. ICS was performed using BD ICS kit as per manufacturer's instructions with overnight incubation (4°C) of permeabilized cells with antibodies. Intracellular staining of transcription factors (TFs) was performed using Foxp3 staining kit (eBiosciences) according to

manufacturer's instructions or by fixing the cells with fixation buffer (BioLegend) for 20 min followed by permeabilization with ice-cold methanol (20 min) and staining for TFs. All TFs were stained at RT for 40 min. Antibodies are listed in table S5. All flow cytometry samples were acquired on LSRII (BD Biosciences) or MACSQuant (Miltenyi) flow cytometers and analyzed by FlowJo software (Version 10.4.2, TreeStar). Cell sorting was performed using FACS ARIA III (BD Biosciences) on T_{FH} cells or (IL-4)4Get$^+$ CD44$^+$ CD4$^+$ T cells.

Staining for IgE B cells

The protocol was adapted from (*65*). Cells obtained from mediastinal lymph nodes (MedLNs) were incubated on ice for 30 min with viability dye, FC-Block (2.4G2), unlabeled anti-IgE (RME-1) to saturate surface and CD23 or Fc receptor bound IgE. Surface staining was performed after this step. Cells were then fixed with and permeabilized with BD intracellular staining kit and stained with fluorochrome conjugated anti-IgE (using same clone that was used to saturate surface IgE), anti-IgG1, and anti-IL-13Rα1 on ice for 30 to 40 min. All incubations prior to fixing cells were done with staining buffer (1X PBS containing 2% FBS and 1 mM EDTA).

Human PBMC stimulation

Peanut study: Peripheral blood mononuclear cells (PBMCs) from healthy control and peanut allergic individuals were stimulated with 100 μg/ml crude peanut extract and stained for T_{FH} markers and cytokines as described (*40*). Aeroallergen study: PBMCs were isolated with gradient centrifugation using Lymphoprep (StemCell Technologies), and the cells were frozen until use. CD4$^+$ T cells were isolated from PBMCs using EasySep Human CD4$^+$ T Cell Enrichment Kit (StemCell Technologies) following the manufacturer's protocol, and the purity was confirmed by flow cytometry. The enriched CD4$^+$ T cells were incubated overnight, 1×10^6 cells/ml in complete IMDM (IMDM supplemented with 10% heat-inactivated fetal bovine serum, 100 U/ml penicillin/streptomycin, 2 mM L-glutamine, 10 mM HEPES, 0.1 mM nonessential amino acids, and 1 mM sodium pyruvate) at 37°C + 5% CO_2. Cells were stimulated for production of cytokines with PMA (50 ng/ml) + ionomycin (1 μg/ml) in the presence of Brefeldin A (GolgiPlug from BD Biosciences) for 6 hours. After stimulation, cells were stained for analysis by flow cytometry. CD4$^+$ T cells were incubated with Ghost Dye Violet 510 (TonboBiosciences) to stain dead cells for 10 min at room temperature. Fluorochrome-conjugated surface antibodies were incubated for 15 min at room temperature. Cell-surface antibodies against CD3 (UCHT1), CD4 (RPA-T4), and CD45RA (HI100) were all from TonboBiosciences. Anti-CXCR5/CD185 (RF8B2,) was from BD Biosciences, and anti-PD-1/CD279 (EH12.2H7) from BioLegend. Cells were then fixed and permeabilized with Fixation/Permeabilization Solution Kit with BD GolgiPlug from BD Biosciences. Intracellular staining was performed for 30 min at 4°C using anti-IL-4 (MP4-25D2), and anti-IL-13 (JES10-5A2) antibodies from BioLegend. FACS analysis was performed on a BD LSR Symphony (BD Biosciences), and data were analyzed with FlowJo software (TreeStar, Ashland, OR).

Enzyme-linked immunosorbent assay (ELISA)

Sera from immunized mice were collected on day 12 post primary and/or 8 to 9 days post boost. ELISA was performed as described elsewhere (*66*). Serum samples were analyzed by ELISA for measurement of total, NP-specific, peanut-specific, or OVA-specific antibodies. Briefly, for antigen-specific antibodies, 20 μg/ml of NP16-OVA, NP4-BSA or NP7-BSA, NP40-BSA, or crude peanut extract (Lot: 287729, Greer Laboratories), in carbonate buffer was coated on 96-well MaxiSorp plates (Thermo Fisher Scientific) overnight. For total antibodies ELISA, 2 μg/ml anti-mouse IgE (BD Pharmingen) capture antibodies in phosphate buffered saline was coated on 96-well MaxiSorp plates overnight. Plates were blocked with 1% BSA in PBS at 37°C for 1 hour followed by the addition of serially diluted serum with a 2-hour incubation at 37°C. Antigen-specific or total antibody or each isotype was detected with anti-mouse IgE-HRP, anti-IgG1-HRP, or anti-IgG2c-HRP (Southern Biotech) and incubated at 37°C. For total antibodies, a starting concentration of 100 ng/ml purified mouse IgE (BD Biosciences) was used as a standard. NP4-BSA or NP7-BSA was used to detect high-affinity IgE depending on the lot. Serum from mice immunized with NP-OVA and alum, or complete Freund's adjuvant or *Alternaria* extract or peanut with cholera toxin were used as reference standards to calculate arbitrary units for IgG1, IgG2c, and IgE, respectively. Plates were developed with stabilized chromogen tetramethylbenzidine (Life Sciences) and stopped with 3 N hydrochloric acid before reading at 450 nm on a microplate reader (Molecular Devices). Mouse mast cell protease 1 (MMCP-1) ELISA was performed with MMCP-1 ELISA kit (Invitrogen) according to the manufacturer's instructions.

Passive cutaneous anaphylaxis (PCA)

PCA was performed as described earlier (*6*). Briefly, ~20 μl of serum from immunized and boosted mice were injected into ear pinnae of naïve B6 recipients. Twenty-four hours later, the recipient mice were challenged with 100 μg NP7-BSA together with 1% Evans blue (i.v.). Thirty minutes later, the mice were euthanized and ear pinnae were harvested and incubated in formamide for 48 to 72 hours at 56°C to release the dye. The extent of vascular leakage was measured spectrophotometrically at 650 nm using Evans blue as the standard.

Microscopy

Mediastinal lymph nodes were snap frozen in OCT tissue-freezing solution and stored at −80°C. Tissues were cut into 7-μm sections and processed as described previously (*21*). Tissues were stained with anti-IgD (11-26.c.2a), PNA (Vector Labs), anti-CD4 (RM4-5); anti-human CD4 (RPA-T4); and anti-PD-1 (RMP1-30). Images were obtained from a laser-scanning confocal microscope (Leica TCS SP5; Lens: Leica HCX PL APO 20x/0.70 Oil) or immunofluorescence microscope (Nikon Eclipse Ti; Camera: Retiga 2000R; Lens: Nikon Plan Apo DIC N1 10X/0.45 and Nikon Plan Fluor DIC N2 20X/0.5). Adobe Photoshop or ImageJ software was used for image analysis and the measurement of GC size and T cell counting.

Cytokine ELISPOT assay

MultiScreen HTS plates were coated overnight at 4°C with anti-IL-21 (IL-21 Elispot kit, eBioscience). Sorted cells were cultured (2.5×10^4 cells/well) with PMA (50 ng/ml) and ionomycin (1 μg/ml) for 36 hours at 37°C followed by the addition of primary then secondary detection antibodies. Spots were developed with Vector Blue (Vector Laboratories) and quantified using an ImmunoSpot analyzer (Cellular Technology Limited).

Quantitative PCR (qPCR)

RNA from sorted T_{FH} cells was isolated using the QIAGEN RNeasy Micro Kit in accordance with the manufacturer's protocol. cDNA was prepared using the Power SYBR Green Cells-to-CT Kit (ThermoFisher) in accordance with the manufacturer's protocol. Real-time PCR was performed using KAPA SYBR Fast Master Mix (Kapa Biosystems) and Low ROX (Kapa Biosystems) and run on the QuantStudio3 (Applied Biosystems). cDNA expression was analyzed by the ΔC_t (change in cycle threshold) method normalized to values of *Hprt* obtained in parallel reactions during each cycle. The following primers were used: *Il4*: forward 5′-AGATCATCGGCATTTTGAACG-3′, reverse 5′-TTTGGCACATCCATCTCCG-3′; *Il13*: forward 5′-GCTTATTGAGGAGCTGAGCAACA-3′, reverse 5′- GGCCAGGTCCACACTCCATA-3′; *Hprt*: forward 5′-CTGGTGAAAAGGACCTCTCG-3′, reverse 5′-TGAAGTACTCATTATAGTCAAGGGCA-3′.

Single-cell labeling, capture, library preparation, and RNA sequencing

TCRβ$^+$ CD4$^+$ CD44$^+$ PD1$^+$ CXCR5$^+$ T_{FH} cells from WT mice or IL-4$^+$ (GFP) TCRβ$^+$ CD4$^+$ CD44$^+$ cells from *Il4* "4Get" reporter mice were sorted 7 days after immunization with *Alternaria* extract (10 μg) and NP19-OVA (25 μg). Cells were stimulated with PMA and ionomycin for 30 min. For both single-cell RNA sequencing (scRNA-seq) experiments, cell suspensions from each mouse sample were labeled with cell hashing antibodies (BioLegend TotalSeq anti-mouse Hashtag #3-6) according to the manufacturer's protocol (BioLegend protocol #5009). Cells were washed and suspended in PBS containing 0.04% BSA and immediately processed as follows. Cells were counted on Countess II automated cell counter (ThermoFisher), and 12,000 cells (4000 cells from each hashtagged mouse) were loaded onto one lane of a 10X Chromium microfluidic chip. Single cell capture, barcoding and library preparation were performed using the 10X Chromium platform, version 2 chemistry for the first

experiment and version 3 chemistry for the second, and according to the manufacturer's protocol (#CG00052) with modifications for generating the hashtag library (*67*) BioLegend protocol #5009. cDNA and libraries were checked for quality on Agilent 4200 Tapestation, quantified by KAPA qPCR, and pooled using a ratio of 95% gene expression library and 5% hashtag library before sequencing, one on a single lane of an Illumina HiSeq4000 and the other on 16.67% of lane of an Illumina NovaSeq 6000 S2 flow cell, both targeting 6000 barcoded cells with an average sequencing depth of 50,000 reads per cell.

scRNA-seq data processing, quality control, and analysis

Illumina base call (bcl) files for the 10X V2 and V3 libraries were converted to FASTQ files using Cell Ranger mkfastq versions 2.2.0 and 3.02, respectively (10X Genomics). Cell Ranger count versions 2.2.0 and 3.0.2 (10X Genomics) were used to align reads from each library to the same mm10 reference genome (GRCm38.84, 10X Genomics reference version 2.1.0), generate digital counts matrices, and call viable cells (n = 3956 and n = 7674, respectively) (*68*). Processing and mapping statistics for both libraries are listed in tables S1 and S2.

All of the following analyses were performed using the Scanpy Python package (version 1.3) (*69*). Biological replicate identities for each cell were captured by the use of hashtag oligo antibodies (HTO) as described in (*67*). HTO library FASTQs were processed through the CITE-Seq-Count tool (version 1.3.3, https://github.com/Hoohm/CITE-seq-Count), producing cell by HTO count matrices for both libraries. Biological replicate labels for each cell were inferred using the HTO count matrices as prescribed in the HTODemux function of the Seurat package (version 2.3.3, https://github.com/satijalab/seurat). Cells that were determined to be HTO multiplets (e.g., doublets, triplets) were excluded from further analysis. Cells were further excluded from downstream analysis based on filtering by the following criteria: UMI counts per cell, gene count per cell, fraction of transcripts mapped to mitochondrial genes, cumulative hemoglobin expression. This quality control process (shown in fig. S6, A and B) yielded n = 3811 and n = 4096 filtered cells for the T_{FH} cell and the IL-4$^+$ CD4 T cell libraries, respectively, with specific exclusion criteria listed in table S3. Genes were removed if they were expressed in fewer than three cells, resulting in filtered gene expression matrices 3811 filtered cells by 12,861 filtered genes and 4096 filtered cells by 14,542 filtered genes, respectively.

The expression matrix of the T_{FH} cell–sorted library was normalized such that the median UMI count in each cell was equal to the median UMI count across the dataset and then log transformed and scaled to zero mean and unit variance on a per-gene basis. 2D and 3D UMAP embeddings of the scaled, log-transformed single-cell expression profiles were produced as follows: (i) the 1200 most highly variable genes (HVGs), as measured by dispersion, were selected; (ii) using the scaled, transformed expression at these HVGs, computing the first 50 principal components (PCs); (iii) these PCs are used to construct a k = 10 nearest neighbor graph (k-NN graph, where distance is measured using cosine distance); (iv) the UMAP embeddings were computed from this k-NN graph (*70*). We observe that cells from each of the biological replicates are well-mixed in the UMAP embeddings (fig. S6C) and each replicate contributes roughly equally to all clusters (fig. S6M). Cluster labels were assigned via the Leiden community detection algorithm on this k-NN graph, yielding 11 clusters (shown in fig. S6E) (*71*). Marker genes were identified via a "one-versus-rest" methodology comparing mean expression of every gene within each cluster which were used to assign putative subtypes. Representative markers used to identify populations of interest and exclude other populations are shown in fig. S6K. These marker genes were used to assign cellular identities to clusters. Specifically, we isolated clusters 1 to 6 and 8, consisting of n = 3002 cells.

The expression matrix of the *Il4*/GFP$^+$ sorted cell library was processed similarly as shown in fig. S6 B, D, F, and N. After a preliminary 2D embedding and cluster analysis, a small population of B cells was removed (fig. S6L) and the remaining n = 3863 T cells were reanalyzed. To explore the specific subpopulations of IL-13$^+$, all cells expressing one or more *Il13* transcripts were isolated and analyzed separately. Six-hundred HVGs were selected, and we were careful to exclude mitochondrial and ribosomal genes, sex-linked genes such as *Xist*, and cell-cycle and proliferation genes from these HVGs. PCs were computed using the log-transformed, normalized expression signatures at these HVGs and the first ten PCs were used to construct a k = 10 cosine distance k-NN and 2D UMAP embedding. Low-resolution (0.2) Leiden community detection was used to identify three subpopulations of IL-13$^+$ cells. All cells expressing one or more *Bcl6* transcript were analyzed identically (as shown in fig. S6). Leiden community detection with resolution 0.1 was used to identify two subpopulations of *Bcl6*$^+$ cells.

Differential expression analysis between pairs of clusters was performed using edgeR (version 3.24.3), where each cell acts as a single sample (*72*, *73*). For each comparison, raw counts for cells in the two clusters of interest were isolated and processed using glmQLFTest assuming a two-group design matrix according to the edgeR User's Guide. There are several tools designed to identify differential genes in single cell transcriptomic data; recent studies have shown edgeR and DESeq2 to balance precision and recall in DEG analysis, and to perform similar to if not better than DEG analysis tools designed for scRNA-seq (*74*).

Immunoblotting

CD4$^+$ T cells were isolated using CD4 T cell purification kit through negative selection (Stem Cell Technologies). Three million cells were lysed in immunoprecipitation assay buffer with protease inhibitors (Roche), and cell lysates were run on SDS-PAGE and transferred onto nitrocellulose membrane. After blocking with 5% nonfat milk in Tris-buffered saline with 5% tween for 1 hour at room temperature, membranes were incubated with anti-mouse DOCK8 antibody (Takara) at 4°C overnight. Goat anti-rabbit IgG(H+L)-HRP polyclonal detection antibody (1:5000) (Invitrogen) was incubated with membrane before assessing chemiluminescence signal with ECL substrate on ChemiDoc Imaging System (Bio-Rad). The housekeeping protein β-actin was used to normalize protein concentrations.

In vitro culture

Mediastinal lymph node cells were isolated from mice immunized with *Alternaria* extract (10 μg) and NP20-OVA (25 μg). Fifty thousand cells/well were cultured in 96-well U-bottom plates with 1 μg CD40 (HM40-3) in the presence of 2 ng of IL-4 (Peprotech) and 50 ng of IL-13 (R&D) for 3 days in complete RPMI 1640. IgE plasma cells were analyzed by flow cytometry.

T_{reg} cell suppression assay

Naïve CD45.1$^+$ CD4$^+$ T cells were isolated by negative selection with magnetic beads (Miltenyi) and labeled with carboxyfluorescein succinimidyl ester (CFSE) (Life Technologies) and used as responders. Regulatory T cells (T_{reg}), CD45.2$^+$ CD4$^+$ CD25$^+$ from WT or *Dock8*$^{-/-}$ mice were isolated by negative selection followed by positive selection with T_{reg} isolation kit (Miltenyi). The cells were plated at a concentration of 3×10^4 cells per well at ratio of 1 T_{reg}:2 responder T cells. Cells were stimulated with 0.5 μg/ml of α-CD3 and 2 μg/ml of α-CD28. After incubation at 37°C for 72 hours, proliferation of responder cells was assessed by flow cytometry and compared to no-T_{reg} controls as an assessment of T_{reg} suppressive abilities.

Mixed bone marrow chimeras

Recipient WT CD45.1$^+$ mice were irradiated with two doses of 600 rad 3 hours apart. One or two hours after the second irradiation, 5×10^5 bone marrow cells from WT or *Il13*$^{-/-}$ mice mixed with 5×10^5 bone marrow cells from *Cd4*^{Cre}*Bcl6*$^{fl/fl}$ mice were adoptively transferred by i.v. injection into irradiated recipient mice. All experiments with bone marrow chimeric mice were performed 10 to 16 weeks after bone marrow transplant.

Dendritic cell migration assay

Mice were immunized intranasally with 50 μg of OVA-Alexa Fluor 647 (Molecular Probes) and 1 μg of LPS (Invivogen). MedLNs were harvested 18 hours after immunization, minced, and digested with collagenase IV (1 mg/ml; Sigma-Aldrich) for 40 min at 37°C. Single-cell suspensions were prepared, stained, and then analyzed on an LSRII (BD Biosciences) or MACSQuant (Miltenyi Biotec) flow cytometer.

In vivo T cell proliferation and T_{FH} differentiation

To assess proliferation, $CD4^+$ T cells from OT-II *Dock8*$^{-/-}$ ($CD45.2^+$) or OT-II WT ($CD45.1.2^+$) mice were prepared from the spleen and lymph nodes by negative selection using the EasySep CD4 T Cell Isolation kit (STEMCELL Technologies) according to the manufacturer's instructions. For T cell proliferation assays, OTII cells were labeled with 1 μM carboxyfluorescein diacetate succinimidyl ester (CFSE) before transfer in to $CD45.1^+$ recipient mice and CFSE dilution was used to assess proliferation. For T_{FH} cell identification, OT-II cells were not labeled with CFSE and were gated using $CD44^+CXCR5^+PD1^+$. A total of 2×10^5 purified OTII cells were transferred into mice by retro-orbital injection. Mice were intranasally immunized 24 hours later with 10 μg of NP-OVA (Biosearch) and 2 μg of LPS (Sigma). MedLNs were harvested 3 days (for T cell proliferation) or 6 days after immunization (for T_{FH} cell analyses). Single–cell suspensions were prepared, stained, and then analyzed on an LSRII flow cytometer (BD Biosciences).

Statistical analysis

ANOVA or Student's *t* test were performed on normally distributed data (analyzed by Shapiro-Wilk test). Mann-Whitney *U* or Kruskal-Wallis *H* tests were used otherwise. A *P*-value of <0.05 was considered significant. Data were analyzed with Prism 7 (GraphPad Software).

REFERENCES AND NOTES

1. H. C. Oettgen, R. S. Geha, IgE regulation and roles in asthma pathogenesis. *J. Allergy Clin. Immunol.* **107**, 429–441 (2001). doi: 10.1067/mai.2001.113759; pmid: 11240941
2. H. Mita, H. Yasueda, K. Akiyama, Affinity of IgE antibody to antigen influences allergen-induced histamine release. *Clin. Exp. Allergy* **30**, 1583–1589 (2000). doi: 10.1046/j.1365-2222.2000.00921.x; pmid: 11069567
3. R. Suzuki *et al*., Molecular editing of cellular responses by the high-affinity receptor for IgE. *Science* **343**, 1021–1025 (2014). doi: 10.1126/science.1246976; pmid: 24505132
4. J. Wang *et al*., Correlation of IgE/IgG4 milk epitopes and affinity of milk-specific IgE antibodies with different phenotypes of clinical milk allergy. *J. Allergy Clin. Immunol.* **125**, 695–702.e6 (2010). doi: 10.1016/j.jaci.2009.12.017; pmid: 20226304
5. J. S. He *et al*., IgG1 memory B cells keep the memory of IgE responses. *Nat. Commun.* **8**, 641 (2017). doi: 10.1038/s41467-017-00723-0; pmid: 28935935
6. H. Xiong, J. Dolpady, M. Wabl, M. A. Curotto de Lafaille, J. J. Lafaille, Sequential class switching is required for the generation of high affinity IgE antibodies. *J. Exp. Med.* **209**, 353–364 (2012). doi: 10.1084/jem.20111941; pmid: 22249450
7. K. Shimoda *et al*., Lack of IL-4-induced Th2 response and IgE class switching in mice with disrupted Stat6 gene. *Nature* **380**, 630–633 (1996). doi: 10.1038/380630a0; pmid: 8602264
8. K. Takeda *et al*., Essential role of Stat6 in IL-4 signalling. *Nature* **380**, 627–630 (1996). doi: 10.1038/380627a0; pmid: 8602263
9. J. Zhu *et al*., Conditional deletion of Gata3 shows its essential function in T_H1-T_H2 responses. *Nat. Immunol.* **5**, 1157–1165 (2004). doi: 10.1038/ni1128; pmid: 15475959
10. T. Kobayashi, K. Iijima, A. L. Dent, H. Kita, Follicular helper T cells mediate IgE antibody response to airborne allergens. *J. Allergy Clin. Immunol.* **139**, 300–313.e7 (2017). doi: 10.1016/j.jaci.2016.04.021; pmid: 27325434
11. A. P. Meli, G. Fontés, C. Leung Soo, I. L. King, T follicular helper cell-derived IL-4 is required for IgE production during intestinal helminth infection. *J. Immunol.* **199**, 244–252 (2017). doi: 10.4049/jimmunol.1700141; pmid: 28533444
12. A. Noble, J. Zhao, Follicular helper T cells are responsible for IgE responses to Der p 1 following house dust mite sensitization in mice. *Clin. Exp. Allergy* **46**, 1075–1082 (2016). doi: 10.1111/cea.12750; pmid: 27138589
13. J. J. Dolence *et al*., Airway exposure initiates peanut allergy by involving the IL-1 pathway and T follicular helper cells in mice. *J. Allergy Clin. Immunol.* **142**, 1144–1158.e8 (2018). doi: 10.1016/j.jaci.2017.11.020; pmid: 29247716
14. H. E. Liang *et al*., Divergent expression patterns of IL-4 and IL-13 define unique functions in allergic immunity. *Nat. Immunol.* **13**, 58–66 (2012). doi: 10.1038/ni.2182; pmid: 22138715
15. R. Morita *et al*., Human blood $CXCR5^+CD4^+$ T cells are counterparts of T follicular cells and contain specific subsets that differentially support antibody secretion. *Immunity* **34**, 108–121 (2011). doi: 10.1016/j.immuni.2010.12.012; pmid: 21215658
16. Y. Harada *et al*., The 3′ enhancer CNS2 is a critical regulator of interleukin-4-mediated humoral immunity in follicular helper T cells. *Immunity* **36**, 188–200 (2012). doi: 10.1016/j.immuni.2012.02.002; pmid: 22365664
17. A. Sahoo *et al*., Batf is important for IL-4 expression in T follicular helper cells. *Nat. Commun.* **6**, 7997 (2015). doi: 10.1038/ncomms8997; pmid: 26278622
18. P. Vijayanand *et al*., Interleukin-4 production by follicular helper T cells requires the conserved Il4 enhancer hypersensitivity site V. *Immunity* **36**, 175–187 (2012). doi: 10.1016/j.immuni.2011.12.014; pmid: 22326582
19. A. Williams *et al*., Hypersensitive site 6 of the Th2 locus control region is essential for Th2 cytokine expression. *Proc. Natl. Acad. Sci. U.S.A.* **110**, 6955–6960 (2013). doi: 10.1073/pnas.1304720110; pmid: 23569250
20. J. Zhu, T helper 2 (Th2) cell differentiation, type 2 innate lymphoid cell (ILC2) development and regulation of interleukin-4 (IL-4) and IL-13 production. *Cytokine* **75**, 14–24 (2015). doi: 10.1016/j.cyto.2015.05.010; pmid: 26044597
21. J. S. Weinstein *et al*., TFH cells progressively differentiate to regulate the germinal center response. *Nat. Immunol.* **17**, 1197–1205 (2016). doi: 10.1038/ni.3554; pmid: 27573866
22. I. Yusuf *et al*., Germinal center T follicular helper cell IL-4 production is dependent on signaling lymphocytic activation molecule receptor (CD150). *J. Immunol.* **185**, 190–202 (2010). doi: 10.4049/jimmunol.0903505; pmid: 20525889
23. X. Liu *et al*., Bcl6 expression specifies the T follicular helper cell program in vivo. *J. Exp. Med.* **209**, 1841–1852 (2012). doi: 10.1084/jem.20120219; pmid: 22987803
24. H. C. Su, H. Jing, Q. Zhang, DOCK8 deficiency. *Ann. N. Y. Acad. Sci.* **1246**, 26–33 (2011). doi: 10.1111/j.1749-6632.2011.06295.x; pmid: 22236427
25. H. C. Su, H. Jing, P. Angelus, A. F. Freeman, Insights into immunity from clinical and basic science studies of DOCK8 immunodeficiency syndrome. *Immunol. Rev.* **287**, 9–19 (2019). doi: 10.1111/imr.12723; pmid: 30565250
26. J. K. Krishnaswamy *et al*., Migratory $CD11b^+$ conventional dendritic cells induce T follicular helper cell-dependent antibody responses. *Sci. Immunol.* **2**, eaam9169 (2017). doi: 10.1126/sciimmunol.aam9169; pmid: 29196450
27. K. L. Randall *et al*., Dock8 mutations cripple B cell immunological synapses, germinal centers and long-lived antibody production. *Nat. Immunol.* **10**, 1283–1291 (2009). doi: 10.1038/ni.1820; pmid: 19898472
28. F. D. Finkelman, M. E. Rothenberg, E. B. Brandt, S. C. Morris, R. T. Strait, Molecular mechanisms of anaphylaxis: Lessons from studies with murine models. *J. Allergy Clin. Immunol.* **115**, 449–457 (2005). doi: 10.1016/j.jaci.2004.12.1125; pmid: 15753886
29. E. Janssen *et al*., Dedicator of cytokinesis 8-deficient patients have a breakdown in peripheral B-cell tolerance and defective regulatory T cells. *J. Allergy Clin. Immunol.* **134**, 1365–1374 (2014). doi: 10.1016/j.jaci.2014.07.042; pmid: 25218284
30. A. K. Singh *et al*., DOCK8 regulates fitness and function of regulatory T cells through modulation of IL-2 signaling. *JCI Insight* **2**, e94275 (2017). doi: 10.1172/jci.insight.94275; pmid: 28978795
31. D. Zotos *et al*., IL-21 regulates germinal center B cell differentiation and proliferation through a B cell-intrinsic mechanism. *J. Exp. Med.* **207**, 365–378 (2010). doi: 10.1084/jem.20091777; pmid: 20142430
32. K. Ozaki *et al*., A critical role for IL-21 in regulating immunoglobulin production. *Science* **298**, 1630–1634 (2002). doi: 10.1126/science.1077002; pmid: 12446913
33. A. Suto *et al*., Interleukin 21 prevents antigen-induced IgE production by inhibiting germ line Cε transcription of IL-4-stimulated B cells. *Blood* **100**, 4565–4573 (2002). doi: 10.1182/blood-2002-04-1115; pmid: 12393685
34. N. Wood *et al*., IL-21 effects on human IgE production in response to IL-4 or IL-13. *Cell. Immunol.* **231**, 133–145 (2004). doi: 10.1016/j.cellimm.2005.01.001; pmid: 15919378
35. K. Takatsu, T. Kouro, Y. Nagai, Interleukin 5 in the link between the innate and acquired immune response. *Adv. Immunol.* **101**, 191–236 (2009). doi: 10.1016/S0065-2776(08)01006-7; pmid: 19231596
36. M. Kubo, T follicular helper and T_H2 cells in allergic responses. *Allergol. Int.* **66**, 377–381 (2017). doi: 10.1016/j.alit.2017.04.006; pmid: 28499720
37. M. Mohrs, K. Shinkai, K. Mohrs, R. M. Locksley, Analysis of type 2 immunity in vivo with a bicistronic IL-4 reporter. *Immunity* **15**, 303–311 (2001). doi: 10.1016/S1074-7613(01)00186-8; pmid: 11520464
38. N. Debeuf, E. Haspeslagh, M. van Helden, H. Hammad, B. N. Lambrecht, Mouse models of asthma. *Curr. Protoc. Mouse Biol.* **6**, 169–184 (2016). pmid: 27248433
39. X. M. Li *et al*., A murine model of peanut anaphylaxis: T- and B-cell responses to a major peanut allergen mimic human responses. *J. Allergy Clin. Immunol.* **106**, 150–158 (2000). doi: 10.1067/mai.2000.107395; pmid: 10887318
40. D. Chiang *et al*., Single-cell profiling of peanut-responsive T cells in patients with peanut allergy reveals heterogeneous effector T_H2 subsets. *J. Allergy Clin. Immunol.* **141**, 2107–2120 (2018). doi: 10.1016/j.jaci.2017.11.060; pmid: 29408715
41. Y. Wang *et al*., IgE sequences in individuals living in an area of endemic parasitism show little mutational evidence of antigen selection. *Scand. J. Immunol.* **73**, 496–504 (2011). doi: 10.1111/j.1365-3083.2011.02525.x; pmid: 21284686
42. G. J. McKenzie *et al*., Impaired development of Th2 cells in IL-13-deficient mice. *Immunity* **9**, 423–432 (1998). doi: 10.1016/S1074-7613(00)80625-1; pmid: 9768762
43. G. J. McKenzie, P. G. Fallon, C. L. Emson, R. K. Grencis, A. N. McKenzie, Simultaneous disruption of interleukin (IL)-4 and IL-13 defines individual roles in T helper cell type 2-mediated responses. *J. Exp. Med.* **189**, 1565–1572 (1999). doi: 10.1084/jem.189.10.1565; pmid: 10330435
44. T. R. Ramalingam *et al*., Unique functions of the type II interleukin 4 receptor identified in mice lacking the interleukin 13 receptor alpha1 chain. *Nat. Immunol.* **9**, 25–33 (2008). doi: 10.1038/ni1544; pmid: 18066066
45. A. Ballesteros-Tato *et al*., T follicular helper cell plasticity shapes pathogenic T helper 2 cell-mediated immunity to inhaled house dust mite. *Immunity* **44**, 259–273 (2016). doi: 10.1016/j.immuni.2015.11.017; pmid: 26825674
46. A. Glatman Zaretsky *et al*., T follicular helper cells differentiate from Th2 cells in response to helminth antigens. *J. Exp. Med.* **206**, 991–999 (2009). doi: 10.1084/jem.20090303; pmid: 19380637
47. S. Nakayamada *et al*., Early Th1 cell differentiation is marked by a Tfh cell-like transition. *Immunity* **35**, 919–931 (2011). doi: 10.1016/j.immuni.2011.11.012; pmid: 22195747
48. S. Keles *et al*., Dedicator of cytokinesis 8 regulates signal transducer and activator of transcription 3 activation and promotes T_H17 cell differentiation. *J. Allergy Clin. Immunol.* **138**, 1384–1394.e2 (2016). doi: 10.1016/j.jaci.2016.04.023; pmid: 27350570
49. C. J. Kearney, K. L. Randall, J. Oliaro, DOCK8 regulates signal transduction events to control immunity. *Cell. Mol. Immunol.* **14**, 406–411 (2017). doi: 10.1038/cmi.2017.9; pmid: 28366940
50. H. Wu *et al*., An inhibitory role for the transcription factor Stat3 in controlling IL-4 and Bcl6 expression in follicular helper T cells. *J. Immunol.* **195**, 2080–2089 (2015). doi: 10.4049/jimmunol.1500335; pmid: 26188063
51. A. Erazo *et al*., Unique maturation program of the IgE response in vivo. *Immunity* **26**, 191–203 (2007). doi: 10.1016/j.immuni.2006.12.006; pmid: 17292640
52. M. Yazdanbakhsh, P. G. Kremsner, R. van Ree, Allergy, parasites, and the hygiene hypothesis. *Science* **296**, 490–494 (2002). doi: 10.1126/science.296.5567.490; pmid: 11964470
53. J. S. He *et al*., Biology of IgE production: IgE cell differentiation and the memory of IgE responses. *Curr. Top. Microbiol. Immunol.* **388**, 1–19 (2015). doi: 10.1007/978-3-319-13725-4_1; pmid: 25553792
54. C. M. Fitzsimmons, F. H. Falcone, D. W. Dunne, Helminth allergens, parasite-specific IgE, and its protective role in human immunity. *Front. Immunol.* **5**, 61 (2014). doi: 10.3389/fimmu.2014.00061; pmid: 24592267

55. T. J. Looney *et al*., Human B-cell isotype switching origins of IgE. *J. Allergy Clin. Immunol.* **137**, 579–586.e7 (2016). doi: 10.1016/j.jaci.2015.07.014; pmid: 26309181
56. R. A. Hoh *et al*., Single B-cell deconvolution of peanut-specific antibody responses in allergic patients. *J. Allergy Clin. Immunol.* **137**, 157–167 (2016). doi: 10.1016/j.jaci.2015.05.029; pmid: 26152318
57. S. M. McCormick, N. M. Heller, Commentary: IL-4 and IL-13 receptors and signaling. *Cytokine* **75**, 38–50 (2015). doi: 10.1016/j.cyto.2015.05.023; pmid: 26187331
58. S. L. LaPorte *et al*., Molecular and structural basis of cytokine receptor pleiotropy in the interleukin-4/13 system. *Cell* **132**, 259–272 (2008). doi: 10.1016/j.cell.2007.12.030; pmid: 18243101
59. L. Pattarini *et al*., TSLP-activated dendritic cells induce human T follicular helper cell differentiation through OX40-ligand. *J. Exp. Med.* **214**, 1529–1546 (2017). doi: 10.1084/jem.20150402; pmid: 28428203
60. C. J. Kim *et al*., The transcription factor Ets1 suppresses T follicular helper type 2 cell differentiation to halt the onset of systemic lupus erythematosus. *Immunity* **49**, 1034–1048.e8 (2018). doi: 10.1016/j.immuni.2018.10.012; pmid: 30566881
61. S. E. Ashley *et al*., Genetic variation at the Th2 immune gene IL13 is associated with IgE-mediated paediatric food allergy. *Clin. Exp. Allergy* **47**, 1032–1037 (2017). doi: 10.1111/cea.12942; pmid: 28544327
62. M. Pykäläinen *et al*., Association analysis of common variants of STAT6, GATA3, and STAT4 to asthma and high serum IgE phenotypes. *J. Allergy Clin. Immunol.* **115**, 80–87 (2005). doi: 10.1016/j.jaci.2004.10.006; pmid: 15637551
63. M. Huebner *et al*., Patterns of GATA3 and IL13 gene polymorphisms associated with childhood rhinitis and atopy in a birth cohort. *J. Allergy Clin. Immunol.* **121**, 408–414 (2008). doi: 10.1016/j.jaci.2007.09.020; pmid: 18037162
64. N. Krug *et al*., Blood eosinophils predict therapeutic effects of a GATA3-specific DNAzyme in asthma patients. *J. Allergy Clin. Immunol.* **140**, 625–628.e5 (2017). doi: 10.1016/j.jaci.2017.02.024; pmid: 28342914
65. Z. Yang, B. M. Sullivan, C. D. Allen, Fluorescent in vivo detection reveals that IgE^+ B cells are restrained by an intrinsic cell fate predisposition. *Immunity* **36**, 857–872 (2012). doi: 10.1016/j.immuni.2012.02.009; pmid: 22406270
66. J. S. He *et al*., The distinctive germinal center phase of IgE^+ B lymphocytes limits their contribution to the classical memory response. *J. Exp. Med.* **210**, 2755–2771 (2013). doi: 10.1084/jem.20131539; pmid: 24218137
67. M. Stoeckius *et al*., Cell Hashing with barcoded antibodies enables multiplexing and doublet detection for single cell genomics. *Genome Biol.* **19**, 224 (2018). doi: 10.1186/s13059-018-1603-1; pmid: 30567574
68. G. X. Zheng *et al*., Massively parallel digital transcriptional profiling of single cells. *Nat. Commun.* **8**, 14049 (2017). doi: 10.1038/ncomms14049; pmid: 28091601
69. F. A. Wolf, P. Angerer, F. J. Theis, SCANPY: Large-scale single-cell gene expression data analysis. *Genome Biol.* **19**, 15 (2018). doi: 10.1186/s13059-017-1382-0; pmid: 29409532
70. E. Becht *et al*., Dimensionality reduction for visualizing single-cell data using UMAP. *Nat. Biotechnol.* **37**, 38–44 (2018). doi: 10.1038/nbt.4314; pmid: 30531897
71. V. A. Traag, L. Waltman, N. J. van Eck, From Louvain to Leiden: Guaranteeing well-connected communities. *Sci. Rep.* **9**, 5233 (2019). doi: 10.1038/s41598-019-41695-z; pmid: 30914743
72. M. D. Robinson, D. J. McCarthy, G. K. Smyth, edgeR: A Bioconductor package for differential expression analysis of digital gene expression data. *Bioinformatics* **26**, 139–140 (2010). doi: 10.1093/bioinformatics/btp616; pmid: 19910308
73. A. T. Lun, Y. Chen, G. K. Smyth, It's DE-licious: A recipe for differential expression analyses of RNA-seq experiments using quasi-likelihood methods in edgeR. *Methods Mol. Biol.* **1418**, 391–416 (2016). doi: 10.1007/978-1-4939-3578-9_19; pmid: 27008025
74. A. Dal Molin, G. Baruzzo, B. Di Camillo, Single-cell RNA-sequencing: Assessment of differential expression analysis methods. *Front. Genet.* **8**, 62 (2017). doi: 10.3389/fgene.2017.00062; pmid: 28588607

ACKNOWLEDGMENTS

We thank M. Firla for technical assistance; M. Wimsatt for the illustration; E. Gelfand (National Jewish Health, CO) for the *Il13*$^{-/-}$ bone marrow; C. Allen (UCSF) for IgE GC B cell staining protocol; R. D. Chow (Yale University) for discussions on analysis of scRNA-seq data; and the Single Cell Biology Laboratory led by P. Robson at the Jackson Laboratory for Genomic Medicine, for help with scRNA-seq experiments. **Funding:** This work was supported by Food Allergy Research and Education Ira and Diana Riklis Family Research Award in Food Allergy, R01 AI136942, and R01 AI108829 (to S.C.E.), and by R21 AI135221 and R21 AI133440 (to A.W.). U.G. is a recipient of Gershon-Trudeau Fellowship from Immunobiology at Yale University. B.Z. is a recipient of Ph.D. fellowship awarded by Agency for Science, Technology, and Research, Singapore. T.S. is a recipient of Robert E. Leet and Clara Guthrie Patterson Trust Mentored Research Award. **Author contributions:** U.G. and S.C.E. designed the study. U.G., J.S.C., M.A.C., J.D.S.G., B.Z., W.F.F., D.C., Y.L., W.S., J.J., J.A.G., L.X., J.S.W., M.C.B., A.W., and S.C.E. performed and/or analyzed experiments. U.G., J.S.C., A.W., and S.C.E wrote the manuscript. T.S., M.C.B., J.E.C., J.S.W., A.W., and S.C.E. provided resources, reagents, and funding. A.W. and S.C.E. supervised the study. **Competing interests:** None. **Data and materials availability:** The accession number for the RNA-seq datasets is GSE132798. The data is available in the Gene Expression Omnibus database. All other data needed to evaluate the conclusions in this paper are present either in the main text or the supplementary materials.

SUPPLEMENTARY MATERIALS

science.sciencemag.org/content/365/6456/eaaw6433/suppl/DC1
Figs. S1 to S16
Tables S1 to S5
References

28 January 2019; accepted 18 July 2019
Published online 1 August 2019
10.1126/science.aaw6433

RESEARCH ARTICLE SUMMARY

MALARIA

Validation of the protein kinase *Pf*CLK3 as a multistage cross-species malarial drug target

Mahmood M. Alam*, Ana Sanchez-Azqueta*, Omar Janha*, Erika L. Flannery, Amit Mahindra, Kopano Mapesa, Aditya B. Char, Dev Sriranganadane, Nicolas M. B. Brancucci, Yevgeniya Antonova-Koch, Kathryn Crouch, Nelson Victor Simwela, Scott B. Millar, Jude Akinwale, Deborah Mitcheson, Lev Solyakov, Kate Dudek, Carolyn Jones, Cleofé Zapatero, Christian Doerig, Davis C. Nwakanma, Maria Jesús Vázquez, Gonzalo Colmenarejo, Maria Jose Lafuente-Monasterio, Maria Luisa Leon, Paulo H. C. Godoi, Jon M. Elkins, Andrew P. Waters, Andrew G. Jamieson, Elena Fernández Álvaro, Lisa C. Ranford-Cartwright, Matthias Marti, Elizabeth A. Winzeler, Francisco Javier Gamo, Andrew B. Tobin†

INTRODUCTION: Despite the positive effects of intervention strategies that include insecticide-impregnated bed nets and artemisinin-based drug therapies, malaria still kills nearly 500,000 people per year and infects more than 200 million individuals globally. This, together with the emerging resistance of the parasite to frontline antimalarials, means that there is an urgent need for novel treatments that not only offer a cure for malaria but also prevent transmission. We show that by inhibiting an essential protein kinase that is a key regulator of RNA processing, we are able to kill the parasite in the blood and liver stages as well as prevent the development of the sexual-stage gametocytes, thereby blocking transmission to the mosquito.

RATIONALE: Our group has previously published a list of 36 protein kinases that are essential for blood-stage survival of the most virulent form of the human malaria parasite, *Plasmodium falciparum*. Here, we focused on one of these protein kinases from the *P. falciparum* CLK (cyclin-dependent–like kinase) family, *Pf*CLK3, and reasoned that inhibition of this protein kinase by a small drug-like molecule would be effective at killing blood-stage parasites. We further hypothesized that because *Pf*CLK3 plays a key role in RNA splicing, inhibition of this kinase would be effective at killing the parasite at all stages of the life cycle where RNA splicing is required. This would include blood, liver, and sexual stages.

RESULTS: By screening a focused library of nearly 30,000 compounds, we identified a probe molecule that selectively inhibited *Pf*CLK3 and killed blood-stage *P. falciparum*. Using a combination of evolved resistance and chemogenetics, we established that our probe molecule had parasiticidal activity by inhibition of *Pf*CLK3. We further showed that inhibition of *Pf*CLK3 in parasites resulted in a reduction in more than 400 gene transcripts known to be essential for parasite survival. The finding that the vast majority of the genes down-regulated by *Pf*CLK3 inhibition contained introns supported the notion that inhibition of *Pf*CLK3 killed the malaria parasite by preventing the splicing of essential parasite genes. Because there is a high degree of homology between orthologs of CLK3 in other *Plasmodium* species, it might be expected that our probe molecule would both inhibit CLK3 contained in other malaria parasite species and have effective parasiticidal activity in these parasites. This was indeed found to be the case, with our molecule showing potent inhibition of CLK3 from *P. vivax* and *P. berghei* as well as killing the blood stages of *P. berghei* and *P. knowlesi*. Furthermore, we demonstrated that CLK3 inhibition also kills liver-stage *P. berghei* parasites and prevents *P. berghei* infection in mice. Finally, we showed that inhibition of *Pf*CLK3 prevents the development of *P. falciparum* gametocytes, thereby blocking the infection of mosquitoes.

ON OUR WEBSITE

Read the full article at http://dx.doi.org/10.1126/science.aau1682

CONCLUSION: We found that inhibition of the essential malaria protein kinase CLK3 can kill multiple species of malaria parasites at the blood stage as well as killing liver-stage parasites and blocking transmission of the parasite to mosquitoes by preventing gametocyte development. In this way, we validate *Plasmodium* spp. CLK3 as a target that can offer prophylactic, curative, and transmission-blocking potential. ■

The list of author affiliations is available in the full article online.
*These authors contributed equally to this work.
†Corresponding author. Email: andrew.tobin@glasgow.ac.uk
Cite this article as M. M. Alam *et al.*, *Science* **365**, eaau1682 (2019). DOI: 10.1126/science.aau1682

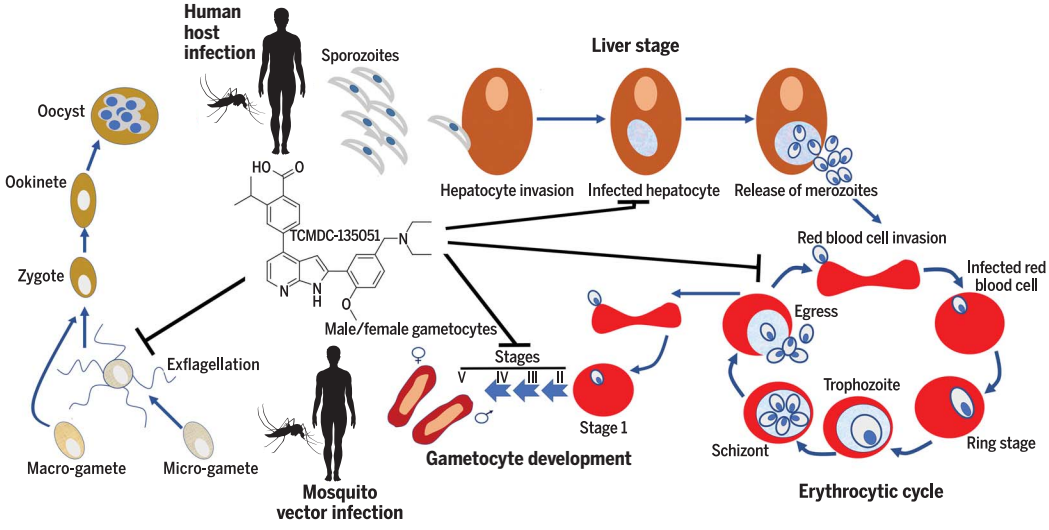

***Pf*CLK3: A new drug target for malaria.** Inhibition of the malaria parasite protein kinase CLK3 with our probe molecule TCMDC-135051 inhibits the development of liver-stage parasites, kills asexual blood-stage parasites at the trophozoite and schizont stages of the erythrocytic cycle, blocks the development of sexual gametocytes that infect mosquitoes, and blocks exflagellation that results in male gametes.

RESEARCH ARTICLE

MALARIA

Validation of the protein kinase *Pf*CLK3 as a multistage cross-species malarial drug target

Mahmood M. Alam[1]*, Ana Sanchez-Azqueta[2]*, Omar Janha[2]*, Erika L. Flannery[3], Amit Mahindra[4], Kopano Mapesa[4], Aditya B. Char[5], Dev Sriranganadane[6], Nicolas M. B. Brancucci[7], Yevgeniya Antonova-Koch[8], Kathryn Crouch[1], Nelson Victor Simwela[1], Scott B. Millar[1], Jude Akinwale[9], Deborah Mitcheson[10], Lev Solyakov[9], Kate Dudek[9], Carolyn Jones[9], Cleofé Zapatero[11], Christian Doerig[12], Davis C. Nwakanma[13], Maria Jesús Vázquez[11], Gonzalo Colmenarejo[14], Maria Jose Lafuente-Monasterio[11], Maria Luisa Leon[11], Paulo H. C. Godoi[6], Jon M. Elkins[15], Andrew P. Waters[1], Andrew G. Jamieson[4], Elena Fernández Álvaro[11], Lisa C. Ranford-Cartwright[5], Matthias Marti[1], Elizabeth A. Winzeler[8], Francisco Javier Gamo[11], Andrew B. Tobin[2]†

The requirement for next-generation antimalarials to be both curative and transmission-blocking necessitates the identification of previously undiscovered druggable molecular pathways. We identified a selective inhibitor of the *Plasmodium falciparum* protein kinase *Pf*CLK3, which we used in combination with chemogenetics to validate *Pf*CLK3 as a drug target acting at multiple parasite life stages. Consistent with a role for *Pf*CLK3 in RNA splicing, inhibition resulted in the down-regulation of more than 400 essential parasite genes. Inhibition of *Pf*CLK3 mediated rapid killing of asexual liver- and blood-stage *P. falciparum* and blockade of gametocyte development, thereby preventing transmission, and also showed parasiticidal activity against *P. berghei* and *P. knowlesi*. Hence, our data establish *Pf*CLK3 as a target for drugs, with the potential to offer a cure—to be prophylactic and transmission blocking in malaria.

Despite artemisinin-based combination therapies offering effective frontline treatment for malaria, there are still more than 200 million cases of malaria worldwide each year, resulting in an estimated 500,000 deaths. This, combined with the fact that there is now clear evidence for the emergence of resistance not only to artemisinin (*1*, *2*) but also to partner drugs including piperaquine and mefloquine (*3*, *4*), means that there is an urgent need for novel therapeutic strategies to cure malaria while also preventing transmission. Global phosphoproteomic studies on the most virulent species of human malaria, *Plasmodium falciparum*, have established protein phosphorylation as a key regulator of a wide range of essential parasite processes (*5*–*8*). Furthermore, of the 65 eukaryotic protein kinases in the parasite kinome (*9*), more than half have been reported to be essential for blood-stage survival (*8*–*12*). These studies, together with the generally accepted potential of targeting protein kinases in the treatment of numerous human diseases (*13*, *14*), suggest that inhibition of parasite protein kinases might offer a viable strategy for the treatment of malaria (*6*, *15*)

To directly test this hypothesis, we focused on one of the four members of the *P. falciparum* cyclin-dependent–like (CLK) protein kinase family, *Pf*CLK3 (PF3D7_1114700), a protein kinase essential for maintaining the asexual blood stage of both *P. falciparum* (*8*, *12*) and *P. berghei* (*10*, *11*). In mammalian cells, the CLK protein kinase family and the closely related SRPK family are crucial mediators of multiple phosphorylation events on splicing factors, including serine-arginine–rich (SR) proteins, which are necessary for the correct assembly and catalytic activity of spliceosomes [reviewed in (*16*)]. A key member of the human CLK family is the splicing factor kinase PRP4 kinase (PRPF4B), which homology-based studies have identified as the closest related human kinase to *Pf*CLK3 (*17*, *18*). PRPF4B plays an essential role in the regulation of splicing by phosphorylation of accessory proteins associated with the spliceosome complex (*19*). The finding that *Pf*CLK3 can phosphorylate SR proteins in vitro (*20*) supports the notion that *Pf*CLK3, like the other members of the *Pf*CLK family (*17*), plays an essential role in parasite pre-mRNA processing (*18*).

High-throughput screen identifies selective *Pf*CLK3 inhibitors

We established high-throughput inhibition assays for two essential members of the *Pf*CLK family, *Pf*CLK1 and *Pf*CLK3 (fig. S1). Both of these protein kinases were purified as active recombinant proteins (fig. S2A) and were used in a high-throughput time-resolved florescence resonance energy transfer (TR-FRET) assay, showing robust reproducibility in 1536-well assay format ($Z' > 0.7$) (fig. S2, B to H). This assay was used to screen 24,619 compounds, comprising 13,533 compounds in the Tres Cantos Anti-Malarial Set (TCAMS) (*21*), 1115 in the Protein Kinase Inhibitor Set (PKIS) (*22*), and 9970 in the MRCT index library (*23*), at a single dose (10 μM). Hits were defined as those compounds that were positioned >3 standard deviations from the mean of the percent inhibition distribution curve (Fig. 1, A and B) and that also showed >40% inhibition. This identified 2579 compounds (consisting of MRCT = 250, PKIS = 4, TCAMS = 2325), which, together with the 259 compounds identified as "the kinase inhibitor set" from within the Medicines for Malaria Venture (MMV) box, a collection of 400 antimalarial compounds (*24*), were used to generate concentration inhibition curves (Fig. 1C and table S1). On the basis of the selectivity criterion of a difference of more than 1.5 log units in the negative logarithm of the half-maximal inhibition (pIC_{50}), 28% of the hits showed specific inhibition of *Pf*CLK1 and 13% specifically inhibited *Pf*CLK3, whereas 23% of the compounds inhibited both *Pf*CLK3 and *Pf*CLK1; the remainder (36%) were inactive (Fig. 1, C and D, and table S1). Exemplar molecules from each of these three classes are shown in fig. S3.

Highlighted in Fig. 1C is TCMDC-135051, which showed the highest selectivity and potency for inhibition of *Pf*CLK3. TCMDC-135051 also showed lower activity against the closely related human kinase CLK2 (29% sequence identity with *Pf*CLK3)

[1]Wellcome Centre for Integrative Parasitology, University of Glasgow, Glasgow G12 8QQ, UK. [2]Centre for Translational Pharmacology, Institute of Molecular Cell and Systems Biology, University of Glasgow, Glasgow G12 8QQ, UK. [3]Novartis Institute for Biomedical Research, Emeryville, CA 94608, USA. [4]School of Chemistry, University of Glasgow, Glasgow G12 8QQ, UK. [5]Institute of Biodiversity, Animal Health and Comparative Medicine, College of Medical, Veterinary and Life Science, University of Glasgow, Glasgow G12 8QQ, UK. [6]Structural Genomics Consortium, Universidade Estadual de Campinas, Campinas, São Paulo 13083-886, Brazil. [7]Department of Medical Parasitology and Infection Biology, Swiss Tropical and Public Health Institute, 4051 Basel, Switzerland. [8]Skaggs School of Pharmaceutical Sciences, UC Health Sciences Center for Immunology, Infection and Inflammation, University of California, San Diego, School of Medicine, La Jolla, CA 92093, USA. [9]Medical Research Council Toxicology Unit, University of Leicester, Leicester LE1 9HN, UK. [10]Department of Molecular Cell Biology, University of Leicester, Leicester LE1 9HN, UK. [11]Diseases of the Developing World, GlaxoSmithKline, 28760 Tres Cantos, Madrid, Spain. [12]Biomedical Science Cluster, School of Health and Biomedical Sciences, Royal Melbourne Institute of Technology, Melbourne, VIC 3000, Australia. [13]MRC Unit the Gambia, Fajara, Banjul, The Gambia. [14]Biostatistics and Bioinformatics Unit, IMDEA Food Institute, 28049 Madrid, Spain. [15]Structural Genomics Consortium, Nuffield Department of Clinical Medicine, University of Oxford, Oxford OX3 7DQ, UK.
*These authors contributed equally to this work.
†Corresponding author. Email: andrew.tobin@glasgow.ac.uk

by a factor of ~100 (table S1). Similarly, TCMDC-135051 showed no evidence of interacting with the human ortholog of *Pf*CLK3, PRPF4B. This was seen in thermostability assays, using differential scanning fluorimetry, where staurosporine, acting as a positive control, increased the melting temperature of PRPF4B by 2.40° ± 0.14°C. In contrast, TCMDC-135051 showed no change in PRPF4B thermostability (fig. S4A). Furthermore, in a mass spectrometry–based PRPF4B activity assay, the published inhibitor Compound A (*25*) showed inhibition of PRPF4B, whereas TCMDC-135051 at concentrations up to 50 μM showed no inhibitory activity (fig. S4B). In further counterscreens, TCMDC-135051 showed no activity against the *P. falciparum* protein kinases *Pf*PKG and *Pf*CDPK1 (fig. S5, A to C). Thus, TCMDC-135051 showed selective inhibition of *Pf*CLK3 when compared against the closely related human kinases PRPF4B and CLK2, as well as the closest parasite kinase, *Pf*CLK1, and other parasite kinases (*Pf*PKG, *Pf*CDPK1).

TCMDC-135051 is a member of a series of molecules that were contained in the high-throughput screen with the same chemical scaffold. This series showed similar inhibitory activity against *Pf*CLK3 (fig. S6). Note that the TCMDC-135051 is part of the TCAMS and has previously been shown to have antiparasiticidal activity (half-maximal response EC_{50} = 320 nM); the structure has been published (*21*). However, resynthesis of TCMDC-135051, together with nuclear magnetic resonance (NMR) analysis, has determined the correct structure for TCMDC-135051 to be the one shown in Fig. 1C and fig. S3.

Parasite strains resistant to TCMDC-135051 show mutations in *Pf*CLK3

We next sought to confirm that *Pf*CLK3 was the target of TCMDC-135051 parasiticidal activity. Exposing *P. falciparum* Dd2 parasites to increasing concentrations of TCMDC-135051 resulted in the emergence of three independent lines that showed decreased sensitivity to TCMDC-135051 but no change in sensitivity to chloroquine or artemisinin (Fig. 2A and Table 1). Whole-genome sequencing of the three resistant lines revealed mutations in *Pf*CLK3 (lines TM051A and TM051C) and a mutation in the putative RNA processing protein PfUSP39 (PF3D7_1317000) (line TM051B; Fig. 2B and Table 1). The resistant clone TM051A, which contained the mutation $Pro^{196} \rightarrow Arg$ (P196R) in the N-terminal region outside the *Pf*CLK3 kinase domain (Fig. 2B), showed the smallest change in sensitivity to TCMDC-135051 (factor of 4.2 shift in EC_{50} relative to parental Dd2 parasites). Examination of the in vitro enzymatic properties of the P196R mutant found in TM051A did not detect any changes in enzyme kinetics or sensitivity to inhibition by TCMDC-135051 relative to the wild-type kinase; this finding suggests that this mutation could potentially stabilize the protein or be otherwise involved in the interaction between *Pf*CLK3 and its substrates or regulatory proteins.

The line TM051C, containing a $His^{259} \rightarrow Pro$ (H259P) mutation in *Pf*CLK3, showed the largest degree of resistance to TCMDC-135051, with a shift in EC_{50} by a factor of >11 in the death curve (Fig. 2C and Table 1). Evaluation of the enzymatic properties of the H259P mutant revealed that the mutant kinase possessed ~3 times the activity of the wild-type kinase, whereas the Michaelis constant K_m for adenosine triphosphate (ATP) was similar between mutant and wild-type kinases (Fig. 2, D and E). The fact that His^{259} resides outside of the kinase domain suggests that this amino acid is within a regulatory region that controls enzymatic activity.

In contrast to the other two resistant lines, TM051B did not contain a mutation in *Pf*CLK3 but rather contained a mutation, $Phe^{103} \rightarrow Ile$ (F103I), within the putative zinc-finger ubiquitin-binding domain of ubiquitin-specific peptidase–39 (*Pf*USP39). The human and yeast orthologs of *Pf*USP39 [small nuclear ribonucleoprotein (snRNP) assembly-defective protein–1 (Sad1)] are members of the deubiquitinase family that are essential components of the U4/U6-U5 tri-snRNP complex necessary for spliceosome activity (*26*–*28*). The position of the F103I mutation within the zinc-finger ubiquitin-binding domain of *Pf*USP39 may be of importance because this domain has been implicated in the interaction of USP39/Sad1 with the spliceosome (*27*). Hence, the involvement of *Pf*USP39 in the same pathway/function as *Pf*CLK3, together with the mutations found in *Pf*CLK3 itself in the other two resistant lines, supports the notion that the parasiticidal activity of TCMDC-135051 is via inhibition of *Pf*CLK3.

Genetic target validation of *Pf*CLK3

To further confirm *Pf*CLK3 as the target of TCMDC-135051 parasiticidal activity, we designed a variant of *Pf*CLK3 that showed reduced sensitivity to TCMDC-135051. To generate this variant, we took advantage of the highly selective inhibition of *Pf*CLK3 over *Pf*CLK1 shown by TCMDC-135051. By exchanging amino acids within subdomain V of the *Pf*CLK3 kinase domain

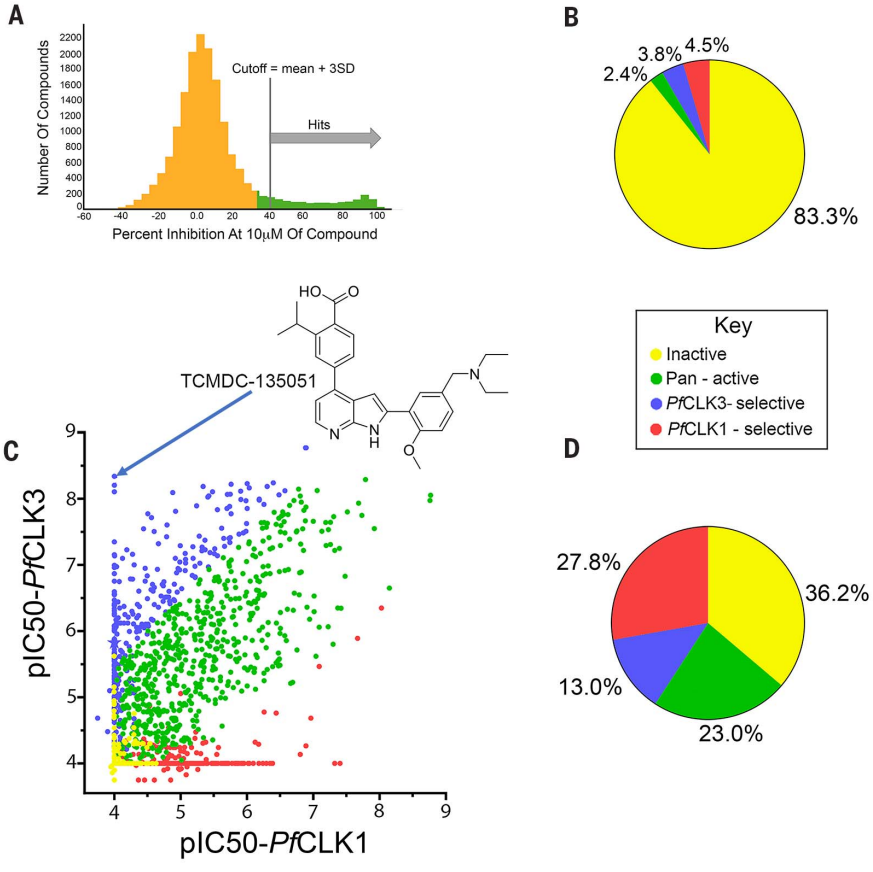

Fig. 1. High-throughput screen identifies inhibitors of *Pf*CLK1 and *Pf*CLK3. (**A**) Percent inhibition distribution pattern of compounds screened against *Pf*CLK3, binned in 5% intervals. Active "hit" compounds were defined as those that were positioned >3 SDs from the mean. (**B**) Pie chart summary of the primary single-dose screen. (**C**) Hit compounds were used in concentration response curves. Shown is a comparison of pIC_{50} values for inhibition of *Pf*CLK3 versus *Pf*CLK1. TCMDC-135051 (structure shown) is highlighted as the most potent and selective *Pf*CLK3 hit. (**D**) The same data as shown in (C) but in pie chart format of compounds designated as inactive, pan-active (active against both *Pf*CLK1 and *Pf*CLK3), or selective for either *Pf*CLK1 or *Pf*CLK3.

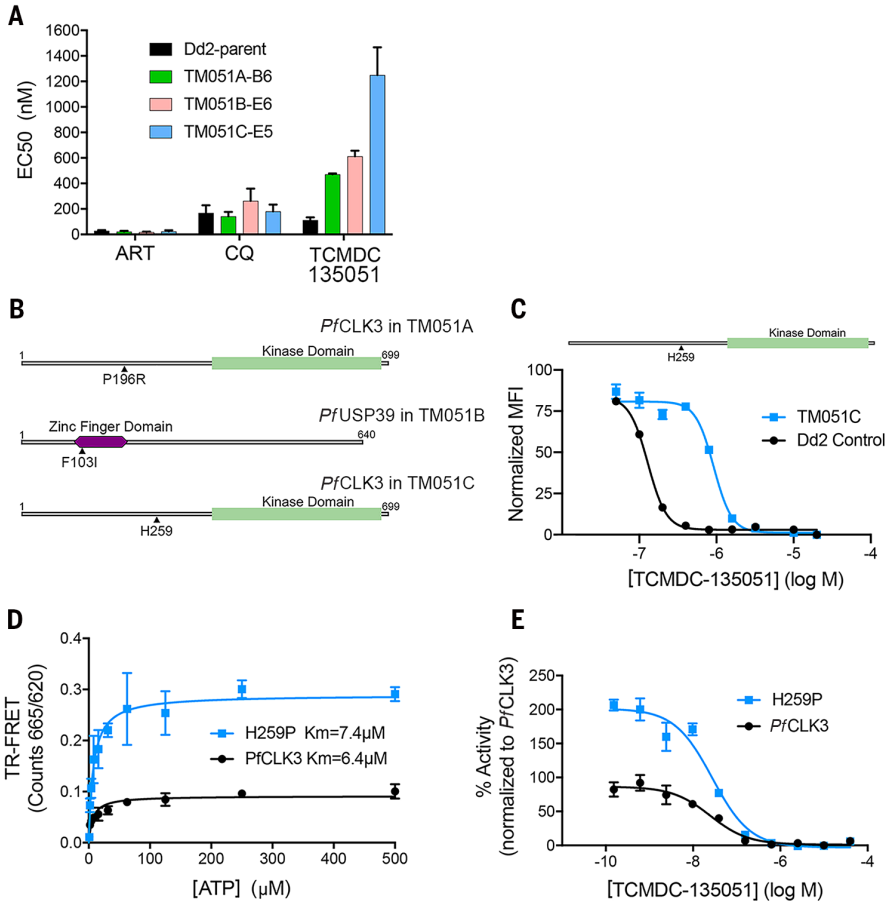

Fig. 2. Parasites adapted to become less sensitive to TCMDC-135051 harbored mutations in the *pfclk3* gene. (**A**) To generate TCMDC-135051–resistant parasite lines, we cultured Dd2 parasites with increasing concentrations of TCMDC-135051 over a 2-month period. This protocol resulted in three lines that were less sensitive to TCMDC-135051 but displayed unchanged sensitivity to artemisinin (ART) and chloroquine (CQ). (**B**) Illustration of the position of the mutations in the *pfclk3* gene and *pfusp39* gene in the drug-resistant mutant lines. (**C**) The line showing the greatest change in sensitivity to TCMDC-135051, TM051C, expressed a mutant form of *Pf*CLK3 (H259P) (illustrated). Shown are death curves for parental and TM051C lines. MFI, mean fluorescence intensity. (**D**) Enzyme activity of recombinant *Pf*CLK3 and the H259P mutant determined at varying ATP concentrations to derive a K_m for ATP. (**E**) TCMDC-135051 kinase inhibition curves for *Pf*CLK3 and the H259P mutant at K_m ATP concentrations for each enzyme. Data are means ± SEM of at least three independent experiments.

with equivalent residues in the kinase domain of *Pf*CLK1 (fig. S1), a variant of *Pf*CLK3 was generated where Gly^{449} in *Pf*CLK3 was substituted by a proline residue (G449P) (Fig. 3A). This recombinant variant protein showed a factor of ~3 log shift in sensitivity for inhibition by TCMDC-135051 (Fig. 3, B and C) [*Pf*CLK3 pIC_{50} = 7.35 ± 0.12 (IC_{50} = 0.04 μM), G449P pIC_{50} = 4.66 ± 0.16 (IC_{50} = 21.87 μM)]. The G449P variant also showed a slightly lower enzymatic activity (Fig. 3D) [*Pf*CLK3 maximal rate of reaction (V_{max}) = 1.24, G449P V_{max} = 0.88] but higher K_m for ATP (fig. S7A) (*Pf*CLK3 K_m = 6.29, G449P K_m = 81.3) relative to wild-type *Pf*CLK3. Single-crossover homologous recombination targeting the *Pf*CLK3 locus with a construct designed to insert the coding sequence for the G449P mutant (Fig. 3E) generated two independent clones (A3 and A8) that expressed the G449P mutant in place of the wild-type *Pf*CLK3 (Fig. 3, F and G). Integration of the plasmid at the target locus was verified by polymerase chain reaction (PCR) of genomic DNA (Fig. 3F), and Western blotting confirmed the expression of the G449P mutant, which was epitope-tagged with a hemagglutinin (HA) tag at the C terminus (Fig. 3G). The growth rate of the G449P-expressing mutant parasites was not different from that of control 3D7 parasites (fig. S7B). The activity of TCMDC-135051 in parasite viability assays was significantly reduced by ~1.5 log units in both clones of G449P (Fig. 3H) [negative logarithm of the half-maximal effect (pEC_{50}) of TCMDC-135051 in the Dd2 wild type, 6.35 ± 0.038 (EC_{50} = 0.45 μM); in the A3 strain, 4.86 ± 0.13 (EC_{50} = 13.80 μM); in the A8 strain, 4.94 ± 0.051 (EC_{50} = 11.48 μM)], providing further evidence that TCMDC-135051 kills parasites via inhibition of *Pf*CLK3.

Previous efforts to make inhibitor-insensitive versions of apicomplexan protein kinases have focused on the mutation of the gatekeeper residue, a key residue in the ATP binding pocket that can provide steric hindrance to ATP competitive protein kinase inhibitors (*5*, *29*, *30*). In contrast, our approach was based on a comparison of residues between two highly related kinases (*Pf*CLK1 and *Pf*CLK3) that showed differential

Table 1. Adaptive resistance to TCMDC-135051. Dd2 parasites were exposed to subthreshold concentrations of TMDC-135051, and three lines were isolated that were less sensitive to TCMDC-135051 but had unchanged sensitivity to artemisinin and chloroquine. Shown are nucleotide changes and associated amino acid changes in genes from the resistance lines as well as the identity and annotated function of the mutant genes. EC_{50} values associated with each line for artemisinin, chloroquine, and TCMDC-135051 are shown, as well as the relative (fold) change in IC_{50} for TCMDC-135051 compared to Dd2 parent parasites. Data are means ± SEM of three experiments.

Line	Chr	Position (mutation)	Mutation	Gene	Annotation	EC_{50} Artemisinin (μM)	EC_{50} Chloroquine (μM)	EC_{50} TCMDC-135051 (μM)	Fold change
Dd2 (parent)						0.028 ± 0.006	0.169 ± 0.059	0.113 ± 0.021	
TM051A	11	556351 (C-G)	P196R	Pf3D7_1114700	*Pf*CLK3	0.022 ± 0.006	0.142 ± 0.034	0.471 ± 0.007	4.2
TM051B	13	708652 (T-A)	F103I	Pf3D7_1317000	U4/U6.U5 tri-snRNP-associated protein (*Pf*USP39)	0.018 ± 0.004	0.263 ± 0.096	0.613 ± 0.044	5.4
TM051C	11	556540 (A-C)	H259P	Pf3D7_1114700	*Pf*CLK3	0.023 ± 0.010	0.180 ± 0.054	1.25 ± 0.217	11.1

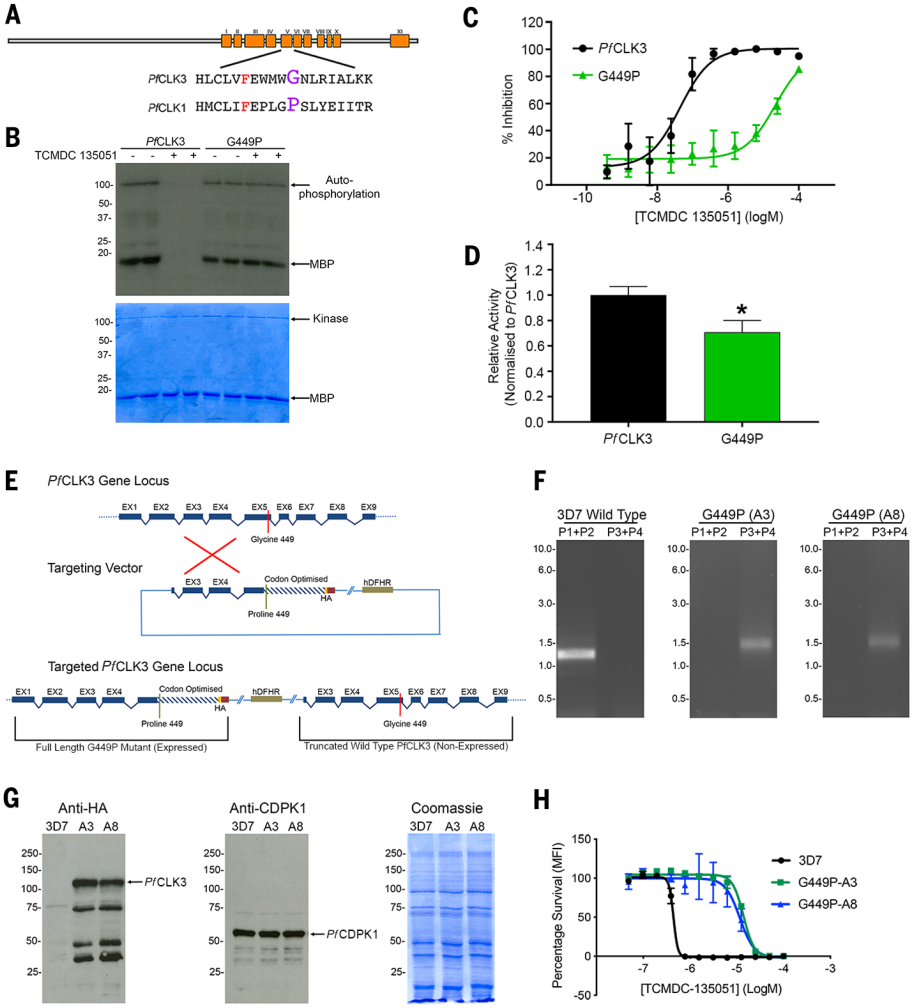

Fig. 3. Chemogenetic validation of *Pf*CLK3 as a target for the parasiticidal activity of TCMDC-135051. (**A**) Schematic of the primary amino acid sequence of *Pf*CLK3 showing the 11 kinase subdomains and the sequence of subdomain V of *Pf*CLK1 and *Pf*CLK3. A, Ala; C, Cys; E, Glu; F, Phe; G, Gly; H, His; I, Ile; K, Lys; L, Leu; M, Met; N, Asn; P, Pro; R, Arg; S, Ser; T, Thr; V, Val; W, Trp; Y, Tyr. (**B**) Gel-based assay of the phosphorylation of myelin basic protein (MBP) by *Pf*CLK3 and a Gly^{449} → Pro variant (G449P). The top gel is an autoradiograph and the bottom a Coomassie stain of the same gel. (**C**) TCMDC-135051 inhibition of recombinant *Pf*CLK3 and the G449P mutant. (**D**) Maximal kinase activity of recombinant *Pf*CLK3 compared to the activity of the G449P mutant. (**E**) Schematic of gene targeting strategy that would result in the expression of the G449P mutant (containing a triple HA tag) in place of wild-type *Pf*CLK3. (**F**) The recombination event illustrated in (E) was identified in cloned G449P parasite cultures by PCR (A3 and A8). (**G**) Expression of the triple HA-tagged G449P mutant in genetically engineered parasite cultures (G449P) was determined by Western blotting. Left, gel probe of lysates with antibodies to HA; center, a loading control probed with antibodies to *Pf*CDPK1; right, a Coomassie stain of the lysate preparations used in the Western blots. (**H**) Growth inhibition curves of TCMDC-135051 against parent 3D7 parasites and G449P parasites (A3 and A8). Data in (C), (D), and (H) are means ± SEM of at least three independent experiments. *$P < 0.05$ (t test).

sensitivity to an inhibitor. By swapping residues between the kinases, we introduced inhibitor insensitivity into our target kinase (e.g., *Pf*CLK3) in a strategy that could be applied to other protein kinases.

Inhibition of *Pf*CLK3 prevents trophozoite-to-schizont transition

To characterize the phenotypic response to *Pf*CLK3 inhibition and to understand *Pf*CLK3 function, we treated *P. falciparum* 3D7 parasites synchronized at ring stage (time point zero) with 1 μM TCMDC-135051. The parasites progressed to late ring stage (time point 20 hours) (Fig. 4A) but did not progress further to trophozoite stage (time point 30 and 40 hours), arresting with a condensed and shrunken appearance (Fig. 4A). Similar effects were observed if the parasites were treated at mid-ring stage (time point 10 hours). Treatment of the parasite at later time points (20 or 30 hours) blocked development of the parasite from the trophozoite to the schizont stage. The fact that the parasites at the schizont stage were not viable was further evidenced by the absence of ring-stage parasites when the culture was continued to the 50-hour time point (Fig. 4A). These data indicated that *Pf*CLK3 inhibition prevented the transition of the parasites at early stages (ring to trophozoite) as well as late stages (trophozoite to schizont) of development and did not allow parasites to reach the next invasion cycle (Fig. 4A). These data further indicated that *Pf*CLK3 inhibition resulted in rapid killing, with no evidence that the compound resulted in quiescence from which the parasite could recover after drug withdrawal. These features were confirmed in parasite reduction rate assays, which showed that treatment of parasites with 10 × EC_{50} of TCMDC-135051 completely killed the parasite in 48 hours; viable parasites could not be observed despite maintaining the parasite culture for 28 days after withdrawal of TCMDC-135051 (Fig. 4B).

Inhibition of *Pf*CLK3 disrupts transcription

Because *Pf*CLK3 has been proposed to regulate RNA processing (*20*) and is closely related to the human kinases PRPF4B and CLK2 that are involved in RNA splicing (*19*), we investigated changes in gene transcription in parent Dd2 parasites and the drug-resistant stain TM051C in response to exposure to TCMDC-135051. RNA isolated from trophozoite-stage parasites was extracted after treatment with 1 μM TCMDC-135051 for 60 min, during which the Dd2 and TM051C parasites maintained normal morphology. Genome-wide transcriptional patterns were determined using oligonucleotide microarray chips that probed 5752 *P. falciparum* genes (*31*). Under these conditions, 779 gene transcripts were significantly down-regulated in response to *Pf*CLK3 inhibition in the Dd2 parasites and 155 genes were up-regulated (Fig. 4C and table S2). That the majority of these transcriptional changes were due to inhibition of *Pf*CLK3 and not off-target events was supported by the fact that under the same conditions, only six genes were up-regulated and 88 down-regulated in the resistant TM051C parasite strain (Fig. 4D and table S3). By subtracting the transcriptional changes observed in the TM051C strain, defined here as "off-target," from those observed with the Dd2 parent, the transcriptional changes due to "on-target" inhibition of *Pf*CLK3 were defined

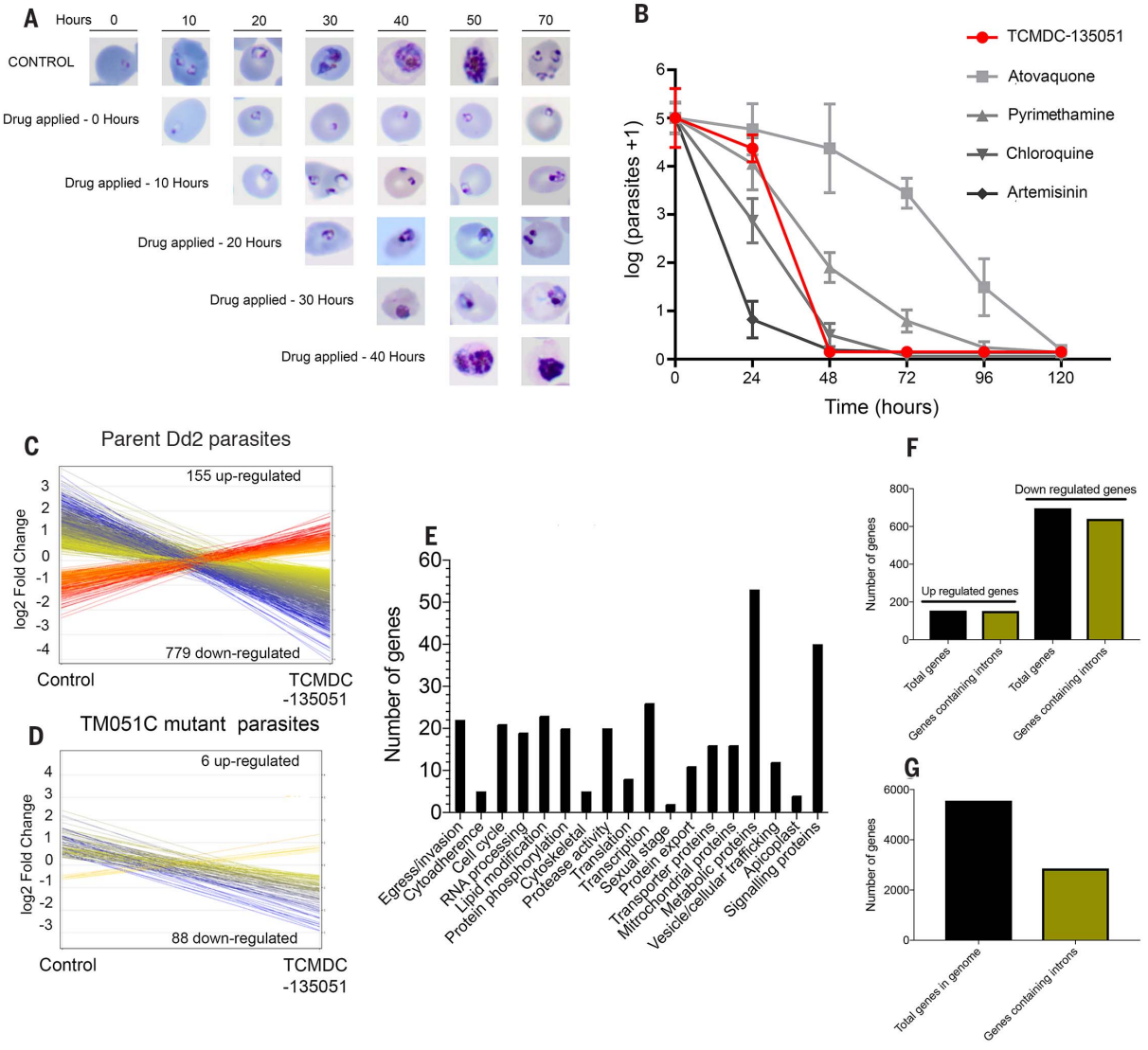

Fig. 4. Inhibition of *Pf*CLK3 prevents trophozoite-to-schizont transition, kills the parasite with rapid kinetics, and disrupts gene transcription. (**A**) Smears of synchronized blood-stage *P. falciparum* cultures after treatment with TCMDC-135051 (2 μM) were taken at the indicated times after TCMDC-135051 administration. (**B**) The in vitro parasite reduction rate in the presence of 10 × EC_{50} of TCMDC-135051 was used to determine the onset of action and rate of killing. Data are means ± SEM. Previous results reported on standard antimalarials tested at 10 × EC_{50} using the same conditions are shown for comparison (*44*). (**C** and **D**) Illustration of the genes that are designated as significantly changing (moderate *t* test, $n = 4$) in transcription after treatment with TCMDC-135051 (1 μM, 60 min) of either (C) parent Dd2 parasites or (D) TM051C mutant parasites. Each line represents the $\log_2$ fold change in the probes used in the microarray. Numbers of genes represented by the probes are indicated. (**E**) Summary of the parasite processes associated with the genes where transcription is statistically significantly down-regulated after TCMDC-135051 treatment. (**F**) Assessment of intron-containing genes among genes that are up-regulated and down-regulated in Dd2 parasites after TCMDC-135051 treatment. (**G**) Assessment of intron-containing genes in the *P. falciparum* genome (data derived from Plasmodb).

(table S4). Among these "on-target" down-regulated genes were those involved in key parasite processes, such as egress and invasion, cytoadherence, parasite protein export, and involvement in sexual stages, as well as housekeeping functions including metabolism, RNA processing, lipid modification, and mitochondrial function (Fig. 4E and table S4). Of the 696 "on-target" genes identified as down-regulated by *Pf*CLK3 inhibition (table S4), 425 matched those that have recently been determined to be essential for asexual *P. falciparum* survival (*12*) (table S4).

Gene ontology enrichment analysis was used to determine biological functions that were disproportionally down-regulated by *Pf*CLK3 inhibition. In this analysis, genes associated with key biological functions, particularly protein modification, phospholipid biosynthesis, and lipid modification, were significantly overrepresented among those genes that were down-regulated (fig. S8 and table S5). We found that 93% of the "on-target" down-regulated genes contained introns (Fig. 4F and table S4), versus 52% of genes in the *P. falciparum* genome that are annotated as containing introns (*32*) (Fig. 4G). Hence, *Pf*CLK3 inhibition significantly affected the transcription of genes that contained introns ($P < 0.0001$, Pearson χ^2 test), further supporting its role in splicing.

In addition to the nearly 700 genes down-regulated in response to *Pf*CLK3 inhibition, there were 154 genes that were significantly

up-regulated (table S4). Among these were genes associated with RNA processing, such as splicing factor 1 (PF3D7_1321700) and pre-mRNA splicing factor SYF1 (PF3D7_1235900), indicating that at least some of the up-regulated genes may represent compensatory mechanisms. In support of this notion was the finding that *Pf*CLK3 itself was within the up-regulated genes (table S4).

Cross-species and in vivo activity of TCMDC-135051

It might be predicted that the close similarity between orthologs of CLK3 in different malaria parasite species would result in TCMDC-135051 showing similar activities against CLK3 from different *Plasmodium* species. This indeed was the case, as in vitro kinase assays using recombinant *Pv*CLK3 (*P. vivax*) and *Pb*CLK3 (*P. berghei*) (fig. S9, A and B) showed that TCMDC-135051 had near-equipotent inhibition at these two orthologs, with pIC_{50} values of 7.47 ± 0.12 (IC_{50} = 0.033 μM) and 7.86 ± 0.10 (IC_{50} = 0.013 μM), respectively (fig. S10, A and B). Furthermore, in asexual blood-stage cultures of both *P. knowlesi* (an experimental model for *P. vivax*) and *P. berghei* [a rodent malaria model used for in vivo drug testing (*33*)], inhibition of CLK3 by TCMDC-135051 resulted in parasiticidal activity in both of these *Plasmodium* species (Fig. 5, A and B). The potent and efficacious effects of TCMDC-135051 in blood *P. berghei* cultures prompted an investigation of the in vivo activity of TCMDC-135051 in mice infected with *P. berghei*. Twice-daily intraperitoneal dosing of TCMDC-135051 into mice infected with *P. berghei* resulted in a dose-related reduction in parasitemia over a 5-day infection period, where the maximal dose (50 mg/kg) resulted in near-complete clearance of parasites from peripheral blood (Fig. 5C).

Activity of TCMDC-135051 at liver invasion and sporozoite development

TCMDC-135051 showed potent activity against *P. berghei* sporozoites in a liver invasion and development assay (*34*) in which the compound showed a pEC_{50} value of 6.17 ± 0.10 (EC_{50} = 0.40 μM) (fig. S11), although hepatocyte toxicity (fig. S11) was observed but only significantly at 10 μM (fig. S11).

Targeting *Pf*CLK3 reduces transmission to the mosquito vector

The effects of *Pf*CLK3 inhibition on sexual-stage parasites were tested in an assay developed using the *P. falciparum Pf*2004 parasite strain, which shows high levels of gametocyte production (*35*). TCMDC-135051 showed potent parasiticidal activity in asexual-stage *Pf*2004 (fig. S12A) [pEC_{50} in *Pf*2004 = 6.58 ± 0.01 (EC_{50} = 0.26 μM)] similar to that seen in asexual 3D7 and Dd2 parasites. In addition, TCMDC-135051 showed inhibitory activity between commitment of infected red blood cells to stage II gametocytes [pEC_{50} = 6.04 ± 0.11 (EC_{50} = 0.91 μM)] (fig. S12B).

These in vitro studies were followed by mosquito membrane feeding assays to test directly the impact of *Pf*CLK3 inhibition on transmission of *P. falciparum* to the mosquito vector. In these experiments, stage II gametocytes (from 3D7 parasites) were exposed to TCMDC-135051 and allowed to develop to stage V in the continued presence of drug. These experiments showed a concentration-dependent decrease in stage V gametocyte number (Fig. 5D). When analyzed using a generalized linear mixed model (GLMM), this effect had a potency of EC_{50} = 0.8 μM (Fig. 5E). Furthermore, the inhibition of *Pf*CLK3 showed a statistically significant decrease in exflagellation (Fig. 5, F and G; EC_{50} = 0.2 μM), which, combined with the effect on gametocyte number, contributed to a statistically significant reduction in transmission, as measured by the prevalence of oocysts in the gut of mosquitos in membrane feeding assays (Fig. 5, H and I).

These studies were further extended to test the effects of *Pf*CLK3 inhibition on stage V gametocytes. Although exposure of stage V gametocytes to TCMDC-135051 for 24 hours did not affect gametocyte number (fig. S13, A and B), a small but significant reduction in exflagellation (~25% reduction, $P < 2 \times 10^{-16}$ as determined by GLMM) was observed at the highest concentration tested (fig. S13, C and D). A more pronounced effect was observed in membrane feeding experiments where mosquito transmission was significantly reduced by ~50% (fig. S13, E and F, $P = 4.33 \times 10^{-6}$). A reduction of mosquito infection prevalence of 50% is likely to have a major effect in field conditions where infection rates in mosquitos are usually <5%.

Discussion

Our results identify *Pf*CLK3 as a valid and druggable antimalarial target for both sexual and asexual stages of parasite development,

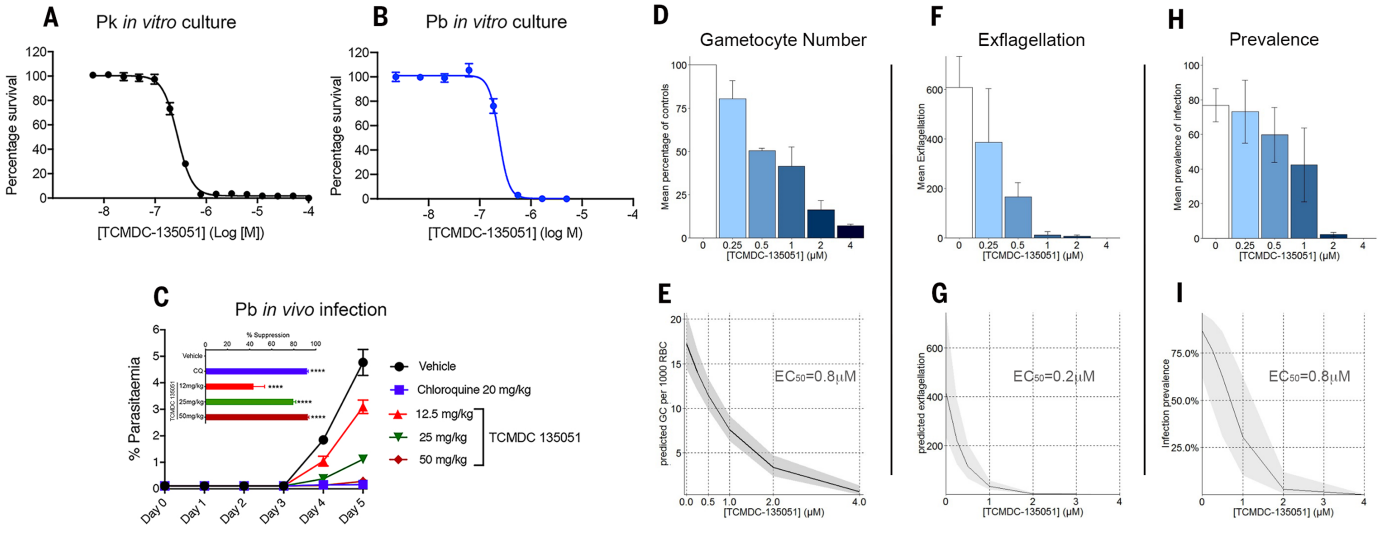

Fig. 5. Inhibition of *Pf*CLK3 has parasiticidal activity at multiple parasite species, shows in vivo parasiticidal activity in *P. berghei*, blocks gametocyte development, and reduces transmission to the mosquito vector. (**A** and **B**) Concentration effect curve of TCMDC-135051 on blood-stage *P. knowlesi* (A) and *P. berghei* (B) parasites. (**C**) TCMDC-135051 *P. berghei* in vivo growth inhibition curves and day 4 percentage suppression plots (inset). Error bars are SD from *n* = 4 mice groups. Statistical comparisons between mice treated with drug and vehicle are shown using one-way analysis of variance and Dunnett multiple-comparisons test. ****$P < 0.0001$. (**D** to **I**) Concentration effect of exposure of stage II to V *P. falciparum* (clone 3D7) gametocytes to TCMDC-135051 on gametocyte (GC) numbers in culture [(D) and (E)], exflagellation [(F) and (G)], and prevalence (number of mosquitos with oocyst infection per number of mosquitos dissected) of infection of *Anopheles coluzzii* mosquitos [(H) and (I)]. (D), (F), and (H) show means ± SEM of four independent experiments; (E), (G), and (I) show the predicted effects of drug concentrations according to the maximal GLMM, with the shaded area indicating 95% confidence intervals. From the GLMM analysis, the approximate EC_{50} values were calculated.

including the liver stage. This suggests that targeting *Pf*CLK3 might be a novel strategy for developing curative treatments for malaria by clearance of asexual blood-stage parasites and as a potential prophylactic by targeting the liver stage; moreover, the parasiticidal activity afforded by *Pf*CLK3 inhibition at gametocytes would indicate that through this mechanism, transmission to the insect vector could also be affected. Because splicing of essential transcripts occurs at many stages of the parasite life cycle, it is attractive to hypothesize that inhibition of *Pf*CLK3, which has been implicated in the phosphorylation of splicing factors necessary for the assembly and activity of the spliceosome (*17*, *18*, *20*), would have a wide-ranging impact on parasite viability. In support of this notion is the finding that *Pf*CLK3 inhibition down-regulated more than 400 essential parasite transcripts. Interestingly, the majority of down-regulated transcripts are from genes that contain introns (91%), providing further evidence that *Pf*CLK3 is involved in RNA splicing and that disruption of this essential process at multiple life-cycle stages is the likely mechanism by which inhibitors of *Pf*CLK3 have parasiticidal activity.

The similarity of CLK3 orthologs in *Plasmodium* spp. suggests that inhibitors might also have activity across a number of *Plasmodium* species. This was confirmed here by almost equipotent inhibition of the kinase activity of *Pv*CLK3, *Pb*CLK3, and *Pf*CLK3 by TCMDC-135051. This in vitro action was mirrored by ex vivo activity in *P. berghei* and *P. falciparum* but also in *P. knowlesi* (a model for *P. vivax*), indicating that inhibition of *Plasmodium* CLK might have cross-species activity. This, coupled to the reduction in transmission after *Pf*CLK3 inhibition, points to *Pf*CLK3 satisfying many of the criteria set by MMV for a suitable target for next-generation antimalarials—namely, a target that can deliver rapid, multistage parasite killing across multiple species with action as a transmission blocker (*36*).

One of the major barriers associated with the development of protein kinase inhibitors is the issue of selectivity, because the ATP binding pocket, to which the majority of protein kinase inhibitors bind, is very similar between protein kinases (*37*). Here, TCMDC-135051 showed surprising selectivity toward *Pf*CLK3 even when compared to its paralog in *P. falciparum Pf*CLK1 and its human ortholog (PRPF4B) and the closely related human kinase CLK2. Furthermore, our transcriptional studies revealed very few off-target events, and adaptive resistance and chemogenetic resistance were associated with single point mutations in *Pf*CLK3; these findings indicate that the selectivity of TCMDC-135051 for *Pf*CLK3 observed in vitro was maintained in the parasite. The fact that a hit from a library screen can show such selectivity against human and parasite kinases provides encouragement that *Pf*CLK3-selective inhibitors can be generated that might provide therapeutic efficacy with low off-target toxicity.

Lipid kinases such as phosphatidylinositol 4-kinase are considered promising targets (*38*) in malaria, and there is abundant evidence that phosphorylation and phosphosignaling are crucial for the viability of both asexual and sexual stages of the malaria parasite (*5*, *8*, *10*, *11*). Essential parasite protein kinase targets have been identified (*8*, *11*), and academic and industrial laboratories have gained much experience in the design of protein kinase inhibitor drugs (*14*, *37*). But despite these developments, the targeting of parasite protein kinases in antimalarial drug development is only in its infancy (*6*, *39*). By focusing on an essential parasite kinase and taking advantage of high-throughput phenotypic screens of commercial and academic libraries (*21*, *40*, *41*) as a starting point to screen for inhibitors, we have identified a probe molecule that has not only established the validity of *Pf*CLK3 as a target in malaria but also determined that this protein kinase is susceptible to selective pharmacological inhibition by small drug-like molecules. In this way, our study lends weight to the argument that targeting the essential parasite protein kinases identified through global genomic studies might be a valid therapeutic strategy in the development of molecules that meet many of the criteria set for the next generation of antimalarial drugs.

Methods summary

See supplementary materials for details.

High-throughput screening

Compounds were tested in single shot at 10 μM, or in dose response from 100 μM (11-point, 3-fold serial dilutions). Screening was performed in 1536-well plates, with final reaction and read-out volumes of 4 μl and 6 μl, respectively. The results from the high-throughput screening were further analyzed using Activity Base (ID Business Solutions Ltd., Surrey, UK). For each test compound, percent inhibition was plotted against compound concentration.

Evolution of compound-resistant lines and whole-genome sequencing

The *P. falciparum* Dd2 strain was cultured in triplicate in the presence of increasing concentrations of TCMDC-135051 to generate resistant mutants as described (*42*). After approximately 60 days of selection, parasites were cloned in 96-well plates by limiting dilution (*43*). The half-maximal (50%) inhibitory concentration was determined in dose-response format using a SYBR Green-I–based cell proliferation assay as described (*41*). To determine genetic variants that arose during selection, genomic DNA was sequenced on an Illumina Mi-seq and single-nucleotide variants were detected using the Genome Analysis Toolkit (GATK v1.6).

Generation of G449 mutant parasite

A fragment of the *Pf*CLK3 gene containing part of exon2, exon 3, exon 4, and part of exon 5 (1143 bp), corresponding to 655 to 1797 bp in clk3 genomic sequence, was amplified using primer CLK3-HR1 and CLK3-HR2 and the amplified product named as *Pf*CLK3. The homologous region (CLK3-HR) was cloned in pHH1-derived vector using restriction sites HpaI and BglII. The rest of the clk3 gene sequence downstream of CLK3-HR, corresponding to 1798 to 3152 bp of the *Pf*Clk3 genomic sequence, was modified by removing introns and the stop codon, and the coding sequence was optimized for *E. coli* codon usage to make it dissimilar to *Pf*clk3 genomic sequence. This fragment of gene, which we named as *Pf*CLK3-codon optimized (CLK3-CO), was commercially synthesized and included BglII recognition site at 5′ and XhoI recognition site at 3′. CLK3-CO was cloned downstream of CLK3-HR region in the parent plasmid using BglII and XhoI restriction sites in such a way that the triple HA tag sequence in the parent plasmid remained in frame with the *Pf*Clk3 sequence. The BglII restriction site that was artificially introduced for cloning purpose was mutated back to original *Pf*CLK3 coding sequence by site-directed mutagenesis using CLK3-BglII-KN1 and CLK3-BglII-KN2 primers. Site-directed mutagenesis was used again to mutate Gly in *Pf*CLK3 at position 449 to Ala. The targeting vector generated was used for transfection of schizont-stage parasites.

REFERENCES AND NOTES

1. J. Straimer *et al*., K13-propeller mutations confer artemisinin resistance in Plasmodium falciparum clinical isolates. *Science* **347**, 428–431 (2015). doi: 10.1126/science.1260867; pmid: 25502314
2. F. Ariey *et al*., A molecular marker of artemisinin-resistant Plasmodium falciparum malaria. *Nature* **505**, 50–55 (2014). doi: 10.1038/nature12876; pmid: 24352242
3. C. Amaratunga *et al*., Dihydroartemisinin-piperaquine resistance in Plasmodium falciparum malaria in Cambodia: A multisite prospective cohort study. *Lancet Infect. Dis.* **16**, 357–365 (2016). doi: 10.1016/S1473-3099(15)00487-9; pmid: 26774243
4. R. Leang *et al*., Evidence of Plasmodium falciparum Malaria Multidrug Resistance to Artemisinin and Piperaquine in Western Cambodia: Dihydroartemisinin-Piperaquine Open-Label Multicenter Clinical Assessment. *Antimicrob. Agents Chemother.* **59**, 4719–4726 (2015). doi: 10.1128/AAC.00835-15; pmid: 26014949
5. M. M. Alam *et al*., Phosphoproteomics reveals malaria parasite Protein Kinase G as a signalling hub regulating egress and invasion. *Nat. Commun.* **6**, 7285 (2015). doi: 10.1038/ncomms8285; pmid: 26149123
6. C. Doerig, J. C. Rayner, A. Scherf, A. B. Tobin, Post-translational protein modifications in malaria parasites. *Nat. Rev. Microbiol.* **13**, 160–172 (2015). doi: 10.1038/nrmicro3402; pmid: 25659318
7. E. Lasonder, M. Treeck, M. Alam, A. B. Tobin, Insights into the Plasmodium falciparum schizont phospho-proteome. *Microbes Infect.* **14**, 811–819 (2012). doi: 10.1016/j.micinf.2012.04.008
8. L. Solyakov *et al*., Global kinomic and phospho-proteomic analyses of the human malaria parasite Plasmodium falciparum. *Nat. Commun.* **2**, 565 (2011). doi: 10.1038/ncomms1558; pmid: 22127061
9. C. Doerig *et al*., Protein kinases of malaria parasites: An update. *Trends Parasitol.* **24**, 570–577 (2008). doi: 10.1016/j.pt.2008.08.007; pmid: 18845480
10. E. Bushell *et al*., Functional Profiling of a Plasmodium Genome Reveals an Abundance of Essential Genes. *Cell* **170**, 260–272. e8 (2017). doi: 10.1016/j.cell.2017.06.030
11. R. Tewari *et al*., The systematic functional analysis of Plasmodium protein kinases identifies essential regulators of mosquito transmission. *Cell Host Microbe* **8**, 377–387 (2010). doi: 10.1016/j.chom.2010.09.006; pmid: 20951971
12. M. Zhang *et al*., Uncovering the essential genes of the human malaria parasite Plasmodium falciparum by saturation mutagenesis. *Science* **360**, eaap7847 (2018). doi: 10.1126/science.aap7847
13. S. Gross, R. Rahal, N. Stransky, C. Lengauer, K. P. Hoeflich, Targeting cancer with kinase inhibitors. *J. Clin. Invest.* **125**, 1780–1789 (2015). doi: 10.1172/JCI76094; pmid: 25932675

14. L. N. Johnson, Protein kinase inhibitors: Contributions from structure to clinical compounds. *Q. Rev. Biophys.* **42**, 1–40 (2009). doi: 10.1017/S0033583508004745; pmid: 19296866
15. C. Doerig *et al*., Malaria: Targeting parasite and host cell kinomes. *Biochim. Biophys. Acta* **1804**, 604–612 (2010). doi: 10.1016/j.bbapap.2009.10.009; pmid: 19840874
16. Z. Zhou, X. D. Fu, Regulation of splicing by SR proteins and SR protein-specific kinases. *Chromosoma* **122**, 191–207 (2013). doi: 10.1007/s00412-013-0407-z; pmid: 23525660
17. S. Agarwal *et al*., Two nucleus-localized CDK-like kinases with crucial roles for malaria parasite erythrocytic replication are involved in phosphorylation of splicing factor. *J. Cell. Biochem.* **112**, 1295–1310 (2011). doi: 10.1002/jcb.23034; pmid: 21312235
18. E. Talevich, A. Mirza, N. Kannan, Structural and evolutionary divergence of eukaryotic protein kinases in Apicomplexa. *BMC Evol. Biol.* **11**, 321 (2011). doi: 10.1186/1471-2148-11-321; pmid: 22047078
19. M. Schneider *et al*., Human PRP4 kinase is required for stable tri-snRNP association during spliceosomal B complex formation. *Nat. Struct. Mol. Biol.* **17**, 216–221 (2010). doi: 10.1038/nsmb.1718; pmid: 20118938
20. S. Kern *et al*., Inhibition of the SR protein-phosphorylating CLK kinases of Plasmodium falciparum impairs blood stage replication and malaria transmission. *PLOS ONE* **9**, e105732 (2014). doi: 10.1371/journal.pone.0105732; pmid: 25188378
21. F. J. Gamo *et al*., Thousands of chemical starting points for antimalarial lead identification. *Nature* **465**, 305–310 (2010). doi: 10.1038/nature09107; pmid: 20485427
22. P. Dranchak *et al*., Profile of the GSK published protein kinase inhibitor set across ATP-dependent and-independent luciferases: Implications for reporter-gene assays. *PLOS ONE* **8**, e57888 (2013). doi: 10.1371/journal.pone.0057888; pmid: 23505445
23. R. Axel, Scents and sensibility: A molecular logic of olfactory perception (Nobel lecture). *Angew. Chem. Int. Ed.* **44**, 6110–6127 (2005). doi: 10.1002/anie.200501726; pmid: 16175526
24. T. Spangenberg *et al*., The open access malaria box: A drug discovery catalyst for neglected diseases. *PLOS ONE* **8**, e62906 (2013). doi: 10.1371/journal.pone.0062906; pmid: 23798988
25. Q. Gao *et al*., Evaluation of cancer dependence and druggability of PRP4 kinase using cellular, biochemical, and structural approaches. *J. Biol. Chem.* **288**, 30125–30138 (2013). doi: 10.1074/jbc.M113.473348; pmid: 24003220
26. J. M. Fraile *et al*., USP39 Deubiquitinase Is Essential for *KRAS* Oncogene-driven Cancer. *J. Biol. Chem.* **292**, 4164–4175 (2017). doi: 10.1074/jbc.M116.762757; pmid: 28154181
27. H. Hadjivassiliou, O. S. Rosenberg, C. Guthrie, The crystal structure of S. cerevisiae Sad1, a catalytically inactive deubiquitinase that is broadly required for pre-mRNA splicing. *RNA* **20**, 656–669 (2014). doi: 10.1261/rna.042838.113; pmid: 24681967
28. O. V. Makarova, E. M. Makarov, R. Lührmann, The 65 and 110 kDa SR-related proteins of the U4/U6.U5 tri-snRNP are essential for the assembly of mature spliceosomes. *EMBO J.* **20**, 2553–2563 (2001). doi: 10.1093/emboj/20.10.2553; pmid: 11350945
29. R. Hui, M. El Bakkouri, L. D. Sibley, Designing selective inhibitors for calcium-dependent protein kinases in apicomplexans. *Trends Pharmacol. Sci.* **36**, 452–460 (2015). doi: 10.1016/j.tips.2015.04.011; pmid: 26002073
30. S. Lourido *et al*., Calcium-dependent protein kinase 1 is an essential regulator of exocytosis in Toxoplasma. *Nature* **465**, 359–362 (2010). doi: 10.1038/nature09022; pmid: 20485436
31. B. F. Kafsack, H. J. Painter, M. Llinás, New Agilent platform DNA microarrays for transcriptome analysis of Plasmodium falciparum and Plasmodium berghei for the malaria research community. *Malar. J.* **11**, 187 (2012). doi: 10.1186/1475-2875-11-187; pmid: 22681930
32. M. J. Gardner *et al*., Genome sequence of the human malaria parasite Plasmodium falciparum. *Nature* **419**, 498–511 (2002). doi: 10.1038/nature01097; pmid: 12368864
33. D. A. Fidock, P. J. Rosenthal, S. L. Croft, R. Brun, S. Nwaka, Antimalarial drug discovery: Efficacy models for compound screening. *Nat. Rev. Drug Discov.* **3**, 509–520 (2004). doi: 10.1038/nrd1416; pmid: 15173840
34. J. Swann *et al*., High-Throughput Luciferase-Based Assay for the Discovery of Therapeutics That Prevent Malaria. *ACS Infect. Dis.* **2**, 281–293 (2016). doi: 10.1021/acsinfecdis.5b00143; pmid: 27275010
35. N. M. Brancucci, I. Goldowitz, K. Buchholz, K. Werling, M. Marti, An assay to probe Plasmodium falciparum growth, transmission stage formation and early gametocyte development. *Nat. Protoc.* **10**, 1131–1142 (2015). doi: 10.1038/nprot.2015.072; pmid: 26134953
36. J. N. Burrows *et al*., New developments in anti-malarial target candidate and product profiles. *Malar. J.* **16**, 26 (2017). doi: 10.1186/s12936-016-1675-x; pmid: 28086874
37. R. Roskoski Jr., A historical overview of protein kinases and their targeted small molecule inhibitors. *Pharmacol. Res.* **100**, 1–23 (2015). doi: 10.1016/j.phrs.2015.07.010; pmid: 26207888
38. C. W. McNamara *et al*., Targeting Plasmodium PI(4)K to eliminate malaria. *Nature* **504**, 248–253 (2013). doi: 10.1038/nature12782; pmid: 24284631
39. I. S. Lucet, A. Tobin, D. Drewry, A. F. Wilks, C. Doerig, Plasmodium kinases as targets for new-generation antimalarials. *Future Med. Chem.* **4**, 2295–2310 (2012). doi: 10.4155/fmc.12.183; pmid: 23234552
40. W. A. Guiguemde *et al*., Chemical genetics of Plasmodium falciparum. *Nature* **465**, 311–315 (2010). doi: 10.1038/nature09099; pmid: 20485428
41. D. Plouffe *et al*., In silico activity profiling reveals the mechanism of action of antimalarials discovered in a high-throughput screen. *Proc. Natl. Acad. Sci. U.S.A.* **105**, 9059–9064 (2008). doi: 10.1073/pnas.0802982105; pmid: 18579783
42. M. Rottmann *et al*., Spiroindolones, a potent compound class for the treatment of malaria. *Science* **329**, 1175–1180 (2010). doi: 10.1126/science.1193225; pmid: 20813948
43. I. D. Goodyer, T. F. Taraschi, Plasmodium falciparum: A simple, rapid method for detecting parasite clones in microtiter plates. *Exp. Parasitol.* **86**, 158–160 (1997). doi: 10.1006/expr.1997.4156; pmid: 9207746
44. L. M. Sanz *et al*., P. falciparum in vitro killing rates allow to discriminate between different antimalarial mode-of-action. *PLOS ONE* **7**, e30949 (2012). doi: 10.1371/journal.pone.0030949; pmid: 22383983

ACKNOWLEDGMENTS

We thank the Proteomics facility of LaCTAD (Laboratório Central de Tecnologias de Alto Desempenho em Ciências da Vida, UNICAMP, Campinas, Brazil); A. da Silva Santiago, A. M. Fala, and P. Zonzini Ramos for assistance with PRPF4B protein production; Aché Laboratórios Farmacêuticos for provision of compound A; E. Peat and D. Armstrong for the maintenance of the IBAHCM/Glasgow University mosquito insectaries; the Scottish National Blood Transfusion service for the provision of human blood and serum; N. Emami (Stockholm University) for assistance with serum supplies; P. Johnson (IBAHCM, University of Glasgow) for discussions on GLMM; and R. Tewari for providing the *P. berghei* cDNA library. **Funding:** Supported by an MRC Toxicology Unit program grant (A.B.T., M.M.A.), MRC Developmental Gap Fund (A.S.-A.), Lord Kelvin Adam Smith Fellowship (M.M.A.), GSK Open Lab Foundation Award (A.S.-A.), joint MRC Toxicology Unit and MRC Unit the Gambia PhD program (O.J.), and Daphne Jackson Fellowship (D.M.). A.P.W., M.M., M.M.A., K.C., N.V.S., and S.B.M. are supported by Wellcome Centre for Integrative Parasitology Core support award WT104111AIA. E.A.W. is supported by grants from the NIH (5R01AI090141 and R01AI103058) and by grants from the Bill & Melinda Gates Foundation (OPP1086217, OPP1141300) as well as by Medicines for Malaria Venture (MMV). Drug WR99210 for selection of transgenic parasites was a gift from Jacobus Pharmaceuticals. M.M. is supported through WT award 172862-01 and a Wolfson Merit award from the Royal Society. The Structural Genomics Consortium (SGC) is a registered charity (number 1097737) that receives funds from AbbVie, Bayer Pharma AG, Boehringer Ingelheim, the Canada Foundation for Innovation, the Eshelman Institute for Innovation, Genome Canada, the Innovative Medicines Initiative (European Union [EU]/European Federation of Pharmaceutical Industries and Associations [EFPIA]) (ULTRA-DD grant no. 115766), Janssen, Merck & Company, Merck KGaA, Novartis Pharma AG, the Ontario Ministry of Economic Development and Innovation, Pfizer, the São Paulo Research Foundation (FAPESP number 2013/50724-5), Takeda, and the Wellcome Trust (106169/ZZ14/Z). E.F.A. was supported by the Tres Cantos Lab Foundation (grant TC125). A.B.C. was supported by a Scottish Funding Council Global Challenges Research Fund award to L.C.R.-C. **Author contributions:** A.B.T. conceived the project, designed experiments, analyzed data, and was the primary author; M.M.A., A.S.-A., O.J., and L.C.R.-C. designed experiments, conducted experiments, analyzed data, and contributed to writing; E.L.F., A.M., K.M., A.B.C., D.S., N.M.B.B., S.B.M., Y.A.K., N.V.S., J.A., D.M., L.S., K.D., C.J., C.Z., M.J.V., M.J.L.-M., and M.L.L. conducted experiments; G.C. and K.C. conducted data analysis; P.H.C.G., J.M.E., D.C., D.C.N., A.P.W., A.G.J., E.F.A., M.M., E.A.W., and F.J.G. contributed to experimental design and to writing the manuscript. **Competing interests:** The authors declare no conflicts of interest. **Data and materials availability:** The GSK compounds were obtained under a materials transfer agreement from GSK. All other data are available in the manuscript or the supplementary materials. Some of the data in this manuscript have been deposited at www.biorxiv.org/content/10.1101/404459v1.article-info.

SUPPLEMENTARY MATERIALS

science.sciencemag.org/content/365/6456/eaau1682/suppl/DC1
Materials and Methods
Figs. S1 to S13
Tables S1 to S5
References (*45*–*51*)

11 July 2018; resubmitted 15 March 2019
Accepted 12 July 2019
10.1126/science.aau1682

RESEARCH ARTICLE

COMPUTER SCIENCE

Superhuman AI for multiplayer poker

Noam Brown[1,2]* and Tuomas Sandholm[1,3,4,5]*

In recent years there have been great strides in artificial intelligence (AI), with games often serving as challenge problems, benchmarks, and milestones for progress. Poker has served for decades as such a challenge problem. Past successes in such benchmarks, including poker, have been limited to two-player games. However, poker in particular is traditionally played with more than two players. Multiplayer games present fundamental additional issues beyond those in two-player games, and multiplayer poker is a recognized AI milestone. In this paper we present Pluribus, an AI that we show is stronger than top human professionals in six-player no-limit Texas hold'em poker, the most popular form of poker played by humans.

Poker has served as a challenge problem for the fields of artificial intelligence (AI) and game theory for decades (*1*). In fact, the foundational papers on game theory used poker to illustrate their concepts (*2*, *3*). The reason for this choice is simple: No other popular recreational game captures the challenges of hidden information as effectively and as elegantly as poker. Although poker has been useful as a benchmark for new AI and game-theoretic techniques, the challenge of hidden information in strategic settings is not limited to recreational games. The equilibrium concepts of von Neumann and Nash have been applied to many real-world challenges such as auctions, cybersecurity, and pricing.

The past two decades have witnessed rapid progress in the ability of AI systems to play increasingly complex forms of poker (*4*–*6*). However, all prior breakthroughs have been limited to settings involving only two players. Developing a superhuman AI for multiplayer poker was the widely recognized main remaining milestone. In this paper we describe Pluribus, an AI capable of defeating elite human professionals in six-player no-limit Texas hold'em poker, the most commonly played poker format in the world.

Theoretical and practical challenges of multiplayer games

AI systems have reached superhuman performance in games such as checkers (*7*), chess (*8*), two-player limit poker (*4*), Go (*9*), and two-player no-limit poker (*6*). All of these involve only two players and are zero-sum games (meaning that whatever one player wins, the other player loses). Every one of those superhuman AI systems was generated by attempting to approximate a Nash equilibrium strategy rather than by, for example, trying to detect and exploit weaknesses in the opponent. A Nash equilibrium is a list of strategies, one for each player, in which no player can improve by deviating to a different strategy. Nash equilibria have been proven to exist in all finite games—and many infinite games—though finding an equilibrium may be difficult.

Two-player zero-sum games are a special class of games in which Nash equilibria also have an extremely useful additional property: Any player who chooses to use a Nash equilibrium is guaranteed to not lose in expectation no matter what the opponent does (as long as one side does not have an intrinsic advantage under the game rules, or the players alternate sides). In other words, a Nash equilibrium strategy is unbeatable in two-player zero-sum games that satisfy the above criteria. For this reason, to "solve" a two-player zero-sum game means to find an exact Nash equilibrium. For example, the Nash equilibrium strategy for Rock-Paper-Scissors is to randomly pick Rock, Paper, or Scissors with equal probability. Against such a strategy, the best that an opponent can do in expectation is tie (*10*). In this simple case, playing the Nash equilibrium also guarantees that the player will not win in expectation. However, in more complex games, even determining how to tie against a Nash equilibrium may be difficult; if the opponent ever chooses suboptimal actions, then playing the Nash equilibrium will indeed result in victory in expectation.

In principle, playing the Nash equilibrium can be combined with opponent exploitation by initially playing the equilibrium strategy and then over time shifting to a strategy that exploits the opponent's observed weaknesses (for example, by switching to always playing Paper against an opponent that always plays Rock) (*11*). However, except in certain restricted ways (*12*), shifting to an exploitative nonequilibrium strategy opens oneself up to exploitation because the opponent could also change strategies at any moment. Additionally, existing techniques for opponent exploitation require too many samples to be competitive with human ability outside of small games. Pluribus plays a fixed strategy that does not adapt to the observed tendencies of the opponents.

Although a Nash equilibrium strategy is guaranteed to exist in any finite game, efficient algorithms for finding one are only proven to exist for special classes of games, among which two-player zero-sum games are the most prominent. No polynomial-time algorithm is known for finding a Nash equilibrium in two-player non-zero-sum games, and the existence of one would have sweeping surprising implications in computational complexity theory (*13*, *14*). Finding a Nash equilibrium in zero-sum games with three or more players is at least as hard (because

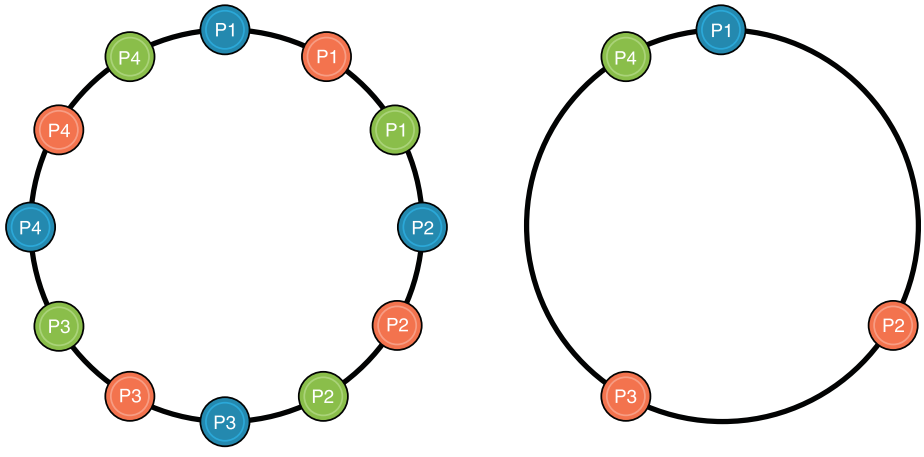

Fig. 1. An example of the equilibrium selection problem. In the Lemonade Stand Game, players simultaneously choose a point on a ring and want to be as far away as possible from any other player. In every Nash equilibrium, players are spaced uniformly around the ring. There are infinitely many such Nash equilibria. However, if each player independently chooses one Nash equilibrium to play, their joint strategy is unlikely to be a Nash equilibrium. (**Left**) An illustration of three different Nash equilibria in this game, distinguished by three different colors. (**Right**) Each player independently chooses one Nash equilibrium. Their joint strategy is not a Nash equilibrium.

[1]Computer Science Department, Carnegie Mellon University, Pittsburgh, PA 15213, USA. [2]Facebook AI Research, New York, NY 10003, USA. [3]Strategic Machine, Inc., Pittsburgh, PA 15213, USA. [4]Strategy Robot, Inc., Pittsburgh, PA 15213, USA. [5]Optimized Markets, Inc., Pittsburgh, PA 15213, USA.
*Corresponding author. Email: noamb@cs.cmu.edu (N.B.); sandholm@cs.cmu.edu (T.S.)

a dummy player can be added to the two-player game to make it a three-player zero-sum game). Even approximating a Nash equilibrium is hard (except in special cases) in theory (*15*), and in games with more than two players, even the best complete algorithm can only address games with a handful of possible strategies per player (*16*). Moreover, even if a Nash equilibrium could be computed efficiently in a game with more than two players, it is not clear that playing such an equilibrium strategy would be wise. If each player in such a game independently computes and plays a Nash equilibrium, the list of strategies that they play (one strategy per player) may not be a Nash equilibrium and players might have an incentive to deviate to a different strategy. One example of this is the Lemonade Stand Game (*17*), illustrated in Fig. 1, in which each player simultaneously picks a point on a ring and wants to be as far away as possible from any other player. The Nash equilibrium is for all players to be spaced uniformly along the ring, but there are infinitely many ways this can be accomplished and therefore infinitely many Nash equilibria. If each player independently computes one of those equilibria, the joint strategy is unlikely to result in all players being spaced uniformly along the ring. Two-player zero-sum games are a special case where even if the players independently compute and select Nash equilibria, the list of strategies is still a Nash equilibrium.

The shortcomings of Nash equilibria outside of two-player zero-sum games, and the failure of any other game-theoretic solution concept to convincingly overcome them, have raised the question of what the right goal should even be in such games. In the case of six-player poker, we take the viewpoint that our goal should not be a specific game-theoretic solution concept but rather to create an AI that empirically consistently defeats human opponents, including elite human professionals.

The algorithms that we used to construct Pluribus, discussed in the next two sections, are not guaranteed to converge to a Nash equilibrium outside of two-player zero-sum games. Nevertheless, we observe that Pluribus plays a strong strategy in multiplayer poker that is capable of consistently defeating elite human professionals. This shows that even though the techniques do not have known strong theoretical guarantees on performance outside of the two-player zero-sum setting, they are nevertheless capable of producing superhuman strategies in a wider class of strategic settings.

Description of Pluribus

The core of Pluribus's strategy was computed through self-play, in which the AI plays against copies of itself, without any data of human or prior AI play used as input. The AI starts from scratch by playing randomly and gradually improves as it determines which actions, and which probability distribution over those actions, lead to better outcomes against earlier versions of its strategy. Forms of self-play have previously been used to generate powerful AIs in two-player zero-sum games such as backgammon (*18*), Go (*9*, *19*), Dota 2 (*20*), StarCraft 2 (*21*), and two-player poker (*4*–*6*), though the precise algorithms that were used have varied widely. Although it is easy to construct toy games with more than two players in which commonly used self-play algorithms fail to converge to a meaningful solution (*22*), in practice self-play has nevertheless been shown to do reasonably well in some games with more than two players (*23*).

Pluribus's self-play produces a strategy for the entire game offline, which we refer to as the blueprint strategy. Then during actual play against opponents, Pluribus improves upon the blueprint strategy by searching for a better strategy in real time for the situations in which it finds itself during the game. In subsections below, we discuss both of those phases in detail, but first we discuss abstraction, forms of which are used in both phases to make them scalable.

Abstraction for large imperfect-information games

There are far too many decision points in no-limit Texas hold'em to reason about individually. To reduce the complexity of the game, we eliminate some actions from consideration and also bucket similar decision points together in a process called abstraction (*24*, *25*). After abstraction, the bucketed decision points are treated as identical. We use two kinds of abstraction in Pluribus: action abstraction and information abstraction.

Action abstraction reduces the number of different actions the AI needs to consider. No-limit Texas hold'em normally allows any whole-dollar bet between $100 and $10,000. However, in practice there is little difference between betting $200 and betting $201. To reduce the complexity of forming a strategy, Pluribus only considers a few different bet sizes at any given decision point. The exact number of bets it considers varies between 1 and 14 depending on the situation. Although Pluribus can limit itself to only betting one of a few different sizes between $100 and $10,000, when actually playing no-limit poker, the opponents are not constrained to those few options. What happens if an opponent bets $150 while Pluribus has only been trained to consider bets of $100 or $200? Generally, Pluribus

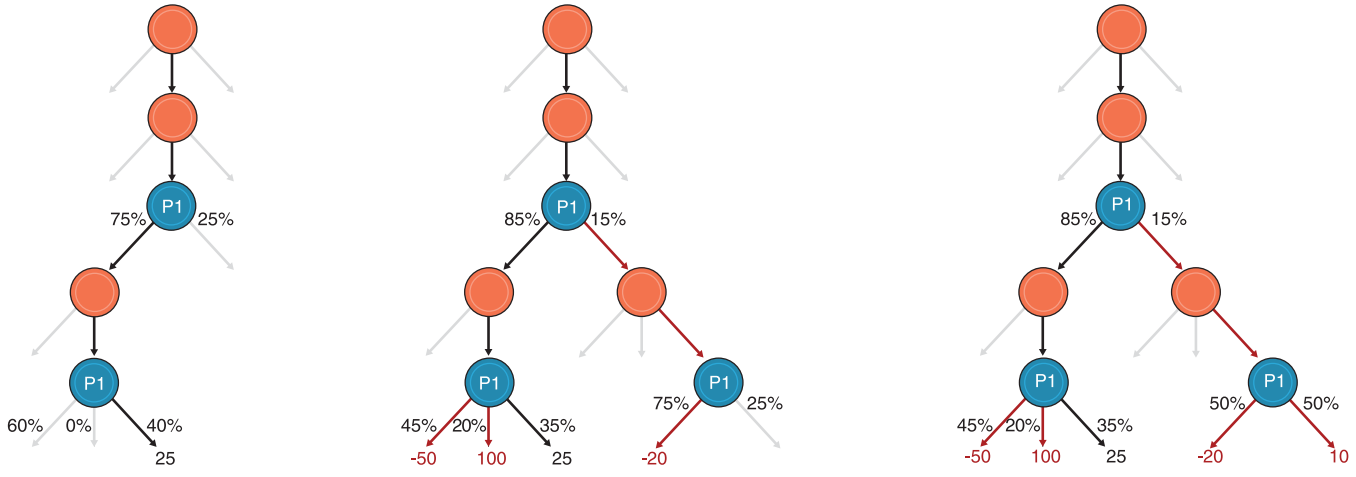

Fig. 2. A game tree traversal via Monte Carlo CFR. In this figure, player P_1 is traversing the game tree. (**Left**) A game is simulated until an outcome is reached. (**Middle**) For each P_1 decision point encountered in the simulation in the left panel, P_1 explores each other action that P_1 could have taken and plays out a simulation to the end of the game. P_1 then updates its strategy to pick actions with higher payoff with higher probability. (**Right**) P_1 explores each other action that P_1 could have taken at every new decision point encountered in the middle panel, and P_1 updates its strategy at those hypothetical decision points. This process repeats until no new P_1 decision points are encountered, which in this case is after three steps but in general may be more. Our implementation of MCCFR (described in the supplementary materials) is equivalent but traverses the game tree in a depth-first manner. (The percentages in the figure are for illustration purposes only and may not correspond to actual percentages that the algorithm would compute.)

will rely on its search algorithm (described in a later section) to compute a response in real time to such "off-tree" actions.

The other form of abstraction that we use in Pluribus is information abstraction, in which decision points that are similar in terms of what information has been revealed (in poker, the player's cards and revealed board cards) are bucketed together and treated identically (*26*–*28*). For example, a 10-high straight and a 9-high straight are distinct hands but are nevertheless strategically similar. Pluribus may bucket these hands together and treat them identically, thereby reducing the number of distinct situations for which it needs to determine a strategy. Information abstraction drastically reduces the complexity of the game, but it may wash away subtle differences that are important for superhuman performance. Therefore, during actual play against humans, Pluribus uses information abstraction only to reason about situations on future betting rounds, never the betting round that it is actually in. Information abstraction is also applied during offline self-play.

Self-play through improved Monte Carlo counterfactual regret minimization

The blueprint strategy in Pluribus was computed using a variant of counterfactual regret minimization (CFR) (*29*). CFR is an iterative self-play algorithm in which the AI starts by playing completely at random but gradually improves by learning to beat earlier versions of itself. Every competitive Texas hold'em AI for at least the past 6 years has computed its strategy using some variant of CFR (*4*–*6*, *23*, *28*, *30*–*34*). We use a form of Monte Carlo CFR (MCCFR) that samples actions in the game tree rather than traversing the entire game tree on each iteration (*33*, *35*–*37*).

On each iteration of the algorithm, MCCFR designates one player as the traverser whose current strategy is updated on the iteration. At the start of the iteration, MCCFR simulates a hand of poker based on the current strategy of all players (which is initially completely random). Once the simulated hand is completed, the AI reviews each decision that was made by the traverser and investigates how much better or worse it would have done by choosing the other available actions instead. Next, the AI reviews each hypothetical decision that would have been made following those other available actions and investigates how much better it would have done by choosing the other available actions, and so on. This traversal of the game tree is illustrated in Fig. 2. Exploring other hypothetical outcomes is possible because the AI knows each player's strategy for the iteration and can therefore simulate what would have happened had some other action been chosen instead. This counterfactual reasoning is one of the features that distinguishes CFR from other self-play algorithms that have been deployed in domains such as Go (*9*), Dota 2 (*20*), and StarCraft 2 (*21*).

The difference between what the traverser would have received for choosing an action versus what the traverser actually achieved (in expectation) on the iteration is added to the counterfactual regret for the action. Counterfactual regret represents how much the traverser regrets having not chosen that action in previous iterations. At the end of the iteration, the traverser's strategy is updated so that actions with higher counterfactual regret are chosen with higher probability.

For two-player zero-sum games, CFR guarantees that the average strategy played over all iterations converges to a Nash equilibrium, but convergence to a Nash equilibrium is not guaranteed outside of two-player zero-sum games. Nevertheless, CFR guarantees in all finite games that all counterfactual regrets grow sublinearly in the number of iterations. This, in turn, guarantees in the limit that the average performance of CFR on each iteration that was played matches the average performance of the best single fixed strategy in hindsight. CFR is also proven to eliminate iteratively strictly dominated actions in all finite games (*23*).

Because the difference between counterfactual value and expected value is added to counterfactual regret rather than replacing it, the first iteration in which the agent played completely randomly (which is typically a very bad strategy) still influences the counterfactual regrets, and therefore the strategy that is played, for iterations far into the future. In the original form of CFR, the influence of this first iteration decays at a rate of $\frac{1}{T}$, where T is the number of iterations played. To more quickly decay the influence of these early "bad" iterations, Pluribus uses a recent form of CFR called Linear CFR (*38*) in early iterations. (We stop the discounting after that because the time cost of doing the multiplications with the discount factor is not worth the benefit later on.) Linear CFR assigns a weight of T to the regret contributions of iteration T. Therefore, the influence of the first iteration decays at a rate of $\frac{1}{\sum_{t=1}^{T} t} = \frac{2}{T(T+1)}$. This leads to the strategy improving more quickly in practice while still maintaining a near-identical worst-case bound on total regret. To speed up the blueprint strategy computation even further, actions with extremely negative regret are not explored in 95% of iterations.

The blueprint strategy for Pluribus was computed in 8 days on a 64-core server for a total of 12,400 CPU core hours. It required less than 512 GB of memory. At current cloud computing spot instance rates, this would cost about $144 to produce. This is in sharp contrast to all the other recent superhuman AI milestones for games, which used large numbers of servers and/or farms of graphics processing units (GPUs). More memory

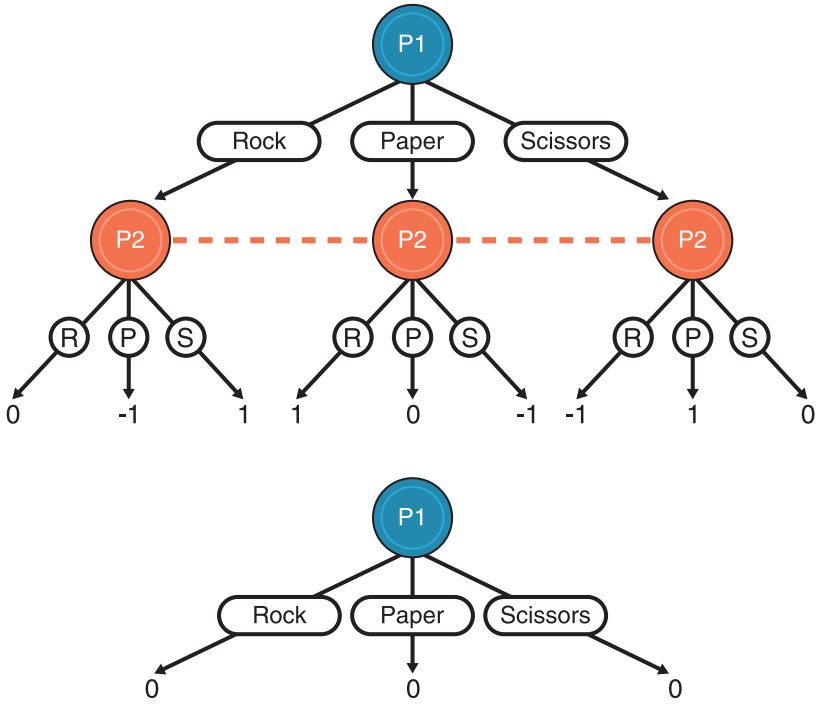

Fig. 3. Perfect-information game search in Rock-Paper-Scissors. (**Top**) A sequential representation of Rock-Paper-Scissors in which player 1 acts first but does not reveal her action to player 2, who acts second. The dashed lines between the player 2 nodes signify that player 2 does not know which of those nodes he is in. The terminal values are shown only for player 1. (**Bottom**) A depiction of the depth-limited subgame if player 1 conducts search (with a depth of one) using the same approach as is used in perfect-information games. The approach assumes that after each action, player 2 will play according to the Nash equilibrium strategy of choosing Rock, Paper, and Scissors with $\frac{1}{3}$ probability each. This results in a value of zero for player 1 regardless of her strategy.

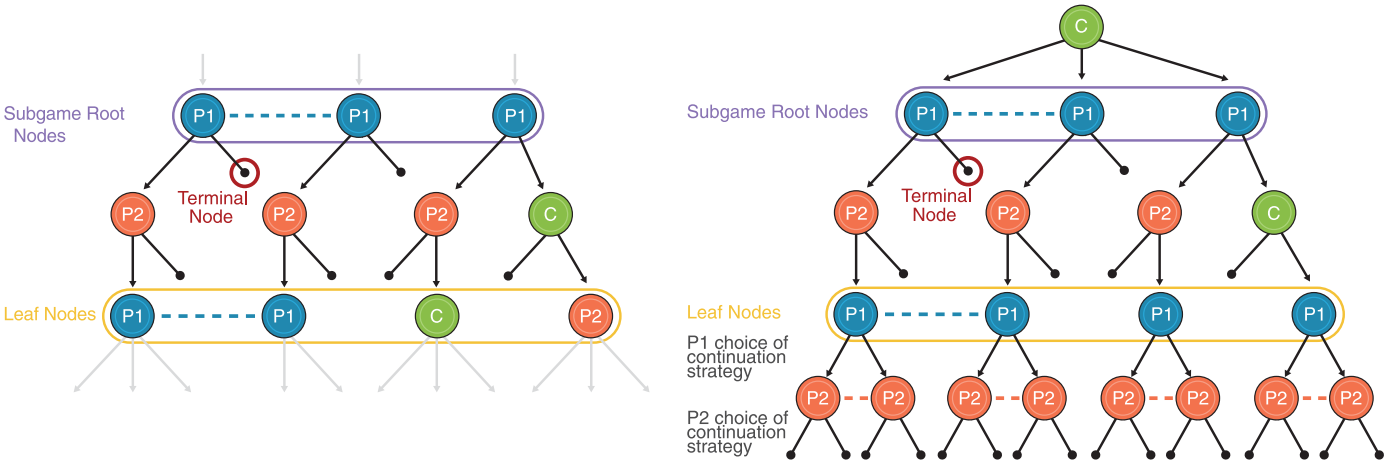

Fig. 4. Real-time search in Pluribus. The subgame shows just two players for simplicity. A dashed line between nodes indicates that the player to act does not know which of the two nodes she is in. (**Left**) The original imperfect-information subgame. (**Right**) The transformed subgame that is searched in real time to determine a player's strategy. An initial chance node reaches each root node according to the normalized probability that the node is reached in the previously computed strategy profile (or according to the blueprint strategy profile if this is the first time in the hand that real-time search is conducted). The leaf nodes are replaced by a sequence of new nodes in which each player still in the hand chooses among k actions, with no player first observing what another player chooses. For simplicity, $k = 2$ in the figure. In Pluribus, $k = 4$. Each action in that sequence corresponds to a selection of a continuation strategy for that player for the remainder of the game. This effectively leads to a terminal node (whose value is estimated by rolling out the remainder of the game according to the list of continuation strategies that the players chose).

and computation would enable a finer-grained blueprint that would lead to better performance but would also result in Pluribus using more memory or being slower during real-time search. We set the size of the blueprint strategy abstraction to allow Pluribus to run during live play on a machine with no more than 128 GB of memory while storing a compressed form of the blueprint strategy in memory.

Depth-limited search in imperfect-information games

The blueprint strategy for the entire game is necessarily coarse-grained owing to the size and complexity of no-limit Texas hold'em. Pluribus only plays according to this blueprint strategy in the first betting round (of four), where the number of decision points is small enough that the blueprint strategy can afford to not use information abstraction and have a lot of actions in the action abstraction. After the first round (and even in the first round if an opponent chooses a bet size that is sufficiently different from the sizes in the blueprint action abstraction), Pluribus instead conducts real-time search to determine a better, finer-grained strategy for the current situation it is in. For opponent bets on the first round that are slightly off the tree, Pluribus rounds the bet to a nearby on-tree size [using the pseudoharmonic mapping (*39*)] and proceeds to play according to the blueprint as if the opponent had used the latter bet size.

Real-time search has been necessary for achieving superhuman performance in many perfect-information games, including backgammon (*18*), chess (*8*), and Go (*9*, *19*). For example, when determining their next move, chess AIs commonly look some number of moves ahead until a leaf node is reached at the depth limit of the algorithm's lookahead. An evaluation function then estimates the value of the board configuration at the leaf node if both players were to play a Nash equilibrium from that point forward. In principle, if an AI could accurately calculate the value of every leaf node (e.g., win, draw, or loss), this algorithm would choose the optimal next move.

However, search as has been done in perfect-information games is fundamentally broken when applied to imperfect-information games. For example, consider a sequential form of Rock-Paper-Scissors, illustrated in Fig. 3, in which player 1 acts first but does not reveal her action to player 2, followed by player 2 acting. If player 1 were to conduct search that looks just one move ahead, every one of her actions would appear to lead to a leaf node with zero value. After all, if player 2 plays the Nash equilibrium strategy of choosing each action with $\frac{1}{3}$ probability, the value to player 1 of choosing Rock is zero, as is the value of choosing Scissors. So player 1's search algorithm could choose to always play Rock because, given the values of the leaf nodes, this appears to be equally good as any other strategy.

Indeed, if player 2's strategy were fixed to always playing the Nash equilibrium, always playing Rock would be an optimal player 1 strategy. However, in reality, player 2 could adjust to a strategy of always playing Paper. In that case, the value of always playing Rock would actually be -1.

This example illustrates that in imperfect-information subgames (the part of the game in which search is being conducted) (*40*), leaf nodes do not have fixed values. Instead, their values depend on the strategy that the searcher chooses in the subgame (that is, the probabilities that the searcher assigns to his actions in the subgame). In principle, this could be addressed by having the value of a subgame leaf node be a function of the searcher's strategy in the subgame, but this is impractical in large games. One alternative is to make the value of a leaf node conditional only on the belief distribution of both players at that point in the game. This was used to generate the two-player poker AI DeepStack (*5*). However, this option is extremely expensive because it requires one to solve huge numbers of subgames that are conditional on beliefs. It becomes even more expensive as the amount of hidden information or the number of players grows. The two-player poker AI Libratus sidestepped this issue by only doing real-time search when the remaining game was short enough that the depth limit would extend to the end of the game (*6*). However, as the number of players grows, always solving to the end of the game also becomes computationally prohibitive.

Pluribus instead uses a modified form of an approach that we recently designed—previously only for two-player zero-sum games (*41*)—in which the searcher explicitly considers that any or all players may shift to different strategies beyond the leaf nodes of a subgame. Specifically, rather than assuming that all players play according to a single fixed strategy beyond the leaf nodes (which results in the leaf nodes having a single fixed value), we instead assume that each player may choose between k different strategies, specialized to each player, to play for the remainder of the game when a leaf node is reached. In the experiments in this paper, $k = 4$. One of the four continuation strategies that we use in the experiments is the

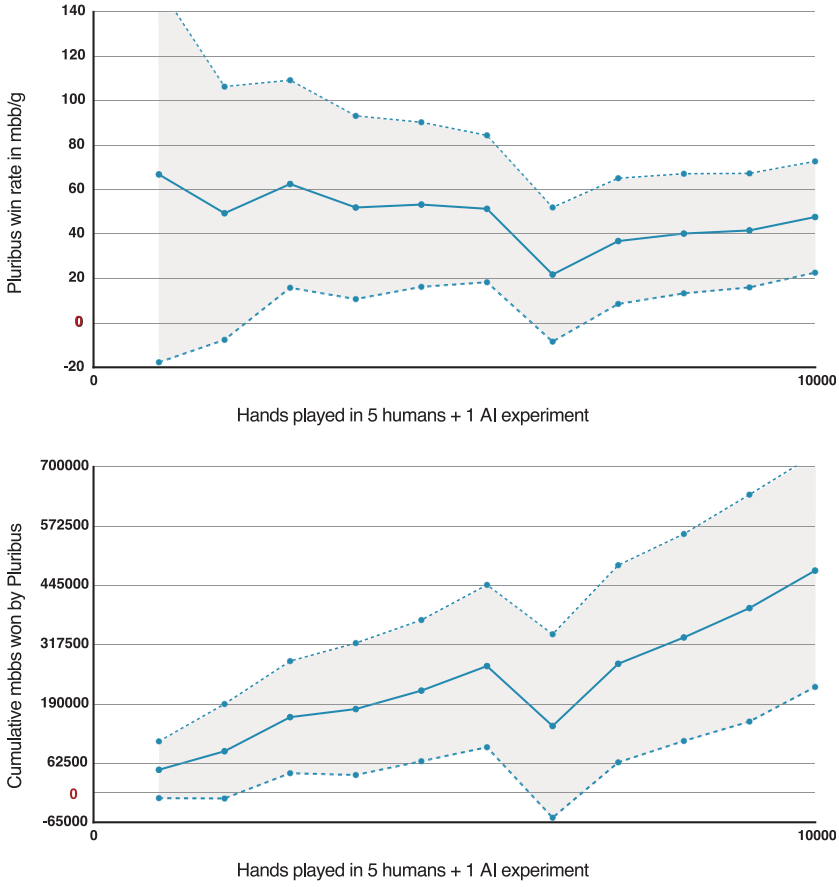

Fig. 5. Performance of Pluribus in the 5 humans + 1 AI experiment. The dots show Pluribus's performance at the end of each day of play. (**Top**) The lines show the win rate (solid line) plus or minus the standard error (dashed lines). (**Bottom**) The lines show the cumulative number of mbbs won (solid line) plus or minus the standard error (dashed lines). The relatively steady performance of Pluribus over the course of the 10,000-hand experiment also suggests that the humans were unable to find exploitable weaknesses in the bot.

precomputed blueprint strategy; another is a modified form of the blueprint strategy in which the strategy is biased toward folding; another is the blueprint strategy biased toward calling; and the final option is the blueprint strategy biased toward raising. This technique results in the searcher finding a strategy that is more balanced because choosing an unbalanced strategy (e.g., always playing Rock in Rock-Paper-Scissors) would be punished by an opponent shifting to one of the other continuation strategies (e.g., always playing Paper).

Another major challenge of search in imperfect-information games is that a player's optimal strategy for a particular situation depends on what the player's strategy is for every situation the player could be in from the perspective of her opponents. For example, suppose the player is holding the best possible hand. Betting in this situation could be a good action. But if the player bets in this situation only when holding the best possible hand, then the opponents would know that they should always fold in response.

To cope with this challenge, Pluribus keeps track of the probability it would have reached the current situation with each possible hand according to its strategy. Regardless of which hand Pluribus is actually holding, it will first calculate how it would act with every possible hand, being careful to balance its strategy across all the hands so as to remain unpredictable to the opponent. Once this balanced strategy across all hands is computed, Pluribus then executes an action for the hand it is actually holding. The structure of a depth-limited imperfect-information subgame as used in Pluribus is shown in Fig. 4.

Pluribus used one of two different forms of CFR to compute a strategy in the subgame, depending on the size of the subgame and the part of the game. If the subgame is relatively large or it is early in the game, then Monte Carlo Linear CFR is used just as it was for the blueprint strategy computation. Otherwise, Pluribus uses an optimized vector-based form of Linear CFR (*38*) that samples only chance events (such as board cards) (*42*).

When playing, Pluribus runs on two Intel Haswell E5-2695 v3 CPUs and uses less than 128 GB of memory. For comparison, AlphaGo used 1920 CPUs and 280 GPUs for real-time search in its 2016 matches against top Go professional Lee Sedol (*43*), Deep Blue used 480 custom-designed chips in its 1997 matches against top chess professional Garry Kasparov (*8*), and Libratus used 100 CPUs in its 2017 matches against top professionals in two-player poker (*6*). The amount of time that Pluribus takes to conduct search on a single subgame varies between 1 and 33 s, depending on the particular situation. On average, Pluribus plays at a rate of 20 s per hand when playing against copies of itself in six-player poker. This is roughly twice as fast as professional humans tend to play.

Experimental evaluation

We evaluated Pluribus against elite human professionals in two formats: five human professionals playing with one copy of Pluribus (5H+1AI), and one human professional playing with five copies of Pluribus (1H+5AI). Each human participant has won more than $1 million playing poker professionally. Performance was measured by using the standard metric in this field of AI, milli big blinds per game (mbb/game). This measures how many big blinds (the initial money the second player must put into the pot) were won on average per thousand hands of poker. In all experiments, we used the variance-reduction technique AIVAT (*44*) to reduce the luck factor in the game (*45*) and measured statistical significance at the 95% confidence level using a one-tailed t test to determine whether Pluribus is profitable.

The human participants in the 5H+1AI experiment were Jimmy Chou, Seth Davies, Michael Gagliano, Anthony Gregg, Dong Kim, Jason Les, Linus Loeliger, Daniel McAulay, Greg Merson, Nicholas Petrangelo, Sean Ruane, Trevor Savage, and Jacob Toole. In this experiment, 10,000 hands of poker were played over 12 days. Each day, five volunteers from the pool of professionals were selected to participate on the basis of availability. The participants were not told who else was participating in the experiment. Instead, each participant was assigned an alias that remained constant throughout the experiment. The alias of each player in each game was known, so that players could track the tendencies of each player throughout the experiment. $50,000 was divided among the human participants on the basis of their performance to incentivize them to play their best. Each player was guaranteed a minimum of $0.40 per hand for participating, but this could increase to as much as $1.60 per hand on the basis of performance. After applying AIVAT, Pluribus won an average of 48 mbb/game (with a standard error of 25 mbb/game). This is considered a very high win rate in six-player no-limit Texas hold'em poker, especially against a collection of elite professionals, and implies that Pluribus is stronger than the human opponents. Pluribus

was determined to be profitable with a p value of 0.028. The performance of Pluribus over the course of the experiment is shown in Fig. 5. (Owing to the extremely high variance in no-limit poker and the impossibility of applying AIVAT to human players, the win rate of individual human participants could not be determined with statistical significance.)

The human participants in the 1H+5AI experiment were Chris "Jesus" Ferguson and Darren Elias. Each of the two humans separately played 5000 hands of poker against five copies of Pluribus. Pluribus does not adapt its strategy to its opponents and does not know the identity of its opponents, so the copies of Pluribus could not intentionally collude against the human player. To incentivize strong play, we offered each human $2000 for participation and an additional $2000 if he performed better against the AI than the other human player did. The players did not know who the other participant was and were not told how the other human was performing during the experiment. For the 10,000 hands played, Pluribus beat the humans by an average of 32 mbb/game (with a standard error of 15 mbb/game). Pluribus was determined to be profitable with a p value of 0.014. (Darren Elias was behind Pluribus by 40 mbb/game with a standard error of 22 mbb/game and a p value of 0.033, and Chris Ferguson was behind Pluribus by 25 mbb/game with a standard error of 20 mbb/game and a p value of 0.107. Ferguson's lower loss rate may be a consequence of variance, skill, and/or his use of a more conservative strategy that was biased toward folding in unfamiliar difficult situations.)

Because Pluribus's strategy was determined entirely from self-play without any human data, it also provides an outside perspective on what optimal play should look like in multiplayer no-limit Texas hold'em. Pluribus confirms the conventional human wisdom that limping (calling the "big blind" rather than folding or raising) is suboptimal for any player except the "small blind" player who already has half the big blind in the pot by the rules, and thus has to invest only half as much as the other players to call. Although Pluribus initially experimented with limping when computing its blueprint strategy offline through self-play, it gradually discarded this action from its strategy as self-play continued. However, Pluribus disagrees with the folk wisdom that "donk betting" (starting a round by betting when one ended the previous betting round with a call) is a mistake; Pluribus does this far more often than professional humans do.

Conclusions

Forms of self-play combined with forms of search have led to a number of high-profile successes in perfect-information two-player zero-sum games. However, most real-world strategic interactions involve hidden information and more than two players. This makes the problem very different and considerably more difficult both theoretically and practically. Developing a superhuman AI for multiplayer poker was a widely recognized milestone in this area and the major remaining milestone in computer poker. In this paper we described Pluribus, an AI capable of defeating elite human professionals in six-player no-limit Texas hold'em poker, the most commonly played poker format in the world. Pluribus's success shows that despite the lack of known strong theoretical guarantees on performance in multiplayer games, there are large-scale, complex multiplayer imperfect-information settings in which a carefully constructed self-play-with-search algorithm can produce superhuman strategies.

REFERENCES AND NOTES

1. D. Billings, A. Davidson, J. Schaeffer, D. Szafron, *Artif. Intell.* **134**, 201–240 (2002).
2. J. von Neumann, *Math. Ann.* **100**, 295–320 (1928).
3. J. Nash, *Ann. Math.* **54**, 286 (1951).
4. M. Bowling, N. Burch, M. Johanson, O. Tammelin, *Science* **347**, 145–149 (2015).
5. M. Moravčík *et al*., *Science* **356**, 508–513 (2017).
6. N. Brown, T. Sandholm, *Science* **359**, 418–424 (2018).
7. J. Schaeffer, *One Jump Ahead: Challenging Human Supremacy in Checkers* (Springer-Verlag, New York, 1997).
8. M. Campbell, A. J. Hoane Jr., F.-H. Hsu, *Artif. Intell.* **134**, 57–83 (2002).
9. D. Silver *et al*., *Nature* **529**, 484–489 (2016).
10. Recently, in the real-time strategy games Dota 2 (*20*) and StarCraft 2 (*21*), AIs have beaten top humans, but as humans have gained more experience against the AIs, humans have learned to beat them. This may be because for those two-player zero-sum games, the AIs were generated by techniques not guaranteed to converge to a Nash equilibrium, so they do not have the unbeatability property that Nash equilibrium strategies have in two-player zero-sum games. (Dota 2 involves two teams of five players each. However, because the players on the same team have the same objective and are not limited in their communication, the game is two-player zero-sum from an AI and game-theoretic perspective.)
11. S. Ganzfried, T. Sandholm, in *International Conference on Autonomous Agents and Multi-Agent Systems (AAMAS)* (2011), pp. 533–540.
12. S. Ganzfried, T. Sandholm, *ACM Trans. Econ. Comp. (TEAC)* **3**, 8 (2015). Best of EC-12 special issue.
13. C. Daskalakis, P. W. Goldberg, C. H. Papadimitriou, *SIAM J. Comput.* **39**, 195–259 (2009).
14. X. Chen, X. Deng, S.-H. Teng, *J. Assoc. Comput. Mach.* **56**, 14 (2009).
15. A. Rubinstein, *SIAM J. Comput.* **47**, 917–959 (2018).
16. K. Berg, T. Sandholm, *AAAI Conference on Artificial Intelligence (AAAI)* (2017).
17. M. A. Zinkevich, M. Bowling, M. Wunder, *ACM SIGecom Exchanges* **10**, 35–38 (2011).
18. G. Tesauro, *Commun. ACM* **38**, 58–68 (1995).
19. D. Silver *et al*., *Nature* **550**, 354–359 (2017).
20. OpenAI, OpenAI Five, https://blog.openai.com/openai-five/ (2018).
21. O. Vinyals *et al*., AlphaStar: Mastering the Real-Time Strategy Game StarCraft II, https://deepmind.com/blog/alphastar-mastering-real-time-strategy-game-starcraft-ii/ (2019).
22. L. S. Shapley, *Advances in Game Theory*, M. Drescher, L. S. Shapley, A. W. Tucker, Eds. (Princeton Univ. Press, 1964).
23. R. Gibson, Regret minimization in games and the development of champion multiplayer computer poker-playing agents, Ph.D. thesis, University of Alberta (2014).
24. T. Sandholm, in *AAAI Conference on Artificial Intelligence (AAAI)* (2015), pp. 4127–4131. Senior Member Track.
25. T. Sandholm, *Science* **347**, 122–123 (2015).
26. M. Johanson, N. Burch, R. Valenzano, M. Bowling, in *International Conference on Autonomous Agents and Multiagent Systems (AAMAS)* (2013), pp. 271–278.
27. S. Ganzfried, T. Sandholm, in *AAAI Conference on Artificial Intelligence (AAAI)* (2014), pp. 682–690.
28. N. Brown, S. Ganzfried, T. Sandholm, in *International Conference on Autonomous Agents and Multiagent Systems (AAMAS)* (2015), pp. 7–15.
29. M. Zinkevich, M. Johanson, M. H. Bowling, C. Piccione, in *Neural Information Processing Systems (NeurIPS)* (2007), pp. 1729–1736.
30. E. G. Jackson, *AAAI Workshop on Computer Poker and Imperfect Information* (2013).
31. M. B. Johanson, Robust strategies and counter-strategies: from superhuman to optimal play, Ph.D. thesis, University of Alberta (2016).
32. E. G. Jackson, *AAAI Workshop on Computer Poker and Imperfect Information* (2016).
33. N. Brown, T. Sandholm, in *International Joint Conference on Artificial Intelligence (IJCAI)* (2016), pp. 4238–4239.
34. E. G. Jackson, *AAAI Workshop on Computer Poker and Imperfect Information Games* (2017).
35. M. Lanctot, K. Waugh, M. Zinkevich, in M. Bowling, *Neural Information Processing Systems (NeurIPS)* (2009), pp. 1078–1086.
36. M. Johanson, N. Bard, M. Lanctot, R. Gibson, M. Bowling, in *International Conference on Autonomous Agents and Multiagent Systems (AAMAS)* (2012), pp. 837–846.
37. R. Gibson, M. Lanctot, N. Burch, D. Szafron, M. Bowling, in *AAAI Conference on Artificial Intelligence (AAAI)* (2012), pp. 1355–1361.
38. N. Brown, T. Sandholm, *AAAI Conference on Artificial Intelligence (AAAI)* (2019).
39. S. Ganzfried, T. Sandholm, in *International Joint Conference on Artificial Intelligence (IJCAI)* (2013), pp. 120–128.
40. Here we use the term "subgame" the way it is usually used in AI. In game theory, that word is used differently by requiring a subgame to start with a node where the player whose turn it is to move has no uncertainty about state—in particular, no uncertainty about the opponents' private information.
41. N. Brown, T. Sandholm, B. Amos, in *Neural Information Processing Systems (NeurIPS)* (2018), pp. 7663–7674.
42. M. Johanson, K. Waugh, M. Bowling, M. Zinkevich, in *International Joint Conference on Artificial Intelligence (IJCAI)* (2011), pp. 258–265.
43. E. P. DeBenedictis, *Computer* **49**, 84–87 (2016).
44. N. Burch, M. Schmid, M. Moravcik, D. Morill, M. Bowling, in *AAAI Conference on Artificial Intelligence (AAAI)* (2018), pp. 949–956.
45. Owing to the presence of AIVAT and because the players did not know each others' scores during the experiment, there was no incentive for the players to play a risk-averse or risk-seeking strategy to outperform the other human.

ACKNOWLEDGMENTS

We thank P. Ringshia for building a graphical user interface and thank J. Chintagunta, B. Clayman, A. Du, C. Gao, S. Gross, T. Liao, C. Kroer, J. Langas, A. Lerer, V. Raj, and S. Wu for playing against Pluribus as early testing. **Funding:** This material is based on Carnegie Mellon University research supported by the National Science Foundation under grants IIS-1718457, IIS-1617590, IIS-1901403, and CCF-1733556 and by the ARO under award W911NF-17-1-0082, as well as XSEDE computing resources provided by the Pittsburgh Supercomputing Center. Facebook funded the player payments. **Author contributions:** N.B. and T.S. designed the algorithms. N.B. wrote the code. N.B. and T.S. designed the experiments and wrote the paper. **Competing interests:** The authors have ownership interest in Strategic Machine, Inc., and Strategy Robot, Inc., which have exclusively licensed prior game-solving code from the Carnegie Mellon University laboratory of T.S., which constitutes the bulk of the code in Pluribus. **Data and materials availability:** The data presented in this paper are shown in the main text and supplementary materials. Because poker is played commercially, the risk associated with releasing the code outweighs the benefits. To aid reproducibility, we have included the pseudocode for the major components of our program in the supplementary materials.

SUPPLEMENTARY MATERIALS

science.sciencemag.org/content/365/6456/885/suppl/DC1
Supplementary Text
Table S1
References (*46*–*52*)
Data File S1

31 May 2019; accepted 2 July 2019
Published online 11 July 2019
10.1126/science.aay2400

ARCHAEOLOGY

Late Upper Paleolithic occupation at Cooper's Ferry, Idaho, USA, ~16,000 years ago

Loren G. Davis[1]*, David B. Madsen[2], Lorena Becerra-Valdivia[3], Thomas Higham[3], David A. Sisson[4], Sarah M. Skinner[1], Daniel Stueber[5], Alexander J. Nyers[6], Amanda Keen-Zebert[7], Christina Neudorf[7], Melissa Cheyney[1], Masami Izuho[8], Fumie Iizuka[8,9], Samuel R. Burns[1], Clinton W. Epps[10], Samuel C. Willis[11], Ian Buvit[1]

Radiocarbon dating of the earliest occupational phases at the Cooper's Ferry site in western Idaho indicates that people repeatedly occupied the Columbia River basin, starting between 16,560 and 15,280 calibrated years before the present (cal yr B.P.). Artifacts from these early occupations indicate the use of unfluted stemmed projectile point technologies before the appearance of the Clovis Paleoindian tradition and support early cultural connections with northeastern Asian Upper Paleolithic archaeological traditions. The Cooper's Ferry site was initially occupied during a time that predates the opening of an ice-free corridor (≤14,800 cal yr B.P.), which supports the hypothesis that initial human migration into the Americas occurred via a Pacific coastal route.

Archaeological evidence predating the appearance of the Clovis Paleoindian tradition (CPT) (*1*) in the Americas by ~13,250 calibrated years before the present (cal yr B.P.) (*2*) is found at a small number of reliably dated sites (*3*–*13*) (fig. S1). These sites share technological attributes similar to Late Upper Paleolithic (LUP) sites in northeastern Asia, including flake- and blade-based stone tool traditions, use of informal lithic tools, lack of fluted bifacial technology, and use of stemmed and lanceolate projectile points (*13*–*15*). We present data from the Cooper's Ferry site in western Idaho (Fig. 1) that extend the timing of human populations south of Late Wisconsinan ice sheets to ~16,000 cal yr B.P. We describe results of excavation and analyses of stone tools and lithic tool production debris, remains from food processing, and multiple cultural features within buried stratigraphic contexts [lithostratigraphic unit 3 (LU3) to LU5] dated using accelerator mass spectrometry (AMS) radiocarbon and luminescence dating methods (*16*).

Background and setting

The Cooper's Ferry site is located within an alluvial terrace at the confluence of Rock Creek and the lower Salmon River of western Idaho (fig. S2). The Niimíipuu (the Nez Perce Tribe) refer to this place as an ancient village site named Nipéhe (*17*, *18*). Davis led excavation of a 2 m–by–2 m unit (unit A) in 1997 that uncovered a Western Stemmed tradition (WST) equipment cache associated with radiocarbon ages of 11,370 ± 40 yr B.P. (Beta-114949; 13,300 to 13,115 cal yr B.P.) and 11,410 ± 120 yr B.P. (TO-7349; 13,475 to 13,060 cal yr B.P.) (*19*, *20*). From 2009 to 2018, Davis led more-extensive excavations of two blocks measuring 7 m by 13 m (area A) and 12 m by 12 m (area B) (figs. S3 and S4). Here, we focus discussion on the area A record.

Stratigraphy

The stratigraphy of area A includes nine LUs and two pedostratigraphic units (table S1 and fig. S5) (*19*). The earliest radiocarbon samples and archaeological materials, which we report here, come from LU3 and LU2. A paleosol, called the Rock Creek Soil, is associated with LU3 and includes a rubified A horizon, calcic B horizon, and loessal C horizon. LU3 is an aeolian loess

[1]Department of Anthropology, Oregon State University, 238 Waldo Hall, Corvallis, OR 97331, USA. [2]Texas Archeological Research Laboratory, University of Texas, Austin, TX 78758, USA. [3]Oxford Radiocarbon Accelerator Unit, Research Laboratory for Archaeology and the History of Art, School of Archaeology, 1 South Parks Road, Oxford OX1 3TG, UK. [4]Bureau of Land Management, Cottonwood Field Office, 2 Butte Drive, Cottonwood, ID 83522, USA. [5]University of Victoria, Department of Anthropology, P.O. Box 1700 STN CSC, Victoria, BC V8W 2Y2, Canada. [6]Northwest Archaeometrics, P.O. Box 2427, Corvallis, OR 97339, USA. [7]Division of Earth and Ecosystem Sciences, Desert Research Institute, 2215 Raggio Parkway, Reno, NV 89512, USA. [8]Tokyo Metropolitan University, Faculty of Humanities and Social Sciences, 1-1 Minami-Osawa, Hachioji-shi, Tokyo, Japan 192-0397. [9]School of Social Sciences, Humanities and Arts, University of California, Merced, Merced, CA, USA. [10]Oregon State University, Department of Fisheries and Wildlife, 104 Nash Hall, Corvallis, OR 97331, USA. [11]Oregon Parks and Recreation Department, Stewardship Section, 725 Summer Street, NE, Suite C, Salem, OR 97301, USA.
*Corresponding author. Email: loren.davis@oregonstate.edu

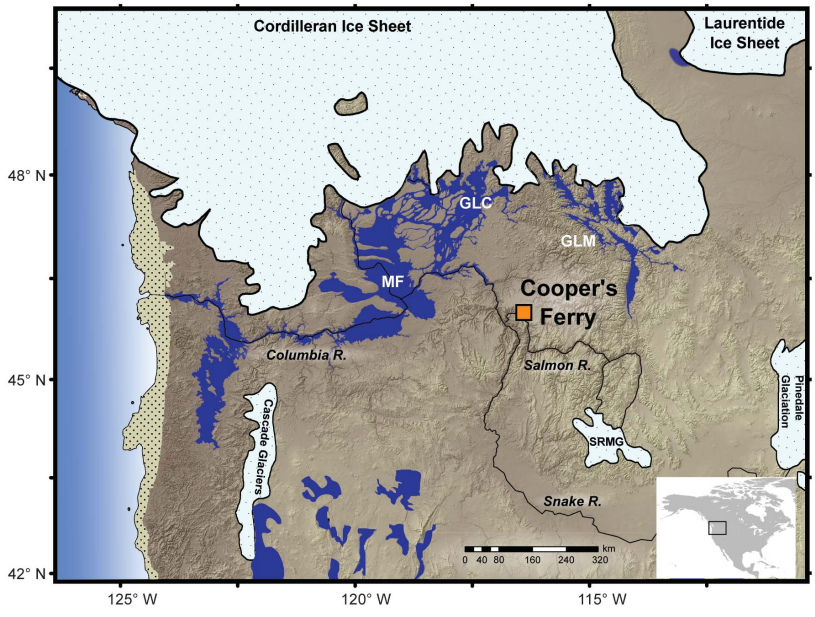

Fig. 1. Location map for the Cooper's Ferry site. Projected regional environmental aspects at ~16,000 cal yr B.P. are based on modeled extents of Cordilleran and Laurentide glacial ice (*41*), Cascade and Salmon River mountain glaciers (SRMG), Pinedale glaciation extents, positions of Glacial Lake Missoula (GLM) and Glacial Lake Columbia (GLC) (*41*), the modeled path of the Missoula Flood (MF) and its impoundment pool (*42*), smaller northern Great Basin pluvial lakes (*43*), and shoreline extents along the Pacific outer continental shelf (shown as a tan dotted area at left) (*44*).

and overlies LU2 and LU1 alluvium. For the purposes of this Report we focus on LU3 to LU1 (Fig. 2). Description of stratigraphic and dating methods and additional details about the geoarchaeological context of younger site deposits are provided in the supplementary materials (*16*).

Geochronology

The Cooper's Ferry site radiocarbon chronology for LU5 to LU3 is based on 21 ages from charcoal and bone samples recovered in situ outside of cultural pit features (Table 1). AMS dating indicates that LU5 dates from ~9250 to 9000 cal yr B.P., LU4 dates from ~11,930 to 10,410 cal yr B.P., and LU3 dates between ~15,660 and 13,260 cal yr B.P. Optically stimulated luminescence (OSL) analysis of potassium feldspar grains sampled from LU5, LU4, and upper LU3 sediments dated to 12,170 ± 2320 years ago (±1 SD), 12,730 ± 2400 years ago, and 13,710 ± 2620 years ago, respectively (Fig. 2 and table S2). Except for dates obtained from within-pit features, all other radiocarbon and OSL measurements (n = 25) were incorporated into a Bayesian age model (Fig. 3). Within the general outlier model, OxA-38106, OxA-38050, OxA-38104, OxA-X-2792-42, and D-AMS 029851 were identified as outliers (>60% probability), most likely due to bioturbation (*16*). The outliers are down-weighted in the model and, in general, the sequence shows good age-depth congruence. Modeled output places the start of LU3 at 16,560 to 15,280 cal yr B.P. (95.4% confidence) and LU4 at 12,740 to 11,440 cal yr B.P. (95.4% confidence), and all dated events span 6140 to 10,120 years (95.4% confidence).

Archaeological evidence originating within LU3

We uncovered and mapped 189 lithic artifacts in situ within LU3, including 161 pieces of debitage, 27 stone tools, and 1 piece of fire-cracked rock

Table 1. Accelerator mass spectrometry chronometric data. RN is the reading number. The percent collagen is the yield of extracted collagen as a function of the starting weight of bone samples. C:N is the atomic weight ratio of carbon to nitrogen. %C is the percentage of carbon in the combusted sample. Stable isotope ratios of C and N are expressed in per mil (‰) relative to Vienna Pee Dee belemnite and ambient inhalable reservoir. The calibrations were done using the OxCal 4.3 software (*46*) and the IntCal13 calibration curve (*47*). Missing chronometric data (*) are due to a lack in reporting or measurement on behalf of the laboratories. CI, confidence interval; –, not determined.

RN	Laboratory no.	Material	Northing (m)	Easting (m)	Elevation (masl)	LU	% collagen	C:N	%C	$\delta^{13}C$ (‰)	$\delta^{15}N$ (‰)	Date		
												yr B.P.	±1 SD	cal yr B.P. (95.4% CI)
52918	OxA-37,170	Bone	78.432	101.000	412.531	Lower LU6	6	3.2	45	–20.2	3.8	7984	40	9000–8655
29234	OxA-37,169	Bone	81.120	100.500	412.463	Mid LU5	4.16	3.4	43	–19.1	6.8	8141	38	9250–9000
59697	D-AMS 029851	Charcoal	79.842	106.657	411.981	Lower LU4	–	–	37	–20.8	–	7944	39	8985–8640
56440	OxA-38,048	Bone	79.922	106.325	412.295	Upper LU4	3.15	3.4	33	–19.6	7.6	9775	50	11,265–11,105
56817	OxA-X-2792-41	Bone	82.162	101.510	412.043	Lower LU4	1.4	3.4	19	–19.5	5.7	9110	50	10,410–10,190
56199	OxA-38,103	Bone	80.880	103.292	412.036	Lower LU4	3.4	3.2	41	–19.8	6.9	10,055	55	11,930–11,310
59391	OxA-X-2792-42	Bone	79.782	106.188	412.027	Lower LU4	2.1	3.3	22	–19.8	5.6	13,165	70	16,070–15,560
50554	OxA-37,171	Bone	81.182	102.243	412.027	Lower LU4	1.2	3.2	44	–20.1	6.9	10,005	40	11,705–11,280
56422	OxA-X-2792-43	Bone	80.900	103.327	411.990	Lower LU4	0.7	3.4	24	–20.5	6.6	10,050	60	11,930–11,285
57483	D-AMS 029850	Charcoal	82.795	107.393	412.009	Mid LU4	–	–	30	–21.3	–	9714	57	11,245–10,795
–	TO-7349	Charcoal	79.20	100.30	411.900	Near surface of LU3	*	*	*	*	*	11,410	120	13,475–13,060
58223	OxA-X-2792-45	Bone	82.630	103.708	411.785	Upper LU3	1.1	3.5	12	–20.4	9.6	11,630	80	13,610–13,275
58628	OxA-38,104	Bone	82.185	100.293	411.695	Mid LU3	6.8	3.2	35	–20	6.9	7605	40	8515–8345
56446	D-AMS 029846	Charcoal	82.676	108.954	411.692	Mid LU3, within F129 (hearth feature)	–	–	22	–34.3	–	12,348	71	14,785–14,075
59379	OxA-38,050	Charcoal	79.916	107.376	411.684	Mid LU3	–	–	29	–28.8	–	7831	40	8765–8535
56461	D-AMS 029749	Charcoal	82.945	108.417	411.667	Mid LU3, within F129 (hearth feature)	–	–	21	–20.8	–	12,598	54	15,195–14,670
56623	D-AMS 029847	Charcoal	82.986	108.388	411.642	Mid LU3, within F129 (hearth feature)	–	–	21	–21.2	–	12,472	61	15,030–14,250
56624	D-AMS 029848	Charcoal	80.020	108.459	411.641	Mid LU3	–	–	22	–19.9	–	12,363	49	14,725–14,120
53495	OxA-37,284	Bone	79.838	103.08	411.552	Lower LU3	5.16	3.5	31	–20.2	5.9	12,475	60	15,035–14,260
58720	OxA-38,051	Charcoal	78.267	102.672	411.572	Lower LU3	–	–	–	–	–	13,070	80	15,945–15,335
58398	OxA-X-2792-48	Bone	80.995	103.020	411.486	Lower LU3	1.6	3.3	28	–21	6.6	12,830	65	15,575–15,105
23283	OxA-38,106	Bone	82.520	102.629	411.310	Lower LU3	1.2	3.4	42	–20.9	4.5	7985	40	9005–8655
–	Beta-114949	Charcoal	79.530	101.450	410.880	Within PFA2	*	*	*	–22	*	11,370	40	13,300–13,115
56823	OxA-38,049	Bone	80.167	103.276	411.868	Within F134	5.4	3.3	32	–20.2	5.5	10,010	50	11,745–11,270
58673	OxA-38,052	Bone	80.375	103.944	411.247	Within F134	1.97	3.2	42	–19.3	7.8	13,335	75	16,265–15,795
59294	OxA-38,197	Bone	82.514	103.536	411.221	Within F144	1.1	3.4	9.4	–20.2	10.4	11,720	80	13,745–13,410
59291	OxA-38,105	Bone	80.931	105.994	411.415	Within F135	4.4	3.2	38	20	10.2	9955	50	11,615–11,240

(FCR), and also 86 faunal bone fragments and 1 river mussel shell fragment (Fig. 2 and tables S3 and S4). Most bone fragments lack clear anatomical features but likely represent medium- to large-bodied mammals. Stone tools include basal fragments of 2 stemmed projectile points (Fig. 4, A to C), 4 biface fragments (Fig. 4, D to F and H), 2 blades (Fig. 4, G and I), and 19 modified flake tools (Fig. 4 and fig. S6). Stemmed point base 73-60685 (Fig. 4A) lay below OxA-X-2792-45 (13,610 to 13,275 cal yr B.P.) and above OSL sample CFA-017 (13,710 ± 2620 years ago). Stemmed point base 73-42800 (Fig. 4B) lay below TO-7349 (13,475-13,060 cal yr B.P.) and above OxA-X-2792-45 (13,610 to 13,275 cal yr B.P.; OxA-38104 is an outlier and thus excluded from this discussion).

In addition to these in situ finds, we identified four features originating within LU3. Features 142 and 144 (F142 and F144) were pits that originated at ~411.72 meters above sea level (masl), stratigraphically below OxA-X-2792-45 (13,610 to 13,275 cal yr B.P.). Whereas F142 was relatively shallow, F144 extended downward to the top of LU1 and contained two pieces of debitage, one modified flake tool, and two bone fragments—one returning an AMS age of 11,720 ± 80 yr B.P. (OxA-38,197; 13,745 to 13,410 cal yr B.P.). F129, present from ~411.73 to 411.58 masl, was a concentration of darker charcoal-bearing sediment within a small basin surrounded by a 2- to 3-cm-thick layer containing oxidized and ashy sediment, charcoal, nine bone fragments, one modified flake tool, and five pieces of debitage. We interpret F129 as a hearth (fig. S8). Three charcoal fragments from F129 date to 12,348 ± 71 yr B.P. (D-AMS 029846; 14,785 to 14,075 cal yr B.P.), 12,472 ± 61 yr B.P. (D-AMS 029847; 15,030 to 14,250 cal yr B.P.), and 12,598 ± 54 yr B.P. (D-AMS 029847; 15,195 to 14,670 cal yr B.P.), whereas charcoal found ~2.5 m away at the same elevation returned an AMS age of 12,363 ± 49 yr B.P. (D-AMS 029848; 14,725 to 14,120 cal yr B.P.). F143 was a pit that originated at ~411.62 masl and extended down to ~411.39 masl (fig. S9). A biface fragment, 15 pieces of debitage, a fragment of tooth enamel interpreted as *Equus* sp. (fig. S10) (*16*), and 7 mammal bone fragments—probably including extinct horse—were found inside and immediately surrounding F143. We interpret F143 as a food processing station. F143 is dated by its stratigraphic position between the slightly higher F129, which dates between 15,000 and 14,410 cal yr B.P. [95.4% confidence; $\chi^2(2) = 5.255$ (5%, 5.991)], and the lower stratigraphic position of three radiocarbon estimates of 12,475 ± 60 yr B.P. (OxA-37,284; 15,035 to 14,260 cal yr B.P.), 12,830 ± 65 yr B.P. (OxA-X-2792-48; 15,575 to 15,105 cal yr B.P.), and 13,070 ± 80 yr B.P. (OxA-38,051; 15,945 to 15,335 cal yr B.P.). Given the slight westward downslope of LU3 stratigraphy,

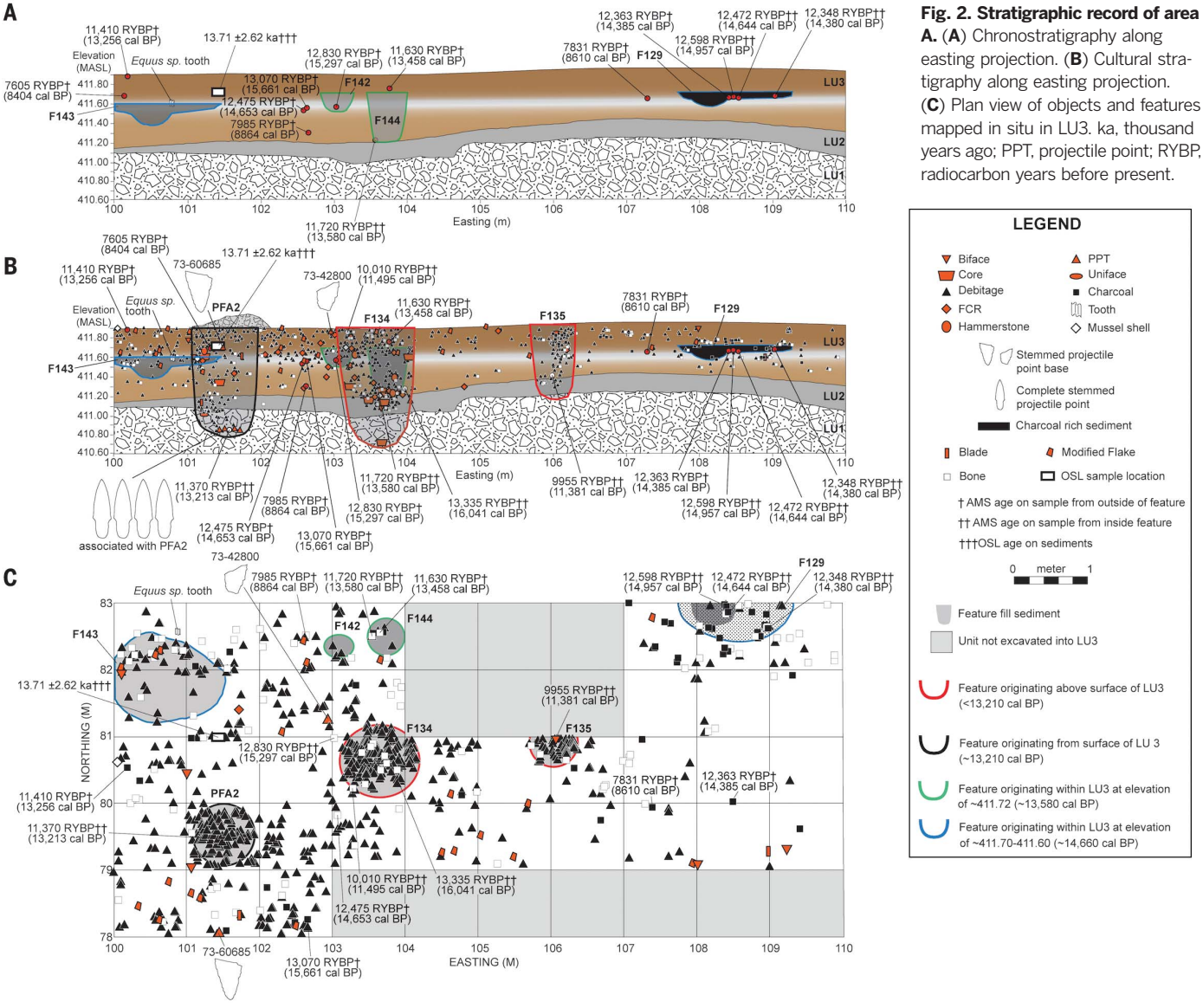

Fig. 2. Stratigraphic record of area A. (**A**) Chronostratigraphy along easting projection. (**B**) Cultural stratigraphy along easting projection. (**C**) Plan view of objects and features mapped in situ in LU3. ka, thousand years ago; PPT, projectile point; RYBP, radiocarbon years before present.

F129 and F143 probably occupied a contemporaneous surface. The LU3 deposit between 411.55 masl and the lower contact with LU2 contained 43 pieces of debitage, 20 bone fragments, and a piece of charcoal excavated in situ below the stratigraphic position of OxA-38,051 (15,945 to 15,335 cal yr B.P.) (Fig. 2). These lower materials are objects discarded during repeated periods of human occupation at Cooper's Ferry, which Bayesian modeling suggests began at 16,560 to 15,280 cal yr B.P. (95.4% confidence) (Fig. 3).

Debitage recovered in situ within LU3 is made primarily from local cryptocrystalline silicate (CCS) and secondarily from fine-grained igneous toolstone. Debitage analysis reveals early to late biface reduction based on the presence of medium to small bifacial percussion flakes and a smaller number of pressure flakes (tables S5 and S6). Lithic tool maintenance is reflected by a CCS burination flake bearing an exhausted unifacial working edge (fig. S6U) and by an igneous toolstone chopper tool edge rejuvenation flake. Artifact 73-61176 (fig. S6V) is an early-stage bifacial overshot thinning flake discovered in situ at 411.455 masl with a finely faceted bifacial platform and distal termination that removed a square edge from an opposing tool margin. This debitage was found in situ below the stratigraphic position of the three oldest radiocarbon ages, dating 15,310 to 15,100 cal yr B.P. (95.4% confidence range). Overall, the quantities of provenienced lithic debitage, tools, cultural features, and bone and charcoal fragments increase from the surface of LU3 and peak at ~411.60 masl, reflecting the presence of intact buried archaeological components (fig. S11).

Archaeological evidence intersecting the surface of LU3

Three pit features were excavated into the LU3 surface, including pit feature A2 (PFA2), F134, and F135. Pit feature A2 originates from the surface of LU3, as evidenced by a gravel cairn that marks its top. It contains 4 WST projectile points, 1 core, 1 hammerstone, 3 blades, 2 unifaces, 2 modified flakes, 724 debitage pieces, and 65 bone fragments (*19*, *20*) (figs. S12 and S13). F134 is a cylindrical pit defined at the surface of LU3 but lacking a clear upper surface. F134 intrudes down through LU2 and into LU1 and contains 131 debitage pieces, 15 FCR fragments, 1 modified flake tool, 1 hammerstone, 1 cobble tool, 3 biface fragments, 1 projectile point blade fragment, 34 bone fragments, and 3 wood charcoal fragments. F134 also contains six angular to subrounded boulder–sized clasts of fine-grained volcanic rock bearing evidence of percussive testing and multiple large flake removals (Fig. 2 and fig. S14). F135 is another cylindrical pit that lacks a defining upper limit. F135 extends downward into the LU1 and contains 1 fragmentary biface, 74 debitage pieces, 2 FCR fragments, 11 bone fragments, and 15 wood charcoal fragments (Fig. 2 and fig. S15). Because F134 and F135 originate at or slightly above the LU3-LU4 boundary, it is unclear whether they date to

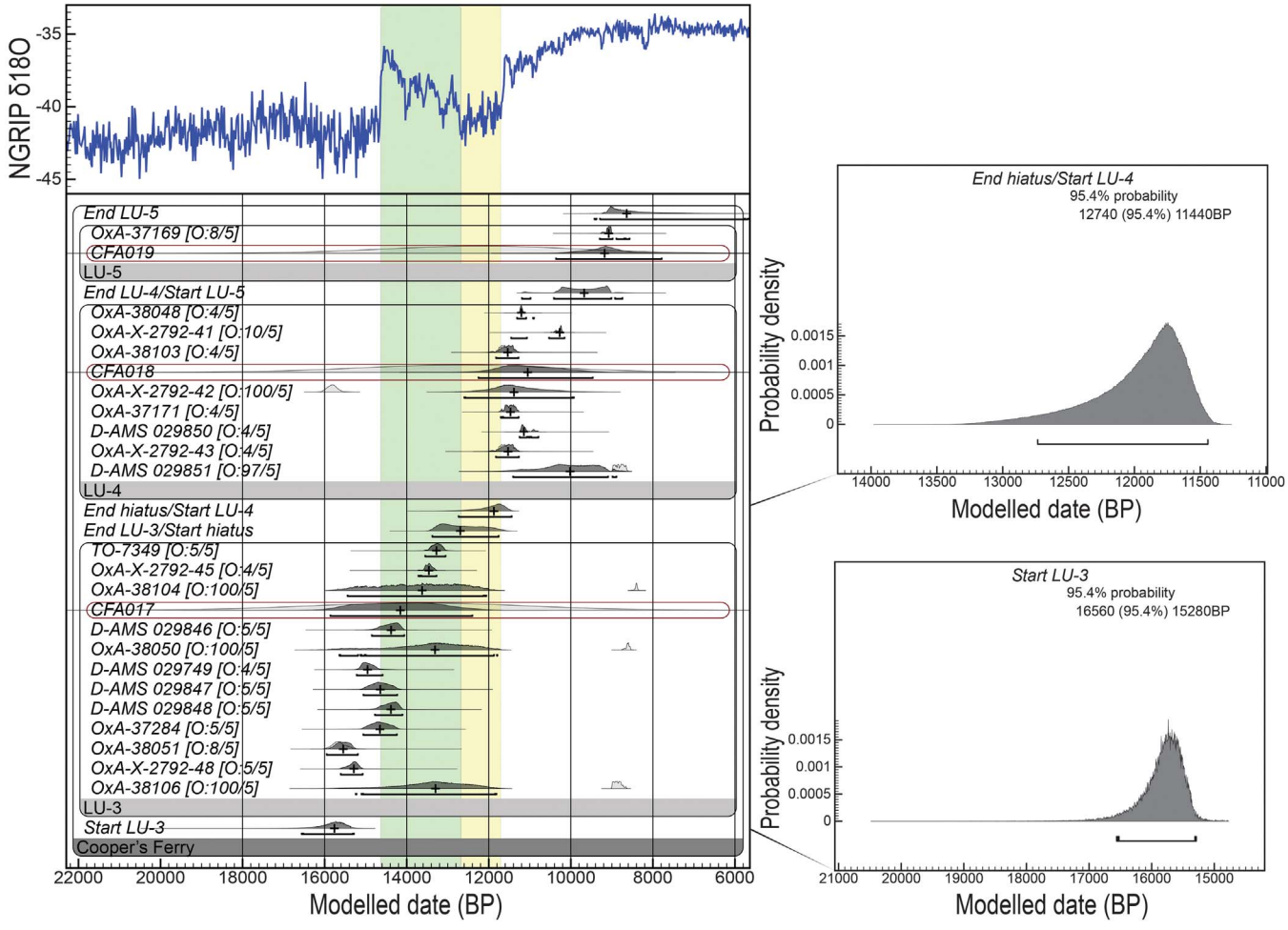

Fig. 3. Bayesian age model of Cooper's Ferry, area A. OSL dates (e.g., CFA017) are outlined in red. The output of the general outlier analysis is noted next to laboratory names for each date. The green vertical band represents the span of Greenland Interstadial 1 (GI-1; Bølling-Allerød), whereas the yellow vertical band indicates Greenland Stadial 1 (GS-1; Younger Dryas). The modeled output estimates the start of LU3 at 16,560 to 15,280 cal yr B.P. (95.4% confidence; prior to GI-1) and the start of LU4 to 12,740 to 11,440 cal yr B.P. (95.4% confidence; mainly during GS-1). NGRIP, North Greenland Ice Core Project.

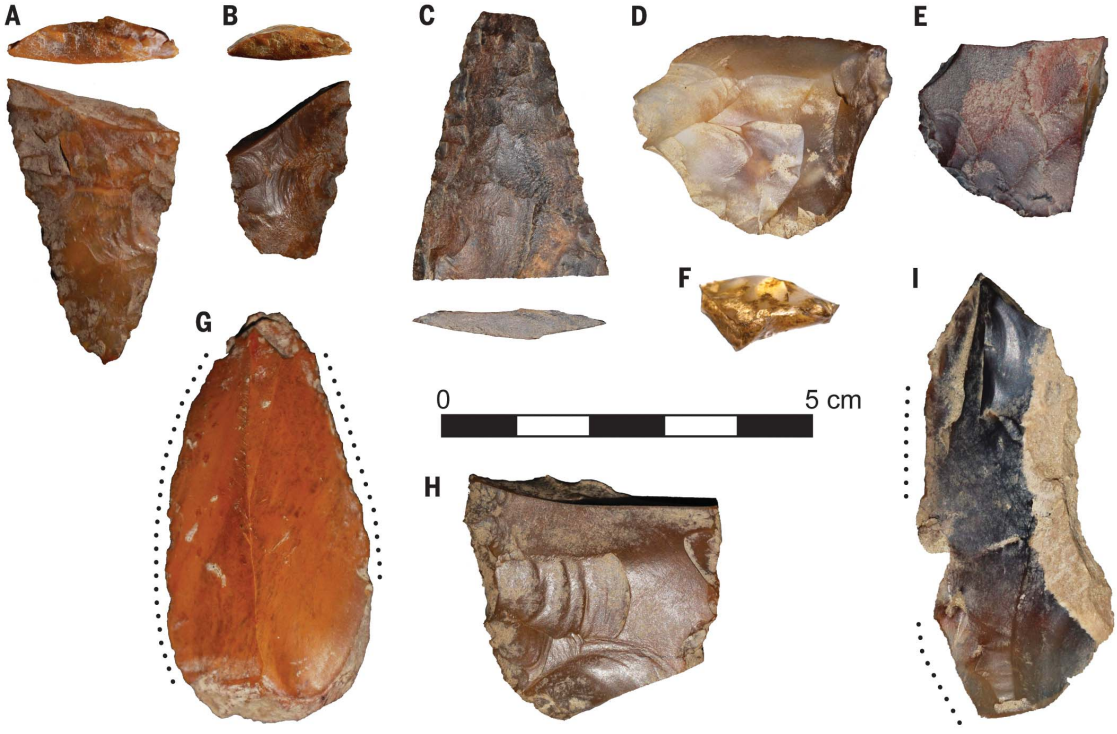

Fig. 4. Lithic tools excavated in situ from LU3. (**A**) Stemmed projectile point haft fragment from LU3 (73-60685; RN 56938). (**B**) Stemmed projectile point haft fragment from LU3 (73-42800; RN 50948). (**C**) Blade fragment of projectile point from LU3 (73-62464; RN 59067). (**D**) Biface preform fragment (73-61085; RN 57401). (**E**) Biface preform fragment (73-63034; RN 59076). (**F**) Biface preform fragment (73-61870; RN 58316). (**G**) Macroblade (73-62953; RN 59385). (**H**) Biface preform fragment (73-62887; RN 59367). (**I**) Macroblade (73-60855; RN 57072). Dots show areas with use wear.

the end of the LU3 occupational phase or the beginning of the LU4 occupational phase. A projectile point blade fragment made on CCS (73-62464) was discovered on the surface of LU3 (Fig. 4C).

Technological antecedents

Stemmed projectile points appear throughout Africa, the Levant, and Europe after 50,000 years ago (*21*) and are associated with late Pleistocene evidence of human presence along the northern Pacific Rim (*22*). In Japan and Korea, Hakuhen-Sentoki projectile points dating from 30,000 to 23,000 cal yr B.P. are made by retouching the proximal end of a thick, pointed blade (*23*). The eponymous "bifacial stemmed point" type, seen mainly in Japan from 16,000 to 13,000 cal yr B.P., was often made on macroflakes or blades with contracting bases and elaborative bifacial retouch (*24*–*28*). Regional variants include the Tachikawa type on Hokkaido, the Kosegawsawa type in northern Honshu near the Sea of Japan, and the Yanagimata type in central and western Honshu. The Tachikawa type bears strong morphological similarities to the contracting margin stemmed point bases from LU3 at Cooper's Ferry (Fig. 5). Stemmed projectile points that are morphologically different from specimens from Cooper's Ferry appeared at Kamchatka's Ushki Lake site by ~13,440 to 12,640 cal yr B.P. (*29*) but were absent earlier from Beringia (*15*), suggesting that their origins lie elsewhere. The age, morphology, and technology of Cooper's Ferry LU3 artifacts share notable similarities with the nonfluted projectile point traditions dated from ~16,000 to 13,000 cal yr B.P. in Japan.

The artifacts contained within LU3 and PFA2 temporally precede and partially overlap with the CPT but represent a separate technological tradition distinguished by flake- and macroblade-based lithic tool production, including but not limited to stemmed, lanceolate, and foliate projectile point forms; Levallois-like and discoidal unidirectional and multidirectional core design; predetermined flake and macroblade blanks; and flake and blade tools. These technological attributes are seen among North and South American sites that predate the CPT, most recently discovered in stratified context beneath Clovis artifacts at the Gault and Friedkin sites in Texas (*2*–*13*). We interpret this temporal and technological affinity to signal a cultural connection with Upper Paleolithic northeastern Asia, which complements current evidence of shared genetic heritage between late Pleistocene peoples of northern Japan and North America (*30*). Although these archaeological connections require further study, the contemporaneous use of stemmed projectile point technologies in northeastern Asia and North America during the late Pleistocene represents an emerging Upper Paleolithic archaeological pattern that precedes the CPT (*13*). Adopting this terminology brings the earliest archaeological period of the Americas into conceptual alignment with the rest of the world and affirms the strength of observed technological connections to northeast Asia (*13*).

Implications for the peopling of the Americas

A small number of reliably dated archaeological sites now provide evidence that humans were present in the Americas by at least 14,500 cal yr B.P. and even before 15,000 cal yr B.P. (*3*–*13*) (fig. S1). Recent genetically based estimates for the presence of people in the Americas suggest that an isolated population moved south of the ice sheets sometime after ~19,500 cal yr B.P. (*31*, *32*) and split into two major branches of northern and southern Native Americans sometime between ~17,500 and 14,600 cal yr B.P. (*33*, *34*). Bayesian age modeling and archaeological evidence from the lower portion of LU3 indicate that humans were initially present at the Cooper's Ferry site 16,560 to 15,280 cal yr B.P. (95.4% confidence level) within this timeframe of initial population expansion. The migration route these peoples employed to initially enter North America is hypothesized to have occurred either via an interior migration from eastern Beringia southward through a deglaciated ice-free corridor (IFC) that opened between continental ice sheets during the late Pleistocene (*16*, *35*) or by a combination of boat transport and walking south along the margin of glaciated and unglaciated Pacific shorelines (*35*–*40*). Models favoring migration through an IFC argue for its opening by ~14,800 cal yr B.P., providing time for humans to migrate from eastern Beringia and move throughout the Americas shortly before the appearance of the CPT (*36*). Cooper's Ferry provides direct evidence for human settlement south of Late Wisconsinan ice sheets in the upper Columbia River basin before the earliest hypothesized opening of the IFC at ~14,800 cal yr B.P. This evidence refutes the IFC hypothesis and leads us to deduce that humans initially migrated

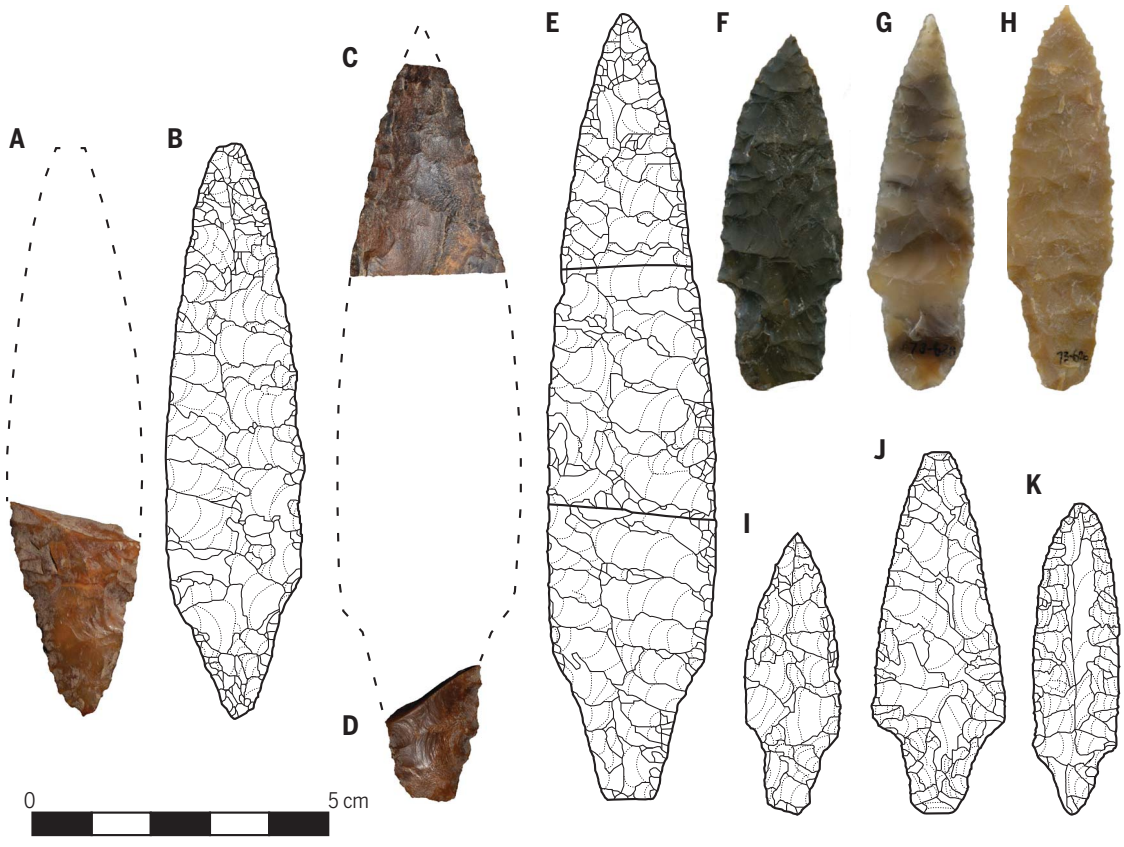

Fig. 5. Comparison of Cooper's Ferry projectile points with late Pleistocene age Tachikawa-type stemmed points from the Kamishiritaki 2 site on Hokkaido, Japan. (**A**) Stemmed projectile point haft fragment from LU3 (73-60685; RN 56938). (**B**) Illustration of Japanese Upper Paleolithic stemmed projectile point from the Kamishiritaki 2 site [redrawn from (*45*)]. (**C**) Blade fragment of projectile point from LU3 (73-62464; RN 59067). (**D**) Stemmed projectile point haft fragment from LU3 (73-42800; RN 50948). (**E**) Illustration of Japanese Upper Paleolithic stemmed projectile point from the Kamishiritaki 2 site [redrawn from (*45*)] as one possible comparison for the reconstructed stemmed projectile point shown in (C) and (D). (**F**) Stemmed projectile point from PFA2 (73-627). (**G**) Stemmed projectile point from PFA2 (73-628). (**H**) Stemmed projectile point from PFA2 (73-626). (**I** to **K**) Illustrations of Japanese Upper Paleolithic stemmed projectile points from the Kamishiritaki 2 site [redrawn from (*45*)].

into the Americas along the Pacific coast. This does not preclude subsequent human migrations through the IFC at a later time, as suggested by paleogenomics (*34*), but such possible population movements do not represent the initial peopling of the Americas.

REFERENCES AND NOTES

1. B. A. Bradley, M. B. Collins, C. A. Hemmings, *Clovis Technology* (International Monographs in Prehistory no. 17, Berghahn Books, 2010).
2. M. R. Waters, T. W. Stafford Jr., *Science* **315**, 1122–1126 (2007).
3. T. D. Dillehay, *Monte Verde: A Late Pleistocene Settlement in Chile*, vol. 2, *The Archaeological Context and Interpretation* (Smithsonian Institution Press, 1997).
4. J. M. Adovasio, J. Donahue, R. Stuckenrath, *Am. Antiq.* **55**, 348–354 (1990).
5. D. F. Overstreet, M. F. Kolb, *Geoarchaeology* **18**, 91–114 (2003).
6. M. R. Waters *et al.*, *Science* **331**, 1599–1603 (2011).
7. D. L. Jenkins *et al.*, *Science* **337**, 223–228 (2012).
8. T. D. Dillehay *et al.*, *Quat. Res.* **77**, 418–423 (2012).
9. J. J. Halligan *et al.*, *Sci. Adv.* **2**, e1600375 (2016).
10. T. D. Dillehay *et al.*, *Sci. Adv.* **3**, e1602778 (2017).
11. T. J. Williams *et al.*, *Sci. Adv.* **4**, eaar5954 (2018).
12. M. R. Waters *et al.*, *Sci. Adv.* **4**, eaat4505 (2018).
13. T. J. Williams, D. B. Madsen, *PaleoAmerica* 10.1080/20555563.2019.1606668 (2019).
14. T. Goebel, I. Buvit, Eds., *From the Yenisei to the Yukon: Interpreting Lithic Assemblage Variability in Late Pleistocene/Early Holocene Beringia* (Center for the Study of the First Americans, 2011).
15. K. E. Graf, I. Buvit, *Curr. Anthropol.* **58**, S583–S603 (2017).
16. See supplementary materials.
17. Schwede (*18*) identified this locale as "Nipéheme." However, Nakia Williamson-Cloud, Nez Perce Tribe Cultural Resource Program Director, explained that the proper reference to this ancient village location is "Nipéhe."
18. M. L. Schwede, thesis, Washington State University, Pullman, WA (1966).
19. L. G. Davis, C. E. Schweger, *Geoarchaeology* **19**, 685–704 (2004).
20. L. G. Davis, A. J. Nyers, S. C. Willis, *Am. Antiq.* **79**, 596–615 (2014).
21. J. Shea, *J. Arch. Sci.* **33**, 823–846 (2006).
22. J. M. Erlandson, T. J. Braje, *Quat. Int.* **239**, 28–37 (2011).
23. K. Morisaki, in *Emergence and Diversity of Modern Human Behavior in Paleolithic Asia*, Y. Kaifu, M. Izuho, T. Goebel, H. Sato, A. Ono, Eds. (Texas A&M University Press, 2015), pp. 376–388.
24. G. K. Lee, K. Sano, *Archaeol. Anthropol. Sci.* **11**, 2453–2465 (2019).
25. Y. Kudo, *Curr. Res. Pleist* **23**, 11–14 (2006).
26. K. Nagai, *Anthropol. Sci.* **115**, 223–226 (2007).
27. H. Sato, M. Izuho, K. Morisaki, *Quat. Int.* **237**, 93–102 (2011).
28. D. Natsuki, *Ronshu Oshorokko* **5**, 59–77 (2018).
29. T. Goebel, M. R. Waters, M. Dikova, *Science* **301**, 501–505 (2003).
30. N. Adachi, K. Shinoda, M. Izuho, in *Emergence and Diversity of Modern Human Behavior in Paleolithic Asia*, Y. Kaifu, M. Izuho, T. Goebel, H. Sato, A. Ono, Eds. (Texas A&M University Press, 2015), pp. 406–417.
31. T. Pinotti *et al.*, *Curr. Biol.* **29**, 149–157.e3 (2019).
32. B. Llamas *et al.*, *Sci. Adv.* **2**, e1501385 (2016).
33. J. V. Moreno-Mayar *et al.*, *Nature* **553**, 203–207 (2018).
34. C. L. Scheib *et al.*, *Science* **360**, 1024–1027 (2018).
35. M. Margold *et al.*, *Quat. Res.* 10.1017/qua.2019.10 (2019).
36. B. A. Potter *et al.*, *Science* **359**, 1224–1225 (2018).
37. K. Fladmark, *Am. Antiq.* **44**, 55–69 (1979).
38. C. A. S. Mandryk, H. Josenhans, D. W. Fedje, R. W. Mathewes, *Quat. Sci. Rev.* **20**, 301–314 (2001).
39. L. G. Davis, S. C. Willis, S. J. Macfarlan, in *Meeting at the Margins*, D. Rhode, Ed. (Univ. of Utah Press, 2012), pp. 47–64.
40. A. J. Lesnek, J. P. Briner, C. Lindqvist, J. F. Baichtal, T. H. Heaton, *Sci. Adv.* **4**, eaar5040 (2018).
41. A. S. Dyke, in *Quaternary Glaciations—Extent and Chronology. Part II: North America*, J. Ehlers, P. L. Gibbard, Eds. (Elsevier, 2004), pp. 373–424.
42. R. B. Waitt Jr., *Geol. Soc. Am. Bull.* **96**, 1271–1286 (1985).
43. R. B. Morrison, in *Quaternary Nonglacial Geology: Conterminous U.S., The Geology of North America*, vol. K-2, R. B. Morrison, Ed. (Geol. Soc. Am., 1991), pp. 283–320.
44. J. Clark, J. Mitrovica, J. Alder, *J. Arch. Sci.* **52**, 12–23 (2014).
45. Hokkaido Archaeological Operation Center, "Shirataki Sites II: Kamishirataki 2 Site, Kamishirataki 6 Site, and Kitashiyubetsu 4 Site, Shirataki Village" (in Japanese) (Hokkaido Archaeological Operation Center, 2001).
46. C. Bronk Ramsey, *Radiocarbon* **43**, 355–363 (2001).
47. P. J. Reimer *et al.*, *Radiocarbon* **55**, 1869–1887 (2013).

ACKNOWLEDGMENTS

E. Lundelius and E. Davis made independent identifications of the *Equus* sp. tooth fragment from digital images. K. Ames and C. Garcia-Des Lauriers commented on an earlier version of this paper. L.G.D. extends his gratitude to the Nez Perce Tribe and

N. Williamson-Cloud for their support of archaeological research at the Cooper's Ferry site. L.G.D. acknowledges J. Cramer and R. Cramer for their vision and generosity in establishing the Keystone Archaeological Fund and C. Rector for supporting the Bernice Peltier Huber Charitable Trust. The excavations were performed by archaeology field school staff members, students, and interns from the University of Alberta (1997), Oregon State University (2009 to 2018), and the Nez Perce tribe (2017 to 2018). A.K.-Z. thanks R. Pober for contributing to field and laboratory work on luminescence dating and K. Rodrigues for contributions to laboratory analysis. L.G.D. and D.A.S. express their deepest appreciation for many summers of shared conversations and lively discussions about Cooper's Ferry with Ken Ames, and we dedicate this paper to him. **Funding:** Cooper's Ferry project work in area A was funded through challenge cost share agreements between the Bureau of Land Management's Cottonwood field office and the University of Alberta (1997; agreement 1422-D-065-A-96-0007) and with Oregon State University (2009 to 2019; assistance agreements L09AC15147 and L14AC00232), by the Bernice Peltier Huber Charitable Trust, the Keystone Archaeological Research Fund, and Oregon State University. M.I. was funded from a Grant-in-Aid for Scientific Research on Innovative Areas (grant no. 1802 for FY2016–2020) from the Ministry of Education, Culture, Sports, Science and Technology, Japan. A.K.-Z. received support from the General Frederick West Lander Endowment. **Author contributions:** L.G.D., D.A.S., S.M.S., and A.J.N. conducted LU3 to LU1 excavations and archaeological data management. L.G.D. and D.B.M. conducted geoarchaeological investigations and wrote the corresponding supplementary materials section. L.G.D., D.S., S.C.W., and S.R.B. conducted the artifact and feature analysis and wrote the corresponding supplementary materials section. M.C., C.W.E., and L.G.D. conducted archaeofaunal bone analyses and wrote the corresponding supplementary materials section. L.B.V. and T.H. conducted radiocarbon and Bayesian analyses and wrote corresponding main text and supplementary materials sections. A.K.-Z. and C.N. conducted the OSL analysis and wrote the corresponding supplementary materials section. L.G.D. and D.B.M. wrote the introduction, background, and results sections of the main text and corresponding supplementary materials section. L.G.D., D.B.M., M.I., F.I., and I.B. wrote the main text interpretation and discussion sections. All authors reviewed the final draft. **Competing interests:** The authors declare no competing interests. **Data and materials availability:** All data are available in the main text or the supplementary materials. The Cooper's Ferry archaeological collection is curated at the Oregon State University Department of Anthropology.

SUPPLEMENTARY MATERIALS

science.sciencemag.org/content/365/6456/891/suppl/DC1
Materials and Methods
Supplementary Text
Figs. S1 to S17
Tables S1 to S6
References (*48*–*80*)

11 May 2019; accepted 1 August 2019
10.1126/science.aax9830

ARCHAEOLOGY

Archaeological assessment reveals Earth's early transformation through land use

ArchaeoGLOBE Project*†

Environmentally transformative human use of land accelerated with the emergence of agriculture, but the extent, trajectory, and implications of these early changes are not well understood. An empirical global assessment of land use from 10,000 years before the present (yr B.P.) to 1850 CE reveals a planet largely transformed by hunter-gatherers, farmers, and pastoralists by 3000 years ago, considerably earlier than the dates in the land-use reconstructions commonly used by Earth scientists. Synthesis of knowledge contributed by more than 250 archaeologists highlighted gaps in archaeological expertise and data quality, which peaked for 2000 yr B.P. and in traditionally studied and wealthier regions. Archaeological reconstruction of global land-use history illuminates the deep roots of Earth's transformation and challenges the emerging Anthropocene paradigm that large-scale anthropogenic global environmental change is mostly a recent phenomenon.

Human societies have transformed and managed landscapes for thousands of years, altering global patterns of biodiversity, ecosystem functioning, and climate (*1*–*6*). Despite increasing interest in the early global environmental changes caused by human activities, from changes in fire regimes and wild animal and plant populations by hunter-gatherers to increasingly intensive forms of agriculture, the global extent, intensity, temporal trajectory, and environmental consequences of Earth's transformation through human land use remain poorly understood outside the archaeological community (*7*–*9*).

Human transformation of environments around the world began with late-Pleistocene hunting and gathering societies and increased throughout the most recent interglacial interval with the emergence of agriculture and urbanized societies. Agricultural land use is implicated in anthropogenic global environmental changes ranging from greenhouse gas emissions and climate change (*5*, *6*, *10*) to widespread deforestation, soil erosion, and altered fire regimes, as well as species introductions, invasions, and extinctions (*4*, *8*, *11*). Such changes are evident even in tropical rainforests and savanna environments long considered pristine (*12*, *13*). However, existing models of long-term changes in global land use (*5*, *14*, *15*) differ substantially in their representation of these early transformations (*8*, *16*), largely owing to limited incorporation of disparate empirical data from archaeology and palaeoecology (*17*, *18*). As a result, global models and assessments of early anthropogenic influence on climate, habitats, biodiversity, and other environmental changes remain poorly characterized (*4*, *10*, *18*, *19*).

Efforts to map land-cover change over the past 10,000 years from pollen data have increased during the past decade, and high-quality regional reconstructions are now available for Europe and the Northern Hemisphere (*20*–*24*). However, global reconstructions that combine both land-use and land-cover change using a range of data sources are rare (*18*, *25*) and have difficulty incorporating environmental data from archaeological sites (*26*). Here, we present a global assessment of archaeological expert knowledge on land use from 10,000 years before the present (yr B.P.) to 1850 CE, showing that existing global reconstructions underestimate the impact of early human land use on Earth's current ecology.

A global synthesis of archaeological knowledge

Archaeologists often study human alterations of environments, but most studies are qualitative or have a local or specialized topical focus [e.g., (*27*–*33*)]. To assess and integrate archaeological knowledge toward synthesis at a global scale, the ArchaeoGLOBE Project used a crowdsourcing approach (*34*, *35*). Archaeologists with land-use expertise were invited to contribute to a detailed questionnaire describing levels of land-use knowledge at 10 time intervals across 146 regional analytical units covering all continents except Antarctica. Contributors selected individual regions where they had expertise; 255 individual archaeologists completed a total of 711 regional questionnaires, resulting in complete, though uneven, global coverage (Fig. 1 and table S1). The result is an expert-based meta-analysis that uses semi-subjective (ranked) survey data to generate regional assessments of land use over time.

Regional-scale archaeological knowledge contributions were sufficient to assess land-use changes in all 146 regions between 10,000 yr B.P. and 1850 CE (Figs. 1 and 2). Overall, self-reported regional land-use expertise increased linearly from 10,000 yr B.P., peaked for 2000 yr B.P., and dropped off sharply thereafter (Fig. 2B), reflecting the decreasing emphasis on environmental archaeological methods in time periods with more abundant material remains and/or historical records. Quality of archaeological data pertaining to past land use (Fig. 2C), determined by the pervasiveness of archaeological surveys, as well as floral and faunal analyses in each region, followed a trend similar to that for expertise, although the peak was somewhat later and more pronounced, and the drop-off was less severe.

Global trends in expertise and data quality, and in published excavations, were heterogeneous across the globe, with consistently higher expertise and data quality across time in regions including, but not limited to, sections of Southwest Asia, Europe, Northern China, Australia, and North America, almost certainly reflecting a greater intensity of archaeological research in these areas. Other areas evidenced relatively low expertise among survey respondents and data quality until the most recent periods, especially parts of Africa, Southeast Asia, and South America.

Global patterns of regional land-use change

In 120 regions (82% of all regions, 88% of inhabited regions at 10,000 yr B.P.), foraging (practices of foraging, hunting, gathering, and fishing) was common (practiced across 1 to 20% of land in region) or widespread (practiced across >20% of region) at 10,000 yr B.P. and declined thereafter (Fig. 3, A and B). Foraging was less than widespread in 40% of all regions by 8000 yr B.P., a decline that expanded to 63% of regions by 3000 yr B.P. By 1850 CE, 73% of regions were assessed with less than widespread foraging, with 51% at the "minimal" (practiced across <1% of land in region) or "none" prevalence levels.

Regional trends of foraging (Fig. 4B and fig. S6D) reveal early declines from 10,000 to 6000 yr B.P. in Southwest Asia, with other regions exhibiting declines in foraging lifeways either gradually, beginning ~4000 yr B.P., or with hardly any declines at all until after 3000 yr B.P. This pattern is congruent with recent global assessments indicating that the majority of domesticated species appeared in the interval from 8000 to 4000 yr B.P., with a smaller number in earlier intervals (*28*).

The current dataset draws attention to the prevalence of agricultural economies across the globe (Fig. 4A) rather than focusing on centers of initial domestication, of which there are now at least 11 worldwide (*28*). At 10,000 yr B.P., these centers were limited to minimal or common components in parts of Southwest Asia. Subsequently, agriculture became much more widespread both through secondary dispersal from

*ArchaeoGLOBE Project authors and affiliations are listed in the supplementary materials.
†Corresponding authors: Erle Ellis (ece@umbc.edu); Lucas Stephens (lucas.s.stephens@gmail.com)

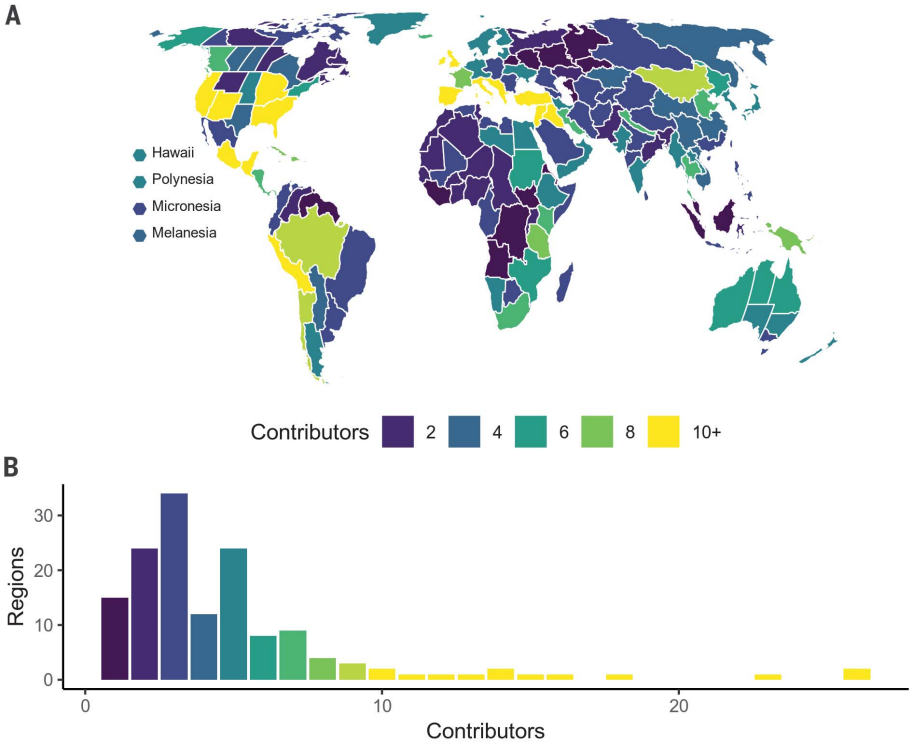

Fig. 1. Archaeological knowledge contributions. (**A**) Geographic distribution of knowledge contributions across 146 regions. The four island regions at left are aggregated into indicator panels with exaggerated areas (Eckert IV projection). (**B**) Histogram showing the distribution of 711 total contributions across regions.

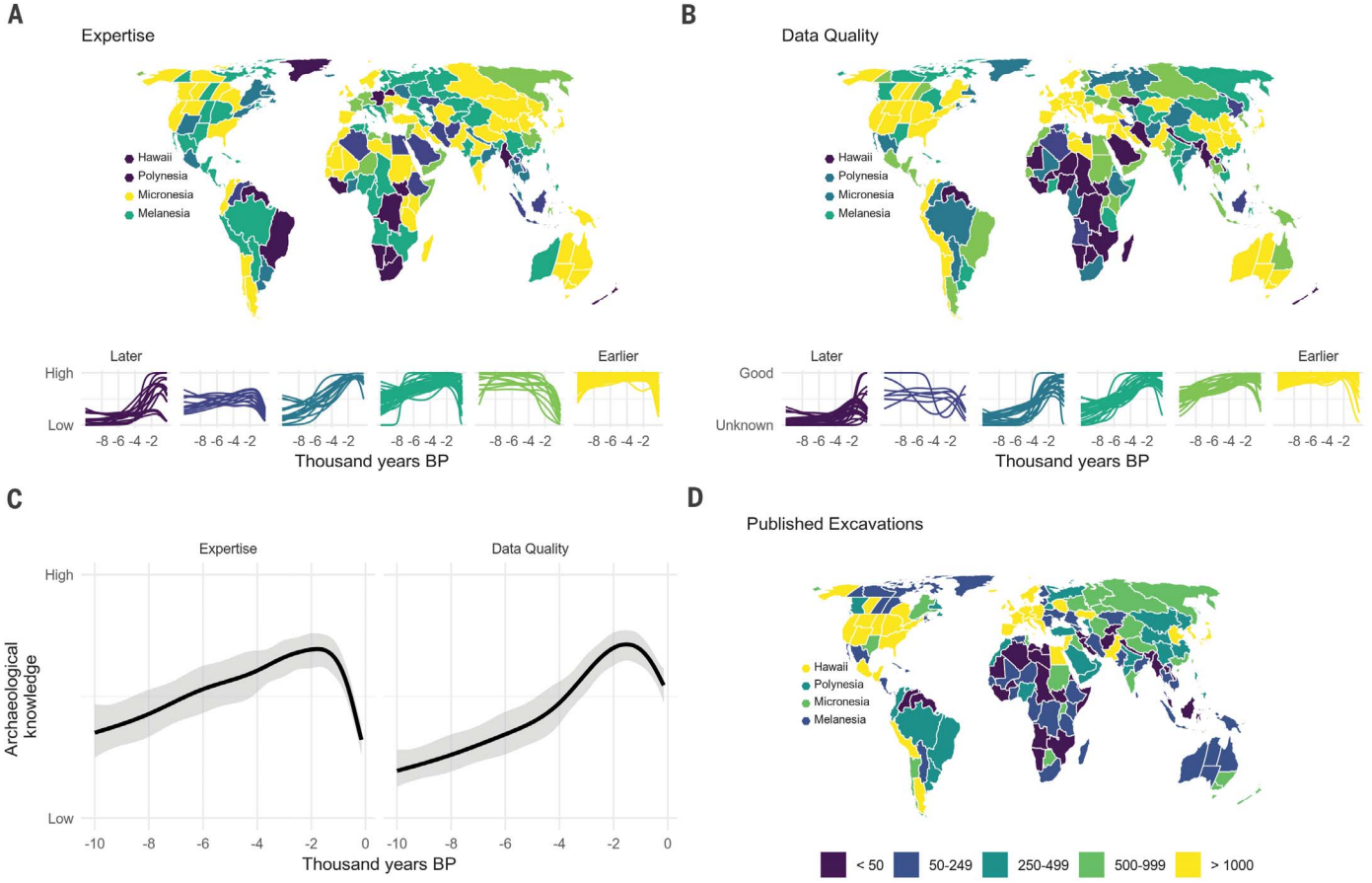

Fig. 2. Archaeological expertise, data quality, and published excavations. (**A**) Regional trends in land-use expertise estimated using a generalized additive mixed model, grouped according to a *k*-means clustering algorithm to show regions with similar temporal trends. (**B**) Regional trends in data quality. (**C**) Global trends in expertise and data quality with 95% confidence intervals. (**D**) Estimated number of published excavations per region.

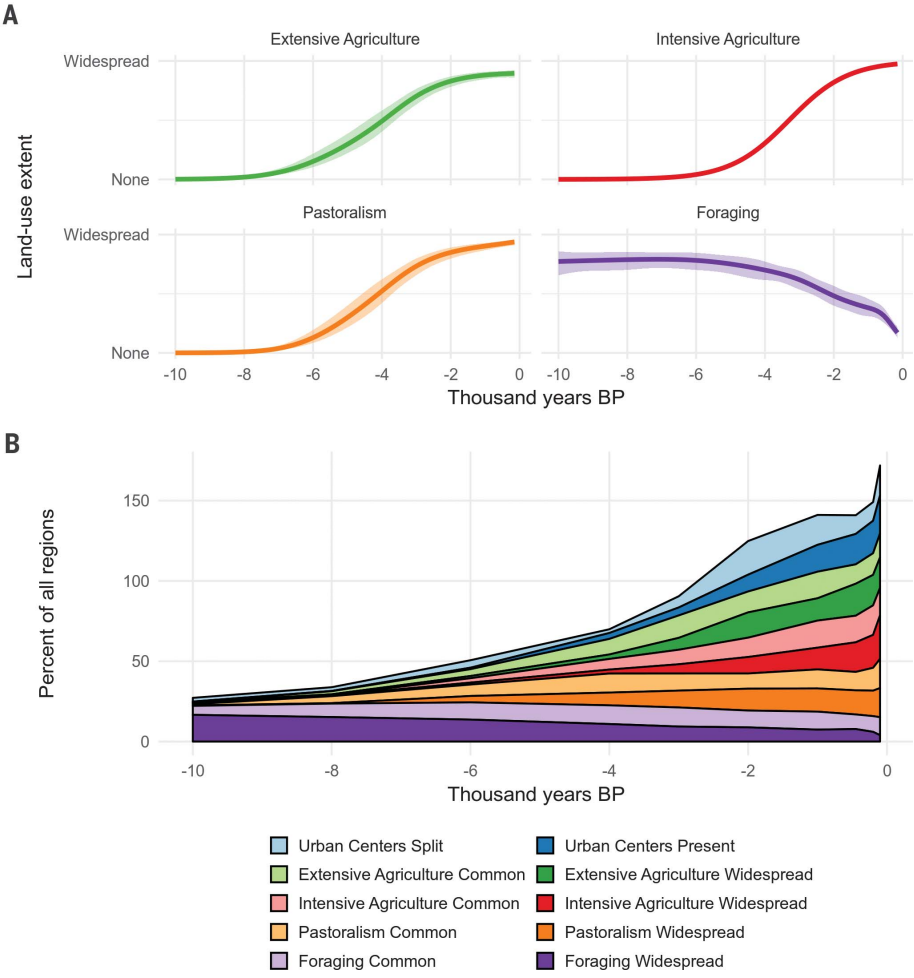

Fig. 3. Summary of global land-use trends. (**A**) Generalized additive mixed-model trends for the extent of each land-use type across all regions with 95% confidence intervals. (**B**) Cumulative summary of regions per land-use category based on consensus assessments (Common, >1 to 20% regional land area; Widespread, >20% regional land area), with presence or absence of urban centers. Categories are nonexclusive, resulting in plot values >100% for all regions.

Southwest Asia and eastern China and through new domestications in the Americas, New Guinea, and Africa. By 6000 yr B.P., 42% of land units had at least minimal extensive agriculture (swidden or shifting cultivation and other forms of non-continuous cultivation), and it was common in >14% of units. Intensive agriculture (all forms of continuous cultivation) was geographically constricted (the Mediterranean, Southwest Asia, South Asia, and eastern China) and common in only a few regions (12 at 6000 yr B.P.) of suitable climatic conditions until 4000 to 3000 yr B.P., spreading more broadly only after 2000 yr B.P. (65 regions with at least common intensive agriculture at 2000 yr B.P.).

This study also illuminates the relationships between different modes of land use. Pastoralism was connected to agricultural centers of origin in Southwest Asia, East Asia, and the Andes, suggesting a close relationship between both types of production. By 10,000 yr B.P., both agriculture and pastoralism were established in the earliest source regions with a focus first around Southwest Asia and the Mediterranean, but by 8000 yr B.P., pastoralism had spread farther from Southwest Asia, perhaps because of the proximity of this region to arid environments where herding was more productive than farming (Fig. 4A). In the Americas, pastoralism was restricted to its origin in the Andes (present from 8000 yr B.P.) until after 1500 CE with the introduction of western domesticates.

After 6000 yr B.P., the geographic spread of extensive agriculture shows a markedly different pattern than that of pastoralism because of its dispersal from additional source locations in East Asia and the Americas. Over the same time period, pastoralism spread across northern Africa and central Asia and was common or widespread across much of Eurasia and Africa by 4000 yr B.P., including many regions where neither form of agriculture was common until between 4000 and 3000 yr B.P. Not until 3000 yr B.P. was extensive agriculture (75 regions) practiced commonly at a greater geographic scale than pastoralism (64 regions). Patterns of regional land use demonstrate the importance of pastoralist production across arid regions (Fig. 4A), including arid and northern regions where agriculture was unsuitable, and document that the type of management practiced on western Eurasian herd animals was highly adaptable and transferable.

Early onset of intensive land use: Assessments versus models

Regional onsets of intensive agriculture, described by archaeologists, were generally earlier than estimates of cultivated crop areas derived from the most commonly used, spatially explicit global reconstruction of land-use history [the HYDE dataset (*14*)]. ArchaeoGLOBE findings complement previous regional (e.g., Europe) land-cover studies based on palaeoecological data (*36*, *37*). Of the 130 ArchaeoGLOBE regions currently making up Earth's agricultural regions (regions with >1% crop area in HYDE at 2000 CE), 69 archaeological onsets were earlier when assessed at the "common" level, in regions encompassing 54% of global crop area at 2000 CE (Fig. 5C), and >67 were earlier at the "widespread" level (56% of global crop area at 2000 CE; Fig. 5D). Although 26 archaeological onsets at the common level were later than HYDE, including 13 regions later by >1000 years (8.4% of global crop area at 2000 CE), ArchaeoGLOBE onsets were >1000 years earlier in 27 regions encompassing 21.8% of global crop area in 2000. At the widespread level, archaeological onsets were later by ≤250 years in just three regions (5% of 2000 global crop area) and earlier by >1000 years in 21 regions, accounting for 22.0% of global crop area in 2000. By contrast, a comparison with KK10, a less commonly applied historical land-cover change reconstruction known for representing early agricultural transformation of land, showed generally earlier onsets of intensive land use than did ArchaeoGLOBE [fig. S7; (*15*)].

Discussion

The ArchaeoGLOBE dataset highlights broad patterns and consistencies in archaeological data while also identifying exceptions and knowledge gaps. Our data show geographical variability in total number of respondents, expertise level, and data quality, suggesting that the breadth of archaeological knowledge differs greatly from one region to another. Potential causes of geographical inconsistencies in archaeological knowledge include the varying conditions under which archaeologists work, the cumulative legacy and positive feedback of early research interests, and the physical accessibility (both real and perceived) of archaeological sites [see also (*38*)]. Although we made rigorous efforts to recruit archaeological knowledge contributions as widely as possible, biases in the dataset also derive from the anglophone orientation of key project investigators, as well as the limitations of their professional networks. These biases exacerbate historical geographical

biases in the pursuit and construction of archaeological knowledge, including the application of environmental archaeological methods. ArchaeoGLOBE respondents may not form a representative sample of global archaeologists, but it is still clear that several regions have seen more intensive archaeological research. Regional hotspots of intensive study are concentrated heavily in Europe, Southwest Asia, and portions of the Americas, a pattern also observed for ecological field sites (*39*) and UNESCO World Heritage sites (*40*).

Regional cold spots that have received much less attention are concentrated in Southeast Asia and Central and West Africa, where resources available for archaeological fieldwork and training are limited. Nonetheless, experts in these regions were able to contribute generalized accounts of land-use trajectories. For instance, archaeobotanical investigations of the cultivation and domestication of indigenous cereals in sub-Saharan Africa (*41*–*43*) are beginning to shed light on earlier and more extensive forms of agriculture. Similar less-investigated indigenous agricultural practices likely characterize parts of Southeast Asia and northern India during the mid-Holocene [e.g., (*44*–*46*)]. Hence, the ArchaeoGLOBE project can help archaeologists prioritize future collection of empirical data and local capacity building to improve the reliability of global perspectives.

Deepening the Anthropocene

Archaeologists and anthropologists have broadly defined "domestication" and, to a lesser extent, "agriculture" [e.g., (*28*)]. However, "hunting and gathering" is a more varied and complex subsistence adaptation than originally conceptualized. Its definition generates debate among scholars by blurring countless variances in land use, resource management, and anthropogenic environmental change. Foraging, or "foraging/hunting/gathering/fishing," was used here to describe subsistence economies and land-use practices that generally exhibit lower amounts of direct human alteration of ecosystems and control of plant and animal life cycles [see (*47*)]. Within this broad category are many forms of resource procurement and land management that have drastically changed landscapes, and we now recognize that foragers may have initiated dramatic and sometimes irreversible environmental change [e.g., (*48*)]. In addition to altering biotic communities around the world through transport and propagation of favored species, extensive early land use by hunter-gatherers may also indicate widespread use of fire to enhance success in hunting and foraging (*49*). Systematic burning has implications for the global carbon cycle through increased greenhouse gas emissions, for water cycles through changes in vegetation and evapotranspiration, and for temperatures through changes in albedo (*50*, *51*).

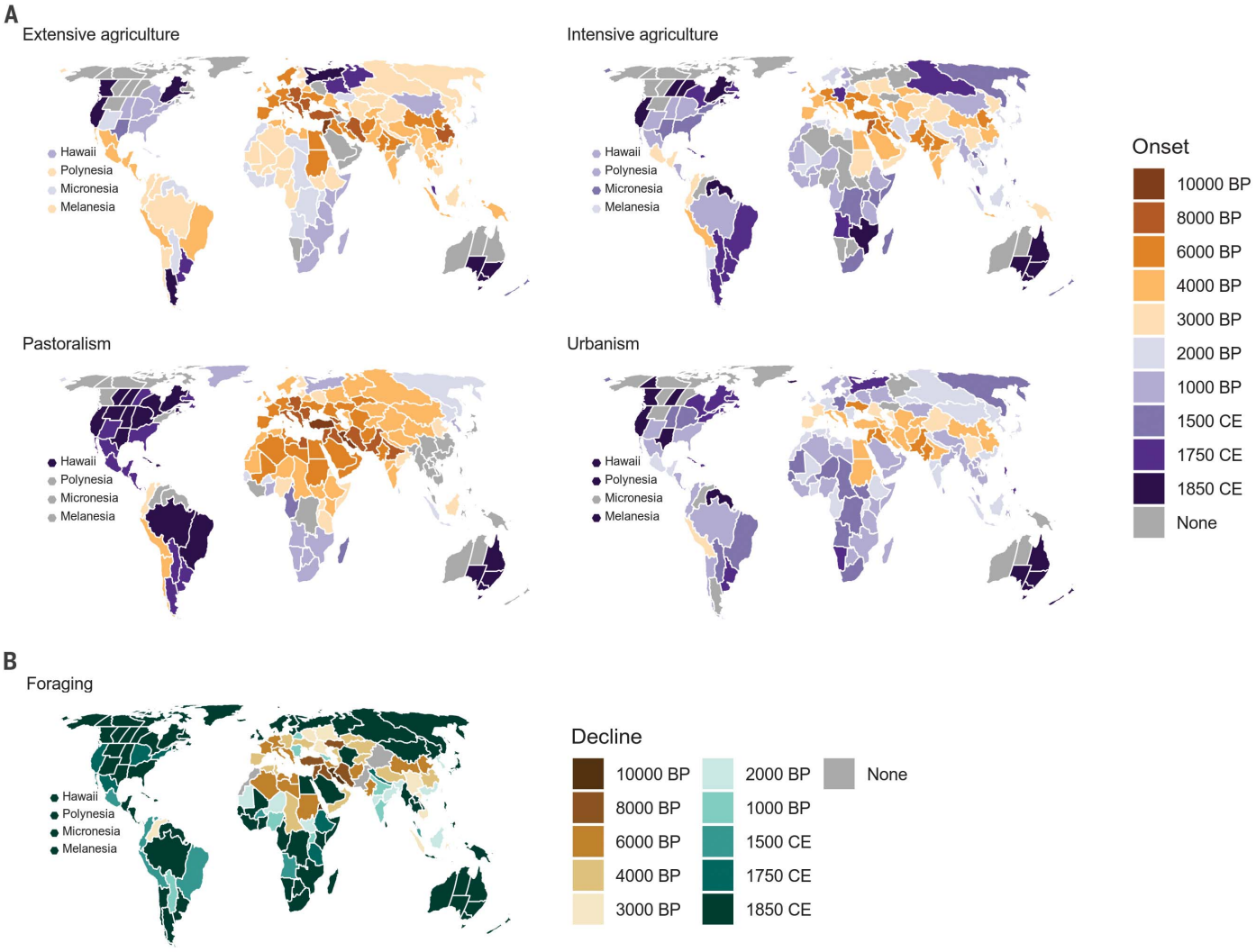

Fig. 4. Regional onsets of land-use categories and decline of foraging. (**A**) Onsets representing the earliest time step assessed at the "common" prevalence level (1 to 20% land area) for extensive agriculture, intensive agriculture, and pastoralism; the earliest time step was assessed as "present" for urbanism. (**B**) Decline representing the latest time step assessed at the "common" prevalence level for foraging.

Globally widespread evidence of hunter-gatherer land use indicates that ecological conditions across most of the terrestrial biosphere were influenced extensively by human activities even before the domestication of plants and animals. Although our dichotomous parsing of hunter-gatherers and agriculturalists is primarily operational, such divisions are still useful. Our data seem to support a unilineal trajectory toward increasingly intensive land use and the replacement of foraging with pastoralism and agriculture, a process that appears largely irreversible over the long term. Such trends also mask more complex pathways, as well as reversals at the local scale in numerous regions. In some parts of the world, agriculture did not simply replace foraging but merged with it and ran in parallel for some time, either as a

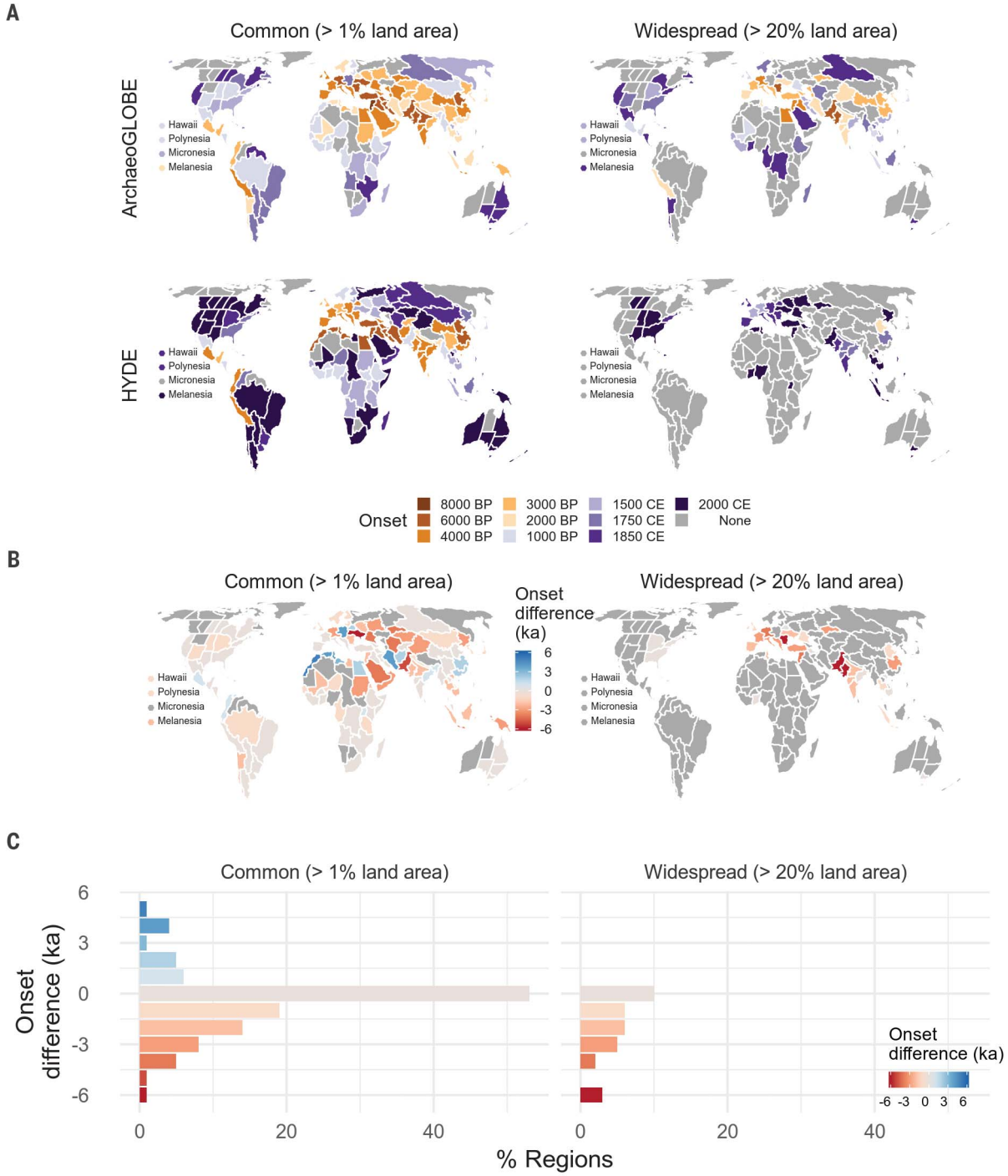

Fig. 5. Comparisons of agricultural onset in ArchaeoGLOBE versus HYDE. (**A**) Onset of intensive agriculture covering ≥1% regional area (common level) and ≥20% regional area (widespread level) in both the ArchaeoGLOBE and HYDE datasets; regions colored in gray did not surpass the associated threshold by 1850 CE for ArchaeoGLOBE and by 2000 CE for HYDE. (**B**) Map of differences in onset of intensive agriculture at common and widespread levels (in thousands of years; negative numbers highlight earlier ArchaeoGLOBE estimates). (**C**) Distributions of onset timing differences at common and widespread levels, same data and scale as (B).

patchwork of different peoples or seasonal shifts. The environmental effects of such mixed-mode land use are difficult to see in the archaeological and paleoecological record and are perhaps often missed in the dichotomous view of replacement by more advanced systems. Through time, as land became increasingly densely occupied and land use more intensive, opportunities for flexibility in subsistence strategies and the resilience that this supported were reduced.

This global archaeological assessment of early land use reveals a much earlier and more widespread global onset of intensive agriculture than the spatially explicit global historical reconstruction most commonly used to inform modeling studies of preindustrial vegetation and climate change [HYDE; (*14*)]. However, archaeological onsets of intensive agriculture appeared slightly later than those reported in the less widely used KK10 reconstruction (*15*). Substantial methodological differences and uncertainties between archaeological estimates and historical reconstructions mean that comparisons among ArchaeoGLOBE, HYDE, and KK10 must be treated with caution (*52*). The regional land-use estimates of our study represent a first step toward more accurate, empirically grounded, spatially explicit global reconstructions of long-term changes in land use and provide reference points and procedural approaches to constrain and correct these biases in future work. Our hope is that our global archaeological assessment, and the collaborative approach that it represents, will help to stimulate and support future efforts, such as work currently in progress through the PAGES LandCover6k initiative (*18*, *25*), toward the common goal of understanding early land use as a driver of long-term global environmental changes across the Earth system, including changes in climate.

REFERENCES AND NOTES

1. B. D. Smith, M. A. Zeder, *Anthropocene* **4**, 8–13 (2013).
2. P. V. Kirch, *Annu. Rev. Environ. Resour.* **30**, 409–440 (2005).
3. W. F. Ruddiman, E. C. Ellis, J. O. Kaplan, D. Q. Fuller, *Science* **348**, 38–39 (2015).
4. N. L. Boivin *et al*., *Proc. Natl. Acad. Sci. U.S.A.* **113**, 6388–6396 (2016).
5. J. O. Kaplan *et al*., *Holocene* **21**, 775–791 (2011).
6. D. Q. Fuller *et al*., *Holocene* **21**, 743–759 (2011).
7. E. C. Ellis, M. Maslin, N. Boivin, A. Bauer, *Nature* **540**, 192–193 (2016).
8. E. C. Ellis *et al*., *Proc. Natl. Acad. Sci. U.S.A.* **110**, 7978–7985 (2013).
9. D. M. J. S. Bowman *et al*., *J. Biogeogr.* **38**, 2223–2236 (2011).
10. W. F. Ruddiman *et al*., *Rev. Geophys.* **54**, 93–118 (2016).
11. E. C. Ellis, *Philos. Trans. A Math. Phys. Eng. Sci.* **369**, 1010–1035 (2011).
12. P. Roberts, C. Hunt, M. Arroyo-Kalin, D. Evans, N. Boivin, *Nat. Plants* **3**, 17093 (2017).
13. F. Marshall *et al*., *Nature* **561**, 387–390 (2018).
14. K. Klein Goldewijk, A. Beusen, J. Doelman, E. Stehfest, *Earth Syst. Sci. Data* **9**, 927–953 (2017).
15. J. O. Kaplan, K. M. Krumhardt, The KK10 Anthropogenic land cover change scenario for the preindustrial Holocene, link to data in NetCDF format. PANGEA (2011).
16. M.-J. Gaillard *et al*., *Clim. Past* **6**, 483–499 (2010).
17. K. Klein Goldewijk, M.-J. Gaillard, K. Morrison, M. Madella, N. Whitehouse, *PAGES Mag* **24**, 81 (2016).
18. M.-J. Gaillard, K. Morrison, M. Madella, N. Whitehouse, *PAGES Mag* **26**, 3 (2018).
19. C. N. H. McMichael, F. Matthews-Bird, W. Farfan-Rios, K. J. Feeley, *Proc. Natl. Acad. Sci. U.S.A.* **114**, 522–527 (2017).
20. A. Dawson *et al*., *PAGES Mag* **26**, 34–35 (2018).
21. J. W. Williams, P. Tarasov, S. Brewer, M. Notaro, *J. Geophys. Res. Biogeosci.* **116**, G01017 (2011).
22. B. Pirzamanbein *et al*., *Ecol. Complex.* **20**, 127–141 (2014).
23. A.-K. Trondman *et al*., *Glob. Chang. Biol.* **21**, 676–697 (2015).
24. M. Zanon, B. A. S. Davis, L. Marquer, S. Brewer, J. O. Kaplan, *Front. Plant Sci.* **9**, 253 (2018).
25. K. D. Morrison *et al*., *PAGES Mag.* **26**, 8–9 (2018).
26. T. A. Kohler *et al*., *PAGES Mag* **26**, 68–69 (2018).
27. J. W. Lewthwaite, A. Sherratt, "Chronological atlas," in *Cambridge Encyclopedia of Archeology*, A. Sherrat, Ed. (Cambridge Univ. Press, 1980).
28. G. Larson *et al*., *Proc. Natl. Acad. Sci. U.S.A.* **111**, 6139–6146 (2014).
29. J. M. Erlandson, T. J. Braje, *Anthropocene* **4**, 1–7 (2013).
30. K. W. Kintigh *et al*., *Proc. Natl. Acad. Sci. U.S.A.* **111**, 879–880 (2014).
31. B. S. Arbuckle *et al*., *PLOS ONE* **9**, e99845 (2014).
32. S. S. Downey, W. R. Haas Jr., S. J. Shennan, *Proc. Natl. Acad. Sci. U.S.A.* **113**, 9751–9756 (2016).
33. K. W. Kintigh *et al*., *Adv. Archaeol. Pract.* **3**, 1–15 (2015).
34. Materials and methods are available as supplementary materials.
35. S. Bartling, S. Friesike, Eds., *Opening Science: The Evolving Guide on How the Internet Is Changing Research, Collaboration and Scholarly Publishing* (Springer, 2014).
36. A. Bevan *et al*., *Holocene* **29**, 703–707 (2019).
37. N. Roberts *et al*., *Sci. Rep.* **8**, 716 (2018).
38. T. A. Surovell *et al*., *Am. Antiq.* **82**, 288–300 (2017).
39. L. J. Martin, B. Blossey, E. Ellis, *Front. Ecol. Environ.* **10**, 195–201 (2012).
40. B. S. Frey, P. Pamini, L. Steiner, *Int. Rev. Law Econ.* **60**, 1–19 (2013).
41. K. Manning, R. Pelling, T. Higham, J.-L. Schwenniger, D. Q. Fuller, *J. Archaeol. Sci.* **38**, 312–322 (2011).
42. F. Winchell, C. J. Stevens, C. Murphy, L. Champion, D. Fuller, *Curr. Anthropol.* **58**, 673–683 (2017).
43. A. U. Kay *et al*., *J. World Prehist.* **32**, 179–228 (2019).
44. T. Denham, *Antiquity* **87**, 250–257 (2013).
45. C. O. Hunt, R. J. Rabett, *J. Archaeol. Sci.* **51**, 22–33 (2014).
46. D. Q. Fuller, C. Murphy, *General Anthropology* **21**, 1–8 (2014).
47. D. Rindos *et al*., *Curr. Anthropol.* **21**, 751–772 (1980).
48. H. Raymond, *Annu. Rev. Anthropol.* **36**, 177–190 (2007).
49. D. M. J. S. Bowman *et al*., *Science* **324**, 481–484 (2009).
50. M. Pfeiffer, A. Spessa, J. O. Kaplan, *Geosci. Model Dev.* **6**, 643–685 (2013).
51. N. Nakicenovic, R. Swart, *Emissions Scenarios. Special Report of the Intergovernmental Panel on Climate Change* (2000); https://www.osti.gov/etdeweb/biblio/20134132.
52. J. Kaplan *et al*., *Land (Basel)* **6**, 91 (2017).
53. ArchaeoGLOBE Project, ArchaeoGLOBE Public Data, Version 3, Harvard Dataverse (2019).
54. ArchaeoGLOBE Project, ArchaeoGLOBE Regions, Version 6, Harvard Dataverse (2019).
55. ArchaeoGLOBE Project, ArchaeoGLOBE Repository, Version 2, Harvard Dataverse (2019).

ACKNOWLEDGMENTS

Funding: This material is based upon work supported by the National Science Foundation under grant no. CNS 1125210 awarded to E.C.E. in 2011. The full list of author, affiliations, and contributions is in the supplementary materials. **Author contributions**: L.S. led the project team and designed the research. E.E. conceived of and designed the research. D.F., N.B., T.R., N.G., A.K., B.M., C.M.B., J.D.R., J.H., and E.B. assisted with research design. L.S., D.F., N.B., T.R., N.G., A.K., B.M., C.G.D.A., C.M.B., T.D., K.D., J.D., L.J., P.R., J.D.R., H.T., M.A., A.L.J., M.M.S.V., M.A., S.A., G.A., M.T.B., T.B., F.B., T.B., P.I.B., N.G.J.C., J.M.C., A.D.C., C.C., M.N.C., J.C., P.R.C., R.A.C., M.C., A.C., L.D., S.D.L., J.F.D., W.E.D., K.J.E., J.M.E., D.E., E.F., P.F., G.F., R.F., S.M.F., R.F., E.G., S.G., R.C.G., J.D.G., J.H., P.H., P.H., K.A.H., C.H., J.W.I., A.J., J.G.K., B.K., C.K., T.R.K., F.L., D.L., G-A.L., M.J.L., H.B.L., J.A.L-S., S.M., R.M., J.M.M., S.M., M.D.M., A.V.M., M.M., G.M.M., J.M., A.N., S.N., T.M.P., C.E.P., L.P., A.R.R., S.R., G.R.S., K.R., R.S., V.S., P.S., P.S., O.S., I.A.S., A.S., R.J.S., R.N.S., M.L.S., M.J.S., K.M.S., J.T., T.L.T., S.U. M.C.U., M.H.W., C.W., P.R.W., D.K.W., N.W., M.Z., and A.Z., contributed and interpreted data. J.O.K., M-J.G., and K.K.G. interpreted data. L.S., N.G., B.M., M.A., S.M.G., J.P., A.T., and E.E. conducted data analysis. L.S., D.F., N.B., T.R., N.G., A.K., B.M., C.G.D.A., T.D., K.D., J.D., L.J., P.R., J.D.R., H.T., A.L.J., M.M.S.V., J.O.K., M-J.G., K.K.G., and E.E. drafted the article. **Competing interests**: The authors declare no competing interests. **Data and materials availability**: All project data are in the public domain (CC-0) and available at Harvard Dataverse (*53*–*55*).

SUPPLEMENTARY MATERIALS

science.sciencemag.org/content/365/6456/897/suppl/DC1
Materials and Methods
Figs. S1 to S7
Tables S1 to S4
ArchaeoGLOBE Project Author List
References (*56*–*60*)

22 February 2019; accepted 29 July 2019
10.1126/science.aax1192

REPORT

MANTLE CHEMISTRY

Deep magma ocean formation set the oxidation state of Earth's mantle

Katherine Armstrong*, Daniel J. Frost†, Catherine A. McCammon, David C. Rubie, Tiziana Boffa Ballaran

The composition of Earth's atmosphere depends on the redox state of the mantle, which became more oxidizing at some stage after Earth's core started to form. Through high-pressure experiments, we found that Fe^{2+} in a deep magma ocean would disproportionate to Fe^{3+} plus metallic iron at high pressures. The separation of this metallic iron to the core raised the oxidation state of the upper mantle, changing the chemistry of degassing volatiles that formed the atmosphere to more oxidized species. Additionally, the resulting gradient in redox state of the magma ocean allowed dissolved CO_2 from the atmosphere to precipitate as diamond at depth. This explains Earth's carbon-rich interior and suggests that redox evolution during accretion was an important variable in determining the composition of the terrestrial atmosphere.

Present-day noble gas abundances indicate that impacts caused extensive losses of Earth's proto-atmosphere during accretion (*1*, *2*). A substantial fraction of the atmosphere must therefore have formed by degassing of Earth's interior (*3*, *4*). The oxidation state of the upper mantle during the first 500 million years of Earth's history had a major influence on the composition and evolution of the atmosphere, as it controlled the redox state of degassing volatile species (*5*–*7*). Before Earth's metallic core was fully formed, the mantle was strongly reduced and would have degassed to produce an atmosphere dominated by the reduced gas species CO, CH_4, and H_2 (*7*, *8*). If this state had persisted, these reduced species would have prevented the rise of atmospheric O_2 (*9*). The upper mantle appears, however, to have been substantially more oxidized by the time the first minerals and rocks were formed. Redox conditions are quantified by the oxygen fugacity (f_{O_2}), and f_{O_2} values recorded by the oldest rocks indicate that the redox state of the upper mantle had increased by about 5 log units by the beginning of the geologic record. Subsequent changes appear to have been relatively minor (*10*–*14*). This oxidation event allowed the more oxidized species CO_2 and H_2O to degas from the mantle.

The main mechanism proposed to explain the increase in mantle redox state in the past has been oxidation by H_2O accompanied by the loss of H_2 to space (*8*, *15*). Although this almost certainly occurred to some extent, the question remains as to whether there would be sufficient H_2O left inside Earth after core formation to accomplish this. It is also unclear why Mars, a seemingly more volatile-rich planet than Earth, has an apparently more reduced primitive mantle (*16*–*18*). An alternative oxidation mechanism is based on FeO disproportionation caused by crystallization of bridgmanite, the dominant lower-mantle mineral. Experimental studies show that bridgmanite has a high $Fe^{3+}/\Sigma Fe$ ratio when in equilibrium with iron metal (*19*–*23*). This implies that the equilibrium $3FeO = Fe^0 + 2FeO_{1.5}$, involving ferric and ferrous iron components in mineral phases, shifted to the right as the lower mantle formed. This resulted in the disproportionation of FeO and the precipitation of iron metal (Fe^0). Segregation of precipitated iron metal from the crystallizing lower mantle into the core could have raised the bulk oxygen content of the entire mantle after convective mixing (*19*). We show that the same FeO disproportionation mechanism must occur in silicate liquid at conditions approaching those of the lower mantle, and hypothesize that the increase in the oxidation state of Earth's mantle was an inevitable consequence of the formation of one or more deep magma oceans.

We describe the f_{O_2} of a silicate melt using the equilibrium

$$FeO + {}^1\!/_4 O_2 = FeO_{1.5} \quad (1)$$

and the expression

$$f_{O_2} = \left(\frac{a^{melt}_{FeO_{1.5}}}{a^{melt}_{FeO} \times K} \right)^4 \quad (2)$$

where a^{melt}_{FeO} is the activity of the FeO component in the silicate melt and K is the equilibrium constant. At ambient pressure, K is such that silicate melts in equilibrium with metallic iron contain negligible Fe_2O_3. For this to change at higher pressures, the volume change for Eq. 1, $\Delta V_{[1]}$, must be negative.

We can determine the sign of $\Delta V_{[1]}$ by examining whether the $Fe^{3+}/\Sigma Fe$ ratio of a silicate melt increases with pressure at a constant temperature and buffered oxygen fugacity. Previous studies performed up to 7 GPa (*24*, *25*) indicated a positive $\Delta V_{[1]}$, which is consistent with the 1-bar volumes and compressibilities (*26*), although it has been proposed that this may change at higher pressures (*27*). We extended these measurements through a series of multianvil experiments to 23 GPa. We chose a relatively polymerized andesitic silicate melt composition to facilitate

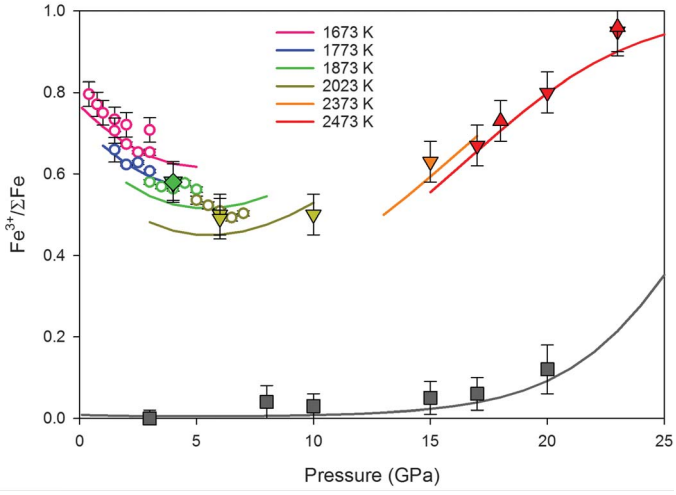

Fig. 1. Ferric iron contents of quenched silicate melts buffered at different oxygen fugacities. We buffered the experimental oxygen fugacity either by the assemblage Ru + O_2 = RuO_2 (colored symbols indicate temperatures), which has an oxygen fugacity of ~ΔIW +8, or by equilibrium with Fe metal (gray squares), ~ΔIW −2. Downward- and upward-pointing triangles indicate initially fully oxidized and fully reduced starting materials, respectively. Results from previous studies are shown as open circles (*24*, *25*). All starting compositions were andesitic except an experiment at 4 GPa that had a MORB melt composition (green diamond). The curves show the fit of our model to the experimental data. The gray curve is calculated for liquid iron metal saturation at 2373 K. The experimental temperature uncertainties are ~50 K.

Bayerisches Geoinstitut, University of Bayreuth, D-95447 Bayreuth, Germany.
*Present address: Peter A. Rock Thermochemistry Laboratory, University of California, Davis, CA, USA.
†Corresponding author. Email: dan.frost@uni-bayreuth.de

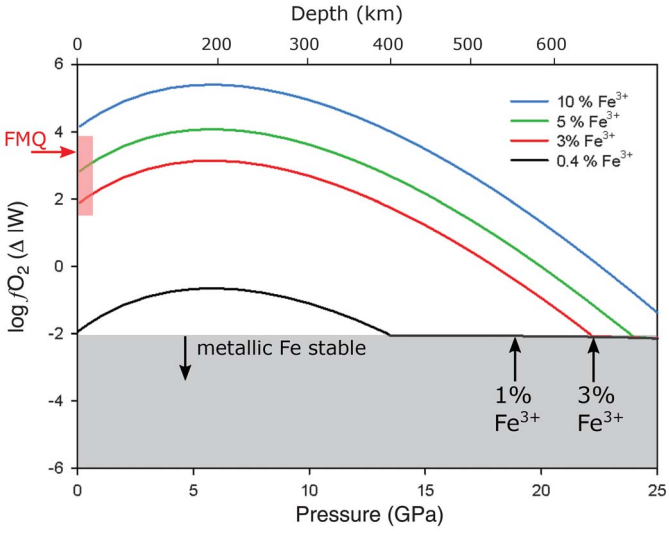

Fig. 2. Magma ocean oxygen fugacity profiles for different bulk $Fe^{3+}/\Sigma Fe$ percentages. We normalized the oxygen fugacity to the iron-wüstite buffer (ΔIW). The value of the FMQ (fayalite, magnetite, quartz) buffer is indicated by the red arrow. The present-day range in upper mantle f_{O_2} is approximated by the vertical red bar. We assume a mantle adiabatic potential temperature of 2273 K. The gray shaded region indicates the f_{O_2} where metallic iron precipitates. Metallic iron precipitation buffers the oxygen fugacity, flattening it with increasing pressure. A magma ocean containing initially only 0.4% ferric iron will start to precipitate metallic iron at ~400 km. If the metal separates to the core, the ferric iron content of the magma ocean will rise to values indicated by the vertical arrows. Once the ferric iron content of the magma ocean reaches 3%, the near-surface f_{O_2} is within the range for the present-day mantle.

glass formation when quenching at high pressures. We used two starting compositions so that we could approach the equilibrium $Fe^{3+}/\Sigma Fe$ ratio both from an initially more oxidized and a more reduced composition. We equilibrated melts with a Ru-RuO_2 buffer, placed in the sample capsule, that resulted in an f_{O_2} approximately 8 log units above the iron-wüstite oxygen buffer (ΔIW +8). The relatively high f_{O_2} makes the measurements more reliable and is not problematic because $\Delta V_{[1]}$ should be independent of f_{O_2}.

After equilibration at high pressure, we analyzed the $Fe^{3+}/\Sigma Fe$ ratios of the quenched silicate melts using Mössbauer spectroscopy. Above 10 GPa, the silicate melt crystallized upon quenching instead of forming a glass. We assumed that the $Fe^{3+}/\Sigma Fe$ ratios of the silicate melts were unmodified by crystallization. The $Fe^{3+}/\Sigma Fe$ ratios we determined near the boundary between glass and crystallized melts were similar, and we did not have any multivalent elements in large enough concentrations to cause major changes in speciation through electron exchange during quenching (*28*).

We found an initial decrease in the $Fe^{3+}/\Sigma Fe$ ratio with increasing pressure (Fig. 1), consistent with a positive $\Delta V_{[1]}$, but the trend reversed above 10 GPa, indicating a negative $\Delta V_{[1]}$. We rationalized this behavior as being due to the compressibility of the Fe_2O_3 melt component becoming greater than that of FeO at high pressure. This could be caused by a pressure-induced change in coordination of Fe^{3+} in the melt (*7*, *29*). We fit the data with a thermodynamic expression for Eq. 1 that describes the $Fe^{3+}/\Sigma Fe$ ratio of the melt as a function of temperature, pressure, f_{O_2}, and melt composition (*24*, *30*). We used a modified third-order Tait equation of state (*31*, *32*) to describe the volumes of the iron oxide components in the melt, allowing us to fit a model to the pressure dependence of the $Fe^{3+}/\Sigma Fe$ ratio (*28*) by refining the iron components' bulk moduli and their pressure derivatives. We tested for the effects of melt composition by performing an experiment at 4 GPa on a mid-ocean ridge basalt (MORB) composition. The resulting melt had an $Fe^{3+}/\Sigma Fe$ ratio almost identical to that of the andesitic melt at the same conditions, which is consistent with predictions (*24*, *30*). We also performed additional experiments at low oxygen fugacities by equilibrating andesitic melts with iron metal. We found constant low $Fe^{3+}/\Sigma Fe$ ratios within error up to 10 GPa, but an increase at higher pressures. Our thermodynamic model reproduces these data well, demonstrating that $\Delta V_{[1]}$, which governs the pressure dependence of the melt $Fe^{3+}/\Sigma Fe$, is essentially independent of f_{O_2}. The increase in Fe_2O_3 stability above 10 GPa results in a substantial proportion of Fe_2O_3 in the melt when in equilibrium with metallic iron. This means that a melt with a negligible Fe_2O_3 content that is transported to pressures above 10 GPa must precipitate iron metal to produce the appropriate equilibrium Fe_2O_3 melt content through the oxidation of FeO.

The accretion of planetary embryos through giant impacts likely resulted in multiple phases of extensive or even complete melting of the proto-Earth (*33*–*36*). We used our model to calculate f_{O_2} as a function of depth though a magma ocean (Fig. 2) created by such a giant impact, by assuming that vigorous convection (*37*, *38*) produced a well-mixed magma with a homogeneous $Fe^{3+}/\Sigma Fe$ ratio. We performed the calculation for a bulk silicate Earth composition, which resulted in a small shift in the f_{O_2}–$Fe^{3+}/\Sigma Fe$ relationship for the melt relative to the andesitic melts due to changes in the activities of the iron components (*28*).

To calculate f_{O_2} as a function of depth, we first take the hypothetical case of an initially reduced magma ocean that is in equilibrium with Fe metal near the surface (Fig. 2). Such a magma ocean would have an $Fe^{3+}/\Sigma Fe$ ratio of ~0.004 and an f_{O_2} of approximately ΔIW −2. For simplicity, we have ignored the effect of Ni, which would raise the f_{O_2} of metal iron equilibrium by up to 1 log unit by forming a Ni-Fe metallic liquid (*28*). For this constant $Fe^{3+}/\Sigma Fe$ ratio, the melt f_{O_2} initially increases slightly with increasing depth and is no longer metal-saturated until 200 km, where the trend reverses because of the sign change of $\Delta V_{[1]}$. Below 400 km, the f_{O_2} of the magma reaches a value at which metallic iron is again stable. At this depth, FeO would disproportionate and precipitate iron metal in order to reach the equilibrium Fe_2O_3 content. With increasing pressure, the negative sign of $\Delta V_{[1]}$ implies that both metal and Fe_2O_3 are produced and the melt $Fe^{3+}/\Sigma Fe$ ratio increases, while the f_{O_2} of the melt flattens out as a result of buffering by iron metal.

If the precipitated metal segregates to the core, the net result is an increase in the Fe_2O_3 content of the silicate liquid. The separation of 0.1 weight percent metal to the core, followed by convective homogenization, would raise the $Fe^{3+}/\Sigma Fe$ of the magma to 0.03 (Fig. 2), which is close to estimates of the present-day mantle (*39*). Greater $Fe^{3+}/\Sigma Fe$ ratios may well have been reached through the separation of more iron metal to the core from progressively greater magma ocean depths, as the ratio of 0.03 estimated for the present-day upper mantle is probably lower than that of the bulk silicate Earth.

Our model shows that for a constant $Fe^{3+}/\Sigma Fe$ ratio, maintained by convection, a gradient in melt f_{O_2} with depth is established. A melt with a ratio of 0.03 remains in equilibrium with metallic iron at lower mantle depths but has an f_{O_2} consistent with the degassing of CO_2 and H_2O near the surface (>ΔIW +2). The f_{O_2} gradient is similar to that proposed for the present-day mantle, which may also reach iron metal saturation at a similar depth (*40*). This is supported by recent observations of iron metal–rich inclusions in gem-quality diamonds that formed between 400 and 660 km depth (*41*).

The removal of metal produced by FeO disproportionation may have raised the $Fe^{3+}/\Sigma Fe$ ratio of the mantle even before core formation was complete. Equilibration with core-forming metal during accretion would have reduced mantle $Fe^{3+}/\Sigma Fe$ ratios to very low values. If the later stages of Earth's accretion, starting from a planetary embryo (i.e., a Mars-size body), occurred mainly through multiple giant collisions (*33*–*36*), FeO disproportionation within each of the resulting magma oceans would have raised the $Fe^{3+}/\Sigma Fe$ ratio of the mantle once the impactor's core had fully segregated. This implies that a H_2O- and CO_2-dominated atmosphere may have been maintained throughout the final stages of accretion. On the other hand, magma oceans on smaller bodies such as the Moon, Mars,

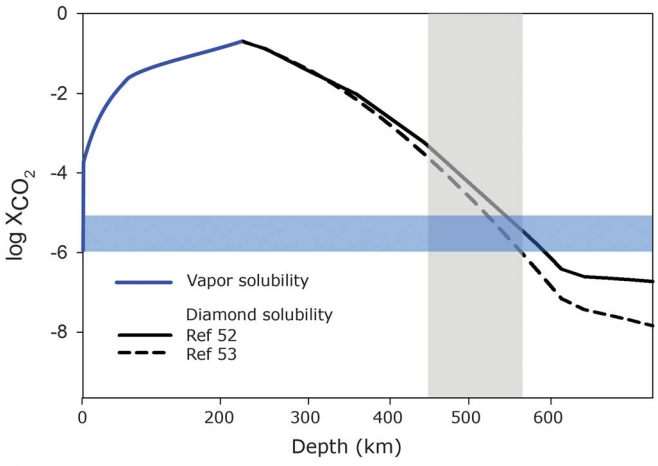

Fig. 3. Carbon dioxide concentration in a magma ocean in equilibrium with diamond. The CO_2 content (in mole fraction) of a CO_2 vapor–saturated melt is shown by the blue curve (*52*); the black curves show the CO_2 content of a diamond-saturated melt, calculated with two different methods (*28*, *52*, *53*). The magma CO_2 concentration is a function of atmospheric CO_2 partial pressure (*7*) but is potentially in the range 1 to 10 ppm, as indicated by the horizontal shaded region. The calculation is performed at 2273 K assuming an oxygen fugacity gradient constrained by a melt with a constant $Fe^{3+}/\Sigma Fe$ ratio of 0.03. The CO_2 content of the melt at diamond saturation drops with depth as f_{O_2} decreases. A melt containing less than 10 ppm CO_2 dissolved at the surface will precipitate diamond at depths of >500 km. The vertical shaded band indicates the approximate conditions, including temperature uncertainty, where diamond is neutrally buoyant in ultramafic melt (*44*, *45*). At depths of >600 km, the melts become saturated in iron metal.

and Vesta were of insufficient depth to cause disproportionation. This explains why their mantles are more reduced [closer to IW (*16*–*18*)], despite Mars forming from more volatile-rich, and therefore potentially more oxidized, material (*42*).

Our experiments were not able to address what happens to the redox conditions in magmas at much higher pressures, which could be relevant for impacts that melted the entire mantle. However, the compressibility of the Fe_2O_3 melt component rivals that of FeO as lower mantle pressures are approached, which may reverse the rising trend in melt $Fe^{3+}/\Sigma Fe$ ratio with pressure. Our model shows some indication of this (Fig. 1) for the more oxidizing conditions. A larger unknown is the impact of electronic spin transitions involving both iron oxide components that could potentially influence the melt $Fe^{3+}/\Sigma Fe$ ratio. These uncertainties are unlikely to negate the effect of FeO disproportionation, even if the latter were restricted to a depth interval near the top of the lower mantle, because the entire magma ocean would pass through this region as a result of convection. The metal produced would ultimately sink to the core, and the increase in Fe_2O_3 would be redistributed to the mantle as a whole through convective mixing.

A gradient in f_{O_2} through a deep magma ocean has been proposed (*7*) to result in a "carbon pump" mechanism that continuously removed small amounts of CO_2 from the overlying atmosphere by dissolution in the magma and subsequent precipitation as diamond in the interior. As Earth experienced a late (Moon-forming) giant impact, this carbon pump might have been important for moving CO_2 from the atmosphere into the mantle. This may explain why, in contrast to other volatile elements such as H and N, a substantial portion of Earth's carbon resides in the mantle (*43*). The carbon pump would operate because a magma ocean in equilibrium with a CO_2-rich atmosphere would still dissolve a few parts per million of CO_2 (*43*). The CO_2 concentration at which the melt reaches carbon (graphite/diamond) saturation, however, would decrease with decreasing f_{O_2} and therefore with depth. This is illustrated in Fig. 3, where we calculate this CO_2 concentration for a magma ocean with an $Fe^{3+}/\Sigma Fe$ of 0.03. As a result of the decrease in f_{O_2}, the CO_2 content of the melt in equilibrium with diamond drops to below 10 ppm at >500 km depth. At such depths, excess carbon would precipitate as diamond and would be neutrally buoyant (*44*, *45*). With time, the diamond content of the mantle would rise, even if the concentration of CO_2 carried by the melt from the surface was low. Venus, on the other hand, may have developed a more CO_2-rich atmosphere because it had not experienced a late giant impact and deep magma ocean formation in which the carbon pump could operate (*46*).

The increase in the oxidation state of the mantle before the end of accretion would also have influenced the conditions under which siderophile (iron metal–loving) elements partitioned into the core, particularly for impactors that were too small to influence mantle f_{O_2}. FeO disproportionation would create an oxidized upper mantle in which small amounts of accreting metal would dissolve. Metal would, however, precipitate again toward lower mantle depths. Siderophile element partitioning would then take place at high pressures and the most oxidizing conditions possible for metal-silicate equilibration in Earth. This may have been important for controlling the proportion of volatile elements that partitioned into the core, particularly if they were delivered predominantly toward the end of accretion (*47*). Earth's apparent depletion of nitrogen might be explained, for example, because it becomes siderophile under such conditions (*48*–*50*). The separation of metal formed through disproportionation would have also prevented highly siderophile elements from becoming overabundant in the silicate Earth toward the final stages of core formation (*51*).

REFERENCES AND NOTES

1. H. E. Schlichting, S. Mukhopadhyay, *Space Sci. Rev.* **214**, 34 (2018).
2. H. Genda, Y. Abe, *Nature* **433**, 842–844 (2005).
3. J. M. Tucker, S. Mukhopadhyay, *Earth Planet. Sci. Lett.* **393**, 254–265 (2014).
4. H. Lammer *et al.*, *Astron. Astrophys. Rev.* **26**, 2 (2018).
5. L. R. Kump, J. F. Kasting, M. E. Barley, *Geochem. Geophys. Geosyst.* **2**, 2000GC000114 (2001).
6. L. Schaefer, B. Fegley Jr., *Icarus* **186**, 462–483 (2007).
7. M. M. Hirschmann, *Earth Planet. Sci. Lett.* **341–344**, 48–57 (2012).
8. J. F. Kasting, D. H. Eggler, S. P. Raeburn, *J. Geol.* **101**, 245–257 (1993).
9. D. C. Catling, M. W. Claire, *Earth Planet. Sci. Lett.* **237**, 1–20 (2005).
10. D. Canil, *Nature* **389**, 842–845 (1997).
11. J. W. Delano, *Orig. Life Evol. Biosph.* **31**, 311–341 (2001).
12. D. Trail, E. B. Watson, N. D. Tailby, *Nature* **480**, 79–82 (2011).
13. S. Aulbach, V. Stagno, *Geology* **44**, 751–754 (2016).
14. R. W. Nicklas *et al.*, *Geochim. Cosmochim. Acta* **250**, 49–75 (2019).
15. Z. D. Sharp, F. M. McCubbin, C. K. Shearer, *Earth Planet. Sci. Lett.* **380**, 88–97 (2013).
16. C. D. K. Herd, L. E. Borg, J. H. Jones, J. J. Papike, *Geochim. Cosmochim. Acta* **66**, 2025–2036 (2002).
17. M. Wadhwa, *Rev. Mineral. Geochem.* **68**, 493–510 (2008).
18. E. A. Pringle, P. S. Savage, J. Badro, J.-A. Barrat, F. Moynier, *Earth Planet. Sci. Lett.* **373**, 75–82 (2013).
19. D. J. Frost *et al.*, *Nature* **428**, 409–412 (2004).
20. Y. Nakajima, D. J. Frost, D. C. Rubie, *J. Geophys. Res.* **117**, B08201 (2012).
21. A. Rohrbach *et al.*, *Nature* **449**, 456–458 (2007).
22. S.-H. Shim *et al.*, *Proc. Natl. Acad. Sci. U.S.A.* **114**, 6468–6473 (2017).
23. D. Andrault *et al.*, *Geochem. Perspect. Lett.* **6**, 5–10 (2018).
24. H. S. C. O'Neill *et al.*, *Am. Mineral.* **91**, 404–412 (2006).
25. H. L. Zhang, M. M. Hirschmann, E. Cottrell, A. C. Withers, *Geochim. Cosmochim. Acta* **204**, 83–103 (2017).
26. V. C. Kress, I. S. E. Carmichael, *Contrib. Mineral. Petrol.* **108**, 82–92 (1991).
27. L. Schaefer, L. T. Elkins-Tanton, *Philos. Trans. R. Soc. A.* **376**, 20180109 (2018).
28. See supplementary materials.
29. Q. Liu, R. A. Lange, *Am. Mineral.* **91**, 385–393 (2006).
30. K. D. Jayasuriya, H. St. C. O'Neill, A. J. Berry, S. J. Campbell, *Am. Mineral.* **89**, 1597–1609 (2004).
31. Y. K. Huang, C. Y. Chow, *J. Phys. D* **7**, 2021–2023 (2002).
32. T. J. B. Holland, R. Powell, *J. Metamorph. Geol.* **29**, 333–383 (2011).
33. W. B. Tonks, H. J. Melosh, *J. Geophys. Res.* **98**, 5319–5333 (1993).
34. J. de Vries *et al.*, *Prog. Earth Planet. Sci.* **3**, 7 (2016).
35. C. B. Agnor, R. M. Canup, H. F. Levison, *Icarus* **142**, 219–237 (1999).
36. L. T. Elkins-Tanton, *Annu. Rev. Earth Planet. Sci.* **40**, 113–139 (2012).
37. Y. S. Solomatov, in *Origin of the Earth and Moon*, R. Canup, K. Righter, Eds. (Univ. of Arizona Press, 2000), pp. 323–338.
38. D. C. Rubie, H. J. Melosh, J. E. Reid, C. Liebske, K. Righter, *Earth Planet. Sci. Lett.* **205**, 239–255 (2003).
39. A. B. Woodland, J. Kornprobst, A. Tabit, *Lithos* **89**, 222–241 (2006).
40. D. J. Frost, C. A. McCammon, *Annu. Rev. Earth Planet. Sci.* **36**, 389–420 (2008).
41. E. M. Smith *et al.*, *Science* **354**, 1403–1405 (2016).
42. G. Dreibus, H. Wänke, *Icarus* **71**, 225–240 (1987).
43. M. M. Hirschmann, *Earth Planet. Sci. Lett.* **502**, 262–273 (2018).
44. E. Ohtani, M. Maeda, *Earth Planet. Sci. Lett.* **193**, 69–75 (2001).
45. A. Suzuki, E. Ohtani, T. Kato, *Science* **269**, 216–218 (1995).
46. S. A. Jacobson, D. C. Rubie, J. Hernlund, A. Morbidelli, M. Nakajima, *Earth Planet. Sci. Lett.* **474**, 375–386 (2017).

47. M. Schönbächler, R. W. Carlson, M. F. Horan, T. D. Mock, E. H. Hauri, *Science* **328**, 884–887 (2010).
48. B. Marty, *Earth Planet. Sci. Lett.* **313–314**, 56–66 (2012).
49. M. Roskosz, M. A. Bouhifd, A. P. Jephcoat, B. Marty, B. O. Mysen, *Geochim. Cosmochim. Acta* **121**, 15–28 (2013).
50. C. Dalou, M. M. Hirschmann, A. von der Handt, J. Mosenfelder, L. S. Armstrong, *Earth Planet. Sci. Lett.* **458**, 141–151 (2017).
51. D. C. Rubie *et al*., *Science* **353**, 1141–1144 (2016).
52. B. Guillot, N. Sator, *Geochim. Cosmochim. Acta* **75**, 1829–1857 (2011).
53. M. S. Duncan, R. Dasgupta, K. Tsuno, *Earth Planet. Sci. Lett.* **466**, 115–128 (2017).

ACKNOWLEDGMENTS

We thank D. Krauße for assistance with EPMA, and H. Schulze, R. Njul, and A. Rother for sample preparation. Discussions with L. Schaefer and M. Hirschmann are greatly appreciated. **Funding:** Supported by the DFG-SPP program 1833 "Building a Habitable Earth" through grant FR 1555/10-1 and through the DFG international research and training group "Deep Volatile Cycles," GRK 2156/1. **Author contributions:** D.J.F. and D.C.R. conceived the project. K.A. performed experiments, analyzed data, and derived the thermodynamic model. C.M. collected and analyzed Mössbauer spectra. T.B.B. collected and analyzed XRD data. K.A. and D.J.F. wrote the manuscript. **Competing interests:** Authors declare no competing interests. **Data and materials availability:** All data are available in the main text or the supplementary materials.

SUPPLEMENTARY MATERIALS

science.sciencemag.org/content/365/6456/903/suppl/DC1
Materials and Methods
Supplementary Text
Figs. S1 to S7
Tables S1 to S6
References (*54*–*75*)

26 April 2019; accepted 2 August 2019
10.1126/science.aax8376

SUPERCONDUCTIVITY

Dynamical charge density fluctuations pervading the phase diagram of a Cu-based high-T_c superconductor

R. Arpaia[1,2]*, S. Caprara[3,4], R. Fumagalli[1], G. De Vecchi[1], Y. Y. Peng[1]†, E. Andersson[2], D. Betto[5], G. M. De Luca[6,7], N. B. Brookes[5], F. Lombardi[2], M. Salluzzo[7], L. Braicovich[1,5], C. Di Castro[3,4], M. Grilli[3,4], G. Ghiringhelli[1,8]*

Charge density modulations have been observed in all families of high–critical temperature (T_c) superconducting cuprates. Although they are consistently found in the underdoped region of the phase diagram and at relatively low temperatures, it is still unclear to what extent they influence the unusual properties of these systems. Using resonant x-ray scattering, we carefully determined the temperature dependence of charge density modulations in $YBa_2Cu_3O_{7-\delta}$ and $Nd_{1+x}Ba_{2-x}Cu_3O_{7-\delta}$ for several doping levels. We isolated short-range dynamical charge density fluctuations in addition to the previously known quasi-critical charge density waves. They persist up to well above the pseudogap temperature T^*, are characterized by energies of a few milli–electron volts, and pervade a large area of the phase diagram.

Cuprate high-temperature superconductors (HTSs) deviate from the Landau Fermi liquid paradigm as a result of the quasi–two-dimensionality of their layered structure and the large electron-electron repulsion. The doping (p)–temperature (T) phase diagram encompasses, at low T, the antiferromagnetic and the superconducting orders and, at higher T, the pseudogap region, which is characterized by a reduction of the quasi-particle density of states in some sections of the Fermi surface below the crossover temperature T^*. In the pseudogap state and up to optimal doping $p \sim 0.17$, short- to medium-range incommensurate charge density wave (CDW) order emerges and competes weakly with superconductivity. Theoretical proposals of CDW (*1*–*3*) and of low-energy charge fluctuations (*4*) were first put forward not long after the discovery of HTS; experimental evidence from surface and bulk sensitive techniques came initially in selected materials (*5*–*8*) and later in all cuprate families (*9*–*14*). Moreover, long-range tridimensional CDW (3D CDW) order has been observed inside the superconducting dome (for $p \sim 0.08$ to 0.17) in special circumstances, such as in high magnetic fields that weaken superconductivity or in epitaxially grown samples (*15*–*17*). Finally, the recent observation of charge density modulations in overdoped $(Bi,Pb)_{2.12}Sr_{1.88}CuO_{6+\delta}$ outside the pseudogap regime (*18*) hints at a wider than expected occurrence of this phenomenon.

The relevance of charge density modulations for the unconventional normal state and the superconducting properties of HTS is currently being debated. In some theoretical models, long- and short-range CDW orders are seen as epiphenomena on top of a fundamentally peculiar metallic state, where the endpoint at $T = 0$ of the pseudogap boundary line ($p^* \sim 0.19$ to 0.21) marks the physical onset of a non–Fermi liquid metallic phase (*19*–*24*). In alternative scenarios, charge density modulations are instead pivotal to the anomalous properties of cuprates (*1*, *25*–*27*). In such scenarios, CDW orders are expected to be critical [i.e., associated with the divergence of a correlation length at a quantum critical point (QCP)] and to permeate, through charge density fluctuations (CDFs), a much broader area of the phase diagram. In this context, short-range correlations extending up to room temperature have recently been observed in the electron-doped cuprate $Nd_{2-x}Ce_xCuO_4$ (*13*). To establish to what extent static and fluctuating charge density modulations contribute to the phase diagram, we have measured them in $YBa_2Cu_3O_{7-\delta}$ and $Nd_{1+x}Ba_{2-x}Cu_3O_{7-\delta}$ as a function of doping and temperature. We have discovered that CDFs are present over a broad region of the phase diagram, which strengthens the importance of charge density modulations in determining the normal-state properties of cuprates; additionally, our findings are consistent with the previously known short- to medium-range CDW orders being precursors of the long-range charge modulation detected in the presence of high magnetic fields, pointing toward CDW orders as a quasi-critical phenomenon.

We measured resonant inelastic x-ray scattering (RIXS) on five $YBa_2Cu_3O_{7-\delta}$ (YBCO) and $Nd_{1+x}Ba_{2-x}Cu_3O_{7-\delta}$ (NBCO) thin films spanning a broad range of oxygen doping, going from the antiferromagnetic (AF) region, where T^* is not even defined, passing through the underdoped (UD) and the optimally doped (OP) regime, up to the slightly overdoped region (i.e., beyond the pseudogap line) (fig. S1) (*28*–*30*). Measurements were performed at the Cu L_3 edge (~930 eV), over broad in-plane wave vector ranges ($q_{||} = 0.2$ to 0.4 reciprocal lattice units, r.l.u.) and temperature ranges ($T = 20$ to 270 K). Figure 1C shows the quasi-elastic (near-zero energy loss) component of the RIXS spectra as a function of $q_{||} = (H, 0)$ taken on sample UD60 (NBCO, $p \approx 0.11$) at different temperatures. A clear peak is present in the whole temperature range under investigation. The intensity of the peak decreases as the temperature increases, with little temperature dependence above 200 K. A quasi-elastic peak, robust versus temperature, is also present in samples UD81 (YBCO, $p \approx 0.14$; Fig. 1B) and OP90 (NBCO, $p \approx 0.17$; Fig. 1A). In contrast, the antiferromagnetic sample (NBCO AF) shows no peaks above the linear background (Fig. 1D). These data highlight the existence of a genuine quasi–T-independent scattering signal representative of short-range charge modulations; although this peak was present in previously published x-ray scattering data on YBCO, $Bi_2Sr_{2-x}La_xCuO_{6+\delta}$, $La_{2-x}Sr_xCuO_4$, and other cuprates, it had been considered to be part of the "high-temperature" background and subtracted out; consequently, it had not been thoroughly discussed (*10*, *12*, *31*–*33*). Note that no peak is present in the (H, H) direction, where a featureless linear shape is observed that can be used as a linear background in the fitting of the scans along $(H, 0)$ (Fig. 2, A to C). The scattering peak intensity is approximatively linear versus $1/T$ (Fig. 1C, inset): The extrapolation to very high temperature ($1/T = 0$) provides an estimate of the intrinsic background of the signal, stemming mainly from the scattering from low-energy phonons and surface imperfections (fig. S3) (*28*).

We decomposed the $(H, 0)$ scans by least-squares fitting to extract the peak intensity, width, and position. Figure 2 shows the results for sample UD60. At high temperatures, the quasi-elastic intensity can be fitted by assuming a single, broad Lorentzian profile on top of a linear background (Fig. 2B). At lower temperatures, two peaks are necessary: a broad peak (BP), very similar to that measured at higher temperature, and a narrow peak (NP) centered at a nearby value of H. We also scanned along K while fixing $H = H_{NP}$ at the maximum of the NP in the $(H, 0)$ scan; there, the shape consists of a narrow and a broad peak, both centered at $K = 0$. Because the temperature dependence of the K-scans follows that of the H-scans (fig. S2) (*28*), the quasi-elastic peak in the reciprocal space can be modeled by a double 2D Lorentzian, a broad one and a narrow one, centered respectively at $q_c^{NP} = (0.325, 0)$ and at $q_c^{BP} = (0.295, 0)$ (Fig. 2E).

[1]Dipartimento di Fisica, Politecnico di Milano, I-20133 Milano, Italy. [2]Quantum Device Physics Laboratory, Department of Microtechnology and Nanoscience, Chalmers University of Technology, SE-41296 Göteborg, Sweden. [3]Dipartimento di Fisica, Università di Roma "La Sapienza," I-00185 Roma, Italy. [4]CNR-ISC, I-00185 Roma, Italy. [5]ESRF, European Synchrotron, F-38043 Grenoble, France. [6]Dipartimento di Fisica "E. Pancini," Università di Napoli Federico II, Complesso Monte Sant'Angelo, I-80126 Napoli, Italy. [7]CNR-SPIN, Complesso Monte Sant'Angelo, I-80126 Napoli, Italy. [8]CNR-SPIN, Dipartimento di Fisica, Politecnico di Milano, I-20133 Milano, Italy.
*Corresponding author. E-mail: riccardo.arpaia@chalmers.se (R.A.); giacomo.ghiringhelli@polimi.it (G.G.) †Present address: International Center for Quantum Materials, School of Physics, Peking University, CN-100871 Beijing, China.

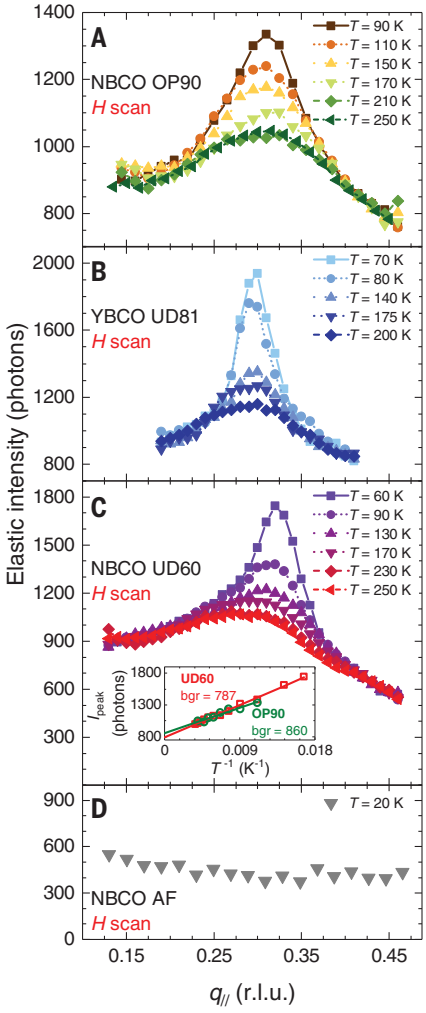

Fig. 1. Quasi-elastic scan along the (*H*, 0) direction for several $YBa_2Cu_3O_{7-\delta}$ and $Nd_{1+x}Ba_{2-x}Cu_3O_{7-\delta}$ films with different oxygen dopings. The quasi-elastic intensity was determined by integrating the Cu L_3 RIXS spectra measured at different $q_{||}$ values in the energy interval [−0.2 eV, +0.15 eV]. The measurements were performed at different temperatures on the following samples: (**A**) Optimally doped NBCO, $p \approx 0.17$. (**B**) Underdoped YBCO, $p \approx 0.14$. (**C**) Underdoped NBCO, $p \approx 0.11$. (**D**) Insulating NBCO, $p < 0.05$. The inset in (C) shows the peak intensity I_{peak} versus T^{-1} for samples OP90 (circles) and UD60 (squares). The extrapolation to $T \rightarrow \infty$ provides an estimate of the intrinsic background of the signal (bgr).

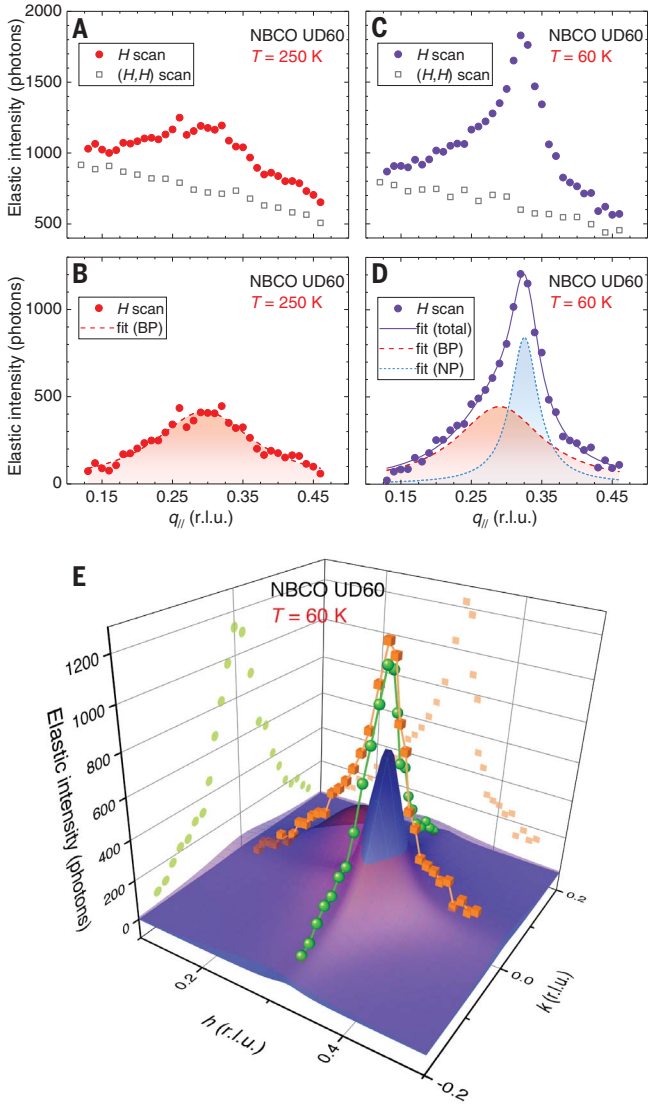

Fig. 2. Two distinct peaks in fits to NBCO UD60 data. (**A**) Quasi-elastic scan measured along (*H*, 0) on sample UD60 at $T = 250$ K (red circles). (**B**) After subtracting the linear background, given by the quasi-elastic scan measured along the Brillouin zone diagonal [open squares in (A)], a clear peak is still present, which can be fitted by a Lorentzian profile (dashed line). (**C**) Same as (A), but at $T = 60$ K (violet circles). (**D**) After subtracting the linear background [open squares in (C)], the data can be fitted with a sum of two Lorentzian profiles (solid line): one broader (dashed line), similar to that measured at 250 K, and the second one narrower and more intense (dotted line). (**E**) The 3D sketch shows the quasi-elastic scans measured along *H* (cubes) and along *K* (spheres) at $T = 60$ K on sample UD60, together with the Lorentzian profiles used to fit them. A narrow peak (NP, blue surface) emerges at $q_c^{NP} = (0.325, 0)$ from a much broader peak (BP, red surface) centered at $q_c^{BP} = (0.295, 0)$.

Figure 3 summarizes the outcome of the fittings for the samples UD60 and OP90, whereas fig. S6 reports the corresponding results for the UD81 sample. The NP presents all the characteristics previously observed in several underdoped cuprates and commonly attributed to the incommensurate CDWs. The BP shares with the NP the position in the reciprocal space (although with small differences; see fig. S7), but it has a very different, almost constant, temperature dependence. Therefore, we attribute the BP to very short-range charge modulations (i.e., to CDFs), as depicted by the reddish region of the *T*-*p* phase diagram of Fig. 4A. Whereas the full width at half maximum (FWHM) of the NP follows a critical temperature dependence, the temperature dependence of the BP width is much weaker in the accessible temperature range and within our experimental uncertainties. Finally, although the amplitude of the NP (i.e., the peak height) is larger than that of the BP at low temperature, the total "volume" (i.e., the integrated scattering intensity) is always dominated by the BP, at least in the accessible *T* range above the critical temperature T_c (Fig. 3).

To further clarify the double character of the phenomenon and to assess the possible dynamical character of the CDFs, we studied the energy associated with the BP by exploiting the high resolution of our instruments. We measured Cu L_3 RIXS spectra on the OP90 and UD60 samples at selected temperatures and at the wave vector of the BP maximum. At all temperatures, the main peak is slightly broader than the instrumental resolution (40 meV) and is not centered at zero energy loss, with the inelastic component stronger at higher *T* (fig. S10) (*28*). Contributions to this quasi-elastic peak come from phonons, from elastic diffuse scattering from the sample surface, and from charge fluctuations. The phonon peak intensity is either *T*-independent (for phonons with energies higher than 30 meV) or decreases upon cooling down (at lower energies); scattering from the surface is constant with *T*. The scattering related to CDWs is the only component expected to grow in intensity with decreasing *T*. Figure 4B shows the quasi-elastic component of three spectra taken on the optimally doped sample at 90 K, 150 K, and 250 K, and $q_{||} = (0.31, 0)$, after subtraction of the phonon contribution, as estimated from the (*H*, *H*) scan (see figs. S11 to S13 for details on how the

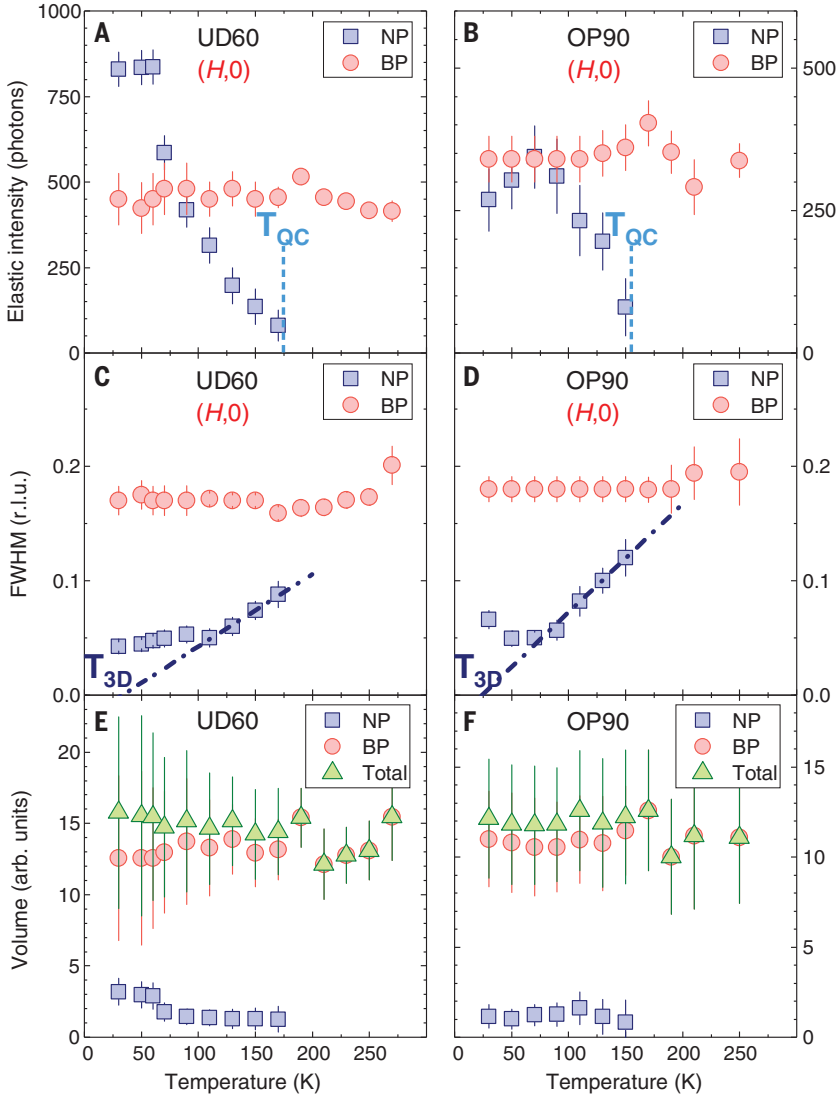

Fig. 3. Characteristics of the two charge density modulation peaks. The graphs show the temperature dependence of the parameters of the two Lorentzian profiles used to describe the quasi-elastic peaks of samples UD60 and OP90 (squares refer to the narrow peak, circles to the broad peak). (**A** and **B**) Intensity. (**C** and **D**) FWHM. T_{QC} is 175 K for sample UD60 and 155 K for sample OP90. T_{3D} is 33 K for sample UD60 and 24 K for sample OP90. (**E** and **F**) Volume of the charge density modulations. The total volume (triangles), given by the sum of the volumes of the two peaks, is dominated by the broad peak.

additional phonon contribution and elastic scattering were subtracted). To better extract the charge density contribution, we subtracted the higher-T spectra from the lower-T ones; in Fig. 4, C and D, we show the 150 K–250 K and 90 K–150 K difference spectra. The resulting peaks are narrower than the original spectra. The higher-T difference is evidently centered at $\omega_0 \approx$ 15 meV, whereas the lower-T difference is almost elastic. This means that the BP, still dominant at high T, has a fluctuating nature, whereas the NP emerges at lower T as a nearly static, quasi-critical CDW.

These results can be interpreted within the theory mentioned above, based on the charge density instability of the high-doping correlated Fermi liquid (*1*, *23*, *24*). We fitted the three quasi-elastic peaks in Fig. 4B (see also fig. S11) by using the dynamical charge susceptibility, proportional to the correlation function of the density fluctuations $\langle n(q, \omega)n(-q, \omega)\rangle$ in Fourier space, as obtained from a standard dynamical Ginzburg-Landau approach in Gaussian approximation (*34*, *35*). Its imaginary part, multiplied by the Bose function, gives the response function for the charge density modulation and represents the intensity of the low-energy peak in the RIXS spectra $I(q, \omega)$. Then the spectra in Fig. 4B can be fitted with this theory, assuming a characteristic energy $\omega_0 \approx$ 15 meV for these overdamped charge fluctuations at 150 K and 250 K; the 90 K curve is better fitted with $\omega_0 \approx$ 7 meV, indicating that the NP is associated with lower or null energy. Similar fittings for the UD60 sample give $\omega_0 \approx$ 6 meV at high temperatures and 3 meV at 90 K (*28*).

The broad peak is therefore generated by dynamical CDFs, with pure 2D character related to individual CuO_2 planes, and is characterized by a noncritical behavior. Its ultrashort-range nature is confirmed by a correlation length—given by the FWHM $\propto \xi^{-1}$ values—of $2\xi \approx 4a$, which is comparable to the modulation period (3.4a; see fig. S8). The narrow peak, by contrast, comes from quasi-critical CDWs appearing only below the onset temperature T_{QC} (crosses in the phase diagram of Fig. 4A) (*28*). Quasi-critical CDW orders compete with superconductivity, as highlighted by the intensity and ξ saturation (or decrease) below T_c (Fig. 3 and figs. S4 to S6). In the relatively narrow temperature range above the occurrence of such competition, the linear extrapolation to zero of the NP width provides an estimate of the critical temperature T_{3D}, below which, in the absence of superconductivity, ξ would diverge (i.e., a static 3D CDW order would form). The values of T_{3D} of our three samples (Fig. 3, C and D, and fig. S6C), indicated as squares in the phase diagram of Fig. 4A, are in fairly good agreement with the onset of the long-range 3D CDWs (T_{3D}^{H}), obtained in high magnetic fields by NMR (*13*), and hard x-ray scattering experiments (*14*) (blue region in Fig. 4A). For OP90, T_{3D} is relatively low because the doping corresponds roughly to the p_c value of the QCP. Moreover, a scan taken at 62 K on overdoped YBCO (OD83, $p \approx 0.18$) shows that already at low temperatures, only the dynamical CDFs survive at $p > p_c$ (see fig. S9). Therefore, from the similarity between the T_{3D} in our films and the T_{3D}^{H} reported in the literature at the same oxygen doping levels, we can speculate that, were it not for the competing superconducting order that quenches the critical behavior of CDWs, 3D CDWs would occur for $p < p_c$ and $T < T_{3D}$ without any application of magnetic field. The static 3D CDW dome is centered at $p \approx 1/8$ and is delimited by two QCPs at $p \approx 0.08$ and 0.17 (*36*, *37*); inside that doping range, above T_{3D} and below T_{QC}, quasi-critical CDWs—precursors of the static 3D CDWs—are present.

The phase diagram of Fig. 4A visualizes the scenario of a continuous crossover from the pure 2D dynamical CDF at high T and all dopings, to a quasi-critical CDW (still 2D) below T_{QC} and for $0.08 < p < 0.17$, to the static 3D CDW usually hindered by superconductivity. Although disregarded up to now, dynamical CDFs represent the bulk of the iceberg of the CDW phenomenon in cuprates. Indeed, they pervade a large part of the phase diagram and coexist with both quasi-critical CDWs and, possibly, 3D CDWs (Fig. 4A), and their total scattering intensity (the volume of the associated BP) dominates at all T (Fig. 3, E and F, and fig. S6E). Moreover, they do not compete with superconductivity.

This picture is consistent with the theoretical proposal of (*1*, *25*). Owing to the weak coupling of CuO_2 planes, CDW orders have a marked 2D

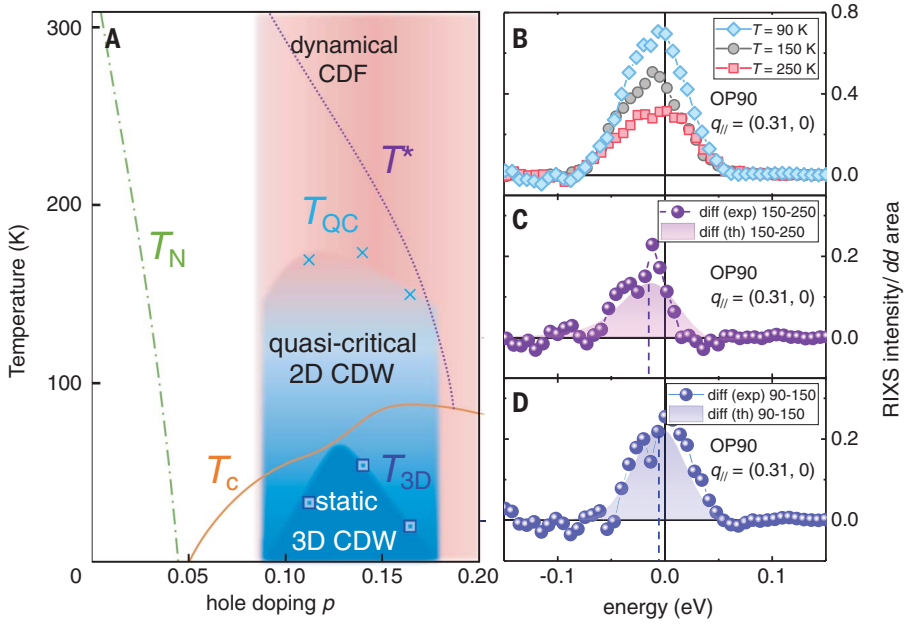

Fig. 4. Static and dynamic charge order in the phase diagram of the HTS cuprates. (**A**) The *T*-*p* phase diagram of cuprates is typically marked by the antiferromagnetic, pseudogap, and superconducting regions (respectively characterized by the onset temperatures T_N, T^*, and T_c). Our results prove that most of these regions are pervaded by charge density modulations of some sort. The narrow peak describes the CDWs, manifesting in a region (pale blue) below T_{QC} (crosses). These 2D CDWs are quasi-critical and are precursors of the static 3D CDWs (blue region). Even though we cannot directly access this dome without a magnetic field, the temperatures T_{3D} (squares) that we infer from the *T* dependence of the NP FWHM are in agreement with those previously determined by NMR and hard x-ray scattering experiments (*15*, *16*). The broad peak describes short-range charge density fluctuations (CDFs), which dominate the phase diagram (red region), coexisting both with the quasi-critical 2D CDWs and with superconductivity, and persisting even above T^*. In contrast, CDFs disappear in undoped/antiferromagnetic samples (white region), whereas their occurrence between $p \sim 0.05$ and $p \sim 0.08$ has yet to be determined. To evaluate the characteristic energies ω_0 associated with the BP, we measured high-resolution RIXS spectra at various temperatures on the samples OP90 and UD60. (**B**) Quasi-elastic component of the spectra (after subtraction of the phonon contribution) at $T = 90$, 150, and 250 K, measured on sample OP90 at $q_{||} = (0.31, 0)$. (**C** and **D**) The experimental 150 K–250 K and 90 K–150 K difference spectra, presented in (B), are shown (spheres), together with the theoretical calculation (solid areas). The data are in agreement with the theory, assuming $\omega_0 \approx 15$ meV at 150 and 250 K and $\omega_0 \approx 7$ meV at 90 K [dashed lines in (C) and (D)].

character and, because of strong quantum thermal dynamical fluctuations, they acquire a truly static character only below T_{3D}. For YBCO and NBCO, T_{3D} is smaller than T_c, thus requiring strong magnetic fields or epitaxially grown samples to suppress superconductivity to obtain static 3D CDWs.

Although this theory can explain most of the experimental findings, some questions remain open. Other cuprate families will have to be tested and the doping region extended to confirm the general applicability of the dynamic CDF scenario. A BP, centered at $q_{||} \approx q_c^{NP}$ and persisting at high temperatures, has been observed over the past few years in other cuprates (*13*, *38*), pointing toward a universality of the CDF phenomenon. However, none of the aforementioned experiments has been conclusive in this respect, because a complete temperature dependence and/or a discrimination of the quasi-elastic signal from the inelastic one was missing. The actual relation between the quasi-critical CDW and the dynamical CDF must also be fully clarified, with particular reference to the possible spatial separation or coexistence of the two phenomena, ultimately linked to the role of disorder in the samples studied by scanning tunneling microscope (*7*, *39*, *40*) and micro–x-ray scattering (*41*) experiments.

The most intriguing finding of this work is the ubiquitous presence (both in temperature and doping) of a broad peak caused by dynamical CDFs, which have small energies of a few meV and extend over a broad momentum range. Therefore, they provide quite an effective low-energy scattering mechanism for all the quasi-particles on the Fermi surface. This makes these excitations an appealing candidate for producing the linear temperature dependence of the resistivity in the normal state and other marginal Fermi liquid phenomena that, since the early days of HTS (*42*), have been the most prominently peculiar properties of the cuprates.

REFERENCES AND NOTES

1. C. Castellani, C. Di Castro, M. Grilli, *Phys. Rev. Lett.* **75**, 4650–4653 (1995).
2. C. Castellani, C. Di Castro, M. Grilli, *Z. Phys. B* **103**, 137–144 (1996).
3. S. A. Kivelson *et al.*, *Rev. Mod. Phys.* **75**, 1201–1241 (2003).
4. V. J. Emery, S. A. Kivelson, *Physica C* **209**, 597–621 (1993).
5. J. M. Tranquada, B. J. Sternlieb, J. D. Axe, Y. Nakamura, S. Uchida, *Nature* **375**, 561–563 (1995).
6. A. Bianconi *et al.*, *Phys. Rev. Lett.* **76**, 3412–3415 (1996).
7. C. Howald, H. Eisaki, N. Kaneko, M. Greven, A. Kapitulnik, *Phys. Rev. B* **67**, 014533 (2003).
8. M. Vershinin *et al.*, *Science* **303**, 1995–1998 (2004).
9. J. E. Hoffman *et al.*, *Science* **295**, 466–469 (2002).
10. T. Wu *et al.*, *Nat. Commun.* **6**, 6438 (2015).
11. G. Ghiringhelli *et al.*, *Science* **337**, 821–825 (2012).
12. J. Chang *et al.*, *Nat. Phys.* **8**, 871–876 (2012).
13. R. Comin, A. Damascelli, *Annu. Rev. Condens. Matter Phys.* **7**, 369–405 (2016).
14. E. H. da Silva Neto *et al.*, *Phys. Rev. B* **98**, 161114 (2018).
15. T. Wu *et al.*, *Nature* **477**, 191–194 (2011).
16. S. Gerber *et al.*, *Science* **350**, 949–952 (2015).
17. M. Blüschke *et al.*, *Nat. Commun.* **9**, 2978 (2018).
18. Y. Y. Peng *et al.*, *Nat. Mater.* **17**, 697–702 (2018).
19. P. W. Anderson, *Science* **235**, 1196–1198 (1987).
20. P. W. Anderson, *Phys. Rev. Lett.* **64**, 1839–1841 (1990).
21. X.-G. Wen, P. A. Lee, *Phys. Rev. Lett.* **76**, 503–506 (1996).
22. T. M. Rice, K.-Y. Yang, F. C. Zhang, *Rep. Prog. Phys.* **75**, 016502 (2012).
23. R.-G. Cai, L. Li, Y.-Q. Wang, J. Zaanen, *Phys. Rev. Lett.* **119**, 181601 (2017).
24. S. Sachdev, E. Berg, S. Chatterjee, Y. Schattner, *Phys. Rev. B* **94**, 115147 (2016).
25. S. Andergassen, S. Caprara, C. Di Castro, M. Grilli, *Phys. Rev. Lett.* **87**, 056401 (2001).
26. S. Caprara, C. Di Castro, G. Seibold, M. Grilli, *Phys. Rev. B* **95**, 224511 (2017).
27. X. Montiel, T. Kloss, C. Pépin, *Phys. Rev. B* **95**, 104510 (2017).
28. See supplementary materials.
29. M. Salluzzo *et al.*, *Phys. Rev. B* **72**, 134521 (2005).
30. R. Arpaia, E. Andersson, E. Trabaldo, T. Bauch, F. Lombardi, *Phys. Rev. Mater.* **2**, 024804 (2018).
31. R. Comin *et al.*, *Science* **343**, 390–392 (2014).
32. T. P. Croft, C. Lester, M. S. Senn, A. Bombardi, S. M. Hayden, *Phys. Rev. B* **89**, 224513 (2014).
33. The reason is the large background of the energy-integrated resonant x-ray scattering scans, caused by the various inelastic contributions resolved in the RIXS spectra (often improperly called "fluorescence" background). In the attempt to single out the CDW contribution, a reference scan measured at "high" temperature and meant to be the intrinsic background was subtracted out from the low-*T* scans, therefore assigning the charge order contribution exclusively to the *T*-dependent part of the signal.
34. J. A. Hertz, *Phys. Rev. B* **14**, 1165–1184 (1976).
35. A. J. Millis, *Phys. Rev. B* **48**, 7183–7196 (1993).
36. S. Badoux *et al.*, *Nature* **531**, 210–214 (2016).
37. H. Jang *et al.*, *Phys. Rev. B* **97**, 224513 (2018).
38. H. Miao *et al.*, *Proc. Natl. Acad. Sci. U.S.A.* **114**, 12430–12435 (2017).
39. S. H. Pan *et al.*, *Nature* **413**, 282–285 (2001).
40. Y. Kohsaka *et al.*, *Phys. Rev. Lett.* **93**, 097004 (2004).
41. G. Campi *et al.*, *Nature* **525**, 359–362 (2015).
42. C. M. Varma, P. B. Littlewood, S. Schmitt-Rink, E. Abrahams, A. E. Ruckenstein, *Phys. Rev. Lett.* **63**, 1996–1999 (1989).
43. R. Arpaia *et al.*, Raw data for "Dynamical charge density fluctuations pervading the phase diagram of a Cu-based high-T_c superconductor"; http://dx.doi.org/10.5281/zenodo.2641214 (2019).

ACKNOWLEDGMENTS

We acknowledge insightful discussions with B. Keimer, M. Le Tacon, T. P. Devereaux, M. Moretti, M. Rossi, W. S. Lee, S. Kivelson, and C. Pépin. The experimental data were collected at the beam line ID32 of the European Synchrotron (ESRF) in Grenoble (France) using the ERIXS spectrometer designed jointly by the ESRF and Politecnico di Milano. **Funding:** Supported by ERC-P-ReXS project 2016-0790 of the Fondazione CARIPLO and Regione Lombardia (Italy); the Swedish Research Council (VR) under the project

2017-00382 "Evolution of nanoscale charge order in superconducting YBCO nanostructures" (R.A.); and the University of Rome Sapienza, under the projects Ateneo 2017 prot. RM11715C642E8370 and Ateneo 2018 prot. RM11816431DBA5AF (S.C., C.D.C., and M.G.).
Author contributions: G.G., M.G., L.B., C.D.C., and R.A. conceived and designed the experiments with suggestions from S.C., N.B.B., and M.S.; R.F., Y.Y.P., G.G., L.B., R.A., G.D.V., G.M.D.L., M.S., E.A., F.L., D.B., and N.B.B. performed the RIXS measurements; R.A., G.G., G.D.V., Y.Y.P., and L.B. analyzed the RIXS experimental data; S.C., C.D.C., and M.G. performed the theoretical calculations; G.M.D.L. and M.S. grew and characterized the NBCO films; R.A., E.A., and F.L. grew and characterized the YBCO films; R.A., G.G., M.G., and C.D.C. wrote the manuscript with input from F.L., L.B., N.B.B., R.F., Y.Y.P., and contributions from all authors. **Competing interests:** G.G. is a member of the Science Advisory Council of the ESRF. **Data and materials availability:** All experimental data shown in the main text and in the supplementary materials are accessible at the Zenodo repository (*43*).

SUPPLEMENTARY MATERIALS

science.sciencemag.org/content/365/6456/906/suppl/DC1
Materials and Methods
Supplementary Text
Figs. S1 to S13
References (*44*–*54*)

16 August 2018; accepted 30 July 2019
10.1126/science.aav1315

ORGANIC CHEMISTRY

Redox-neutral organocatalytic Mitsunobu reactions

Rhydian H. Beddoe[1], Keith G. Andrews[1], Valentin Magné[1], James D. Cuthbertson[1], Jan Saska[1], Andrew L. Shannon-Little[1], Stephen E. Shanahan[2], Helen F. Sneddon[3], Ross M. Denton[1]*

Nucleophilic substitution reactions of alcohols are among the most fundamental and strategically important transformations in organic chemistry. For over half a century, these reactions have been achieved by using stoichiometric, and often hazardous, reagents to activate the otherwise unreactive alcohols. Here, we demonstrate that a specially designed phosphine oxide promotes nucleophilic substitution reactions of primary and secondary alcohols in a redox-neutral catalysis manifold that produces water as the sole by-product. The scope of the catalytic coupling process encompasses a range of acidic pronucleophiles that allow stereospecific construction of carbon-oxygen and carbon-nitrogen bonds.

Alcohols are important feedstocks (*1*–*5*) for chemical synthesis because they are abundant and inexpensive and can be converted into a wide range of additional functional groups by using, among others, nucleophilic substitution reactions (*6*). The ideal (hypothetical) nucleophilic substitution would involve direct stereospecific displacement of the hydroxyl group with concomitant elimination of water (Fig. 1A) (*7*). In practice, kinetic and thermodynamic barriers prevent direct substitution, and therefore, additional chemical activating agents must be used. However, conventional methods, such as the Mitsunobu protocol (Fig. 1B) (*8*, *9*), involve hazardous stoichiometric reagents that are incongruous with the principle of atom economy (*10*). Nevertheless, this method is used very frequently and remains the state of the art in terms of stereospecific nucleophilic substitution (*11*). Therefore, it is clear that alternative catalytic substitution reactions would have a major impact on chemical synthesis and eventually replace the inherently inefficient current methods (*12*). To date, a variety of strategies have been devised to enable catalytic coupling of π-activated alcohols and nucleophiles, which include Brønsted or Lewis acid catalysis (*13*) and transition metal–catalyzed substitution (*14*). In many cases, these reactions occur through stabilized carbocation intermediates and, necessarily, generate racemic products. However, there are notable examples in which excellent stereoselectivity has been achieved (*15*). A conceptually different approach to catalytic nucleophilic substitution termed "borrowing hydrogen" (*16*–*18*) involves oxidation of the alcohol, condensation with a nucleophile, and then reduction to achieve the product of a direct substitution reaction. Despite these advances, the development of catalytic methods that enable stereospecific bimolecular substitution of nonactivated chiral alcohols remains a major challenge (*19*, *20*). Although some progress has been made by using cyclopropenone catalysis (*21*), most effort to date has been focused on modifying the original Mitsunobu protocol by redox recycling of the stoichiometric reagents. Although this approach is intuitive, implementation is challenging because recycling the phosphine reagent requires a stoichiometric reductant and recycling the azo oxidant requires a mutually compatible stoichiometric oxidant (Fig. 1C).

An early reaction of this type was reported in 2006 and involved the use of substoichiometric [10 mole % (mol %)] azodicarboxylate, which was recycled by using di(acetoxy)iodobenzene as a stoichiometric oxidant, in combination with two equivalents of triphenylphosphine (Fig. 1C) (*22*). Further work reported by Taniguchi, Košmrlj, and co-workers in 2013 and in 2016 resulted in a more efficient recycling protocol using a modified arylazocarboxylate that was elegantly regenerated through aerobic oxidation with an iron phthalocyanine cocatalyst by using molecular oxygen as the terminal oxidant (Fig. 1C) (*23*, *24*). These processes were successful in rendering the Mitsunobu reaction catalytic with respect to the oxidant, but stoichiometric phosphine was still required. Protocols catalytic in phosphine or both species suffered from limited output (*25*, *26*). Although these catalytic variants are valuable, any catalytic Mitsunobu reaction based on redox recycling will always require a stoichiometric oxidant and reductant, which places a ceiling on the level of atom economy that can be achieved (*27*).

Conscious of these limitations, we questioned whether an alternative catalysis manifold could be developed in which the oxidation state of phosphorus was invariant (*28*, *29*). Such a manifold would require the unconventional step of generating a Mitsunobu-active phosphorus species from phosphorus(V) in a catalytic sense. We therefore designed a cycle based on phosphine oxide catalyst **1** (Fig. 1D), which we reasoned would be activated by the acidic pronucleophile and undergo cyclization and dehydration to afford oxyphosphonium salt **2**. Although this transformation, which involves cleavage of the strong phosphorus-oxygen formal double bond, appears very challenging, we were aware that phosphine oxides containing two hydroxyaryl groups had been observed to undergo thermal dehydration at 200°C to afford isolable pentavalent phosphoranes (*30*). As in the classical Mitsunobu reaction, the counteranion associated with phosphonium salt **2** may engage in nonproductive, reversible bonding and exchange at phosphorus (*11*), but ultimately, ring-opening by the alcohol would afford the conventional intermediate, the alkoxyphosphonium-nucleophile ion pair **3**. Subsequent nucleophilic substitution between the alkoxyphosphonium salt and associated counter anion should then afford the substitution product and regenerate phosphine oxide **1**, closing the catalytic cycle. This approach was particularly attractive because there is no redox change and water is generated as the sole by-product. Furthermore, if this catalytic dehydration system could be validated, it would expand the field of phosphorus-based organocatalysis (*31*–*37*) and allow further reaction development. Herein, we demonstrate phosphine oxide **1** functions as an efficient catalyst for Mitsunobu inversion in the designed manifold.

We began our investigation by examining the role of the acidic pronucleophile, which in our proposed cycle (Fig. 1D), participates in the initial dehydration step. Experiments were performed with catalyst **1** (a bench-stable solid, prepared on a multigram scale in two steps without chromatography; see materials and methods) and (+)-2-octanol [>99% enantiomeric excess (e.e.)] as a representative nonactivated alcohol. Azeotropic removal of water from either toluene or xylenes by using a Dean-Stark trap is critical to the cycle because the phosphonium salt intermediates are kinetically and thermodynamically unstable with respect to hydrolysis, which returns the phosphine oxide. Pronucleophiles with low Brønsted acidity [for example, benzoic acid, $pK_a(H_2O) = 4.2$] did not promote measurable catalysis, but as acidity increases [for example, 4-nitrobenzoic acid, $pK_a(H_2O) = 3.4$], the catalysis manifold becomes active. Presumably, dehydration requires sufficient protic activation of the strong phosphorus-oxygen bond. However, with increasing acidity, elimination reactions and acid-promoted coupling, which occurs with retention of configuration, also become increasingly competitive. This leads to a second acidity boundary, and optimization identified dinitrobenzoic acid [$pK_a(H_2O) = 1.4$] as an efficient coupling partner for inversion (tables S1 and S2). The inverted ester product was formed in a yield of 84% and an e.e. of 98%.

Having optimized the conditions, we then explored the scope of the catalytic Mitsunobu coupling reaction. Stoichiometric esterification

[1]GlaxoSmithKline Carbon Neutral Laboratories for Sustainable Chemistry, School of Chemistry, University of Nottingham, Nottingham NG7 2GA, UK. [2]Jealott's Hill International Research Centre, Jealott's Hill, Bracknell, Berkshire RG42 6EY, UK. [3]Green Chemistry, GlaxoSmithKline, Medicines Research Centre, Stevenage, Hertfordshire SG1 2NY, UK.
***Corresponding author. Email: ross.denton@nottingham.ac.uk**

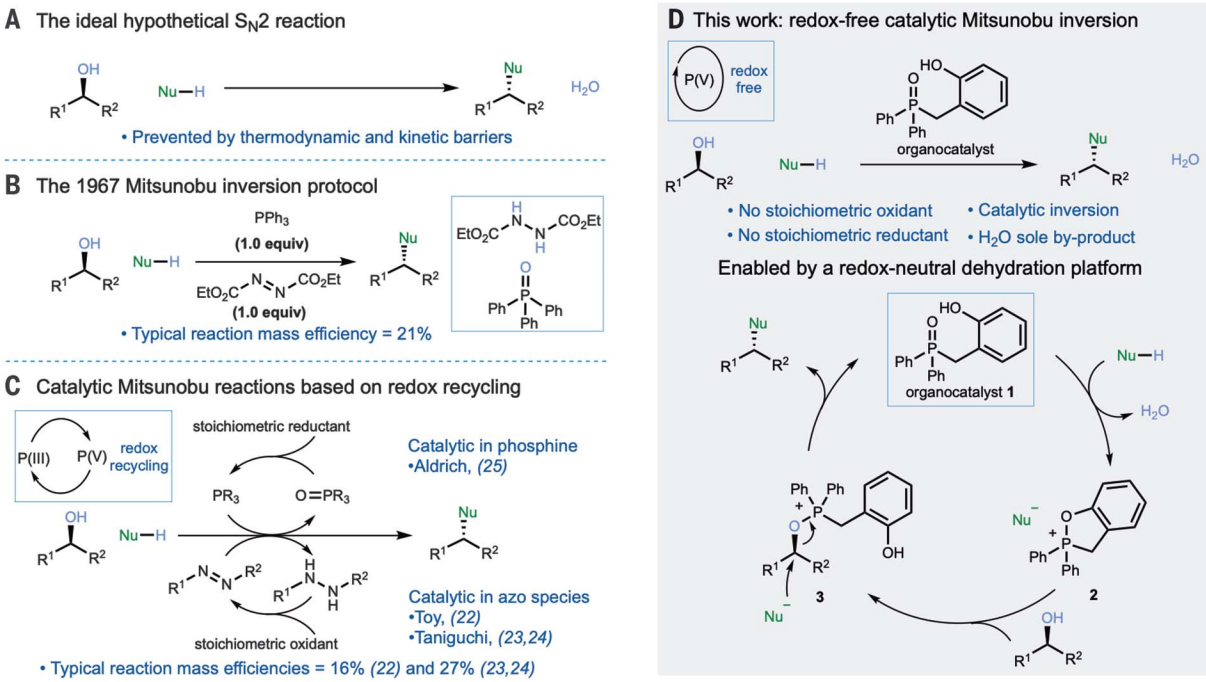

Fig. 1. Approaches to bimolecular nucleophilic substitution reactions of alcohols. (**A**) The ideal hypothetical S_N2 reaction involving direct displacement of the leaving group, inversion of stereochemistry, and generation of water as the sole by-product. (**B**) The 1967 Mitsunobu protocol for nucleophilic substitution of alcohols with inversion of stereochemistry. equiv, equivalent. (**C**) Catalytic variants of the Mitsunobu reaction based on recycling with exogenous redox reagents. (**D**) Design of a redox-free catalytic Mitsunobu inversion based on a phosphorus organocatalysis platform.

methods generally require activated carboxylic acid derivatives, coupling reagents, or strongly acidic conditions. As such, catalytic access to substitution products of both primary and secondary alcohols is valuable. As shown in Fig. 2, primary alcohols bearing functional groups potentially sensitive to strong acid, including ester (**5a**), amide (**5b**), phthalimide (**5c**), and nitrile (**5d**), were esterified under the reaction conditions. β-Citronellol also afforded the desired ester product (**5e**) with little isomerization of the sensitive trisubstituted alkene. Notably, substrates containing a phosphine-sensitive alkyl bromide (**5h**) and azide (**5i**) coupled efficiently, which would likely be problematic when using a catalytic P(III) redox-cycling strategy. It was also possible to use *p*-toluenesulfonic acid monohydrate as a pronucleophile (**5j**). This provides access to a valuable alkyl tosylate electrophile, avoiding use of a toxic sulfonyl chloride and the associated stoichiometric base.

A hallmark of the Mitsunobu reaction is secondary alcohol inversion. Acyclic, cyclic, and benzylic chiral nonracemic secondary alcohols were found to undergo efficient inversion reactions with either 2,4-dinitrobenzoic acid or 2-nitrobenzoic acid. Substrates containing ether (**5l**), alkene (**5m**), aryl chloride (**5o**), sulfone (**5q**), and silyl ether (**5r**) functional groups afforded the corresponding inverted esters in good to excellent yields. Benzylic alcohols **4t** and **4u** gave the desired ester products with excellent yields and high levels of inversion when the less acidic 2-nitrobenzoic acid was used as the coupling partner. In these more sensitive cases, competing elimination erodes the yield, whereas loss of stereochemical integrity presumably occurs from Fischer esterification or racemizing first-order nucleophilic substitution (S_N1) reactions. Electron-deficient alcohols were also challenging substrates; however, in the case of alcohol **4l**, low reactivity could be overcome by increasing the catalyst loading, which gave **5l** with excellent yield and selectivity. The desired inverted ester was also obtained when natural 5α-cholestan-3β-ol (**4v**) was subjected to the reaction conditions. In the case of cholesterol (**5x**) and *exo*-norborneol (**5w**), the corresponding esters were formed with retention of configuration due to anchimeric participation of the alkene and the nature of the bicyclic ring system, respectively (*38*).

We next sought to extend the method to encompass carbon-nitrogen and carbon-sulfur bond formations. Using dibenzenesulfonimide as a pronucleophile allowed access to a range of *N*,*N*-bis-sulfonamide derivatives (**5y** to **5ab**). The *N*,*N*-bis-sulfonamide moiety can be deprotected to afford either the sulfonamide or primary amine (*39*). The utility of this reaction was demonstrated in the efficient synthesis of the orthogonally protected diamine **5z** from amino alcohol precursor **4z**. Critically, reaction with (+)-2-octanol was shown to occur with excellent inversion of stereochemistry (**5ab**). Thioester (**5ac**) was also accessed by using thiobenzoic acid and 1-decanol as coupling partners, demonstrating the viability of carbon-sulfur bond formation, albeit with lower efficiency.

Often, the ester products formed by Mitsunobu inversion are immediately hydrolyzed to yield the inverted alcohol. The non-natural isomer of steroid 5α-cholestan-3β-ol, **7**, was synthesized on scale (4.37 g, 56%) in two steps by using a catalytic Mitsunobu esterification protocol followed by ester hydrolysis, with only a solvent exchange between the steps. Catalyst **1** and the carboxylic acid were recovered from the final mixture in 91 and 87% yield, respectively, and subsequently reused in catalytic esterification of substrates **5f** and **5g** with no loss of yield. In principle, this recycling strategy could be considered an effective implementation of the ideal inversion reaction depicted in Fig. 1A.

To further demonstrate the scope and applicability of the new Mitsunobu protocol, we next investigated the use of phenols as coupling partners. Although phenol itself is not acidic enough to participate in catalytic Mitsunobu couplings directly as a pronucleophile, we reasoned that a one-pot tosylation-etherification protocol could be developed. This was exemplified through the synthesis of the antituberculosis agent thiocarlide **10** (Fig. 2). A catalytic Mitsunobu reaction between isoamyl alcohol and *p*-toluenesulfonic acid monohydrate afforded isoamyl tosylate, which was reacted with 4-nitrophenol in situ to afford the ether product **9**. This one-pot etherification protocol provides a convenient and atom-economical alternative to existing phenol alkylation reactions and avoids stoichiometric and toxic alcohol-activating agents such as *p*-toluenesulfonyl chloride or phosphorus tribromide.

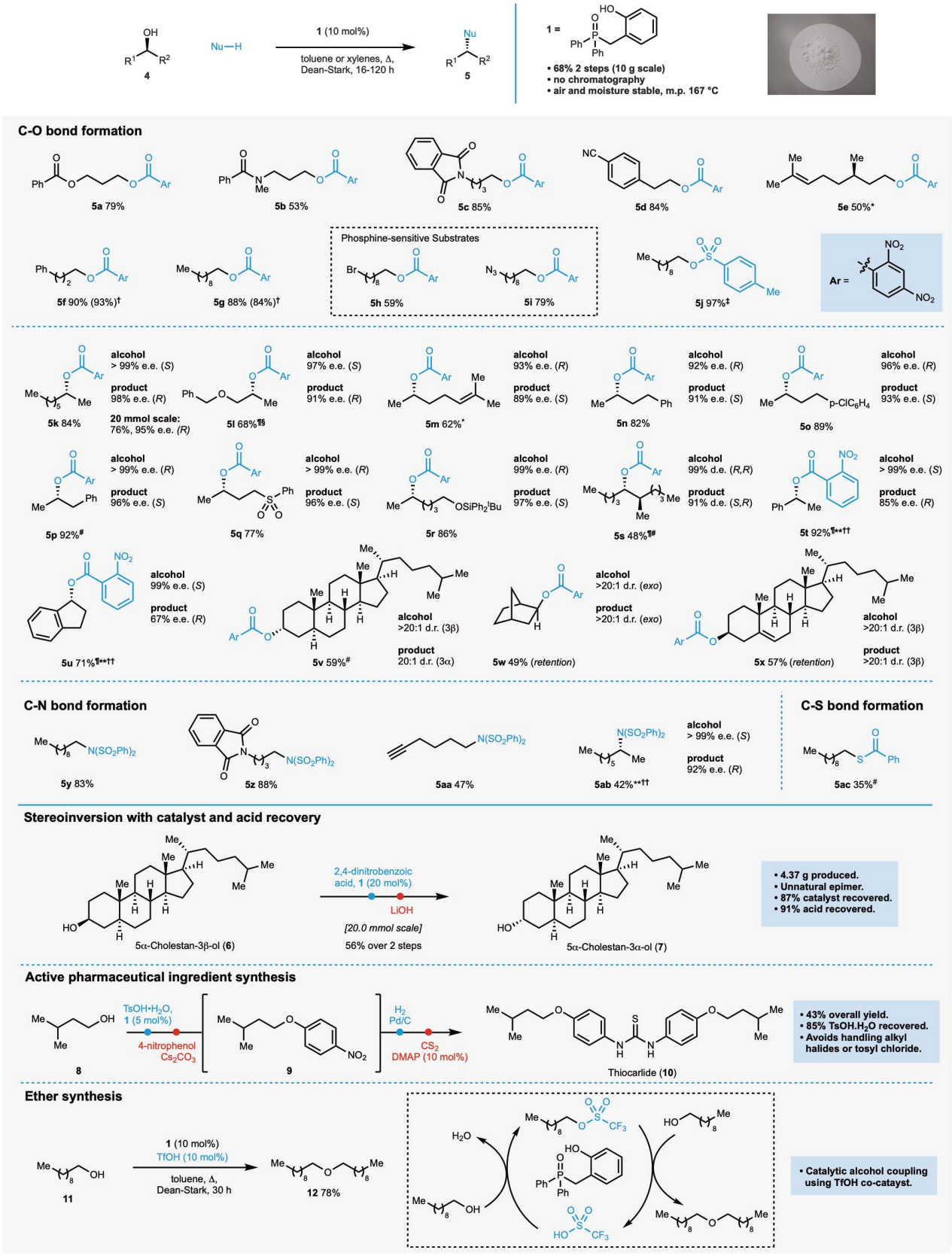

Fig. 2. Substrate scope of the catalytic Mitsunobu inversion reaction. Reactions carried out in either toluene or xylenes (1- to 2-mmol scale with respect to the alcohol unless otherwise stated); all yields are isolated yields. *Isomerization of alkene accounts for ~10% of the yield. †Reaction performed with reclaimed acid and catalyst. ‡5 mol % of catalyst used. §40 mol % catalyst used. ¶Portion-wise addition of the acid. #20 mol % of catalyst used. **25 mol % of catalyst used. ††2 equivalents of alcohol used. DMAP, 4-dimethylaminopyridine; d.e., diastereoisomeric excess; d.r., diastereoisomeric ratio; m.p., melting point.

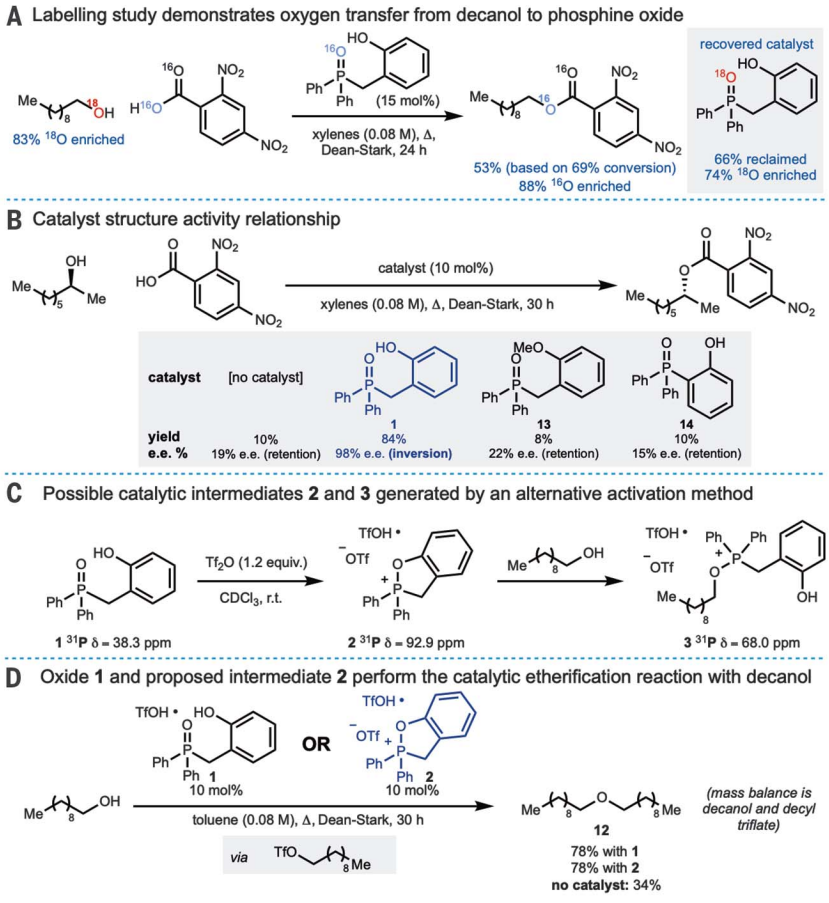

Fig. 3. Mechanistic investigation. (**A**) Oxygen-18 labeling demonstrates transfer of oxygen from the alcohol substrate to the catalyst. (**B**) Catalyst analogs, which cannot engage in cyclization and formation of proposed phosphonium intermediate **2**, are not active catalysts. (**C**) Synthesis of possible catalytic intermediates **2** and **3**. (**D**) Phosphonium intermediate **2** catalyzes etherification of decanol in analogy to phosphine oxide **1**. r.t., room temperature.

The tosic acid was recovered (87%) from the crude reaction mixture. Subsequent reduction and thiourea formation afforded the active pharmaceutical ingredient **10**. This synthesis demonstrates that the catalytic Mitsunobu protocol is valuable in contexts other than inversion and that alternative acidic pronucleophiles can be used.

Finally, we were able to demonstrate a manifold in which the coupled alcohol product can act directly as an electrophile. When triflic acid is used with phosphine oxide **1** as a cocatalyst (Fig. 2), the Mitsunobu-generated alkyl triflate (*40*) is reactive enough to undergo in situ alkylation with remaining alcohol to afford the symmetrical ether **12** and regenerate the triflic acid cocatalyst (materials and methods). This phosphine oxide–cocatalyst manifold (Fig. 2) may allow the development of reactions in which toxic alkylating agents are formed and reacted with a range of nucleophiles in situ, avoiding the need to handle such species.

To assess the catalytic dehydration platform depicted in Fig. 1D, we carried out mechanistic studies beginning with an isotope labeling experiment, whereby 2,4-dinitrobenzoic acid and ^{18}O-enriched 1-decanol were subjected to the reaction conditions (Fig. 3A). The ester product was obtained with high ^{16}O incorporation, and the recovered catalyst was found to contain 74% ^{18}O. This result, along with the excellent enantioselectivities obtained for secondary alcohol substrates, is consistent with the expected oxygen transfer from the alcohol to the catalyst. We next examined structural changes to the catalyst. An initial control experiment in the absence of the catalyst yielded the benzoic ester product in 10% yield after 30 hours with 19% e.e. for the retention product (Fig. 3B). We presume that the loss of stereochemical integrity during the reaction arises through a combination of a Fischer esterification and a racemizing S_N1 mechanism. We next probed the posited role of the hydroxyl group using phosphine oxides **13** and **14**, neither of which were catalytically active (Fig. 3B). In both cases, formation of the proposed five-membered phosphonium species **2** is precluded. Phosphine oxide **14** has a ^{31}P shift [39.4 parts per million (ppm)] similar to the active catalyst **1** (38.3 ppm), indicating a similar amount of phosphoryl activation (phosphonium character) and demonstrating a role for the hydroxyl group beyond simple hydrogen-bond activation of the phosphorus-oxygen bond.

We next sought to identify reaction intermediates by monitoring the reaction using ^{31}P and ^{1}H nuclear magnetic resonance (NMR) spectroscopy. However, the only phosphorus species observed in aliquots of the catalytic reaction was the phosphine oxide **1** (figs. S8 and S9). Given that activated phosphonium intermediates are typically hydrolytically sensitive and that phosphine oxide activation requires dehydration at elevated temperature under Dean-Stark conditions, we designed an alternative method to access possible catalytic intermediates avoiding the generation of water. To this end, activation of phosphine oxide **1** with triflic anhydride at room temperature (Fig. 3C) resulted in a species, whose ^{31}P, ^{13}C, and ^{1}H NMR data were consistent with phosphonium triflate **2**. Subsequent addition of decanol afforded the acyclic alkoxyphosphonium triflate **3**. Finally, phosphonium triflate **2** was demonstrated to be catalytically active and promoted etherification in analogy to phosphine oxide **1** (Fig. 3D). In summary, the experiments described above and in the supplementary material are congruous with the catalytic cycle depicted in Fig. 1D, where dehydration to afford phosphonium intermediates is likely to be turnover-limiting and dependent on a geometrically important hydroxyl group; hydrogen-bond availability alone is insufficient to account for the reactivity. The labeling study and stereochemical inversion are consistent with the carbon-nucleophile bond formation occurring from an alkoxyphosphonium salt–nucleophile ion pair in accord with the classical Mitsunobu reaction.

The elimination of redox chemistry in our catalytic Mitsunobu protocol obviates the need for terminal oxidants and reductants and results in substantially increased reaction mass efficiency of 65% (fig. S14) (*41*). The established organophosphorus-catalyzed dehydration manifold has potential applications in a range of other classical phosphorus-mediated transformations.

REFERENCES AND NOTES

1. S. V. Pronin, C. A. Reiher, R. A. Shenvi, *Nature* **501**, 195–199 (2013).
2. J. Jin, D. W. C. MacMillan, *Nature* **525**, 87–90 (2015).
3. C. C. Nawrat, C. R. Jamison, Y. Slutskyy, D. W. C. MacMillan, L. E. Overman, *J. Am. Chem. Soc.* **137**, 11270–11273 (2015).
4. P. H. Huy, T. Hauch, I. Filbrich, *Synlett* **27**, 2631–2636 (2016).
5. L. Wu, T. Moteki, A. A. Gokhale, D. W. Flaherty, F. D. Toste, *Chem* **1**, 32–58 (2016).
6. C. K. Ingold, *Structure and Mechanisms in Organic Chemistry* (Cornell Univ. Press, 1953).
7. J. An, R. M. Denton, T. H. Lambert, E. D. Nacsa, *Org. Biomol. Chem.* **12**, 2993–3003 (2014).
8. O. Mitsunobu, M. Yamada, *Bull. Chem. Soc. Jpn.* **40**, 2380–2382 (1967).
9. O. Mitsunobu, *Synthesis* **1981**, 1–28 (1981).
10. B. M. Trost, *Science* **254**, 1471–1477 (1991).
11. K. C. K. Swamy, N. N. B. Kumar, E. Balaraman, K. V. P. P. Kumar, *Chem. Rev.* **109**, 2551–2651 (2009).
12. D. J. C. Constable *et al.*, *Green Chem.* **9**, 411–420 (2007).
13. M. Dryzhakov, E. Richmond, J. Moran, *Synthesis* **48**, 935–959 (2016).
14. B. Sundararaju, M. Achard, C. Bruneau, *Chem. Soc. Rev.* **41**, 4467–4483 (2012).
15. S. Krautwald, D. Sarlah, M. A. Schafroth, E. M. Carreira, *Science* **340**, 1065–1068 (2013).

16. A. J. A. Watson, J. M. J. Williams, *Science* **329**, 635–636 (2010).
17. M. H. S. A. Hamid *et al*., *J. Am. Chem. Soc.* **131**, 1766–1774 (2009).
18. T. Yan, B. L. Feringa, K. Barta, *Nat. Commun.* **5**, 5602 (2014).
19. A. Bunrit *et al*., *J. Am. Chem. Soc.* **137**, 4646–4649 (2015).
20. P. T. Marcyk *et al*., *Angew. Chem. Int. Ed.* **58**, 1727–1731 (2019).
21. E. D. Nacsa, T. H. Lambert, *Org. Lett.* **15**, 38–41 (2013).
22. T. Y. S. But, P. H. Toy, *J. Am. Chem. Soc.* **128**, 9636–9637 (2006).
23. D. Hirose, T. Taniguchi, H. Ishibashi, *Angew. Chem. Int. Ed.* **52**, 4613–4617 (2013).
24. D. Hirose, M. Gazvoda, J. Košmrlj, T. Taniguchi, *Chem. Sci.* **7**, 5148–5159 (2016).
25. J. A. Buonomo, C. C. Aldrich, *Angew. Chem. Int. Ed.* **54**, 13041–13044 (2015).
26. D. Hirose, M. Gazvoda, J. Košmrlj, T. Taniguchi, *Org. Lett.* **18**, 4036–4039 (2016).
27. S. Davey, *Nat. Chem.* **5**, 358 (2013).
28. S. P. Marsden, A. E. McGonagle, B. McKeever-Abbas, *Org. Lett.* **10**, 2589–2591 (2008).
29. X. Tang, C. Chapman, M. Whiting, R. Denton, *Chem. Commun.* **50**, 7340–7343 (2014).
30. D. Hellwinkel, W. Krapp, *Chem. Ber.* **111**, 13–41 (1978).
31. H. Guo, Y. C. Fan, Z. Sun, Y. Wu, O. Kwon, *Chem. Rev.* **118**, 10049–10293 (2018).
32. T. V. Nykaza, T. S. Harrison, A. Ghosh, R. A. Putnik, A. T. Radosevich, *J. Am. Chem. Soc.* **139**, 6839–6842 (2017).
33. C. B. Caputo, L. J. Hounjet, R. Dobrovetsky, D. W. Stephan, *Science* **341**, 1374–1377 (2013).
34. N. L. Dunn, M. Ha, A. T. Radosevich, *J. Am. Chem. Soc.* **134**, 11330–11333 (2012).
35. M. C. Hilton *et al*., *Science* **362**, 799–804 (2018).
36. Z. Lao, P. H. Toy, *Beilstein J. Org. Chem.* **12**, 2577–2587 (2016).
37. L. Longwitz, T. Werner, *Pure Appl. Chem.* **91**, 95–102 (2019).
38. B. R. Castro, *Org. React.* **29**, 1–53 (1983).
39. P. A. Sibbald, F. E. Michael, *Org. Lett.* **11**, 1147–1149 (2009).
40. B. Dhakal, L. Bohé, D. Crich, *J. Org. Chem.* **82**, 9263–9269 (2017).
41. R. H. Beddoe, H. F. Sneddon, R. M. Denton, *Org. Biomol. Chem.* **16**, 7774–7781 (2018).

ACKNOWLEDGMENTS

We acknowledge support from K. Butler, S. Aslam, and B. Pointer-Gleadhill from the University of Nottingham Analytical Services. Reach Separations, Ltd., is acknowledged for providing analytical services. **Funding:** We acknowledge funding from the EPSRC (grants EP/R030693/1 and EP/L015633/1), the Leverhulme Trust (RPG-2014-190), Syngenta, GlaxoSmithKline, and The School of Chemistry, University of Nottingham. **Author contributions:** R.M.D. designed the experiments. R.H.B., K.G.A., V.M., J.D.C., J.S., and A.L.S.-L. carried out the experiments. All of the authors analyzed the data. R.M.D., R.H.B., and K.G.A. drafted the manuscript. **Competing interests:** The authors declare no competing interests. **Data and materials availability:** All data are available in the main text or the supplementary materials.

SUPPLEMENTARY MATERIALS

science.sciencemag.org/content/365/6456/910/suppl/DC1
Materials and Methods
Figs. S1 to S14
Tables S1 to S3
HPLC and SFC Traces
NMR Spectra
References (*42*–*80*)

20 March 2019; accepted 9 July 2019
10.1126/science.aax3353

MAGNETISM

Skyrmion lattice with a giant topological Hall effect in a frustrated triangular-lattice magnet

Takashi Kurumaji[1]*, Taro Nakajima[1], Max Hirschberger[1], Akiko Kikkawa[1], Yuichi Yamasaki[1,2,3], Hajime Sagayama[4], Hironori Nakao[4], Yasujiro Taguchi[1], Taka-hisa Arima[1,5], Yoshinori Tokura[1,6]

Geometrically frustrated magnets can host complex spin textures, leading to unconventional electromagnetic responses. Magnetic frustration may also promote topologically nontrivial spin states such as magnetic skyrmions. Experimentally, however, skyrmions have largely been observed in noncentrosymmetric lattice structures or interfacial symmetry-breaking heterostructures. Here, we report the emergence of a Bloch-type skyrmion state in the frustrated centrosymmetric triangular-lattice magnet Gd_2PdSi_3. We observed a giant topological Hall response, indicating a field-induced skyrmion phase, which is further corroborated by the observation of in-plane spin modulation probed by resonant x-ray scattering. Our results may lead to further discoveries of emergent electrodynamics in magnetically frustrated centrosymmetric materials.

In geometrically frustrated magnets, where competing interactions among localized spins cannot be simultaneously satisfied, conventional magnetic orders are suppressed. Consequently, spins strongly fluctuate and can form a disordered state known as a spin-liquid state (*1*) or occasionally find a route to various spin textures, including spin-spiral orders or more-complex noncoplanar orders (*2*, *3*). These spin states are mutually competing in energy, resulting in a complex magnetic phase diagram with respect to temperature, magnetic field, and pressure. An emerging spin state can be characterized from the perspective of geometrical correlation of spin vectors ($\mathbf{S}_i$) on neighboring sites (i, j, k) in a lattice. For example, the vector spin chirality $\mathbf{S}_i \times \mathbf{S}_j$ describes the handedness of a spin spiral (*4*), and the scalar spin chirality $\mathbf{S}_i \cdot (\mathbf{S}_j \times \mathbf{S}_k)$ is connected to time-reversal symmetry breaking (*5*, *6*). These composite spin parameters couple with charge degrees of freedom in a correlated electron system, causing unconventional electromagnetic responses (*7*–*10*). Exploration of previously unknown spin textures via magnetic frustration has been one of the recent central directions in condensed matter physics.

Spin configurations are characterized by topological numbers, which remain intact under local deformation or weak fluctuations (*11*). Since the discovery of magnetic skyrmion states in chiral magnets (*12*, *13*), this concept has attracted growing interest. The magnetic skyrmion is a vortex-like nanometric spin structure that carries an integer topological number describing how many times magnetic moments within a skyrmion wrap a sphere (*14*). This quantization defines the particle nature of this spin texture with sensitivity to the electronic current and external electric and magnetic fields, highlighting the potential of magnetic skyrmions as information carriers (*15*). Extensive studies have successfully identified skyrmion-hosting materials in the form of both bulk compounds (*16*) and multilayer thin-film structures (*17*). From those, one can establish an empirical design principle for skyrmions (*18*, *19*): They appear in crystallographic lattice structures that lack inversion symmetry in or at the interfaces. These asymmetries cause the relativistic Dzyaloshinskii-Moriya (DM) interaction (*20*, *21*), which inherently prefers twisted spin configurations. More recently, this dogma has been challenged in theories (*22*–*24*) that propose spontaneous symmetry breaking by stabilizing the skyrmion state in centrosymmetric lattices via magnetic frustration. However, experimental realization and observation of unconventional electronic responses have remained elusive.

Here, we demonstrate that the metallic magnet Gd_2PdSi_3, composed of a triangular-lattice network of Gd atoms (Fig. 1A) in the centrosymmetric hexagonal structure, hosts a skyrmion-lattice (SkL) state upon the application of a magnetic field (H) perpendicular to the triangular-lattice plane, which is robust down to the lowest measured temperature. The transition into the topological spin state is characterized by a prominent topological Hall response (*25*, *26*), in sharp contrast to the adjacent magnetic phases. Using resonant x-ray scattering (RXS), we identify the long-range order of Gd spins modulated in the triangular lattice plane. The spin texture of the field-induced SkL phase is consistent with a triangular-lattice of Bloch-type skyrmions (Fig. 1B).

Gd_2PdSi_3 belongs to a family of rare-earth intermetallics of the form R_2PdSi_3 (R, rare-earth element) (*27*). Its crystal structure is derived from the simple AlB_2-type structure, with a triangular-lattice of R atoms sandwiching a nonmagnetic honeycomb-lattice layer composed of Pd and Si atoms (Fig. 1A). Owing to the difference in atomic size, Si and Pd atoms order into a superstructure along both in- and out-of-plane directions (*28*), whereas the overall structure retains centrosymmetry (fig. S1A). This excludes the DM interaction as a source of the skyrmion state. Instead, the Ruderman-Kittel-Kasuya-Yosida (RKKY)–type interaction among the local 4f moments dominates (*29*–*31*); RKKY interactions on the triangular network of 4f moments in R_2PdSi_3 are moderately frustrated (*32*) and show rich magnetic phases, including modulated structures (*33*). Specifically, in Gd_2PdSi_3, metamagnetic transitions have been observed under a magnetic field applied perpendicular to the triangular lattice, accompanied by nonmonotonic variations of longitudinal and transverse transport properties (*34*). These features suggest strong coupling between conduction electrons and Gd spins and indicate that unconventional spin structures may emerge in the triangular-lattice network of Gd 4f moments.

We first compare the magnetic phase diagram determined by the ac susceptibility (χ') for $H \| c$ in Gd_2PdSi_3 (Fig. 1C) with the contour mapping of the topological response of each phase probed by the topological Hall resistivity ρ_{yx}^{T} (Fig. 1D). Owing to the topological nature of skyrmions, they show characteristic emergent electrodynamic responses (*14*). In metallic materials, in particular, the scalar spin chirality of skyrmions acts like a fictitious magnetic field, which generates a transverse motion of electrons; this is known as the topological Hall effect (THE) (*25*, *26*, *35*). The transverse resistivity ρ_{yx} is generally made up of three components

$$\rho_{yx} = R_0 B + R_S M + \rho_{yx}^{T} \quad (1)$$

where the first and second terms are the normal and anomalous Hall resistivities proportional to the magnetic induction field B and the magnetization M, respectively, and the third term represents the topological component. Because the first two terms can be determined from magnetization measurements, ρ_{yx}^{T} can be extracted reliably and is considered a good probe for the existence of skyrmions or related topological spin states in various materials (*36*). As shown in Fig. 1C, peaks in χ' with respect to H (fig. S2) define the phase boundaries for the three magnetic phases (IC-1, A, and IC-2) in addition to the

[1]RIKEN Center for Emergent Matter Science (CEMS), Wako 351-0198, Japan. [2]Research and Services Division of Materials Data and Integrated System (MaDIS), National Institute for Materials Science (NIMS), Tsukuba 305-0047, Japan. [3]PRESTO, Japan Science and Technology Agency (JST), Kawaguchi 332-0012, Japan. [4]Institute of Materials Structure Science, High Energy Accelerator Research Organization, Tsukuba, Ibaraki 305-0801, Japan. [5]Department of Advanced Materials Science, University of Tokyo, Kashiwa 277-8561, Japan. [6]Department of Applied Physics, University of Tokyo, Tokyo 113-8656, Japan.
*Corresponding author. Email: takashi.kurumaji@riken.jp

paramagnetic (PM) state (*34*). In the *H*-*T* phase diagram, we overlay the contour plot of ρ_{yx}^{T} (Fig. 1D), which is deduced from the Hall resistivity measurements. The enhanced topological Hall signal appearing exclusively in the *A*-phase region suggests that in Gd_2PdSi_3 the application of *H* induces topological phase transitions in the context of spin textures. The magnitude of the THE at the lowest temperature is as large as 2.6 microhm·cm, which is one or two orders of magnitude larger than that in other skyrmion-hosting materials such as MnSi (40 nanohm·cm under high pressure) (*25*, *26*, *35*, *37*) and FeGe (0.16 microhm·cm in a thin film) (*38*). This must be partly caused by a shorter wavelength of the spin modulation (~2.5 nm) (fig. S5), which squeezes the emergent magnetic flux of a skyrmion, in contrast to the relatively large size of skyrmions (10 to 100 nm) in typical noncentrosymmetric (chiral or polar) magnets (*36*).

To corroborate the observation of the THE in the *A* phase, we show a typical ρ_{yx}–*H* curve together with the *M* for $H \| c$ at 2 K (Fig. 2A). A sharp positive enhancement of ρ_{yx} is apparent in the region between two stepwise changes of *M*, defining the first-order–like transitions to and from the *A* phase. On the contrary, in the IC-2 phase and higher-field region, ρ_{yx} stays negative with nearly field-linear behavior, at least up to 140 kOe (fig. S3A), where *M* is 13.7 μ_B/f.u. (where μ_B is the Bohr magneton and f.u. is formula unit), approaching the saturation value expected for the value of local Gd moment. In principle, this nearly saturated phase hosts a topologically trivial spin arrangement, allowing us to describe the Hall response with the first two terms in Eq. 1. The black solid line in Fig. 2A shows the fit to the high-field data of ρ_{yx}. The fitting quality is excellent for all measured temperatures (fig. S3A), which allows us to unambiguously extract ρ_{yx}^{T} from ρ_{yx} (Figs. 2B and 1C). The quality of the fit is not substantially affected by using a different formula—e.g., assuming skew scattering type anomalous Hall effect (fig. S4). Figure 2C shows the evolution of the peak in ρ_{yx}^{T} with temperature. Continuous decrease of ρ_{yx}^{T} toward zero around 20 K suggests that this response is affected by the magnitude of the molecular field from 4f moment on the conduction electron through an f-d coupling, consistent with the scalar spin chirality model for the THE (*35*). The effective magnetic field (B_{eff}) for the maximum ρ_{yx}^{T} is around −39 T (*39*), which is a factor of 0.07(≡*P*) smaller than the bare emergent magnetic field (B_{em} ~ −570 T) estimated from the skyrmion density. The polarization factor *P* is one order of magnitude smaller than those in MnSi under pressure (*P* ~ 0.25 to 0.38) and slightly-doped $Mn_{1-x}Fe_xSi$ (*P* ~ 0.3 to 0.45) (*37*). This may be caused by the moderate f-d coupling in the present rare-earth system as compared with the strong d-d coupling in transition metal compounds.

To further examine the nature of the SkL state in the *A* phase, we present the Hall resistivity as a function of the angle between *H* and the *c* axis in the experimental configuration illustrated in the inset of Fig. 2D. At $\phi = 0°(H \| c)$ with *H* = 9.9 kOe in the *A* phase, ρ_{yx} starts from a large positive value. As *H* rotates clockwise away from the *c* axis, the value of ρ_{yx} remains flat until it experiences an abrupt drop to near zero at around $\phi = 45°$. A hysteresis with a width of ~15° is observed between clockwise and counterclockwise rotation scans of *H*, pointing to the first-order nature of this *H*-direction–sensitive phase transition. This should be compared to thin-film systems (*40*, *41*), in which the SkL is confined in a two-dimensional space and survives only when *H* is oriented nearly perpendicular to the lattice plane. Similar behavior may be expected for the present system composed of stacked triangular-lattice layers. The above observation provides a measure of the topological number for the spin texture where the topological Hall signal sharply transitions from finite to zero upon the destabilization of the SkL state. In contrast, at *H* = 40 kOe, far above the upper critical field of the *A* phase, a smooth evolution of ρ_{yx} is observed with negligible hysteresis. This high-field ρ_{yx}, the absolute magnitude of which is much smaller than the SkL signal, follows cosϕ (black solid line in Fig. 2D), indicating that *M* closely follows the

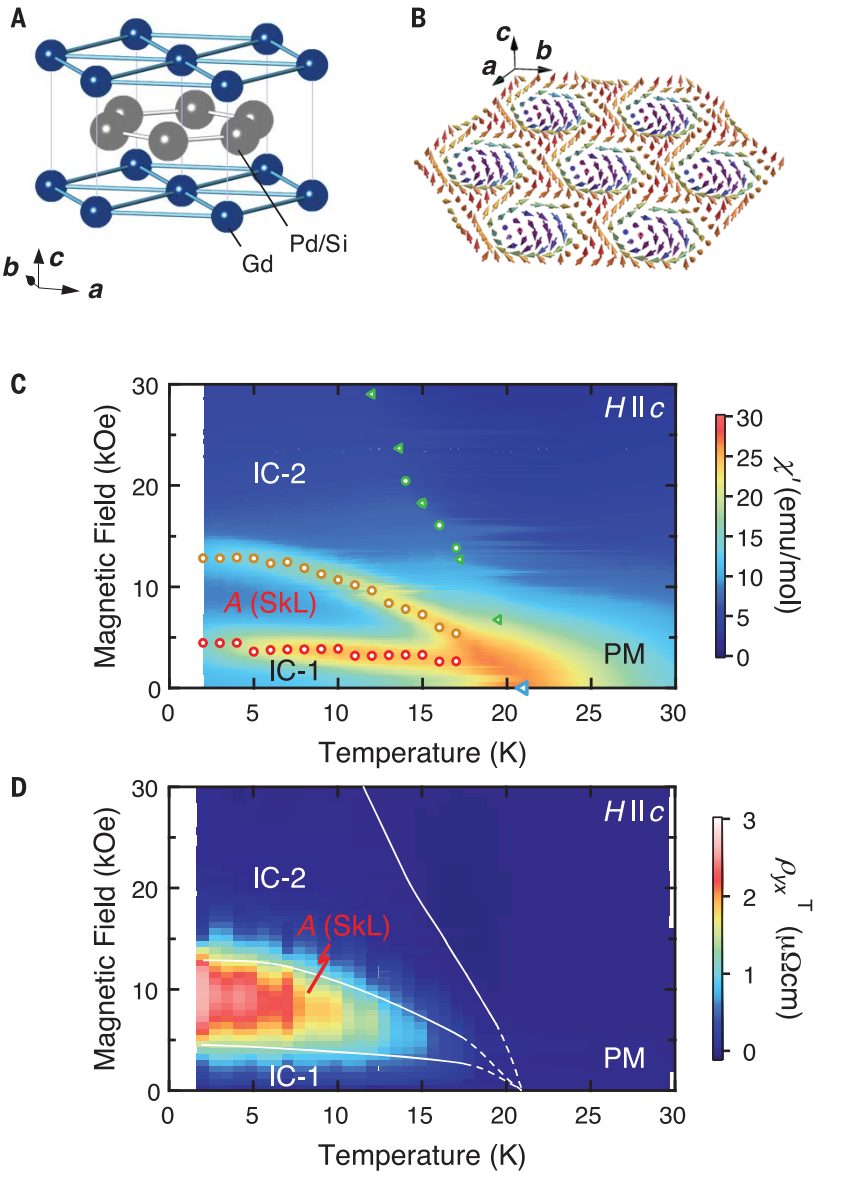

Fig. 1. Phase diagram and THE in Gd_2PdSi_3. (**A**) Basic AlB_2-type crystal structure for Gd_2PdSi_3. (**B**) Illustration of the spin texture in the SkL state. Each arrow indicates a magnetic moment at each Gd site. (**C** and **D**) Contour plot of (C) χ′ and (D) ρ_{yx}^{T} for $H \| c$ (see text for definition). *A* represents the SkL phase and PM the paramagnetic phase. IC-1 and IC-2 denote incommensurate spin-state phases in near-zero and high-field regions, respectively. Circular (triangular) symbols were determined by a peak or a kink in the χ′-*H* (χ′-*T*) scan (fig. S2). emu, electromagnetic units; mol, molar.

rotating H and that the projections of M and B to the c axis produce the first two terms in Eq. 1 as dominant contributions to ρ_{yx} outside the A-phase region.

Having identified the emergence of a topological electromagnetic response in the A phase, we examined the Gd spin structure under H along the c axis by means of the magnetic RXS in resonance with the Gd L_2 edge. We observed the magnetic modulation along in-plane directions represented by the reciprocal-space vector $\mathbf{Q}_1 = (q, 0, 0)$ [and equivalent $\mathbf{Q}_2 = (0, -q, 0)$ and $\mathbf{Q}_3 = (q, -q, 0)$] in the magnetically ordered phase (*39*). Here, q (~ 0.14 reciprocal lattice unit) is the magnetic modulation wave number. In Fig. 3, A and B, we show M and q, respectively, as a function of H, which is applied along the c axis; the data were taken at 5 K. To define the phase boundary for each phase, we show the difference ΔM between the measurements of M for the H-increasing and H-decreasing scans (Fig. 3A). In the IC-1 phase, q is almost independent of H and starts to gradually increase on entering the A phase and, furthermore, the IC-2 state. Despite the clear first-order nature for each transition (vertical gray lines), q shows merely a weak kink at each phase boundary and changes only 4% in total between 0 Oe in the IC-1 phase and 20 kOe in the IC-2 phase. The orientation of the Q vectors with respect to the triangular lattice does not change across these metamagnetic transitions. This restricts the candidate spin textures for each phase to the spin modulations with one or several equivalent Q vectors plus a component of homogeneous magnetization ($q = 0$) along the c axis. This is consistent with the intermediate-field SkL state, which can be seen as a superposition of three spiral spin modulations with their magnetic modulation vectors lying in the triangular-lattice plane and pointing 120° away from each other.

Figure 3C shows the H dependence of the scattering intensities for respective satellite peaks for the three Q vectors measured around a Bragg spot (2, 2, 0) in the H-decreasing scan. Starting from the high-field IC-2 phase region (10 kOe < H < 20 kOe), we observed that the intensity for one of the Q vectors (I_{Q_2}) is markedly weak compared with I_{Q_1} and I_{Q_3}. A fanlike structure (fig. S7A) provides a good explanation for this feature as follows. Polarization analysis of the scattered x-ray, which enables decomposition of the in-plane ($\mathbf{m}_\perp$) and out-of-plane (m_z) components of the modulated magnetic moment (*39*), reveals the negligibly weak modulating m_z component (fig. S6B) for the magnetic structure of the IC-2 state. We thus propose that a possible magnetic structure for the IC-2 state is a fanlike or a transverse conical structure (fig. S7, A and B), both of which lack global scalar spin chirality in accord with the absence of a topological contribution in ρ_{yx}. Of the two proposed magnetic structures, the fan model gives a better fit to the observed intensity, although both fits deviate from experimental observations. The observed imbalance of the scattering intensity among the three Q domains is suggestive of the single-Q nature of this phase and stems perhaps from residual strains on the sample induced by shaping and attaching it on the sample holder (*42*).

With decreasing H (Fig. 3C), the intensities for all the three Q vectors show a stepwise increase upon entering the A phase. Such a simultaneous increase of intensity for every Q is associated with the developing m_z (modulation component), as shown in Fig. 3D, which is absent in the IC-2 phase. This fact points to a noncoplanar spin texture in the topological A phase. When H decreases further (Fig. 3C), the intensity for each Q vector is almost unchanged, whereas a prominent peak in ΔM (Fig. 3A) suggests a first-order phase transition from the A phase to the IC-1 phase. The polarization analysis reveals the presence of an m_z component (fig. S6A) comparable with that of the A phase, suggesting a similarity of the spin configurations for both phases.

Looking back to the polarization analysis for the A phase (Fig. 3D), the intensity $I_{\pi-\pi'}$ for the π-π' channel ($\propto m_z^2$) is of nearly the same magnitude for all $\mathbf{Q}_i$, consistent with the triple-Q nature of the skyrmion state. $I_{\pi-\sigma'}$ ($\propto (\mathbf{m}_\perp \cdot \mathbf{k}_i)^2$) is, on the other hand, correlated with $\mathbf{m}_\perp$ to show clear $\mathbf{Q}_i$ dependence. For the Bloch-type SkL state, the spin texture is composed of a superposition of the three proper-screw spin modulations (Fig. 3E), where $\mathbf{m}_\perp$ is perpendicular to each $\mathbf{Q}_i$ vector (Fig. 3E, inset). As shown in Fig. 3F and the corresponding inset, the direction of $\mathbf{Q}_2$ is particularly closer to $\mathbf{k}_i$ than are the directions of $\mathbf{Q}_1$ and $\mathbf{Q}_3$—i.e., the direction of $\mathbf{m}_\perp$ for $\mathbf{Q}_2$ is closer to the direction normal to $\mathbf{k}_i$ than those for $\mathbf{Q}_1$ and $\mathbf{Q}_3$. This feature is consistent with the $\mathbf{Q}_i$ dependence of $I_{\pi-\sigma'}$. Furthermore, a quantitative comparison between the calculated and observed intensities reveals that the magnetic structures in the A phase can be reproduced by hybridization of the three proper screws with equivalent amplitude plus the uniform moment along z (fig. S6C), consistent with the picture of the Bloch-type SkL state. This spin texture spontaneously breaks the inversion symmetry and potentially hosts domains for handedness of skyrmions. Preference for the Bloch-type spin configuration over the Néel or the antiskyrmion type is consistent with the effect of the dipole-dipole interaction (*14*, *43*), which is generally substantial in Gd compounds.

The scattering intensities in the IC-1 state (fig. S6, A and C) suggest that the IC-1 state may also be of triple-Q nature but forms a spin texture topologically distinct from that of the A phase. A degree of freedom for the phase (φ_i) remains among the three helical modulations

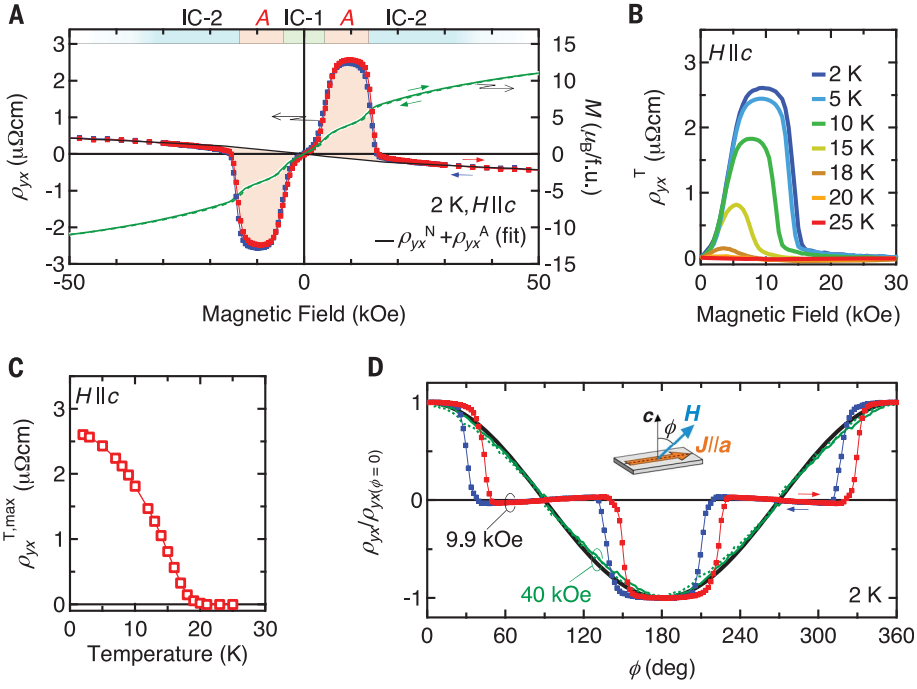

Fig. 2. Temperature and angular dependence of the THE in Gd_2PdSi_3. (**A**) H dependence of ρ_{yx} (left y axis) and M (right y axis) for $H \| c$ at 2 K. The red (blue) curve represents the H-increasing (H-decreasing) scan. The black curve indicates the sum of the normal (ρ_{yx}^N) and anomalous (ρ_{yx}^A) components of Hall resistivity. μ_B, Bohr magneton; f.u., formula unit. (**B**) H dependence of topological Hall component ρ_{yx}^T at various temperatures. (**C**) Temperature dependence of the maximum values of ρ_{yx}^T ($\rho_{yx}^{T,max}$). (**D**) Normalized transverse resistivity at 2 K with H rotating in the ac plane. Red (blue) symbols and green solid (dashed) line are in a (counter)clockwise rotation. The inset defines the rotation angle ϕ. The reference line cosϕ is shown by the black solid line.

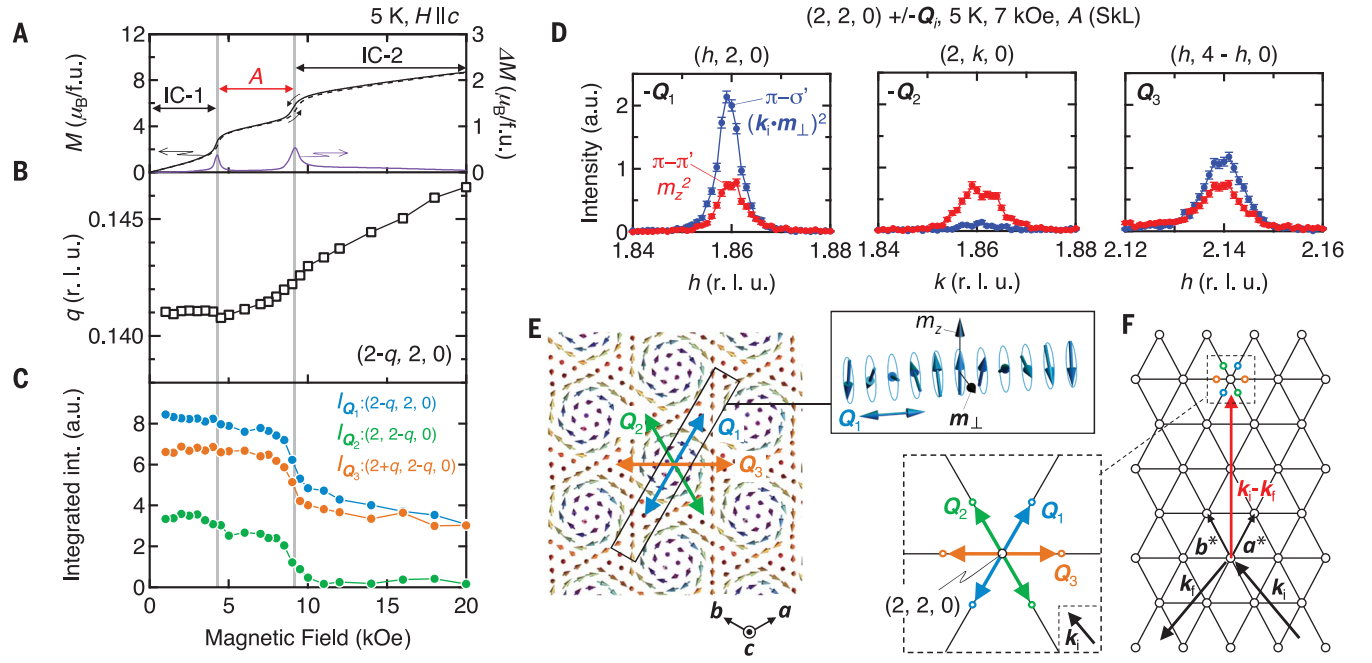

Fig. 3. Analysis of spin textures by RXS. (**A**) *H* dependence of *M* in *H*-increasing (black dashed line) and *H*-decreasing (black solid line) sweeps and the difference between them (Δ*M*, purple solid line). (**B** and **C**) Plots of (B) *q* and (C) integrated intensity for each magnetic satellite peak at $\mathbf{Q}_i$ (*i* = 1, 2, 3) around the Bragg peak (2, 2, 0), measured at 5 K and in an *H*-decreasing sweep. r.l.u., reciprocal lattice units; a.u., arbitrary units. (**D**) Intensity profile of magnetic reflection of each polarization channel for each (−)$\mathbf{Q}_i$ at 5 K with *H*||*c* of 7 kOe in the *A* (SkL)–phase region. Red [blue] circles denote the π-π′ [π-σ′] channel, which is approximately proportional to the m_z^2 [$(\mathbf{k}_i \cdot \mathbf{m}_\perp)^2$] (*39*). π (σ) corresponds to the x-ray polarization parallel (perpendicular) to the (0, 0, *L*) plane. Error bars indicate 1 SD. (**E**) Schematic real-space texture for the Bloch-type SkL state with the definition of $\mathbf{Q}_i$ (*i* = 1, 2, 3). (Inset) Proper-screw–type modulation component propagating along $\mathbf{Q}_1$. m_z and $\mathbf{m}_\perp$ represent the respective *c*-axis and *ab*-plane components of the magnetic moments. (**F**) Illustration of x-ray scattering condition in the reciprocal space. The inset shows a magnified view around (2, 2, 0), indicating the relationship between $\mathbf{Q}_i$ and $\mathbf{k}_i$.

(*39*). When the φ_i for each $\mathbf{Q}_i$ vector is 0 (mod 2π), the triple-*Q* state is equivalent to the Bloch-type SkL state, as exemplified by the *A* phase. For $\varphi_i = \pi/6$, the triple-*Q* state is composed of a triangular-lattice of merons and antimerons (fig. S7C) with no net scalar spin chirality at zero field; this is compatible with the observed features for the IC-1 state (*39*). The possible emergence of a triple-*Q* zero-field ground state (IC-1) may be a notable difference from the conventional noncentrosymmetric skyrmion-hosting systems, which typically show a single-*Q* helical state as the zero-field state (*36*). We also note unconventional features beyond the conventional helical or conical state in the IC-1 phase. As shown in Fig. 2B, ρ_{yx}^{T} starts to gradually increase from zero field before a steep increase characterizing the transition to the skyrmion state, which can be explained by the proposed noncoplanar nature in the IC-1 state: The meron-antimeron lattice can show an *H*-induced scalar spin chirality (*39*).

According to existing theories, skyrmion phase down to the lowest temperature is enabled by the magnetic frustration with support from additional effects, such as magnetic anisotropy owing to the spin-orbit coupling (*23*, *44*) and higher-order RKKY-like interaction (*24*). Notably, it is predicted that the latter mechanism can stabilize a zero-field multiple-*Q* state (albeit not identical with the present IC-1 state) (*45*), suggesting that nearly degenerate multiple-*Q* orders may exist in the ground state of the RKKY-based intermetallics. We observe that the magnetic structure for the IC-1 phase shows a certain ellipticity of the spin-spiral form (fig. S9), which suggests that weak easy-plane anisotropy may play a role in stabilizing the IC-1 state.

In addition to the enhanced THE, it has been theoretically predicted that the skyrmion in a centrosymmetric lattice shows distinctive properties, such as the compatible formation of antiskyrmion with skyrmion (*22*, *23*) and the helicity-dependent current responses (*43*, *44*). These properties provide the skyrmions as individual particles with internal degrees of freedom, which are absent in noncentrosymmetric systems with innate chirality or polarity. The conduction-electron–mediated competing magnetic interactions on a geometrically frustrated lattice will provide a platform for emergent electrodynamics owing to topological spin textures and will provide a link between the concepts of spin topology and magnetic frustration.

REFERENCES AND NOTES

1. L. Balents, *Nature* **464**, 199–208 (2010).
2. H. T. Diep, *Frustrated Spin Systems* (World Scientific, 2004).
3. C. Lacroix, P. Mendels, F. Mila, Eds., *Introduction to Frustrated Magnetism* (Springer Series in Solid State Sciences, vol. 164, Springer, 2011).
4. V. Simonet, M. Loire, R. Ballou, *Eur. Phys. J. Spec. Top.* **213**, 5–36 (2012).
5. V. Kalmeyer, R. B. Laughlin, *Phys. Rev. Lett.* **59**, 2095–2098 (1987).
6. X. G. Wen, F. Wilczek, A. Zee, *Phys. Rev. B* **39**, 11413–11423 (1989).
7. S.-W. Cheong, M. Mostovoy, *Nat. Mater.* **6**, 13–20 (2007).
8. Y. Taguchi, Y. Oohara, H. Yoshizawa, N. Nagaosa, Y. Tokura, *Science* **291**, 2573–2576 (2001).
9. Y. Machida, S. Nakatsuji, S. Onoda, T. Tayama, T. Sakakibara, *Nature* **463**, 210–213 (2010).
10. C. D. Batista, S.-Z. Lin, S. Hayami, Y. Kamiya, *Rep. Prog. Phys.* **79**, 084504 (2016).
11. H. B. Braun, *Adv. Phys.* **61**, 1–116 (2012).
12. S. Mühlbauer *et al.*, *Science* **323**, 915–919 (2009).
13. X. Z. Yu *et al.*, *Nature* **465**, 901–904 (2010).
14. N. Nagaosa, Y. Tokura, *Nat. Nanotechnol.* **8**, 899–911 (2013).
15. A. Fert, V. Cros, J. Sampaio, *Nat. Nanotechnol.* **8**, 152–156 (2013).
16. A. Bauer, C. Pfleiderer, *Generic Aspects of Skyrmion Lattices in Chiral Magnets* (Springer Series in Materials Science, vol. 228, Springer, 2016).
17. W. Jiang *et al.*, *Phys. Rep.* **704**, 1–49 (2017).
18. A. N. Bogdanov, D. A. Yablonskii, *Sov. Phys. JETP* **68**, 101–103 (1989).
19. A. Bogdanov, A. Hubert, *J. Magn. Magn. Mater.* **138**, 255–269 (1994).
20. I. Dzyaloshinskii, *J. Phys. Chem. Solids* **4**, 241–255 (1958).
21. T. Moriya, *Phys. Rev.* **120**, 91–98 (1960).
22. T. Okubo, S. Chung, H. Kawamura, *Phys. Rev. Lett.* **108**, 017206 (2012).
23. A. O. Leonov, M. Mostovoy, *Nat. Commun.* **6**, 8275 (2015).
24. S. Hayami, R. Ozawa, Y. Motome, *Phys. Rev. B* **95**, 224424 (2017).

25. M. Lee, W. Kang, Y. Onose, Y. Tokura, N. P. Ong, *Phys. Rev. Lett.* **102**, 186601 (2009).
26. A. Neubauer *et al*., *Phys. Rev. Lett.* **102**, 186602 (2009).
27. P. A. Kotsanidis, J. K. Yakinthos, E. Gamari-Seale, *J. Magn. Magn. Mater.* **87**, 199–204 (1990).
28. F. Tang *et al*., *Phys. Rev. B* **84**, 104105 (2011).
29. M. A. Ruderman, C. Kittel, *Phys. Rev.* **96**, 99–102 (1954).
30. T. Kasuya, *Prog. Theor. Phys.* **16**, 45–57 (1956).
31. K. Yosida, *Phys. Rev.* **106**, 893–898 (1957).
32. D. S. Inosov *et al*., *Phys. Rev. Lett.* **102**, 046401 (2009).
33. A. Szytuła *et al*., *J. Magn. Magn. Mater.* **202**, 365–375 (1999).
34. S. R. Saha *et al*., *Phys. Rev. B* **60**, 12162–12165 (1999).
35. R. Ritz *et al*., *Phys. Rev. B* **87**, 134424 (2013).
36. N. Kanazawa, S. Seki, Y. Tokura, *Adv. Mater.* **29**, 1603227 (2017).
37. B. J. Chapman, M. G. Grossnickle, T. Wolf, M. Lee, *Phys. Rev. B* **88**, 214406 (2013).
38. S. X. Huang, C. L. Chien, *Phys. Rev. Lett.* **108**, 267201 (2012).
39. See materials and methods and supplementary text.
40. T. Yokouchi *et al*., *Phys. Rev. B* **89**, 064416 (2014).
41. Y. Ohuchi *et al*., *Phys. Rev. B* **91**, 245115 (2015).
42. T. Inami, N. Terada, H. Kitazawa, O. Sakai, *J. Phys. Soc. Jpn.* **78**, 084713 (2009).
43. X. Zhang *et al*., *Nat. Commun.* **8**, 1717 (2017).
44. S.-Z. Lin, S. Hayami, *Phys. Rev. B* **93**, 064430 (2016).
45. R. Ozawa, S. Hayami, Y. Motome, *Phys. Rev. Lett.* **118**, 147205 (2017).
46. T. Kurumaji *et al*., Skyrmion in frustrated triangular-lattice, Version 1.0, Zenodo, (2019); http://doi.org/10.5281/zenodo.3240669.

ACKNOWLEDGMENTS

We thank X. Z. Yu for efforts on Lorentz transmission electron microscopy experiments and L. Ye, K. S. Okada, S. Hayami, H. Ishizuka, Y. Motome, and N. Nagaosa for helpful discussions. **Funding:** X-ray scattering measurements were performed under the approval of the Photon Factory Program Advisory Committee (proposal no. 2015S2-007) at the Institute of Material Structure Science, High Energy Accelerator Research Organization (KEK). This research was supported in part by Grant-in-Aid for Scientific Research (S) no. 24224009, Grant-In-Aid for Young Scientists (B) no. 17K14351, Grant-in-Aid for Scientific Research no. 16H05990 from the Japan Society for the Promotion of Science (JSPS), and PRESTO no. JPMJPR177A from the Japan Science and Technology Agency (JST). M.H. was supported as a JSPS international research fellow (no. 18F18804). **Author contributions:** T.K. and Y.To. conceived the project. T.K., A.K., and Y.Ta. grew the single crystals of Gd_2PdSi_3. T.K. characterized the magnetic and transport properties of the samples with the help of M.H. and A.K. T.N., Y.Y., H.S., H.N., and T.A. performed the resonant x-ray diffraction measurement. T.K., T.N., M.H., T.A., and Y.To. jointly discussed the result and wrote the manuscript with contributions from all authors. **Competing interests:** The authors declare no competing interests. **Data and materials availability:** Data reported in this paper are archived in Zenodo (*46*).

SUPPLEMENTARY MATERIALS

science.sciencemag.org/content/365/6456/914/suppl/DC1
Materials and Methods
Supplementary Text
Figs. S1 to S9
References (*47*–*54*)

7 May 2018; accepted 30 July 2019
Published online 8 August 2019
10.1126/science.aau0968

PLANT SCIENCE

Rhizobial tRNA-derived small RNAs are signal molecules regulating plant nodulation

Bo Ren[1]*, Xutong Wang[1]*, Jingbo Duan[1], Jianxin Ma[1,2]†

Rhizobial infection and root nodule formation in legumes require recognition of signal molecules produced by the bacteria and their hosts. Here, we show that rhizobial transfer RNA (tRNA)-derived small RNA fragments (tRFs) are signal molecules that modulate host nodulation. Three families of rhizobial tRFs were confirmed to regulate host genes associated with nodule initiation and development through hijacking the host RNA-interference machinery that involves ARGONAUTE 1. Silencing individual tRFs with the use of short tandem target mimics or by overexpressing their targets represses root hair curling and nodule formation, whereas repressing these targets with artificial microRNAs identical to the respective tRFs or mutating these targets with CRISPR-Cas9 promotes nodulation. Our findings thus uncover a bacterial small RNA–mediated mechanism for prokaryote-eukaryote interaction and may pave the way for enhancing nodulation efficiency in legumes.

Symbiotic nitrogen fixation by the bacteria Rhizobia, which occurs in specialized root organs known as nodules of legumes, provides usable nitrogen to plants in agricultural and natural ecosystems. The establishment of rhizobia-legume symbiosis is dependent on recognition of signal molecules between the partners. Upon perception of plant flavonoids, rhizobia secrete lipo-chitooligosaccharidic nodulation factors, which induce root hairs to curl around the bacteria and develop infection treads that allow bacteria to penetrate into the cortical cells of the roots to form nodules (*1*). Because symbiotic nitrogen fixation is resource intensive, legumes have evolved a number of mechanisms to control nodule numbers (*2*). Here, we describe a mechanism by which the bacteria regulate nodule numbers.

Transfer RNA (tRNA)–derived small RNA fragments (tRFs) are found in both prokaryotes and eukaryotes. Originally thought to be random degradation products, tRFs are specifically cleaved from mature tRNAs and often accumulate in stressed or virally infected cells (*3*). Some tRFs, akin to microRNAs (miRNAs), are bound by Argonaute (AGO) proteins, suggesting that they may use an miRNA-like mechanism to regulate gene expression (*4*). tRFs can target and repress retrotransposons through an RNA interference (RNAi)–mediated silencing pathway (*5*). We asked whether tRFs are involved in cross-kingdom communications.

We studied the soybean (*Glycine max*) and the rhizobium (*Bradyrhizobium japonicum*) as symbiotic partners to address this question. All 50 rhizobial tRNAs produced tRFs in both the Rhizobium (strain USDA110) culture and the 10-day-old and 20-day-old soybean (cultivar Williams 82) nodules, most were 18 to 24 nucleotides (nt) in size, and abundance varied (Fig. 1A and figs. S1 and S2). Overall, the tRFs in the nodules are more abundant than those in the culture, with 21-nt tRFs—primarily derived from the *3′* ends of the tRNAs—most abundant (figs. S2 and S3 and table S1).

A total of 52 soybean genes in the soybean genome (*6*) were predicted to be targets of 25 distinct 21- or 22-nt rhizobial tRFs, with a relative abundance of >100 copies per million rhizobial small RNA reads (table S1). These tRFs were neither found in small RNA libraries from non-nodule soybean tissues (table S2) (*7*) nor predicted to target rhizobial genes. Of the 52 soybean genes, *GmRHD3a*/*GmRHD3b*, *GmHAM4a*/*GmHAM4b*, and *GmLRX5*—which are orthologs of the *Arabidopsis ROOT HAIR DIRECTIVE 3* (*RHD3*), *HAIRY MERISTEM 4* (*HAM4*), and *LEUCINE-RICH REPEAT EXTENSION-LIKE 5* (*LRX5*), respectively—attracted our attention because these *Arabidopsis* genes are important for root hair and plant development (*8*–*10*). These soybean genes were predicted to be the targets of three rhizobial tRFs—dubbed Bj-tRF001, Bj-tRF002, and Bj-tRF003—which are the predominant products derived from three tRNAs: Val-1-tRNA(CAC), Gly-1-tRNA(UCC), and Gln-1-tRNA(CUG), respectively (Fig. 1A). Enrichment of the three tRFs in the nodules compared with the rhizobium culture

[1]Department of Agronomy, Purdue University, West Lafayette, IN 47907, USA. [2]Center for Plant Biology, Purdue University, West Lafayette, IN 47907, USA.
*These authors contributed equally to this work.
†Corresponding author. Email: maj@purdue.edu

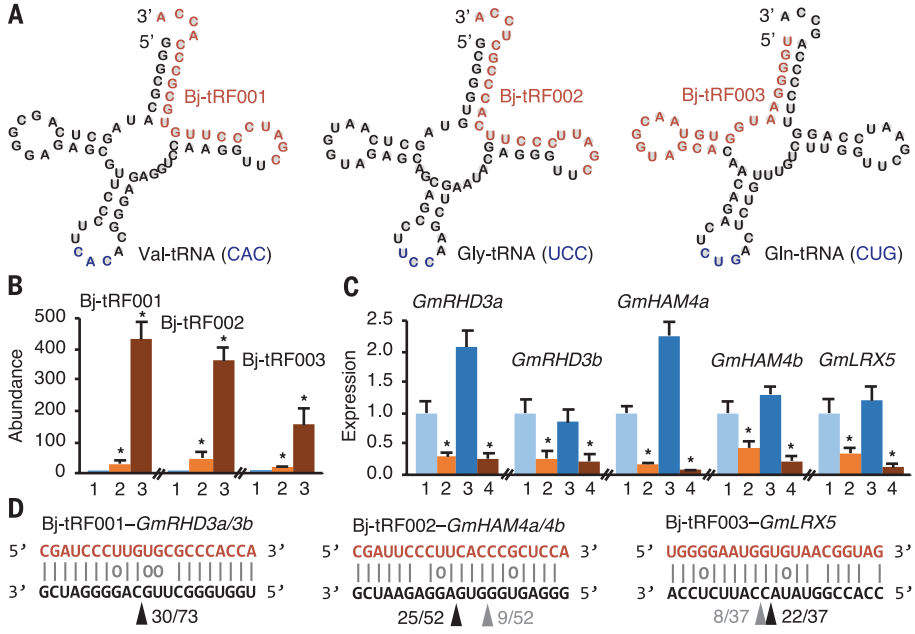

Fig. 1. Rhizobial tRFs and their putative target genes in soybean. (**A**) Origins of three rhizobial tRFs. Anticodons in corresponding tRNAs are colored in blue. (**B**) Abundance of the three tRFs, measured by means of stem-loop quantitative RT-PCR, in free-living *B. japonicum* (*B. j.*) USDA110 (1) and 10–day and 20–day post-inoculation (dpi) nodules (2 and 3, respectively). (**C**) Expression of the putative tRF target genes, measured with quantitative RT-PCR, in the 10-day-old and 20-day-old nodules (2 and 4) and uninoculated soybean roots (1 and 3). Values in (B) and (C), with one set as "1" and the others adjusted accordingly, are shown as means ± SE from three biological replicates. Asterisks indicate the significance level at $P < 0.01$ (Student's t test). (**D**) The three tRFs, their putative target transcripts, and the cleavage sites and frequencies (indicated with arrows and ratios) were detected in the 20-dpi nodules.

was further validated by means of stem-loop quantitative reverse transcription polymerase chain reaction (RT-PCR) (Fig. 1B and fig. S4), and reduced expression of the five soybean genes in the nodules compared with the uninoculated roots was revealed with quantitative RT-PCR (Fig. 1C).

Assuming that the reduced expression of these soybean genes was caused by the rhizobial tRFs through miRNA-like posttranscriptional regulation, cleavage of the mRNAs from these genes at the predicted tRF target sites would have occurred. The mRNAs of these genes were predominantly cleaved at the predicted tRF target sites in the 20-day nodules, whereas none of these sites were cleaved in the uninoculated roots (Fig. 1D and fig. S5). None of these sites are complementary to or were predicted to be targeted by previously identified soybean small RNAs (7) or newly produced ones in this study. Soybean miR171k is the only small RNA predicted to target *GmHAM4a*/*GmHAM4b*, but it was primarily expressed in the uninoculated roots (9.38 counts per million reads) instead of the nodules (0.27 counts per million reads) and thus unlikely to be responsible for the observed repression of *GmHAM4a*/*GmHAM4b* in the nodules.

To determine whether the repression of the *GmRHD3a*/*GmRHD3b*, *GmHAM4a*/*GmHAM4b*, and *GmLRX5* expression in the nodules is associated with nodulation, we created root mutants by means of CRISPR-Cas9 (fig. S6) for each of the five genes and for both copies of each of the two duplicated gene pairs, which were inoculated with USDA110. In all cases examined, expression of the edited genes was reduced (fig. S7), the roots with edited genes produced more nodules than those of the empty-vector transgenic controls, and the double mutants produced the greatest number of nodules (Fig. 2, A and D). We also developed transgenic roots that overexpress *GmRHD3b*, *GmHAM4a*, or *GmLRX5* by the cauliflower mosaic virus (CaMV) *35S* promoter, which exhibited increased expression of these genes and reduced nodule numbers compared with those of the controls (Fig. 2, B and D, and fig. S8A). Thus, these genes are negative regulators of nodulation.

To examine the effects of individual rhizobial tRFs on nodulation, we generated transgenic short tandem target mimic (STTM) soybean roots to silence each of the three rhizobial tRFs (fig. S9). Nodule numbers in the STTM roots were decreased compared with those of the empty-vector transgenic controls (Fig. 2, C and D). As expected, relative abundance of the three tRFs was decreased, and expression of their putative targets was increased (figs. S8B and S10), suggesting that these tRFs are positive regulators of nodulation and may function through repressing their putative target genes.

To understand by which mechanism rhizobial tRFs regulate nodulation, we constructed two artificial miRNA precursors, *aMIR-tRF001* and *aMIR-tRF003*, by replacing the miR172a and miR172a* sequences from the soybean miR172a precursor *MIR172a* with rhizobial tRF001 and its complementary tRF001* or with tRF003 and its complementary tRF003* (fig. S11). *aMIR-tRF001* and *aMIR-tRF003* were expressed separately in Williams 82 hairy roots, under the control of the *35S* promoter, to produce artificial miRNAs amiR-tFR001 and amiR-tFR-003 in the transgenic roots (Fig. 3A). Expression of the putative amiR-tFR001 and amiR-tFR003 targets *GmRHD3a/3b* and *GmLRX5* was reduced compared with that of empty-vector transgenic controls (Fig. 3B), and more nodules were produced in the *aMIR-tRF001* and *aMIR-tRF003* transgenic roots than in respective controls (Fig. 3C). These observations suggest that the artificial miRNA/tRF sequences directly repressed their putative targets to promote nodulation.

To determine whether such sequence complementarity was necessary for the artificial miRNA/tRF-mediated gene regulation, two sets of fusion genes were made by adding each of the 21–base pair (bp) of DNA fragments corresponding to the three putative tRF target sites (wild type) and each of the 21-bp of DNA fragments with 4-bp modification at the detected cleavage site (mutation type) to the coding sequence of the *green fluorescence protein* (*GFP*) gene. The fusion genes were expressed under the control of the *35S* promoter in Williams 82 hairy roots separately (fig. S12A). Reduction of the GFP activity in the "wild-type" roots ~24 hours after inoculation with USDA110 was detected, whereas no change of the GFP activity in the "mutation type" roots

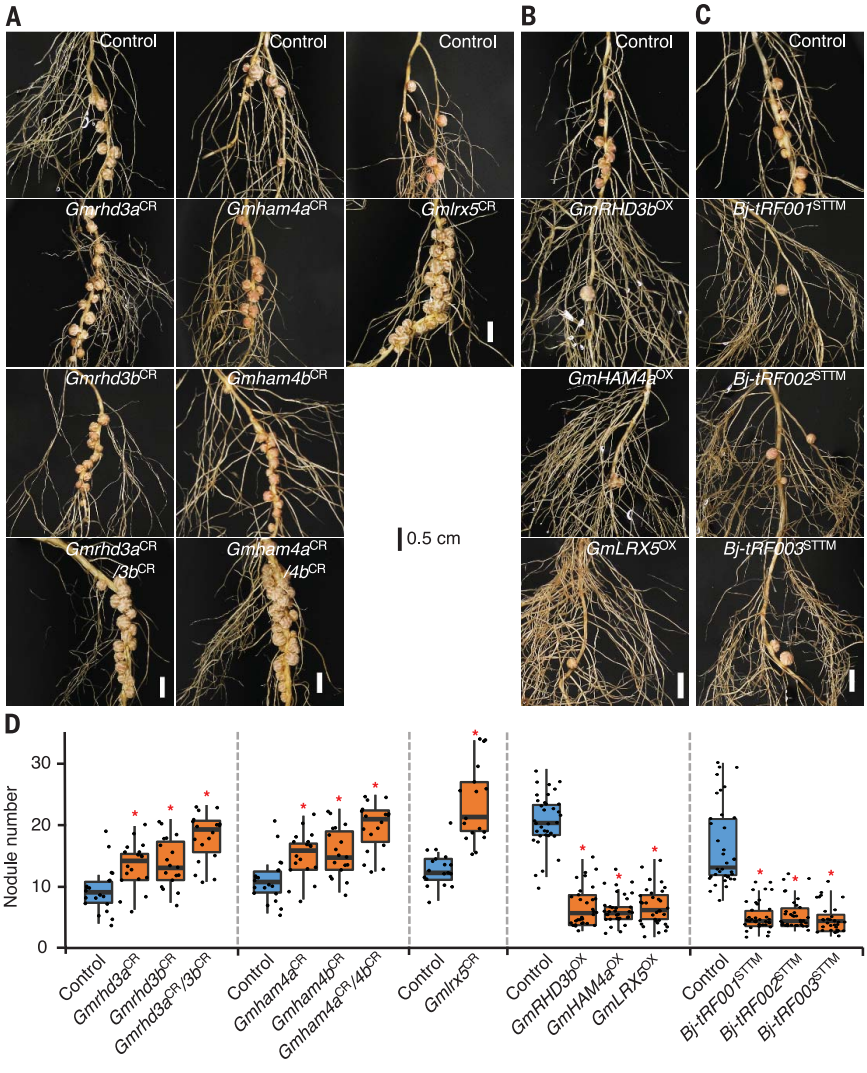

Fig. 2. Modulation of soybean nodulation by rhizobial tRFs and their putative targets. (**A**) Knockouts of the putative tRF targets by means of CRISPR-Cas9 (CR) resulted in increased nodule numbers. (**B**) Overexpression (OX) of the putative tRF targets resulted in decreased nodule numbers. (**C**) Silencing of individual tRFs by means of STTM resulted in decreased nodule numbers. (**D**) Nodule numbers, with all data points represented by dots, are shown as box and whisker plots displaying 95 to 5% interval from three biological replicates (12 plants per replicate) collected 28 days after inoculation. Controls are transgenic roots of empty vectors used for the CRISPR-Cas9 knockouts, the gene-overexpression roots, and the STTM tRF-silencing roots, respectively. Asterisks indicate the significance level of $P < 0.01$ (Student's t test).

was observed (Fig. 3D and fig. S12B). The relative abundance of *GFP* transcripts was consistent with the GFP activity (fig. S12C). These observations indicate that the "wild-type" fusion genes were negatively regulated through base-pairing of their mRNAs at the integrated "target sites" with the rhizobial tRFs.

In *Arabidopsis*, AGO1 is a component of the RNA-induced silencing complexes that mediate miRNA-guided cleavage of target mRNAs (*11*). To determine whether the rhizobial tRFs act through the functional counterpart of AGO1 in soybean, one (GmAGO1b) of the two soybean orthologs of the *Arabidopsis* AGO1 (*12*), whose transcripts are relatively more abundant than those of the other (GmAGO1a) in soybean root nodules (*13*), was fused with the Myc epitope tag and expressed in the hairy roots of Williams 82. The fusion protein was immunoprecipitated by the Myc antibody from the 20-day nodules induced by USDA110. All three rhizobial tRFs were detected in the GmAGO1b-Myc–associated fraction pulled down by the Myc antibody but not detected in the nodule lysate incubated without the antibody, suggesting that these rhizobial tRFs hijacked the soybean AGO1 to catalyze tRF-guided cleavage of target mRNAs in the host cells (Fig. 3E).

Actually, the tRF-mediated regulation of host gene expression was detected at early stages of rhizobial infection. At all five time points from 6 to 72 hours after inoculation with USDA110, the abundance of the three tRFs was increased in the inoculated root hairs compared with the uninoculated root hairs (fig. S13A), whereas the expression of their targets was decreased (fig. S13B). No differences in root hair number and length were observed between the *GmRHD3b*, *GmHAM4a*, and *GmLRX5* overexpression roots and the controls or between the tRF-silencing STTM roots and the controls (fig. S14), but the proportions of deformed and curled root hairs were decreased in the overexpression and STTM roots compared with respective controls (Fig. 4, A to C), suggesting that rhizobial tRFs promote rhizobial infection.

To shed light on the evolutionary conservation and divergence of rhizobial tRF-mediated host gene regulation, we analyzed sequence data from four legumes—soybean, common bean (*Phaseolus vulgaris*), *Medicago truncrtula*, and *Lotus japonica* (*6*)—and 12 rhizobium species (*14*), as well as the *GmRHD3a*/*GmRHD3b*, *GmHAM4a*/*GmHAM4b*, and *GmLRX5* sequences from soybean populations (*15*, *16*). Among 699 soybean accessions, no sequence variation at the three tRF target sites within the five genes was found (fig. S15). Among eight *B. japonicum* strains, no sequence variation at the three tRF sites within respective rhizobial tRNAs was detected (fig. S16). By contrast, sequences at the target sites diverged among the four legumes (fig. S17). In particular, no orthologs of *GmLRX5* were found in the other three legumes (fig. S17). The counterparts of the three rhizobial tRF sequences in respective tRNAs also showed interspecific divergence (fig. S16). *PvRHD3* in common bean, the ortholog of *GmRHD3a/3b*,

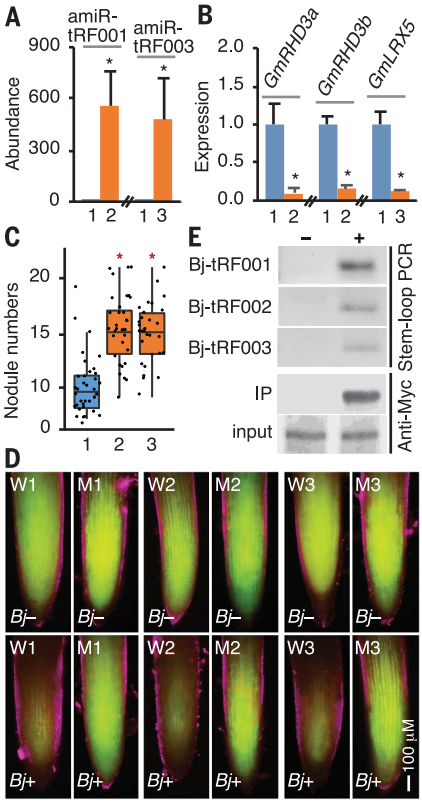

Fig. 3. Rhizobial tRF-guided gene regulation by hijacking the host RNAi machinery. (**A**) Abundance of artificial miRNAs measured with stem-loop quantitative RT-PCR in *aMIR-tRF001* (2) and *aMIR-tRF003* transgenic roots (3) and respective empty-vector transgenic roots (1) 28 days after inoculation. (**B**) Expression of the putative tRF/artificial miRNA targets measured with quantitative RT-PCR in the same samples as described in (A). Values in (A) and (B), with one set as "1" and the others adjusted accordingly, are shown as means ± SE from three biological replicates. Asterisks indicate the significance level at $P < 0.01$ (Student's t test). (**C**) Nodule numbers in the same samples as described in (A), with all data points represented by dots, are shown as box and whisker plots displaying 95 to 5% interval from three biological replicates (12 plants per replicate). (**D**) GFP activity in transgenic roots of "GFP-tRF target site" fusion genes (W1 to W3) and "GFP-mutated tRF target site" fusion genes (M1 to M3) 24 hours after inoculation with USDA110. *Bj*– and *Bj*+ indicate uninoculated and inoculated roots, respectively. (**E**) Association of the three tRFs with soybean GmAGO1b in nodules 28 days after inoculation detected from three experimental replicates. "+" and "–" indicate the GmAGO1b-Myc fusion protein–associated fraction immunoprecipitated by the Myc antibody and the nodule lysate without Myc antibody incubation, respectively.

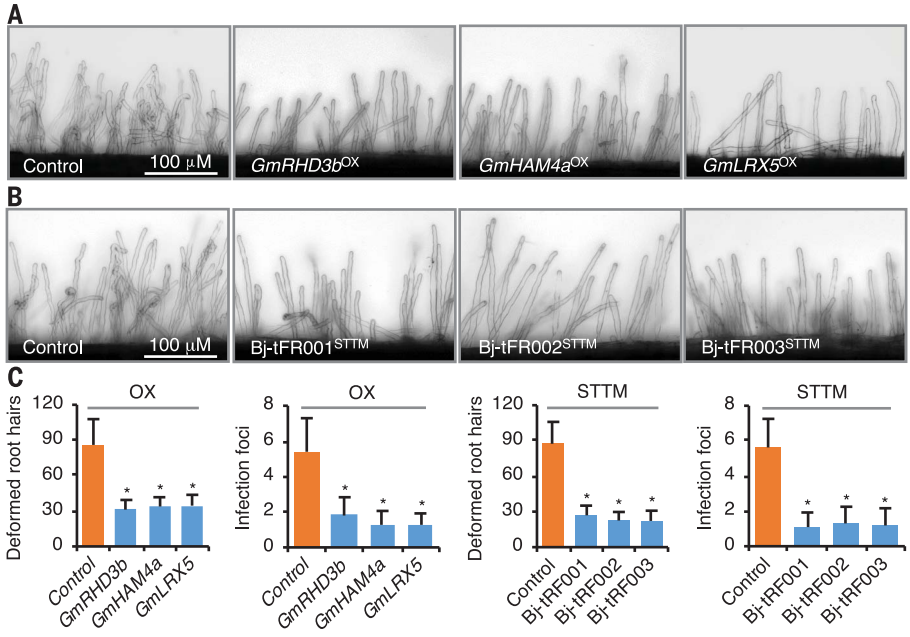

Fig. 4. Modulation of early-stage rhizobial infection by rhizobial tRFs and their targets in soybean. (**A** and **B**) Morphological differences between the root hairs overexpressing the rhizobial tRF targets and the negative control and between the STTM root hairs inhibiting the rhizobial tRF function and the negative control. (**C**) Quantitation of deformed root hairs and curled root hairs with infection foci in samples as exemplified in (A) and (B). The values are shown as means ± SD from three biological replicates ($n = 25$ hairy roots per replicate). Asterisks indicate the significant level at $P < 0.05$ (Student's t test).

does have a tRF001 target site identical to that of *GmRHD3a/3b* (fig. S17), but *Rhizobium etli*, a compatible symbiotic partner of common bean (*17*), does not have the *B. japonicum* Val-1-tRNA (CAC) from which tRF001 was derived. Using the small RNA data from the common bean nodules induced by a *R. etli* strain (*17*), 38 *R. etli* tRNAs were identified to have produced 21-nt tRFs. These tRFs were primarily derived from the 3′ ends of the tRNAs (fig. S18). Ten different 21-nt tRFs, each with a relative abundance of >100 counts per million rhizobial small RNA reads in the common bean nodules, were predicted to target 14 common bean genes, including genes encoding a protein kinase, a GRAS transcription factor, and an APETALA2-like transcription factor that may be involved in nodulation regulation (table S3) (*18*). Nevertheless, none of these 14 putative *R. etli* tRF targets in common bean are orthologs of the 25 putative *B. japonicum* tRF targets in soybean (table S1).

We demonstrate that rhizobial tRFs are positive regulators of rhizobial infection and nodule formation in soybean, playing an important role in balancing plant growth and symbiosis (fig. S19). In addition to the three rhizobial tRFs we investigated, other rhizobial tRFs were predicted to target soybean genes annotated to encode auxin receptors and efflux carriers, RING/U-box proteins, and protein kinases (table S1), which may also affect nodulation (*19*). Such cross-kingdom communications may be common among symbiotic partners, but the nodes of rhizobial tRFs-host gene interactions appear to be diverse.

REFERENCES AND NOTES

1. D. J. Gage, *Microbiol. Mol. Biol. Rev.* **68**, 280–300 (2004).
2. B. J. Ferguson *et al.*, *Plant Cell Environ.* **42**, 41–51 (2019).
3. A. J. Schorn, R. Martienssen, *Trends Cell Biol.* **28**, 793–806 (2018).
4. P. Kumar, J. Anaya, S. B. Mudunuri, A. Dutta, *BMC Biol.* **12**, 78 (2014).
5. A. J. Schorn, M. J. Gutbrod, C. LeBlanc, R. Martienssen, *Cell* **170**, 61–71.e11 (2017).
6. S. Dash *et al.*, *Nucleic Acids Res.* **44**, D1181–D1188 (2016).
7. S. Arikit *et al.*, *Plant Cell* **26**, 4584–4601 (2014).
8. J. Chen, G. Stefano, F. Brandizzi, H. Zheng, *J. Cell Sci.* **124**, 2241–2252 (2011).
9. E. M. Engstrom *et al.*, *Plant Physiol.* **155**, 735–750 (2011).
10. N. Baumberger, C. Ringli, B. Keller, *Genes Dev.* **15**, 1128–1139 (2001).
11. K. Bohmert *et al.*, *EMBO J.* **17**, 170–180 (1998).
12. X. Liu, T. Lu, Y. Dou, B. Yu, C. Zhang, *BMC Bioinformatics* **15**, 4 (2014).
13. A. J. Severin *et al.*, *BMC Plant Biol.* **10**, 160 (2010).
14. T. Fujisawa *et al.*, *Nucleic Acids Res.* **42**, D666–D670 (2014).
15. Z. Zhou *et al.*, *Nat. Biotechnol.* **33**, 408–414 (2015).
16. C. Fang *et al.*, *Genome Biol.* **18**, 161 (2017).
17. D. Formey *et al.*, *Int. J. Mol. Sci.* **17**, 887 (2016).
18. L. P. Íñiguez, B. Nova-Franco, G. Hernández, *Plant Signal. Behav.* **10**, e1062957 (2015).
19. M. Zhu, J. L. Dahmen, G. Stacey, J. Cheng, *BMC Bioinformatics* **14**, 278 (2013).

ACKNOWLEDGMENTS

We thank D. Yu for the pSC1 vector and B. C. Meyers for suggestions. **Funding:** This work was partially supported by the Agriculture and Food Research Initiative of the U.S. Department of Agriculture National Institute of Food and Agriculture (grants 2015-67013-22811 and 2018-67013-27425), Purdue AgSEED program, North Central Soybean Research Program, and Indiana Soybean Alliance. **Author contributions:** B.R., X.W., and J.D. performed the research; B.R., X.W., and J.M. analyzed the data; and J.M. designed the research and wrote the manuscript, with input from B.R., X.W., and J.D. **Competing interests:** This work has been filed for a U.S. Provisional Patent Application. **Data and materials availability:** All data are available in the National Center for Biotechnology Information (accession nos. SRR7986781 to SRR7986788 and SRR7985373), main text, or supplementary materials.

SUPPLEMENTARY MATERIALS

science.sciencemag.org/content/365/6456/919/suppl/DC1
Materials and Methods
Figs. S1 to S19
Tables S1 to S4
References (*20–42*)

30 October 2018; resubmitted 22 April 2019
Accepted 10 July 2019
10.1126/science.aav8907

SYNTHETIC BIOLOGY

Programmed chromosome fission and fusion enable precise large-scale genome rearrangement and assembly

Kaihang Wang*, Daniel de la Torre, Wesley E. Robertson, Jason W. Chin†

The design and creation of synthetic genomes provide a powerful approach to understanding and engineering biology. However, it is often limited by the paucity of methods for precise genome manipulation. Here, we demonstrate the programmed fission of the *Escherichia coli* genome into diverse pairs of synthetic chromosomes and the programmed fusion of synthetic chromosomes to generate genomes with user-defined inversions and translocations. We further combine genome fission, chromosome transplant, and chromosome fusion to assemble genomic regions from different strains into a single genome. Thus, we program the scarless assembly of new genomes with nucleotide precision, a key step in the convergent synthesis of genomes from diverse progenitors. This work provides a set of precise, rapid, large-scale (megabase) genome-engineering operations for creating diverse synthetic genomes.

Efforts to minimize (*1*, *2*), refactor (*3*), recode (*4*, *5*), and reorganize (*2*, *6*) chromosomes and genomes are providing new insights and opportunities. However, in *Escherichia coli*, the workhorse of synthetic biology, the methods necessary to realize a complete set of operations for synthetic genome design are missing. These operations include (i) the iterative replacement of genomic DNA with synthetic DNA, (ii) deletion of genomic DNA, (iii) translocation of large genomic sections, and (iv) inversion of large genomic sections as well as (v) methods for combining large genome sections from distinct strains for the convergent assembly of synthetic genomes. Each operation should be scarless and programmed with nucleotide precision so that genome designs can be precisely and rapidly realized.

Efficient, precise, and robust methods for iterative replacement (>100 kb per step) and deletion of genome sections have been reported (*7*); however, there has been less progress on creating methods for generating precisely programmed inversions or translocations in *E. coli*, with most current methods for inversions relying on sequence-specific recombinases. Moreover, methods for combining large (e.g., 0.5-Mb) sections from distinct genomes rely on classical conjugation (*8*) and its derivatives (*5*, *9*). Although these methods can be useful (*5*, *9*), they are fundamentally limited because (i) they require large regions of homology [commonly at least 3 kb, and sometimes up to 400 kb, between the donor and recipient genomes (*5*)], (ii) undesired chimeras between the two genomes may result, and (iii) the site of crossover between the two genomes is not precisely specified. Indeed, in favorable cases, crossovers are only selected with kilobase resolution.

Chromosome fission and fusion have occurred in natural evolution (*10*, *11*), and these processes may have accelerated evolution (*10*, *12*, *13*). The synthetic splitting and fusion of chromosomes have been explored to a limited extent, primarily in naturally recombinogenic organisms (*13*–*18*). One report excised up to 720 kb from a single region of the *E. coli* genome (*19*) by using natural homologous recombination in *E. coli*. Because the recombination frequency in *E. coli* is generally low (*20*), this approach is presumably very inefficient. A protelomerase of bacteriophage N15 and a *Vibrio* origin of replication were used to divide the circular *E. coli* chromosome into two linear subchromosomes. However, only one characterized arrangement was viable (*21*). Thus, the limited methods for splitting the *E. coli* genome are not general or efficient.

Here, we demonstrate that an *E. coli* genome, without any prior modification, can be efficiently split, by single-step programmed fission, into pairs of synthetic chromosomes. The resulting synthetic chromosomes enable precise, programmed fusions, genomic inversions, and translocations; moreover, they provide a route to assemble new genomes through the precise, convergent assembly of large genomic fragments from distinct strains.

We designed and synthesized a system to precisely split the unmodified genome into two user-defined, circular chromosomes (Fig. 1A) and tested our approach by splitting the *E. coli* MDS42 (*1*) genome (data file S1) into a 3.43- and a 0.56-Mb chromosome. To achieve this, we first introduced Cas9 with appropriate spacers (table S1), the lambda-red recombination machinery, and a fission bacterial artificial chromosome (BAC) (data file S2) into cells. We implemented six Cas9-directed cuts in the DNA of these cells; two of these cuts target the genome, and four of these cuts target the fission BAC (data files S3 and S4). The two cuts in the genome create fragment 1 and fragment 2, and the four cuts in the fission BAC release linker sequence 1 and linker sequence 2. Chromosome 1 (3.43 Mb) containing the genomic origin of replication (*oriC*) was formed through lambda-red–mediated recombination between genomic fragment 1 and linker sequence 1, by virtue of their 50–base pair (bp) regions of homology (table S2). Similarly, chromosome 2 (0.56 Mb) was formed through lambda red–mediated recombination between genomic fragment 2 and linker sequence 2 (Fig. 1A and fig. S1); this linker sequence contained its own replication and segregation machinery.

In the prefission strain, the fission BAC is nonessential and contains a *SacB-Cm*^{R} double selection cassette (this confers resistance to chloramphenicol and sensitivity to sucrose, but cells can grow on sucrose by losing the fission BAC), the *luxABCDE* operon (conferring luminescence), and *rpsL* (conferring sensitivity to streptomycin). After successful fission, the *rpsL* gene is lost, cells are resistant to streptomycin, the *luxABCDE* operon is removed from a strong promoter to chromosome 1 (leading to weaker luminescence), and the *SacB-Cm*^{R} double selection cassette becomes part of chromosome 2 and cannot be lost. Thus, correct postfission cells are selectively sensitized to sucrose.

After execution of the fission protocol, we enriched for cells that had undergone genome fission to generate two chromosomes, through growth on streptomycin and chloramphenicol (table S3). This selects for both loss of *rpsL* and maintenance of *Cm*^{R} in the *SacB-Cm*^{R} double selection cassette and therefore kills cells containing the fission BAC but allows growth of cells that have undergone programmed genome fission.

We characterized individual postfission clones by several independent methods. First, we examined the luminescence of cells and their growth on selective media (Fig. 1B). Successful clones had decreased luminescence with respect to prefission controls, gained sucrose sensitivity, and gained the ability to grow when challenged simultaneously with both chloramphenicol and streptomycin. Second, we performed polymerase chain reactions (PCRs) across the new junctions resulting from fission. Successful postfission clones exhibited bands of the expected size that were not present in prefission clones (Fig. 1C). This confirmed that both fission junctions were as expected. Third, we confirmed the expected restriction enzyme digestion pattern for the postfission genome by pulsed-field gel electrophoresis (fig. S2). Finally, we determined the replicon organization of the genome by de novo assembly; we achieved this by combining the results of short-read (300-bp paired end) and long-read (N50 of ~8.3 kb) sequencing in Unicycler (*22*) to generate one contig per replicon. The postfission assembly formed two circular contigs, which corresponded to the chromosomes expected from fission (fig. S3 and table S4). The

Medical Research Council Laboratory of Molecular Biology, Francis Crick Avenue, Cambridge, England, UK.
*Present address: Division of Biology and Biological Engineering, California Institute of Technology, Pasadena, CA, USA.
†Corresponding author. Email: chin@mrc-lmb.cam.ac.uk

copy number of each chromosome was as expected (table S5).

We demonstrated the scope and generality of fission by programming the splitting of the genome into five additional distinct and diverse pairs of chromosomes (Fig. 2 and figs. S2 to S4). These included a pair in which chromosome 1 is 2.44 Mb and chromosome 2 is 1.55 Mb. Because chromosome 2 has BAC-derived replication and segregation machinery, our data are consistent with BACs being able to maintain megabases of DNA. The only constraints we imposed on the choice of fission sites were that they contained a protospacer adjacent motif (PAM) for Cas9 and lay greater than 30 bp outside any gene. Although a single 2-Mb fission test failed (fig. S5 and table S3), all other experiments we tried led to successful fission (figs. S1 to S4). Fission had only modest effects on the growth of cells (fig. S6). We observed that the genome fissions were present after approximately 105 generations of continuous growth (fig. S7).

We demonstrated that the programmed fusion of synthetic chromosomes, generated by fission, enables the generation of precisely rearranged genomes (Fig. 3). We applied fission to a cell in which ~0.54 Mb, section C (Fig. 2A and figs. S1 and S3), of the genome is watermarked by 2521 synonymous codon changes (*5*) (data file S5); this brought the total number of successful fissions to 7 (Fig. 2A and fig. S1). The resulting cell contained chromosome 1 (3.45 Mb) and a watermarked chromosome 2 (0.54 Mb). After fission, we replaced the *SacB-Cm*^{R} double selection cassette in chromosome 2 with an *oriT-pheS*-Kan*^{R} cassette (table S6). This cell provided a common intermediate for diverse fusions.

We first used fusion to regenerate the original genome. We prepared chromosome 1 for fusion

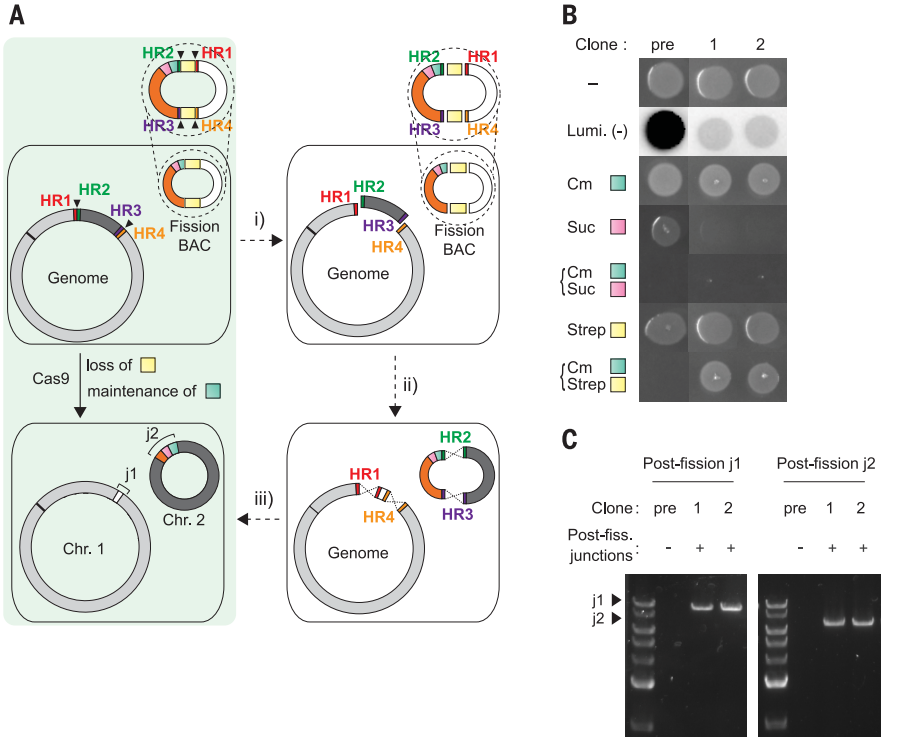

Fig. 1. Programmed genome fission splits the *E. coli* genome into two chromosomes. (**A**) *E. coli* harbors a fission BAC containing a double selection cassette (*sacB-Cm*^{R} shown as pink and green, respectively), *rpsL* (yellow), a *luxABCDE* operon (white), and the BAC replication machinery (orange). During fission, (i) Cas9 induces six cuts (black triangles), splitting the genome into fragment 1 (light gray, containing *oriC* indicated by black line) and fragment 2 (dark gray) and the fission BAC into four pieces (linker sequence 1, linker sequence 2, and two copies of *rpsL*). (ii) Homology regions (HRs) between fragments and their cognate linkers. (iii) Lambda red recombination joins fragments and linkers to yield chromosomes 1 and 2 (Chr. 1 and Chr. 2). Junctions 1 and 2 (j1 and j2) are new junctions. (**B**) Growth and luminescence (Lumi.) of prefission (pre) and postfission (1 and 2) clones are consistent with the generation of two chromosomes (Chr. 1, ~3.43 Mb and Chr. 2, ~0.56 Mb). Cells were stamped in plain LB agar (-), 20 μg/ml chloramphenicol (Cm), 7.5% sucrose (Suc), 100 μg/ml streptomycin (Strep), or the indicated combination. (**C**) PCR of postfission (Post-Fiss.) clones across j1 and j2.

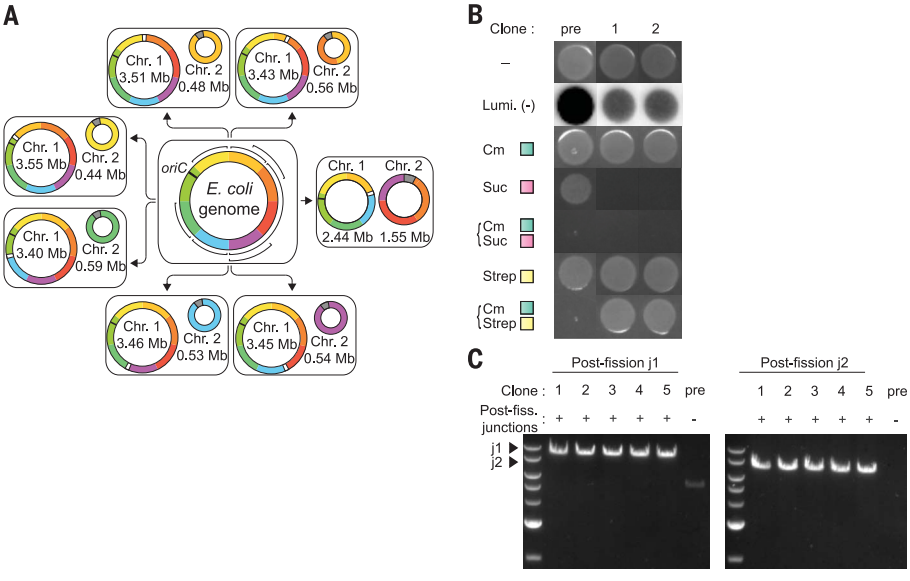

Fig. 2. Fission can be performed throughout the *E. coli* genome. (**A**) Successful fissions performed. Each color on the *E. coli* genome corresponds to ~0.5 Mb. We named the sections A to H. A is dark orange, and the other sections are labeled alphabetically in a clockwise sequence. Linker sequence 1, white; *oriC*, black bar; linker sequence 2, gray. Boundaries and homologies of each fission experiment are provided in table S2. Seven fissions are shown, including the 3.43, 0.56 Mb fission (Fig. 1). The 3.45, 0.54 Mb fission (purple Chr. 2) was performed by using an *E .coli* genome in which a ~0.54-Mb section had been recoded (Fig. 3). (**B**) Growth and luminescence for the generation of the 2.44, 1.55 Mb fission; annotation as in Fig. 1B. Data for other fissions are shown in fig. S4. (**C**) PCR of clones across new junctions for 2.44, 1.55 Mb fission. Postfission clones (1 to 5) exhibit products of the expected size, whereas the prefission control does not. Junction PCRs for other fissions are in fig. S4.

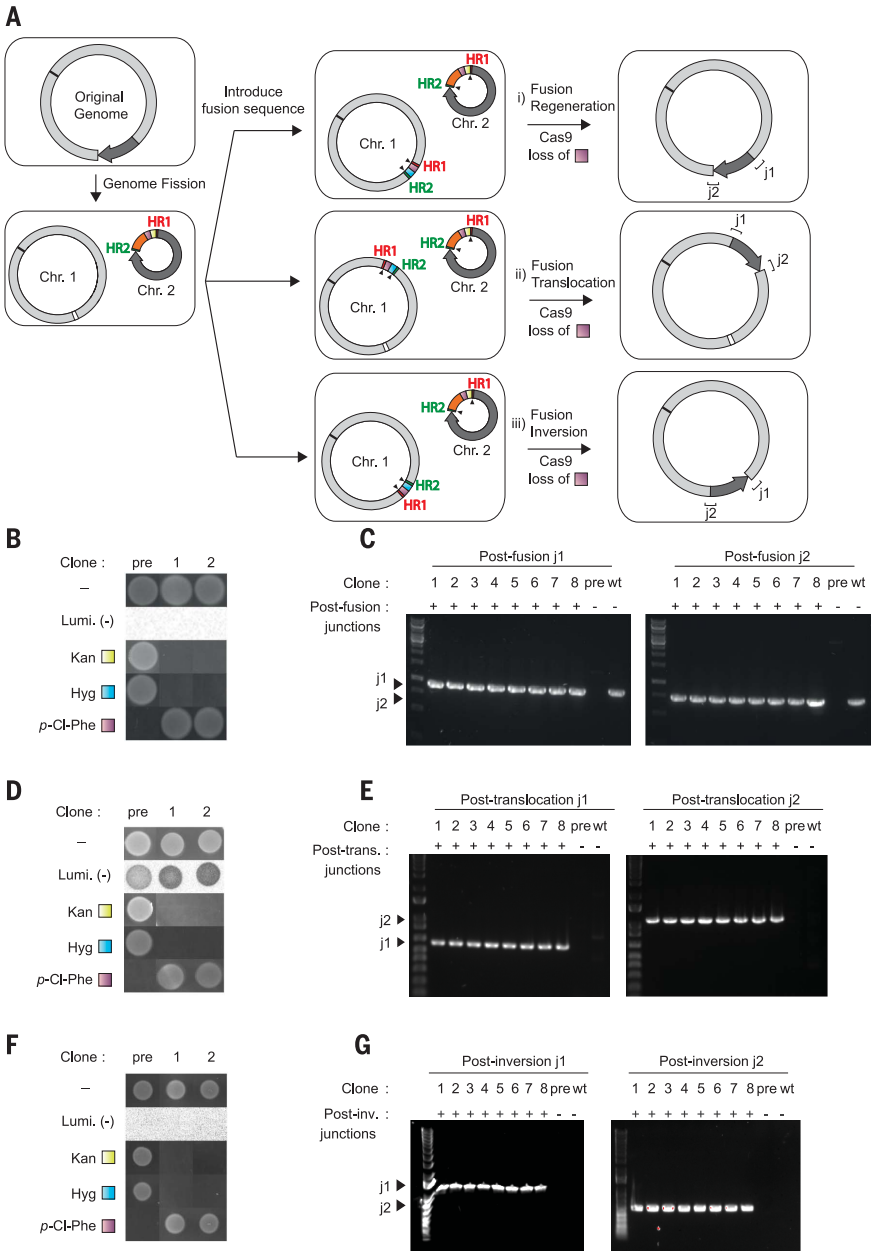

Fig. 3. Programmed chromosomal fusion enables translocations and inversions of large genomic segments from common fission intermediates. (**A**) *E. coli* with two chromosomes (Chr. 1 ~3.45 Mb and Chr. 2 ~0.54 Mb) was generated by fission. The sequence of Chr. 2 is watermarked as described in the text. The color-coding is as in Fig. 1A; a *pheS*-Kan*^{R} double selection cassette (purple and yellow, respectively) is shown. A fusion sequence, consisting of a *pheS*-Hyg*^{R} (purple and blue, respectively) double selection cassette flanked by HR1 and HR2, is introduced in the indicated positions and orientation in Chr. 1 by lambda-red recombination. Cas9 spacer-directed cleavage (black arrows), lambda-red recombination, and selection for fusion products through the loss of *pheS** on 4-chloro-phenylalanine yield the indicated products. (i) Regenerating the original genomic arrangement, (ii) translocation of the 0.54-Mb segment 700 kb away from its original position, and (iii) inversion of the 0.54-Mb segment. (**B**) Growth and luminescence of pre- and postfusion regeneration (1 and 2) clones. Hyg, hygromycin; Kan, kanamycin; *p*-Cl-Phe, 4-chloro-phenylalanine. (**C**) PCR of clones across new junctions for fusion regeneration. Postfusion clones (1 to 8) exhibit products of the expected size, whereas the pre-fusion control does not. wt, wild type. (**D** and **E**) As in (B and C) but for fusion translocation (trans.). (**F** and **G**) As in (B and C) but for fusion inversion (inv.).

by replacing its linker sequence 1 with a fusion sequence for chromosome 2 (oligonucleotide sequences are provided in table S6). This contained a *pheS*-Hyg*^{R} double selection cassette flanked by Cas9 cut sites and homology to fragment 2 in chromosome 2 (Fig. 3A). Fusion was initiated by Cas9-mediated cleavage at either side of the *pheS*-Hyg*^{R} cassette in chromosome 1 and at the ends of the watermarked sequence in chromosome 2, and the resulting homologous ends were joined through lambda red–mediated recombination. We selected the fusion product on 4-chloro-phenylalanine.

We characterized postfusion clones by several independent methods. Successful clones were no longer sensitive to 4-chloro-phenylalanine or resistant to kanamycin or hygromycin (Fig. 3B). PCR across the new junctions generated by fusion led to bands of the correct size that were not present in the prefusion clones (Fig. 3C). We further demonstrated successful fusion by de novo assembly of short-read (300-bp paired end) and long-read (N50 of ~20 kb) sequencing. The prefusion genome formed two circular contigs, whereas all postfusion assemblies formed a single circular contig, which corresponds to the expected fusion product (fig. S3).

We demonstrated that inserting the fusion sequence at different positions in chromosome 1 (500 or 700 kb away from linker sequence 1) (Fig. 3A and fig. S8), followed by initiation of fusion with chromosome 2, enables the selection of genomes bearing defined translocations (Fig. 3, D and E, and figs. S3 and S8). We also demonstrated that inserting the fusion sequence into chromosome 1 in an inverted orientation (Fig. 3A), followed by initiation of fusion with chromosome 2, enables the selection of genomes bearing defined inversions (Fig. 3, F and G, and fig. S3). An attempt at fusion 1.8 Mb away from the linker sequence did not lead to a stable translocation (fig. S8 and table S3).

Next, we combined genome fission, conjugative transplant, and chromosome fusion to precisely combine defined sections of distinct genomes (Fig. 4A). This is a key step in the precise assembly of synthetic genomes from strains containing synthetic sections.

We began with two strains, each containing a different watermarked genomic section [section C or section A (Fig. 2 and fig. S1)], with the target of combining the watermarked sections in a single, chimeric genome. We defined one strain as the donor (data file S5) and the other strain as the recipient (data file S6). We performed fission on the genome of the donor to capture its watermarked sequence in chromosome 2. We then replaced the *SacB-Cm*^{R} double selection cassette in chromosome 2 with an *oriT-pheS*-Kan*^{R} cassette (table S6) and transformed a nontransferable F′ plasmid (*5*) into the donor strain. These steps prepare the donor strain for transplant of chromosome 2 to the recipient.

In parallel, we performed fission on the genome of the recipient to split its genome, at the same position as the donor, into two synthetic

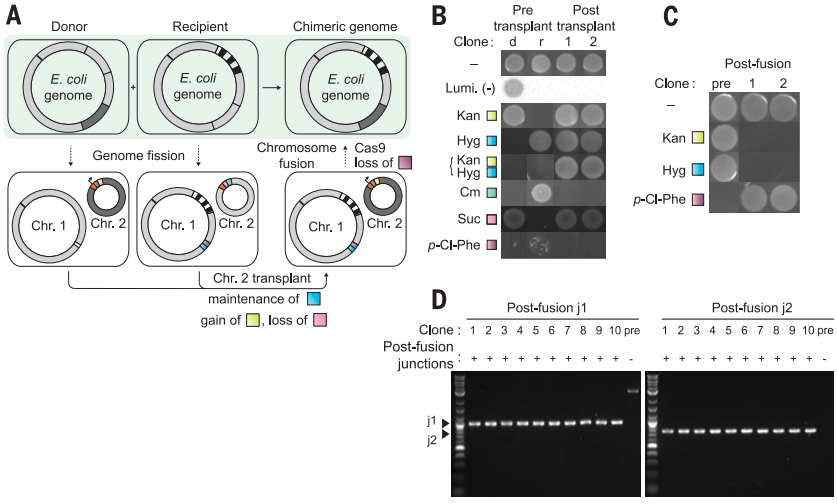

Fig. 4. Precise genome assembly from genomic segments of distinct strains. (**A**) Precisely combining the watermarked region 1 (dark gray) from a donor strain and a watermarked region 2 (black striped) from a recipient strain into a single strain. Fission is performed in parallel in the donor and recipient strains. The resulting donor strain contains a watermarked Chr. 2 containing an *oriT* (black arrow) and a *pheS*-Kan*^{R} double selection cassette (purple and yellow); the remainder of linker sequence 2 is orange. The resulting recipient strain contains an analogous nonwatermarked Chr. 2, with a *sacB-Cm*^{R} cassette (pink and green). The linker sequence 1 (white) is replaced with a fusion sequence containing a *pheS*-Hyg*^{R} cassette (purple and blue) in preparation for fusion. The donor cell is provided with a nontransferable F′ plasmid. Mixing of donor and recipient cells facilitates conjugative transplant of Chr. 2 from the donor to the recipient; selection for *Kan*^{R} and against *sacB*-mediated sucrose sensitivity enables the isolation of cells that have gained a watermarked Chr. 2 and lost the nonwatermarked Chr. 2. Subsequent genome fusion generates a strain in which the watermarked regions 1 and 2 have been precisely combined in a single chromosome. (**B**) Following the process of chromosomal transplant by growth on selective media and luminescence. d, the pretransplant donor; r, pretransplant recipient. (**C**) Following the process of chromosomal fusion through growth on selective media. (**D**) PCR across the new junctions generated by chromosomal fusion yields products of the expected size in the postfusion clones (1 to 10) but not in the prefusion control.

chromosomes. This created a recipient containing a nonwatermarked chromosome 2 (the fission BAC used in the recipient, and therefore chromosome 2, contains a *sacB-Cm*^{R} cassette and does not contain *oriT*) and chromosome 1 that contains the second watermarked region. The linker sequence 1 in chromosome 1 of the recipient was then replaced with a fusion sequence containing a *pheS*-Hyg*^{R} cassette flanked by regions of homology to the fragment of the original genome captured in chromosome 2.

To generate cells that contain both watermarked regions, we mixed donor and recipient cells. We selected for transfer of chromosome 2 from the donor to the recipient and recipient cells in which chromosome 2 from the donor had replaced the endogenous chromosome 2; we termed this overall process chromosome transplant. The resulting recipient cells contained chromosome 2 from the donor and chromosome 1 from the recipient. We generated a single, chimeric genome that contains both the watermarked sequences by fusion of the donor chromosome 2 and the recipient chromosome 1 (Fig. 4, B to D; fig. S3; and data file S7). All attempts at genome assembly were successful.

We demonstrated the efficient programmed, single-step fission of the unmodified *E. coli* genome into diverse megabase-scale chromosomes. These chromosomes provide a common intermediate for the facile creation of diverse genomes. The chromosomes in a single cell can be fused into a single genome to effect precise genomic translocations or precise and scarless inversions. This facilitates the realization of reorganized genome designs and the exploration of modular, synthetic syntenies that may be more amenable to engineering (*2*). Moreover, the transplant of chromosomes between cells, followed by fusion, enables the precise convergent assembly of new genomes. Our work provides the necessary set of precise, rapid, large-scale genome-engineering operations for creating diverse synthetic genomes.

REFERENCES AND NOTES

1. G. Pósfai *et al.*, *Science* **312**, 1044–1046 (2006).
2. C. A. Hutchison 3rd *et al.*, *Science* **351**, aad6253 (2016).
3. L. Y. Chan, S. Kosuri, D. Endy, *Mol. Syst. Biol.* **1**, 0018 (2005).
4. M. J. Lajoie *et al.*, *Science* **342**, 357–360 (2013).
5. J. Fredens *et al.*, *Nature* **569**, 514–518 (2019).
6. J. S. Dymond *et al.*, *Nature* **477**, 471–476 (2011).
7. K. Wang *et al.*, *Nature* **539**, 59–64 (2016).
8. J. Lederberg, E. L. Tatum, *Nature* **158**, 558 (1946).
9. F. J. Isaacs *et al.*, *Science* **333**, 348–353 (2011).
10. D. W. Burt, *Cytogenet. Genome Res.* **96**, 97–112 (2002).
11. G. Giannuzzi *et al.*, *Genome Res.* **23**, 1763–1773 (2013).
12. V. S. Cooper, S. H. Vohr, S. C. Wrocklage, P. J. Hatcher, *PLOS Comput. Biol.* **6**, e1000732 (2010).
13. J. A. Escudero, D. Mazel, *Int. Microbiol.* **20**, 138–148 (2017).
14. D. Ausiannikava *et al.*, *Mol. Biol. Evol.* **35**, 1855–1868 (2018).
15. M. Itaya, T. Tanaka, *Proc. Natl. Acad. Sci. U.S.A.* **94**, 5378–5382 (1997).
16. J. Luo, X. Sun, B. P. Cormack, J. D. Boeke, *Nature* **560**, 392–396 (2018).
17. Y. Shao *et al.*, *Nature* **560**, 331–335 (2018).
18. Y. Ueda *et al.*, *J. Biosci. Bioeng.* **113**, 675–682 (2012).
19. Y. Yamaichi, H. Niki, *EMBO J.* **23**, 221–233 (2004).
20. C. Raeside *et al.*, *mBio* **5**, e01377–e14 (2014).
21. X. Liang, C. H. Baek, F. Katzen, *ACS Synth. Biol.* **2**, 734–740 (2013).
22. R. R. Wick, L. M. Judd, C. L. Gorrie, K. E. Holt, *PLOS Comput. Biol.* **13**, e1005595 (2017).

ACKNOWLEDGMENTS

We thank J. Houseley and J. Ajioka for providing equipment for pulsed-field gel electrophoresis and J.E. Sale for helpful comments on the manuscript. **Funding:** This work was supported by the Medical Research Council (MRC), UK (MC_U105181009 and MC_UP_A024_1008), and an ERC Advanced Grant SGCR, all to J.W.C. **Author contributions:** K.W. designed and implemented the genome manipulation processes reported. K.W., D.d.l.T., and W.E.R. demonstrated scope. D.d.l.T. implemented the de novo assembly approach. J.W.C. defined the direction of research, supervised the project, and wrote the paper with the other authors. **Competing interests:** The authors declare no competing interests. **Data and materials availability:** The sequences for de novo genome assemblies and DNA sequencing data have been deposited in NCBI's GenBank and SRA databases, and their accession numbers are listed in table S4. All other data needed to evaluate the conclusions of the study are present in the paper or the supplementary materials.

SUPPLEMENTARY MATERIALS

science.sciencemag.org/content/365/6456/922/suppl/DC1
Materials and Methods
Figs. S1 to S8
Tables S1 to S6
Data Files S1 to S7
References (*23*–*27*)

17 May 2019; accepted 2 August 2019
10.1126/science.aay0737

ASTROCHRONOLOGY

Solar System chaos and the Paleocene–Eocene boundary age constrained by geology and astronomy

Richard E. Zeebe[1]* and Lucas J. Lourens[2]

Astronomical calculations reveal the Solar System's dynamical evolution, including its chaoticity, and represent the backbone of cyclostratigraphy and astrochronology. An absolute, fully calibrated astronomical time scale has hitherto been hampered beyond ~50 million years before the present (Ma) because orbital calculations disagree before that age. Here, we present geologic data and a new astronomical solution (ZB18a) showing exceptional agreement from ~58 to 53 Ma. We provide a new absolute astrochronology up to 58 Ma and a new Paleocene–Eocene boundary age (56.01 ± 0.05 Ma). We show that the Paleocene–Eocene Thermal Maximum (PETM) onset occurred near a 405-thousand-year (kyr) eccentricity maximum, suggesting an orbital trigger. We also provide an independent PETM duration (170 ± 30 kyr) from onset to recovery inflection. Our astronomical solution requires a chaotic resonance transition at ~50 Ma in the Solar System's fundamental frequencies.

Numerical solutions for the Solar System's orbital motion provide Earth's orbital parameters in the past, which are widely used to date geologic records and investigate Earth's paleoclimate (*1*–*11*). The Solar System's chaoticity imposes an apparently firm limit of ~50 million years before the present (Ma) on identifying a unique orbital solution, as small differences in initial conditions and parameters cause astronomical solutions to diverge around that age [Lyapunov time ~5 million years (Myr); supplementary materials] (*4, 6, 12, 13*). Recent evidence for a chaotic resonance transition (change in resonance pattern; see below) in the Cretaceous (Libsack record) (*9*) confirms the Solar System's chaoticity but does not provide constraints to identify a unique astronomical solution. The unconstrained interval between the Libsack record (90 to 83 Ma) and 50 Ma is too large a gap, allowing chaos to drive the solutions apart (supplementary materials). Thus, proper geologic data around 60 to 50 Ma are essential to selecting a specific astronomical solution and, conversely, the astronomical solution is essential to extending the astronomically calibrated time scale beyond 50 Ma.

We analyzed color reflectance data (a^*, red-to-green spectrum) (*7, 8*) at Ocean Drilling Program (ODP) Site 1262 (supplementary materials), a^*-1262 hereafter, a proxy for changes in lithology (*7*). The related Fe-intensity proxy (*8*) gives nearly identical results (fig. S4). We focus on the section at ~170 to 110 m (~58 to 53 Ma), which exhibits an exceptional expression of eccentricity cycles at Site 1262 (*7, 8, 10, 14, 15*), less so in the preceding (older) section. Our focus interval includes the PETM and Eocene Thermal Maximum 2 (ETM2), extreme global warming events (hyperthermals), considered the best paleo-analogs for the climate response to anthropogenic carbon release (*16*–*18*). The PETM's trigger mechanism and duration remain highly debated (*19*–*21*). Thus, in addition to geological and astronomical implications, unraveling the chronology of events in our studied interval is critical for understanding Earth's past and future climate.

We developed a simple floating chronology, attempting to use a minimum number of assumptions (supplementary materials). We initially used a uniform sedimentation rate throughout the section (except for the PETM) and a root mean square deviation (RMSD) optimization routine to derive ages (for final age model and difference from previous work, see supplementary materials). No additional tuning, wiggle-matching, or preexisting age model was applied to the data. Using our floating chronology, the best fit between the filtered and normalized data target a^{**} (Fig. 1) and a given astronomical solution was obtained through minimizing the RMSD between record and solution by shifting a^{**} along the time axis (offset τ) over a time interval of ±200 thousand years (kyr), with ETM2 centered around 54 Ma (supplementary materials). Before applying the minimization, both a^{**} and the solution were demeaned, linearly detrended, and normalized to their respective standard deviation (Fig. 1).

It turned out that one additional step was necessary for a meaningful comparison between a^{**} and astronomical solutions. Relative to all solutions tested here, a^{**} was consistently offset (shifted toward the PETM after optimizing τ) by about one short eccentricity cycle for ages either younger (some solutions) or older than the PETM (other solutions). The consistent offset relative to the PETM suggests that the condensed PETM interval in the data record is the culprit, for which we applied a correction, also obtained through optimization. At Site 1262, the PETM is marked by a ~16-cm clay layer (<1 weight % $CaCO_3$), largely due to dissolution and some erosion across the interval (*16*, *22*), although erosion of Paleocene (pre-PETM) sediment alone cannot account for the offset of about one short eccentricity cycle (supplementary materials). Sedimentation rates were hence nonuniform across the PETM interval (*8, 10, 16*), and primary lithologic cycles from variations in $CaCO_3$ content are not preserved within the clay layer. Thus, we corrected the condensed interval by stretching a total of k grid points across the PETM by Δz for a total length of $\Delta L = k\Delta z$ and included k as a second parameter in our optimization routine (Fig. 1). Essentially, the correction for the reduction (gap) in carbonate sedimentation across the PETM is determined by the entire record except the PETM itself (supplementary materials). In summary, we minimized the RMSD between data target and solution by a stretch-shift operation, i.e., we simultaneously optimized the number of stretched PETM grid points (k) and the overall time shift (τ) between floating chronology and solution.

Our new astronomical solution, ZB18a [computations build on our earlier work (*6, 23, 24*), supplementary materials], agrees exceptionally well with the final a^{**} record (Fig. 1B) and has the lowest RMSD of all 18 solutions published to date that cover the interval (Table 1). The 18 solutions were computed by multiple investigators, representing different solution classes due to initial conditions, parameters, etc. (supplementary text S6 and S7). Based on ZB18a, we provide a new astronomically calibrated age model to 58 Ma (Fig. 1B and supplementary materials) and a revised age for the Paleocene–Eocene boundary (PEB) of 56.01 ± 0.05 Ma (see supplementary materials for errors). Our PEB age differs from previous ages (*8*, *25*–*27*) but is close to approximate estimates from 405-kyr cycle counting across the Paleocene (*28*) (supplementary materials).

Contrary to current thinking (*8, 14, 20, 27, 29*), the PETM onset therefore occurred temporally near, not distant, to a 405-kyr maximum in Earth's orbital eccentricity [Fig. 1, compare also (*10*)]. As for ETM2 and successive early Eocene hyperthermals (*7. 29*, *30*), this suggests an orbital trigger for the PETM, given theoretical grounding and extensive, robust observational evidence for eccentricity controls on Earth's climate (*2*, *7*–*10*, *14*, *20, 26*–*32*). Note, however, that the onset does not necessarily coincide with a 100-kyr eccentricity maximum (see below). Our analysis also provides an independent PETM main phase duration of 170 ± 30 kyr from onset to recovery inflection (for tie points, see fig. S6 and supplementary materials). This duration might be an underestimate given that sedimentation rates increased during the PETM recovery (compacting the recovery would require additional stretching of the main phase). Our duration is significantly longer than 94 kyr (*20*) but agrees

[1]School of Ocean and Earth Science and Technology, University of Hawaii at Manoa, 1000 Pope Road, MSB 629, Honolulu, HI 96822, USA. [2]Department of Earth Sciences, Faculty of Geosciences, Utrecht University, Princetonlaan 8a, 3584 CB Utrecht, Netherlands.
*Corresponding author. Email: zeebe@soest.hawaii.edu

with the ^{3}He age model at Site 1266 (167^{+34}_{-24} kyr) (*21*) and is consistent with >8 cycles in Si/Fe ratios at Zumaia (*31*), which, we suggest, are full (not half) precession cycles.

If high orbital eccentricity (*e*) also contributed to the long PETM duration ($e \approx 0.025$ to 0.044 during PETM), then the potential for prolonged future warming from eccentricity is reduced due to its currently low values ($e \approx 0.0024$ to 0.0167 during next 100 kyr). A similar argument may hold for eccentricity-related PETM trigger mechanisms. The PETM occurred superimposed on a long-term, multimillion year warming trend (*7*, *30*). Our solution ZB18a shows a 405-kyr eccentricity maximum around the PETM but reduced 100-kyr variability (Fig. 1B). Eccentricity in ZB18a remained high before the PETM for one short eccentricity cycle (Fig. 1B, arrow), suggesting that the combination of orbital configuration and background warming (*30*, *32*) forced the Earth system across a threshold, resulting in the PETM. Although similar thresholds may exist in the modern Earth system, the current orbital configuration (lower *e*) and background climate (Quaternary/Holocene) are different from 56 Ma. None of the above, however, will directly mitigate future warming and is therefore no reason to downplay anthropogenic carbon emissions and climate change.

Table 1. RMSD between *a* record and selected astronomical solutions.†**

Solution	RMSD
ZB18a‡§	0.6820
ZB17a	0.9108
ZB17b	1.0358
La10c	0.7431
La10a	0.9854
La11	1.0009
Va03	0.9611

†Record and solution were demeaned, detrended, and normalized to their standard deviation before calculating RMSD. ‡"Z" and "B" derive from Zeebe-HNBody (*6*). §Lowest RMSD of 18 solutions published to date: ZB17a-k (n = 11) (*6*), La10a-d (n = 4) (*33*), La11 (n = 1) (*13*), La04 (n = 1) (*5*), Va03 (n = 1) (*4*) (7/18 listed).

Our astronomical solution ZB18a shows a chaotic resonance transition (change in resonance pattern) (*33*) at ~50 Ma, visualized by wavelet analysis (*34*) of the classical variables:

$$h = e\sin\varpi; p = \sin(I/2)\sin\Omega, \qquad (1)$$

where e, I, ϖ, and Ω are eccentricity, inclination, longitude of perihelion, and longitude of ascending node of Earth's orbit, respectively (Fig. 2). The wavelet spectrum highlights several fundamental frequencies (*g*'s and *s*'s) of the Solar System, corresponding to eigenmodes. For example, g_3 and g_4 are loosely related to the perihelion precession of Earth's and Mars' orbits (s_3 and s_4 correspondingly to the nodes). The *g*'s and *s*'s are constant in quasiperiodic systems but vary over time in chaotic systems (supplementary materials). The period P_{43} associated with $g_4 - g_3$ switches from ~1.5 to ~2.4 Myr in ZB18a ~50 Ma, characteristic of a resonance transition (Fig. 2, arrow) (*33*). An independent analysis of the *a**-1262 record recently also reconstructed $P_{43} \approx 1.5$ Myr (*35*) within the interval ~56 to 54 Ma. However, our individual *g*-values from ZB18a are different from the reconstructed mean values, although within their 2σ error bounds (supplementary materials).

Notably, parameters required for long-term integrations compatible with geologic observations (e.g., ZB18a versus *a***, Fig. 1) appear somewhat incompatible with our best knowledge of the current Solar System. For instance, ZB18a is part of a solution class featuring specific combinations of number of asteroids and solar quadrupole moment (J_2), with J_2 values lower than recent evidence suggests (supplementary materials). In addition, the La10c solution (*33*) with a small RMSD (Table 1) used the INPOP08 ephemeris, considered less accurate than the more recent INPOP10 used for La11 (*13*). However, La10c fits the geologic data better than La11 does [Table 1 and (*27*)].

The resonance transition in ZB18a is an unmistakable manifestation of chaos and is also key to distinguishing between different solutions before ~50 Ma, e.g., using the $g_4 - g_3$ term.

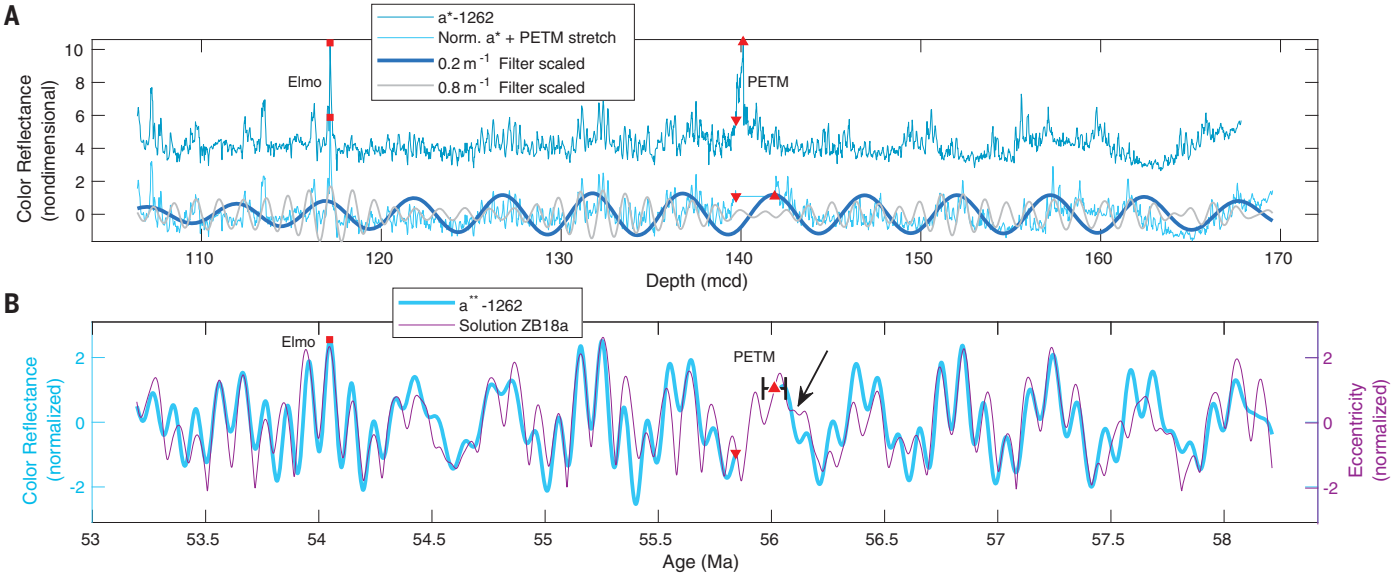

Fig. 1. Data analysis and comparison of color reflectance *a to our astronomical solution ZB18a.** (**A**) *a** at ODP Site 1262 (blue-green), interpolated, demeaned, detrended record (Norm. *a**) including PETM stretch (light-blue); scaled long/short eccentricity cycle filter (blue/gray), PETM onset (up-triangle), PETM recovery inflection (down-triangle), Elmo (square). mcd, meters composite depth. As primary $CaCO_3$ variations within the PETM interval are not preserved due to dissolution and erosion, the interval was cropped. (**B**) Sum of long- and short-cycle filter outputs in the time domain (data target *a***, light blue) and normalized eccentricity of Earth's orbit from our astronomical solution ZB18a (purple). *a*** and ZB18a were demeaned, detrended, and normalized to their respective standard deviation before optimization (RMSD minimization between *a*** and solution by stretch-shift operation, see text). Across the cropped PETM interval, *a*** provides no actual information and is omitted. Up-triangle and error bar indicate our new age for the PEB (PETM onset) of 56.01 ± 0.05 Ma. Arrow indicates the prolonged high-eccentricity period before the PETM (see text).

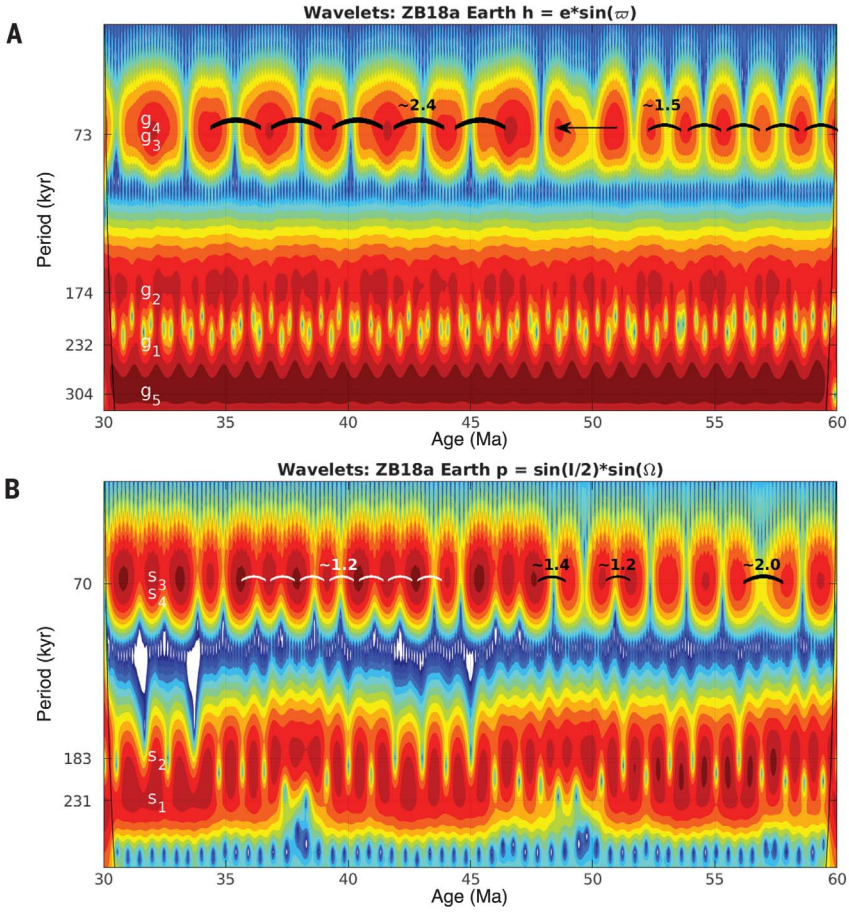

Fig. 2. Wavelet analysis of astronomical solution. Wavelet analysis (*34*) of (**A**) $h = e \sin \varpi$ and (**B**) $p = \sin(I/2) \sin \Omega$ from our astronomical solution ZB18a (see text). *g*'s and s's indicate fundamental frequencies of the Solar System's eigenmodes (multiple frequencies are expressed in the spectrum of a single planet). For example, g_3 and g_4 are loosely related to the perihelion precession of Earth's and Mars' orbits. The wavelet amplitude (red, peaks; blue, valleys) in, e.g., the g_3 and g_4 frequency band is modulated by the period $1/(g_4 - g_3) \approx 2.4$ Myr for ages younger ~45 Ma, where $g_3 \approx 1/74.61$ kyr^{-1} and $g_4 \approx 1/72.33$ kyr^{-1} (*6*). Correspondingly, $1/(s_4 - s_3) \approx 1.2$ Myr. However, in our solution, the period associated with $g_4 - g_3$ switches from ~1.5 Myr to ~2.4 Myr across the resonance transition around 50 Ma (arrow). The ratio $(g_4 - g_3):(s_4 - s_3) \approx 1{:}2$ after ~45 Ma and closer to 1:1 before but appears irregular.

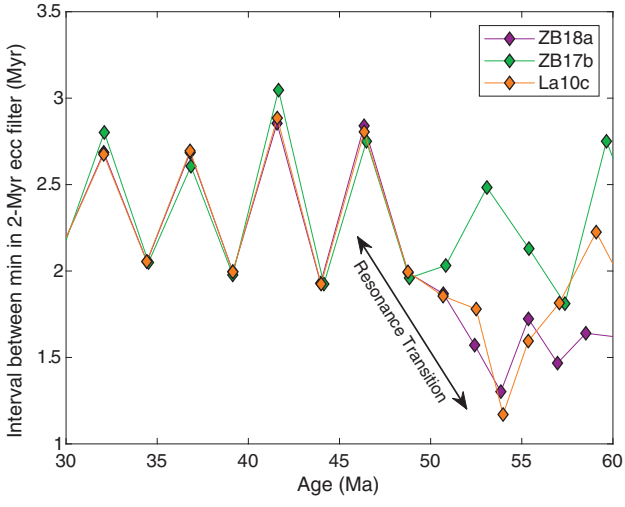

Fig. 3. Resonance transition in selected astronomical solutions. Interval between consecutive minima (Δt_{min}) in 2-Myr Gaussian filter (±60%) of Earth's orbital eccentricity for selected solutions (*6*, *33*). The rise of Δt_{min} around 50 Ma in ZB18a and La10c indicate resonance transitions. However, note distinct pattern of ZB18a before 55 Ma. Hence our solution ZB18a (closest agreement with the data record, Fig. 1) requires that the Solar System underwent a specific chaotic resonance transition pattern between ~60 and 50 Myr BP.

This term modulates the amplitude of eccentricity and, e.g., the interval between consecutive minima in a 2-Myr filter of eccentricity (Fig. 3). Other solutions such as La10c (*33*) also show a resonance transition around 50 Ma. However, the pattern for ZB18a is different before 55 Ma, which is critical for its better fit with the data record from 58 to 53 Ma (smaller RMSD; Table 1 and Fig. 1). For example, $P_{43} \approx 2$ and ~1.6 Myr at ~59 and ~56 Ma in La10c but is rather stable at ~1.5 to 1.6 Myr across this interval in ZB18a. Briefly, to explain the geologic record, our astronomical solution requires that the Solar System is (i) chaotic and (ii) underwent a specific resonance transition pattern between ~60 and 50 Myr BP.

REFERENCES AND NOTES

1. H. Poincaré, *Les Méthodes Nouvelles de la Mécanique Céleste, Vol. 1* (Gauthier-Villars, 1892).
2. M. Milanković, *Kanon der Erdbestrahlung und Seine Anwendung auf das Eiszeitproblem* (Königl. Serb. Akad., 1941).
3. J. D. Hays, J. Imbrie, N. J. Shackleton, *Science* **194**, 1121–1132 (1976).
4. F. Varadi, B. Runnegar, M. Ghil, *Astrophys. J.* **592**, 620–630 (2003).
5. J. Laskar *et al.*, *Astron. Astrophys.* **428**, 261–285 (2004).
6. R. E. Zeebe, *Astron. J.* **154**, 193 (2017).
7. L. J. Lourens *et al.*, *Nature* **435**, 1083–1087 (2005).
8. T. Westerhold *et al.*, *Paleoceanogr. Paleoclimatol.* **22**, 2201 (2007).
9. C. Ma, S. R. Meyers, B. B. Sageman, *Nature* **542**, 468–470 (2017).
10. M. Li, L. R. Kump, L. A. Hinnov, M. E. Mann, *Earth Planet. Sci. Lett.* **501**, 165–179 (2018).
11. C. Spalding, W. W. Fischer, G. Laughlin, *Astrophys. J.* **869**, L17 (2018).
12. A. Morbidelli, *Modern Celestial Mechanics: Aspects of Solar System Dynamics* (Taylor & Francis, 2002).
13. J. Laskar, M. Gastineau, J.-B. Delisle, A. Farrés, A. Fienga, *Astron. Astrophys.* **532**, L4 (2011).
14. S. R. Meyers, *Paleoceanogr. Paleoclimatol.* **30**, 1625–1640 (2015).
15. S. R. Meyers, *Earth Sci. Rev.* **190**, 190–223 (2018).
16. J. C. Zachos *et al.*, *Science* **308**, 1611–1615 (2005).
17. Intergovernmental Panel on Climate Change, T. F. Stocker *et al.*, Eds., *Climate Change 2013: The Physical Science Basis* (Cambridge Univ. Press, 2013).
18. R. E. Zeebe, A. Ridgwell, J. Z. Zachos, *Nat. Geosci.* **9**, 325–329 (2016).
19. F. A. McInerney, S. L. Wing, *Annu. Rev. Earth Planet. Sci.* **39**, 489–516 (2011).
20. U. Röhl, T. Westerhold, T. J. Bralower, J. C. Zachos, *Geochem. Geophys. Geosyst.* **8**, Q12002 (2007).
21. B. H. Murphy, K. A. Farley, J. C. Zachos, *Geochim. Cosmochim. Acta* **74**, 5098–5108 (2010).
22. R. E. Zeebe, J. C. Zachos, *Paleoceanogr. Paleoclimatol.* **22**, PA3201 (2007).
23. R. E. Zeebe, *Astrophys. J.* **798**, 8 (2015a).
24. R. E. Zeebe, *Astrophys. J.* **811**, 9 (2015b).
25. C. Jaramillo *et al.*, *Science* **330**, 957–961 (2010).
26. A. J. Charles *et al.*, *Geochem. Geophys. Geosyst.* **12**, Q0AA17 (2011).
27. T. Westerhold *et al.*, *Clim. Past* **13**, 1129–1152 (2017).
28. F. J. Hilgen, K. F. Kuiper, L. J. Lourens, *Earth Planet. Sci. Lett.* **300**, 139–151 (2010).
29. B. S. Cramer, J. D. Wright, D. V. Kent, M.-P. Aubry, *Paleoceanogr. Paleoclimatol.* **18**, 1097 (2003).
30. J. C. Zachos, H. McCarren, B. Murphy, U. Röhl, T. Westerhold, *Earth Planet. Sci. Lett.* **299**, 242–249 (2010).
31. T. Dunkley Jones *et al.*, *Clim. Past* **14**, 1035–1049 (2018).
32. R. E. Zeebe, T. Westerhold, K. Littler, J. C. Zachos, *Paleoceanogr. Paleoclimatol.* **32**, 440–465 (2017).
33. J. Laskar, A. Fienga, M. Gastineau, H. Manche, *Astron. Astrophys.* **532**, A89 (2011).
34. M. Ghil *et al.*, *Rev. Geophys.* **40**, 3-1–3-41 (2002).

35. S. R. Meyers, A. Malinverno, *Proc. Natl. Acad. Sci. U.S.A.* **115**, 6363–6368 (2018).

ACKNOWLEDGMENTS

Funding: R.E.Z. acknowledges support from the U.S. National Science Foundation (OCE16-58023). This research was supported by the Netherlands Organisation for Scientific Research (NWO-ALW 865.10.001) and by the Netherlands Earth System Science Centre (NESSC 024.002.001) to L.J.L. We are grateful to the International Ocean Discovery Program for drilling and exploring ODP Site 1262.

Author contributions: R.E.Z. and L.J.L. devised the study and wrote the manuscript. L.J.L. was instrumental in guiding the cyclostratigraphic analyses and selecting the a^*-1262 record. R.E.Z. led the numerical integrations for the orbital motion of the Solar System. **Competing interests:** The authors declare no competing interests. **Data and materials availability:** Solutions for Earth's orbital eccentricity and inclination are available at www2.hawaii.edu/~zeebe/Astro.html and www.ncdc.noaa.gov/paleo/study/26970. We provide results from 100 to 0 Ma but caution that the interval 100 to 58 Ma is unconstrained due to chaos.

SUPPLEMENTARY MATERIALS

science.sciencemag.org/content/365/6456/926/suppl/DC1
Materials and Methods
Supplementary Text
Figs. S1 to S8
Tables S1 to S3
References (*36*–*59*)

19 February 2019; accepted 30 July 2019
10.1126/science.aax0612

SIGNAL TRANSDUCTION

Membrane-associated periodic skeleton is a signaling platform for RTK transactivation in neurons

Ruobo Zhou[1,2,3], Boran Han[1,2,3], Chenglong Xia[1,2,3], Xiaowei Zhuang[1,2,3]*

Actin, spectrin, and related molecules form a membrane-associated periodic skeleton (MPS) in neurons. The function of the MPS, however, remains poorly understood. Using super-resolution imaging, we observed that G protein–coupled receptors (GPCRs), cell adhesion molecules (CAMs), receptor tyrosine kinases (RTKs), and related signaling molecules were recruited to the MPS in response to extracellular stimuli, resulting in colocalization of these molecules and RTK transactivation by GPCRs and CAMs, giving rise to extracellular signal–regulated kinase (ERK) signaling. Disruption of the MPS prevented such molecular colocalizations and downstream ERK signaling. ERK signaling in turn caused calpain-dependent MPS degradation, providing a negative feedback that modulates signaling strength. These results reveal an important functional role of the MPS and establish it as a dynamically regulated platform for GPCR- and CAM-mediated RTK signaling.

Signal transduction mediated by cell surface receptors requires precise coordination of a cascade of molecular events. Receptor tyrosine kinases (RTKs) constitute a large class of such cell surface receptors that are expressed across many cell types and perform a broad spectrum of cellular functions, including promotion of cell survival, regulation of cell division and differentiation, and modulation of cellular metabolism and cell-to-cell communication (*1*, *2*). RTKs are activated in response to extracellular signals, initiating a number of intracellular signal transduction cascades to alter gene expression in cells (*1*–*4*). The kinase activity of RTKs can be activated either directly by their cognate ligands or through transactivation by other transmembrane proteins (*1*, *2*, *4*–*7*). Among the RTK transactivators are G protein–coupled receptors (GPCRs), the largest class of cell surface receptors in eukaryotes, and cell adhesion molecules (CAMs), the class of transmembrane proteins responsible for cell-cell interactions (*1*, *4*–*7*). In neurons, RTK transactivation by GPCRs and CAMs, as well as direct activation of RTKs by their cognate ligands, plays important roles in regulating neurite outgrowth and axon guidance, controlling neuronal migration and repair, and modulating synaptogenesis and synaptic transmission (*3*–*8*). However, it is largely unknown how GPCRs, CAMs, RTKs, and related signaling components are spatially organized at the neuronal cell surface and how these molecules are brought together to enable RTK transactivation and downstream signaling.

[1]Howard Hughes Medical Institute, Harvard University, Cambridge, MA 02138, USA. [2]Department of Chemistry and Chemical Biology, Harvard University, Cambridge, MA 02138, USA. [3]Department of Physics, Harvard University, Cambridge, MA 02138, USA.
*Corresponding author. Email: zhuang@chemistry.harvard.edu

Recently, it has been shown that actin, spectrin, and their interacting molecules form a membrane-associated periodic skeleton (MPS) structure in the axons and dendrites of neurons (*9*–*12*). The neuronal MPS contains molecular components homologous to those of the erythrocyte membrane skeleton (*13*), but it adopts a distinct ultrastructure: in neurites, actin filaments are assembled into ring-like structures that are periodically spaced by spectrin tetramers, forming a quasi–one-dimensional lattice structure underneath the plasma membrane with a periodicity of ~190 nm (*9*). This structure is present in distinct types of neurons and across diverse animal species (*14*, *15*). The MPS can organize transmembrane proteins, such as ion channels and adhesion molecules, into periodic distributions along axons (*9*, *11*, *16*–*18*), raising the possibility that this submembrane lattice structure may mediate membrane-associated signal transduction by regulating the distributions of related signaling proteins in space and time.

To test this hypothesis, we applied stochastic optical reconstruction microscopy (STORM) (*19*, *20*), a super-resolution imaging method, to examine the spatial distributions of two transmembrane proteins that are known to transactivate RTKs in neurons (*5*, *7*, *21*, *22*): (i) the cannabinoid type 1 receptor (CB1), the most abundant GPCR in the brain and a therapeutic target for regulating appetite, pain, mood, and memory, and for treating neurodegenerative diseases (*23*); and (ii) the neural cell adhesion molecule 1 (NCAM1), an immunoglobulin superfamily CAM important for neuronal migration, neurite outgrowth and fasciculation, and neural circuit development (*7*). We used two-color STORM to investigate the spatial relationship between the MPS and these membrane proteins in cultured hippocampal neurons (Fig. 1). The MPS was visualized through immunolabeling of the C terminus of βII-spectrin, which is located at the center of each spectrin tetramer connecting adjacent actin rings and is near the binding site for ankyrin, an adaptor protein that can connect transmembrane proteins to the membrane skeleton (*13*, *24*).

Before stimulation with exogenous ligands, CB1 and NCAM1 exhibited a small degree of colocalization with the C terminus of βII-spectrin, i.e., the center of the spectrin tetramer, in axons (Fig. 1, A and C, left). We quantified the degree of colocalization using one-dimensional (1D) cross-correlation analysis by projecting the signals to the longitudinal axis of the axon and calculating the average 1D cross-correlation function between the two color channels over many axon segments. The 1D cross-correlation amplitude, defined as the average amplitude of the peaks at ±190 nm (the period of the MPS), quantifies not only the colocalization between the signaling molecules and the MPS but also the degree of periodicity of these signaling molecules (Fig. 1, B and D, blue). The observed average cross-correlation amplitudes were >10-fold greater than the values derived from single-color–labeled neurons, indicating that the observed colocalization was not the result of cross-talk between the two color channels (fig. S1). Upon treatment with ligands, a CB1 agonist WIN 55,212-2 (hereafter, WIN; inhibition constant K_i = 62 nM) (*23*) or a NCAM1 antibody (NCAM1 Ab) that binds to the extracellular domain to mimic homophilic or heterophilic binding of NCAM (*7*), CB1 or NCAM1, respectively, displayed a substantially higher degree of colocalization with the MPS (Fig. 1, A and C, middle) with a three- to fourfold increase in the cross-correlation amplitudes (Fig. 1, B and D, red), and a significant reduction in the average distance between CB1 or NCAM1 and their nearest-neighbor spectrin tetramer centers (fig. S2). Quantitatively similar ligand-induced increase in colocalization between CB1 or NCAM1 and the MPS was observed using different cell-fixation protocols (fig. S3). Such colocalization was abolished by treatment with the actin depolymerizing drugs latrunculin A (LatA) and cytochalasin D (CytoD) (Fig. 1, A and C, right; B and D, yellow), which is known to disrupt the MPS structure (*10*, *12*). Together, these results indicate ligand-induced recruitment of CB1 and NCAM1 to the MPS. Coimmunoprecipitation experiments also showed increased interaction of CB1 and NCAM1 with the MPS upon ligand treatment (fig. S4), further supporting this notion.

Next, we tested whether the recruitment of CB1 and NCAM1 to the MPS is important for the downstream signaling. It has been shown that, upon ligand binding, both CB1 and NCAM1 can activate the Raf-MEK-ERK signaling cascade through RTK transactivation in neurons (Fig. 2A) (*7*, *22*). We thus measured the level of phosphorylated (activated) ERK (pERK) using an immunofluorescence assay (*25*) to quantify the signaling strength. Upon treatment with either the CB1 agonist WIN or the NCAM1 Ab, we observed a transient increase in pERK signal in neurons,

followed by a decay to basal levels (Fig. 2, B and C, blue), consistent with previous reports (*22*, *26*). Similar ERK activation was observed regardless of whether the analysis was done for axons only or for all neurites (fig. S5). Pretreating the neurons with the CB1-specific antagonist SR141716 (SR; K_i = 2 nM), which has little activity on CB2 (*27*–*29*), abolished the observed WIN-induced pERK signal increase in neurons (Fig. 2C, green), as well as the WIN-induced increase in CB1 and MPS colocalization (Fig. 1B, green).

Disruption of the MPS structure by the LatA/CytoD treatment completely abolished the transient, ligand-induced ERK activation (Fig. 2C, yellow). Similar results were obtained by βII-spectrin knockdown (Fig. 2, C, red, and D), which is also known to disrupt the MPS structure (*10*, *12*). The cell-surface expression levels of CB1 and NCAM1 did not decrease in βII-spectrin knockdown neurons (fig. S6), excluding the possibility that the knockdown effect on ERK activation was the result of a decrease in the surface expression of CB1 or NCAM1. Similar βII-spectrin–dependent, ligand-induced ERK activation was also observed using Western blot analysis (fig. S7). Together, these results suggest that the MPS plays an important role in enabling the CB1- and NCAM1-mediated ERK signaling.

Next, we investigated mechanistically how CB1- or NCAM1-mediated ERK signaling is facilitated by the MPS. To this end, we first examined which step along the signaling pathway is affected by MPS disruption. Both CB1- and NCAM1-mediated RTK transactivations activate protein kinase C (PKC), which in turn activates the ERK cascade in neurons (Fig. 2A) (*5*, *7*, *22*). We added PDBu, a direct PKC activator, to neurons and measured the resulting pERK signal. The PDBu-induced increase in pERK signal was not diminished by βII-spectrin knockdown (fig. S8A), indicating that the MPS did not act directly on the Raf-MEK-ERK cascade downstream of PKC. Previous studies (*5*, *7*, *21*, *22*) have suggested that CB1 and NCAM1 can transactivate two RTK types in neurons, tropomyosin receptor kinase B (TrkB) and fibroblast growth factor receptors (FGFRs). Indeed, the addition of TrkB and FGFR inhibitors, and likewise the knockdown of TrkB and FGFR1, strongly suppressed the increase in pERK signal induced by WIN or NCAM1 Ab (fig. S8, B and C). These results indicate that the ERK signaling in neurons induced by CB1 and NCAM1 ligands was primarily through transactivation of the two RTKs, TrkB and FGFR. To test whether MPS facilitates CB1- and NCAM1-mediated transactivation of these two RTKs or events downstream of TrkB and FGFR activation, we examined whether MPS disruption inhibits the TrkB and FGFR activation induced directly by their own cognate ligands, brain-derived neurotrophic factor (BDNF) for TrkB and basic fibroblast growth factor (bFGF) for FGFR. The pERK signal increase induced by BDNF or bFGF remained quantitatively similar in βII-spectrin knockdown neurons as compared with wild type neurons (fig. S8, D and E), suggesting that the MPS does not act downstream of these RTKs but likely affects their transactivation by CB1 and NCAM1. Supporting this notion, using Western blot analysis, we observed activation (phosphorylation) of TrkB and FGFR upon addition of the CB1 ligand WIN, as well as activation of FGFR by the NCAM1 Ab treatment, both in a βII-spectrin–dependent manner (Fig. 2, E and F).

Next, we used STORM to examine the spatial relationship of the two RTKs, TrkB and FGFR1, to the MPS, as well as to the RTK transactivators

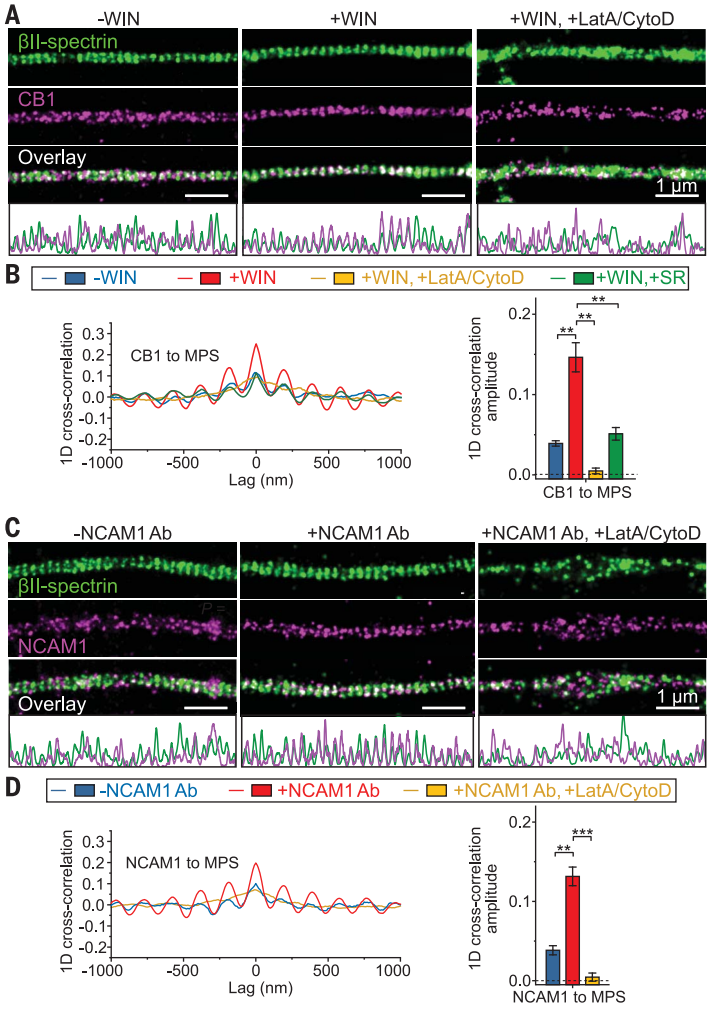

Fig. 1. CB1 and NCAM1 are recruited to the MPS upon cognate ligand binding. (**A**) Two-color STORM images of βII-spectrin (green) and CB1 (magenta) in the axons of untreated neurons (left, "−WIN"), neurons treated with the CB1 agonist WIN (middle, "+WIN"), and neurons pretreated with LatA and CytoD to disrupt the MPS before addition of WIN (right, "+WIN, +LatA/CytoD"). 1D projection traces of βII-spectrin (green) and CB1 (magenta) signals along the axon are shown at the bottom. βII-spectrin was visualized by immunostaining with an antibody against the C terminus of βII-spectrin. CB1 was visualized by immunostaining with CB1 antibody. (**B**) Left: Average 1D cross-correlation functions between the distributions of CB1 and βII-spectrin from many CB1-positive axon segments for the three conditions described in (A), as well as for neurons pretreated with the CB1 antagonist SR before addition of WIN ("+WIN, +SR"). Right: Average 1D cross-correlation amplitudes, defined as the difference between the average of the peaks at ±190 nm and the average of the valleys at ±95 nm and ±285 nm of the average 1D cross-correlation functions. $^{**}P < 0.01$; actual P values (from left to right): 4.4×10^{-3}, 1.6×10^{-3}, and 8.7×10^{-3} (unpaired Student's t test). (**C** and **D**) Same as (A) and (B), but for neurons treated with NCAM1 antibody (NCAM1 Ab) instead of WIN. Neurons were preincubated with NCAM1 Ab at 4°C to allow antibody binding in both "−NCAM1 Ab" and "+NCAM1 Ab" conditions. NCAM1 Ab treatment ("+NCAM1 Ab") was achieved by a temperature increase to stimulate signaling (see supplementary materials and methods), whereas the temperature increase step was skipped in the "−NCAM1 Ab" condition to prevent signaling, as previously described (*26*). NCAM1 was visualized through immunostaining with the NCAM1 antibody. $^{**}P < 0.01$, $^{***}P < 0.001$; actual P values (from left to right): 2.1×10^{-3} and 5.8×10^{-4} (unpaired Student's t test). Data in bar graphs are mean ± SEM (n = 3 biological replicates; 100 to 200 axonal regions were examined per condition). Scale bars: 1 μm.

CB1 and NCAM1. Upon addition of WIN, both RTKs displayed a substantial increase in colocalization with the MPS, which was reflected by a three- to fivefold increase in 1D cross-correlation amplitudes, and disruption of the MPS by LatA/CytoD treatment abolished these colocalizations (Fig. 3A). Co-imaging of CB1 with TrkB or FGFR1 showed little colocalization between these molecules before addition of WIN, whereas the amplitude and periodicity of the 1D cross-correlation functions increased dramatically after WIN addition (Fig. 3B), suggesting ligand-induced colocalizations between CB1 and the two RTKs. MPS disruption by LatA/CytoD treatment or βII-spectrin knockdown completely eliminated this ligand-induced colocalization (Fig. 3B). One potential caveat of this 1D analysis is that the increase in the 1D cross-correlation may only be a reflection of the recruitment of both CB1 and RTKs to the MPS, and it may not necessarily indicate an enhanced spatial proximity between CB1 and RTKs themselves. Thus, we performed 2D cross-correlation analysis between CB1 and the two RTKs (fig. S9A), as well as nearest-neighbor distance analysis between these molecules (fig. S9B), to further probe their colocalization. Both analyses showed that WIN treatment enhanced proximity between CB1 and the two RTKs in an MPS-dependent manner. Similarly, NCAM1 Ab treatment also induced colocalization between NCAM1 and FGFR1 in an MPS-dependent manner (fig. S10). As further support, coimmunoprecipitation experiments showed that the interaction between CB1 and the two RTKs greatly increased upon WIN treatment, and likewise the interaction between NCAM1 and FGFR greatly increased upon NCAM1 Ab treatment, both in an MPS-dependent manner (fig. S11).

We further examined the spatial distributions of Src-family tyrosine kinases, which are known as important mediators of RTK transactivation by GPCRs and CAMs (Fig. 2A) (*4*–*7*, *30*). As expected, preincubation with PP2, a specific Src-family kinase inhibitor, abolished the increase in pERK signal induced by CB1 and NCAM1 ligands in neurons (fig. S12). Notably, Src, a known mediator for GPCR-mediated RTK transactivation (*4*, *6*), also became substantially more colocalized with the MPS upon WIN treatment, and this colocalization was abolished by MPS disruption (Fig. 3C). To test whether this recruitment of Src to the MPS depends on Src activity, we generated three Src mutants with different levels of kinase activities (Src^{Act}, Src^{SH2eng}, and $Src^{SH2\text{-}3eng}$) by introducing mutations that promote the open (active) or closed (inactive) conformation of Src (Fig. 3D) (*31*). The degree of colocalization between the MPS and these Src mutants scaled with their kinase activity in the absence of WIN, and the effect of WIN treatment on the Src-MPS colocalization was substantially reduced for the constitutively active

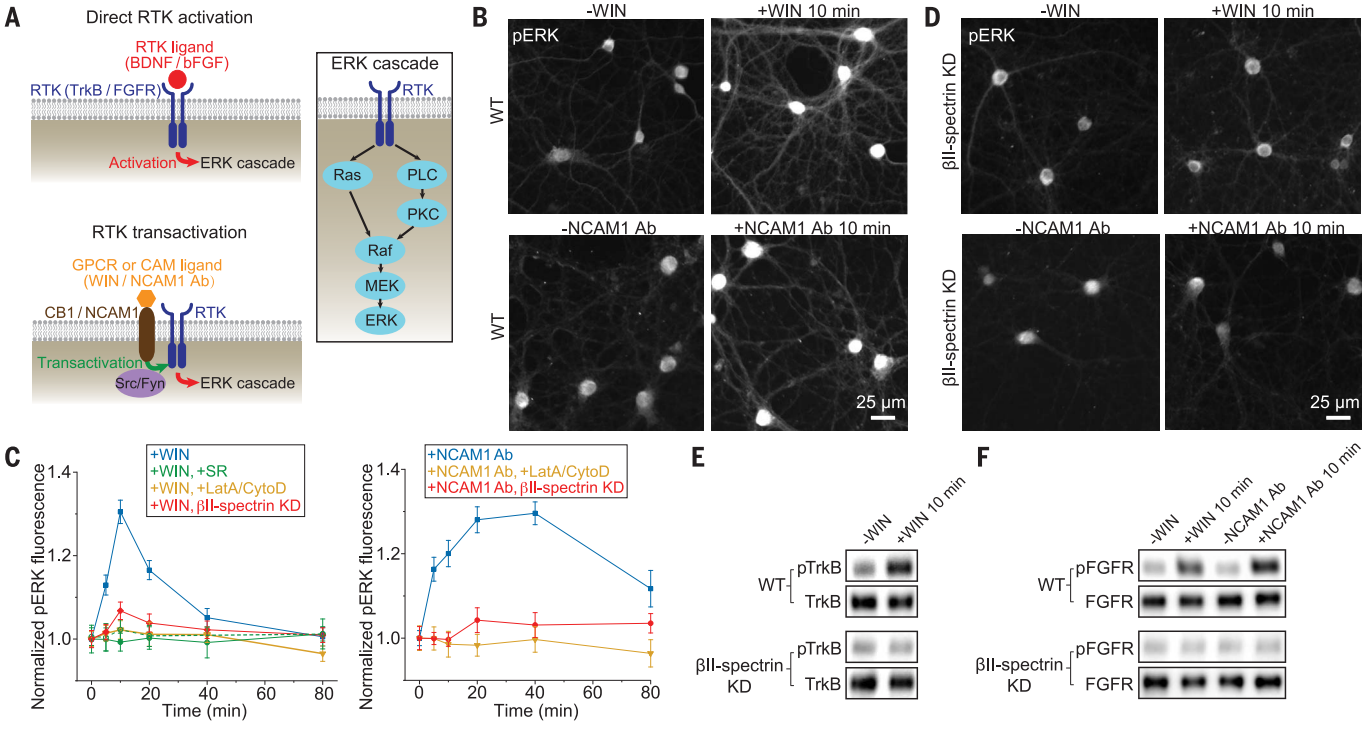

Fig. 2. MPS disruption abolishes RTK transactivation and downstream ERK signaling. (**A**) Left: Diagrams showing direct RTK activation (top) and RTK transactivation (bottom). RTK can be either activated directly by binding of their cognate ligands or transactivated by other transmembrane proteins, such as CB1 (upon binding of CB1 ligand) and NCAM1 (upon binding of NCAM1 Ab). Right: Diagram showing the ERK signaling cascade downstream of RTK. PLC, phospholipase C; MEK, mitogen-activated protein kinase kinase. (**B**) Top: Immunofluorescence images of pERK in wild-type (WT) untreated neurons (left) and WT neurons treated with WIN for 10 min (right). WIN treatment was initiated by addition of WIN at 37°C. Bottom: Same as top, but for treatment with NCAM1 Ab. Neurons were preincubated with NCAM1 Ab at 4°C to allow antibody binding in both "−NCAM1 Ab" and "+NCAM1 Ab" conditions, and NCAM1 Ab treatment ("+NCAM1 Ab") was then initiated by a temperature increase to 37°C, whereas this temperature increase step was eliminated in the "−NCAM1 Ab" condition to prevent signaling. Scale bar: 25 μm. (**C**) Time courses of ERK activation upon WIN addition (left) or upon NCAM1 Ab treatment (right) for WT neurons (blue), WT neurons pretreated with the CB1 antagonist SR (green, closed symbols: 1 μM SR; green, open symbols: 100 nM SR), WT neurons pretreated with LatA and CytoD (yellow), and βII-spectrin knockdown (KD) neurons (red). βII-spectrin KD was induced by adenovirus expressing βII-spectrin shRNA (fig. S6A). Data are mean ± SEM (n = 3 biological replicates; 20 to 30 imaged regions were examined per condition). (**D**) Same as (B), but for βII-spectrin KD neurons instead of WT neurons. (**E**) Western blot analysis for phosphorylated (activated) TrkB (pTrkB) and total TrkB in whole-cell lysates from WT neurons (top) and βII-spectrin KD neurons (bottom) before and 10 min after WIN treatment. (**F**) Western blot analysis for phosphorylated (activated) FGFR (pFGFR) and total FGFR in whole-cell lysates from WT neurons (top) and βII-spectrin KD neurons (bottom) before and 10 min after the initiation of WIN or NCAM1 Ab treatment. Western blots are representative examples from two independent biological replicates.

mutant Src^{Act}, exhibiting only a 48% (instead of a three to fourfold) increase in 1D cross-correlation amplitude, and the WIN-induced increase was completely abolished for the two inactive Src mutants (Src^{SH2eng} and Src$^{SH2-3eng}$) (Fig. 3D and fig. S13). Likewise, Fyn, the Src-family kinase mediating NCAM1-induced RTK transactivation (*30*), also exhibited enhanced colocalization with the MPS upon NCAM1 Ab treatment (fig. S14).

The above results suggest that the MPS acts as a signaling platform that brings CB1, NCAM1, RTKs, and Src-family kinases into proximity to enable RTK transactivation by CB1 and NCAM1. Next, we investigated whether RTK transactivation and the downstream ERK signaling in turn have any effect on the MPS. After WIN or NCAM1 Ab treatment, the MPS was degraded gradually over time (Fig. 4, A and B, and fig. S15, A and B). Preincubation with the CB1-antagonist SR blocked the WIN-induced MPS degradation (Fig. 4, A and C). Preincubation with U0126, an inhibitor (median inhibitory concentration IC_{50} = 60 to 70 nM) of MEK, the kinase upstream of ERK (Fig. 2A), also protected the MPS from degradation (Fig. 4, A and C, and fig. S15, A and C), indicating that the MPS degradation was a result of the ERK signaling. Brain spectrin is the substrate of the calpain protease (*32*) and RTK-induced ERK signaling activates calpain-2 (*33*), raising the possibility that the observed MPS degradation may result from cleavage by calpain. Indeed, we found that inhibiting calpain activity with an inhibitor MDL-28170 (MDL; K_i = 8 nM) or short hairpin RNA (shRNA) against calpain-2 prevented signaling-induced MPS degradation (Fig. 4, A and C, and fig. S15, A and C). With calpain or MEK activities inhibited and hence the MPS retained, the ligand-induced colocalization between signaling molecules and the MPS was also maintained (fig. S16). These results indicate that CB1- and NCAM1-mediated RTK transactivation turns on an ERK-dependent calpain pathway that degrades the MPS. This degradation was reversible: the MPS structure reassembled within a few hours after ligand removal (fig. S17).

Because the MPS structure brings RTKs, RTK transactivators, and Src-family kinases into proximity to facilitate RTK transactivation, we envisioned that the MPS degradation could provide a negative feedback to reduce the strength of ERK signaling induced by RTK transactivation. Indeed, preventing MPS degradation by the calpain inhibitor MDL or calpain-2 knockdown increased ERK signaling induced by both WIN and NCAM1 Ab (Fig. 4, D and E, and fig. S15, D and E), supporting the existence of such a negative feedback loop.

Ligand binding could also induce receptor endocytosis, a process known to positively or

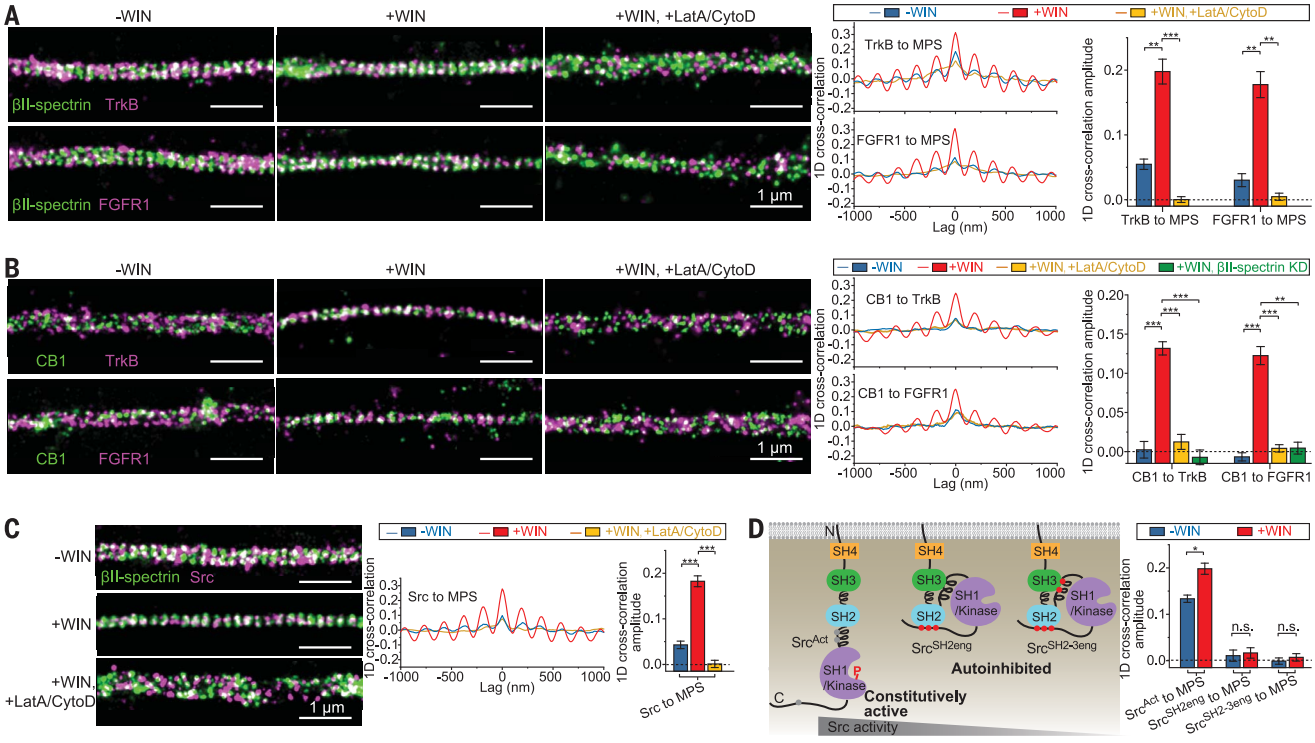

Fig. 3. The MPS functions as a signaling platform that brings RTKs, RTK transactivators, and Src kinases into proximity. (**A**) Left panels: Two-color STORM images of βII-spectrin (green) and TrkB (magenta) (top panels) and of βII-spectrin (green) and FGFR1 (magenta) (bottom panels) in CB1-positive axons of untreated neurons (left, "−WIN"), neurons treated with WIN (middle, "+WIN"), and neurons pretreated with LatA and CytoD before WIN addition (right, "+WIN, +LatA/CytoD"). Right panels: Average 1D cross-correlation functions and 1D cross-correlation amplitudes between the distribution of βII-spectrin and the distributions of RTKs (TrkB or FGFR1) from many CB1-positive axons for the three conditions. $^{**}P < 0.01$, $^{***}P < 0.001$; actual *P* values (from left to right): 2.3×10^{-3}, 5.6×10^{-4}, 2.8×10^{-3}, and 1.2×10^{-3} (unpaired Student's *t* test). (**B**) Similar to (A), but for co-imaging of CB1 instead of βII-spectrin, with the two RTKs. The results for the +WIN condition in βII-spectrin KD neurons are additionally shown in green (+WIN, βII-spectrin KD). $^{**}P < 0.01$, $^{***}P < 0.001$; actual *P* values (from left to right): 6.7×10^{-4}, 7.3×10^{-4}, 3.8×10^{-4}, 5.2×10^{-4}, 6.8×10^{-4}, and 1.0×10^{-3} (unpaired Student's *t* test). (**C**) Similar to (A), but for co-imaging of Src with βII-spectrin. $^{***}P < 0.001$; actual *P* values (from left to right): 6.4×10^{-4}, 2.2×10^{-4} (unpaired Student's *t* test). (**D**) Left: Diagram showing the intramolecular domain organizations of the three Src variants. Src^{Act} is a constitutively active mutant, and gray dots in Src^{Act} indicate the sites modified to disrupt the auto-inhibiting intramolecular domain interactions. Src^{SH2eng} and Src$^{SH2-3eng}$ are inactive mutants, and red dots in these mutants indicate the sites modified to facilitate the auto-inhibiting intramolecular domain interactions. The red "P" represents the major phosphorylation site of activated Src. Right: Average 1D cross-correlation amplitudes between the distributions of βII-spectrin and the three Src mutants. $^{*}P < 0.1$; n.s., not significant ($P > 0.1$); actual *P* values (from left to right): 1.1×10^{-2}, 0.74, and 0.49 (unpaired Student's *t* test). Data in bar graphs are mean ± SEM ($n = 3$ biological replicates; 100 to 200 axonal regions were examined per condition). βII-spectrin and CB1 were visualized as described in Fig. 1; TrkB, FGFR1, and Src variants were visualized by moderate expression of GFP-tagged TrkB, FGFR1, or Src variants through low-titer lentiviral transfection and detection through GFP antibody. Scale bars: 1 μm.

negatively regulate various signaling pathways (*34*, *35*). In addition to providing a platform for recruiting signaling molecules, could the MPS influence the endocytosis of these molecules, which in turn also impacts ERK signaling? To examine whether the MPS affects CB1 endocytosis, we examined how the rate of ligand-induced CB1 endocytosis changed under two MPS perturbation conditions: (i) βII-spectrin knockdown, which disrupts the MPS, and (ii) MDL treatment, which protects the MPS from signaling-induced degradation. βII-spectrin knockdown led to a substantial increase in WIN-induced CB1 endocytosis, whereas MDL treatment inhibited WIN-induced CB1 endocytosis (fig. S18), indicating that the MPS structure can repress endocytosis.

To estimate how much this effect of MPS on CB1 endocytosis would contribute to the observed negative feedback on signaling, we examined the ERK signaling in clathrin heavy chain (CHC) knockdown neurons, as CB1 endocytosis is known to occur in a clathrin-dependent manner in neurons (*36*). Although CHC knockdown inhibited CB1 endocytosis at least as strongly as MDL treatment did (fig. S18), it did not have an appreciable effect on ERK signaling induced by WIN (fig. S19), suggesting that the enhancement in ERK signaling observed under calpain inhibition (Fig. 4E) was not primarily the result of inhibition of endocytosis. Hence, for CB1-mediated RTK transactivation, the negative feedback caused by the signaling-induced MPS degradation was likely a direct effect of the loss of the structural platform for signaling-molecule recruitment. Whether the same is true for NCAM1-mediated RTK transactivation remains to be investigated.

Taken together, our results suggest that the MPS serves as a structural platform for bringing signaling molecules, including GPCRs, CAMs, RTKs, and Src-family kinases, into proximity to enable GPCR- and CAM-mediated transactivation of RTKs and the downstream ERK signaling (Fig. 4F). These signaling molecules were recruited to sites near the center of the spectrin tetramer, where the adaptor protein ankyrin binds. Both spectrin and ankyrin are large scaffolding proteins containing multiple domains, which could provide multiple binding sites for signaling molecules and bring them into proximity to form signaling complexes. It has been shown that GPCR-signaling components, CAMs, and the Src kinase can interact with specific molecular domains of spectrin or ankyrin (*13*, *37*, *38*). It is also possible that some of these signaling molecules are first recruited to the MPS to increase their local concentration, which in turn facilitates the recruitment of other signaling molecules through multivalent interactions. In support of this view, optogenetically induced self-oligomerization of the SH2 domain, a common protein domain in many signaling molecules, including Src and Fyn kinases, has been shown to facilitate complex formation between RTKs and SH2, thereby activating RTKs (*39*). Our results raise the interesting possibility that MPS may facilitate

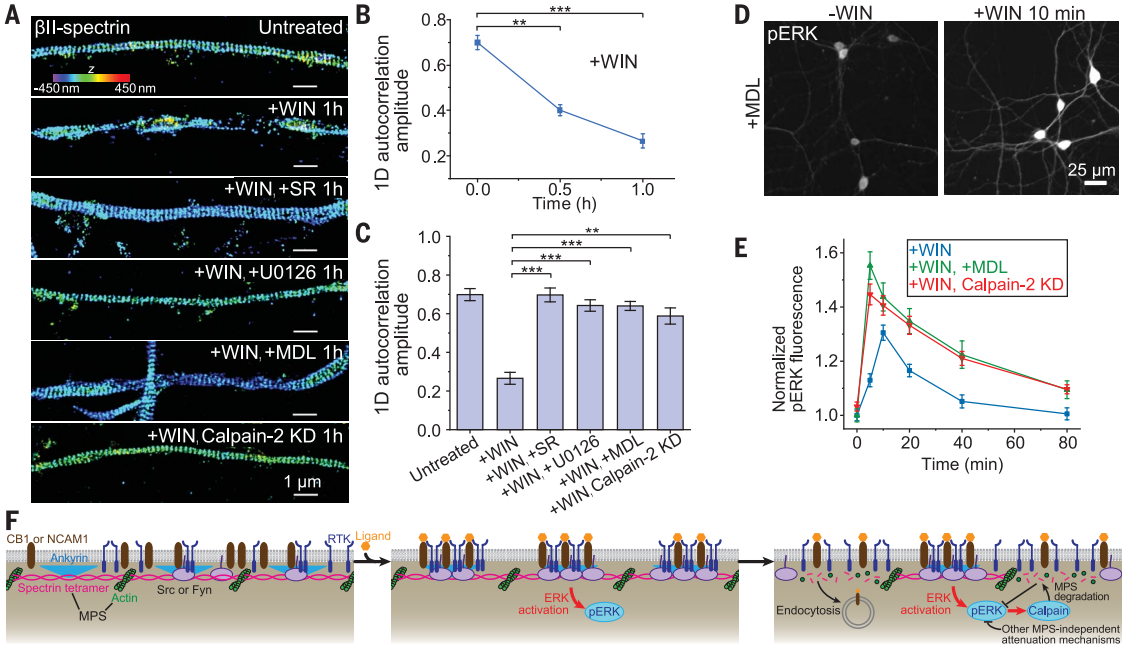

Fig. 4. ERK signaling causes disassembly of the MPS structure, providing a negative feedback for signaling. (**A**) 3D STORM images of βII-spectrin in CB1-positive axons of untreated neurons, neurons treated with WIN for 1 hour in the absence and presence of SR (a CB1 antagonist), U0126 (a MEK inhibitor), MDL (a pan-calpain inhibitor), and calpain-2 KD neurons treated with WIN for 1 hour. Calpain-2 KD was induced by adenovirus expressing calpain-2 shRNA (fig. S15A). Scale bars: 1 μm. Colored scale bar indicates the *z*-coordinate information. (**B**) Average 1D auto-correlation amplitude of the βII-spectrin distribution, indicating the degree of the periodicity in the MPS, calculated from many axon segments at different time points after addition of WIN. $^{**}P < 0.01$, $^{***}P < 0.001$; actual *P* values (from left to right): 1.6×10^{-3} and 5.9×10^{-4} (unpaired Student's *t* test). (**C**) Average 1D auto-correlation amplitudes for the six conditions described in (A). $^{**}P < 0.01$, $^{***}P < 0.001$; actual *P* values (from left to right): 8.0×10^{-4}, 9.2×10^{-4}, 6.3×10^{-4}, and 3.5×10^{-3} (unpaired Student's *t* test). Data in (B) and (C) are mean ± SEM ($n = 3$ biological replicates; 50 to 100 axonal regions were examined per condition). (**D**) Immunofluorescence images of pERK in neurons pretreated with MDL, before (left) and after (right) WIN treatment. Scale bar: 25 μm. (**E**) Time courses of ERK activation upon addition of WIN for control neurons (blue), neurons pretreated with MDL (green), and calpain-2 KD neurons (red). The curve for control neurons is reproduced from Fig. 2C. Data are mean ± SEM ($n = 3$ biological replicates; 20 to 30 imaged regions were examined per condition). (**F**) Schematic showing the MPS functioning as a dynamically regulated platform to recruit signaling molecules and enable RTK transactivation. Upon ligand binding to RTK transactivators (CB1 and NCAM1), these transactivators, RTKs (TrkB and FGFR), and related Src-family tyrosine kinases (Src and Fyn) are recruited to the MPS and brought into proximity of each other, enabling RTK transactivation and downstream ERK signaling. ERK activation in turn induces MPS degradation in a calpain-dependent manner, providing a negative feedback loop to attenuate the strength of ERK signaling. MPS degradation also leads to an increase in receptor endocytosis. Because the ligand-induced increase in the pERK signal was followed by a decay under both control conditions and conditions where the MPS degradation was inhibited by inhibiting calpain activity (Fig. 4E and fig. S15E), other MPS-independent attenuation mechanisms may contribute to the observed pERK signal decay.

multivalent-interaction–mediated phase separation of signaling molecules. Our observations of the recruitment of signaling molecules to the MPS upon ligand stimulation suggest a critical role of the MPS in signaling. Indeed, disruption of the MPS abolished ligand-induced RTK transactivation by CB1 or NCAM1 and the downstream ERK signaling. Furthermore, we demonstrated that the ERK signaling induced reversible MPS degradation in a calpain-protease–dependent manner, which in turn caused an attenuation of signaling strength, providing a negative feedback loop (Fig. 4F). In addition, we observed that MPS can regulate endocytosis, potentially providing another mechanism for signaling regulation. Overall, our results demonstrate that the MPS functions as a dynamically regulated structural platform for GPCR- and CAM-mediated RTK transactivation and signaling, providing a mechanism for regulating signal transduction in neurons.

REFERENCES AND NOTES

1. A. Gschwind, O. M. Fischer, A. Ullrich, *Nat. Rev. Cancer* **4**, 361–370 (2004).
2. M. A. Lemmon, J. Schlessinger, *Cell* **141**, 1117–1134 (2010).
3. V. Latham, R. H. Singer, *Handbook of Cell Signaling* **3**, 293–297 (2003).
4. F. Cattaneo *et al*., *Int. J. Mol. Sci.* **15**, 19700–19728 (2014).
5. P. Doherty, F. S. Walsh, *Mol. Cell. Neurosci.* **8**, 99–111 (1996).
6. L. M. Luttrell, Y. Daaka, R. J. Lefkowitz, *Curr. Opin. Cell Biol.* **11**, 177–183 (1999).
7. D. K. Ditlevsen, G. K. Povlsen, V. Berezin, E. Bock, *J. Neurosci. Res.* **86**, 727–743 (2008).
8. K. Shen, C. W. Cowan, *Cold Spring Harb. Perspect. Biol.* **2**, a001842 (2010).
9. K. Xu, G. Zhong, X. Zhuang, *Science* **339**, 452–456 (2013).
10. G. Zhong *et al*., *eLife* **3**, e04581 (2014).
11. E. D'Este, D. Kamin, F. Göttfert, A. El-Hady, S. W. Hell, *Cell Rep.* **10**, 1246–1251 (2015).
12. B. Han, R. Zhou, C. Xia, X. Zhuang, *Proc. Natl. Acad. Sci. U.S.A.* **114**, E6678–E6685 (2017).
13. V. Bennett, D. N. Lorenzo, *Curr. Top. Membr.* **77**, 143–184 (2016).
14. E. D'Este *et al*., *Sci. Rep.* **6**, 22741 (2016).
15. J. He *et al*., *Proc. Natl. Acad. Sci. U.S.A.* **113**, 6029–6034 (2016).
16. D. Albrecht *et al*., *J. Cell Biol.* **215**, 37–46 (2016).
17. E. D'Este, D. Kamin, F. Balzarotti, S. W. Hell, *Proc. Natl. Acad. Sci. U.S.A.* **114**, E191–E199 (2017).
18. M. Hauser *et al*., *Cell Rep.* **24**, 1512–1522 (2018).
19. M. J. Rust, M. Bates, X. Zhuang, *Nat. Methods* **3**, 793–795 (2006).
20. B. Huang, W. Wang, M. Bates, X. Zhuang, *Science* **319**, 810–813 (2008).
21. P. Berghuis *et al*., *Proc. Natl. Acad. Sci. U.S.A.* **102**, 19115–19120 (2005).
22. O. Asimaki, G. Leondaritis, G. Lois, N. Sakellaridis, D. Mangoura, *J. Neurochem.* **116**, 866–873 (2011).
23. A. C. Howlett *et al*., *Pharmacol. Rev.* **54**, 161–202 (2002).
24. C. Y. Huang, M. N. Rasband, *Ann. N. Y. Acad. Sci.* **1420**, 46–61 (2018).
25. G. Krapivinsky *et al*., *Neuron* **40**, 775–784 (2003).
26. H. Son, J. Seuk Kim, J. Mogg Kim, S. H. Lee, Y. S. Lee, *Biochem. Biophys. Res. Commun.* **298**, 262–268 (2002).
27. S. Hu, W. S. Sheng, R. B. Rock, *PLOS ONE* **8**, e77577 (2013).
28. R. H. Robinson *et al*., *J. Neuroimmune Pharmacol.* **8**, 1239–1250 (2013).
29. M. Rinaldi-Carmona *et al*., *FEBS Lett.* **350**, 240–244 (1994).
30. P. F. Maness, M. Schachner, *Nat. Neurosci.* **10**, 19–26 (2007).
31. R. Krishnamurty *et al*., *Nat. Chem. Biol.* **9**, 43–50 (2013).
32. F. H. Kobeissy *et al*., *Mol. Neurobiol.* **52**, 696–709 (2015).
33. S. Zadran *et al*., *J. Neurosci.* **30**, 1086–1095 (2010).
34. P. P. Di Fiore, P. De Camilli, *Cell* **106**, 1–4 (2001).
35. A. Sorkin, M. von Zastrow, *Nat. Rev. Mol. Cell Biol.* **10**, 609–622 (2009).
36. A. A. Coutts *et al*., *J. Neurosci.* **21**, 2425–2433 (2001).
37. D. S. Wang, R. Shaw, J. C. Winkelmann, G. Shaw, *Biochem. Biophys. Res. Commun.* **203**, 29–35 (1994).
38. J. H. Nedrelow, C. D. Cianci, J. S. Morrow, *J. Biol. Chem.* **278**, 7735–7741 (2003).
39. L. J. Bugaj *et al*., *Nat. Commun.* **6**, 6898 (2015).

ACKNOWLEDGMENTS

We thank H. Babcock and Y. Fu for helping with two-color STORM imaging setup construction and data analysis, K. Xu for providing the software for processing the two-color STORM imaging data, and M. Rasband for providing the adenoviruses expressing shRNA against βII-spectrin. **Funding:** This work is supported in part by the National Institutes of Health. R.Z. is an HHMI Fellow of the Life Sciences Research Foundation. X.Z. is a Howard Hughes Medical Institute investigator. **Competing interests:** The authors declare no competing interests. **Author contributions:** R.Z. and X.Z. designed the experiments. R.Z. and C.X. performed the experiments. R.Z. and B.H. performed data analysis. R.Z. and X.Z. wrote the manuscript with input from B.H. and C.X. **Data and materials availability:** All data are available in the manuscript or supplementary materials.

SUPPLEMENTARY MATERIALS

science.sciencemag.org/content/365/6456/929/suppl/DC1
Materials and Methods
Figs. S1 to S19
References (*40*–*48*)

8 January 2019; accepted 2 August 2019
10.1126/science.aaw5937

Hybrid Microscopes

Despite sharing many optical components, conventional microscopes have always existed in two basic configurations: upright or inverted. While most labs have to purchase two separate microscopes for viewing different samples, Echo has developed the world's first hybrid microscope that can be flipped to perform in either configuration. Users can quickly tailor their microscope to suit their specific needs and will appreciate the intuitive touchscreen. Touchscreen functions drive cameras and illumination, replacing manual turrets and levers. No more clicking is needed—just tap to count or draw lines to measure. Traditional eyepieces have been replaced with iPad Pro tablets to provide easier viewing and crystal-clear images through their Liquid Retina display. Restore settings from previously captured images to accurately reproduce experiments. Share findings in seconds with Dropbox, AirDrop, USB, and other iOS file-sharing options.

Echo
For info: 858-429-9565
discover-echo.com

EV Isolation System for Serum and Plasma

System Biosciences offers the SmartSEC HT EV Isolation System for Serum & Plasma, the first kit on the market that enables extracellular vesicle (EV) isolation in a 96-well plate-based format. With SmartSEC HT, you get high yields of highly pure EVs needed for biomarker discovery, diagnostic development, therapeutic development, and more. SmartSEC HT combines all the benefits of size-exclusion chromatography (SEC)—purity, yield, reproducibility, and preservation of EV integrity—with a contaminant-trapping feature that overcomes the limitations of conventional SEC for a fast, easy, EV isolation workflow. Each SmartSEC HT kit comes with optimized amounts of SmartSEC resin already aliquoted into a 96-well filter plate, SmartSEC Isolation Buffer, and two collection plates. Each well of the filter plate can be loaded with 250 µL–500 µL of serum or plasma, and if desired, unused wells can be preserved for future use. The entire system is compatible with standard manual and automated liquid-handling systems.

System Biosciences
For info: 888-266-5066
www.systembio.com

Soft X-Ray Light Source

The 642-1 Soft X-Ray (SXR) light source from McPherson features a six-position anode carousel. Users can easily change anode target materials without breaking vacuum. Using different anode materials allows for tuning of the emitted electronvolt energy. The vacuum housing of the source features standard NW40K vacuum flanges (optionally DN40CF). It also features two equivalent output beams, which enable sample/reference comparison and device calibration. The new source is easy to set up and provides a reliable emission-line source and a means for at-wavelength calibration, or metrology of SXR lithography materials, multilayers, or grazing-incidence optical systems for astrophysics and other fundamental research.

McPherson
For info: 800-255-1055
www.mcphersoninc.com

Infectious Disease Reagents

The Native Antigen Company is one of the world's leading suppliers of reagents that enable research into vaccine development and diagnostics for emerging and endemic infectious diseases. It specializes in the development and manufacture of native and recombinant viral and bacterial antigens, antibodies, and immunoassays, alongside bespoke product development and custom manufacturing using its proprietary mammalian cell expression system. The Native Antigen Company's team has decades of experience in the isolation and purification of native antigens and high-yield mammalian cell expression systems, ensuring conformity to native type. Its high-quality reagents have been widely adopted by leading pharmaceutical companies, in vitro diagnostic assay manufacturers, and academic groups involved in cutting-edge vaccine research and serology, where correct folding and glycosylation are vital.

The Native Antigen Company
For info: +44-(0)-1865-595230
thenativeantigencompany.com

Targeted Protein Degradation for Drug Discovery

AMS Biotechnology has introduced a new range of homogeneous proximity assays, critical enzymes, and small-molecule inhibitors to assess the chemical adaptor function of proteolysis targeting chimeras (PROTACs). Targeted protein degradation using PROTACs is a promising new therapeutic method in drug discovery. PROTACs can regulate protein degradation through targeted control of ubiquitin E3 ligases. The PROTAC method offers many advantages compared to traditional protein inhibition, which requires sustained protein binding to evoke the intended biological reaction. This can be problematic in the incidence of target overexpression, the presence of competing ligands, or protein mutations that lead to binding resistance. PROTACs bypass these issues by promoting degradation that circumvents the native resistance of proteins against sustained inhibition. Even select weak-binding and promiscuous ligands can be used with PROTACs and still demonstrate high degradation efficacy. Also, ineffectual ligands that do not modulate the cellular functions of the protein of interest can mediate degradation through PROTACs. Whether the ligand is a strong inhibitor, a weak binder, promiscuous, or ineffectual, PROTACs offer the ability to degrade proteins previously believed to be "undruggable" through conventional small-molecule inhibition.

AMS Biotechnology
For info: 617-945-5033
www.amsbio.com

Mass Spectrometer

The Thermo Fisher Scientific Orbitrap Exploris 480 mass spectrometer is a quadrupole-Orbitrap mass spectrometer based on the hardware and instrument-control software designs of the next-generation Thermo Scientific mass spectrometers. Built on the guiding principles of ease-of-use and hardware reliability, its robust system performance boosts sample throughput. Soundness of data is assured with high-resolution accurate-mass (HRAM) selectivity, high scan speed and best-in-class mass spectral quality, all within a compact footprint to conserve bench space. Simplified operation, smart scheduling, and execution of user-selected scan types deliver rich, high-confidence sample insights for users of all skill levels in a wide range of applications, from small molecules to peptides and intact proteins.

Thermo Fisher Scientific
For info: 866-984-3766
www.thermofisher.com

Electronically submit your new product description or product literature information! Go to www.sciencemag.org/about/new-products-section for more information.

Newly offered instrumentation, apparatus, and laboratory materials of interest to researchers in all disciplines in academic, industrial, and governmental organizations are featured in this space. Emphasis is given to purpose, chief characteristics, and availability of products and materials. Endorsement by *Science* or AAAS of any products or materials mentioned is not implied. Additional information may be obtained from the manufacturer or supplier.

Community science: Not just a hobby

Community science groups have an inclusive, open-door ethos that makes them a natural place to learn informally about scientific careers. Members explore, create, and problem-solve as they work together on do-it-yourself projects in conservation, synthetic biology, and more. If you join a community science lab, don't expect a straightforward path to a job. But do expect to meet potential mentors and advisors, make local connections, and gain skills to support your professional development. **By Chris Tachibana**

Michal Galdzicki started doing community science nearly 10 years ago, while getting a Ph.D. in bioinformatics and bioengineering from the University of Washington (UW). The community science movement is still evolving, he says, so even members don't know if they should call it citizen science, DIY for "do it yourself," or something else. Participants may identify as artisans, hackers, or makers, but all celebrate hands-on, open, accessible science. Projects can be about engineering, environmental conservation, art, food, and more—often covering multiple topics at once. For example, Galdzicki originated a DIY-genotyping project for tracking the origin of salmon from markets and restaurants.

Galdzicki now has the title "Data Czar," in charge of integrating information at the Seattle protein-design company Arzeda. He says he constantly applies expertise from his community science work. Especially in a startup company, resourcefulness, low-cost creativity, and on-the-spot problem-solving are essential. Community science projects can develop those capabilities. For him, he says, "DIY actually means 'figure it out yourself.'"

Kevin Chen also benefited from cofounding the community science group Bricobio in 2013 in Montreal. In 2014, he launched the company Hyasynth, which uses engineered microbes to generate cannabis-derived medicines. Bricobio helped with connections, he says, bringing the right people with the right interests together to start the company.

Chen, Galdzicki, and others emphasize that community science is not about career advancement. Its primary goals, Chen says, are around democratization, "breaking down walls to increase access to science and get the public engaged with its tools." Still, being part of the community science world can provide professionally useful skills and connections.

A global mission—with networking opportunities

Community science projects cover a broad spectrum, ranging from collecting weather data with home sensors to culturing microbes to produce milk proteins. Synthetic biology is a common theme, Chen explains, because the history of community science includes sharing BioBricks, which are units of DNA sequences for engineering microbes. Teams for the International Genetically Engineered Machine (iGEM) Foundation Jamboree, held annually since 2003 at the Massachusetts Institute of Technology (MIT) in Cambridge, develop projects for the event using a standard BioBrick kit. Companies including Hyasynth, Ginko Bioworks, and SynBioBeta count "iGEMers" among their founders and employees.

The diversity of people and interests in community science is highlighted by the hundreds of participants at the Global Community Bio Summit at the MIT Media Lab. Activities, Chen says, include productive discussions, useful breakout sections, and global collaborations.

David Kong directs the MIT Community Biotechnology Initiative and founded the Global Community Bio Summit. He describes his work as "helping crystallize global networks around community science." The goal of the Bio Summit, he says, is to move science from individual labs to a collective intelligence that advances it in a coordinated, decentralized fashion.

cont.>

PHOTO: ASGER NØRREGÅRD RASMUSSEN

Upcoming features

Faculty: Moving Your Lab to Another Country—September 13 ■ Neuroscience: Alzheimer's—October 4 ■ Top Employers Survey—October 25

POSTDOC AND YOUNG INVESTIGATOR OPPORTUNITIES

SÃO PAULO
Brazil

The São Paulo Research Foundation (FAPESP), one of the leading Brazilian agencies dedicated to the support of research, has ongoing programs and support mechanisms to bring researchers from abroad to excellence centers in São Paulo.

MORE INFORMATION

YOUNG INVESTIGATOR AWARDS
www.fapesp.br/yia

POSTDOC
www.fapesp.br/en/postdoc

FAPESP
SÃO PAULO
RESEARCH FOUNDATION

WWW.FAPESP.BR/EN

ScienceCareers online @sciencecareers.org
POSTDOCTORAL OPPORTUNITIES

Akiko Otani

Bio Summit attendees meet people who share this broader scientific objective. They can also connect with people in decision-making positions. In 2018, Bio Summit donors and sponsors included the global corporations Scientist.com, MilliporeSigma, and Takeda. **Akiko Otani,** Takeda's director of public–private partnerships, was one of several participants from the pharmaceutical company.

Otani stresses that Takeda's primary goal in sending representatives to the Bio Summit was not recruiting or scouting for employees. Instead, she says, "It was an opportunity to connect with and support people around the world who are doing science in their own communities." Projects such as teaching science to children in India using paper microscopes showed "young scientists doing impressive, innovative things with limited resources." Otani was impressed at the innovation and practical skills demonstrated by attendees that went beyond their academic achievements. She noted that the Bio Summit highlighted a diversity of thoughts, ideas, and people—a perspective that she brought back to Takeda by having Kong present to her team about the community bioscience philosophy.

The spaces where it happens

Global summits are energizing, but the real work of DIY scientists happens in community labs. At first glance, these spaces can resemble traditional academic, government, and for-profit facilities. Seattle's SoundBio Lab, for instance, has incubators, centrifuges, and a pipetting robot. Lab members, however, range from high school students to retirees. Members may be artists incorporating science in their work, programmers contributing computer skills, parents introducing their kids to technology, or entrepreneurs piloting startup ideas.

Like most community labs, SoundBio is governed by a volunteer board. It's funded by donors and a low-cost membership fee. The SoundBio mission is educational, but some community labs are more like incubator spaces for startups, says cofounder **Zach Mueller.** SoundBio literally started "with people sitting around on lawn chairs in Zach's garage," cofounder Galdzicki says. Moving to lab space near UW meant that he, Mueller, cofounder Regina Wu, and early SoundBio members did all the work of creating their nonprofit organization, including paperwork, fundraising, and building lab benches.

Other learning experiences that can result from community science include mentoring, teaching, and collaborating with people with diverse backgrounds and interests. Networking is not a goal of SoundBio but can happen automatically. Many of those working at the lab have local connections: Wu works at Fred Hutchinson Cancer Research Center and Mueller at Amazon, while Yoshi Goto, director of operations and lab manager, has interned at Arzeda.

When Galdzicki started doing community science, his graduate school advisors were **John Gennari,** in UW's Biomedical Informatics and Medical Education department, and **Herbert Sauro,** in UW's Department of Bioengineering. Both supported this outside activity, even for an early-career researcher who had a thesis to complete. Gennari says that his department is interdisciplinary, with projects that include studying patient communications via social media and presenting science to laypeople. Community science aligns with that work and is a way to acquire and practice science communication skills. For that reason, some students and postdocs find that community science complements their research and grounds it in the real world. In addition, Gennari says, "research is intense" and any external activities help "clear your mind."

Community science is also a public-outreach opportunity. Sauro notes that some funding agencies, such as the U.S. National Science Foundation, require outreach activities. By working with the public on projects, scientists learn to explain and justify their research to laypeople. The activity also educates the general population about science, Sauro says. Many science outreach and communication programs are geared toward kids, so he appreciates that community labs include adults. "They vote and pay taxes that pay our salaries," he says, "so they should also be part of science outreach."

Chen says that currently, about half the participants in Montreal's Bricobio are academic scientists. For them, Bricobio is an inspiring, friendly space to build their skills and share their knowledge, he explains. As someone who now hires for his company, Chen observes that community science experience on a CV is noteworthy and demonstrates an ability to think beyond academic science. Others in hiring positions at universities and companies also say they notice citizen science or maker projects, or participation in community science or iGEM, but do not prioritize applications with these activities.

Nonetheless, to some, community science experience demonstrates creativity, genuine interest in the field, and job-related competence, especially for participants who initiate projects or develop them from scratch. Gennari and Sauro said they would look favorably at community science membership that was mentioned in an application from a graduate student, postdoc, or even faculty member. Gennari said he would consider it an indication of organizational and communication skills. Both he and Sauro emphasize, however, that not everyone would agree.

Making and marketing

Somewhat related to community science are maker organizations. These groups often focus on creating tangible items, such as furniture or musical instruments, but the community science and maker movements aren't separated by a clear line. Take **Laura Penman's** work with Copenhagen Maker in Denmark. As part of completing her Master's degree in digital manufacturing at London Metropolitan University, Penman self-built a 3D printer based on open-source designs from ceramicist Jonathan Keep. The printer creates items using organic material, such as coffee grounds, inoculated with fungal spores. The fungi grow into a networked mycelium that can be treated to create a solid, biodegradable material.

When Penman moved to Denmark, she got involved in the maker community—not to find a job, but to meet people. "As a byproduct," she says, "I found people who helped my professional development by pushing me to try out ideas." For example, through the community, Penman met a professor at

cont.>

PHOTO: TAKEDA PHARMACEUTICALS

DISCOVER THE FUTURE

a leading position at SciLifeLab

To further strengthen our research environment and complement research areas already present at SciLifeLab, we are now looking to recruit an outstanding young group leader to a new SciLifeLab Fellows position.

The fellow will become an associate at the SciLifeLab research center, as well as contract a position at Stockholm University.

SciLifeLab Fellows position / Assistant Professor in Neurochemistry

Focused on molecular techniques to visualize and manipulate activity in the nervous system.

Read more at: www.scilifelab.se/fellows.

Application deadline: September 10, 2019.

About SciLifeLab

As a national hub for molecular biosciences in Sweden, SciLifeLab (Science for Life Laboratory) facilitates cutting-edge, multi-disciplinary life science research and promotes its translation to the benefit of society. The center focuses on both health and environmental research and is jointly operated by its four founder universities: KTH Royal Institute of Technology, Karolinska Institutet, Stockholm University, and Uppsala University. About 200 research groups, 1500 researchers and 40 national infrastructure facilities are associated with SciLifeLab.

Featured participants

Arzeda
www.arzeda.com

Bricobio
www.brico.bio

Copenhagen Maker
www.copenhagenmaker.com

Hyasynth
hyasynthbio.com

International Genetically Engineered Machine Competition
igem.org

MIT Media Lab
www.media.mit.edu

SoundBio
sound.bio

Takeda
www.takeda.com

University of Washington
www.washington.edu

the IT University of Copenhagen Digital Design Department who provided her with informal advice and mentoring for her maker project and her career.

Penman now works for 3Shape, which makes 3D scanners and software. Getting the job did not involve maker connections, though. One day, Penman bicycled past the company's building, noticed the name, and then checked the company's employment page. Penman says the 3D printing project was an asset that helped her CV stand out, though. Reflecting on these experiences, she says the career benefits of community science or maker participation are "hard to predict, but can be huge as long as you're not expecting a direct link to a job."

Even now, as an engineer for a 3D company, Penman still participates in Copenhagen Maker. Her motivations align with those of Galdzicki and Chen, whose day jobs and community lab work use related competencies. The difference, the three say, is that community science allows for more creativity. The work is driven by member and community interests rather than company directives and has few constraints beyond the usual need for time and funding.

Copenhagen Maker has a professionalization side, though, says **Stine Broen Christensen,** leader of the Copenhagen Maker Festival. A goal of the nonprofit organization is making technology accessible to the public through education, urban development, and democracy initiatives. Another is showcasing small businesses that originated as community science or maker projects. As an example of a science-based small business that uses the Copenhagen Maker Festival to interact with the public and promote its product, Broen Christensen names PlatoScience. Started by a neuroscientist and a product designer, the company makes personal neurostimulation headsets to increase focus and productivity.

Copenhagen Maker also runs Underbroen, a space for startups and small- and medium-sized enterprises "to go from maker to market," Christensen says. The space brings entrepreneurs together and encourages them to share knowledge, resources such as 3D printing and milling equipment, and skills such as programming and graphic design.

Occasionally life- and career-changing

Participants in community science, maker spaces, and events like the Global Bio Summit or iGEM emphasize that these activities do not lead directly to a job. Sometimes, though, joining the community can be career changing. **Japheth Kelly** was a computer science student at Ashesi University in Accra, Ghana, when he saw a poster in the library about iGEM.

"[Community science is about] … breaking down walls to increase access to science and get the public engaged with its tools."
– Kevin Chen (lower left corner)

The iGEM Jamboree brings thousands of participants to MIT, including teams from community labs such as SoundBio, which sends a group of high school students. Kelly's team members were from his university. Not only were they the first iGEM team from the West African region, he says, "we were all engineers with no biology background." Recruited and led by faculty member Elena Rosca, the team quickly got trained in synthetic biology methods and developed their project to use engineered bacteria to reduce the toxicity of gold mining in Ghana. The team won a silver medal for their work and the Chairman's Award for iGEM spirit and values.

For Kelly, the project led to a job growing the scientific and synthetic biology community in his region. He is now an iGEM Ambassador and travels around Africa, raising awareness about iGEM with young scientists and industry and academic leaders who could support them. The job requires researching a country's education policies, pitching to funders, and aligning university and company interests with solutions that a synthetic biology team can provide.

Kelly's career plans are to work in industry, get more education, and return to Ghana to teach. He says his iGEM work, which was reported extensively in the media, has been recognized by employers. He adds that the challenges of the experience were actually opportunities. Lack of funding seemed like a disadvantage, "but I learned skills from presenting and giving pitches to investors," he says. "I learned to tell a story that can get us help with our projects." His team dealt with equipment that had to go abroad to get repaired and customs agencies that didn't understand materials sent to them for synthetic biology. Overcoming these barriers gave his team problem-solving experience that they now present to employers as a valuable skill.

Now, when Kelly talks to students about getting involved with science at a grassroots level, he tells them, "You need heart and determination to get through the hard, long nights in the lab when you often get results you weren't expecting, but you'll get help from a network that will bring other opportunities to your door. If I, Japheth Kelly, a nonbiologist, can do it, I say you definitely can, too."

PHOTO: COURTESY OF KEVIN CHEN

Chris Tachibana is a freelance writer who specializes in life sciences.

SESYNC Request for Proposal: 2020 Postdoctoral Fellowship Program

Applications due November 8, 2019

The National Socio-Environmental Synthesis Center (SESYNC) invites applications from early-career scholars (≤ 4 years post Ph.D.) for two-year postdoctoral fellowships that begin **June 1, 2020**. Primarily funded by the National Science Foundation, SESYNC is an international leader in supporting interdisciplinary socio-environmental synthesis research. We support a vigorous postdoctoral program that currently includes ~15 postdoctoral fellows undertaking original socio-environmental (S-E) synthesis research.

Position Summary: Fellows are in residence at SESYNC full time at our Center in Annapolis, Maryland. Each works with a Collaborating Mentor of their choosing that extends the fellow's current network of collaborators; the mentor may be affiliated with any organization or institution. Successful candidates will use *synthesis methods* to address a problem arising from, or associated with, the relationship between humans and nature. Priority will be given to projects that have the potential to advance understanding of socio-environmental systems. SESYNC encourages applications from candidates who will take advantage of ecological, social or geoscience data sets (e.g., geospatial, hyperspectral, etc.), ongoing experiments, or modeling results. The fellowship provides a competitive salary and travel funds to interact with a mentor and attend conferences. Besides undertaking a synthesis research project, postdoctoral fellows will take part in SESYNC's Socio-Environmental Immersion Program. Unique among environmental postdoctoral programs, a learning component of the program will immerse fellows in theory foundational to understanding socio-environmental systems and prepare them to conduct interdisciplinary and actionable research.

Step by step application details for the program, requirements, and deadlines can be found at **http://sesync.us/postdoc2020**. **Applications are due November 8th**. Please contact us at postdoc.application@sesync.org with questions.

Cleveland Clinic Lerner Research Institute

Postdoctoral Fellowships Available

The Lerner Research Institute is home to basic, translational and clinical research at Cleveland Clinic, ranked one of the nation's top hospitals by *U.S. News and World Report*. With over $140M in federal grants and an annual research budget of over $270M, the Lerner is consistently ranked among the top research institutes in the nation. Postdoctoral fellows routinely obtain grant funding and first-author publications in top-tier journals.

Postdoctoral Job Opportunities:
http://www.lerner.ccf.org/jobs/postdoctoral/
For further information email: RETC@ccf.org

The Lerner Experience

- Opportunity to train among world-class scientists and physician-scientists in a top-ranked healthcare institution
- Multidisciplinary, disease-focused research programs
- 180 principal investigators across 10 departments with over 700,000 square feet of research space
- Competitive salary and benefits package
- Active Postdoctoral Association and 250+ postdocs
- Career development opportunities and support through the Research Education and Trailing Center

City of Cleveland

Cleveland is a multicultural city with nationally acclaimed museums, sports, restaurants, and music and arts programs. Situated on Lake Erie, the area offers stunning views, beaches, and water sports. Low cost of living, with below average traffic and commute times for major cities.

Apply to the Janssen Post-Doc Program!

The Janssen Post-Doc (PD) program offers early career chemical, bioengineering, and biological scientists a best-in-class experience learning and working with world-class drug developers to:

- Address challenging scientific questions
- Broaden your network
- Publish novel research in high-impact journals

Learn more about Post-Doctoral careers, visit us at: **www.careers.jnj.com**

janssen | PHARMACEUTICAL COMPANIES OF Johnson & Johnson

CRTP
CARDIOVASCULAR RESEARCH TRAINING PROGRAM

HEALTH SCIENCES

Postdoctoral Fellowship in Cardiovascular Research

A postdoctoral fellow position is available in the Cardiovascular Research Training Program (CRTP) at the University of New Mexico (UNM) Health Sciences Center (HSC; https://hsc.unm.edu/), funded by a T32 grant from NIH/NHLBI. The goal of the CRTP is to provide exceptional pre- and post-doctoral trainees a broad, multidisciplinary background in cardiovascular and pulmonary research with integration between basic and clinical sciences. This research program provides a rich academic training environment, including the resources, technical approaches, communication skills, and professional interactions that will aid the trainee becoming an independent investigator in cardiovascular research.

The program currently includes 22 faculty mentors at the School of Medicine and College of Pharmacy with research programs in vascular biology, cardiovascular toxicology and development, cell signaling, and clinical and translational research. Specific research interests include systemic and pulmonary hypertension, atherosclerosis, angiogenesis, oxidant signaling, metabolic and mitochondrial dysfunction, ion channels and intracellular calcium dynamics, endothelial biology, air pollutants and vascular injury, ischemic brain injury, adaptive immunity, estrogen receptor signaling, stem cell biology, drug discovery, and sleep apnea.

The University of New Mexico, founded in 1889, is located in the heart of Albuquerque, a metropolitan area of more than 500,000 people situated in the historic Rio Grande River Valley at the base of the majestic Sandia Mountains. Albuquerque is one of the most culturally diverse cities in the country, reflected in its unique architecture, art, and cuisine (https://www.visitalbuquerque.org/). The city's high altitude climate, abundant sunshine, and surrounding mountainous terrain provide many opportunities for outdoor activities, including skiing, golfing, hiking, fishing, and mountain biking.

Minimum requirements: PhD, MD, or equivalent. Applications are restricted to U.S. citizens or permanent residents.

Preferred qualifications: Research experience in cardiovascular physiology, pharmacology or toxicology; strong publication record; excellent communication and laboratory skills.

The CRTP T32 provides an NIH level stipend, and allowances for tuition and fees, health insurance, training-related expenses, and travel to scientific meetings. *Individuals from under-represented minority groups are strongly encouraged to apply.*

Applications must include a letter of interest, CV, and names and email addresses of three references. Direct correspondence to Dr. Thomas C. Resta, **tresta@salud.unm.edu**.

Thomas C. Resta, PhD, FAHA, FAPS, Professor, Dept. of Cell Biology and Physiology, Director, Cardiovascular Research Training Program, University of New Mexico Health Sciences Center, Albuquerque, NM 87131-0001; Phone: 505-272-8822; Email: tresta@salud.unm.edu; Home page: https://vivo.health.unm.edu/display/n524

SCHOOL OF MEDICINE
CASE WESTERN RESERVE UNIVERSITY

Postdoctoral Scholar - Department of Biochemistry

Postdoctoral Position in the Unfolded Protein

Response and Circadian Clock Biology

The laboratory of Dr. J. Alan Diehl in the Department of Biochemistry at the Case Western Reserve University School of Medicine (CWRU) has postdoctoral positions available to investigate stress and nutrient mediated stress sensing by the Unfolded Protein Response during tumor development and progression. Specific points of inquiry include but are not limited to the regulation of non-coding RNAs and the Circadian Clock biology.

The Department of Biochemistry has a highly interactive environment with state-of-the-art facilities and outstanding core laboratories. Excellent stipends and benefits packages are available.

Interested candidates should send a Cover Letter, current CV, and names and contact information for 3 references to: J. Alan Diehl, Chair Department of Biochemistry (**jad283@case.edu**)

The National Academies of
SCIENCES • ENGINEERING • MEDICINE

FORD FOUNDATION FELLOWSHIPS

For Achieving Excellence in College and University Teaching

Through its program of Fellowships, the Ford Foundation seeks to increase the diversity of the nation's college and university faculties by increasing their ethnic and racial diversity, to maximize the educational benefits of diversity, and to increase the number of professors who can and will use diversity as a resource for enriching the education of all students.

The Ford Foundation Fellowship Programs offer approximately 70 predoctoral, 36 dissertation, and 24 postdoctoral awards.

	2020 APPLICATION DEADLINE DATES	Stipend
Predoctoral:	December 17, 2019	$24,000
Dissertation:	December 10, 2019	$25,000
Postdoctoral:	December 10, 2019	$45,000

For more information and to apply online:
www.nas.edu/ford
FordApplications@nas.edu
202-334-2872

SCHOOL OF MEDICINE CENTER FOR NEUROIMAGING

Post-Doctoral Fellow in Brain Imaging Genomics of Alzheimer's Disease

The Brain Imaging Genomics Laboratory of the Indiana University Center for Neuroimaging (CfN) and the Neuroimaging Core of the NIA-funded Indiana Alzheimer Disease Center (IADC), directed by Dr. Andrew Saykin, has openings for outstanding, highly motivated post-doctoral researchers with special interest in the areas of genomics/computational systems biology, cognitive neuroscience, and human brain imaging, to play a major role in state-of-the-science integrative studies of early stage Alzheimer's disease (AD) and related disorders.

Special opportunities afforded by this fellowship include experience working directly with the Genetics Core of the NIA-funded Alzheimer's Disease Neuroimaging Initiative and the IADC, as well as with the IU Network Science Institute (IUNI), which is conducting pioneering integrative studies of systems biology, the human connectome, and networks of AD. The CfN, IADC, and IUNI are highly collaborative transdisciplinary environments with internationally known investigators in Medical Neuroscience, Medical and Molecular Genetics, Computer Science and Bioinformatics.

Applicants should hold a PhD, MD or MD/PhD in bioinformatics, computational genetics, systems biology, neuroscience, or a related discipline, and have high motivation and enthusiasm for research and excellent written and oral communication skills. Preference is given to candidates with experience in one or more of the following areas: medical and molecular genomics, computational systems biology, network analysis, and multimodal MRI and PET neuroimaging.

To apply, please email a cover letter with a brief description of research experience, interests and goals, full CV, and three reference letters to Brad Glazier, Program Administrator (**bsglazie@iu.edu**).

Stony Brook University

Multiple Postdoctoral Positions Fall/Winter 2019

Stony Brook University is recruiting for multiple postdoctoral positions in various sub-specialties, for the upcoming fall and winter months.

Stony Brook has been characterized by innovation, energy and progress, and making ground-breaking discoveries since its beginning half a century ago.

Any interested candidates are invited to visit our JOBS page.

www.stonybrook.edu/postdocjobs

Stony Brook University/SUNY is an equal opportunity, affirmative action employer.

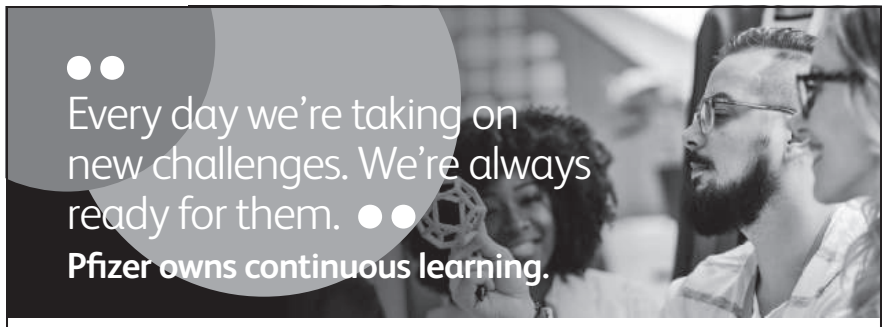

Pfizer Worldwide Research and Development Postdoctoral Program

At Pfizer, postdocs are trained to become successful, independent investigators, capable of formulating and addressing important scientific hypotheses. In addition, trainees receive broad exposure to the process of drug discovery, from idea to clinical trials. Areas of scientific focus include cardiovascular and metabolic diseases, comparative medicine, drug safety, biotherapeutics/protein engineering, inflammation and immunology, medicinal chemistry, oncology, pharmacology, vaccines, and clinical, computational, and genomic sciences.

We recruit highly motivated Ph.D. recipients with an outstanding track record of scientific productivity and a passion for ground-breaking, fast-paced research that facilitates the development of innovative therapies for human diseases. Our program promotes dissemination of research results through publications and participation in scientific meetings, provides opportunities for collaboration with leading academic labs and industry consortia, and offers exceptional professional development training and networking opportunities.

To explore our program and research, visit us online at:
www.pfizer.com/careers/en/postdoctoral-program

pfizercareers.com

Pfizer OWNIT!

EGL Charitable Foundation

The EGL Charitable Foundation invites you to apply to the

Gruss Lipper Post-Doctoral Fellowship Program

Eligibility

- Israeli citizenship
- Candidates must have completed PhD and/or MD/PhD degrees in the Biomedical Sciences at an accredited Israeli University/Medical School or be in their final year of study
- Candidates must have been awarded a postdoctoral position in the U.S. host research institution.

Details regarding the fellowship are available at www.eglcf.org

Application Deadline is September 29, 2019

NIH National Institute of Neurological Disorders and Stroke

Postdoctoral Position – Section on Circuits, Synapses and Molecular Signaling

The Intramural Research Program (IRP) at the National Institutes of Health is the largest biomedical research institute on earth. A combination of world-class investigators, unparalleled facilities, and a unique funding environment provides a rich training environment for postdoctoral fellows.

Position Description: Postdoctoral positions are available in the laboratories of Dr. Lorna Role, Dr. Simon Halegoua, National Institute of Neurological Disorders and Stroke (NINDS), and Dr. David Talmage, National Institute of Mental Health (NIMH) in Bethesda MD. The Role and Talmage laboratories use a wide array of approaches to understand the contribution of cholinergic signaling to memory formation and recall, to understand how axonal signaling contributes to the development and maintenance of cholinergic circuits in the mammalian brain, and to identify novel approaches for reversing or mitigating the adverse effects of altered cholinergic signaling in pathological conditions of memory disorders (AD, PTSD). The Halegoua and Talmage labs decipher the molecular signaling events that mediate acute and chronic hyperalgesic responses of mouse nociceptors to inflammation and injury using an array of sophisticated cell biological, molecular, genetic, and imaging approaches *in vitro* and *in vivo*.

Salary, benefits, and travel opportunities (if applicable) will be commensurate with experience and qualifications.

Qualifications: Candidates should have a Ph.D., M.D. or equivalent degree, less than 4 years of postdoctoral experience, and expertise in electrophysiology, imaging, behavioral analyses, and /or cell biology and molecular biology. Candidates should have excellent writing and communication skills, and an outstanding publication record.

To apply: Interested candidates should send a cover letter, curriculum vitae, bibliography, and contact information of three references to: Lorna Role: lorna.role@nih.gov, David Talmage: David.talmage@nih.gov or Simon Halegoua: simon.halegoua@nih.gov.

DHHS and NIH are Equal Opportunity Employers. Applicants of all races and religions, both sexes and any age are encouraged to apply. All employees are subject to a background investigation. The NIH is dedicated to building a diverse community in its training and employment programs.

Fellowships for Postdoctoral Scholars

Woods Hole Oceanographic Institution

New or recent doctoral recipients are encouraged to submit applications prior to October 15, 2019.

Awards related to the following areas are anticipated: **Applied Ocean Physics & Engineering; Biology**; **Geology & Geophysics**; **Marine Chemistry & Geochemistry**; **Physical Oceanography**; a joint **USGS/WHOI award**; an **Ocean Bottom Seismograph Instrument Center award**; and an **Ocean Twilight Zone award**. Interdepartmental research is also encouraged.

Awards are competitive, with primary emphasis on research promise. Scholarships are 18-months with an annual stipend of $61,200, a health and welfare allowance and a research budget. Recipients are encouraged to pursue their own research interest in association with resident staff. Communication with potential WHOI advisors prior to submitting an application is encouraged. Recipients of awards can begin any time after January 1and before December 1, 2020.

Further information may be obtained at:

www.whoi.edu/postdoctoral

An Equal Opportunity/Affirmative Action Employer

UNIVERSITY OF MICHIGAN

The **Department of Pharmacology** is seeking outstanding recent graduates for **open postdoctoral positions** with experience in cellular electrophysiology in the following research areas; (1) The mechanisms of epileptic encephalopathy with SUDEP linked to human variants in ion channel genes in **Dr. Lori Isom's** lab; (2) The role of ion channels and fuel metabolism in the production of oscillations in intracellular calcium and insulin secretion from pancreatic islets and diabetes; and Modulation of excitatory synaptic transmission by mechanical trauma in cultured cortical neurons in **Dr. Les Satin's** lab; (3) Studies of the neurobiology of drug addiction and obesity in **Dr. Carrie Ferrario's** lab, details here: https://sites.google.com/a/umich.edu/ferrariolab/job-postings; (4) There are also opportunities for postdocs with a variety of expertise to work with faculty on the NIDA-funded Biology of Drug Abuse Training grant, PI, **Dr. John Traynor**: https://sites.google.com/umich.edu/bda/home. Candidates should be highly motivated with a Ph.D., or M.D. degree in a relevant discipline, experience in patch clamping, intracellular recording, cell culture, intravenous drug self-administration, and immunohistochemistry and/or western blotting. Publication record in the English language, peer-reviewed journals and strong verbal and written communication skills are essential. Please send application materials: cover letter (including a statement of past accomplishments and research interests), CV and contact information for 3 references electronically to: Ingrid Shriner-Ward, **ingridw@umich.edu**.

Michigan Medicine conducts background screening and pre-employment drug testing on job candidates upon acceptance of a contingent job offer and may use a third-party administrator to conduct background screenings. Background screenings are performed in compliance with the Fair Credit Report Act. Pre-employment drug testing applies to all selected candidates, including new or additional faculty and staff appointments, as well as transfers from other U-M campuses. The University of Michigan is an Equal Opportunity/Affirmative Action Employer.

EMORY

Postdoctoral position

A postdoctoral position is available in a joined research team at Emory University and Atlanta VA Medical Center to perform basic and translational research on protective and regenerative therapies for neurodegenerative disorders. Cellular/molecular, optogenetics/optochemogenetics, electrophysiological methods and animal behavioral tests will be applied. The fellow will work independently to develop his/her research career with full support. Should have PhD or MD degree with experience in neuroscience or molecular biology or biochemistry research. Must be self-motivated for research and teamwork. Salary and fringe benefits will be paid according to NIH standard. Send application to **spyu@emory.edu**.

Washington University in St. Louis School of Medicine

There is an opportunity for **post-doctoral research** in the laboratory of Dr. Grant Challen (Washington University, St. Louis, USA), which studies how genetic mutations influence the function of blood-forming stem cells in the bone marrow (hematopoietic stem cells = '"HSCs") and contribute to the development of blood cancers. The Challen lab using cutting-edge techniques such as next-generation sequencing, CRISPR/Cas9 and high-throughput flow cytometry in model systems incorporating cancer cell lines, transgenic mouse models, and primary cells from human patients.

The successful candidate will have the opportunity to work on any number of projects investigating how epigenetic modifications influence HSC fate decisions, and how genetic mutations in epigenetic regulators contribute to clonal expansion of mutant HSCs in clonal hematopoiesis and predispose for transformation to hematopoietic malignancies. The post-doctoral scholar will be responsible for managing their own projects (under the mentorship of Dr. Challen) as well as contributing to ongoing projects with other trainees. Must have troubleshooting skills, independent analytical thinking and research planning skills as well as demonstrated ability to work independently and communicate with the laboratory staff and investigators. Experience in flow cytometry and small animal handling is desirable. For more information about our lab research please visit our website (www.challenlab.com) and follow us on Twitter (@challenlab). Qualified candidates can contact Dr. Grant Challen (**grantchallen@wustl.edu**) with CV and research statement attached.

Washington University is an Equal Opportunity Employer.

Gender and Women's Studies
UNIVERSITY OF WISCONSIN-MADISON

Wittig Postdoctoral Fellowship in Feminist Biology

The Wittig Postdoctoral Fellowship in Feminist Biology offers the opportunity to combine research in a Fellow's area of interest with teaching at the University of Wisconsin-Madison. We seek a highly motivated new or recent PhD in one of the biological sciences or public health or MD, who wants to develop research skills in an area of biology related to gender and teaching skills in feminist approaches to biology. Research can be conducted in any hosting faculty lab at the University; please specify the agreement to host in the research proposal. During the two-year fellowship, the Fellow will teach one undergraduate course per semester for the Department of Gender & Women's Studies such as GWS 530, Biology and Gender. GWS will provide mentorship in teaching and in feminist theory and methods.

To apply, please submit cover letter, CV, 5-page research proposal, signed agreement from hosting lab, and contact information for three references (one of whom is head of the hosting lab) to: Elizabeth Morris, **emorris@wisc.edu**, with "Postdoctoral application-your name" in the subject line. The deadline for 2020-22 applications is February 12, 2020. The Wittig postdoc is administered through the Center for Research on Gender & Women. For more information, contact the CRGW Administrator, Elizabeth Morris, emorris@wisc.edu, or the CRGW Director, Prof. Janet Hyde, jshyde@wisc.edu. Link to job listing: https://jobs.wisc.edu/research#gws

Cincinnati Children's

Molecular Cardiovascular Biology

TENURED TRACK FACULTY POSITIONS IN MOLECULAR CARDIOVASCULAR BIOLOGY (Assistant, Associate, Full Professor)

The Division of Molecular Cardiovascular Biology, within The Heart Institute at Cincinnati Children's is looking for qualified Ph.D., M.D. or M.D.-Ph.D. candidates with a research program that investigates or can be applied to the investigation of the molecular biology of cardiac muscle. Candidates with a skeletal muscle research focus will also be considered.

The Heart Institute at Cincinnati Children's has brought together clinical care, research and education programs, all directed at providing comprehensive care for children with heart and muscle disease and developing novel therapeutic avenues for treatment. The Heart Institute at Cincinnati Children's is one of the strongest pediatric clinical heart programs in the country.

This is an excellent opportunity to join our existing faculty of world – renowned researches in developmental cardiac biology, pediatric and adult disease-based heart research, and skeletal muscle and muscular dystrophy biology. The successful candidate will receive a generous startup package.

Cincinnati Children's is ranked third among all Honor Roll hospitals in the 2019-20 *U.S. News & World Report* survey of best children's hospitals and receives the third-most NIH funds of any pediatric institution in the United States.

A letter of interest, accompanied by a complete curriculum vitae and the names of three references should be electronically sent to: **Jeff.Molkentin@cchmc.org**

Cincinnati Children's is an Equal Opportunity Employer.

Massachusetts Institute of Technology

Department of Earth, Atmospheric and Planetary Sciences

Assistant Professorship in Climate-Related Sciences

The MIT Department of Earth, Atmospheric and Planetary Sciences includes a vibrant and interdisciplinary group in climate science that we seek to expand. We are especially interested in physical oceanography, atmospheric chemistry, and atmospheric dynamics, but we encourage applications from outstanding candidates in all sub disciplines of climate science. We seek candidates who use any approach or combination of approaches, including observation, theory, modeling, and experimentation. Candidates should have the potential for innovation and leadership in research and a commitment to teaching at the undergraduate and graduate levels.

Applicants must hold a Ph.D. in earth sciences or related field by the start of employment. Our intent is to hire at the assistant professor level, but more senior appointments may also be considered. Applications from women and underrepresented minorities are strongly encouraged. A complete application must include a cover letter, curriculum vitae, one- to two-page descriptions each of research and teaching plans, and three letters of recommendation.

Please explicitly commit to our department's code of conduct https://eapsweb.mit.edu/about/code-conduct) in submitted cover letters.

Applications are being accepted at Academic Jobs Online: https://academicjobsonline.org/ajo/jobs/14201

To receive full consideration, complete applications must be received by November 1, 2019. Complete applications will be considered starting September 15 until November 1, 2019.

Search Contact: Ms. Karen Fosher, HR Administrator, EAPS, 54-924 Massachusetts Institute of Technology, 77 Massachusetts Avenue, Cambridge, MA 02139-4307, email: kfosher@mit.edu

MIT is an Equal Opportunity/Affirmative Action employer

http://web.mit.edu

MUSC MEDICAL UNIVERSITY of SOUTH CAROLINA

Tenure Track Faculty Position in Regenerative Medicine and Cell Biology

Department of Regenerative Medicine and Cell Biology

Up to two tenure track faculty positions at the Assistant or Associate Professor level are available for researchers that focus on a topic broadly related to the digestive system. Candidates whose research complements existing department strengths, which include tissue engineering, pluripotent stem cell differentiation, digestive disease research, and molecular biology of cell function, are particularly encouraged to apply. Successful applicants will become members of the Digestive Disease Research Center, a recently developed priority of the MUSC strategic plan that provides core facilities, pilot project funding, and a rich mentoring environment for junior investigators. Competitive salary, laboratory space and start-up funds are available. Research at MUSC is supported by several excellent core facilities specializing in imaging, genetically modified mice and rats, drug discovery, proteomics, genomics, and flow cytometry. Information about the Department can be found at https://medicine.musc.edu/departments/regenerative-medicine.

Applicants should provide a research plan and a curriculum vitae including the names of three references through the MUSC employment portal: **http://careers.pageuppeople.com/756/cw/en-us/job/516847/univ-open-rank-tenure-track-faculty**. Review of applications will begin in September and continue until the position is filled.

The Medical University of South Carolina in Charleston has approximately 2,200 graduate and professional students that are supported by 1300 faculty members. Total annual research funding exceeds $250 million. This includes funding that supports the NCI–designated Hollings Cancer Center, a Clinical and Translational Science Award, and multiple institutional training grants that support graduate student stipends. Charleston is a unique coastal city of half a million residents that has a rich history, numerous arts and cultural events, an exceptional culinary environment, and offers extensive outdoor beach and recreation opportunities. Information can be found at http://www.charlestoncvb.com/.

MUSC is an Affirmative Action/Equal Opportunity Employer.

Yale University
School of Medicine

FACULTY POSITION AT THE ASSISTANT PROFESSOR LEVEL

DEPARTMENT OF CELLULAR AND MOLECULAR PHYSIOLOGY

The Department of Cellular and Molecular Physiology is conducting a search for new faculty members at the assistant professor level.

The search seeks candidates whose research connects the properties of molecules to the properties of physiological systems.

Excellent opportunities are available for collaborative research, as well as for graduate and medical student teaching. Candidates must hold a Ph.D., M.D., or equivalent degree. Applicants should include a curriculum vitae, a statement of research interests and future goals, and should arrange to have three letters of reference sent. Applicants should apply at the following website:

http://apply.interfolio.com/66568

Application Deadline: **October 18, 2019**

Yale University is an Affirmative Action/Equal Opportunity Employer and welcomes applications from women, persons with disabilities, protected veterans, and members of minority groups.

By **Luis Alexis Rodríguez-Cruz**

Between two worlds

I sat alone in my room, glued to my computer screen, watching events unfold 3000 kilometers away. Back home in Puerto Rico in July, thousands were marching to Old San Juan, demanding that Governor Ricardo Rosselló resign, and I was proud of them. I, however, was in Vermont, pursuing my Ph.D. I had left Puerto Rico because of the academic opportunities available elsewhere—a trade-off many scientists make as we pursue our training and careers. But I still feel deeply connected to my home. I stayed up late following what was happening and talking with friends who were marching, including one who suffered violence at the hands of the police. I was furious at myself for not being there.

My first instinct was to buy a plane ticket home. I didn't want to neglect my academic work, but before I'm a Ph.D. student, I'm a Puerto Rican. I have a responsibility to get involved in what happens there. But the tickets were too expensive. I couldn't go.

I remembered when Hurricane Maria hit Puerto Rico 2 years earlier. I was not home to help my family and community—I had left for Vermont a month before the storm. Since then, I have sought counseling to deal with my feelings of isolation and helplessness about being away, and I have worked on building meaningful relationships with friends and colleagues in Vermont. But it only took the first protest to remind me that I have one foot here and another in Puerto Rico. I was desperate to participate in this historic moment.

"The first protest [reminded] me that I have one foot here and another in Puerto Rico."

I tried to focus on my dissertation proposal, but it was no use. I pushed myself to go to work every day, but even reading scientific articles was hard.

Speaking with my counselor helped me figure out the way forward. I realized that I was focused on what I *wanted* to do instead of what I *could* do. There were still ways I could help from Vermont.

I got in touch with my friend and colleague Bianca Valdés, a Ph.D. student at the University of Puerto Rico, whom I know through an initiative to train scientists to get involved in policymaking called the Puerto Rico Science Policy Action Network (PR-SPAN). We came up with a rapid, feasible way for me to contribute: write an online letter in which Puerto Rican scientists could express our support for Rosselló's resignation. We wanted to emphasize that, although Rosselló is also a scientist, he does not represent the Puerto Rican scientific community or the values needed to govern.

After a daylong flurry of writing and editing, and with the help of former PR-SPAN member Jesús Alvelo, who is currently a science and technology policy fellow with AAAS (which publishes *Science*), we had the letter posted. In just a few hours, it got about 100 signatures. It was even picked up by the press.

I also teamed up with a few Puerto Rican friends in Vermont to take pictures with signs urging Rosselló to resign, which we posted on social media. We wanted to show our support for the protestors back home as well as make non-Puerto Rican members of our networks aware of what was happening there. I had thought of trying something like this before my meeting with my counselor but had not pushed hard enough. Now, I decided to just set a time and make it happen. Only three of us were able to make it, but it was still great to feel that sense of community, and I was happy about our small contribution to the cause.

Perhaps counterintuitively, taking these actions also helped me get back on track with my academic work. I felt I was doing my part—however minor—to support the people of Puerto Rico, so when I was at work, I was able to focus on my science.

As students and scientists, we cannot alienate ourselves from the issues that matter to us. We must be engaged. And the many of us who are far from home to pursue our scientific research can find ways to engage from afar. ■

Luis Alexis Rodríguez-Cruz is a Ph.D. student at the University of Vermont in Burlington. Do you have an interesting career story? Send it to SciCareerEditor@aaas.org.

ILLUSTRATION: ROBERT NEUBECKER

Published by AAAS